



저작자표시-비영리-변경금지 2.0 대한민국

이용자는 아래의 조건을 따르는 경우에 한하여 자유롭게

- 이 저작물을 복제, 배포, 전송, 전시, 공연 및 방송할 수 있습니다.

다음과 같은 조건을 따라야 합니다:



저작자표시. 귀하는 원저작자를 표시하여야 합니다.



비영리. 귀하는 이 저작물을 영리 목적으로 이용할 수 없습니다.



변경금지. 귀하는 이 저작물을 개작, 변형 또는 가공할 수 없습니다.

- 귀하는, 이 저작물의 재이용이나 배포의 경우, 이 저작물에 적용된 이용허락조건을 명확하게 나타내어야 합니다.
- 저작권자로부터 별도의 허가를 받으면 이러한 조건들은 적용되지 않습니다.

저작권법에 따른 이용자의 권리는 위의 내용에 의하여 영향을 받지 않습니다.

이것은 [이용허락규약\(Legal Code\)](#)을 이해하기 쉽게 요약한 것입니다.

[Disclaimer](#)

**Thesis for the Degree of
Doctor of Philosophy**

**Collision Response of Cylindrical Structures
and Their Residual Strengths**

The Graduate School
University of Ulsan

Department of Naval Architecture and Ocean Engineering

Quang Thang Do

Collision Response of Cylindrical Structures and Their Residual Strengths

Supervisors: Professors Sang-Rai Cho and Hyun Kyoung Shin

A Thesis

Submitted to
the Graduate School of the University of Ulsan
In partial Fulfillment of the Requirements
for the Degree of

Doctor of Philosophy

by

Quang Thang Do

Department of Naval Architecture
and Ocean Engineering
Ulsan, Korea

December 2018

Collision Response of Cylindrical Structures and Their Residual Strengths

This certifies that the thesis of Quang Thang Do is approved



Committee Chair: Prof. Joo Sung Lee



Committee Member: Dr. Young Sik Jang



Committee Member: Prof. Hyun Kyoung Shin



Committee Member: Prof. Jungsoo Ryue



Committee Member: Prof. Sang-Rai Cho

Department of Naval Architecture and
Ocean Engineering Ulsan, Korea

December 2018

Abstract

Fabricated ring- and stringer-stiffened cylinders or unstiffened tubular members have been used by marine structure engineers for a long time as major components of submarine pressure hulls, main legs of fixed or floating types of offshore platforms and floating offshore wind turbine foundations. During their service lifetime, these structures may be prone to get damaged caused by accidents such as ship collisions, groundings, or slamming. Among these accidents, ship collisions have been highlighted as the most serious ones owing to the damage or even catastrophic loss of the cylinder structural integrity. The present thesis deals with the structural behavior of offshore structural components subjected to accidental loads arising from the collision and their residual strength under combined axial compression and radial pressure.

Relevant experimental data of small-scale ring- and stringer-stiffened cylinder and H-shape tubular members are compiled. The aim of the tests was to provide more realistic experimental information to understand the extent damage of these structures under dynamic mass impact as well as hydrostatic pressure loadings. The details of the experimental setup, test procedure, exact material properties, and test results are reported in this study. The experimental data appear to be useful for future benchmarking of numerical and simplified prediction methods for similar structures. Numerical models are developed using the finite element software package ABAQUS, and comparative analysis of experiments is conducted. In the numerical analysis, the effects of boundary conditions and the strain-rate sensitivity of the material and other dynamic effects on these structures were considered carefully. The accuracies of numerical assessment of impact response and their residual strength are discussed.

Dynamic impact test on H-shape tubular member at room and low-temperatures are also conducted. The fracture response and failure mode of offshore tubular structures under low-velocity mass impact are discussed. Furthermore, a new simple critical failure strain formulation has been provided during considering the size of the fine mesh in the contact area between the offshore tubular member and ship collision. The accuracy and reliability of formulation have been validated with experimental results. Thus, the proposed equation can be used to a collision scenario similar to that of the current study.

Rigorous parametric studies of full-scale ring- and stringer-stiffened cylinder examples and H-shape tubular members are performed using the numerical method which has been validated with the experimental results obtained from the tests reported in this study and other test data available in the open literature. Based on the numerical results, simple design formulations were derived for predicting the extent of local denting damage and the residual strength of the damaged

structures. The simple formulas can be used for quick estimation of residual strength under various loadings. The accuracy of the derived formulation has been quantified by comparing with test results and numerical predictions, showing a good agreement for all the loading cases. These formulations can be useful for the purposes of the design of these structures under the risk conditions of marine structures.

Acknowledgements

This thesis is based on the work done at the Department of Naval Architecture and Ocean Engineering, the Graduate School, University of Ulsan, during the period of March 2016 to December 2018 and supervised by Professors Sang-Rai Cho and Hyun Kyoung Shin, to whom the author wishes to express his sincere gratitude for their kinds of support and guidance.

This study was supported by the Korea Institute of Energy Technology Evaluation and Planning (KETEP), Ministry of Trade, Industry & Energy (MOTIE) of the Republic of Korea (Nos. 20154030200970 and 20163010024620). This financial support is greatly acknowledged.

Sincere thanks are given to Professor Joo Sung Lee, Professor Jungsoo Ryue and Dr. Young Sik Jang for their willingness to serve as members of the thesis committee and providing useful comments and suggestions which improved the quality of the work.

The author would like to thank the following people: The graduate students from Ultimate Limit State Analysis Laboratory, especially Teguh Muttaqie and Park Sang Hyun for their devotion and effort shown for the experiments conducted within the scope of this study.

Dr. Burak Can Cerik, from the Department of Naval Architecture and Ocean Engineering, Inha University, is thanked for the exchange of ideas, fruitful discussions and friendship, during his stay in Ulsan, Korea in 2014, Spring and continuously afterward.

I am very grateful to Dr. Huynh Van Vu of Nha Trang University for his long support and for introducing me to ULSAN laboratory. I also would like to warmly thank all my friends at University of Ulsan for their support and for making these years enjoyable.

And finally, I am deeply indebted to all of my families for their endurance and financial and vital moral support.

Quang Thang Do
Ulsan, Korea
December 2018.

*Dedicated to my wife and my family,
thanks for your love and support*

Contents

Abstract.....	i
Contents	v
List of Figures.....	xi
List of Tables.....	xix
List of Symbols	xxi
Chapter 1 Introduction.....	1
1.1 Background and motivation.....	1
1.2 Aims and scope of work.....	8
1.3 Outline of the thesis	9
Chapter 2 Overview of research on ship collisions with offshore installations	11
2.1 Introduction.....	11
2.2 General impact mechanics in ship-platform collision.....	11
2.3 Impact deformation and residual strength of cylindrical shell ($R/t > 30$).....	17
2.4 Impact deformation and residual strength of tubular member.....	21
2.4.1 Impact deformation of unstiffened tubular member	21
2.4.2 Residual strength of damaged unstiffened tubular member.....	23
2.5 Rules and regulations	25
2.6 Final remarks	26
Chapter 3 Collision response of ring- and stringer-stiffened cylinders	28
3.1 Introduction.....	28
3.2 Dynamic impact tests on ring-stiffened cylinders	31
3.2.1 Test models	31
3.2.1.1 Dimensions	31
3.2.1.2 Material properties	34
3.2.1.3 Initial shape imperfection measurement	38
3.2.1.4 Experimental set-up	40
3.2.1.5 Test results.....	44
3.2.2 Nonlinear finite element modeling.....	53
3.2.2.1 Element and boundary conditions.....	53

3.2.2.2	Material properties definition.....	55
3.2.3	Numerical results and discussion.....	57
3.2.3.1	Damage generation	57
3.2.3.2	Energy partition.....	63
3.2.3.3	Effect of strain-rate hardening definition.....	64
3.2.3.4	Effect of boundary conditions.....	66
3.3	Dynamic impact tests on stringer-stiffened cylinders.....	67
3.3.1	Test models	67
3.3.1.1	Dimensions	67
3.3.1.2	Material properties	69
3.3.1.3	Initial shape imperfection measurement	72
3.3.1.4	Experimental set-up	73
3.3.1.5	Test results.....	76
3.3.2	Nonlinear finite element modeling.....	82
3.3.2.1	Element and boundary conditions.....	82
3.3.2.2	Material properties definition.....	85
3.3.3	Numerical results and discussion.....	86
3.3.3.1	Damage generation	86
3.3.3.2	Energy partition.....	91
3.3.3.3	Effect of strain-rate hardening definition.....	92
3.3.3.4	Effect of boundary conditions.....	93
3.4	Parametric study.....	95
3.4.1	Ring-stiffened cylinder.....	95
3.4.1.1	Effect of impact location and angle	95
3.4.1.2	Effect of impact velocity.....	96
3.4.1.3	Effect of ring-stiffeners	98
3.4.1.4	Effect of striker header shapes	99
3.4.2	Stringer-stiffened cylinder	101
3.4.2.1	Effect of impact location and angle	101
3.4.2.2	Effect of impact velocity.....	102
3.4.2.3	Effect of stringer-stiffeners	104
3.4.2.4	Effect of striker header shapes	106
3.5	Derivation of approximate equations to predict the extent damage.....	107

3.5.1 Ring-stiffened cylinder.....	108
3.5.2 Stringer-stiffened cylinder	115
3.6 Final remarks	120
Chapter 4 Fracture response of tubular structures to lateral collision at room and sub-zero temperatures.....	122
4.1 Introduction.....	122
4.2 Details of experiments.....	125
4.2.1 Test models	125
4.2.1.1 Dimensions of the test models	125
4.2.1.2 Material properties	126
4.2.2 Experimental set-up	128
4.2.2.1 Experimental set-up at room temperature	128
4.2.2.2 Experimental set-up at sub-zero temperature.....	131
4.2.3 Strain gauge arrangement.....	132
4.3 Test results.....	133
4.3.1 Drop test on H-Shape tubular model at room temperature	134
4.3.1.1 Plastic damage on brace and chord.....	134
4.3.1.2 Fracture at T-joint	138
4.3.2 Drop test on H-Shape tubular model at sub-zero temperature	144
4.4 Numerical simulations of collision test.....	151
4.4.1 Finite element modelling	151
4.4.2 Boundary conditions	152
4.4.3 Material properties definition.....	153
4.5 Numerical results and discussion.....	154
4.5.1 Drop tests at room temperature	154
4.5.2 Drop tests at sub-zero temperature.....	161
4.6 Parametric study	165
4.6.1 Derivation of approximate equation to predict the extent damage	165
4.6.1.1 Modification factor for maximum deflection.....	165
4.6.1.2 Modification factor for overall bending damage	166
4.6.1.3 Local denting damage equation	166
4.6.2 Deriving a simple fracture criterion	166
4.6.3 Failure modes of single and H-shape tubular members	169

4.7 Final remarks	172
Chapter 5 Experiments on the residual strength of damaged ring- and stringer-stiffened cylinders subjected to hydrostatic pressure	173
5.1 Introduction	173
5.2 Test models	175
5.2.1 Material properties	175
5.2.2 Damage generation and measurements	175
5.3 Hydrostatic pressure test on ring-stiffened cylinder	175
5.3.1 Test procedures	175
5.3.2 Strain gauge arrangement.....	177
5.3.3 Test results and discussion	178
5.3.3.1 Intact models: RS-I and RS-II.....	178
5.3.3.2 Damaged models: RS-C-1, RS-C-2, RS-C-3 and RS-C-4	181
5.4 Hydrostatic pressure test on stringer-stiffened cylinder	186
5.4.1 Test procedures	186
5.4.2 Strain gauge arrangements	186
5.4.3 Test results and discussion	188
5.4.3.1 Intact models: SS-I.....	188
5.4.3.2 Damaged models: SS-C-1; SS-C-2	193
5.5 Numerical analysis	198
5.5.1 Finite element modelling	198
5.5.2 Residual stresses and initial imperfection	198
5.5.3 Residual strength analysis.....	202
5.5.4 Numerical results and discussions	204
5.5.4.1 Ring-stiffened cylinder	204
5.5.4.2 Stringer-stiffened cylinder	208
5.6 Parametric study	213
5.6.1 Ring-stiffened cylinders.....	213
5.6.1.1 Effect of impact location.....	213
5.6.1.2 Effect of impact velocity	214
5.6.1.3 Effect of ring-stiffeners	215
5.6.1.4 Effect of striker header shapes	216
5.6.2 Stringer-stiffened cylinders.....	217

5.6.2.1 Effect of impact location	217
5.6.2.2 Effect of impact velocity	217
5.6.2.3 Effect of stringer-stiffeners	218
5.6.2.4 Effect of striker header shapes	219
5.7 Final remarks	221
Chapter 6 Predictions on the residual strength of damaged ring- and stringer-stiffened cylinders under hydrostatic pressure	222
6.1 Introduction.....	222
6.2. Ring-stiffened cylinder	222
6.2.1 Description of numerical model.....	222
6.2.2 Failure mode interaction formula for intact case	223
6.2.3 Failure mode formula for damage case	225
6.2.4 Accuracy of the proposed formulation.....	230
6.2.5 Results and discussion	231
6.3. Stringer-stiffened cylinder	231
6.2.1 Description of test data	231
6.2.2 Failure mode equation for intact case	232
6.2.3 Failure mode formula for damage case	233
6.2.4 Accuracy of the proposed formulation.....	236
6.2.5 Results and discussion	236
6.4. Final remarks	236
Chapter 7 Residual strength formulations of damaged ring- and stringer-stiffened cylinders under combined axial compression and radial pressure	237
7.1 Introduction.....	237
7.2 Validation of numerical modeling technique.....	238
7.2.1 Description of test data	238
7.2.2 Finite element modeling.....	239
7.2.3 Validation of numerical method	240
7.3. Ring-stiffened cylinder	243
7.2.1 Description of numerical model.....	243
7.2.2 Ultimate strength formulations of intact ring-stiffened cylinder	243
7.2.3 Deriving residual strength formulations of damaged ring-stiffened cylinder	245
7.4. Stringer-stiffened cylinder	248

7.3.1 Description of numerical model.....	248
7.3.2 Ultimate strength formulations of intact stringer-stiffened cylinder.....	248
7.3.3 Deriving residual strength formulations of damaged stringer-stiffened cylinder	251
7.5 Final remarks	255
Chapter 8 Conclusions and recommendation for future work.....	256
8.1 Conclusions.....	256
8.2 Recommendations for future work	258
References	259
List of publications.....	274
International Journal.....	274
International Conference	275
Appendix A: Imperfection measurement results for stiffened cylinder.....	277
Appendix B: Typical circumferential shape imperfection pattern observed in test models	285
Appendix C: Properties of tensile test coupons and details of test results for stiffened cylinder models.....	288
Appendix D: Experiments.....	313
D.1 Measured damage extents for ring-and stringer-stiffened models	313
D.2 Accelerometer measurements	324
D.3 Strain measurement for tubular test models	327
D.4 Deformed shape of the experimental models.....	332
Appendix E: Effects of impact location and angles on the extent damage of ring- and stringer-stiffened cylinder	337
Appendix F: Numerical analysis results	339
F.1 Deformed shape of the numerical models	339
F.2 Results of permanent deflection for ring- or stringer-stiffened cylinder under mass impact	341
F.3 Residual strength of damaged ring- or stringer-stiffened cylinder under hydrostatic pressure.....	353
F.4 Residual strength of damaged ring- or stringer-stiffened cylinder under combined axial compression and radial pressure	364

List of Figures

Fig. 1.1 Monthly distribution of collisions in Alaskan waters [7].	2
Fig. 1.2 Collision of the US submarine Greeneville and fishing vessel Ehime Maru	2
Fig. 1.3 Grounding accident of the cruise ship Costa Concordia	3
Fig. 1.4 The Mumbai High North Platform fire.	3
Fig. 1.5 The <i>oil tanker Overseas Ohio</i> after colliding with an iceberg	4
Fig. 1.6 Damages of Ekofisk 2/4-W platform and Big Orange XVIII after collision	5
Fig. 1.7 The Grampian Defender vessel hitting the BP Magnus offshore facility.	5
Fig. 1.8 Cause of oil spills from ships in 1970-2005 [10].	6
Fig. 2.1 Model for assessment of reaction force to deck from DNV-RP-C204 (2010).	12
Fig. 2.2 Energy dissipation for strength, ductile and shared/energy design [26].	13
Fig. 2.3 Strain energy distribution in ship-installation collision [26].	15
Fig. 2.4 Force-displacement curve for a 5000 tons supply vessel by DNV [26].	16
Fig. 2.5 Force-displacement curve for bow with and without bulb	16
Fig. 3.1 Dimensions of the ring-stiffened cylinder for model RS-I (unit: mm).	32
Fig. 3.2 Geometry of the end plate and the end ring for RS-I (Unit: mm).	33
Fig. 3.3 Dimensions of the ring-stiffened cylinder for model RS-II (unit: mm).	33
Fig. 3.4 Geometry of the end plate and the end ring for model RS-II (Unit: mm).	34
Fig. 3.5 Dimension of the tensile test coupons (Unit: mm).	35
Fig. 3.6 Universal testing machine used in tensile tests and sample coupons.	35
Fig. 3.7 Engineering stress-strain curve of cylindrical shell for model RS-C-2.	35
Fig. 3.8 Coupons for high speed tensile tests: (a) Dimensions (unit: mm); (b) After testing	36
Fig. 3.9 Experimental setup for high strain rate tensile testing.	37
Fig. 3.10 Dynamic tensile strain-stress curves for first series model.	37
Fig. 3.11 Dynamic tensile strain-stress curves for first series model.	38
Fig. 3.12 Imperfection profiles of the intact test models, RS-I.	39
Fig. 3.13 Measurements of initial shape imperfections for model RS-II:	40
Fig. 3.14 Impact testing frame & boundary conditions in the experiment.	41
Fig. 3.15 Dimensions of the striking mass and its indenter (Unit: mm): (a) Type I; (b) Type II.	42
Fig. 3.16 Arrangement of the strain gauges.	43
Fig. 3.17 Deformed shape of the models in top view: (a) RS-C-1 and (b) RS-C-2 [115].	44
Fig. 3.18 Deformed shape of the models in top view: (a) RS-C-3 and (b) RS-C-4.	45
Fig. 3.19 Deformed shape of the ring-stiffeners: (a) RS-C-1 and (b) RS-C-2 [115].	45
Fig. 3.20 Longitudinal damage profiles for models: (a) RS-C-1; (b) RS-C-2.	46

Fig. 3.21 Circumferential damage profiles for models: (a) RS-C-1; (b) RS-C-2.	47
Fig. 3.22 Longitudinal damage profiles for models: (a) RS-C-3; (b) RS-C-4.	48
Fig. 3.23 Circumferential damage profiles for models: (a) RS-C-3; (b) RS-C-4.	49
Fig. 3.24 Recorded strain histories of model RS-C-3 for: (a) cylinder shell; (b) ring-stiffeners..	51
Fig. 3.25 Recorded strain histories of model RS-C-4 for: (a) cylinder shell; (b) ring-stiffeners..	52
Fig. 3.26 Force-displacement curves for the test models.	53
Fig. 3.27 Convergence tests for collision analysis.	54
Fig. 3.28 Finite element model for collision analysis.	55
Fig. 3.29 True stress-strain curve at various strain rates for RS-C-3 model.	57
Fig. 3.30 Deformed shape of the models compared with numerical results:	59
Fig. 3.31 Predicted deformed shape of models compared with the test result for models:	60
Fig. 3.32 Comparison of the longitudinal damage profiles obtained.	61
Fig. 3.33 Predicted force-displacement curve of models compared with the test result.	62
Fig. 3.34 Energy histories obtained numerically for model RS-C-1.	63
Fig. 3.35 Force-displacement curves for different strain-rate hardening definitions.	65
Fig. 3.36 Force-displacement curves for different boundary conditions for model RS-C-1.	66
Fig. 3.37 Dimensions of stringer-stiffened cylinder model (unit: mm).	68
Fig. 3.38 Dimensions of end plate and ring (unit: mm).	69
Fig. 3.39 Engineering stress-strain curve of cylindrical shell.	70
Fig. 3.40 Engineering stress-strain curves of high speed tensile tests:	71
Fig. 3.41 Out-of-radius measurement of shell model SS-C-1:	72
Fig. 3.42 Cross sectional shell of models SS-I and SS-C-2 at the mid-bay.	73
Fig. 3.43 Drop testing machine.	74
Fig. 3.44 Dimensions of striker mass and its indenter.	74
Fig. 3.45 Strain gauge arrangements.	76
Fig. 3.46 Dimensions of support plates.	77
Fig. 3.47 Detailed view of experimental boundary conditions.	77
Fig. 3.48 Deformed shape of models: (a) SS-C-1 and (b) SS-C-2.	78
Fig. 3.49 Deformed shape of stringer-stiffeners: (a) SS-C-1 and (b) SS-C-2.	78
Fig. 3.50 Measured longitudinal damage profiles: (a) model SS-C-1; (b) model SS-C-2.	79
Fig. 3.51 Measured circumferential damage profiles: (a) model SS-C-1; (b) model SS-C-2.	80
Fig. 3.52 Strain time histories recorded by the strain gauges placed on cylinder shell.	82
Fig. 3.53 Strain time histories recorded by the strain gauges placed on stringer-stiffeners.	83
Fig. 3.54 Strain time histories recorded by strain gauges placed on ring-stiffeners.	84
Fig. 3.55 Finite element model for collision analysis.	85
Fig. 3.56 Typical true stress-strain curve applied for FE analysis.	86

Fig. 3.57 Predicted deformed shape of models compared with test results:	87
Fig. 3.58 Predicted deformed stringer-stiffener shape compared with test results for SS-C-2. ...	88
Fig. 3.59 Comparison of predicted longitudinal damage profiles with test results:	89
Fig. 3.60 Comparison of strain obtained from numerical predictions and test results	90
Fig. 3.61 Energy time histories for test models obtained numerically.	91
Fig. 3.62 Force-displacement curves for different strain-rate hardening definitions.	93
Fig. 3.63 Force-displacement curves for different boundary conditions.	94
Fig. 3.64 Different impact locations on the ring-stiffened cylinder.	96
Fig. 3.65 Force-displacement curves with various impact locations on ring-stiffened cylinders.	97
Fig. 3.66 Effect of impact angles.	97
Fig. 3.67 Force-displacement curves with increasing impact velocity on ring-stiffened cylinders.	98
Fig. 3.68 Force-displacement curves with various number of ring-stiffened cylinders.	99
Fig. 3.69 Dimensions of striker.....	100
Fig. 3.70 Force-displacement curves for various striker header shapes.	100
Fig. 3.71 Impact with various indenter surfaces: (a) Knife-edge indenter; (b) rectangular indenter and (c) hemispherical indenter.....	101
Fig. 3.72 Impact locations on the stringer-stiffened cylinder.	102
Fig. 3.73 Force-displacement curves with various impact locations on string-stiffened cylinders.	103
Fig. 3.74 Force-displacement curves with increasing impact velocity of.....	104
Fig. 3.75 Force-displacement curves for various number of stringer stiffeners.	105
Fig. 3.76 Force-displacement curves for various stringer-stiffener types.	106
Fig. 3.77 Results from various striker header shapes.	108
Fig. 3.78 Plotted curve to predict the extent damage for ring-stiffened cylinder.	112
Fig. 3.79 Plotting of the proposed formula against basic parameters.....	112
Fig. 3.80 Plotting of the proposed formula against basic parameters.....	113
Fig. 3.81 Plotting of the proposed formula against basic parameters.....	113
Fig. 3.82 Comparison of proposed formulation and the existing formulations.....	114
Fig. 3.83 Plotted curve for prediction of extent damage for stringer-stiffened cylinder.	116
Fig. 3.84 Collision response of stringer-stiffened cylinder with various striker header shapes.	117
Fig. 3.85 Plotting of the proposed formula against basic parameters L_s/R and R/t	118
Fig. 3.86 Plotting of the proposed formula against basic parameters h_{sw}/t_{sw} and h_{rw}/t_{rw}	118
Fig. 3.87 Plotting of the proposed formula against basic parameters E/σ_Y and w_{sf}/t_{sf}	119
Fig. 3.88 Comparison of proposed model with the numerical results of SS-C-1 and SS-C-2. ..	119

Fig. 4.1 Dimensions of H-shape tubular member models (unit: mm).	127
Fig. 4.2 Dimensions of tensile test coupon.	128
Fig. 4.3 Tensile tests results.	128
Fig. 4.4 Dynamic mass impact test setup at room temperature.	129
Fig. 4.5 Dimensions of striker mass: (a) Type I; (b) Type II.	130
Fig. 4.6 Test model OWT-D2-LT in the cold chamber.	131
Fig. 4.7 Dynamic mass impact test setup at room temperature for model D2-LT.	132
Fig. 4.8 Arrangements of strain gauges for room temperature test.	133
Fig. 4.9 Arrangements of strain gauges and thermocouples for sub-zero temperature test.	134
Fig. 4.10 Measurements of deformed shape after collision:	135
Fig. 4.11 Measuring local denting with Vernier calipers.	135
Fig. 4.12 Permanent deformation of models: (a) B2 and (b) C3.	136
Fig. 4.13 Permanent deformation of models: (a) H1 and (b) H2.	137
Fig. 4.14 Permanent deformation of models: (a) H5; (b) G5.	137
Fig. 4.15 Quantities for evaluating local denting and overall-beam deflection damage extents:	138
Fig. 4.16 Permanent deformation of model A1.	139
Fig. 4.17 Deformed shape of models: (a) A2; (b) F1.	139
Fig. 4.18 Idealised profiles of a damage on both brace and chord tubular.	140
Fig. 4.19 Idealised stress distribution in T-joint of tubular member after denting test.	140
Fig. 4.20 Partial fracture damage of models: (a) E3; (b) G6.	141
Fig. 4.21 Partial fracture damage of models: (a) H3; (b) H4.	141
Fig. 4.22 Complete fracture damage of model G4 before releasing boundary condition.	141
Fig. 4.23 Complete fracture damage of models: (a) G1; (b) G2.	142
Fig. 4.24 Complete fracture damage of models: (a) G3; (b) G4.	142
Fig. 4.25 Strain measurement history – Location 1	143
Fig. 4.26 Strain measurement history – location 5:	144
Fig. 4.27 Test processes of model H6-LT.	146
Fig. 4.28 Time history of temperature measured by each thermocouple for model H6-LT.	146
Fig. 4.29 Time history of temperature measured by each thermocouple for model OWT-D2-LT.	147
.....	147
Fig. 4.30 Strain measurement results during cooling time for model H6-LT.	147
Fig. 4.31 Fracture damage of model H6 with fixed boundary condition.	148
Fig. 4.32 Deformed shape of model OWT-D2-LT after impact:	149
Fig. 4.33 Deformed shape of model OWT-D3-LT after impact:	149
Fig. 4.34 Strain time histories recorded at low-temperature for model H6-LT.	150
Fig. 4.35 Strain time histories recorded at room temperature for model H3.	150

Fig. 4.36 Comparison of strain measurements between room temperature and sub-zero temperature collision.....	151
Fig. 4.37 Finite element model for collision analysis.....	152
Fig. 4.38 True stress-strain curve at various strain rates for series G model.....	153
Fig. 4.39 Influence of sub-zero temperature on material behavior [224].	155
Fig. 4.40 Predicted deformed shape of model compared with test result for model B2:.....	156
Fig. 4.41 Force-displacement response for model B2.	156
Fig. 4.42 Collapse mechanism of a beam loaded off-center.....	156
Fig. 4.43 Force-displacement response for model B2.	158
Fig. 4.44 Force-displacement response for different models.....	158
Fig. 4.45 Predicted deformed shape of models compared with test results:.....	159
Fig. 4.46 Force-displacement response for different models.....	159
Fig. 4.47 Predicted deformed shape of model compared with test result for model E3.....	160
Fig. 4.48 Predicted deformed shape of model compared with test result for model G4.	161
Fig. 4.49 Force-displacement response for different models.....	162
Fig. 4.50 Numerical results compared to test results for predicting local shell denting damage.	163
Fig. 4.51 Numerical results compared to test results for predicting overall bending damage....	163
Fig. 4.52 Residual stress distributions at T-joint after cooling process.....	164
Fig. 4.53 Predicted deformed shape of model compared with test result for model D2-LT.	164
Fig. 4.54 Definition of shape factor.	166
Fig. 4.55 Failure strain of experimental models compared to proposed equation.....	168
Fig. 4.56 Comparison of the various fracture criteria for ship collision modelling.....	169
Fig. 4.57 Plotting of failure mode of test models against basic parameters E_k/E_a and L_b/D_b	170
Fig. 4.58 Plotting of failure mode of test models against basic parameters E_k/E_a and D_b/t_b	171
Fig. 4.59 Plotting of failure mode of test models against basic parameters E_k/E_a and D_b/t_b * P_0/P_c	171
Fig. 5.1 Schematic of the hydrostatic test in pressure chamber.....	176
Fig. 5.2 Experimental setup for intact model RS-II under hydrostatic pressure test.....	177
Fig. 5.3 Strain gauge arrangements: (a) model RS-I; (b) models RS-C-1&RS-C-2.....	178
Fig. 5.4 Strain gauge arrangements: (a) model RS-II; (b) models RS-C-3&RS-C-4.	179
Fig. 5.5 Collapsed shape of the model RS-I: (a) Outside (b) Inside.....	180
Fig. 5.6 Collapsed shape of the model RS-II: (a) Outside (b) Inside.....	180
Fig. 5.7 Axial shortening versus pressure of models RS-I and RS-II.....	181
Fig. 5.8 Strain measurement results versus pressure of intact model RS-I.....	182
Fig. 5.9 Circumferential strain measurement results versus pressure of intact model RS-II.....	182

Fig. 5.10 Deformed shape of model RS-C-1: (a) Outside; (b) Inside.....	183
Fig. 5.11 Deformed shape of model RS-C-2: (a) Outside (b) Inside.....	183
Fig. 5.12 Strain measurement results versus pressure of model RS-C-1.....	184
Fig. 5.13 Deformed shape of model RS-C-3: (a) Outside (b) Inside.....	184
Fig. 5. 14 Deformed shape of model RS-C-4: (a) Outside (b) Inside.....	185
Fig. 5. 15 Strain measurement results versus pressure of model RS-C-4.....	185
Fig. 5.16 Schematic of hydrostatic pressure test.....	187
Fig. 5.17 Experimental setup for the hydrostatic pressure test.	187
Fig. 5.18 Arrangements of the strain gauges: (a) SS-I; (b) SS-C-1 & SS-C-2.	188
Fig. 5.19 Record of the applied history pressure for model SS-I.	189
Fig. 5.20 Outside collapse shape of model SS-I.	190
Fig. 5.21 Inside collapse shape of model SS-I.....	191
Fig. 5.22 Deformed cross-section shape of model SS-I.....	191
Fig. 5.23 Axial shortening relative to the pressure of intact model SS-I.....	192
Fig. 5.24 Strain measurement results relative to the pressure of model SS-I.	192
Fig. 5.25 Experimental result of pressure relative to the axial shortening of.....	193
Fig. 5.26 Outside collapse shapes of model SS-C-1.....	194
Fig. 5.27 Collapse shape of model SS-C-1: (a) inside; (b) cross section.....	195
Fig. 5.28 Strain measurement results relative to the pressure of model SS-C-1.	196
Fig. 5.29 Outside collapse shapes of model SS-C-2.....	196
Fig. 5.30 Collapse cross-section shape of model SS-C-2.....	197
Fig. 5.31 Strain measurement results relative to the pressure of model SS-C-2.	197
Fig. 5.32 Contour plot of residual stress of typical plate after cold bending.....	199
Fig. 5.33 Cold bending residual stress distribution for model SS-I.....	200
Fig. 5.34 Residual stress distribution caused by stiffener-shell welding [159].	200
Fig. 5.35 Welding residual stress distribution for model RS-II.....	202
Fig. 5.36 Welding residual stresses distribution obtained from analyses for model RS-II.	202
Fig. 5.37 Welding residual stress distribution for model SS-I.....	203
Fig. 5.38 Hydrostatic pressure analysis modelling.	203
Fig. 5.39 Pressure versus axial shortening curves of model RS-I.	204
Fig. 5.40 Comparison of numerical predictions with test results for model RS-II.....	205
Fig. 5.41 Comparison of strain measurement versus pressure between test and.....	205
Fig. 5.42 Deformed shape of the test model RS-C-1 compared with numerical results.....	206
Fig. 5.43 Deformed shape of the test model RS-C-2 compared with numerical results.....	206
Fig. 5.44 Predicted collapsed shape of damaged model compared with the test.....	207
Fig. 5.45 Numerical analysis results compared to test results.	208

Fig. 5.46 Pressure relative to the axial shortening of intact model SS-I.....	210
Fig. 5.47 Predicted collapsed shape of model SS-I when compared with the test results.	211
Fig. 5.48 Predicted deformed stringer-stiffener shape when compared with the test.....	211
Fig. 5.49 Pressure relative to the axial shortening curves of model SS-C-1 and SS-C-2.....	212
Fig. 5.50 Predicted collapsed shape of test model SS-C-1 when compared with the test results.	212
Fig. 5.51 Predicted collapsed shape of test model SS-C-2 when compared with the test results.	213
Fig. 5.52 Pressure-radial displacement curves with various impact locations.	214
Fig. 5.53 Collapsed shapes: (a) At the mid-bay 30^0 and (b) At the ring stiffener 30^0	214
Fig. 5.54 Pressure-radial displacement curves with various impact velocities.....	215
Fig. 5.55 Pressure-radial displacement curves with various number of ring-stiffened cylinders.	216
Fig. 5.56 Parametric study results with various striker header shapes.	217
Fig. 5.57 Pressure-radial displacement curves with various impact locations	218
Fig. 5.58 Pressure-radial displacement curves with various impact velocities.....	219
Fig. 5.59 Collapsed shapes: (a) shell, (b) stringer-stiffened cylinder.	219
Fig. 5.60 Effect of stringer-stiffener shapes.....	220
Fig. 5.61 Parametric study results with various striker header shapes	220
Fig. 6.1 Procedure for the derivation of knockdown factors.	225
Fig. 6.2 Collapsed shape of damaged model RS-3 ($d/R = 0.016$) under hydrostatic pressure. ..	227
Fig. 6.3 Non-dimensional parameter of pressure versus radial displacement at hit point of.....	227
Fig. 6.4 Best-fit curve for prediction of residual strength for ring-stiffener cylinder.....	228
Fig. 6.5 Plotting of X_m against basic parameters L_s/R and R/t for hydrostatic pressure.....	228
Fig. 6.6 Plotting of X_m against basic parameters h_w/t_w and w_f/t_f for hydrostatic pressure.	229
Fig. 6.7 Plotting of X_m against basic parameters E/σ_Y and L_c/R for hydrostatic pressure.	229
Fig. 6.8 Plotting of X_m against basic parameters P_n/P_Y and P_n/P_Y for hydrostatic pressure.	229
Fig. 6.9 Proposed formulation results compared to test results for predicting	230
Fig. 6.10 Best-fit curve to predict the residual strength for stringer-stiffened cylinder.	234
Fig. 6.11 Plotting of the proposed formula against basic parameters L_s/R and R/t	235
Fig. 6.12 Plotting of the proposed formula against basic parameters h_{sw}/t_{sw} and h_{rw}/t_{rw}	235
Fig. 6.13 Plotting of the proposed formula against basic parameters E/σ_Y and w_{sf}/t_{sf}	235
Fig. 7.1 Damaged platform column [225].	238
Fig. 7.2 Finite element analysis setup for inducing damage to specimens	241
Fig. 7.3 Comparison of force-displacement curves obtained from.....	241
Fig. 7.4 Axial shortening curves for damaged stringer-stiffened cylinder models.....	242

Fig. 7.5 Axial shortening curves for damaged ring-stiffened cylinder models.	243
Fig. 7.6 Collapsed shape of ring-stiffened cylinder model ($R/t = 159$) under combined loadings:	246
Fig. 7.7 Radial pressure versus displacement curves for	246
Fig. 7.8 Ultimate strength interaction curves for damaged ring-stiffened cylinders	247
Fig. 7.9 Best-fit curve for prediction of residual strength of	247
Fig. 7.10 Geometry of stringer stiffened cylinder and loadings considered [227].	248
Fig. 7.11 Collapsed shape of stringer-stiffened cylinder model ($R/t = 210$)	253
Fig. 7.12 Average axial stress-strain curves for model SS-3 ($R/t = 210$).	254
Fig. 7.13 Best-fit curve for prediction of residual strength of	254
Fig. A. 1 Measurements of initial shape imperfections.	284
Fig. C.1 Shell coupon tensile test results for ring-stiffened cylinder model.....	301
Fig. C.2 Ring-stiffener coupon tensile test results for ring-stiffened cylinder model.	301
Fig. C.3 Coupon tensile test results for stringer-stiffener cylinder model.....	302
Fig. C.4 Coupon tensile test results for stringer-stiffener cylinder.....	302
Fig. C.5 Dynamic tensile test set-up.	303
Fig. C.6 Coupon for dynamic tensile test after testing.	304
Fig. D4.1 Deformed shape of model A1.....	332
Fig. D4.2 Deformed shape of model A2.....	333
Fig. D4.3 Deformed shape of model F1.	334
Fig. D4.4 Deformed shape of model D2.....	335
Fig. D4.5 Deformed shape of model D3.....	336
Fig. E.1 Effects of impact location and angles on the extent damage of ring-stiffened cylinder.	337
Fig. E.2 Effects of impact location and angles on the extent damage	338
Fig. F.1 Deformed shape of the various impact locations on ring-stiffened cylinders.	339
Fig. F.2 Deformed shape of the various impact locations on stringer-stiffened cylinders.	340

List of Tables

Table 3.1 Measured dimensions of test models.....	34
Table 3.2 Measured dimensions of test models.....	36
Table 3.3 Summary of out-of-circularity measurements.....	39
Table 3.4 Collision test conditions of test models.....	42
Table 3.5 Results of damaged stringer-stiffened cylinder models.....	50
Table 3.6 True stresses and strains.....	55
Table 3.7 Comparison of the numerical results with the test results for collision models.....	59
Table 3.8 Energy absorption of structural components.....	63
Table 3.9 Permanent displacement comparison for different strain-rate hardening definitions...	65
Table 3.10 Measured dimensions of stringer-stiffened cylinder models.....	68
Table 3.11 Material properties of test models.....	70
Table 3.12 Measurement results of out-of-roundness.....	73
Table 3.13 Impact test conditions for stringer-stiffened cylinder models.....	75
Table 3.14 Results of damaged stringer-stiffened cylinder models.....	81
Table 3.15 Comparison of test results and numerical predictions.....	90
Table 3.16 Energy absorption of structural components.....	92
Table 3.17 Permanent displacement comparison for different strain-rate hardening definitions.....	93
Table 3.18 Scantlings of stringer-stiffener shapes used in parametric studies.....	105
Table 3.19 Summary of collision analysis results with various striker header shapes.....	107
Table 3.20 Properties of the reference ring-stiffened cylinders.....	109
Table 3.21 Dependence of δ_l on non-dimensional geometry and material parameters.....	110
Table 3.22 Properties of the reference stringer-stiffened cylinders.....	115
Table 4.1 Measured dimensions of test models for room temperature (unit: mm).....	126
Table 4.2 Measured dimensions of test models for sub-zero temperature (unit: mm).....	127
Table 4.3 Material properties of test models.....	127
Table 4.4 Impact test conditions for tubular members at room temperature.....	130
Table 4.5 Impact test conditions for tubular members at sub-zero temperature.....	132
Table 4.6 Results of measured damage for each test model at room temperature.....	144
Table 4.7 Results of measured damage for each test model at sub-zero temperature.....	151
Table 4.8 Comparison of test results and numerical results.....	162

Table 5.1 Comparison of experimental results with numerical results and prediction of some guideline rules.	208
Table 5.2 Comparison of the numerical results with the experimental results and prediction of some guideline rules.	209
Table 5.3 Summary results of parametric study with various striker shapes.....	216
Table 6.1 Properties of the reference ring-stiffened cylinders.....	223
Table 6.2 Comparison of the proposed formula and the design code.....	225
Table 6.3 Comparison of the proposed formulation results with the test results.....	230
Table 6.4 Properties of the reference stringer-stiffened cylinders.....	233
Table 6.5 Comparison of the proposed formulation results with the test results.....	236
Table 7.1 Properties of the ring-stiffened cylinder models.....	239
Table 7.2 Properties of the orthogonally stiffened cylinder specimens.....	239
Table 7.3 Comparison of experimental results with numerical results.....	242
Table 7.4 Comparison of the accuracy of existing design formulae and that of the proposed formulation (mean/COV (%)).....	252
Table F.2.1 Comparison of prediction and parametric study result for permanent deflection of the ring-stiffened cylinder under mass impact.....	341
Table F.2.2 Comparison of prediction and parametric study result for permanent deflection of the stringer-stiffened cylinder under mass impact.....	347
Table F3.1 Comparison of the proposed formulation results with numerical results for residual strength of damaged ring-stiffened cylinder under external hydrostatic pressure.....	353
Table F3.2 Comparison of the proposed formulation results with numerical results for residual strength of damaged stringer-stiffened cylinder under external hydrostatic pressure.	358
Table F4.1 Comparison of the proposed formulation results with numerical results for residual strength of damaged ring-stiffened cylinder under combined axial compression and radial pressure.	364
Table F4.2 Comparison of the proposed formulation results with numerical results for residual strength of damaged stringer-stiffened cylinder under combined axial compression and radial pressure.	373

List of Symbols

Roman symbols

- A : Cross-sectional area of tubular or cylinder wall
- A_s : cross-sectional area of ring-frame
- C : Material constant in Cowper-Symonds constitutive equation
- C_s : Indenter shape factor, see Eq. 3.16
- C_L : Impact location factor, see Eq. 3.18
- C_β : Impact angle factor, see Eq. 3.19
- D : Cylinder diameter
- D_{max} : Maximum outer diameter of a dented tubular section, see Fig. 4.15
- D_{min} : Minimum outer diameter of a dented tubular section, see Fig. 4.15
- D_0 : Initial outer diameter of tubular, see Eq. 4.1
- D_b : Outside diameter of bracing pipe
- D_c : Outside diameter of chord pipe
- E : Young's modulus
- E_k : Kinetic energy
- E_a : Strain energy absorption capacity, see Eq. 3.22
- E_{ext} : External energy
- E_{int} : Internal energy
- I : Moment of inertia of tubular section
- I_c : Second moment area of cross section of the ring-frame, including shell thickness
- I_t : Second moment of the whole cross-section of the stringer stiffened cylinder
- I_{zr} : Moment of inertia of ring cross-section about its line of symmetry
- K : Stiffness matrix, see Eq. 4.8
- L : Total length of cylinder or tubular member
- L_s : Ring stiffener spacing
- M : Bending moment
- M_m : Mass matrix, see Eq. 4.8
- M_p : Plastic bending moment resistance, see Eq. 4.14
- N_0 : Plastic axial resistance per unit width
- P : Resistance force or radial pressure
- P_0 : Plastic collapse resistance against local denting, see Eq. 4.13

P_{dam} : Collapse pressure of damaged cylinder
 P_{el} : Failure pressure for local buckling mode, see Eq. 6.13
 $P_{in.}$: Collapse pressure of intact cylinder, see Eq. 6.1
 P_c : Collapse hydrostatic pressure, see Eq. 6.1
 P_r : Collapse radial pressure, see Eq. 7.6
 P_{rm} : von Mises shell buckling pressure under radial pressure alone, see Eq. 7.10
 P_m : Local buckling pressure, see Eq. 6.6
 P_n : Overall buckling pressure, see Eq. 6.7
 P_t : Tripping pressure, see Eq. 6.8
 P_Y : Yield pressure, see Eq. 6.5
 R : mean radius of cylinder
 R_0 : Outside radius of cylinder
 R_s : radius of centroid of ring-frame
 R_i : collision resistance force of struck installation, see Eq. 2.2
 R_u : Reduction factor, see Eq. 6.10
 $R_{ux,r}$: Reduction factor for ring-stiffened cylinders under combined loading, see Eq. 7.12
 $R_{ux,s}$: Reduction factor for stringer-stiffened cylinders under combined loading, see Eq. 7.36
 V_{str} : Structure volume, see Eq. 3.20
 V_{shell} : Structure volume of cylindrical shell, see Eq. 3.20
 X_m : Modeling uncertainty factor
 G : Parameter in the interframe failure
 G' : Shear modulus, $E/2(1 + \nu)$
 J : St. Venant torsional constant, $(w_{fr} t_{fr}^3 + h_{wr} t_{wr}^3)/3$
 T_p : Torsional parameter, $I_z z^2 + \Gamma$
 Z : Batdorf slenderness parameter, see Eq. 7.4
 Γ : Warping constant, $I_z \left(d + \frac{t_{fr}}{2} \right)^2$
 a : Distance from mid-span to point of impact, see Fig. 4.18
 b : Distance from impact point to chord pipe, see Fig. 4.18
 b_{rf} : Ring stiffener flange width
 b_{sf} : Stringer stiffener flange width
 d : Dent depth of cylinder
 d_d : Permanent dent depth at impact point of bracing member
 d_0 : Permanent displacement of overall bending damage at impact point
 l_d : Length of dent depth
 l_0 : Overall length of stringer-stiffened cylinder

n	: Circumferential wave number, see Eq. 3.6
n_s	: Number of stringer stiffeners
n_r	: Number of ring stiffeners
m	: Striker mass
m_{eq}	: Equivalent bending moment per length
m_0	: Fully plastic bending moment of the cylinder wall per unit length
q	: Material coefficients of Cowper and Symonds equation, see Eq. 3.13
t	: Thickness of tubular wall or cylinder shell
t_{eq}	: Equivalent thickness, see Eq. 3.33
t_{rw}	: Ring stiffener web thickness
t_{sw}	: Stringer stiffener web thickness
t_{rf}	: Ring stiffener flange thickness
t_{sf}	: Stringer stiffener flange thickness
h_{rw}	: Ring stiffener web height
h_{sw}	: Stringer stiffener web height
v	: Impact velocity
k_{0n}	: Rotational spring constraint at the shell-stiffener intersection,
	$\frac{Et^3}{3(1-\nu^2)L} \left[1 + \left(\frac{nL}{\pi R} \right)^2 \right]^2$
w_{fr}	: Ring stiffener flange width
w_{fs}	: Stringer stiffener flange width
x	: distance from collision to mid-span of ring-stiffened cylinder

Greek symbols

α	: Mass proportional Rayleigh damping coefficient, see Eq. 4.8
β	: Stiffness proportional Rayleigh damping coefficient, see Eq. 4.8
δ_d	: Non-dimensional dent depth ($\delta_d = d/R$), see Eq. 3.16
ε	: Engineering strain
ε_{HS}	: Hardening start strain
ε_{HSD}	: Dynamic hardening start strain
$\varepsilon_{HS,tr}$: True hardening start strain
$\varepsilon_{pl,tr}$: True plastic strain
ε_{tr}	: True strain
ε_T	: Ultimate tensile strain

ϵ_{TD} : Dynamic ultimate tensile strain
 $\epsilon_{T,tr}$: True ultimate tensile strain
 ϵ_Y : Strain corresponding to initial yield stress
 $\epsilon_{Y,tr}$: True strain corresponding to initial yield stress
 θ : Plastic hinge rotation
 λ_E : Energy ratio, see Eq. 3.20
 ν : Poisson's ratio
 ρ : Material density
 σ : Engineering stress
 σ_0 : Average flow stress, see Eq. 3.32
 σ_e : Elastic buckling stress of the stringer as a column, see Eq. 7.26
 σ_s : Elastic buckling stress for unstiffened shell, see Eq. 7.27
 σ_t : Elastic tripping stress of stringer, see Eq. 7.28
 σ_{iej} : Elastic shell buckling stress for fabricated shell, see Eq. 6.16
 σ_{HS} : Hardening start stress (engineering)
 $\sigma_{HS,tr}$: True hardening start stress
 σ_{tr} : True stress, see Eq. 3.3
 σ_T : Ultimate tensile stress (engineering)
 σ_{TD} : Dynamic ultimate tensile stress (engineering)
 $\sigma_{T,tr}$: True dynamic ultimate tensile stress
 σ_Y : Static yield stress (engineering)
 σ_{YD} : Dynamic yield stress (engineering)
 σ_θ : Average hoop stress at mid-bay, see Eq. 7.5
 σ_{eq} : von Mises equivalent stress, see Eq. 7.18
 σ_{ec} : Elastic column buckling stress for stringer and shell, see Eq. 7.19
 σ_{et} : Elastic tripping stress for stringer and shell, see Eq. 7.20
 σ_{oa} : Elastic overall column buckling stress of stiffened cylinder, see Eq. 7.21
 σ_{es} : Elastic buckling stress for unstiffened shell, see Eq. 7.22
 σ_{el} : Elastic lateral buckling stress of stringer, see Eq. 7.23
 σ_{eg} : Elastic overall buckling stress for shell and ring stiffener, see Eq. 7.24
 σ_{tr} : Elastic tripping stress for ring stiffener, see Eq. 7.25
 $\sigma_{\theta cr}$: Elastic buckling strength of ideal shell structure under radial pressure, see Eq. 7.9
 $\sigma_{xd,r}$: Axial stress of damaged ring-stiffened cylinder under combined loading, see Eq. 7.12
 $\sigma_{xd,s}$: Axial stress of damaged stringer-stiffened cylinder under combined loading, see Eq. 7.36
 $\sigma_{xin,r}$: Axial stress of intact ring-stiffened cylinder under combined loading, see Eq. 7.1
 $\sigma_{xin,s}$: Axial stress of intact stringer-stiffened cylinder under combined loading, see Eq. 7.15

- ρ_L : Local buckling knockdown factor, see Eq. 6.4
- ρ_{OA} : Overall buckling knockdown factor, see Eq. 6.3
- ρ_T : Tripping knockdown factor, see Eq. 6.2
- ρ_x : Axial compression elasto-plastic knockdown factor, see Eq. 7.2
- ρ_θ : Radial pressure elasto-plastic knockdown factor, see Eq. 7.3
- Ψ : partial safety factor, see Eq. 6.22
- η : plasticity reduction factor for non-stress relieved shells, see Eq. 6.15

Abbreviations

- ABS : American Bureau of Shipping
- ALS : Accidental Limit State
- BV : Bureau Veritas
- API : American Petroleum Institute
- COV : Coefficient of Variation
- DNV GL: Det Norske Veritas and Germanischer Lloyd
- IMO : International Maritime Organization
- ISSC : International Ship and Offshore Structures Congress
- KETEP: Korean Institute of Energy Technology Evaluation and Planning
- LPG : Liquefied Petroleum Gas
- LR : Lloyd's Register
- KIMS : Korean Institute of Materials Science
- SLS : Serviceability limit state
- TLP : Tension leg platform
- ULS : Ultimate limit state design

Chapter 1

Introduction

1.1 Background and motivation

Besides the normal operational loads, offshore structures are also exposed to accidental events which may involve ship collision or impact by falling objects from platform decks, fire and explosions, earthquakes, or slamming. Among these accidents, ship collisions have been highlighted to be the most significant cause of damage or even catastrophically loss of offshore installations due to loss of structural integrity. It is accounted for more than 22% of worldwide offshore accidents [1]. Additionally, the International Maritime Organization (IMO) recorded that there is an average annual occurrence of 23.8 collisions during the last decade with very serious casualties [2]. It is also shown that human mistakes are the main causes of accident events. Following human mistake, hazard environmental conditions and equipment failures are also shared significantly. Furthermore, according to the historical records [3-5] are reported that the consequences of most of the accident events can endanger human life and cause financial losses. In the serious accident events, the accidental loads may sink the vessel or collapse of structures which can lead to oil leakage, environmental pollutions. The immediate repair of the damage may be difficult and sometimes impossible owing to economic and technical requirements. Therefore, it is important to minimize the probability of occurrence of accident events and also to reduce the results of these accident events.

Nowadays, more ice melts in the Arctic sea area due to the global warming. Thus, transportations in the Arctic sea during the summer appears to be possible. The concept of the Northern Sea Route has been discussed in recent years. The possibility to operate and freight in the Arctic in summer and the risk for the Arctic operation were reported by DNV GL [6]. However, since shipping in Arctic sea has improved, the probability of occurrence of ship collision with icebergs was also increased accordingly. For instance, Hill [7] presented the collisions of ship and icebergs in Alaska, as shown in Fig. 1.1.

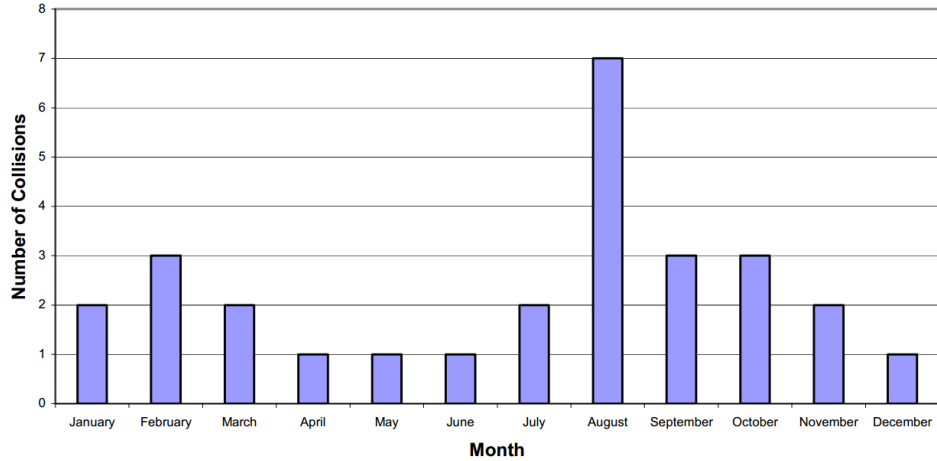


Fig. 1.1 Monthly distribution of collisions in Alaskan waters [7].

During operation of offshore structures, a minor collision will result in only repairable local damage of structure and probably will not call for cease of operation. A major collision, on the other hand, will damage marine structures globally and certainly require a cease of operations. Severe damages to ship structures may sink the vessel and give rise to great economic loss or even severe environmental pollutions and endanger human life. One of the most well-known ship collision with icebergs was Titanic accident in 1912. The sinking of luxury Titanic ship made worldwide injury with more than 1,500 passengers died, which still has a wide influence today. The accident of the US submarine *Greenville* with the fishing vessel *Ehime Maru* in 2001 is shown in Fig. 1.2. More recently in 2012, the Italian cruise ship *Costa Concordia* collided with a underwater rock, resulting in 32 passenger deaths, as indicated in Fig. 1.3.

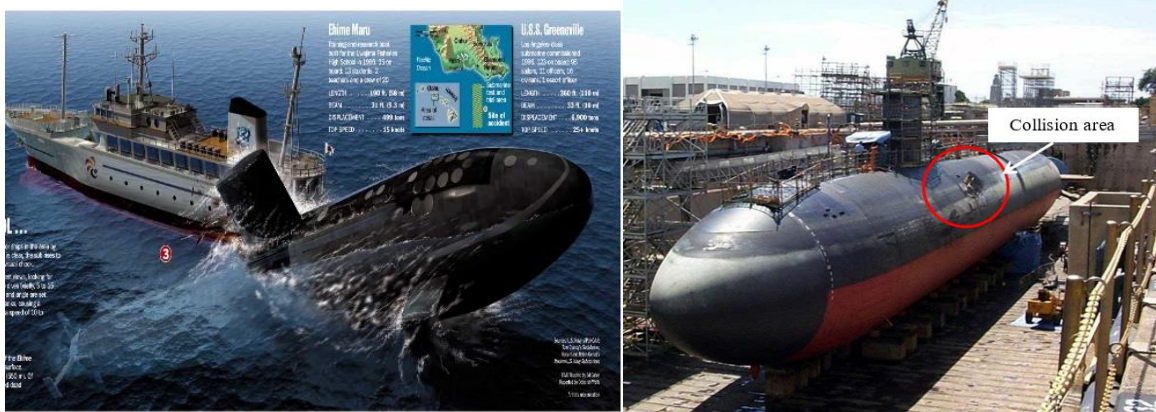


Fig. 1.2 Collision of the US submarine *Greenville* and fishing vessel *Ehime Maru* (source: https://en.wikipedia.org/wiki/USS_Greenville).



Fig. 1.3 Grounding accident of the cruise ship Costa Concordia
(source: https://en.wikipedia.org/wiki/Costa_Concordia_disaster).

In the past several decades, the global oil and natural gas consumptions have been rapidly increased. Thus, a large number of offshore structures were constructed and installed worldwide. However, the probability of collisions between visiting vessels and offshore installation collisions was also increased accordingly. For instance, in the Norwegian Continental Shelf a total of 115 collisions between installations and visiting vessels with work on the field have been reported since 1982, and no less than 26 between 2001 and 2010 [8]. In July 2005, a multipurpose support vessel struck collided with *the Mumbai High North Platform* and it ruptured several marine risers. The resulting gas leak led to catastrophic explosions and fire and 22 persons dead [9], as illustrated in Fig. 1.4.



Fig. 1.4 The Mumbai High North Platform fire.

As one future trend of the offshore oil and gas exploration and exploitation is to march into the arctic regions, ship collisions with ice floes and icebergs may become more frequent. The *oil tanker Overseas Ohio* collided with an iceberg in *Prince William Sound*, Alaska on the 2nd of January, 1994. After the collision, an area of approximately 36 m² of the bulbous bow of the tanker had been deflected 2 meters, as shown in Fig. 1.5. Furthermore, another collision occurred between *Big Orange XVIII* vessel and the unstaffed *Ekofisk 2/4-W* water injection facility at a speed 5 m/s on June 8th, 2009. The crew on the deck lost control of the vessel when entering the 500-meter zone of *Ekofisk 2/4-X* platform and due to failure to control the vessel steer at the emergency situation, the vessel hit *Ekofisk 2/4-W* water injection and bridge support platform. The result of collision created wide-ranging damage to both platform installation and vessel, as shown in Fig. 1.6.

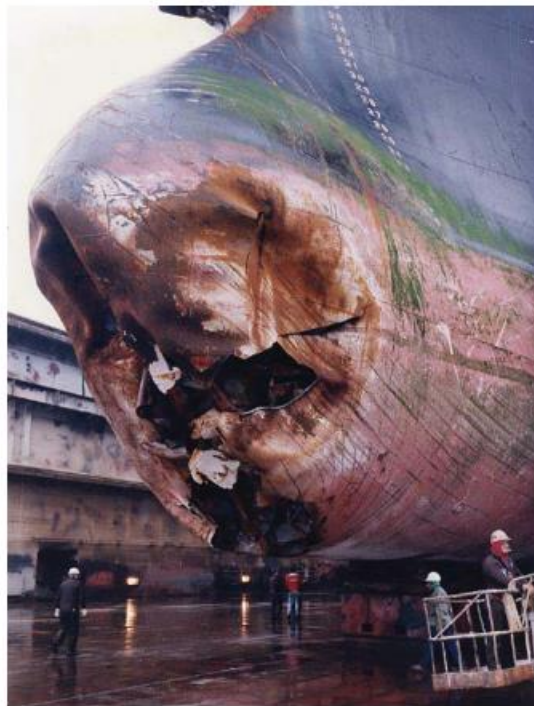


Fig. 1.5 The *oil tanker Overseas Ohio* after colliding with an iceberg in *Prince William Sound*, Alaska [7].



Fig. 1.6 Damages of Ekofisk 2/4-W platform and Big Orange XVIII after collision
(source: <http://www.ptil.no/getfile.php>).

More recently, a collision occurred between the platform supply vessel *Grampian Defender* and *BP Magnus* offshore facility on April 22, 2011. The vessel made contact with the legs of the platform and drifted underneath the walking bridge linked to an adjacent platform resulting in damages to the mast, firefighting monitor and funnel. A photo taken at the time of the incident is shown in Fig. 1.7.



Fig. 1.7 The Grampian Defender vessel hitting the BP Magnus offshore facility
(source: www.maritimeaccident.org).

The environmental issues at sea are closely related to the transportation safety of oil tankers, which may cause oil spills after ship collisions. The causes of oil spill incidents from oil tankers are shown in Fig. 1.8. It is reported by the International Oil Pollution Compensation Funds (IOPCF, 2005) [10]. For example, the *Exxon Valdez* accident in 1989 is considered one of the most

devastating man-made environmental disasters ever to occur at sea. The oil tanker Exxon Valdez slammed into Bligh Reef and spilled more than 11 million gallons of crude oil into the water of Alaska's Prince William Sound region. The coastal ecosystem was severely damaged, with millions of animals died and some species completely perished.

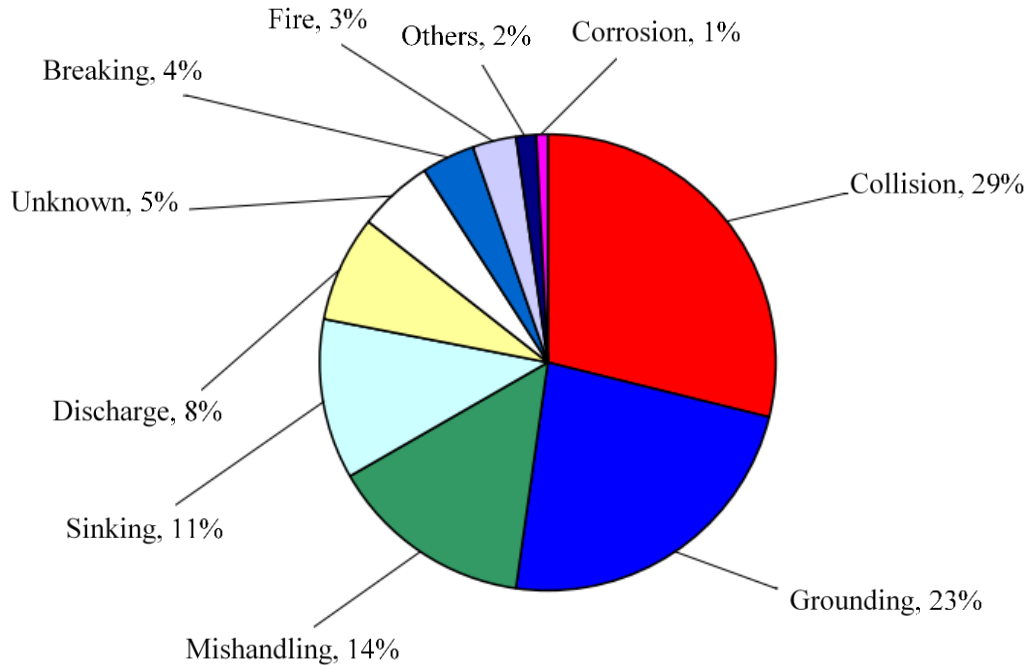


Fig. 1.8 Cause of oil spills from ships in 1970-2005 [10].

Accident collision events not only occur for oil and gas installations but also for recently emerging renewable energy devices: wind turbine farms. Most of the current offshore wind farms are located in shoal waters close to coastline where the risk of collision between OWTs (offshore wind turbines) with passing vessels is considerably high due to dense shipping lanes and heavy traffic. A very recent example of such incident happened at the *Bard Offshore 1* offshore wind farm, when it was under construction in the German North Sea on February 18, 2013. An offshore service and supply vessel has collided with the foundation of a wind turbine and suffered serious damage to the bow fender of the vessel.

In view of the potentially severe consequences of ship collisions, there has been a continuous interest in understanding the underlying collision mechanics and designing crashworthy structures. In the early 80's, with increasing offshore operations in North Sea, collision became a serious concern for stakeholders [11]. This was followed with significant research projects focusing on structural issues in UK [12-13] and Norway [14]. The-state-of-the-art methods developed in this period are summarized in [15]. Most of these methods are statistical or empirical, experimental

and simplified analytical methods. Further developments in the field, the International Conference on Collision and Grounding of Ships and Offshore Structures (ICCGS) was established in 1996. The conference is still very active today with the most recent one held in Ulsan, Korea, 2016. The next ICCGS will be held in Lisbon, Portugal, 2019. Based on the research findings, ship design standards and regulations were also enforced by the classification societies and governments for the safe operation and production. For instance, typical design standards are NORSOK-N003 (2007), NORSOK-N004 (2004), DNV-RP-C204 (2010) and DNV-RP-C208 (2013).

Nowadays, these advances enabled NLFEA (nonlinear finite element analysis) are powerful tools for predicting ship collisions and groundings. Many researchers have published and presented the ship collision simulations in many conference proceedings. Several commercial software packages, such as ABAQUS FEA, LS-DYNA, MSC. DYTRAND and ANSYS, are being widely used in dynamic impact fields. Obviously, ship and offshore structure collision modellings are very complicated procedures. It includes material properties (strain hardening and strain rate effects), geometries, loadings, boundary conditions and others for both striking ships and offshore structures. Numerical techniques offer a means of obtaining a complete solution to these problems. Modeling effort might be considerably extended in comparison with simplified methods. However, once NLFEA is validated, a large number of scenarios can be analyzed and enormous information can be obtained. The main advantage is that NLFEA provides a complete view of the results and the simulation is repeatable. Therefore, NLFEA is recently considered as a tool numerically producing experiments instead of performing costly laboratory scale tests.

On the other hand, there are still no attempts made to perform a comparative analysis of dynamic impact tests on small-scale models of offshore structural components experiments with NLFEA. The extensive research efforts in the field of ship collision and grounding in recent years have no counterpart in the offshore structures. Especially, experiments representing realistic impact conditions are lacking. There are also no widely accepted rational design recommendations based on accidental limit state principles for these structural components.

Within this context, it is important to realize that it is necessary to prevent any catastrophic accidents happening due to the inevitable potential risk of collision. And to ensure platform safety while at the same time avoiding unnecessary and very costly repairs as well as to be able to assess quickly and accurately the consequences and effects on structural strength after the occurrence of collision. The probability of major offshore collisions can be kept at a low level by means of adequate preventive measures and due to considerations for the protection of human lives. For this purpose, it is necessary to understand deep insights into the deformation mechanics of ships and offshore structural collisions and the residual strengths of the damaged structures as a basis for

repair decisions. Therefore, the purpose of the present study is mainly focused on the collision response of cylindrical structures and their residual strength with the current advanced analysis tools. Also, simple design formulations to predict the extent damage due to dynamic mass collision and their residual strength of damaged stiffened cylinders subjected to various loadings were provided. These formulations are very good accuracy and reliability according to the available test data. These formulations are also convenient to use for the purposes of initial design and serviceability limit state assessment of stiffened cylinders under the risk conditions of marine structures.

1.2 Aims and scope of work

The present thesis aims to contribute to the understanding of internal mechanics of ship impact on offshore structural components. The work was carried out as a part of the Korea Institute of Energy Technology Evaluation and Planning (KETEP) and the Ministry of Trade, Industry and Energy (MOTIE) of the Republic of Korea (No. 20124030200110, 20142020103560, 20154030200970, 20163010024620 and 20178520000280).

The objectives of the present work constituted by the following tasks:

- To understand deep insights into the deformation mechanics of ships and offshore structural components including ring- and stringer-stiffened cylinder as well as tubular members during ship collisions.
- To improve the accuracy of ship collision simulations by developing the numerical methodologies. And to understand the numerical simulations of accidental loading on ships and offshore structural components and validations against experimental results.
- To gain improved understanding of the detailed behavior of offshore structural components subjected to impact and their residual strength under various loadings based on the parametric study results obtained through numerical analysis.
- To investigate the residual strength of the floating offshore installations subjected to external hydrostatic pressure or combined axial compression and radial pressure through comparative analysis of experiments on small-scale models with numerical simulations.
- To propose formulations for predicting the extent of local denting damage and the residual strength of the damaged ring and stringer stiffened cylinders under hydrostatic pressure or combined axial compression and radial pressure.
- To establish strength design procedures based on the H-shape tubular member models proposed.

1.3 Outline of the thesis

The present thesis is organized into chapters with separate topics. The chapters are mainly based on the five journal papers published and one paper under preparation. The following papers are presented in the thesis:

- [1] Sang-Rai Cho, **Quang Thang Do**, Hyun Kyoung Shin. Residual strength of damaged ring-stiffened cylinders subjected to external hydrostatic pressure. *Marine Structures* 2017; 56:186–205.
- [2] **Quang Thang Do**, Teguh Muttaqie, Hyun Kyoung Shin, Sang-Rai Cho. Dynamic lateral mass impact on steel stringer-stiffened cylinders. *International Journal of Impact Engineering* 2018; 116:105–26.
- [3] **Quang Thang Do**, Teguh Muttaqie, Sang-Hyun Park, Hyun Kyoung Shin, Sang-Rai Cho. Ultimate strength of intact and dented steel stringer-stiffened cylinders under hydrostatic pressure. *Thin-Walled Structures* 2018; 132:442–60.
- [4] **Quang Thang Do**, Teguh Muttaqie, Sang-Hyun Park, Hyun Kyoung Shin, Sang-Rai Cho. Predicting the collision damage of steel ring-stiffened cylinders and their residual strength under hydrostatic pressure. *Ocean Engineering* 2018; 169:326–43.
- [5] **Quang Thang Do**, Teguh Muttaqie, Dinh Ngoc Can Le, Byeong-Soo Seo, Sang-Hyun Park, Hyun Kyoung Shin, Sang-Rai Cho. Fracture response and failure mode of H-shape tubular structures under dynamic mass impact. *International Journal of Impact Engineering*. (under preparation).
- [6] Sang-Rai Cho, Teguh Muttaqie, **Quang Thang Do**, Ha Young So, Jung-Min Sohn. Ultimate strength formulation considering failure mode interactions of ring-stiffened cylinders subjected to hydrostatic pressure. *Ocean Engineering* 2018; 161:242–256.

The present thesis is organized as follows:

Chapter 1 is mainly focused on the brief introduction of the background, motivation and objectives of the work. **Chapter 2** gives an overview of the research on the response of ships and offshore structure collisions. Fundamental concepts which are necessary for understanding the rest of the thesis are presented. Classification Society's Rules for the marine structural design are also summarized

Chapter 3 studies experimentally the plastic damage responses of ring- and stringer-stiffened cylinders subjected to dynamic mass impact. The details of the experimental setup, test

procedure, material properties, and test results are reported in this chapter. Also, the modeling of numerical analysis method, material property definitions, boundary conditions and convergence tests were conducted. The numerical analysis methodology is verified both with the quasi-static denting test results obtained from the literature and the present test results. The deformation behaviour of ring and stringer stiffened cylinders and the effect of ring and stringer stiffeners in energy dissipation are thoroughly discussed. The phenomena observed in dynamic tests such as strain rate and inertial effects are studied. After validating the numerical strategies with test results, rigorous parametric studies on the actual design of full-scale cylindrical structure examples were performed by changing the design variables. Finally, the deriving of approximate equations for prediction of extent damage was performed.

In **Chapter 4**, the fracture response of tubular structures to lateral collision at room and sub-zero temperature is presented. Numerical analysis results validated by comparing with dynamic impact tests are utilized for understanding the energy dissipation mechanisms and interaction of these with each other. A classification of the impact response is made and simplified analysis procedures are provided. Additionally, the simple critical failure strain was derived for predicting the fracture response at T-joint of tubular member under low-velocity mass impact. Final, rigorous parametric studies on full-scale H-shape tubular structures were carried out by changing the design variables. Based on the results of the test data and parametric studies, the different damage modes of H-shape tubular structures are discussed. A criterion for strength design considerations is also presented.

Chapter 5 focuses on the residual strength of damaged ring- and stringer-stiffened cylinders under hydrostatic pressure. A series of intact and damaged ring- and stringer-stiffened cylinder models were performed under hydrostatic pressure. The numerical analysis methodology for the assessment of residual strength of these structures was developed and verified with test results. In addition, the parametric studies in Chapter 3 were continued to perform for post-damage analysis.

Chapter 6 and **chapter 7**, the residual strength formulations for ring- and stringer-stiffened cylinders subjected to hydrostatic pressure or combined axial compression and radial pressure were provided. The accuracy and reliability of all the derived formulations are established by comparison with the test results and finite element analyses.

Finally, **Chapter 8** summarizes the important findings of the thesis and provides recommendations for future work.

Chapter 2

Overview of research on ship collisions with offshore installations

2.1 Introduction

The topic of ships and offshore structure collisions has attracted the interest of many researchers and engineers during the last four decades and the large methodologies and knowledge have been created. In the first part of this chapter presents the general approach to investigate the ships and offshore structure collisions. Because ships play an important role in the collision scenarios, therefore, the response of ships under the impact is also briefly covered.

In the second and third part of this Chapter, researchers who reported on the behavior of tubular members and cylindrical shells including ring- and stringer-stiffened cylinders during the collision and their subsequent load carrying capacity is reviewed in more detail. A brief review of the response of intact cylindrical shells which is essential to understanding and comparing with the effects of damage is also provided.

In the next part of this Chapter, the quick review of design principles and guidelines is presented. The classifying of each rule and regulations is also considered. Finally, some final remarks and suggestions are provided in the conclusion part of this Chapter.

2.2 General impact mechanics in ship-platform collision

During the occurrence of collision between a marine vehicle and an offshore installation, the kinetic energy of the striking vessel may be dissipated by various energy absorption processes. It is therefore a general approach to investigate initially the possible extent of energy involved, followed by an examination of the various energy absorption processes which will occur during the impact. The energy dissipation capability of each of these processes and the weakening effects induced on the structure must also be studied in a detailed manner before any assessment on the safety of the damaged platform can be carried out and particularly when a code of practice for design against collision is to be formulated.

For the past several decades, an important method has been to decouple the problem into two parts: the external dynamics and the internal mechanics, as suggested by Minorsky [17]. The external dynamics model simplifies the effect of fluid as constant added masses such that the whole collision system is undamped and the conservation of momentum principle applies. This allows for a fast estimation of the dissipated energy with reasonable accuracy. Pedersen and Zhang [18] proposed a closed form theoretical model for the planar external dynamics problem. Stronge [19] developed a solution for three dimensional (3D) impacts. The problem of external dynamics in ship collisions has also been addressed in Brown [20], Tabri [21], etc.

Wang et al. [22] suggested that the external mechanics can be solved either by numerical solution of the equations of motion or by an integrated approach where conservation of energy, momentum and angular momentum during the impact are used to derive analytical expressions for the dissipated energy. The latter is much simple and provided herein. A general case of collision between ships and installations is indicated in Fig. 2.1.

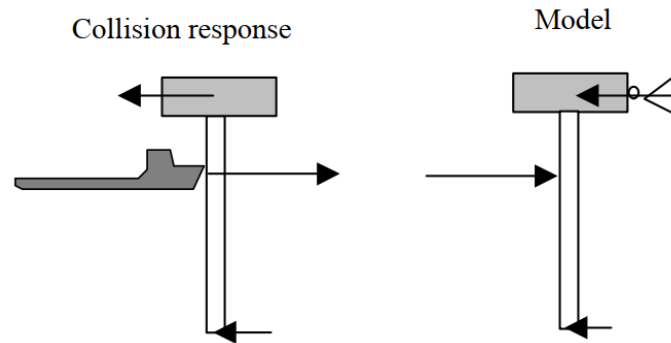


Fig. 2.1 Model for assessment of reaction force to deck from DNV-RP-C204 (2010).

The kinetic energy of the ship striking a platform is determined by:

$$E = 0.5 (m + a) V^2 \quad (2.1)$$

where V is the impact velocity of the ship, m is the striking mass and a is the hydrodynamic added mass.

The value for the added mass of a ship is equal to $0.4 m$ for board side collisions and $0.1 m$ for bow and stern collisions. The magnitudes of the energy involved are 14 MJ and 11 MJ for these two cases of collision as specified in DNV technical notes [23-24]. Such quantities correspond to a supply vessel of 5000 tons displacement, which is the estimated size of future supply ships, with an impact velocity of 2 m/s. This assumes that the ship is suffering from engine trouble with rudder locked, drifting against the platform at a wave height of 4 meters, above which operation of supply vessels in the North Sea area should be abandoned.

There are three types of vessels which may collide with offshore installations: visiting supply vessels, passing vessels and shuttle tankers. Among them, the collision between offshore installations and supply vessels is larger than other two. This is also the main collision scenarios which considered in the standards. Based on the impact energy, Paik and Thayamballi [25] classified the collisions in two type follows: minor collision (low-energy collision) and major collision (high-energy collision). A minor collision is defined as small permanent deformation without tearing or fracture of side shell of the struck structure. A major collision can result in severe damage including fracture.

It is interesting to note that the standard collision event described for OWTs in [28] is a major collision case. A tanker with 160000 DWT may correspond to a displacement of 190000 tons. With added mass and 2 m/s collision velocity, the resulting impact energy is more than 500 MJ. Obviously, this energy is much larger than the standard collision energy defined for supply vessel collision.

When the impact energy is defined based on the collision scenario, the next consideration is assessing how this energy is dissipated in struck structures as strain energy. This corresponds to internal mechanics in collisions, which is concerned with the evaluation of process of deformation and damage, impact response of structures involved in collision. In the design against ships and offshore installation collisions [26] are categorized into three regimes that depend on the relative strength, as shown in Fig. 2.2. These three regimes included ductile design, strength design and shared-energy design.

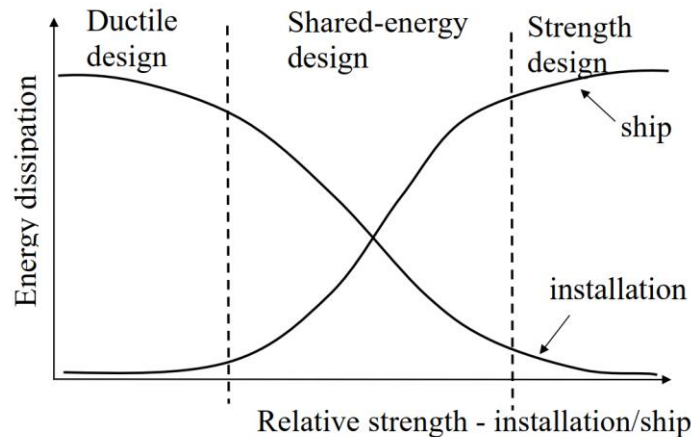


Fig. 2.2 Energy dissipation for strength, ductile and shared/energy design [26].

In ductile design the bow or side of the striking ship is considered to be infinitely rigid. It means that all of the energy is dissipated by the impacted installation or ship structures. This assumption can simplify the calculations because the shape of the striking ship largely dictates the

form of the damage to the struck ship/installation. However, this frequently used assumption results in the struck ship/installation sustaining damage regardless of how much it has been strengthened.

In *strength design*, the striking ship is considered to have a finite strength, and the strengthened struck ship/installation can crush the striking ship, which has to dissipate the major part of the collision energy. This objective is achieved if the struck ship/installation can resist the total crushing force as well as local areas with high force intensities. These design principles resemble those adopted in conventional ultimate limit state (ULS) design. Strength design may be a relevant option in certain cases but often yields an overly conservative and costly solution. Strength design may be necessitated by operational limitations, e.g., the length of downtime because of repair.

In *shared-energy design*, both the striking ship and the installation are considered to deform significantly. Consequently, the distribution of the damage and energy dissipation become considerably difficult to estimate by simple methods, because the bow crushing force cannot be assessed independently of the deformation state of the ship side/installation and vice versa, i.e., the resistance to the penetration of the struck ship/installation depends on the crushing state of the bow.

The relative strength of colliding structures determines the distribution of the energy dissipated. In *ductile design*, ship is relatively rigid compared to installation and in strength design vice versa. Strength design might be desirable for the safety of the installation; however, ductile design is fully acceptable unless the struck installation can resist the direct action of the accidental load without impairment of global integrity. There are cases where strength design is required. For instance, some decks have critical knee braces in the vessel impact zone which should be designed to withstand vessel impact [27-28].

The strain energies can be evaluated in two ways. First, the force-displacement relationship of the ship and the installation is constructed independently and integrated such that the resistance force in both striking ship and struck installation is similar. The sum of the two energy absorption obtained from integration of force-displacement curves should be equal to collision energy. This process is illustrated in Fig. 2.3 and expressed as follows:

$$E_k = E_s + E_i = \int_0^{w_s, max} R_s dw_s + \int_0^{w_i, max} R_i dw_i \quad (2.2)$$

where R_s is collision resistance force of striking ship; R_i is collision resistance force of struck installation.

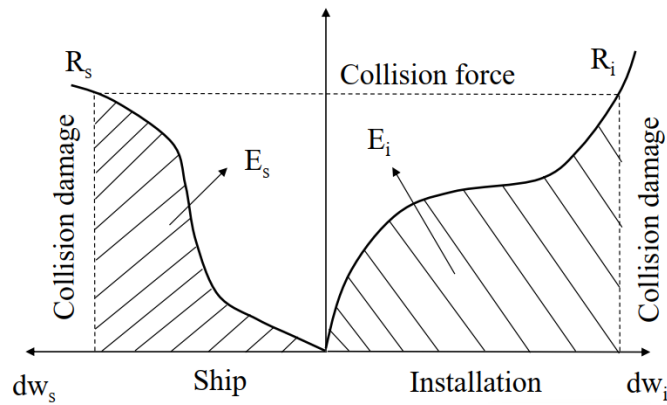


Fig. 2.3 Strain energy distribution in ship-installation collision [26].

Second method is the integrated analysis of colliding structures where both bodies are deformable. This method is more accurate; however, for this purpose the only means is NLFEA which might be computationally burdensome.

Another important consideration is that the standard force-deformation relationship curve for bow impact, which was developed in 1981, is based on a raked bow where crushing occurs in the relatively weak bow superstructure. Supply vessels are now built with a variety of bow shapes (i.e., bulbous bows, X-bows, etc.), which have widely different crushing characteristics from that of the standard vessel considered in NORSOK N-004 [29]. For ship structures, DNV [26] provides force-displacement relationships as shown in Fig. 2.4. These curves were derived using simplified analytical methods three decades ago. Furthermore, for supply vessels and merchant vessels in the range of 2000-5000 tons displacement, the force deformation relationships given in Fig. 2.5 may be used for impacts against jacket legs with diameter 1.5 m – 2.5 m [26].

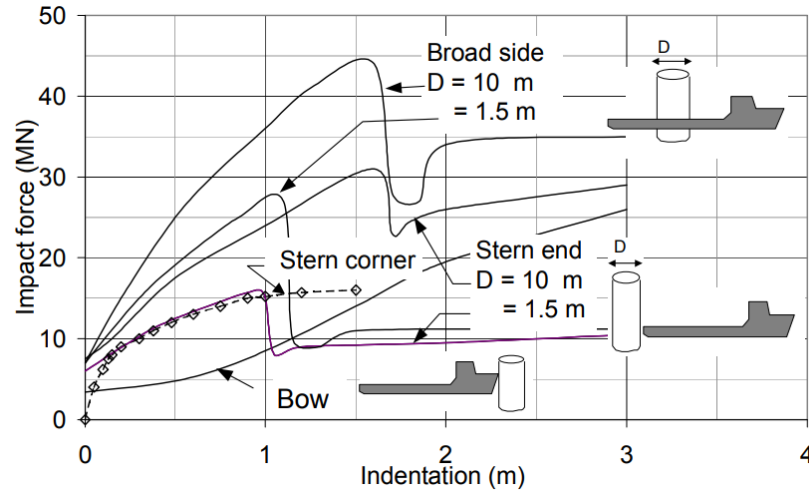


Fig. 2.4 Force-displacement curve for a 5000 tons supply vessel by DNV [26].

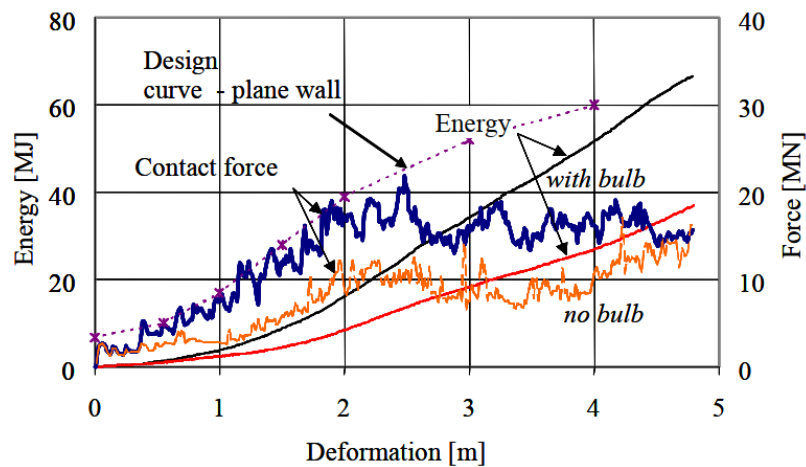


Fig. 2.5 Force-displacement curve for bow with and without bulb (2000-5000 tons) by DNV [26].

Amdahl [30] presented experimental studies with small-scale bow and stern structures and provided simplified analytical methods for crushing load of basic elements. These methods can be used to evaluate impact response of complex ship structures considered as an assembly of basic elements. Furthermore, there are numerous works related with ship collision and it is impossible to review here the vast amount of literature available.

In fact, it is rather complex to establish these curves initially and very difficult to find analytical formulae for the force and durations of impact for general load curves. Therefore, the impact velocity of the striking object even in the case of falling objects from platform is generally assumed to be slow enough that the dynamic effects can be ignored. The impact forces are therefore assumed to act quasi-statically on the structures.

2.3 Impact deformation and residual strength of cylindrical shell ($R/t > 30$)

In offshore installations, bracing tubular members are commonly designed for carrying the axial compressive loading with negligible local buckling of the cylindrical shell. Therefore, to prevent the local buckling occurs, the R/t ratio of bracing members are usually limited to be less than 30 for general structural steel as required by design codes API [31] and DNV [32].

However, in the case of stiffened cylindrical shell which applied to main leg members of fixed platforms or columns of floating rig, the R/t ratios of cylindrical members usually exceed 30. In general, these cylindrical shells are stiffened by rings, stringers or both. Therefore, these types of structures are sensitive to local buckling which can be lead to a catastrophic event due to collision and the subsequent residual strength reduced significantly. The limitation of related publications dealing with this topic, the literature review on the impact response and residual strength of damaged cylindrical shells ($R/t > 30$) is presented here based on the summaries of the researchers.

One of the earliest publication investigated the behavior of cylindrical shells subjected to localized transverse loading was reported by Pippard and Chitty [33] after the end of World War II. They investigated the effects of underwater explosion on the structural integrity of submarine hulls. The submarine pressure hulls are designed as the form of ring-stiffened cylinders. The models were loaded transversely through ball indenter and cylindrical bars, statically and dynamically. The test models were fabricated with the range of R/t ratios from 100 to 250. Various levels of stiffness of the end supports of the specimens were also considered. It is noted that the loading condition and geometry of models described were quite similar to that of a collision between marine vehicles and cylindrical offshore structural members.

Zayas and Dao [34] performed the experiments for representing the column of a semi-submersible offshore rig impacted by the side of support vessel. The ring-stiffened cylinders were designed with scale of 1 to 6.25. The support vessel was modelled as a round-edged ram indenter. The collision load was applied statically over four panels, and three different longitudinal locations were examined. A simplified analytical method based on an idealised elasto-plastic solution was also presented. The cross section of the column was divided into dented regions, where significant radial displacements were expected, and the remaining undented region was available to resist the bending moment. It was assumed that the shell between the rings at the top and bottom of the collision zone underwent plastic elongation and within the dented region, 60% of the material was considered to undergo membrane tensile action. Flexural strain energy of the ring stiffeners was

also investigated by performing a finite element analysis of a typical ring. The amount of energy in the elastic range of the ring was shown to be small when compared to that in the plastic range and once the first plastic hinge was formed the resisting force of the ring did not increase substantially. Thus, it could be assumed that the ring-stiffener's force-indentation relationship was a straight line. Fairly good agreement was obtained in the comparison of results from the analysis and corresponding experimental results.

Smith and Dow [35] presented the residual strength of damaged ring-stiffened cylinders subjected to external pressure. They suggested the form of damaged similar to cause the most serious loss of strength was that involving bending deformation of ring frames. The concentrated radial load was applied and then removed in order to simulate different levels of increments of the damage processes. An ideal rigid plastic collapse mechanism was also formulated assuming the formation of four plastic hinges of the ring frame. The obtained results were consistent with the finite element analysis. The subsequent collapse behaviour of the damaged ring frame was examined at each deformed configuration under external pressure by using the numerical analysis of computer program. The results illustrated that a significant reduction in collapse strength caused by various levels of damage.

Smith and Creswell [36] had been further investigated by using numerical techniques. Three types of damage have been identified which may be caused by the underwater explosion or impact damage. The results found that the influence of damage-induced residual stresses was reduced by about 30% in strength of cylindrical structures. Interestingly, the importance of this effect is that the collapse pressure was not reduced proportionally with the increase in the damage deformation but remains significant even at large damage amplitude. It was also highlighted that the most serious types of damage will be those involved with distortions of the stiffener ring frame which may reduce the collapse pressure to a minimum of about 30% of the squash pressure or to between 40 and 50% of the strength of an undamaged structure containing characteristic imperfections.

Frieze and Sachines [37] also investigated the residual strength of damaged ring-stiffened cylinders using the numerical analysis method. In order to simulate the damaged process, the load was reduced to zero during each increment and the unloaded configuration of the model without residual stresses taken into consideration. These configurations were used as input data for a subsequent residual strength analysis. The load-deflection relationship of the damage process of a single bay shell model with $R/t = 100$ and $L/R = 0.25$ was provided. The subsequent residual strength analysis showed that an increase in damage distortion from two to six times the shell thickness decreased the compressive strength by only up to 10%. The trend in damage effect

suggested the consequences of damage would become increasingly significant as ring-framed cylinder slenderness increased.

Onoufriou et al. [38-41] provided a series quasi-static denting tests on 1/20 small-scale ring-stiffened cylinders. These works were supported by an extensive cohesive research programme in Department of Energy and S.E.R.C. and carried out in various UK Universities. The geometry of the models was as follows: $R/t = 133$ and 267 , $L/R = 0.15$, 0.25 and 0.5 . The models were to be examined for the effects of damage on their residual strength under axial loading. Two series of models were tested. In the first series, the models CY-2 to CY-5 were subjected to mid-bay denting and, in the second, the models CY-6 to CY-9 were subjected primarily to ring-stiffener deformation. Also, in the first series the ring-stiffeners are flat-bar whereas the second series have T-shaped stiffeners.

The results were found that when the models were subjected to mid-panel denting, they exhibited lower lateral stiffness as the slenderness and ring spacing increased. These parameters were less important when the dents were applied to the rings and the bending stiffness of the rings themselves mainly determined the response. In the axial compression tests, the slender shells showed a sudden failure, while the stockier ones suffered a small but significant reduction in stiffness prior to collapse. Furthermore, the location of the dent in relation to the rings did not appear to have any significant effect on the strength. Even in the cases of ring dents including large initial rotation of the stiffener no sign of stiffener distress was observed.

In term of residual strength assessment, it confirmed that the dent location in relation to the rings had little effect on the mechanism of failure and strength reduction. It also indicated that the dent may have an added effect on the strength by acting as a sympathetic imperfection to the critical mode of failure. For models with the presence of well-defined initial imperfections, the failure mode would be dominated by the imperfection and precluding the dent from triggering a critical collapse mode.

Ronalds et al. [42-46] conducted quasi-static denting tests on four small-scale stringer-stiffened cylinders with lateral loading at mid-span, denoted by 3B1, 3B2, 3B3, and 3B4. All specimens had flat-bar ring-stiffeners dividing the specimens into three bays, which were stiffened in the longitudinal direction by 40 (3B1, 3B2) and 20 (3B3, 3B4) stringer stiffeners, respectively. The ranges of geometry were determined with $R/t = 190$ and 254 , $L/R = 0.33$ to 1.1 . Damage was simulated by slowly applying a round-edged wedge to the cylinder radially, with the edge normal to the cylinder axis. The specimens were then loaded axially in small increments using a displacement-loading machine until collapsed.

Walker et al. [47-50] performed a series quasi-static denting tests including ring-stiffened cylinder and stringer-stiffened cylinders. The purpose of the tests on this shell geometry was to investigate further the occurrence of stiffeners tripping under combined axial compression and external pressure. These experiments were also performed at the University of Surrey, UK. It is noted that the dimensions of test models were similar to those provided by Onoufriou and Ronalds. The results were found that collapse behavior of the model under combined loadings was commonly complicated than the damaged model was subjected to pure axial compression. Additionally, the rotational rigidity of the ring stiffeners played a significant role of the buckling characteristics of the models.

Tsang et al. [51-54] provided the combined loading tests on eight-small scale models with R/t ratio of 267 and ring spacing equal to 0.15R. This project was carried out at Imperial College London, UK. The test models were fabricated following to cold bending of steel sheets and then welding processes of ring-stiffener into the shell. Among these models, five models were designed to fail in the inter-frame buckling model and the other two models in overall buckling mode (general instability mode).

Galletly et al. [55-57] presented 35 small-scale single bay ring-stiffened cylinder models with R/t ratio of 100 and L/R ratios of 0.33, 0.74 and 1.15. Among them, eighteen models were fabricated with cold rolling and seam welding but without subsequent stress relieving. Other seventeen models were machined from steel pipes and could consider almost no imperfection. The models were subjected to combined external pressure and axial compression.

Frieze et al. [58] performed a series of combined loading tests on eighteen models. After fabricating model by cold bending and welding processes, these model were subsequently subsequent stress relieving. The R/t ratios of the models were 150 and 300 and L/R ratios ranged from 0.1 to 0.4. The collapse behaviors occurred both axisymmetric and asymmetric buckling modes. A quite simple interaction equation was also provided for predicting the ultimate strength of ring-stiffened cylinder under combined loading. The accuracy of proposed formulation was indicated better than DNV rules and BS5500 for hydrostatic pressure loading capability.

In America, Miller [59-60] carried out the experiments on forty medium scale models with R/t ratios in the range of 242 and 500. Models were designed with angle section ring-stiffeners and subjected to axial compression. Interaction equations have also been proposed.

Croll and Ellinas [61-64] reported a simple analytical approach to the axisymmetric response of cylinders under combined axial compression and external pressure. Based on the estimation of

first material yield and first full plasticity, it provided a reliable measure of the collapse strength for allowable stress and limit state design respectively.

Raymond [65] performed a series experiments on T-ring-stiffened cylinders under quasi-static denting tests at University of Surrey, UK. The local damage was generated using knife-edge indenter. Some of the dented models are subsequently tested under combinations of axial loading and external pressure for the investigation of the collapse behavior of the damaged shells. Undamaged shells are also tested in order to provide a basis of comparison for residual strength of damaged cases.

McCall [66] reported the experimental models with TIG welded steel stiffened cylinder at University of Surrey, UK. Twelve models including plain ring-stiffened and the orthogonally stiffened cylinders were tested under quasi-static denting tests. Then, all of the models were subjected to combined hydrostatic pressure and axial compression. Furthermore, the methods to repair damaged cylindrical thin-walled shells subjected to combined hydrostatic pressure and axial compression are also investigated experimentally.

Recently, MacKay et al. [67] provided details of experimental and numerical investigations on the strength of damaged pressure hulls, which included machined unstiffened and ring-stiffened cylinders with artificial corrosion damage. MacKay et al. [66] conducted numerical analyses of their corroded ring-stiffened models under hydrostatic pressure.

More recently, Do et al. [69-72] presented a series experiment of both ring and stringer stiffened cylinders. Details of test and numerical results for both intact and damaged ring-stiffened cylinders were provided. The damages were generated by dynamic mass impact and their residual strength was tested under hydrostatic. Then, the formulations were also derived based on the regression analysis of the results of a rigorous parametric study by nonlinear finite element analysis for predicting the extent of local denting damage under dynamic lateral mass impact as well as the residual strength of a damaged stiffened cylinder under various loadings. These results are included in the main part of a current thesis.

2.4 Impact deformation and residual strength of tubular member

2.4.1 Impact deformation of unstiffened tubular member

Studies focus on offshore structure load bearing components have been concentrated mostly on tubular members which are used extensively on fixed platforms. The geometries for tubular bracing members are of the ranges: $10 < R/t < 30$ and $20 < L/R < 60$.

Thomas et al. [73] conducted tests on short simply supported aluminum and steel tubes under the action of quasi-static transverse loading applied through a wedge-shape indenter. The ranges of D/t and L/R ratios of tubes were 48-74 and 3-22 respectively. In the tests it was observed that three phases of deformation were apparent as pure crumpling, followed by bending and crumpling and finally complete structural collapse of tube. The principal effect of increasing the length was also found that the amount of deformation experienced by the tube in the first phase of deformation is greatly reduced by an increasing in the length.

Amdahl [74] provided a series tests of small scale tubular members under side collisions. The scenario of these experiments could represented a jacket structure subjected to side collision by a supply vessel. The experimental and analytical investigations were also concluded. The geometries of the tubes tested were in the ranges: $15 < R/t < 25$, $L/R = 8$ and 12 . The deformation behaviour of the specimens were quite similar to those observed by Thomas. Furthermore, based on the experimental and analytical investigation results, the design curves were provided to design tubular member against accidental ship collisions. Then these proposed design curves were published and have been adopted by various researchers in a number of papers [75 - 81].

Cho [82] presented the lateral dynamic impact tests on small-scale tubular members. The geometries of the specimens were of the ranges: $12 < R/t < 20$, $40 < L/R < 74$. This study was one of earliest study which considered the dynamic effects in the collision of tubular members. Because most of the experimental and analytical works reported until Cho's study [80] has been carried out quasi-statically, it means that the dynamic effects can be ignored. The specimens were supported on rollers which would allow free rotation and axial movement of the ends but no lateral movement. The dynamic impact tests were performed by using an inclined runway machine. The damage was generated with various striker masses and different impact velocities.

Cerik et al. [83] reported the dynamic mass impact on 12 small-scale tubular members. The geometries of the tubes tested were in the ranges: $10 < R/t < 30$, $15 < L/R < 45$. The dynamic impact test results are utilised for quantifying modelling uncertainties for nonlinear finite element analyses. Then, rigorous parametric studies were performed to develop force-displacement curves for the tubular members. The results found that the failure mode of impact response of tubular members were classified into three groups based on plastic collapse load and characteristic resistance to local shell denting: Mode I-dominant global beam deformation, mode II –

combination of local denting and beam deformation, and mode III-dominant local shell denting. Additionally, an empirically deduced reduction factor was also proposed to consider the detrimental effect of local shell denting on plastic collapse load of tubular beams.

More recently, Liu et al. [84] performed a series of experimental and numerical studies on the behaviour of scaled tubular components and T-joints subjected to transverse impact loads with knife-edge indenter. The results found that the force-displacement responses show distinctly three stages, which are the initial vibratory stage, the steady deflection stage and the rebounding stages. The tests demonstrate that the brace increases the energy absorption of the chord members, and that the T-joints carries more impact loads when subject to impacts of higher impact velocities.

2.4.2 Residual strength of damaged unstiffened tubular member

In offshore installations, bracing members are commonly designed to apply axial compressive loading. In most cases of minor collision, catastrophic failure of the installation is not expected to occur but damage to a bracing member can happen quite frequently, particularly for jacket type construction, which will in turn affect the capacity of the structure to withstand extreme loads [65]. Therefore, it is very important to know the residual load carrying capacity of a damaged bracing member as well as the energy absorption after it collision. In this section, a summary of various experimental and analytical investigations for the residual strength capacity are reviewed.

Smith et al. [85-88] is the first group of researchers performed investigations on the residual strength of damaged bracing members. Experimental models were carried out on small scale tubulars with R/t ratios of 13 and 23 and column slenderness ratio mainly in the imperfection sensitive range of $0.8 < \lambda < 1.2$ (where $\lambda = (L/\pi R) (\sigma_Y/E)^{1/2}$). Full scale specimens retrieved from decommissioned platform were also tested. The damaged tubulars were applied axial compressive load until collapse with simply supported. Some important findings from their work are summarized. First, local denting damage was caused to reduce the section modulus and eccentricity of the neutral axis. The reduction of strength was insensitive to the location and shape of the denting damage [87]. Second, the effective values of Young's Modulus and yield stress of the dent zone were taken to be 50% and 75% of full material value, respectively. Next, the effect of damage was the greatest when bending was slight and reduced as the departure from straightness increased. Finally, the design curves which were provided based on parametric studies to agree well with test results.

Taby, Moan and Rashed [89-90] carried out a series of 21 tube models which were fabricated R/t ratios from 19 to 30 and slenderness ratios of 0.6 to 1.1. All models were generated damage by quasi-static denting. Then, axial compression was applied to the damaged specimens which were mounted with simply supported end conditions. Plastic analysis has been carried out with the assumption of a three-stage deformation namely plastic dent, ultimate stage and post-ultimate stage. During the dent plasticization stage, only axial compressive strains were considered. In the dent, bending stresses superimposed on the direct stresses and as the axial load continued to increase, yielding started at the middle of the dent and continued until a full plastic hinge line was formed.

Ellinas [91] developed an analytical method based on a member with a reduced effective section which could account for any combination of denting and overall bending. The analysis procedure assumed that once plastic deformation occurred the damaged part of the tube in dented region became ineffective. The load carrying capacity was then obtained on the basis of the reduced section using beam-column analysis, similar in form to that used in current design codes. The evaluation of the initial plastification stress, leading to the formation of plastic hinge at the middle of the dent is similar to that suggested by Taby et al. [89-90].

Ueda et al. [92] provided an experimental study for locally dented tubular under pure bending simple support conditions. A total of 21 tubular models with local denting damage were tested. The range of R/t ratios of test models was from 17 to 32. It is found that predominant effect of a dent was on the ultimate strength of the tube when the dent was placed on the compression side under bending. It also suggested that a dent was not likely to initiate local buckling or affect the rotation capacity of a damaged tube.

Griffiths et al. [93] conducted the tests on tubulars with geometries of the range of ratios: $4 < R/t < 15.5$ and $36 < L/R < 158$. Test models were damaged by impact with a knife edge having a mass of 20 kg dropping from various heights at mid span of tubular. Two types of boundary conditions were considered: direct bearing under the loading and the tube simply supported at its ends. After locally denting, models were tested under axial compression with ball seating at each end to simulate a simply supported condition.

Actually, most of the works discussed have been focused on the residual strength behavior of damaged tubulars under pure axial compression without the effect of external pressure. However, in actual cases, most of the ship/platform collisions happen above the water line. Therefore, the damaged member may have situated under a depth of water where hydrostatic pressure will be quite substantial.

Only Cho [82] has considered this effect of both axial compression and hydrostatic pressure in this area. A series of small scale test model was tested in an intact condition to provide a basis for comparison for damaged tubes with and without pressure loading. The damages were generated by dynamic mass impact with different magnitudes of damage at various locations along the length. Loading conditions included pure axial compression and combined hydrostatic pressure and axial compressive load with the specimen ends supported on spherical sittings.

2.5 Rules and regulations

For the design structural of offshore industry, it is considered four limit state designs follows: Ultimate, serviceability, accidental, and fatigue limit states. Among them, *accidental limit state* (ALS) and *ultimate limit state* (ULS) are relevant applied for design against accidental loads. ULS defines clearly and simply the maximum load carrying capacity. In an accidental event this corresponds to the strength in damaged condition. On the other hand, accidental limit state may be based on different objectives and can be defined using different methodologies.

The ALS can be represented based on critical deformation, critical strain, rupture, absorbed energy or as in ULS design, on the form of force or moment. These define so-called acceptance criteria, which are functional requirements concerned with resistance of installation to accidental effects. Depending on the type of collision, struck installation and definition of acceptable safety level by authorities, individuals or societies the acceptance criteria may vary. Therefore, it is not easy to develop a universally accepted ALS design criterion for all collision events.

There are some class rules play an important role in designing the offshore structures against ship collisions. Typical design standards are Norsok-N003 [94], Norsok-N004 [95], DNV-RP-C204 [96] and DNV-RP-C208 [97]. The current design standard for ship collisions generally follows the content when the standard was first introduced in 1980s [98]. DNV Offshore

Standards, such as DNV OS-A101 [99] and DNV-OS-C101 [100] apply in conjunction with DNV-RP-C204. The safety assessment principles and the design accidental loads are given in [99], which are prescriptive. According to [100] the structures exposed to accidental loads should be checked in ALS is in two steps: first, the resistance to the loads which they are subjected due to the accidental event and second, post-accident resistance against environmental loads when the resistance is reduced by structural damage caused by the design accidental loads.

According to the Norsok-N003 [94] standard, the accidental limit state (ALS) design check should be carried out with a characteristic value of each accidental action which corresponds

to an annual exceedance probability of 10^{-4} per installation. This gives the design collision scenario being a standard supply vessel with a displacement of 5000 tons travelling with a speed of 2 m/s. The standard design energy is thus 11 MJ for the bow/stern collisions and 14 MJ for the broadside collisions considering added mass effects. Nowadays, ship structures and designs have significantly changed for the design of crashworthy structures. For example, according to risk assessment, Moan et al. [101] recommended the design energy should be increased to 50 MJ for supply vessel bow collisions with offshore platforms.

Recently, ABS rule also provided standard for accidental loading assessment. The accidental loading scenario evaluation processes are conducted in risk assessment where initial hazard identification defines potential accidents that can occur to the installation during its life. Then, the risk exposure is developed based on the likelihood and consequence of each event. Generally, the process is idealized as three distinct activities: developing an accidental hazard risk assessment plan, performing a preliminary risk assessment and carrying out a detailed risk assessment.

2.6 Final remarks

Fabricated thin-walled cylindrical shells are widely applied as structural components of offshore installations and therefore it has attracted a lot of research interest. Many valuable experimental models were provided for both collision loadings and the subsequent load under axial compression or combined loadings. A substantial amount of work has been done in the investigation of the effects of damage for offshore structure members.

Based on the research results of previously completed or currently being performed, more and more useful information will be available in the near future. However, there is still a lack of understanding on numerous aspects of offshore installations and ship collisions where more investigations are required. As shown in previous sections, research undertaken so far has been mostly concentrated on the investigation of the behavior of damaged shells subjected to axial compressive load alone. And there is a lack of information and understanding available on the behavior of damaged offshore structures are subjected to combine external pressure and axial compressive loading actions. During the service of offshore installations, the most dominant loading condition on the column members is obviously axial compression resulting from the massive weight of the installation's top-side structure. Thus, when these installations are operated in deeper and deeper water, high water pressure will be also acting on the member. Furthermore, in actual conditions, tidal wave variation will also lead to temporary high-pressure loading on the

structural components as impulsive pressure or slamming loadings. This is therefore a very important area where research effort is required.

To this end, one of the issues currently facing to designers is that there are some class rules and reliable formulations which were predicted the extent damage of the offshore structures and ship collisions. However, until recently, there were no rules or consistently reliable formulations for predicting the residual strength of damaged offshore cylindrical structures subjected to various loadings after a collision. Therefore, it is necessary to spend more attention to assess the residual strength of these structures.

Chapter 3

Collision response of ring- and stringer-stiffened cylinders

3.1 Introduction

In the field of marine structures, fabricated multi-bay ring- and stringer-stiffened cylinders have been used by marine structural engineers for a long time as a major component of submarine pressure hulls or compression elements for floating offshore installations, such as the main legs of tension leg platforms and spars, and more recently, as buoyancy columns for floating offshore wind turbine foundations. In floating offshore installation columns, where the axial compression is dominant, stiffening the cylinder wall in the longitudinal direction is adequate in terms of weight efficiency and buoyancy requirements. When used in conjunction with ring-stiffeners, the stringers form an orthogonal reinforcement against axial compression and hydrostatic pressure loading. However, owing to their fabrication costs and complexity, both stiffening types are commonly used in practice. When structural elements are likely to be damaged in service, it is critical to consider the effects of such damage on the structure's strength and serviceability during the design stage. In order to achieve this, an understanding of the form of damage that is likely to occur is required [8]. Cylindrical shell structures are susceptible to damage due to the impact loads that may arise from accidents involving phenomena such as mass impact and impulsive pressure loading. Among these cases, this study addresses the problem of low-velocity mass impact loading on a ring and stringer-stiffened cylindrical shell.

For ring-stiffened cylinder, only few studies can be found on the behaviour of ring-stiffened cylinder under collision. Walker and Kwok [103] presented experimental and analytical work on quasi-static denting on cylinders. Harding and Onoufriou [104] and Karroum et al. [105] conducted quasi-static denting tests on small-scale ring-stiffened cylinder specimens. The models were to be examined for the effects of damage on their residual strength under axial loading. Two series of models were tested. In the first series, the models CY-2 to CY-5 were subjected to mid bay denting and, in the second, the models CY-6 to CY-9 were subjected primarily to ring-stiffener deformation. Also, in the first series the ring-stiffeners are flat-bar whereas the second series have T-shaped stiffeners. Walker et al. [49,50] reported quasi-static denting tests on both small-scale

ring-stiffened and orthogonally stiffened cylinders. Especially, dynamic impact tests for these structures are lacking.

For stringer-stiffened cylinder, the buckling behaviour of these structures has been thoroughly investigated by numerous researchers, and extensive experimental data for various loading cases are available in the literature [106-109]. However, only a small number of studies can be found on the behaviour of stringer-stiffened cylinders under mass impact. Ronalds et al. [43, 110-112] conducted quasi-static denting tests on four small-scale stringer-stiffened cylinders with lateral loading at mid-span, denoted by 3B1, 3B2, 3B3, and 3B4. All specimens had flat-bar ring-stiffeners dividing the specimens into three bays, which were stiffened in the longitudinal direction by 40 (3B1, 3B2) and 20 (3B3, 3B4) stringer stiffeners, respectively. Damage was simulated by slowly applying a round-edged wedge to the cylinder radially, with the edge normal to the cylinder axis. The specimens were then loaded axially in small increments using a displacement-loading machine. Walker et al. [49-50, 103, 113] performed quasi-static denting tests on two stringer-stiffened cylinders denoted by R5 and R6. These models had three bays each, separated by a plain section circumferential ring stiffener and stiffened in the longitudinal direction by 40 and 20 stringer stiffeners, respectively. The purpose of the tests on this shell geometry was to investigate further the occurrence of stiffeners tripping under hydrostatic pressure initially, and then subjected to axial compressive loading. Furthermore, Cerik [114] performed numerical predictions of the residual strengths of damaged stringer-stiffened cylinders that were subjected to axial compression. The local denting damage was induced by dynamic denting analysis of a lateral load and then subjecting the cylinders to axial compression.

An advantage of using quasi-static denting to impose specified damage is that it provides continuous recording of the damage process, which can be used to develop simplified analysis methods [115-117]. The majority of available experimental works that have investigated marine structure collisions follow the quasi-static approach, and assume that structure's response under a dynamic load as a result of a low-velocity mass impact is similar to the static force-displacement response. However, the dynamic effects of strain rate and inertial forces have not been taken into account. Inertial forces may be neglected because the impact duration is generally longer than the structure's natural period; however, the strain rate effect should be considered in order to predict the impact response accurately [114]. These issues are realistic importance for design against accidental impact loading. Recently, various available experimental and numerical studies related to ship structural components [105, 118-122] subjected to dynamic mass impact loading have demonstrated that accurate prediction of the structural response using nonlinear finite element analysis is not accuracy, unless details of the experimental conditions and exact material characteristics are provided. Moreover, Jones [123] noted that the accuracy of numerical predictions is improved when the dynamic material properties are provided. It is emphasized that

there is a lack of understanding on numerous aspects of dynamic material properties and that the available data in this field is inadequate.

There are analytical studies on unstiffened cylinders subjected to concentrated load, which causes local denting deformation, such as [124-128]. Hoo Fatt and Wierzbicki [129] extended the work of Wierzbicki and Suh [130], which focused on the denting of cylindrical shell of ring-stiffened cylinders. Simplified analysis methods can rapidly assess collisions as long as they comply with the actual structural response. Because these studies are purely theoretical, extensive validation studies with reliable experimental data are required. Moreover, in actual structural responses, the dynamic effects of strain rate and inertial forces should be taken into account to predict the permanent damage accurately. Recently, Cerik et al. [115] modified the model provided by Hoo Fatt and Wierzbicki for ring-stiffened cylinders. These equations have a good accuracy with limited test models. Therefore, further studies need to be considered for validating the analytical method with reliable experimental data.

Nowadays, the nonlinear finite element analysis has become an excellent tool for evaluating the collision response and failure of structures in the ocean engineering field [72]. A numerical evaluation of the residual strength of ring-and stringer-stiffened cylinders under dynamic mass impact was performed by Cho et al. [69] and Do et al. [70]. It was also applied in some offshore structures, including damaged ring-stiffened cylinders [117], pipelines [131] and damaged box girders [132]. Furthermore, a nonlinear finite element analysis was applied to perform ship-collision scenarios and validate the analytical methods [133-135]. Thus, besides its economic efficiency, a carefully performed finite element analysis, validated with reliable test data, could be the most effective way for evaluating the residual strength of damaged ocean engineering structures.

Within this context, this chapter describes experiments conducted on small-scale steel ring-and stringer-stiffened cylinder models that were subjected to dynamic mass impact. The experimental work is significant and can be used to validate predictions for dynamic mass impact loading. The tests were simulated using a nonlinear finite element analysis. Numerical impact simulations were included for an assessment of the dynamic material properties, in order to highlight the effect of strain-rate hardening. Next, an existing model for the local denting behaviour of unstiffened cylinders was revisited and the results obtained by modifying this model were compared with the experimental response. Furthermore, parametric studies were conducted on the stringer-stiffened cylinder models in order to clarify the progressive impact responses. Finally, the formulations based on the regression analysis of the results of a rigorous parametric study by nonlinear finite element analysis were derived for predicting the extent of the local denting damage under dynamic lateral mass impact.

3.2 Dynamic impact tests on ring-stiffened cylinders

In this section, the dynamic mass impact on a series of ring-stiffened cylinders was performed for evaluation of the impact response of ring-stiffened cylinders struck at mid-bay. The striker mass having a rigid knife-edge indenter is used to generate the damage. The numerical simulations were also performed and validated with experimental results. The results in this study have considerable importance providing a reliable and realistic view of the response.

3.2.1 Test models

To fabricate marine ring-stiffened cylinders, flat plates are rolled and then welded to the required curvature to form an unstiffened cylinder. The webs of ring-stiffeners are produced using several pieces of flat plate, and then the rolled flanges are welded together to construct ring-stiffeners. After inserting the ring-stiffeners into the cylinder, longitudinal seam welding is performed, and then the cylinder and stiffeners are joined by welding to complete the ring-stiffened cylinder. Of course, this type of fabrication method, incorporating cold bending and welding, leaves initial shape and material imperfections.

Following the fabricating method described, six nominally identical, internally ring-stiffened steel cylinder models were fabricated. The shells were cold-rolled to the required curvature, and then flat bar ring-stiffeners were internally welded onto the shell. Longitudinal seam welding was conducted to form a cylinder, and finally, the end plate and flange were welded to the cylinder. Two series of steel ring-stiffened cylinders were fabricated with different dimensions. The first series included the models RS-I, RS-C-1, and RS-C-2. The second series comprised the models RS-II, RS-C-3, and RS-C-4. Among them, RS-I and RS-II are the intact models, which are used for comparison with the damaged models to determine the ultimate-strength reduction factor in next chapter. The dimensions, material properties and damage generation process are provided in this section.

3.2.1.1 Dimensions

For first series, the dimensions of the test models are depicted in Fig. 3.1 and 3.2. The outside radius (R_o) and overall length (L) were 400 mm and 1060 mm, respectively. The stiffener spacing reduced gradually towards the ends from 200 mm to 80 mm. The thickness of the shell and stiffener was nominally 4 mm, but the actual values slightly deviated from the nominal value. The measured thicknesses of the shell (t_s) and ring-stiffener (t_w) are provided in Table 3.1. The ring stiffeners

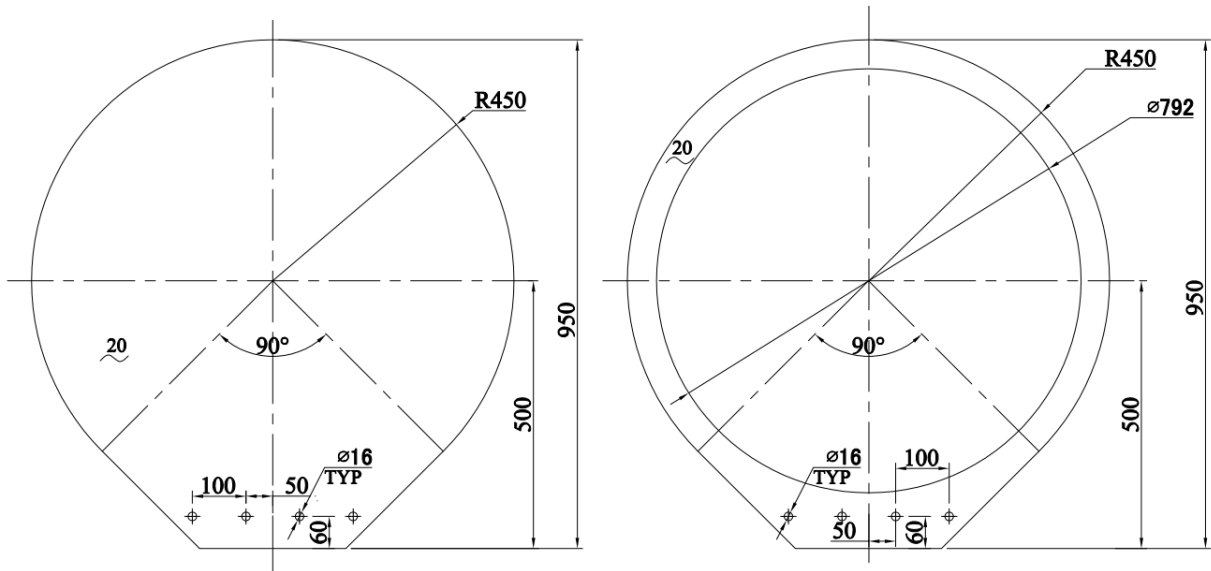


Fig. 3.2 Geometry of the end plate and the end ring for RS-I (Unit: mm).

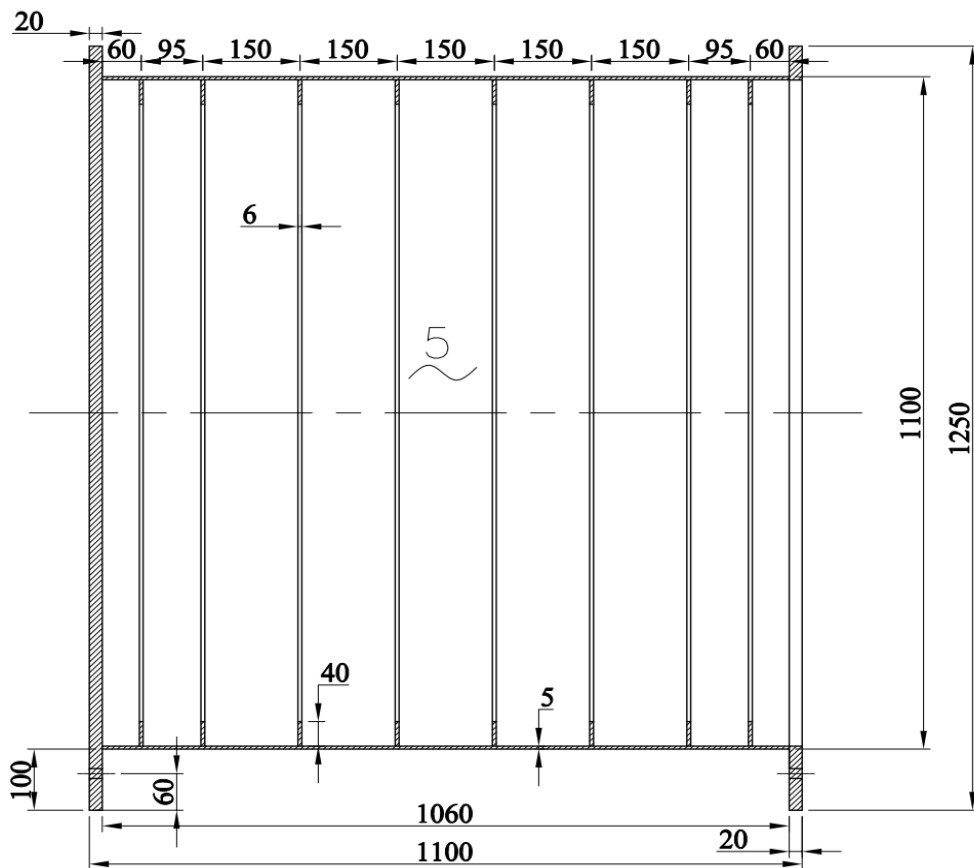


Fig. 3.3 Dimensions of the ring-stiffened cylinder for model RS-II (unit: mm).

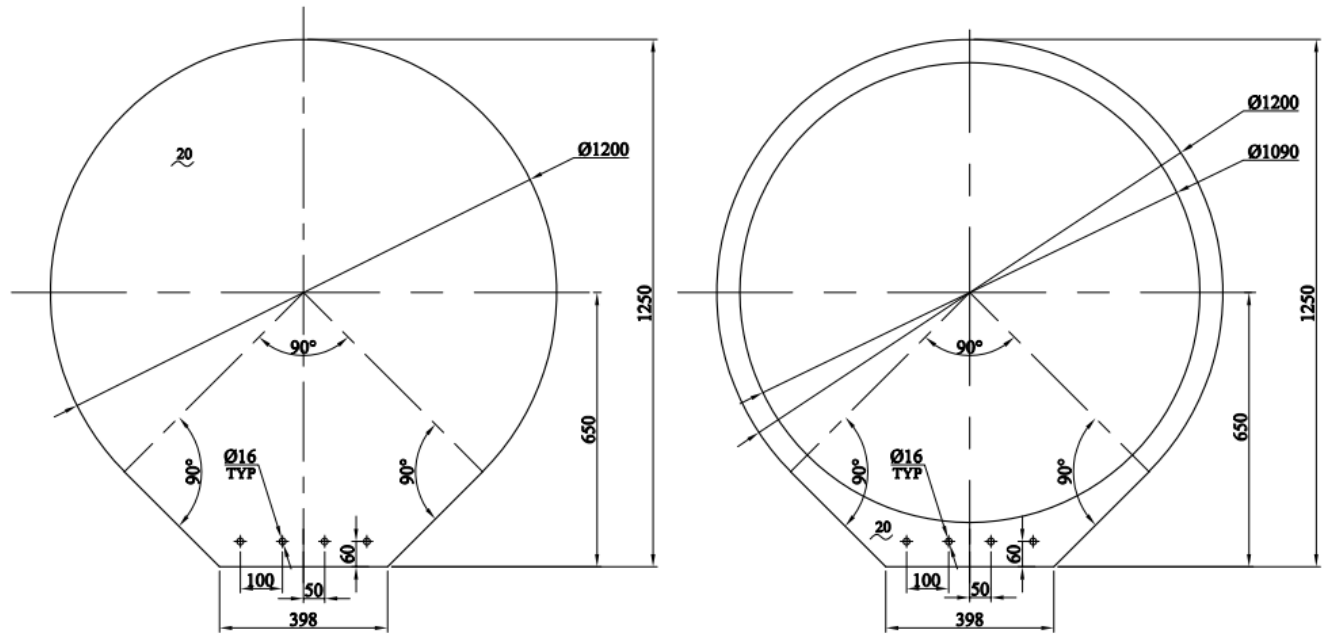


Fig. 3.4 Geometry of the end plate and the end ring for model RS-II (Unit: mm).

Table 3.1 Measured dimensions of test models.

		RS-I	RS-C-1	RS-C-2	RS-II	RS-C-3	RS-C-4
Outside radius (mm)	R_o	400	400	400	550	550	550
Thickness (mm)	t	3.96	3.96	3.95	4.96	4.97	4.94
Total length (mm)	L	1060	1060	1060	1060	1060	1060
Ring-stiffener spacing (mm)	l	200	200	200	150	150	150
Number of rings	n_r	6	6	6	8	8	8
Ring-stiffener web height (mm)	h_{rw}	35.0	35.0	35.0	40.0	40.0	40.0
Ring-stiffener web thickness (mm)	t_{rw}	3.94	3.94	4.0	5.92	5.81	5.81

3.2.1.2 Material properties

The mechanical properties of material were obtained from tensile coupon test [136], under procedures given in Korean Standard, the coupon is cut off from each parent plate of the cylinder shell. It is taken in order to provide an accurate representation of the experimental material of models. The tensile test coupon dimensions are shown in Fig. 3.5. From each parent plate of the cylinder shell and ring-stiffeners, five flat coupons were cut and tested using the universal testing machine, shown in Fig. 3.6. An example engineering stress-strain curves of cylindrical shells for model RS-C-2 are provided in Fig. 3.7. The average mechanical properties are shown in Table 3.2.

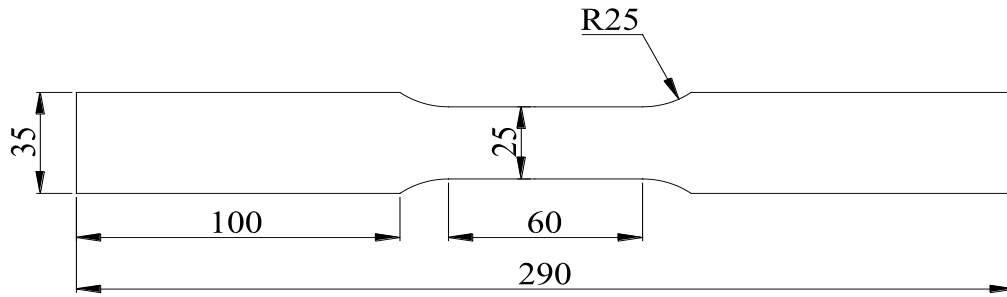


Fig. 3.5 Dimension of the tensile test coupons (Unit: mm).



Fig. 3.6 Universal testing machine used in tensile tests and sample coupons.

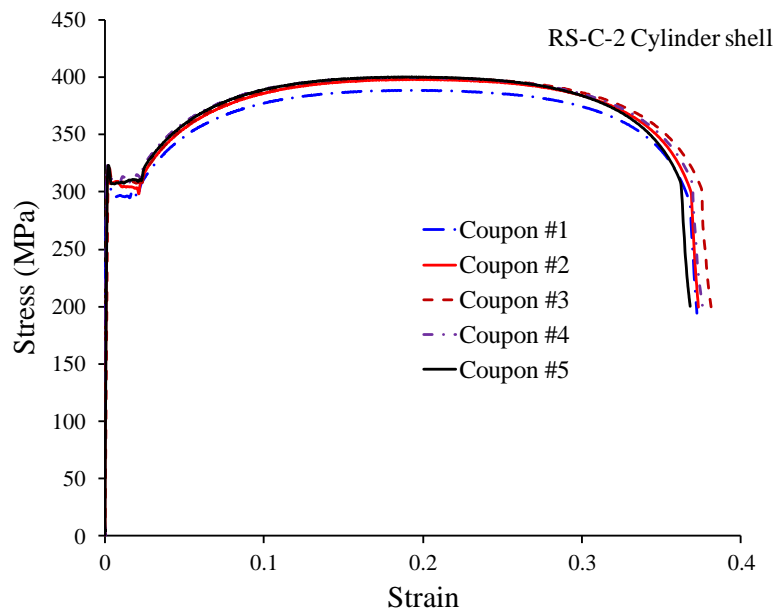
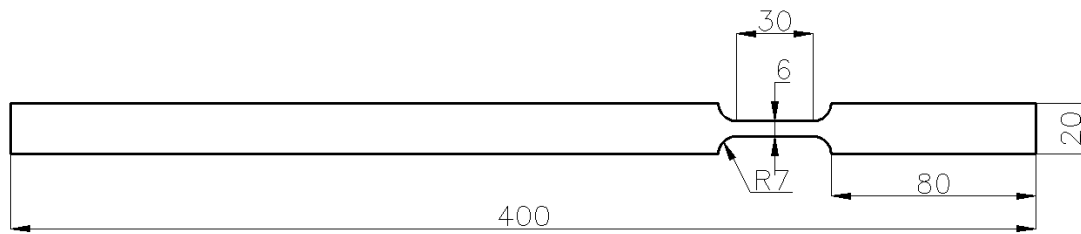


Fig. 3.7 Engineering stress-strain curve of cylindrical shell for model RS-C-2.

Table 3.2 Measured dimensions of test models.

Model		RS-I	RS-C-1	RS-C-2	RS-II	RS-C-3	RS-C-4
Yield strength (MPa)	σ_Y	306.5	302.2	309	274.9	274.9	274.9
Ultimate strength (MPa)	σ_T	398.3	396.2	397.3	370.5	370.5	370.5
Elasticity modulus (GPa)	E	204456	191394	200099	202404	202404	202404
Hardening start strain	ε_{HS}	0.0225	0.0227	0.0224	0.0145	0.0145	0.0145
Ultimate tensile strain	ε_T	0.196	0.196	0.194	0.234	0.234	0.234
Fracture strain	ε_F	0.373	0.376	0.366	0.427	0.427	0.427

The dynamic tensile tests were also performed by following the procedures of ISO 26203-2:2011 [137]. The dimensions and test results of the dynamic tensile test coupon for high strain rates are shown in Fig.3.8. In this figure, the average thickness of the tensile test coupons is 1.98 mm. The tests were conducted with various strain rate values corresponding to 10/s, 50/s and 100/s. The dynamic tensile test setup is shown in Fig. 3.9. The strain was measured using a high-speed camera while the force was measured by load cells and two strain gauges attached on both sides of the coupon. The dynamic tensile stress-strain curves were obtained from the Instron VHS-65/80-25 servo hydraulic machine, as shown in Fig. 3.9. It is noted that some coupons were failed to obtain the results. The unfiltered dynamic tensile strain-stress curves obtained for the first series (RS-I, RS-C-1 and RS-C-2) are shown in Fig. 3.10. The filtered dynamic tensile strain-stress curves obtained for the first series (RS-I, RS-C-1 and RS-C-2) are depicted in Fig. 3.11.



(a)



(b)

Fig. 3.8 Coupons for high speed tensile tests: (a) Dimensions (unit: mm); (b) After testing.

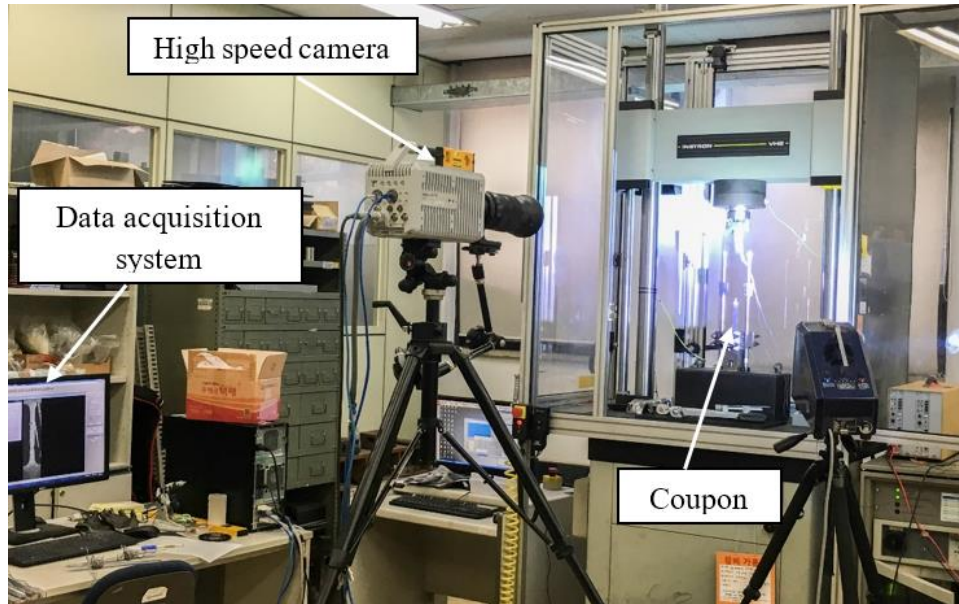


Fig. 3.9 Experimental setup for high strain rate tensile testing.

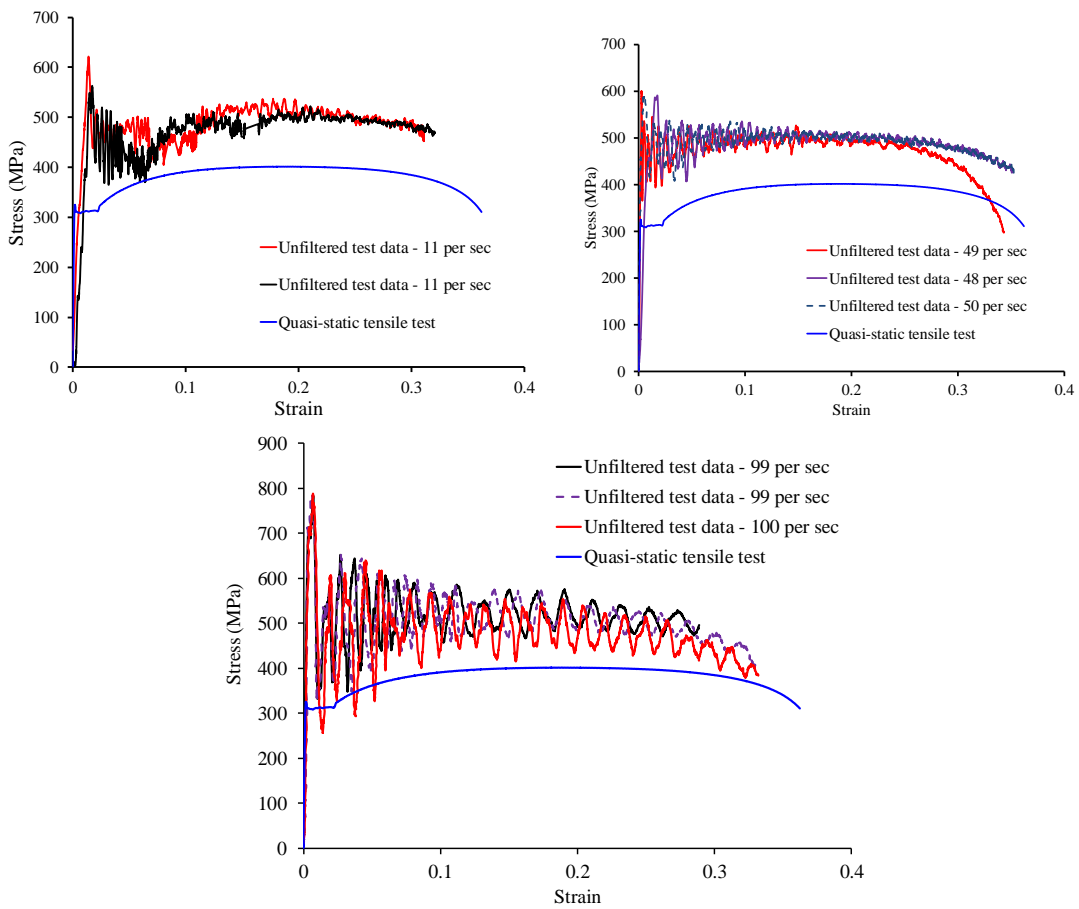


Fig. 3.10 Dynamic tensile strain-stress curves for first series model.

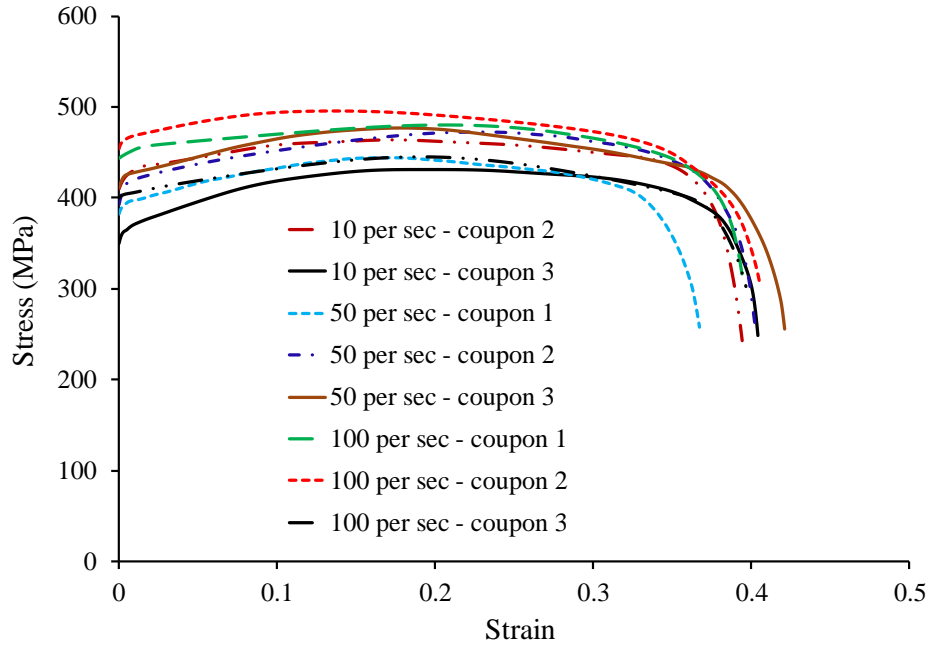


Fig. 3.11 Dynamic tensile strain-stress curves for first series model.

3.2.1.3 Initial shape imperfection measurement

For the first series, before performing the collision tests, the initial imperfections were measured using a two-point bridge gauge. On the inner and outer surface of the models, the longitudinal grid lines were drawn at every 10° . The circumferential grid lines were drawn at each ring-stiffener location and at the middle of each bay. The relative radial deflections of the cross points were measured using a two-point bridge gauge along every circumferential grid line. This procedure corresponds to radial measurement of shape imperfections. The total number of deflection points measured on every circumferential grid line was 36. The two-point bridge gage readings were converted to out-of-roundness values by performing Fourier series expansion [138]. The imperfection profiles of the intact model are shown in Fig. 3.12. In this figure, 0° line corresponds to the longitudinal weld line. The magnitudes of the imperfections are exaggerated by 10 times. The maximum out-of-circularity values occur near the longitudinal weld line. More details of initial imperfection measurement can be found in Appendix A and B.

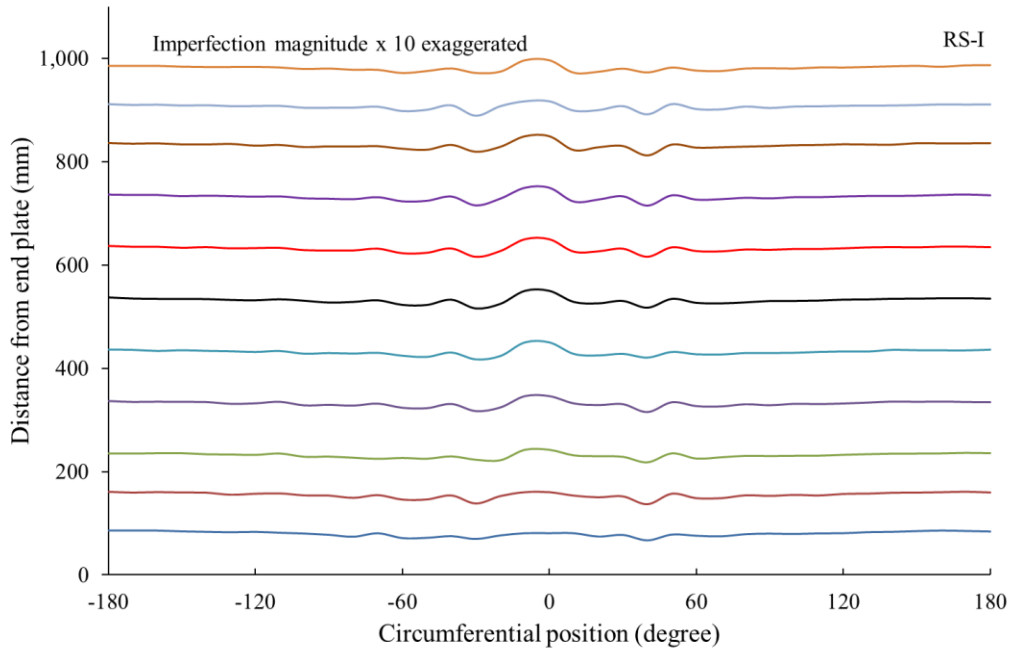
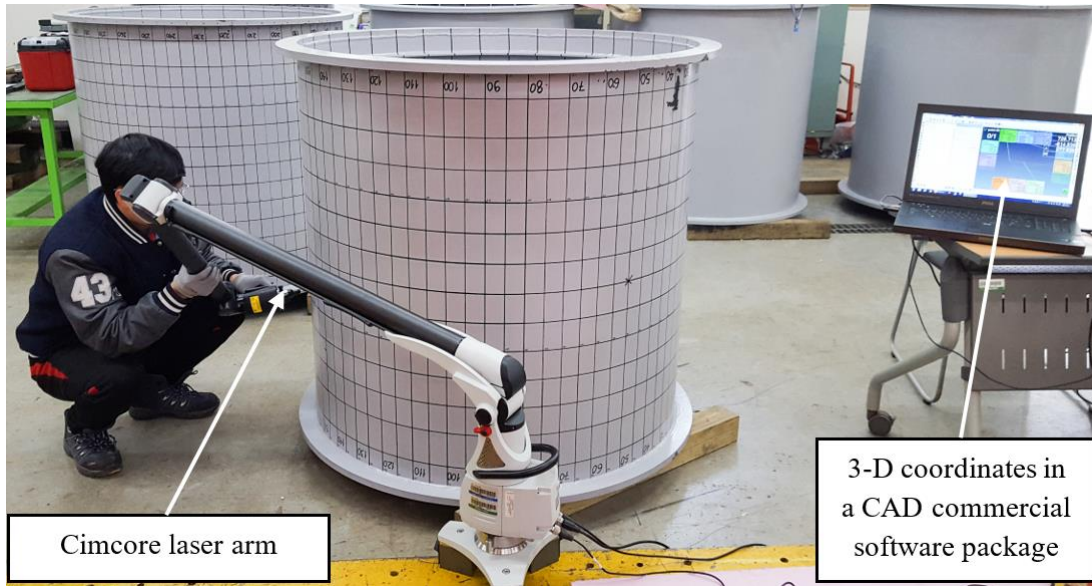


Fig. 3.12 Imperfection profiles of the intact test models, RS-I.

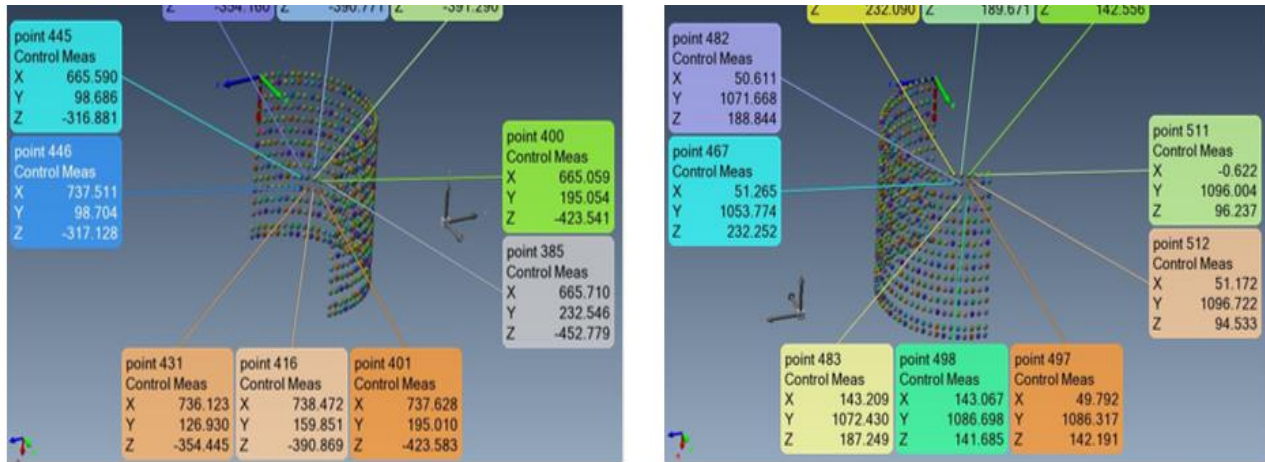
For the second series, the initial imperfections were measured using a Cimcore laser arm. The CAD commercial software was used to convert the recorded imperfection results to 3-D coordinates, which will be applied for modelling in the finite element analysis. The initial imperfection measurement setup is depicted in Fig. 3.13. The summary of maximum out-of-circularity is provided in Table 3.3. The maximum out-of-circularity values were smaller than the tolerable imperfection level for ring-stiffened cylinders specified in PD5500 [139], which is 0.5% of the cylinder radius, R .

Table 3.3 Summary of out-of-circularity measurements.

Model	RS-I	RS-C-1	RS-C-2	RS-II	RS-C-3	RS-C-4
Max. out-of-circularity	0.42 % R	0.36%R	0.44%R	0.37%R	0.42%R	0.46%R
Location	6 th bay, weld line (0 degrees)	3 rd bay, weld line (0 degrees)	2 nd bay, weld line (0 degrees)	2 nd bay, weld line (0 degrees)	4 th bay, weld line (0 degrees)	3 rd bay, weld line (0 degrees)



(a)



(b)

Fig. 3.13 Measurements of initial shape imperfections for model RS-II:

(a) CimCore device; (b) 3-D coordinates.

3.2.1.4 Experimental set-up

The experiment was conducted using a free-fall testing frame, as illustrated in Fig. 3.14. There is a pulley at the top of the frame tower that guides and holds an electromagnet attached to the striking mass. The height of the striking mass can be varied in order to achieve the desired impact energy. Once the electromagnetic force has been cut off, the striking mass falls and accelerates due to gravity. The velocity of the striking mass is simply determined by equating its potential energy to its kinetic energy prior to impact.

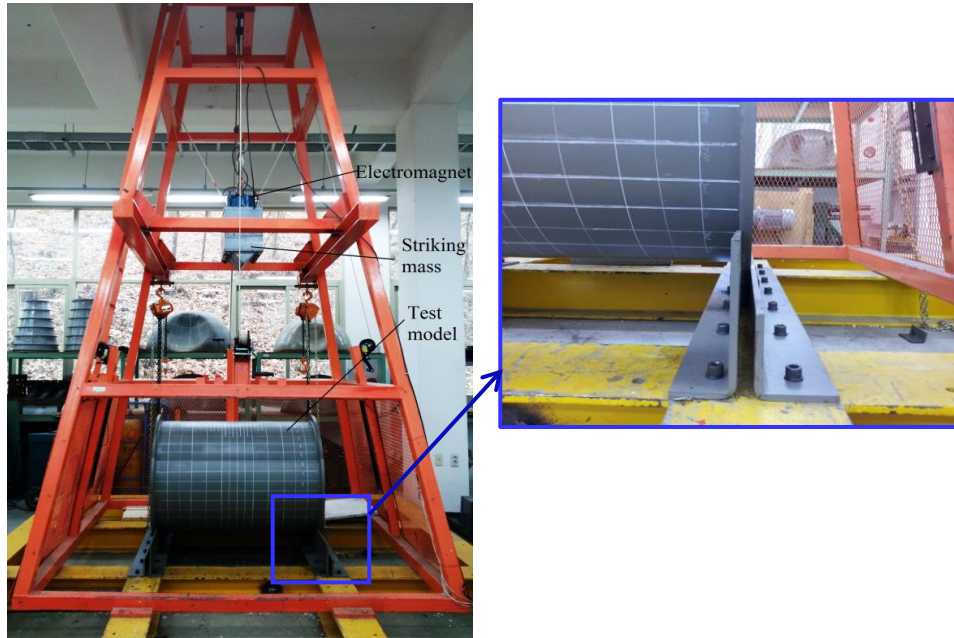


Fig. 3.14 Impact testing frame & boundary conditions in the experiment.

It is important to describe the boundary conditions in the experiment in details because the impact response is highly sensitive to the provided restraints in some cases. The models were firmly fixed to 10 mm thick support plates using 4 bolts. The support plates were bolted to the rigid foundation of the testing frame in Fig. 3.14. Note that the support plates were in contact with the end plate and the end ring only. Therefore, some part of the bottom of the end plate and the end ring were fixed. On the upper part, the displacements and rotations were free. Consequently, the cylinder shell remained circular at both ends, but depending on the stiffness of the end plate and the end ring, the axial translation and rotations were partially restrained.

The striking mass is 295 kg and 500 kg for striker type I and II, respectively. The tip is rounded with a radius of 5 mm and 10 mm for type I and type II, respectively. The dimensions of the striking mass and its indenter surface are given in Fig. 3.15. The details of impact test conditions for each model are shown in Table 3.4.

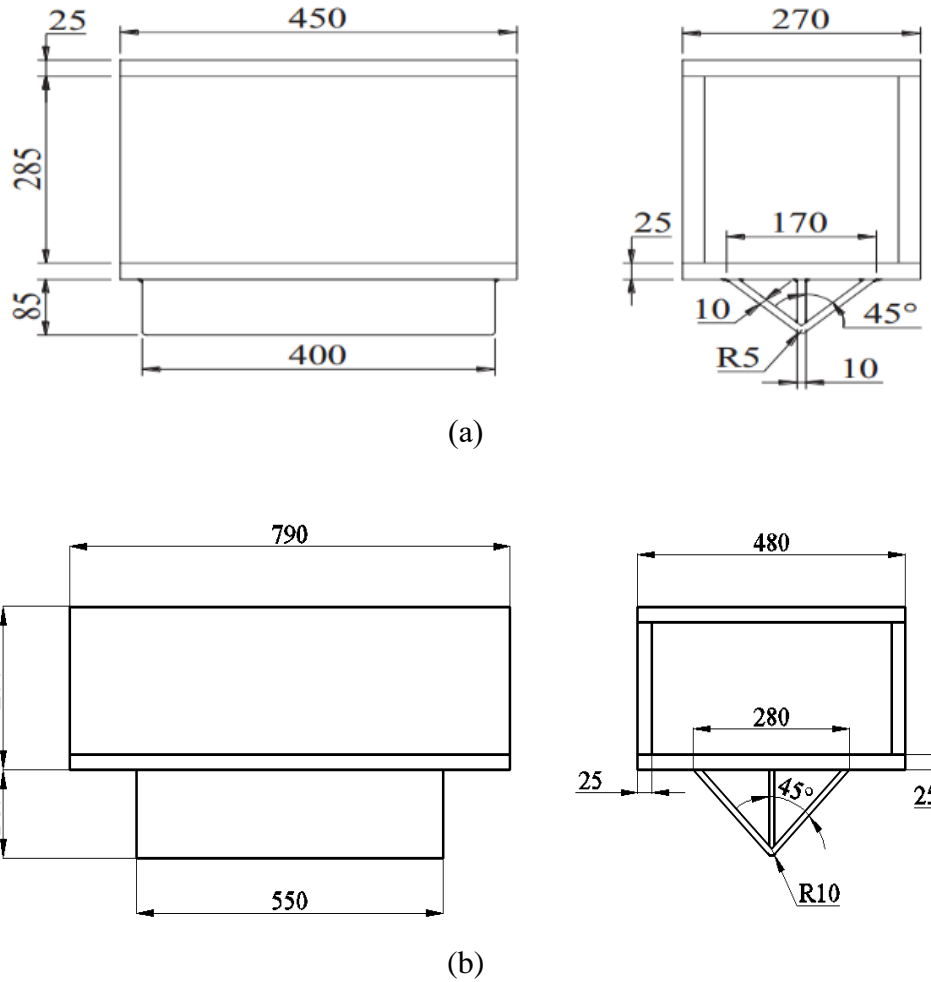


Fig. 3.15 Dimensions of the striking mass and its indenter (Unit: mm): (a) Type I; (b) Type II.

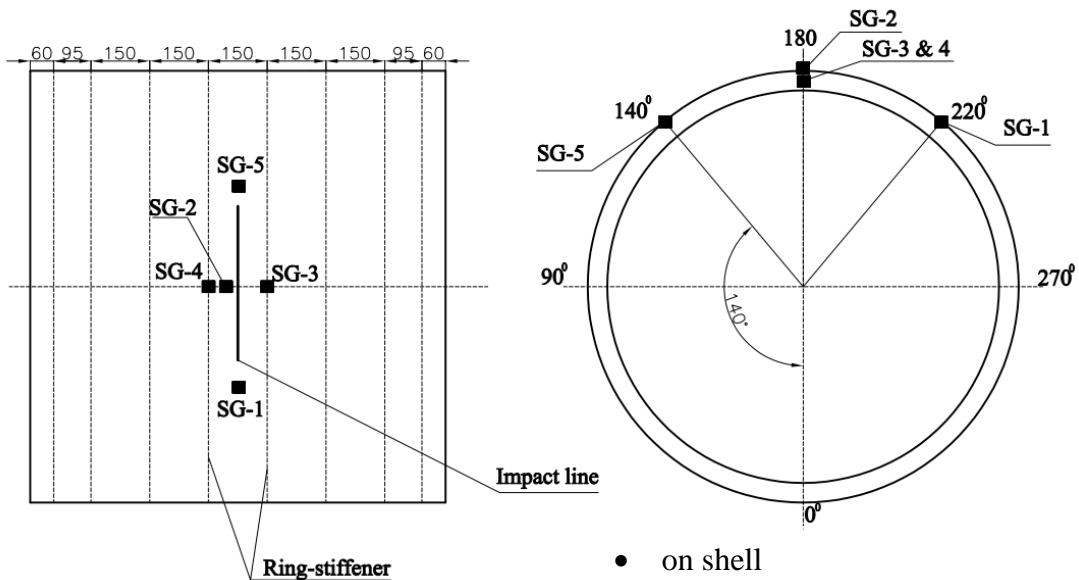
Table 3.4 Collision test conditions of test models.

Model	RS-C-1	RS-C-2	RS-C-3	RS-C-4
Drop height (mm)	1600	1200	1200	1600
Collision velocity (m/s)	5.602	4.852	4.852	5.602
Striker mass (kg)	295	295	500	500
Kinetic energy (J)	4629	3472	5249	7846

With this experimental setup, direct measurement of impact force and deflection throughout impact is not possible. Still, an indirect measurement method was employed. Four accelerometers were affixed on the upper surface of the striking mass to record the acceleration history. By utilizing Newton’s law of motion and double integration of acceleration history recorded during impact, dynamic force-displacement curve can be obtained. After impact, it is assumed that the indenter remains in contact with the struck model. Therefore, the indenter and

the impact region of the struck model have the common velocity and the displacement throughout the entire response. The permanent deflection of the model can be obtained when both bodies are not in contact anymore.

Strain gauges were placed at five positions to obtain more details about the impact response of the models. At each position two strain gauges were affixed. First two positions, SG-1 and SG-2, are 30 mm beside the impact line. The strain gauges at these locations are on the inner surface of the cylinder. In order to understand the deformation behavior of the ring stiffeners, strain gauges, SG-3 and SG-4, were placed on the surface of the ring-stiffeners bordering the mid bay. The last position, SG-5, is at center plane and on the generator line at 220° degrees away from the top generator line on the inner surface of the cylinder. The arrangement of the strain gauges is sketched in Fig. 3.16.



- on shell
 - SG-1 (140° , 530 mm from End plate)
 - SG-2 (180° , 500 mm from End plate)
 - SG-5 (220° , 530 mm from End plate)
- on ring-stiffener
 - SG-3 (180° , 605 mm, 525 mm)
 - SG-4 (180° , 455 mm, 525 mm)

Fig. 3.16 Arrangement of the strain gauges.

3.2.1.5 Test results

The deformed shapes of the models RS-C-1, RS-C-2, RS-C-3, and RS-C-4 are shown in Fig. 3.17 and Fig. 3.18, respectively. The damage can be described as local denting at the impact region. The local dent causes flattening of the cross section having a length of the width of the indenter. At the ends of the flattened dent section there is outward bulging of the shell. The large dent is limited in the mid-bay. The boundaries of the local dent are semi-ellipses. After carefully checking the damage profile, it was found that the impact location shifted away from prescribed position towards the open end. The inevitable rotation of the striking mass when it leaves the electromagnet is likely the main cause.

In Fig. 3.19, the deformed shape of the ring-stiffeners is shown. The upper parts of the ring stiffeners adjacent to damage zone is completely flattened. At the ends of this flattened part, strain concentration is noticeable. The ring-stiffeners bordering the bay adjacent to the mid-bay are also deformed as the cracked coating confirms. The shape of the ring-stiffeners remains unaffected except the flattened parts. Also, the damage spreads in the longitudinal direction when the flattened part is tilted with a small degree of rotation outward. This means that the ring-stiffeners are tripped.

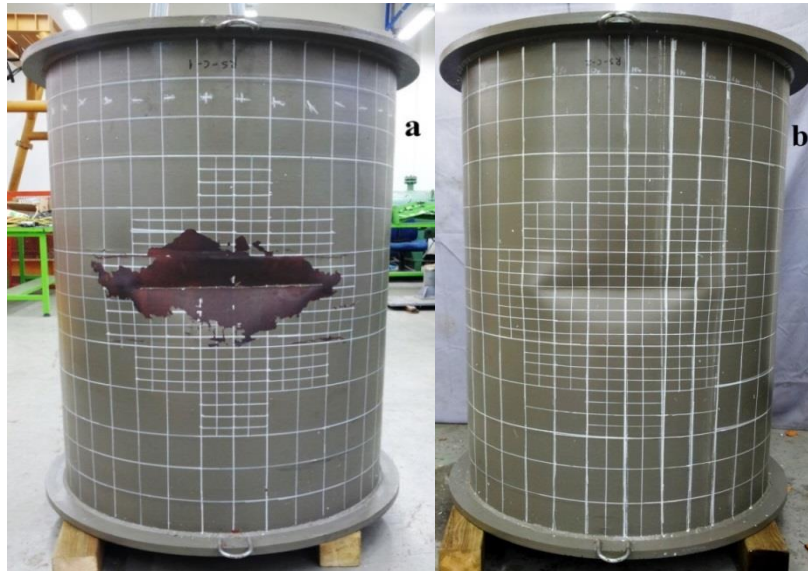


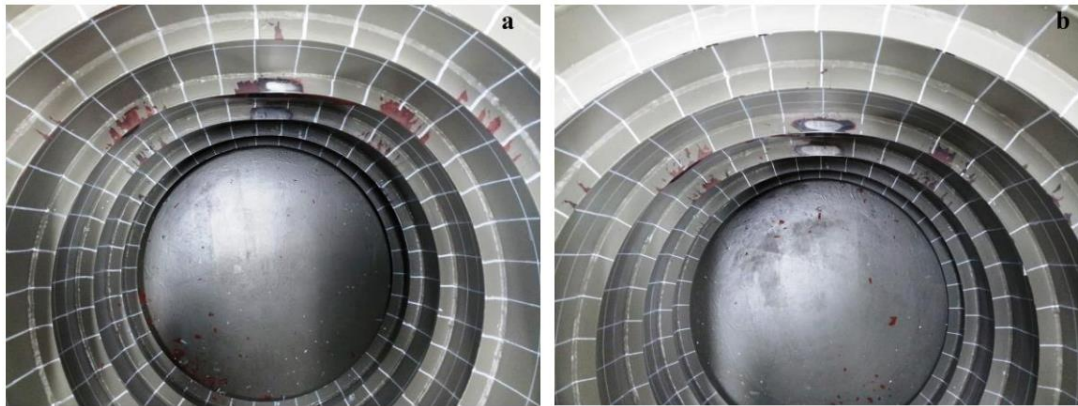
Fig. 3.17 Deformed shape of the models in top view: (a) RS-C-1 and (b) RS-C-2 [115].



(a)

(b)

Fig. 3.18 Deformed shape of the models in top view: (a) RS-C-3 and (b) RS-C-4.



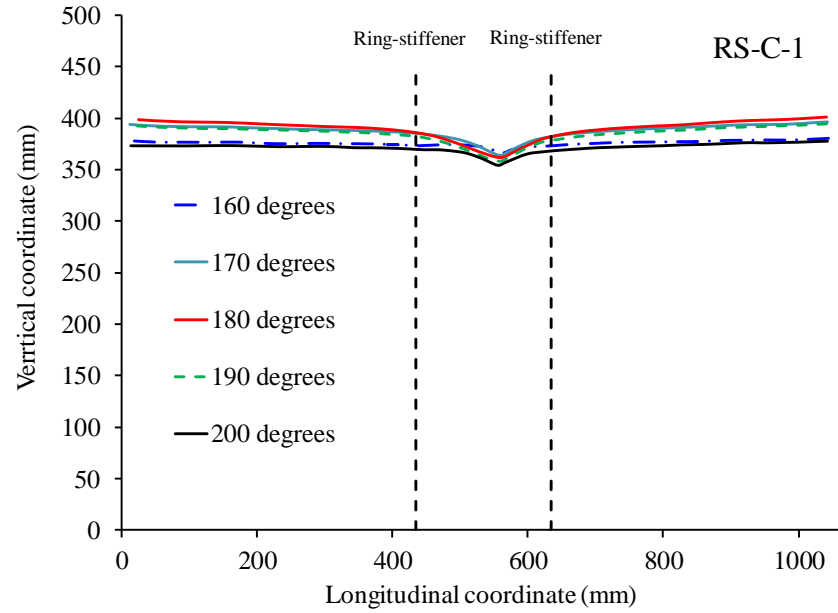
(a)

(b)

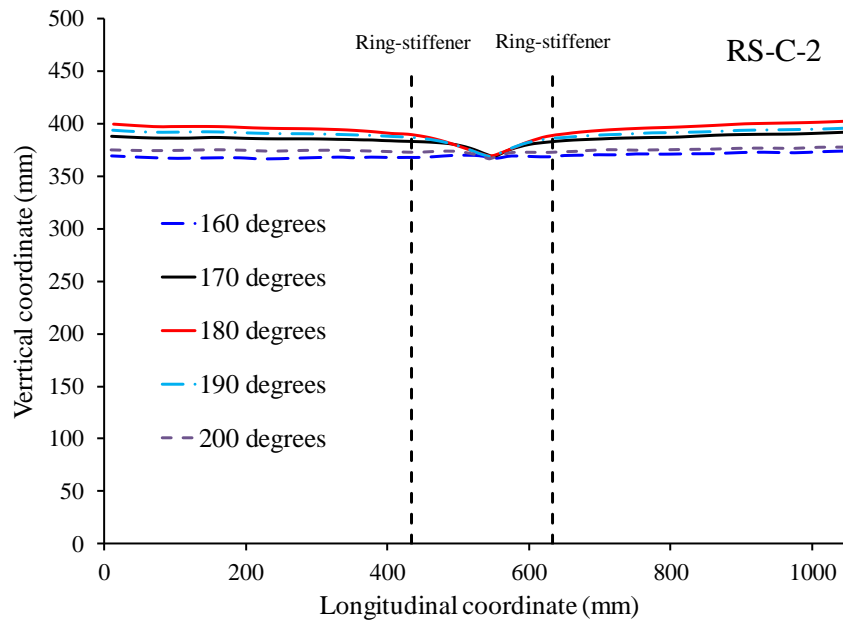
Fig. 3.19 Deformed shape of the ring-stiffeners: (a) RS-C-1 and (b) RS-C-2 [115].

The damage profiles and extents were measured using *CimCore* portable measuring arm device. By doing this, the exact hit location and the eccentricities in loading could be determined. The longitudinal and circumferential damage profiles for each model are shown from Fig. 3.20 to Fig. 3. 23, respectively. It is clear from the circumferential damage profile of RS-C-1 that the dent line is not horizontal due to large rotation of the striking mass before hitting the model. For RS-C-2, this rotation is small. For both models the longitudinal damage profiles prove that the ring-stiffeners do not much limit the damage in mid-bay. The outward bulging in dented cross-section is noticeable.

The tilting of ring-stiffeners bordering the mid-bay was also measured. The maximum out-of-plane displacement at the toe of stiffener web is taken as reference. It was recognized that the dent line shift along longitudinal axis has significantly affected the deformation of ring-stiffeners where the tilting of the ring-stiffener closer to the dent line is much larger.

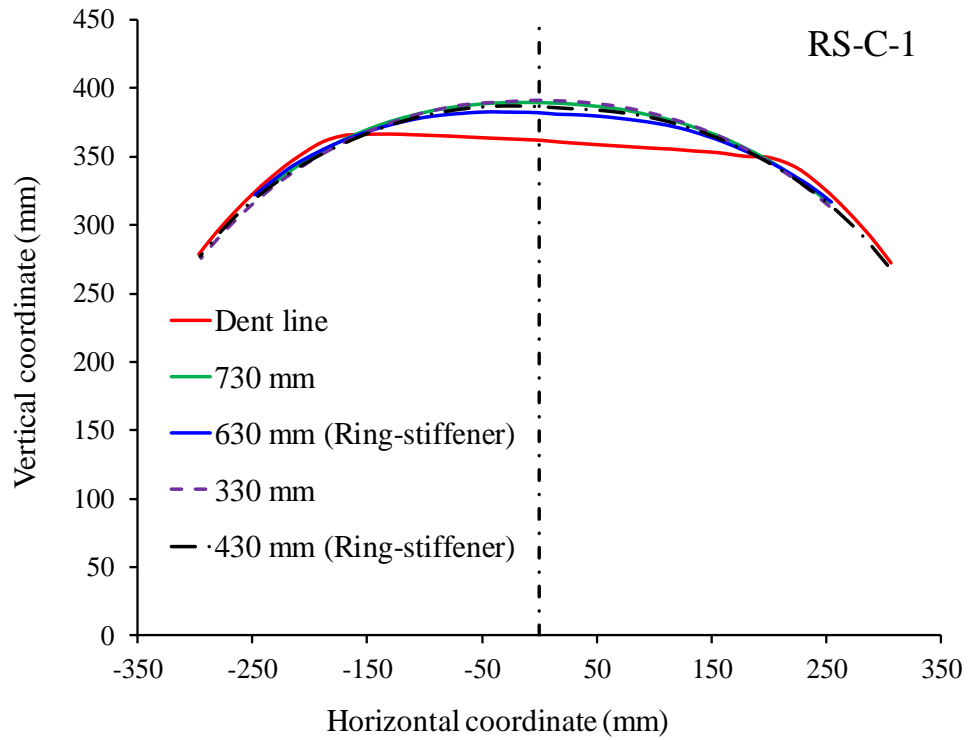


(a)

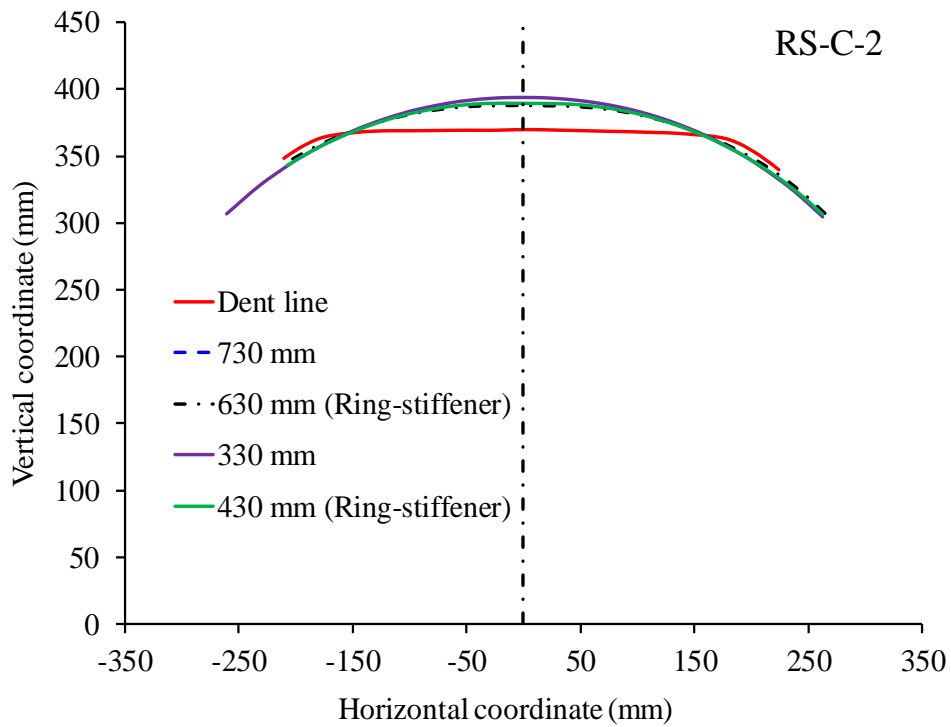


(b)

Fig. 3.20 Longitudinal damage profiles for models: (a) RS-C-1; (b) RS-C-2.

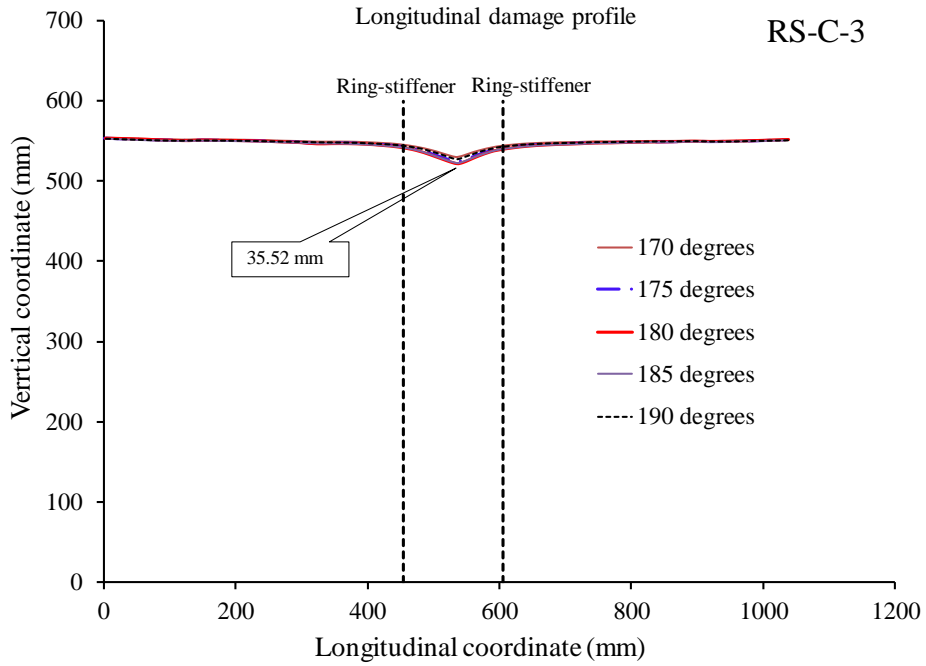


(a)

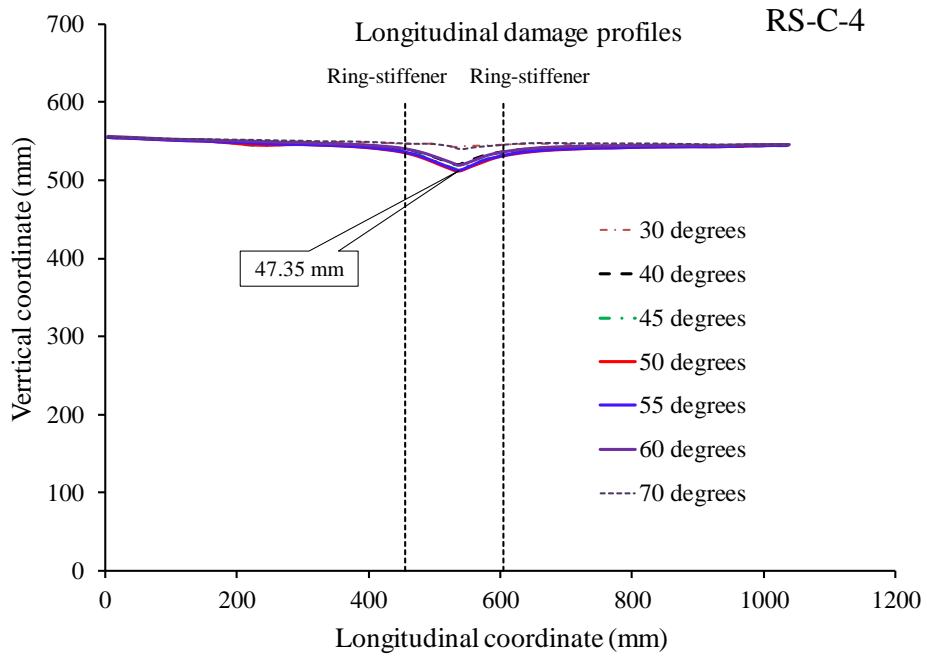


(b)

Fig. 3.21 Circumferential damage profiles for models: (a) RS-C-1; (b) RS-C-2.

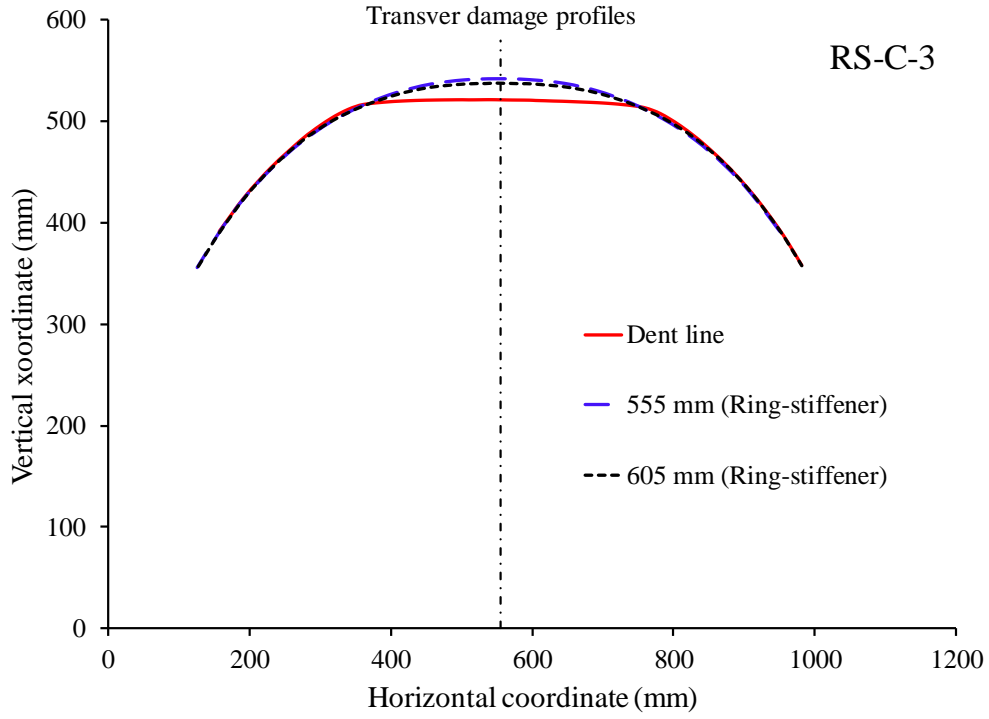


(a)

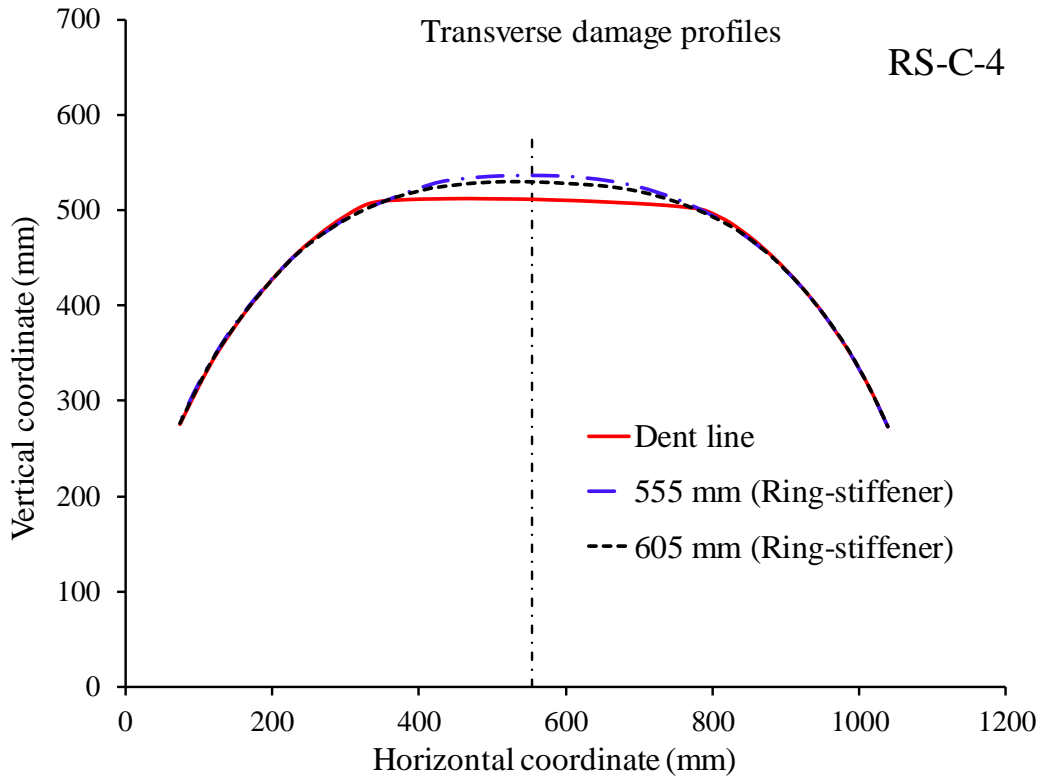


(b)

Fig. 3.22 Longitudinal damage profiles for models: (a) RS-C-3; (b) RS-C-4.



(a)



(b)

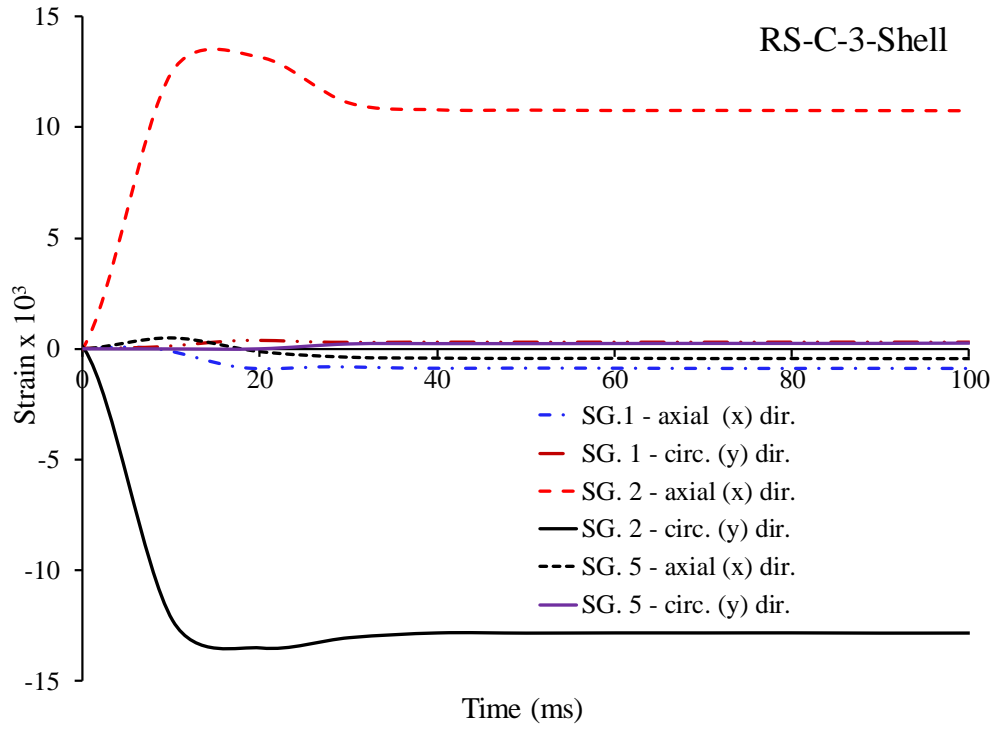
Fig. 3.23 Circumferential damage profiles for models: (a) RS-C-3; (b) RS-C-4.

The results of the damage extent measurements and permanent dent depth of the all models are listed in Table 3.5. The rotation of the dent line with respect to the longitudinal axis and vertical axis (centre plane) was also calculated, and is displayed in this table.

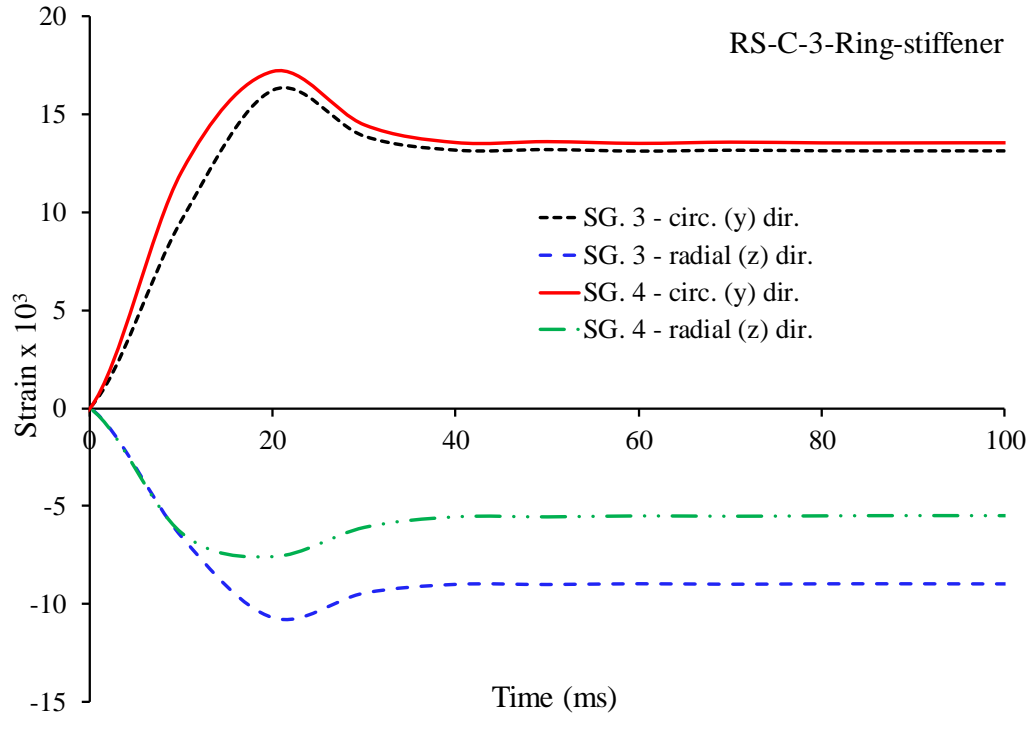
Table 3.5 Results of damaged stringer-stiffened cylinder models.

Model	SS-C-1	SS-C-2	SS-C-3	SS-C-4
Permanent dent depth (mm), d	45.92	34.14	35.52	47.35
Non- dimensional permanent dent depth, δ_d	0.115	0.085	0.065	0.086
Longitudinal shift impact line (mm)	27.15	16.3	9.0	7.0
Rotation angle of dent line about longitudinal axis ($^{\circ}$)	2.65	0.59	0.0	1.5
Rotation angle of dent line about vertical axis ($^{\circ}$)	0.87	1.67	0.0	0.0
Tilting of center ring-stiffener in denting area ($^{\circ}$)	6.98	5.34	4.35	7.56
Tilting of side ring-stiffener in denting area ($^{\circ}$)	2.72	1.33	1.20	1.0

The strain measurements give more details for understanding the deformation process. The filtered strain histories are shown in Figs. 3.24 and 3.25 for cylinder shell and ring-stiffeners of models RS-C-3 and RS-C-4, respectively. For model RS-C-3, according to the strain measurements at position 2 where closest to the impact line, the cylinder shell deformation is largest in both longitudinal and circumferential directions due to membrane stretching marked with high tensile and compressive strains. The strain measurements at position 1 and 5 are quite small when compared to other position. Because these positions are located far from the impact line. However, strain measurements at position 3 and 4, where strain gauges placed on ring-stiffeners, were high compressive and tensile strain in both radial and circumferential directions. For model RS-C-4, the strain measurements were obtained similar trend occur with model RS-C-3, but the strain magnitude of RS-C-4 is 30% higher than that of the RS-C-3 as a result of the increase in impact energy.

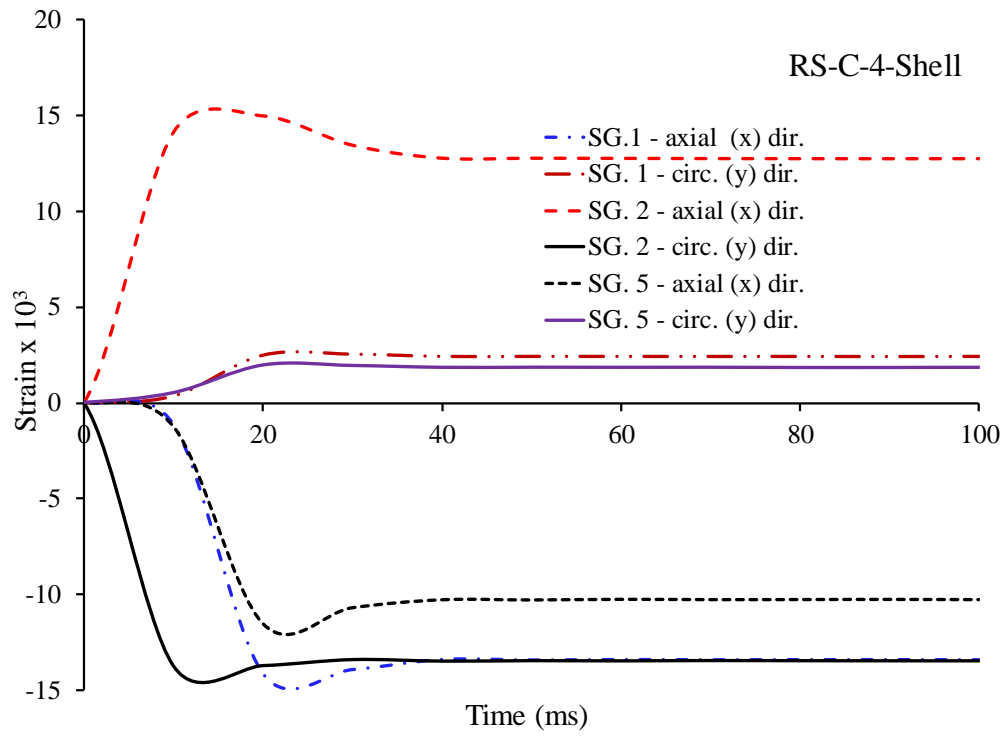


(a)

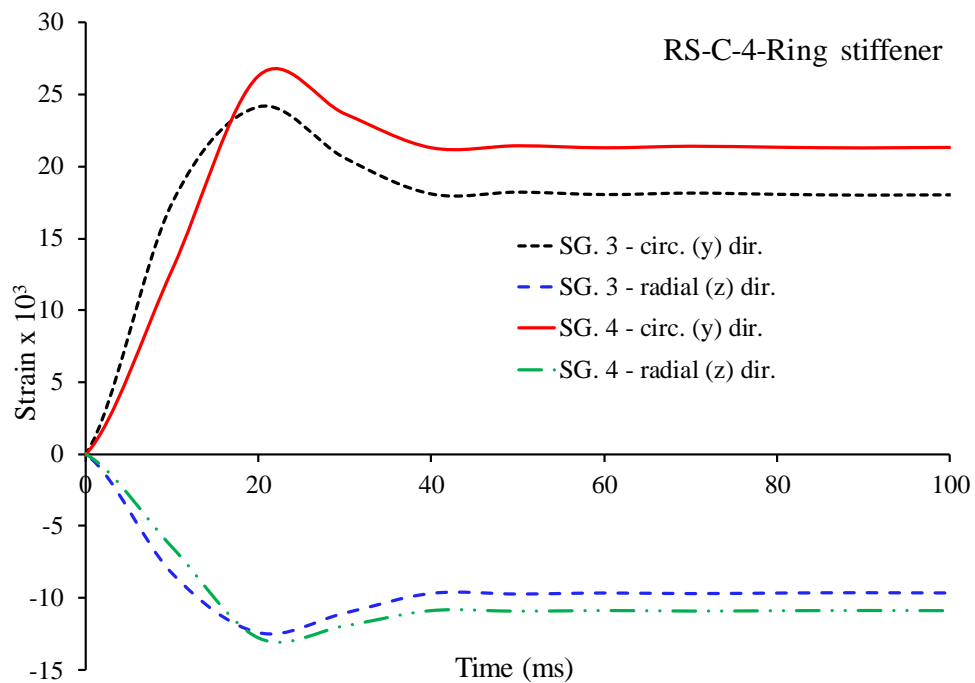


(b)

Fig. 3.24 Recorded strain histories of model RS-C-3 for: (a) cylinder shell; (b) ring-stiffeners.



(a)



(b)

Fig. 3.25 Recorded strain histories of model RS-C-4 for: (a) cylinder shell; (b) ring-stiffeners.

The force-displacement curves were obtained by combining the calculated force history from the acceleration data and displacement history, as shown in Fig. 3.26. Generally, the impact response is similar to the response of unstiffened cylinders and quasi-statically dented ring-stiffened cylinder models [104]. When the indentation increases, the slope of the force-displacement curve gradually decreases. In addition to the oscillations because of the dynamic nature of the problem, there are no sudden peak and trough, which indicate clear effect of deformation of the ring-stiffeners on the impact resistance and the dent depth.

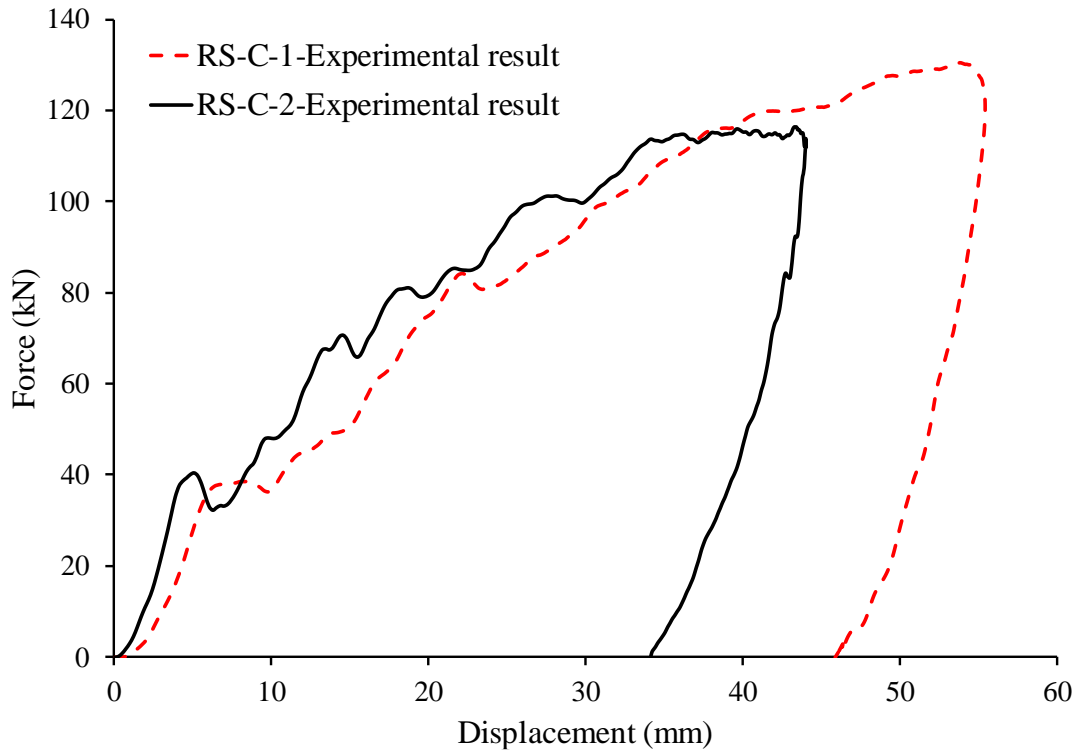


Fig. 3.26 Force-displacement curves for the test models.

3.2.2 Nonlinear finite element modeling

3.2.2.1 Element and boundary conditions

For the numerical analysis, the shell and ring-stiffeners were modelled using four-node curved shell elements (Abaqus S4R), with hourglass regulation and reduced integration. Thickness integration was performed using the Simpson rule, with five integration points throughout the thickness. The knife-edge striker was assumed to be rigid, and the R3D4 element was used. The contact between the indenting surface and struck model was defined using the general contact option in Abaqus. This contact algorithm uses a penalty method as the contact constraint.

The convergence test was performed by changing the mesh sizes of the modelling to select the optimum ones. In the study, the mesh size of the contact region was half of the outer region size. The convergence test results are shown in Fig. 3.27. As seen in the figure, when the element number was 43,400, the maximum deflection converged to a certain value, which was 97.1 % of the 170000 element case. The selected element size for the contact region (fine mesh) was 5 mm x 5 mm and that of the outer region (coarse mesh) was 10 mm x 10 mm.

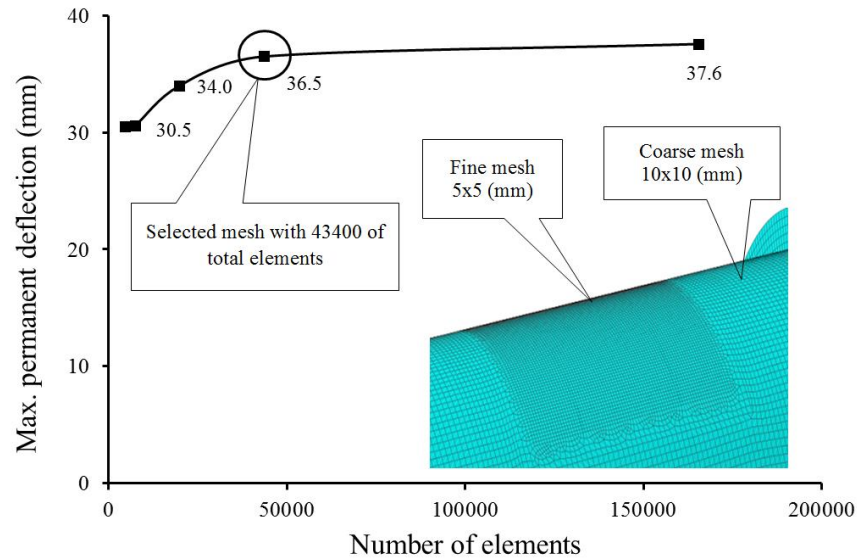


Fig. 3.27 Convergence tests for collision analysis.

In order to provide an accurate representation of the experimental support and simplify the numerical model, part of the supporting structures was modelled as a fixture, as illustrated in Fig. 3.28. The boundary conditions of the cylinders were fixed in all degrees of freedom at the bottom of the end flange as in the experimental conditions. The thickness of the end flange was 20 mm. It is similar to the effect of heavy bulkheads in the actual structures. For the striker, the mass and velocity were applied to the reference points to simulate the predicted impact energy. It should be noted that the rigid striker motions were governed by the reference point motions by assigning the initial collision velocity for the reference point in the vertical direction.

Following impact, the model vibrates elastically; therefore, Rayleigh damping was utilised to overcome these vibrations and rapidly attain a static equilibrium state. Rayleigh damping involves damping associated with low-frequency oscillations, which is proportional to mass and damping associated with high-frequency oscillations, which is proportional to stiffness. The former is used to include a damping matrix in dynamic analysis, which is obtained by multiplying the mass matrix of the system with the coefficient α . The coefficient α was set as the lowest natural

frequency of the model, which was obtained by means of modal analysis.

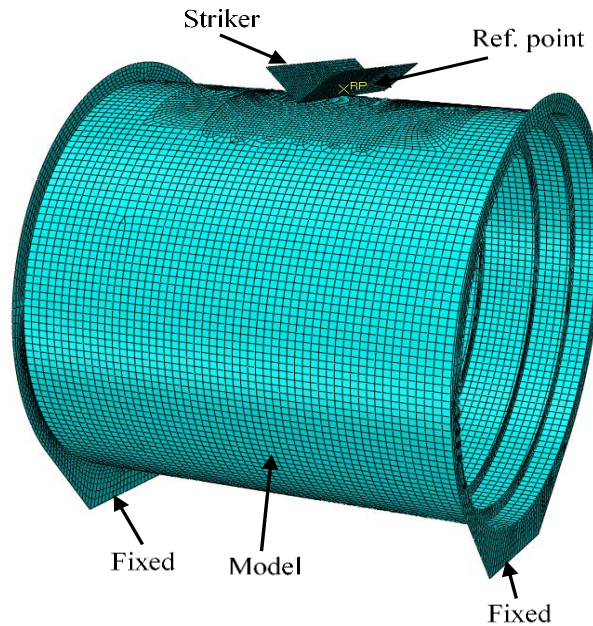


Fig. 3.28 Finite element model for collision analysis.

3.2.2.2 Material properties definition

For the collision analysis, the material properties were defined using the equations proposed by Cho et al. [140]. These equations were derived using the results of the large number of dynamic tensile tests on various steels. Deviations of the yield and ultimate tensile strengths and strains were quite small. Firstly, using the engineering strains and stresses of the yield, hardening-start and ultimate tensile points obtained from the static tensile tests, the corresponding true values were calculated using Eqs. (3.1) and (3.2). The true stresses and strains calculated are tabulated in Table 3.6.

Table 3.6 True stresses and strains.

$\sigma_{Y,tr}$	$\varepsilon_{Y,tr}$	$\sigma_{HS,tr}$	$\varepsilon_{HS,tr}$	$\sigma_{T,tr}$	$\varepsilon_{T,tr}$
306.8	0.00149	312.3	0.0194	469.1	0.1664

$$\sigma_{tr} = \sigma(\varepsilon + 1) \quad (3.1)$$

$$\varepsilon_{tr} = \ln(\varepsilon + 1) \quad (3.2)$$

where

σ, ε : engineering stress and strain, respectively.

σ_{tr} , ε_{tr} : true stress and strain, respectively.

$\sigma_{Y,tr}$, $\sigma_{HS,tr}$, $\sigma_{T,tr}$: true yield strength, true hardening start stress and true ultimate tensile strength, respectively.

$\varepsilon_{HS,tr}$, $\varepsilon_{T,tr}$: true hardening start strain and true ultimate tensile strain, respectively.

By substituting the values from Table 3.6 into Eqs. (3.3)-(3.5), the constitutive equation can be obtained considering the yield plateau and strain hardening.

$$\sigma_{tr} = E\varepsilon_{tr} \quad \text{when } 0 < \varepsilon_{tr} \leq \varepsilon_{Y,tr} \quad (3.3)$$

$$\sigma_{tr} = \sigma_{Y,tr} + (\sigma_{HS,tr} - \sigma_{Y,tr}) \frac{\varepsilon_{tr} - \varepsilon_{Y,tr}}{\varepsilon_{HS,tr} - \varepsilon_{Y,tr}} \quad \text{when } \varepsilon_{Y,tr} < \varepsilon_{tr} \leq \varepsilon_{HS,tr} \quad (3.4)$$

$$\sigma_{tr} = \sigma_{HS,tr} + K(\varepsilon_{tr} - \varepsilon_{HS,tr})^n \quad \text{when } \varepsilon_{HS,tr} < \varepsilon_{tr} \quad (3.5)$$

where

$$n = \frac{\sigma_{T,tr}}{\sigma_{T,tr} - \sigma_{HS,tr}} (\varepsilon_{T,tr} - \varepsilon_{HS,tr}) \quad (3.6)$$

$$K = \frac{\sigma_{T,tr} - \sigma_{HS,tr}}{(\varepsilon_{T,tr} - \varepsilon_{HS,tr})^n} \quad (3.7)$$

In order to consider the strain-rate hardening effects on the constitutive relationships, the equations provided in Ref. 140 were used. The equations were derived by using the results of dynamic tensile tests on various steels, including SS41, AH36, and HSLA. The dynamic values of yield strength, ultimate tensile strength, hardening start strain and ultimate tensile strain, expressed in terms of the strain rate $\dot{\varepsilon}$, were obtained using Eqs. (3.8) - (3.11). The true stress-equivalent plastic strain data generated from those equations for various strain rates (10 s^{-1} , 20 s^{-1} , 50 s^{-1} , 70 s^{-1} , 100 s^{-1} and 150 s^{-1}) are plotted in Fig. 3.29. The true plastic strain was calculated by means of Eq. (3.12) in order to apply the numerical model.

$$\frac{\sigma_{YD}}{\sigma_Y} = 1 + 0.3(E/1000\sigma_Y)^{0.5}(\dot{\varepsilon})^{0.25} \quad (3.8)$$

$$\frac{\sigma_{TD}}{\sigma_{YD}} = 1 + [0.16(\sigma_T/\sigma_{YD})^{3.325}(\dot{\varepsilon})^{1/15}]^{0.35} \quad (3.9)$$

$$\frac{\varepsilon_{HSD}}{\varepsilon_{HSS}} = 1 + 0.1(E/1000\sigma_Y)^{1.73}(\dot{\varepsilon})^{0.33} \quad (3.10)$$

$$\frac{\varepsilon_{TD}}{\varepsilon_T} = 1 - 0.117[(E/1000\sigma_T)^{2.352}(\sigma_T/\sigma_Y)^{0.588}](\dot{\varepsilon})^{0.2} \quad (3.11)$$

$$\varepsilon_{pl,tr} = \varepsilon_{tr} - \frac{\sigma_{tr}}{E} \quad (3.12)$$

where

σ_{YD} : dynamic yield strength;

σ_{TD} : dynamic ultimate tensile strength;

ε_{HSS} : static hardening start strain;

ε_{HSD} : dynamic hardening start strain;
 ε_{TD} : dynamic ultimate tensile strain;
 ε_T : static ultimate tensile strain;
 $\varepsilon_{pl,tr}$: true plastic strain.

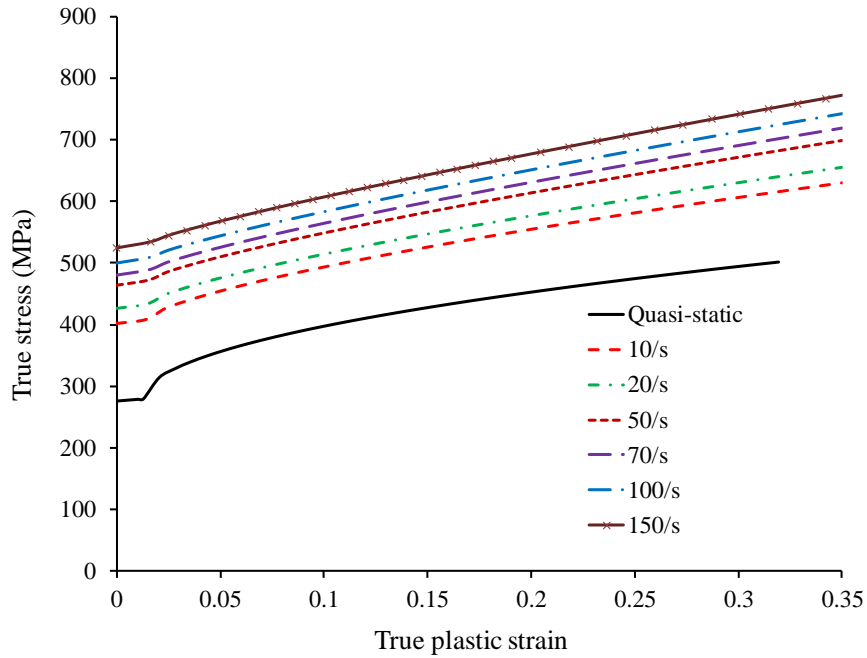


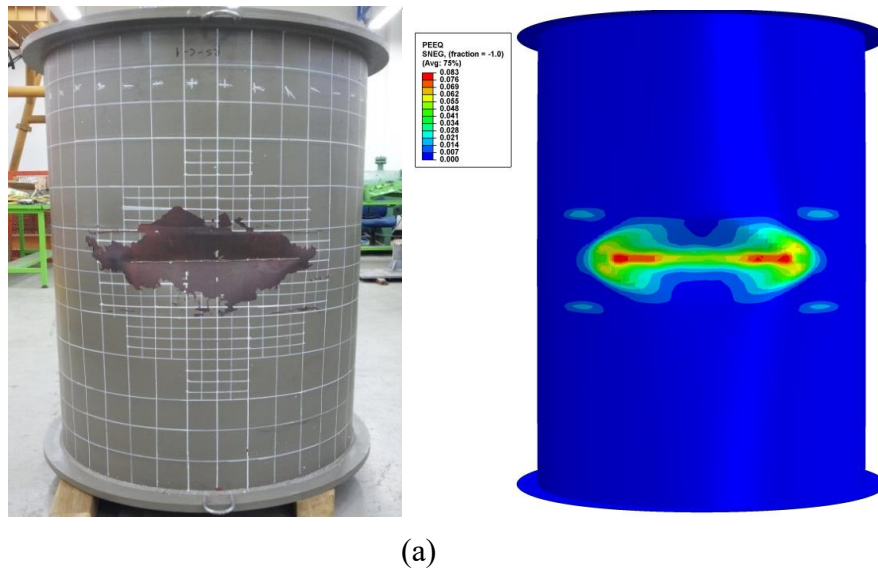
Fig. 3.29 True stress-strain curve at various strain rates for RS-C-3 model.

3.2.3 Numerical results and discussion

3.2.3.1 Damage generation

The deformed shapes of the models RS-C-1, RS-C-2, RS-C-3 and RS-C-4 compared with numerical results were shown in Fig. 3.30 and Fig. 3.31, respectively. In this figure, the equivalent plastic strain is highlighted, which is the distribution of the residual strains after the collision tests. There is a similar deformed shape between experimental and numerical results. The upper parts of the ring stiffeners adjacent to damage zone are completely flattened. The ring-stiffeners bordering the bay adjacent to the mid-bay are also deformed as the cracked coating confirms. The damage spreads in the longitudinal direction when the flattened part is tilted with a small degree of rotation outward. In addition, the numerically predicted longitudinal damage shapes are compared with the measured values in Fig. 3.32.

The numerically predicted responses were compared with the test responses using the force-displacement curves. The numerical analysis setup was modified to include the eccentricities in the previously mentioned loading. The results are shown in Fig. 3.33. The displacement here is the indentation on the cylinder, which is equal to the lateral displacement of the striking mass. Based on the accelerometer measurements, the displacement corresponds to the dent depth were generated. It is noted that the numerical results are consistent with the test results. The overall tendencies and peak force magnitudes were accurately predicted in the numerical analyses. More detail, the permanent deflection of model RS-C-1 and RS-C-2 in experimental results was 45.92 mm and 34.14 mm while that of numerical results was 44.84 mm and 36.5 mm, respectively. It means the difference between test and numerical results around 3%. In addition, there is a small discrepancy in the permanent deformations, but considering the uncertainties and errors in the experiments, this discrepancy is expected. Particularly for RS-C-1, the force levels were slightly overestimated when the displacement increased, which resulted in lower permanent deformations than the actual ones. The major cause of these differences may be the impact location and hit angle, which cannot be exactly estimated in the experiments and included in the numerical analyses.



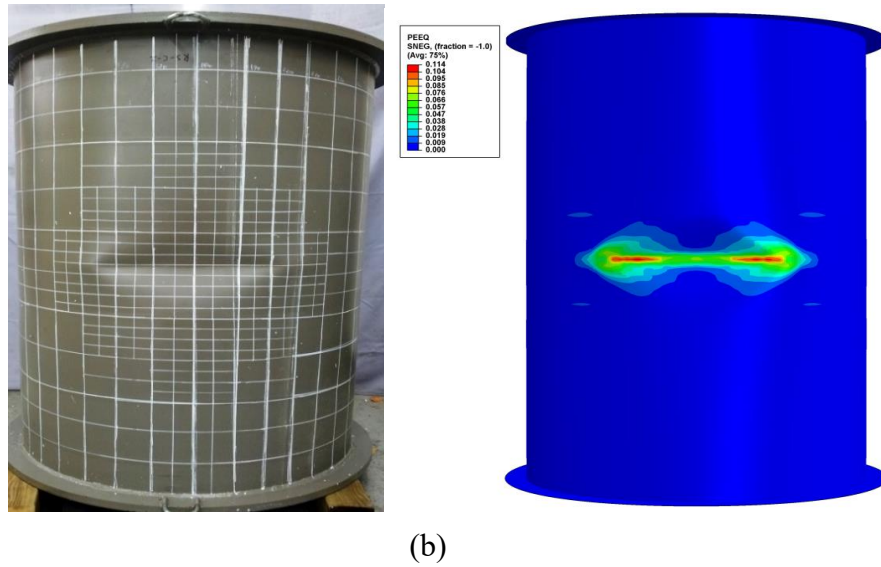
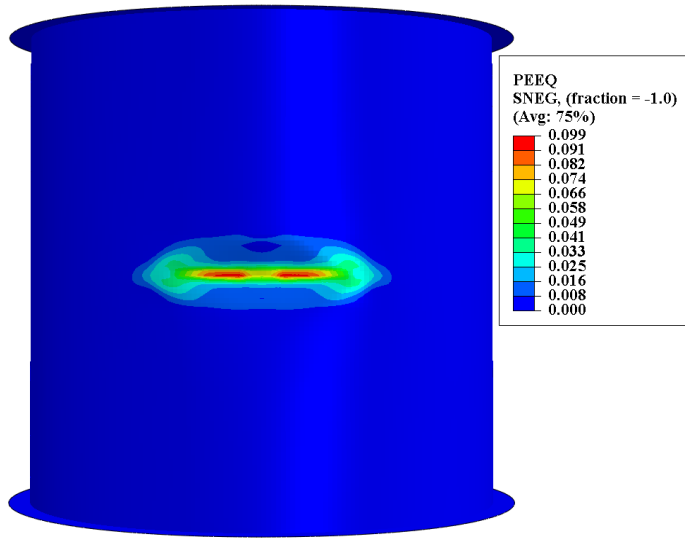
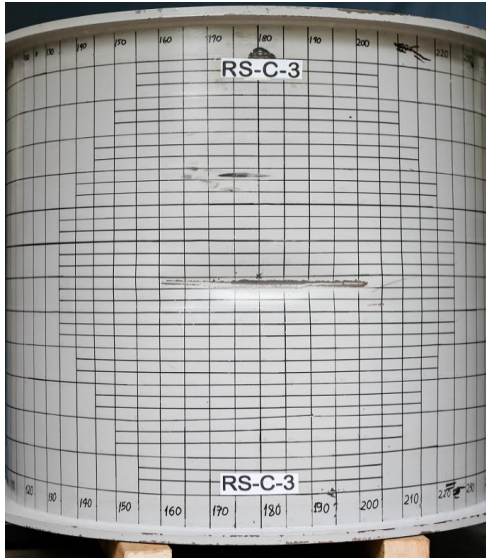


Fig. 3.30 Deformed shape of the models compared with numerical results:
 (a) RS-C-1 and (b) RS-C-2.

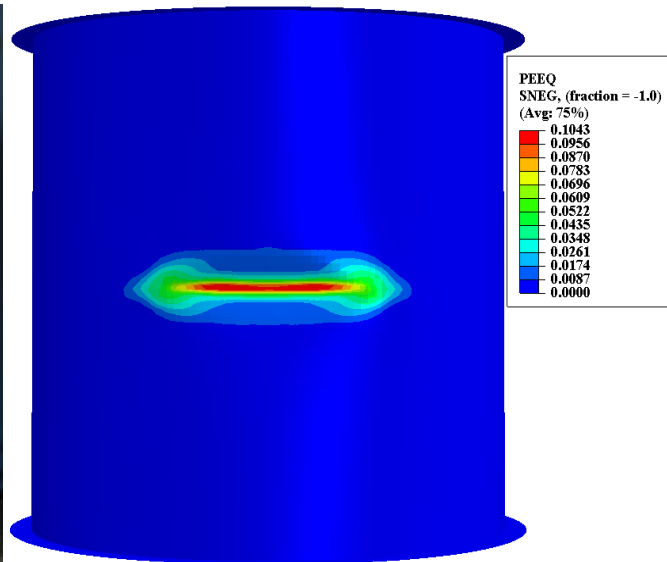
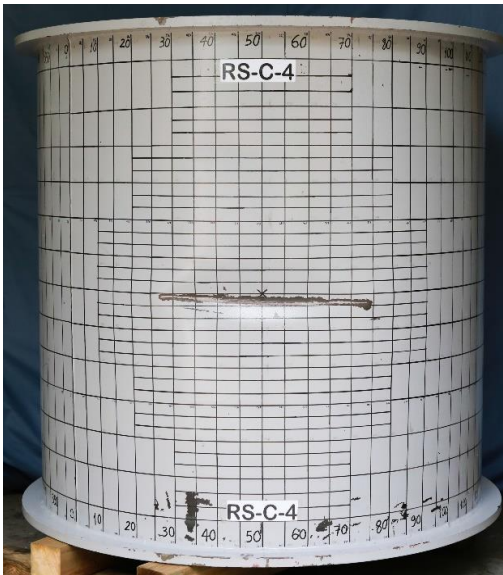
Generally, a good agreement was achieved between the numerical analysis and experimental results. Detailed comparisons of the permanent dent depth (d) and modelling uncertainty factor (X_m) are presented in Table 3.7. The mean of the X_m is 0.967, while the quite small coefficient of variation (COV) is 3.98 %. Therefore, it is concluded that good accuracy in the collision analysis was achieved.

Table 3.7 Comparison of the numerical results with the test results for collision models.

	RS-C-1	RS-C-2	RS-C-3	RS-C-4
Test result, d (mm)	45.92	34.14	35.52	47.35
FEA result, d (mm)	44.84	36.10	37.69	49.52
Bias (FEA/Test), X_m	0.976	1.057	1.061	1.046



(a)



(b)

Fig. 3.31 Predicted deformed shape of models compared with the test result for models:
(a) RS-C-3; (b) RS-C-4.

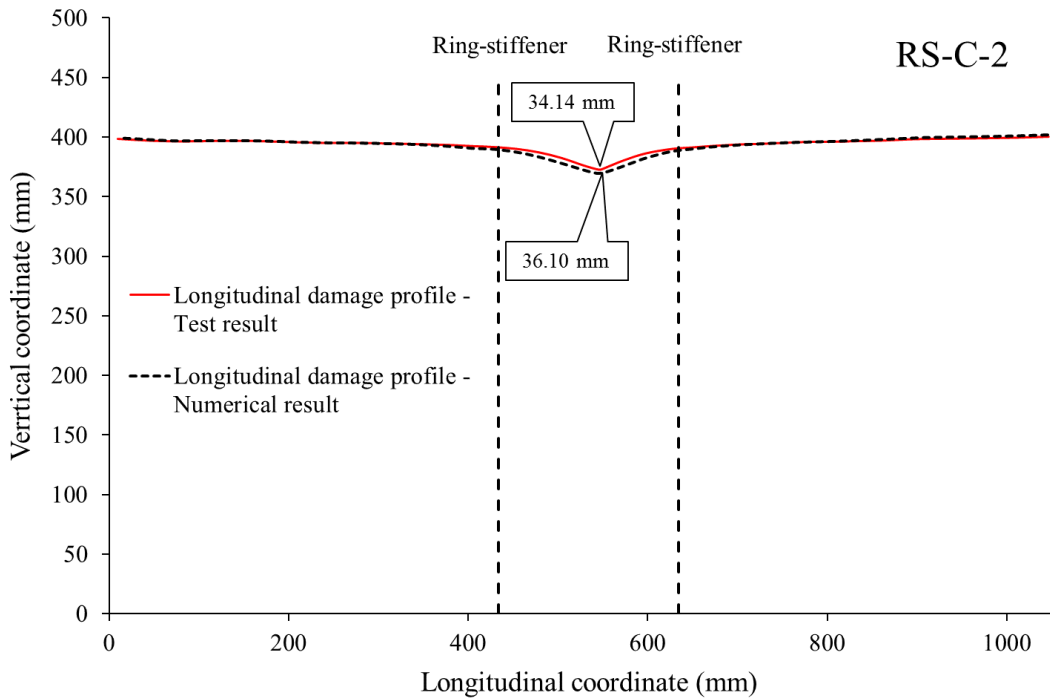
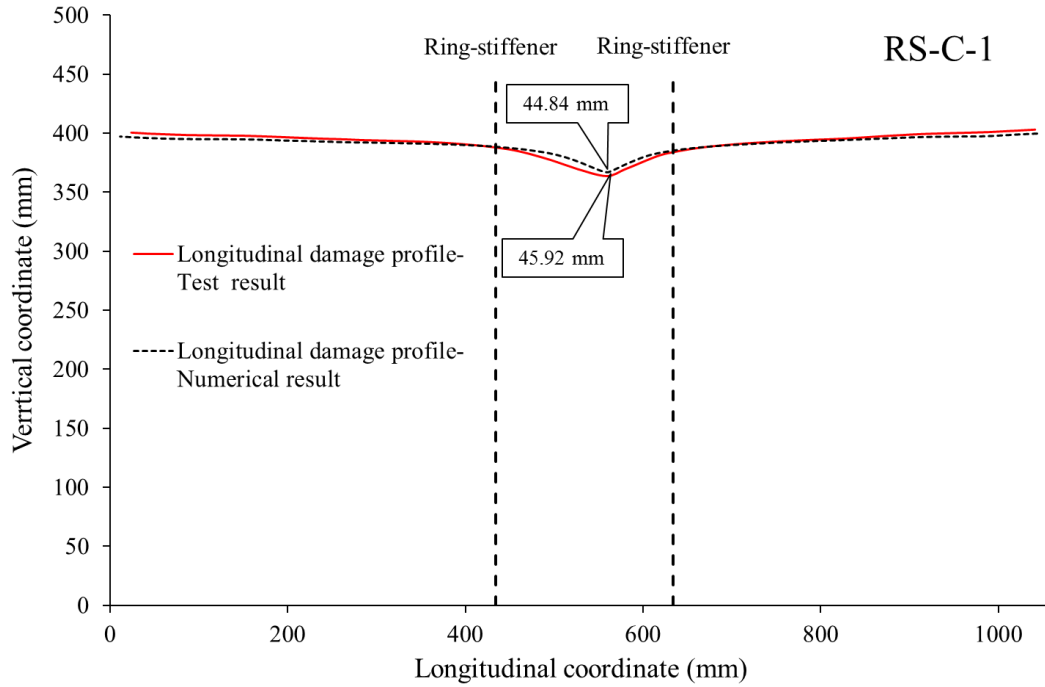


Fig. 3.32 Comparison of the longitudinal damage profiles obtained from experimental and numerical prediction.

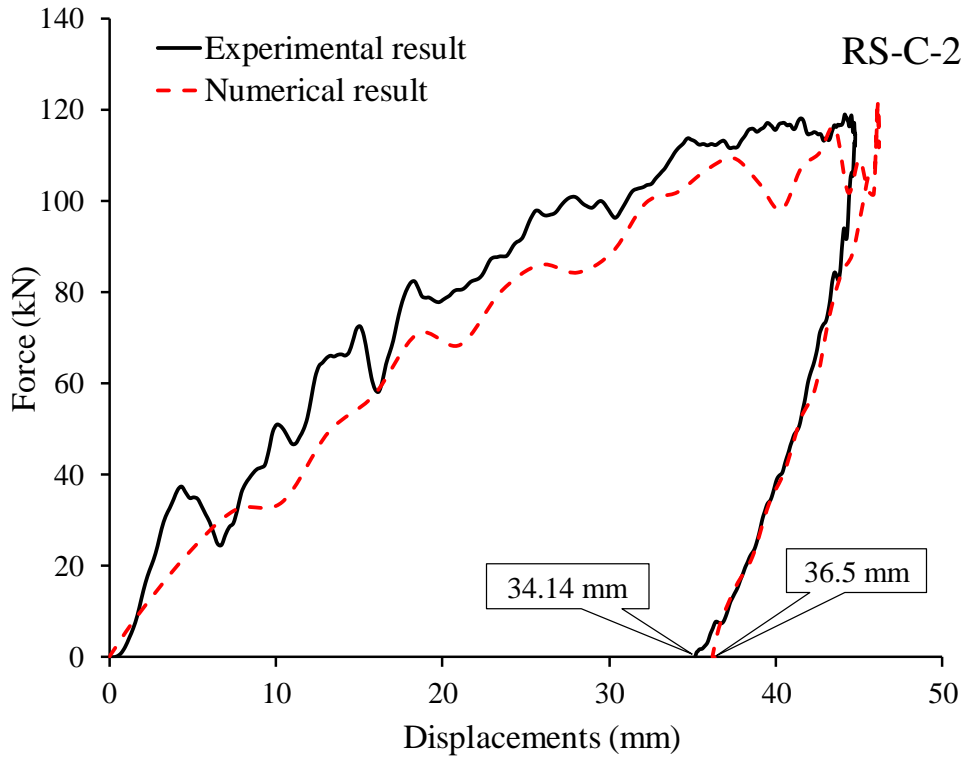
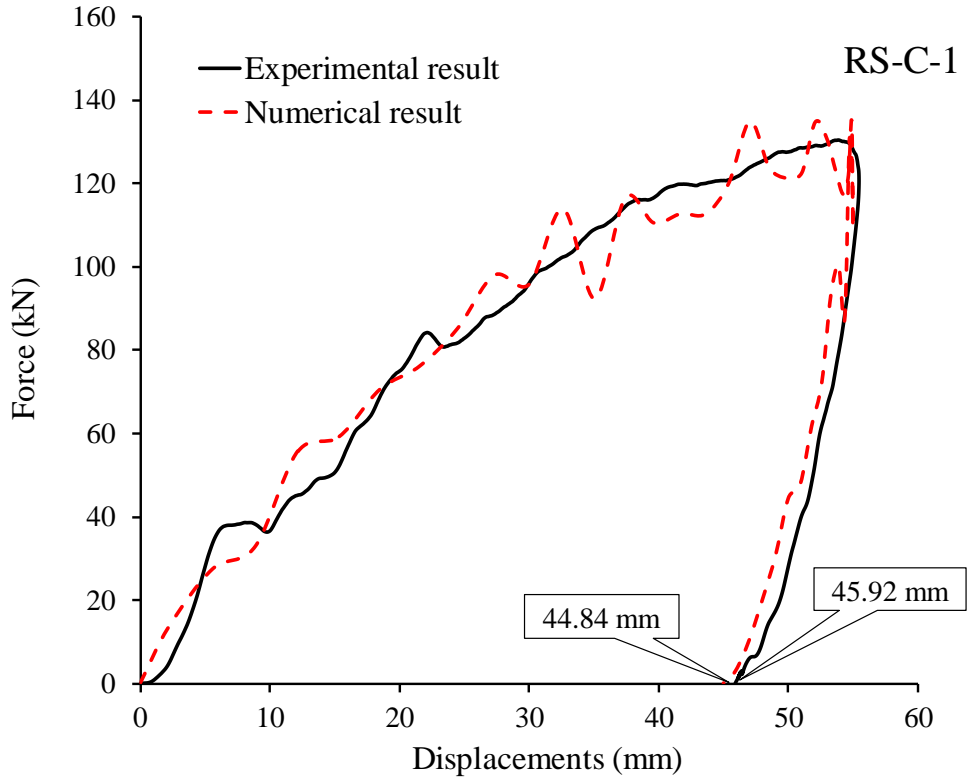


Fig. 3.33 Predicted force-displacement curve of models compared with the test result.

3.2.3.2 Energy partition

The energy partition throughout the impact duration is supplied further insights into the effect of each component structures such as cylindrical shell, ring-stiffeners as well as end plate, which could not be detected in the responses of force-displacement. In Fig. 3.34, the total internal and the plastic strain energy histories for the whole struck model, the cylinder shell and the ring-stiffeners of model RS-C-1 are shown. It is clear that the energy dissipated in the cylinder shell is the largest while that of the end plate is the lowest. As indicated in Table 3.8, approximately 65.38% and 33.67% of the total impact energy is dissipated by the cylindrical shell deformation and ring-stiffeners, respectively, while that of the end plate accounts for only around 0.95%. It indicates that the ring-stiffeners are also played a quite vital role in resisting collision.

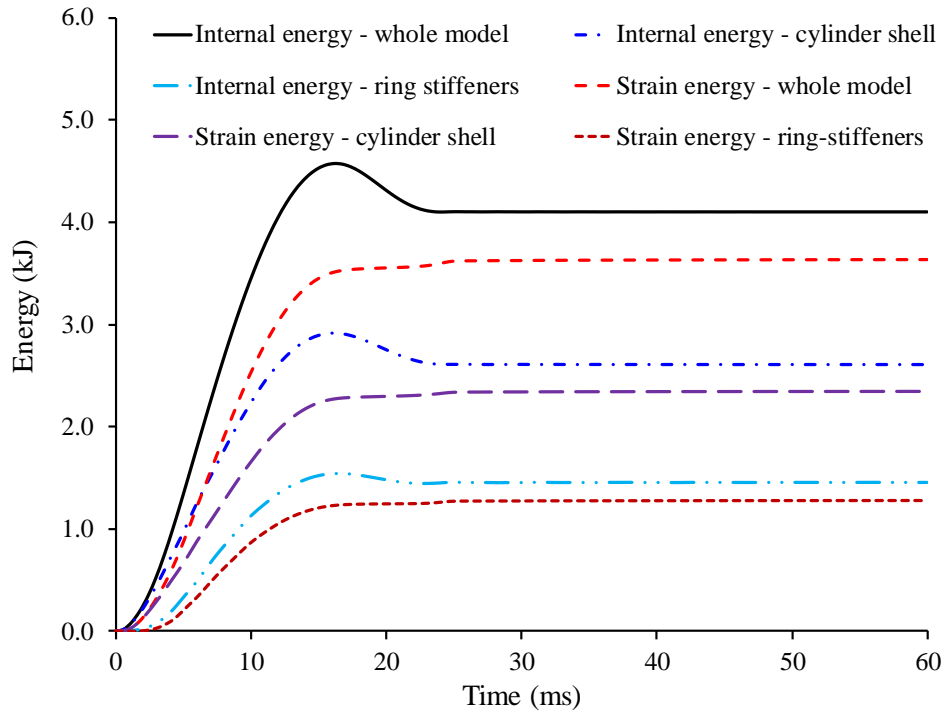


Fig. 3.34 Energy histories obtained numerically for model RS-C-1.

Table 3.8 Energy absorption of structural components.

Structural component	SS-C-1	
	Internal energy	Plastic energy
Cylinder shell	65.38 %	66.25 %
Ring-stiffeners	33.67 %	33.60 %
End plates	0.95 %	0.15 %

3.2.3.3 Effect of strain-rate hardening definition

It is well known that the strength of steel structures subjected to dynamic loading is sensitive to strain rate, the dynamic flow stress increase when increasing strain rate. Therefore, consideration of the strain rate effect by means of selecting material constant coefficients in the Cowper-Symonds equation as Eq. (3.13) can be discussed. The stress-strain dependence is assumed similar at all strain-rate levels, the strain-rate hardening behaviour was defined by simply scaling quasi-static plasticity data with a dynamic hardening factor, which is the ratio of the dynamic to static yield strength. The dynamic hardening factor depends only on the strain-rate magnitude and can be expressed as a power-law function, as proposed by Cowper and Symonds [141]. The coefficients in the Cowper and Symonds equation are common used as $D = 40.4 \text{ s}^{-1}$ and $q = 5$ for mild steel, and $D = 3200 \text{ s}^{-1}$ and $q = 5$ for high tensile steel. Furthermore, D can be calculated using Eq. (3.14), as provided by Lee and Kim [142].

$$\sigma_{YD} = \sigma_Y \left[1 + \left(\frac{\dot{\epsilon}_p}{D} \right)^{1/q} \right] \quad (3.13)$$

where

σ_{YD} : dynamic yield stress;

σ_Y : static yield stress;

$\dot{\epsilon}_p$: equivalent strain rate;

D, q : material constants for a particular material;

$$D = \begin{cases} 92000 \exp\left(\frac{\sigma_Y}{364}\right) - 193779 & \text{for } \sigma_Y > 271 \\ 40 & \text{for } \sigma_Y \leq 271 \end{cases} \quad (3.14)$$

Figure 3.35 displays the numerical investigation results for the effects of strain-rate hardening definitions on the force-displacement curves for the tested model RS-C-1. It is clearly illustrated that the overall response tendencies of the force-displacement curves are not affected by the strain-rate definitions. The stiffness of the struck model was increased or decreased following by the strain-rate effect definitions; therefore, the permanent deflection is dependent on these definitions. A detailed comparison of permanent deflection between the numerical and experimental results is provided in Table 3.9. It should be noted that, for this particular case, negligence of the strain-rate effect results in a 7.7 % larger permanent deflection for RS-C-1. When the Cowper-Symonds equation is used with the coefficients $D = 40.4$ and $D = 3200$, and determined by Eq. (3.14), the differences are 4.6, 2.0 and 5.6 %, respectively. Interestingly, when using the

direct input of test data, the permanent deflection of the numerical result is only 1.9% larger than that of the test result. Therefore, it is suggested that the dynamic material properties should be used to define plasticity at high strain rates in numerical simulations.

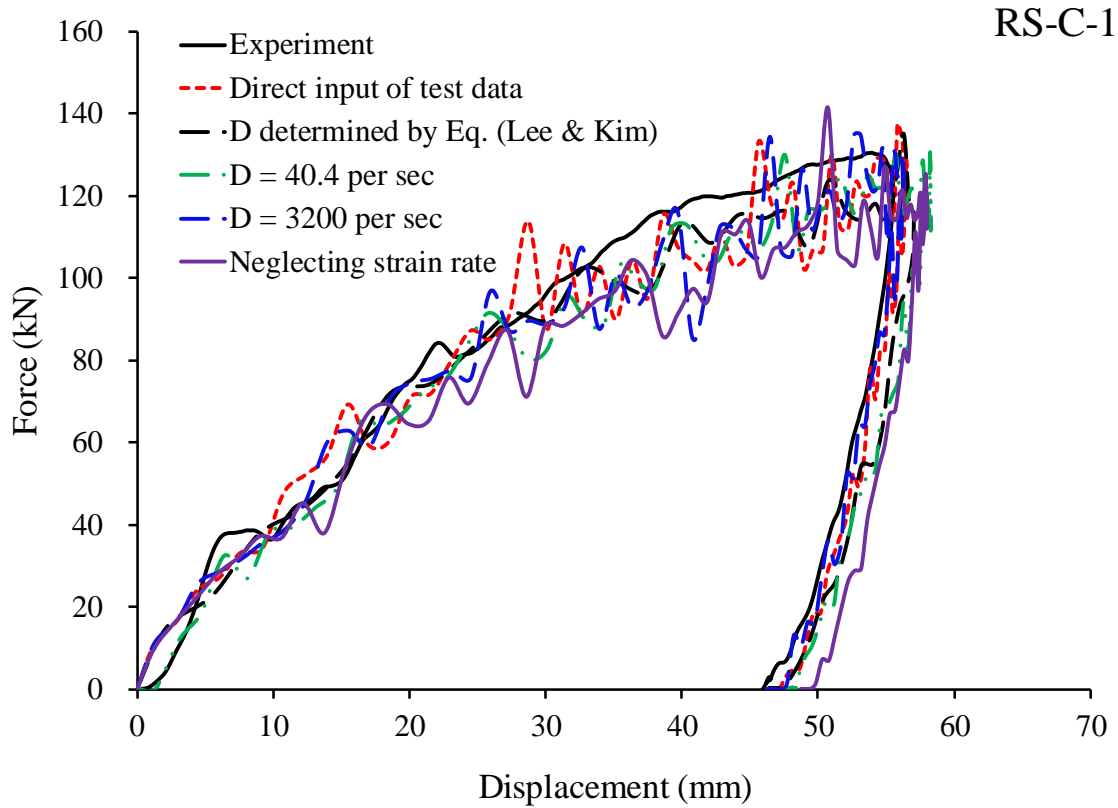


Fig. 3.35 Force-displacement curves for different strain-rate hardening definitions.

Table 3.9 Permanent displacement comparison for different strain-rate hardening definitions.

	Permanent deflection, d_d (mm)		X_m Num. pred./ test result
	Numerical predictions	Test result	
Direct input of test data [140]	46.84	45.92	1.019
$D = 40.4/s$	48.05		1.046
$D = 3200/s$	46.85		1.020
D determined by Eq. (3.14)	48.51		1.056
Neglecting the strain-rate effect	49.46		1.077

3.2.3.4 Effect of boundary conditions

The effect of these on restraining the axial displacement and rotation of the cylinder ends affects the cylinder shell's membrane resistance. In order to clarify this issue, the effect of idealising the boundary conditions was assessed by means of comparison with the fully modelled experimental conditions. Three types of boundary conditions were considered: fully fixed at the cylinder ends (case 1); free axial translations, restrained rotations and radial translations (case 2); only restrained radial translations at the cylinder ends (case 3). A comparison was carried out for the impact conditions of RS-C-1, and the resulting force-displacement curves are displayed in Fig. 3.36.

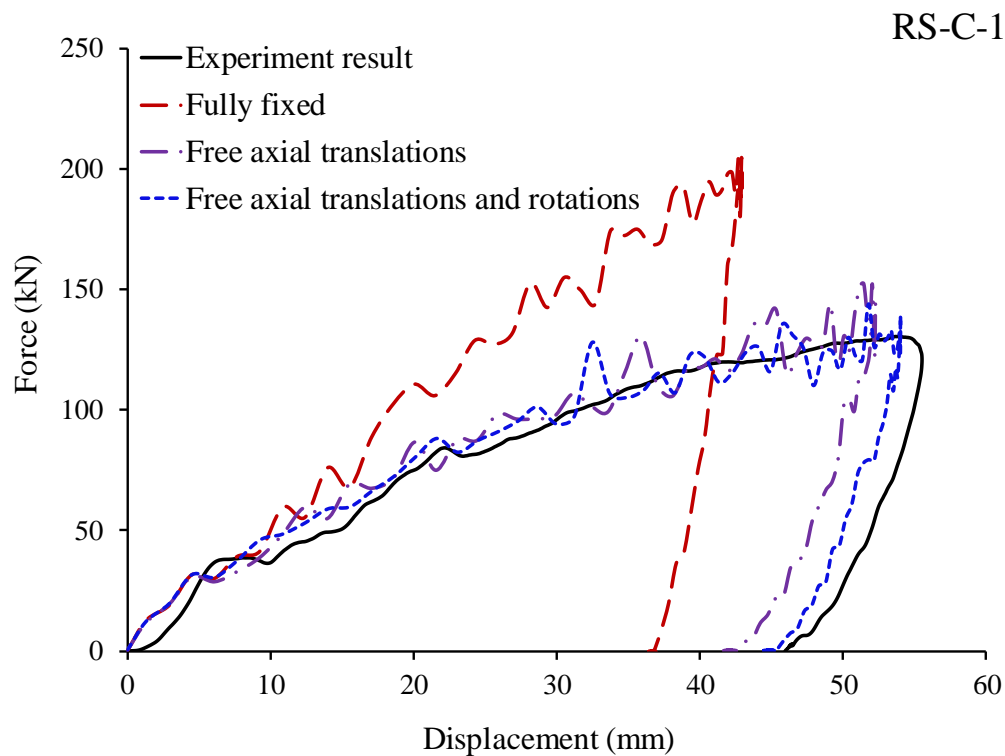


Fig. 3.36 Force-displacement curves for different boundary conditions for model RS-C-1.

In term of the comparing the permanent deflection prediction for each boundary condition with the experimental result, it is not surprising that the fully fixed condition does not effectively represent the actual case because the upper part of the end plate and ring were not restrained during the tests. Although the energy dissipated by the end plate and the end ring is not significant, their effect on restraining the axial translation of the cylinder ends affects the membrane resistance of the cylinder shell. However, similar results were obtained for case 2 of free axial translations and case 3 of free axial translations and rotations between the test and numerical results. Generally,

case 3, which was closely represented the actual case give the best prediction of the permanent deflection. It is concluded that the effect of the boundary conditions for any collision analysis should be considered carefully.

3.3 Dynamic impact tests on stringer-stiffened cylinders

This section describes experiments conducted on two small-scale steel stringer-stiffened cylinder models that were subjected to dynamic mass impact. The experimental work is significant and can be used to validate predictions for dynamic mass impact loading. The tests were simulated using a nonlinear finite element analysis. Numerical impact simulations were included for an assessment of the dynamic material properties, in order to highlight the effect of strain-rate hardening. The striker mass having a rigid knife-edge indenter is used to generate the damage. The results in this study have considerable importance providing a reliable and realistic view of the response.

3.3.1 Test models

3.3.1.1 Dimensions

Two internally stringer-stiffened steel cylinder models, which were fabricated and are denoted by SS-C-1 and SS-C-2, were tested. The model manufacturing process followed the standard methods and techniques for full-scale structures of this type. The stringer-stiffened cylinders were designed to reduce the influence of the boundary conditions on the buckling behaviour. The stringers and rings were dimensioned so that elastic tripping would be eliminated and these members could attain their maximum plastic strength. The cylinder shell was cut from 3-mm-thick steel sheets, cold-bent using rollers and welded to form a cylinder. The shell and stiffener thicknesses were nominally 3 mm; however, actual values were measured using an ultrasonic device and determined to be an average of 2.98 mm, which is marginally less than the nominal value. The outside diameter (D_o) and overall length (L) were 1100 and 1060 mm, respectively. In total, there were 20 stringers, which were flat bars with scantling as 65×5 mm. The ring-stiffeners were cut from flat sheets with a thickness of 5 mm, and the ring-stiffener web depth (h_{rw}) was 200 mm. The width and thickness of the ring-stiffened flange were 50 and 5 mm, respectively, while the stiffener spacing was 600 mm. A circular plate of 20-mm thickness was welded onto the left end of the cylinder, while a flange of 20-mm thickness was welded onto the right end. Similar to the effect of heavy bulkheads in actual structures, these end conditions ensured

that the cylinder ends remained circular. The end plate and ring had extensions at the bottom, which were bolted to the support plates. The scantlings and configuration of these models were determined by considering the requirement of conducting hydrostatic pressure testing for examining the residual strength of the damaged stringer-stiffened cylinder. The hydrostatic pressure testing facility required that one end be open and the other closed. The measured thicknesses of the models are provided in Table 3.10, and the test model dimensions are depicted in Figs. 3.37 and 3.38. The four holes at the bottom of the end plate and end ring are intended for bolting with the supports.

Table 3.10 Measured dimensions of stringer-stiffened cylinder models.

Model		SS-C-1	SS-C-2
Radius, R		550	550
Shell thickness, t		2.98	2.97
Total length, L		1060	1060
Stringer-stiffener	web height, h_{sw}	65.0	65.0
	web thickness, t_{st}	4.89	4.87
	web height, h_{sw}	200	200
Ring-stiffener	web thickness, t_{sw}	4.90	4.92
	flange width, b_{rf}	50.0	50.0
	flange thickness, t_{rf}	4.89	4.88

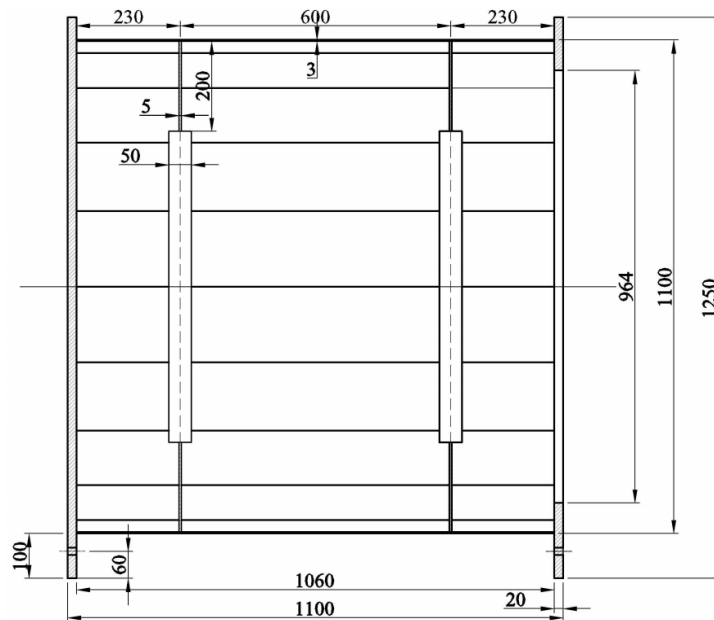


Fig. 3.37 Dimensions of stringer-stiffened cylinder model (unit: mm).

3.3.1.2 Material properties

The models were fabricated from a general-purpose structural steel material, namely, SS41. The mechanical properties were obtained by performing quasi-static tensile tests following the procedures listed in the Korean Standard KS B 0802 [136]. Six flat coupons were cut from each parent plate of the cylinder shell, ring-stiffeners and stringer-stiffeners and tested using a universal testing machine. Negligible variations were noted in the yield strength and Young's modulus, and these were further reduced by ensuring that all models were fabricated from a single steel sheet. Engineering stress-strain curves of cylindrical shells are provided in Fig. 3.39. The average mechanical properties of test models are given in Table 3.11.

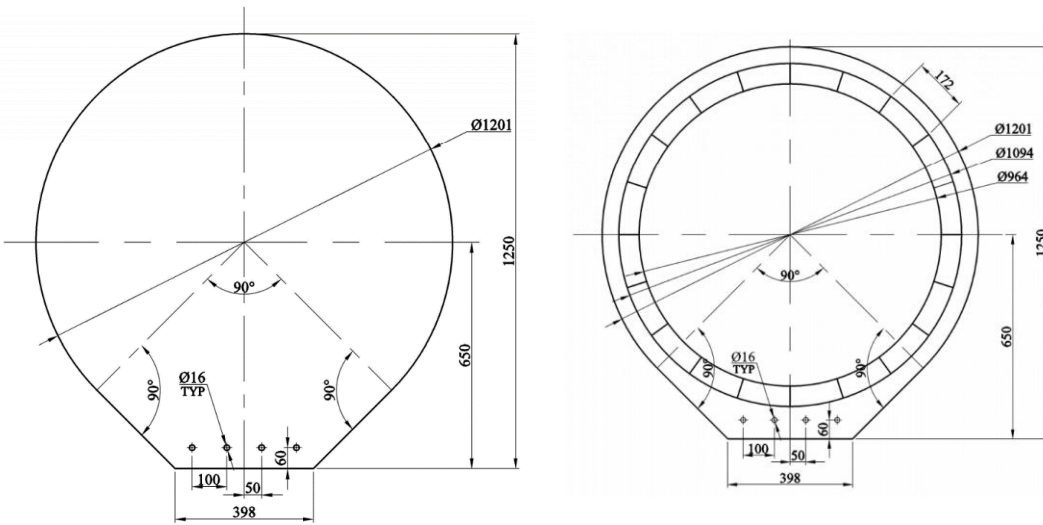


Fig. 3.38 Dimensions of end plate and ring (unit: mm).

The high speed tensile tests were also performed by following the procedures of ISO 26203-2:2011 [137]. The tests were conducted with various strain rate values corresponding to 10/s, 50/s and 100/s. The high speed tensile test setup is shown in Fig. 40 in previous section. The strain was measured using a high-speed camera while the force was measured by load cells and two strain gauges attached on both sides of the coupon. The dynamic tensile stress-strain curves were obtained from the Instron VHS-65/80-25 servo hydraulic machine as shown in Fig. 3.39. It is noted that some coupons were failed to obtain the results. The details of tensile test result on each coupon are given in Appendix C.

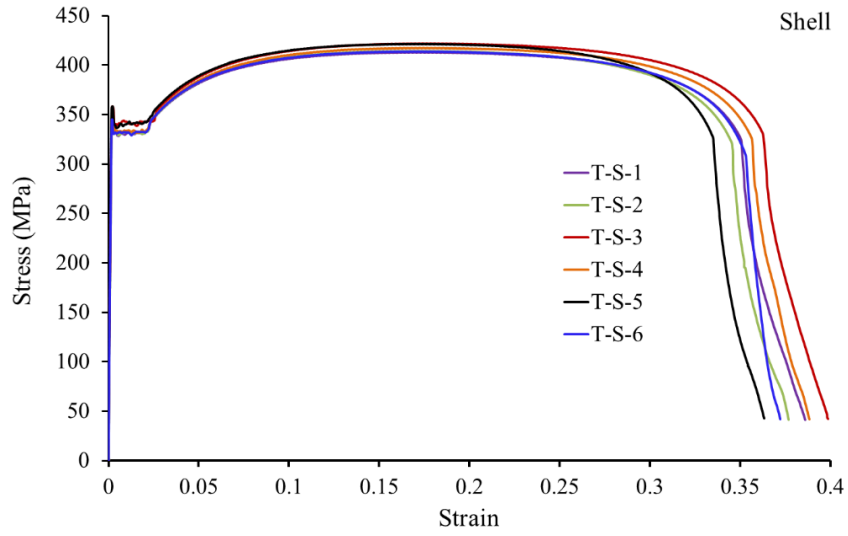
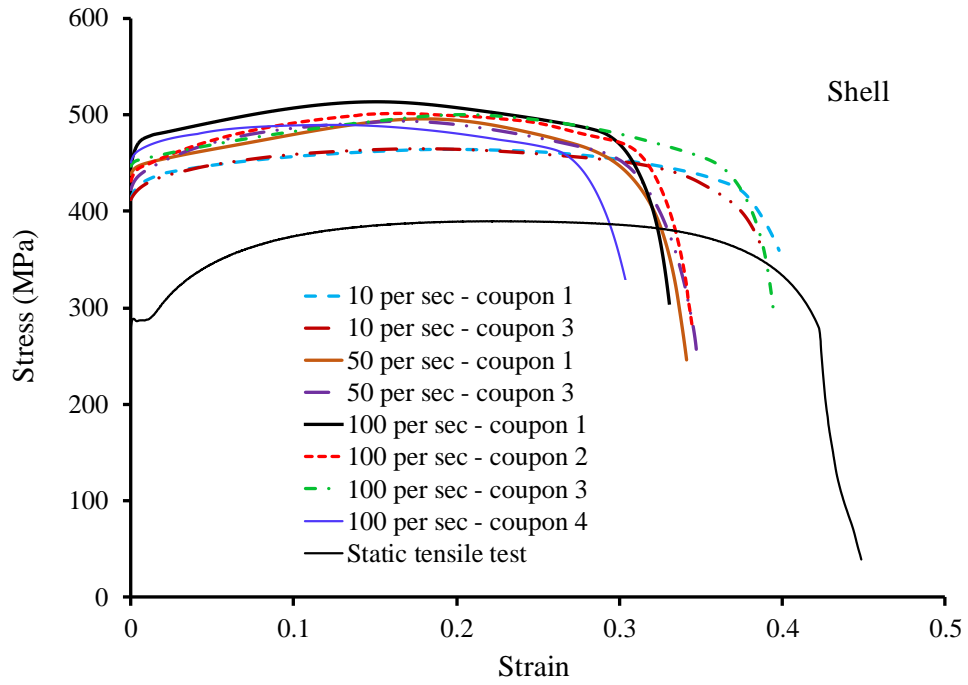


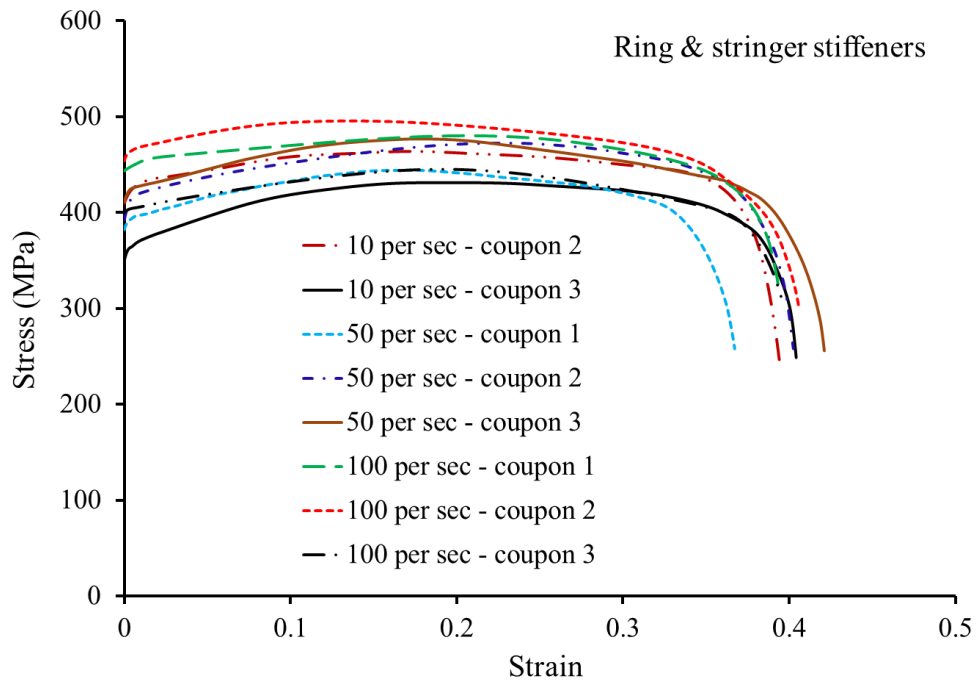
Fig. 3.39 Engineering stress-strain curve of cylindrical shell.

Table 3.11 Material properties of test models.

	Cylinder shell	Ring-stiffener		Stringer-stiffener
		web	flange	
Yield strength, σ_Y (MPa)	335.9	258.9	295.2	264.8
Ultimate tensile strength, σ_T (MPa)	417.0	390.5	394.5	389.5
Young's modulus, E (MPa)	210200	203100	203100	206500
Hardening start strain, ε_{HS}	0.0223	0.0133	0.0142	0.0149
Ultimate tensile strain, ε_T	0.1727	0.2328	0.2292	0.2288
Fracture strain, ε_F	0.3811	0.4697	0.4606	0.4622



(a)



(b)

Fig. 3.40 Engineering stress-strain curves of high speed tensile tests:
(a) Shell and (b) Ring & stringer stiffeners.

3.3.1.3 Initial shape imperfection measurement

The initial model imperfections were measured before mounting them onto the testing frame. The longitudinal grid lines were drawn at intervals of 5° on the inner and outer surfaces of the models. The circumferential grid lines were drawn with 50 mm spacing. The out-of-roundness of the cylinders was evaluated at each longitudinal point of these lines, based on the measurements obtained using a laser portable arm with a precision of 0.05 mm. A high-end version device, the CimCore laser probe, was used to capture the point and convert it into 3D coordinates in commercial CAD software packages. Prior to measurement, levelling was conducted and the reference point was obtained to minimise errors during measurement. This procedure corresponds to a radial measurement of the shape. The measurements were performed from the outside for 21 points on one line. A total of 1512 measurement points were used to construct the complete circular shell, as illustrated in Fig. 3.41.

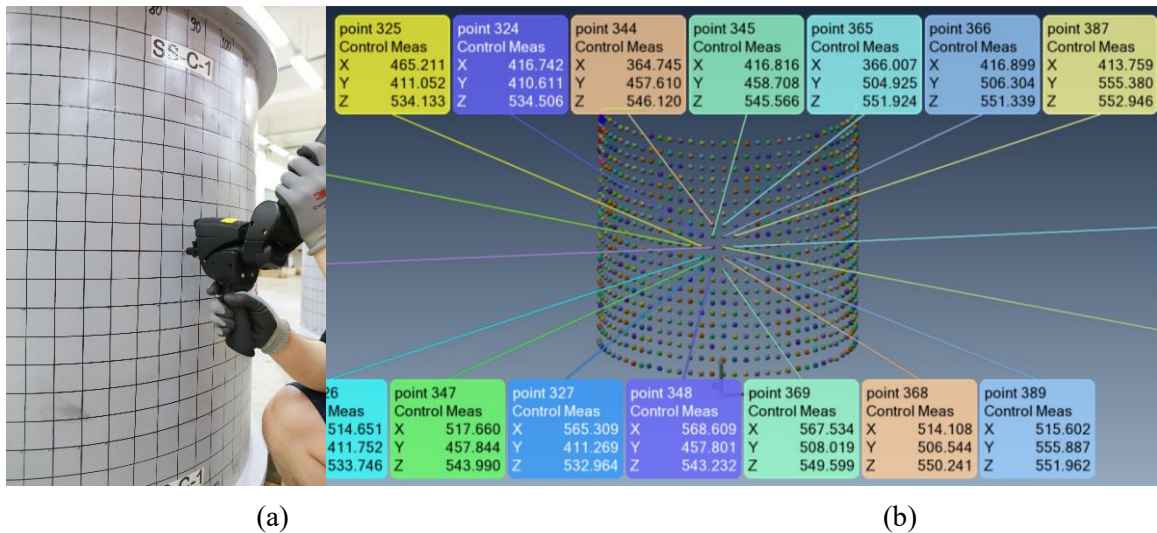


Fig. 3.41 Out-of-radius measurement of shell model SS-C-1:
 (a) CimCore device and (b) 3-D coordinates.

The cross-sectional shell of the initial imperfection of models SS-I and SS-C-2 are shown in Fig. 3.42. In the figure, the magnitude of initial deflection was exaggerated by 10 times. The out-of-roundness measurement results are summarised in Table 3.12. The maximum out-of-roundness values were smaller than 0.5% of the cylinder radius R , which was the upper limit of tolerable imperfection for stringer-stiffened cylinders according to API [143].

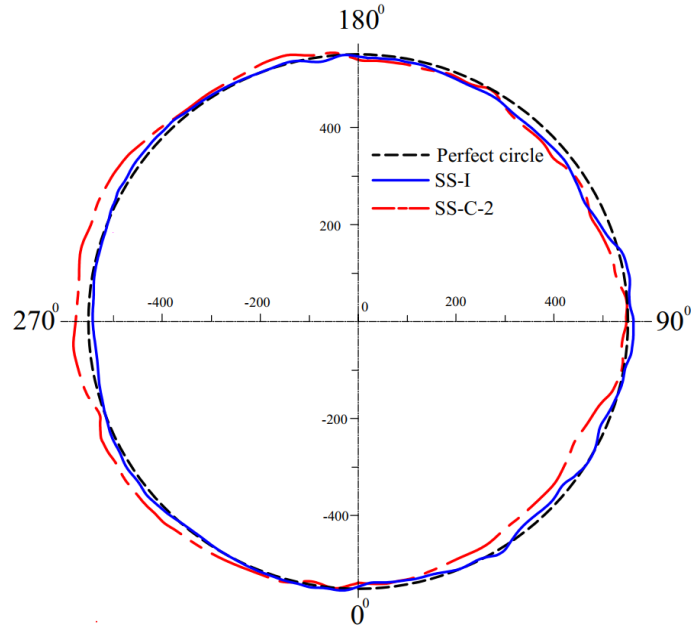


Fig. 3.42 Cross sectional shell of models SS-I and SS-C-2 at the mid-bay.

Table 3.12 Measurement results of out-of-roundness.

Model	SS-C-1	SS-C-2
Max. out-of-roundness	0.38% R	0.41 % R
Location	230 mm*, weld line (0^0)	830 mm*, weld line (0^0)

Note: * indicates distance from end-plate.

3.3.1.4 Experimental set-up

The experiment was conducted using a free-fall testing frame, as illustrated in Fig. 3.43. This testing frame was used successfully in earlier impact tests for ring-stiffened cylinders. There is a pulley at the top of the frame tower that guides and holds an electromagnet attached to the striking mass. The height of the striking mass can be varied in order to achieve the desired impact energy. Once the electromagnetic force has been cut off, the striking mass falls and accelerates due to gravity. The velocity of the striking mass is determined straightforwardly by equating its potential energy to its kinetic energy prior to impact.

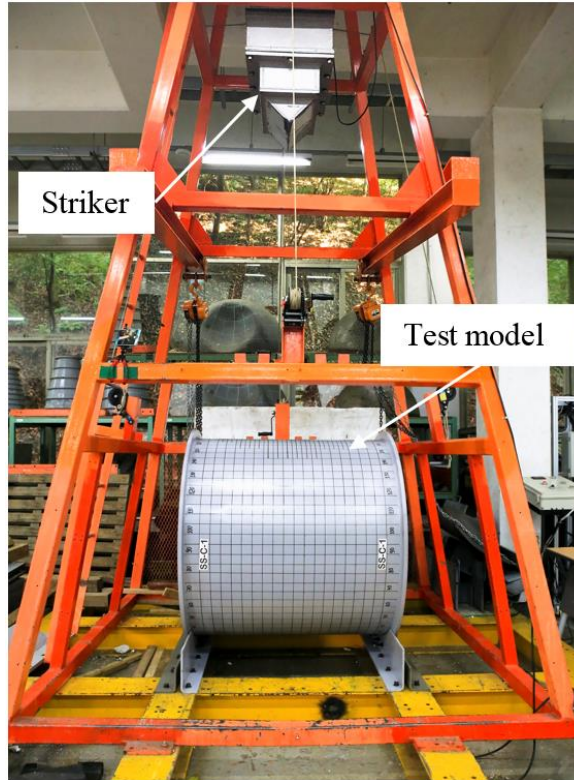


Fig. 3.43 Drop testing machine.

The striking masses applied were 500 and 600 kg for the SS-C-1 and SS-C-2 models, respectively. The striker had an indenter with a knife-edge tip and was rounded with a radius of 10 mm. Different striking masses and drop heights were used for each model. The dimensions of the striking mass and its indenter surface are presented in Fig. 44, while the experimental conditions for each model are listed in Table 3.13.

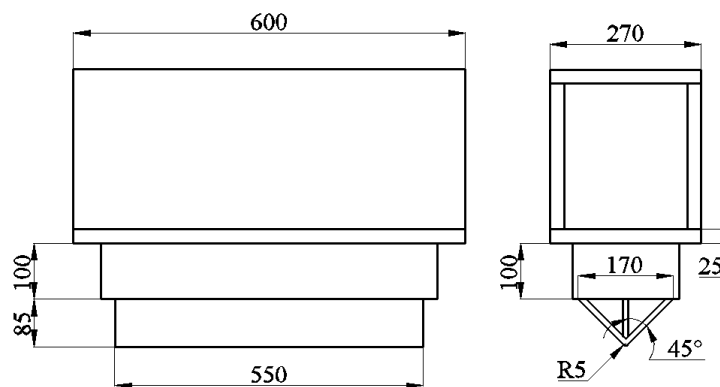


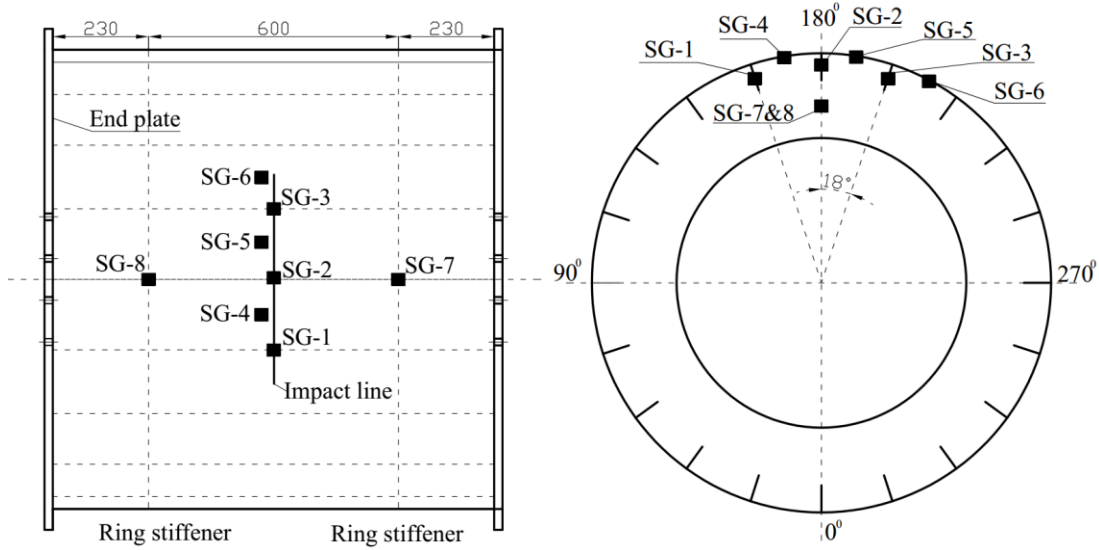
Fig. 3.44 Dimensions of striker mass and its indenter.

Table 3.13 Impact test conditions for stringer-stiffened cylinder models.

Model	SS-C-1	SS-C-2
Drop height, H (mm)	1600	1580
Impact velocity, v (m/s)	5.60	5.57
Striking mass, M (kg)	500	600
Kinetic energy, E_k (J)	7848	9300

Two-direction strain gauges were bonded in eight positions. The first three strain gauges were placed on the surface of the stringer-stiffeners bordering the mid-bay, located along the expected impact line. The second three strain gauges were placed on the inner surface of the cylindrical shell, 30 mm alongside the expected impact line. The final two strain gauges were placed on the surface of the ring-stiffener webs. The arrangement of the strain gauges is indicated in Fig. 3.45.

It is critical to describe the experimental boundary conditions in detail, because the impact response is highly sensitive to the restraints provided in certain cases [119, 123]. The models were firmly fixed to 10-mm-thick support plates using four bolts, as illustrated in Fig. 3.46. The support plates were in turn bolted to the rigid foundation of the testing frame. A detailed view of the boundary conditions is provided in Fig. 3.47. It should be note that the support plates were in contact with only the end plate and ring; therefore, a certain portion of the end plate and ring bottom was fixed. On the upper part, the displacements and rotations were free. Consequently, the cylinder shell remained circular at both ends; however, the axial translation and rotations were partially restrained, depending on the stiffness of the end plate and ring.



- On stringer-stiffener
 - Position 1 (162° , 530 mm*)
 - Position 2 (180° , 530 mm)
 - Position 3 (198° , 530 mm)
- On shell
 - Position 4 (170° , 500 mm)
 - Position 5 (190° , 500 mm)
- On ring-stiffener
 - Position 7 (180° , 830 mm, 425 mm)
 - Position 8 (180° , 230 mm, 425 mm)

Note: * indicates distance from end-plate

Fig. 3.45 Strain gauge arrangements.

3.3.1.5 Test results

The deformed shapes of the models are illustrated in Fig. 3.48. Following careful assessment of the damage profile, it was determined that the impact location of the SS-C-1 model shifted 11 mm from the mid-bay towards the open end. For the SS-C-2 model, the impact location was determined as being approximately at the mid-bay, for which the striking mass rotation when it leaves the electromagnet is likely to be the main cause. The damage can be described as a local denting in the impact region. The local dent results in a flattening of the cross-section, with a length equal to that of the indenter. The damage can be defined as a flattened section around the perimeter, an outward bulging of the zone adjacent to the dent and semi-elliptical-shaped flattened zones on either side of the dent zone.

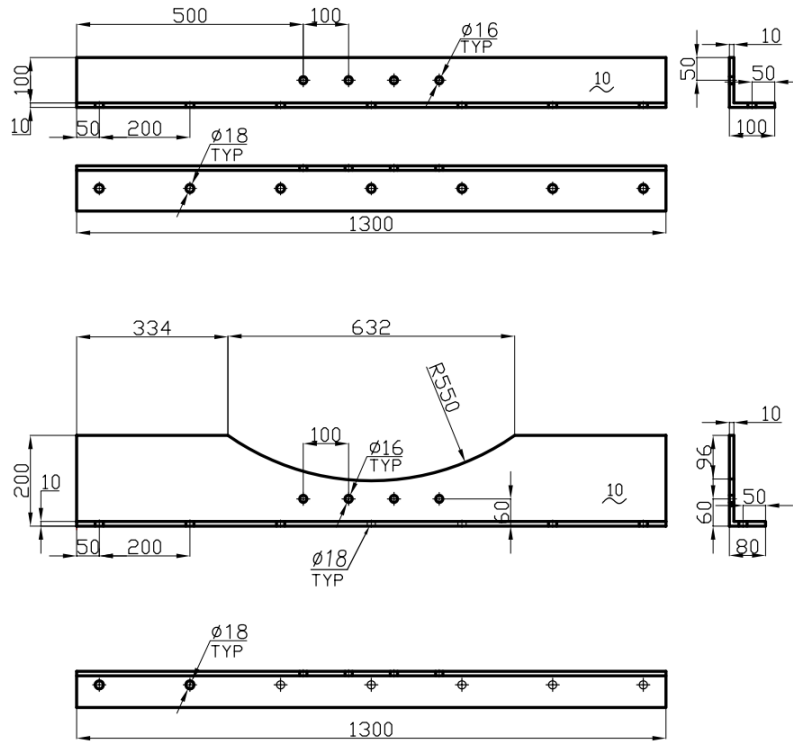


Fig. 3.46 Dimensions of support plates.

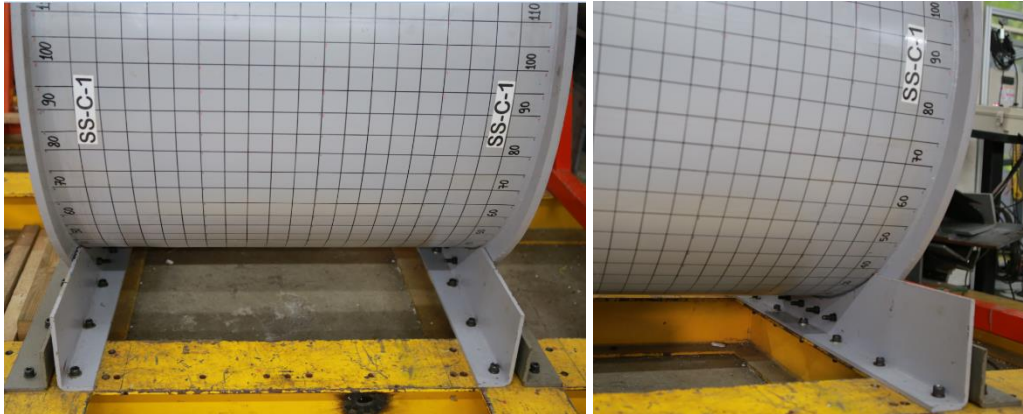


Fig. 3.47 Detailed view of experimental boundary conditions.

Figure 3.49 illustrates the deformed shape of the stringer-stiffeners, where the upper parts of the stringer-stiffeners adjacent to the damage zone were completely flattened. The inner span of a given stringer between two ring-stiffeners collapsed as a beam, with a clear three-hinge mechanism. The stringers acted as beams that resisted loading until they formed plastic hinges and therefore yielded to the indenter loading. Furthermore, the larger elastic spring-back following retraction of the indenter was noticeable in the actual tests. Consequently, the permanent

deformation was smaller in the test results. It is also noteworthy that local tripping of stringer-stiffeners was apparent in the joint of the stringer-stiffeners with ring-stiffeners.

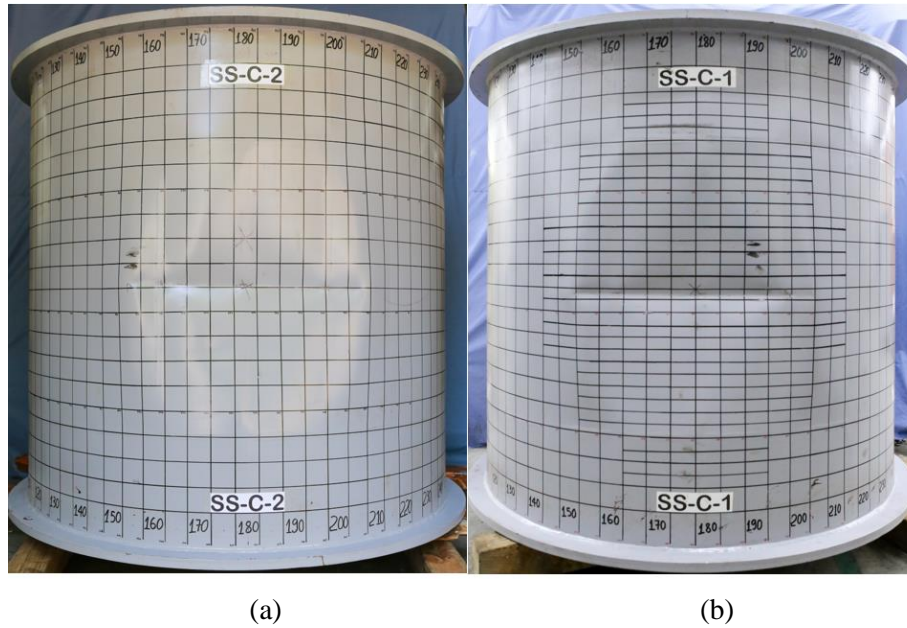


Fig. 3.48 Deformed shape of models: (a) SS-C-1 and (b) SS-C-2.

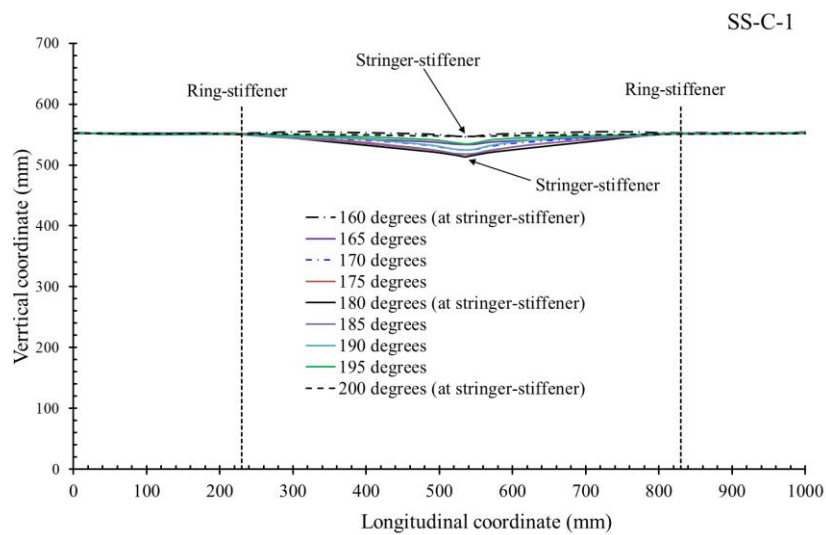


Fig. 3.49 Deformed shape of stringer-stiffeners: (a) SS-C-1 and (b) SS-C-2.

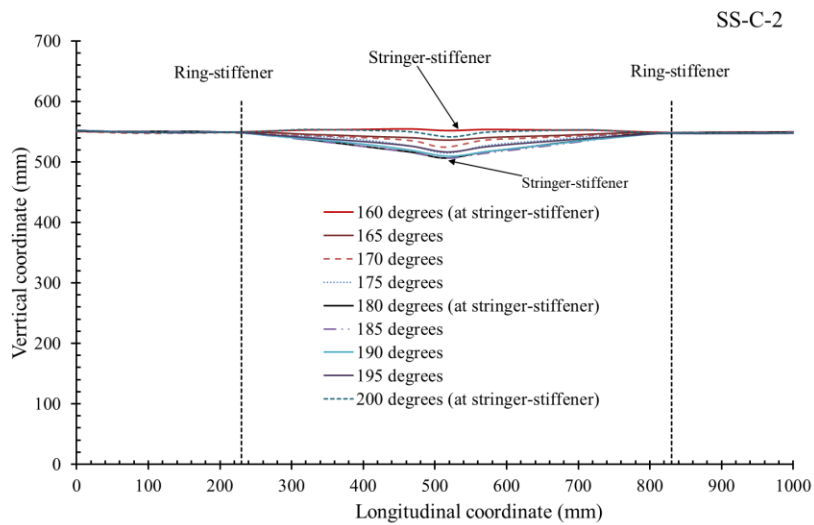
The damage profiles and extents were measured using the CimCore portable measuring arm device, which enabled determination of the exact hit location and loading eccentricities. The longitudinal and circumferential damage profiles for each model are illustrated in Figs. 3.50 and 3.51, respectively. For both models, the longitudinal damage profiles indicate that the stringer-stiffeners limit the damage in the mid-bay significantly. It is also noteworthy that the ring-stiffeners prevent the damage from spreading to adjacent bays. In Fig. 3.51, the circumferential damage profile of SS-C-1 indicates that the impact line appears to be horizontal; however, for SS-C-2, the impact line was inclined as a result of the large striking mass rotation before hitting the model. An

outward bulging of the stringer-stiffener is noticeable under the indenter in the dented cross-section.

The tilting of the stringer-stiffeners and ring-stiffeners bordering the mid-bay was also measured. The maximum out-of-plane displacement at the toe of the stringer-stiffener web was considered in the reference. It was observed that rotation of the dent line about the vertical axis significantly affected the deformation of the stringer-stiffeners. The results of the damage extent measurements and permanent dent depth of the two models are listed in Table 3.14. The rotation of the dent line with respect to the longitudinal axis and vertical axis (centre plane) was also calculated, and is displayed in this table.

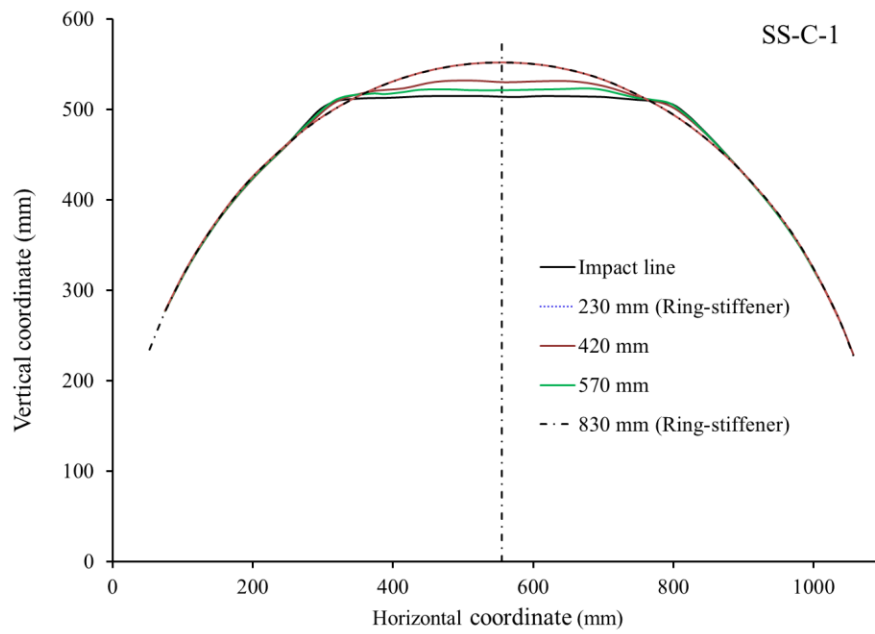


(a)

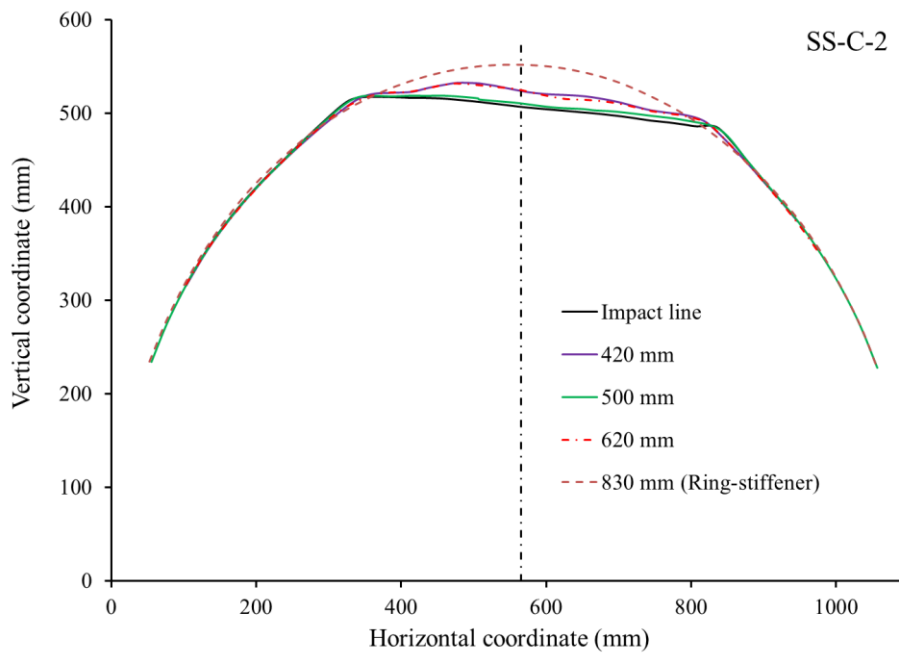


(b)

Fig. 3.50 Measured longitudinal damage profiles: (a) model SS-C-1; (b) model SS-C-2.



(a)



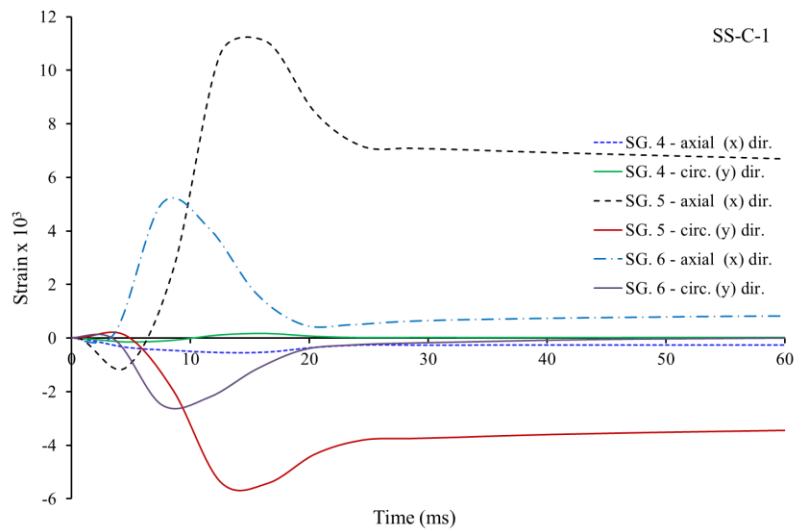
(b)

Fig. 3.51 Measured circumferential damage profiles: (a) model SS-C-1; (b) model SS-C-2.

Table 3.14 Results of damaged stringer-stiffened cylinder models.

Model	SS-C-1	SS-C-2
Permanent dent depth (mm), d_d	36.80	43.20
Non- dimensional permanent dent depth, δ_d	0.067	0.079
Longitudinal shift impact line (mm)	12.0	2.0
Rotation angle of dent line about longitudinal axis ($^\circ$)	0.0	5.0
Rotation angle of dent line about vertical axis ($^\circ$)	0.0	2.1
Tilting of center stringer-stiffener in denting area ($^\circ$)	5.68	8.56
Tilting of side stringer-stiffener in denting area ($^\circ$)	4.35	5.72
Tilting of ring-stiffener ($^\circ$)	0.0	0.0

The strain measurements provide additional details for understanding the deformation processes. The arrangements of the strain gauges are illustrated in Fig. 3.44 in the previous section. The filtered strain histories for the cylinder shell, stringer-stiffeners and ring-stiffeners are displayed in Figs. 3.52, 3.53 and 3.54, respectively. According to the strain measurements in positions 5 and 6 for both models, cylinder shell deformation occurred mainly in the longitudinal direction, because membrane stretching was accompanied by high tensile strains. In the circumferential direction, the strains were compressive. In particular, the strain magnitude of SS-C-2 is 28% higher than that of the SS-C-1 as a result of the increase in impact energy. It should be noted that the strains in the circumferential direction attained their permanent value earlier; thus, deformation begins when the circumferential curvature flattens and results in compressive membrane strains. Furthermore, the cylindrical shells were subjected to significantly higher tensile strain than the material yield strain.



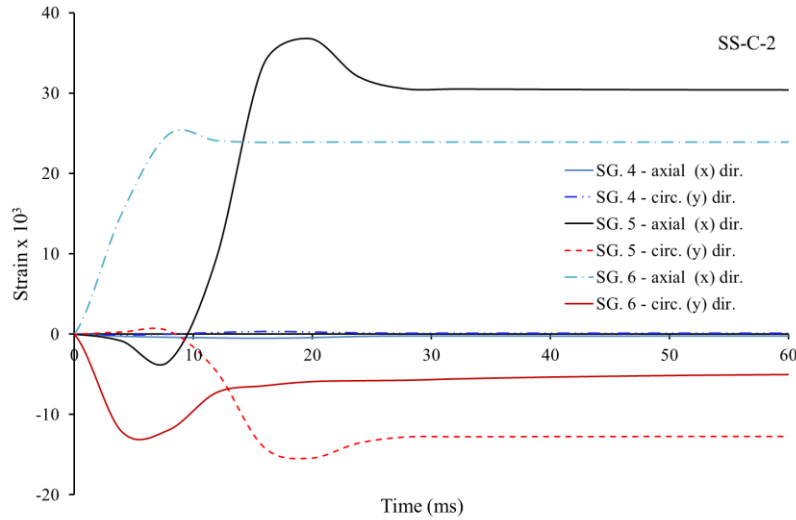


Fig. 3.52 Strain time histories recorded by the strain gauges placed on cylinder shell.

As observed in Fig. 3.53, the stringers in the position under the indenter predictably underwent extensive compressive strain. However, at position 3 of SS-C-1 and position 1 of SS-C-2, the strain is tensile, with marginal magnitude. Because of the loading eccentricity and asymmetrical end conditions, the measured strain levels vary at these two positions on the ring-stiffener. At a distance from the dent zone, the strain level in position 7 is higher than that in position 8 for both models, as illustrated in Fig. 3.54.

3.3.2 Nonlinear finite element modeling

3.3.2.1 Element and boundary conditions

For the numerical analysis, the shell, stringer-stiffeners and ring-stiffeners were modelled using four-node curved shell elements (Abaqus S4R), with hourglass regulation and reduced integration. Thickness integration was performed using the Simpson rule, with five integration points throughout the thickness. The knife-edge striker was assumed to be rigid, and the R3D4 element was used. The contact between the indenting surface and struck model was defined using the general contact option in Abaqus. This contact algorithm uses a penalty method as the contact constraint.

A convergence test was performed by varying the mesh sizes during modelling in order to select the optimum sizes. In this study, the contact region mesh size was half that of the outer region. The selected element size for the contact region was 5×5 mm and that for the outer region was 10×10 mm. This mesh size is adequate for capturing the deformed cylinder shell shape and force-displacement response precisely. It is noteworthy that a finer mesh results in elements with

edge sizes that are smaller than the shell thickness, which causes problems in contact calculations. The surfaces of the shell elements were offset outwards in order to avoid overlapping of materials. The thickness of the elements at the weld joints was not increased. It was considered that this assumption would not result in significant discrepancies between the actual and simulated responses.

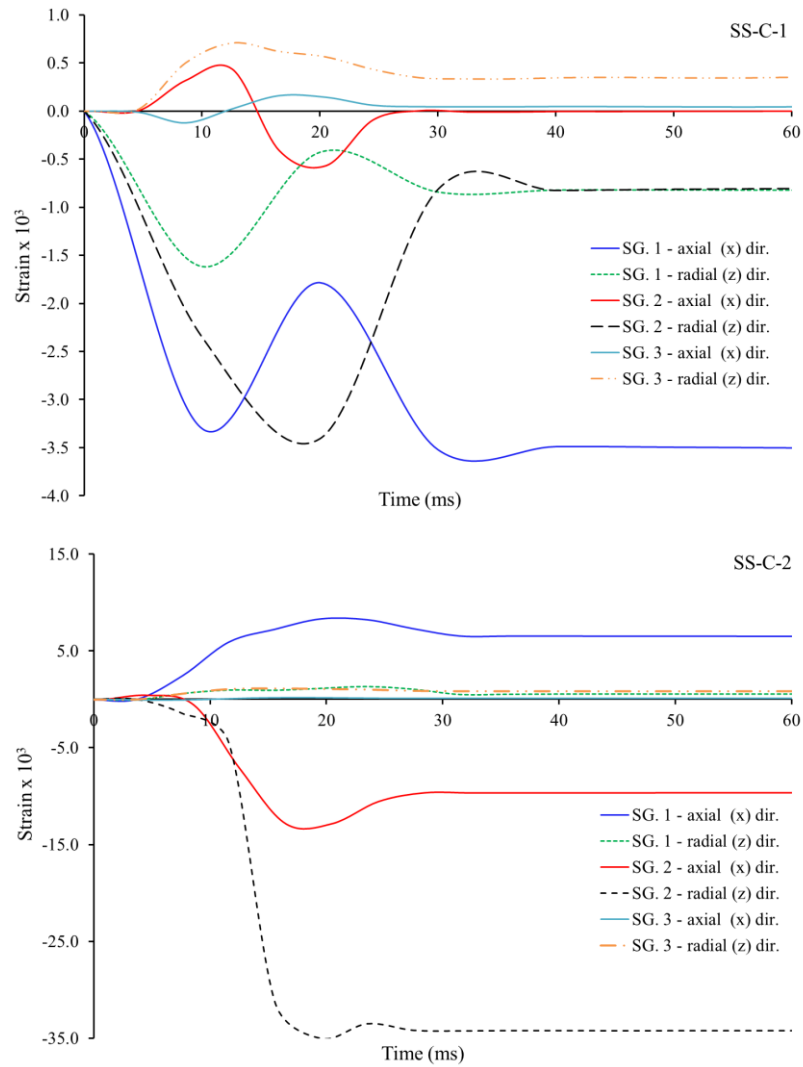


Fig. 3.53 Strain time histories recorded by the strain gauges placed on stringer-stiffeners.

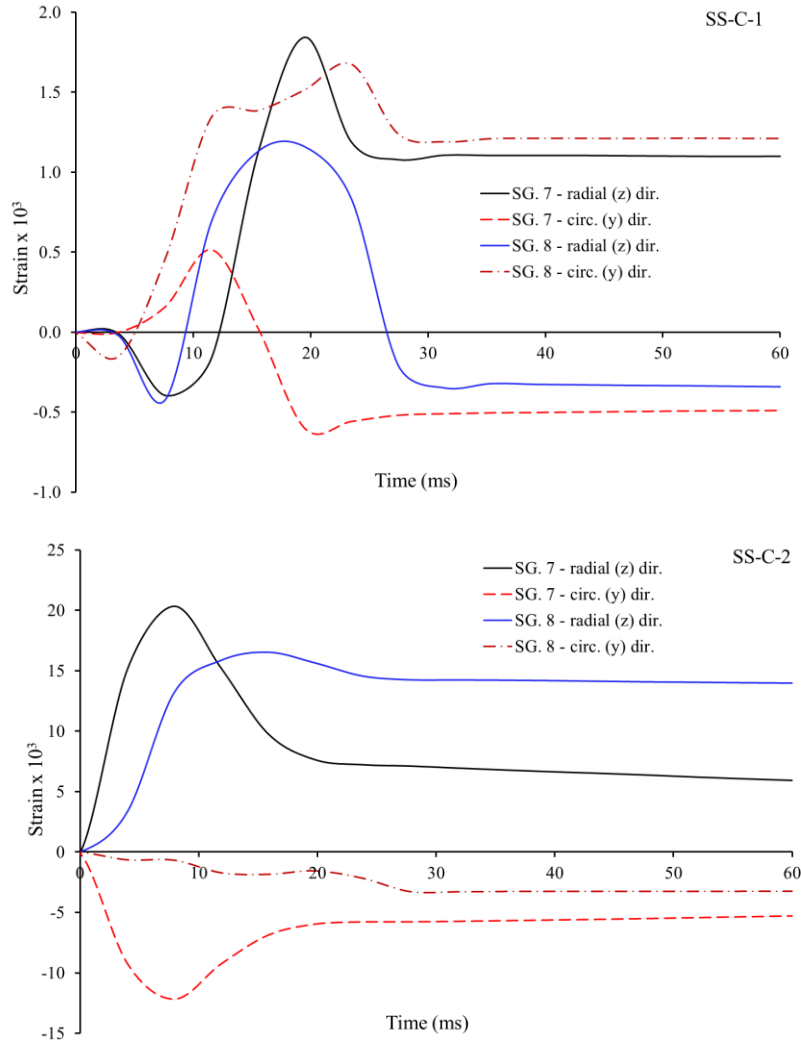


Fig. 3.54 Strain time histories recorded by strain gauges placed on ring-stiffeners.

In order to provide an accurate representation of the experimental support and simplify the numerical model, part of the supported structures was modelled as a fixture, as illustrated in Fig. 3.55. The fixtures were securely fixed at four bottom bolt holes in order to simulate the clamped boundary conditions in the experiment. For the striker, the mass and velocity were applied to the reference points to simulate the predicted impact energy. It should be noted that the rigid striker motions were governed by the reference point motions by assigning the initial collision velocity for the reference point in the vertical direction.

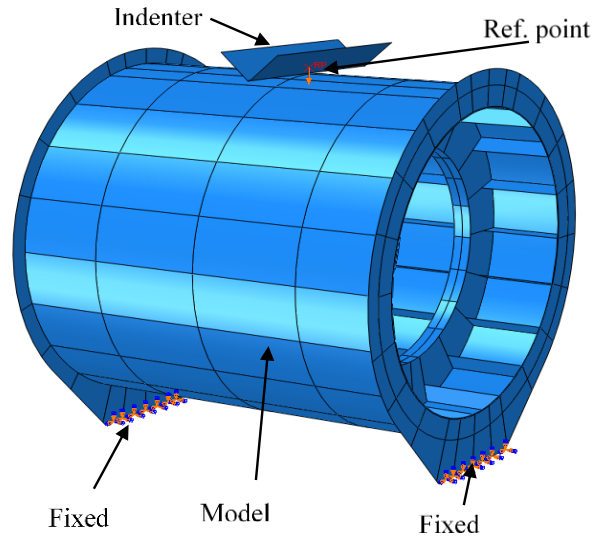


Fig. 3.55 Finite element model for collision analysis.

Following impact, the model vibrates elastically; therefore, Rayleigh damping was utilised to overcome these vibrations and rapidly attain a static equilibrium state. Rayleigh damping involves damping associated with low-frequency oscillations, which is proportional to mass, and damping associated with high-frequency oscillations, which is proportional to stiffness. The former is used to include a damping matrix in dynamic analysis, which is obtained by multiplying the mass matrix of the system with the coefficient α . The coefficient α was set as the lowest natural frequency of the model, which was obtained by means of modal analysis.

3.3.2.2 Material properties definition

The material properties were defined the same procedures as previous section 3.2.2.2. The true stress-equivalent plastic strain data generated from those equations for various strain rates (10 s^{-1} , 20 s^{-1} , 50 s^{-1} , 70 s^{-1} , 100 s^{-1} and 150 s^{-1}) are plotted in Fig. 3.56.

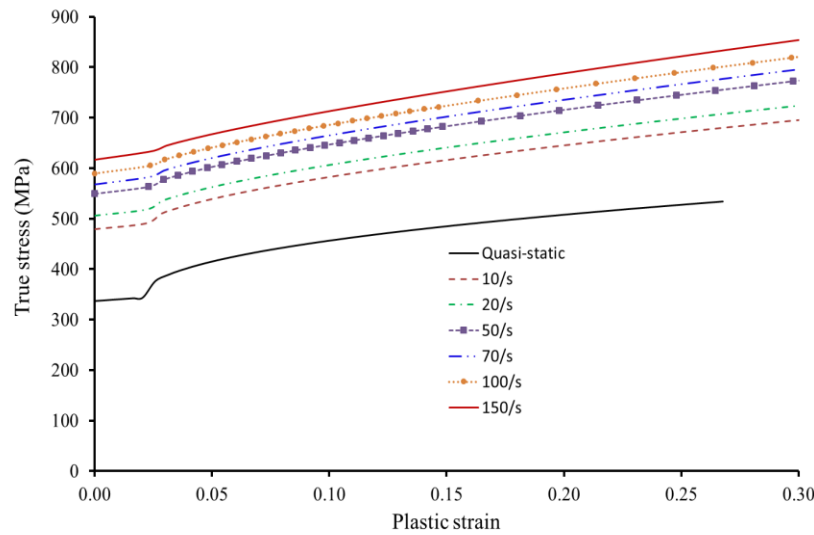


Fig. 3. 56 Typical true stress-strain curve applied for FE analysis.

3.3.3 Numerical results and discussion

3.3.3.1 Damage generation

The dented shapes and residual stress distributions for models SS-C-1 and SS-C-2 following collision test and numerical results are illustrated in Figs. 3.57 and 3.58. In these figures, the contours of the von Mises stresses are shown. As mentioned earlier, all the previously reported experiments the damages were generated in quasi-static manners [110-113]. Therefore, there are some differences from the damages generated by dynamic impact tests of this study. Firstly, the quasi-statically obtained damages were expanded over the adjacent bays in longitudinal direction, which are similar to those reported for ring-stiffened cylinders [114-118]. On the contrary, however, the dynamically obtained damages are confined in the bay of contact. Secondly, the denting lines of the static damages were straight, but those of dynamic tests were curvy which can be seen in Fig. 3.51.

In the inner span of a given stringer between two ring-stiffeners collapsed as a beam, with a clear three-hinge mechanism. The stringers acted as beams that resisted loading until formed plastic hinges and therefore yielded to the striker loading. As the dent depth increased, the flattened section around the perimeter extended and the stringers adjacent the centre stringer began to deform together with the shell and collapse. It is also notable that the ring-stiffeners prevented the extent of damage spreading to adjacent bays. It can be concluded that the T-ring stiffeners were adequately stiff or strong for preventing an extension of the damaged zone or localising the buckles in the shell skin and stringer stiffeners. The heavy end ring on these models played an important

role in the denting process and in some cases might be representative of bulkheads in an actual column. The T-ring stiffeners at closer spacing would improve the collision resistance and are necessary when designing the column for combined axial compression and external pressure loading.

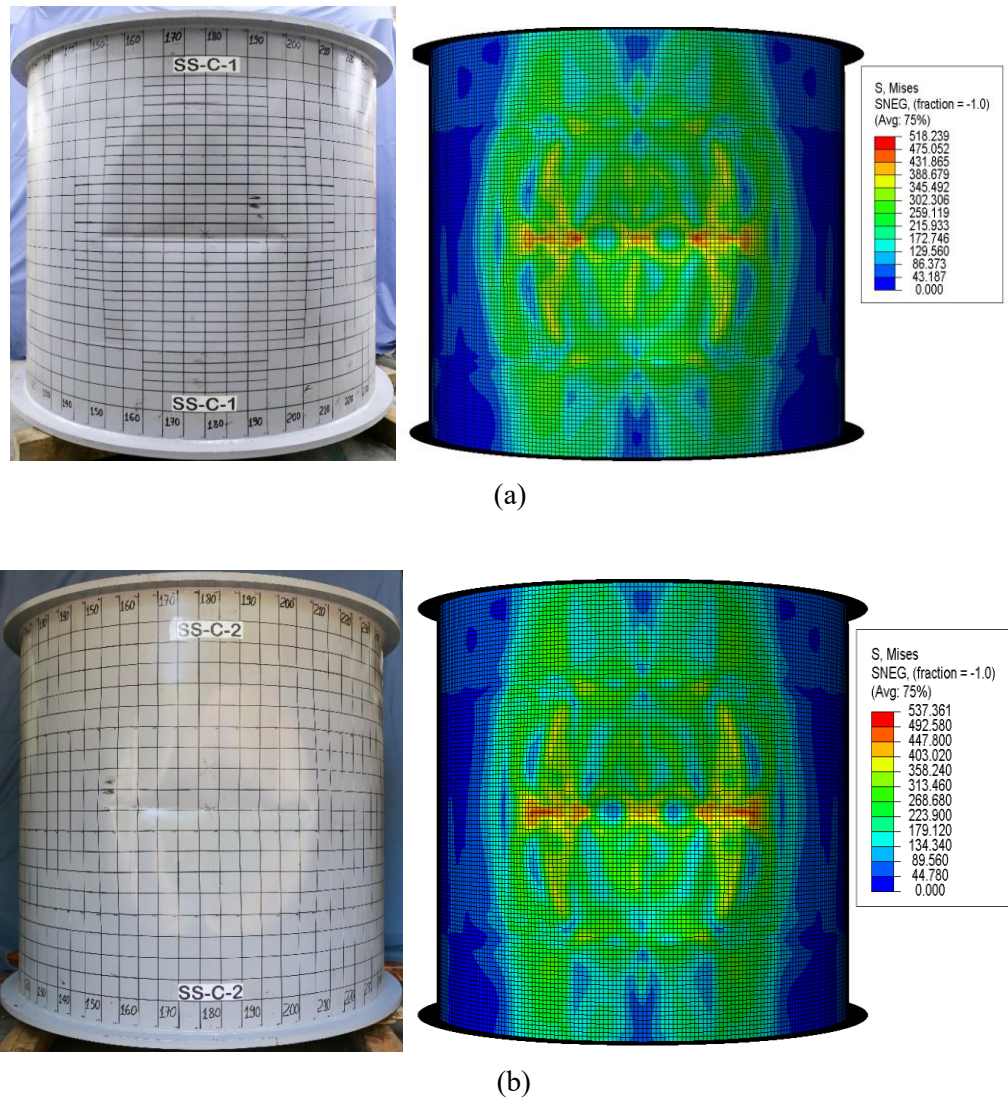


Fig. 3.57 Predicted deformed shape of models compared with test results:
(a) model SS-C-1; (b) model SS-C-2.



Fig. 3.58 Predicted deformed stringer-stiffener shape compared with test results for SS-C-2.

Furthermore, it is also noteworthy that local tripping of stringer-stiffeners was apparent near the ring-stiffeners. It is evident that the stringers play a significant role in resisting impact, while the ring-stiffeners are flexural fixed for the axial restraint. This phenomenon only occurs in dynamic mass impact when a load is rapidly applied over a short duration. This may be considered to be due to the effects of inertial force, strain rate and vibration on the structure responses. This information enables one to understand and validate the dynamic impact responses of stringer-stiffened cylinders, which has not yet been considered in the open literature. This stands in contrast with the previous studies which were presented by Ronalds et al. [110-112] and Walker et al. [113]. For these studies, there is no local tripping of the rings or of the stringers. The reason for this is that the local denting damage was generated by the quasi-static denting and neglecting the effects of inertial force and strain rates.

The numerically predicted longitudinal damage shapes are compared with the measured values in Fig. 3.59. A reasonable agreement is observed between the predictions and test results. The predictions of the permanent dent depth were compared with that of the experimental results, and the variation between the numerical predictions and test results was found to be approximately 4.2% as shown in Table 3.15. Additionally, the comparison of strain measurement between test and numerical results of model SS-C-2 are also provided in Fig. 3.60. It is clear that the permanent plastic deformation strains of numerical results were reached earlier than that of experimental strains, which were around 10 ms and 20 ms, respectively.

It is also noted that the definition of strain rate hardening adopted in the analysis are appropriate for this type of dynamic impact problem. The ranges of strain rate obtained from numerical analysis were 0.42/s to 33.1/s and 0.65/s to 46.1/s for models SS-C-1 and SS-C-2, respectively. Therefore, the ranges of strain rate input data in numerical analysis (10 s^{-1} , 20 s^{-1} , 50 s^{-1} , 70 s^{-1} , 100 s^{-1} and 150 s^{-1}) are appropriated. Furthermore, the comparisons of strain obtained from experimental and numerical predictions in Fig. 3.60 were shown a good agreement.

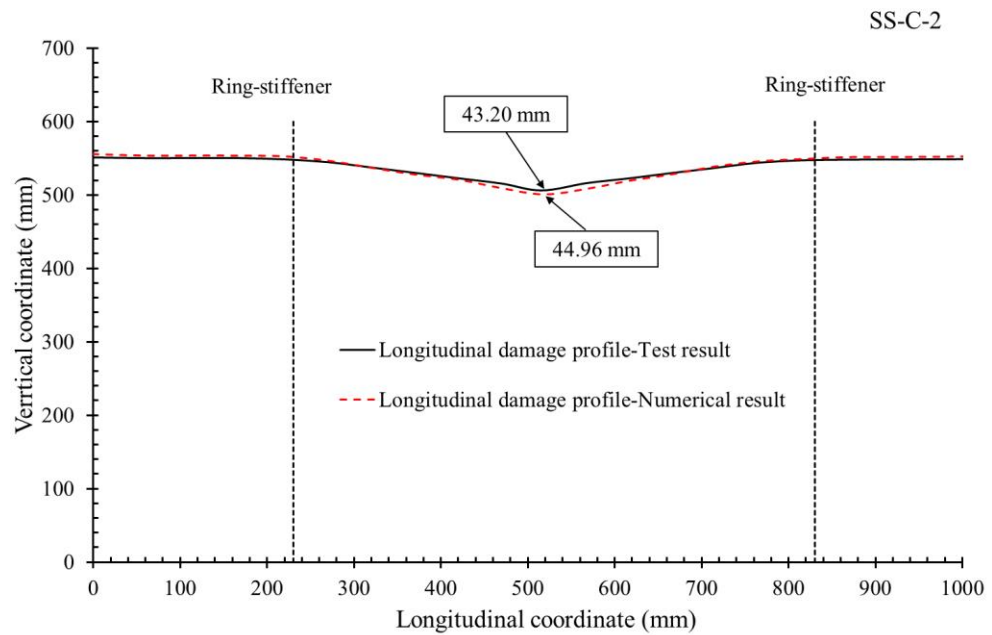
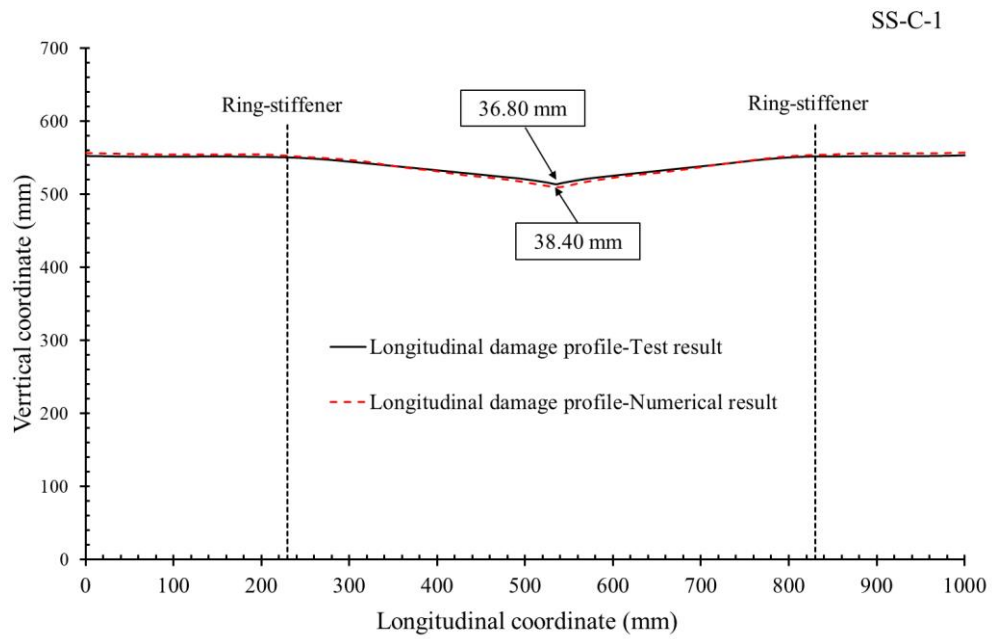
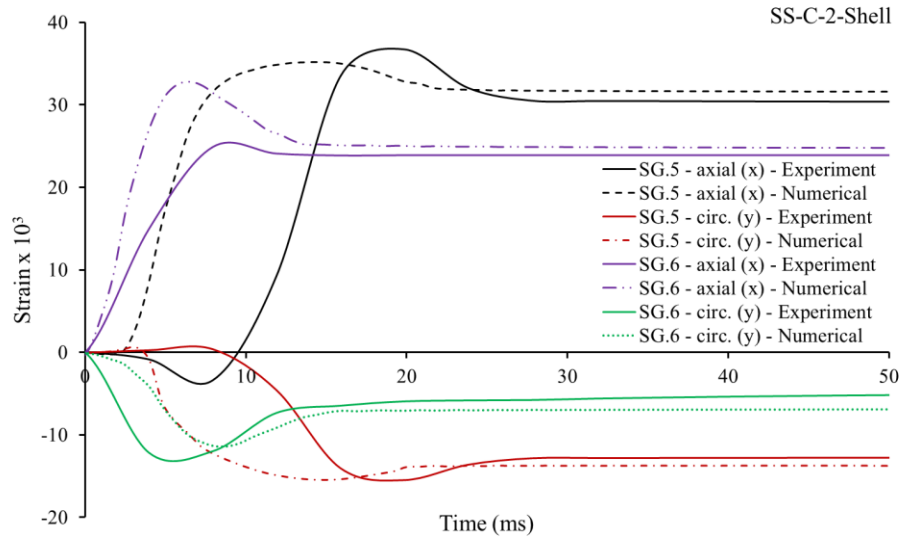
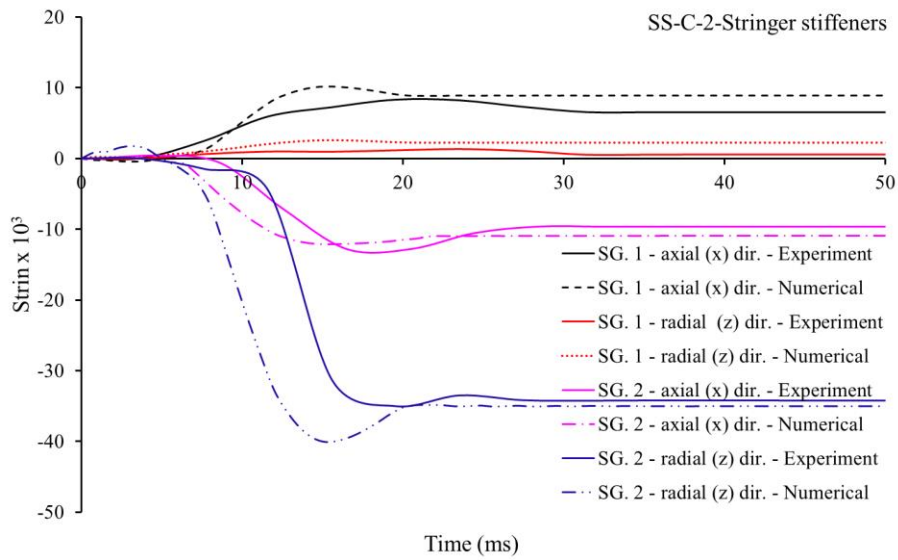


Fig. 3.59 Comparison of predicted longitudinal damage profiles with test results:
 (a) model SS-C-1; (b) model SS-C-2.



(a)



(b)

Fig. 3.60 Comparison of strain obtained from numerical predictions and test results for SS-C-2: (a) Shell; (b) Stringer stiffeners.

Table 3.15 Comparison of test results and numerical predictions.

Model	Permanent dent depth, d_a (mm)		X_m Num. pred./ test result
	Test result	Numerical prediction	
SS-C-1	36.80	38.40	1.043
SS-C-2	43.20	44.96	1.041

3.3.3.2 Energy partition

The energy partition throughout the impact duration is supplied further insights into the effect of each component structures such as cylindrical shell, stringer-stiffeners as well as ring-stiffeners, which could not be detected in the responses of force-displacement. Figure 3.61 illustrates the total internal and plastic strain energy histories for the whole struck model, cylinder shell, stringer-stiffeners and ring-stiffeners of both models. In this study, the energy dissipated in the stringer-stiffener is the largest for both models. As indicated in Table 3.16, approximately 55% and 43% of the total impact energy is dissipated by the stringer-stiffener deformation and cylinder shell, respectively, while that of the end plate and ring-stiffeners accounts for only around 1.5% and 0.5%, respectively. It indicates that the stringer-stiffeners played a vital role in resisting collision.

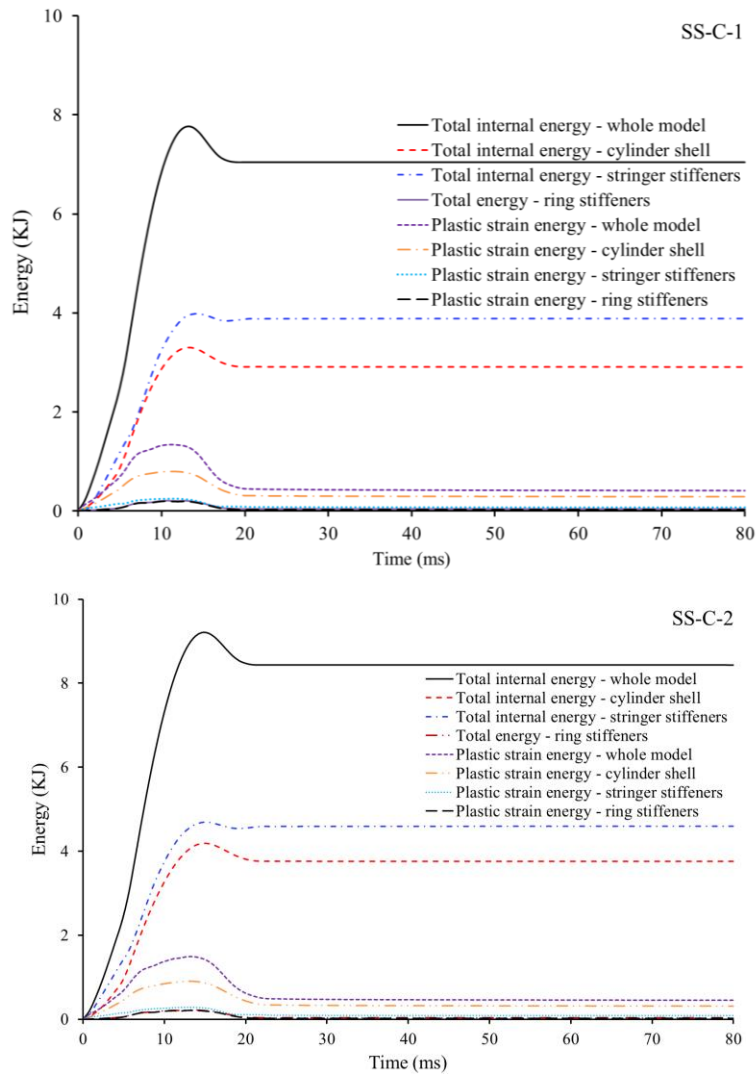


Fig. 3.61 Energy time histories for test models obtained numerically.

Table 3.16 Energy absorption of structural components.

Structural component	SS-C-1		SS-C-2	
	Internal energy	Plastic energy	Internal energy	Plastic energy
Cylinder shell	41.30 %	69.62 %	44.45 %	69.22 %
Stringer-stiffeners	55.26 %	18.72 %	54.50 %	19.61 %
Ring-stiffeners	0.56 %	5.78 %	0.46 %	5.24 %
End plates	0.13 %	2.13 %	0.12 %	1.91 %

3.3.3.3 Effect of strain-rate hardening definition

It is well known that the strength of steel structures subjected to dynamic loading is sensitive to strain rate, the dynamic flow stress increase when increasing strain rate. Therefore, consideration of the strain rate effect by means of selecting material constant coefficients in the Cowper-Symonds equation Eq. (3.13) can be discussed. The stress-strain dependence is assumed similar at all strain-rate levels, the strain-rate hardening behaviour was defined by simply scaling quasi-static plasticity data with a dynamic hardening factor, which is the ratio of the dynamic to static yield strength. The dynamic hardening factor depends only on the strain-rate magnitude and can be expressed as a power-law function, as proposed by Cowper and Symonds [141]. The coefficients in the Cowper and Symonds equation are common used as $D = 40.4 \text{ s}^{-1}$ and $q = 5$ for mild steel, and $D = 3200 \text{ s}^{-1}$ and $q = 5$ for high tensile steel. Furthermore, D can be calculated using Eq. (3.14), as provided by Lee and Kim [142].

Figure 3.62 displays the numerical investigation results for the effects of strain-rate hardening definitions on the force-displacement curves for the tested model SS-C-1. It is clearly illustrated that the overall response tendencies of the force-displacement curves are not affected by the strain-rate definitions. The stiffness of the struck model was increased or decreased following by the strain-rate effect definitions; therefore, the permanent deflection is dependent on these definitions. A detailed comparison of permanent deflection between the numerical and experimental results is provided in Table 3.17. It should be noted that, for this particular case, negligence of the strain-rate effect results in a 17.1% larger permanent deflection for SS-C-1. When the Cowper-Symonds equation is used with the coefficients $D=40.4$ and $D =3200$, and determined by equation (3.14), the differences are 5.20, 12.30 and 5.70%, respectively. Interestingly, when using the direct input of test data, the permanent deflection of the numerical result is only 4.30% larger than that of the test result. Therefore, it is suggested that the dynamic material properties should be used to define plasticity at high strain rates in numerical simulations.

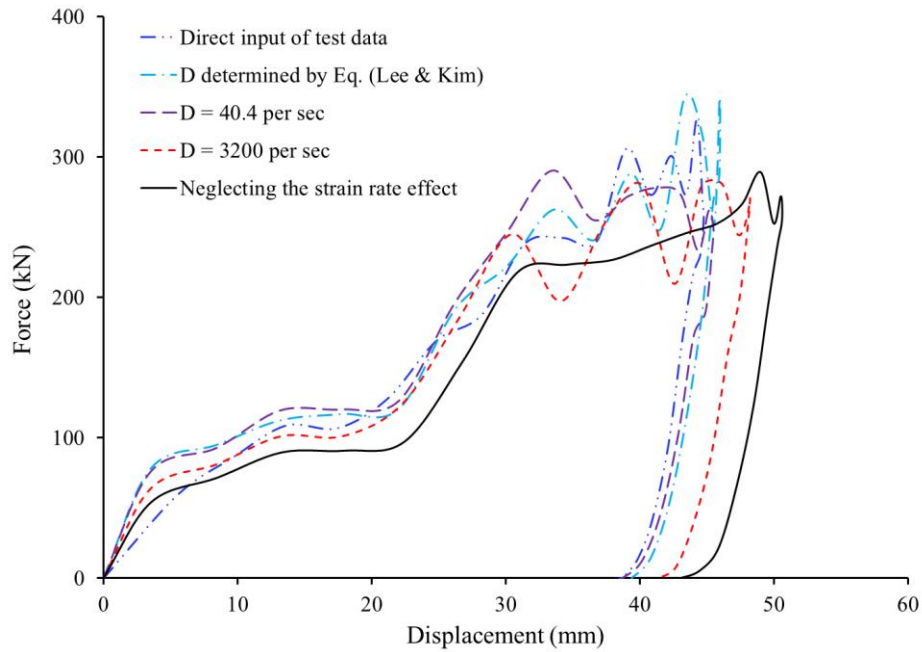


Fig. 3.62 Force-displacement curves for different strain-rate hardening definitions.

Table 3.17 Permanent displacement comparison for different strain-rate hardening definitions.

	Permanent deflection, d_d (mm)		X_m Num. pred./ test result
	Numerical predictions	Test result	
Direct input of test data [140]	38.40		1.043
$D = 40.4/s$	38.70		1.052
$D = 3200/s$	41.31		1.123
Cowper-Symonds with coefficient obtained from equation (13)	38.90	36.80	1.057
Neglecting the strain-rate effect	43.08		1.171

3.3.3.4 Effect of boundary conditions

As indicated in Table 3.16, the end plate and fixture may not dissipate a significant amount of energy. However, the effect of these on restraining the axial displacement and rotation of the cylinder ends affects the cylinder shell's membrane resistance. In order to clarify this issue, the

effect of idealising the boundary conditions was assessed by means of comparison with the fully modelled experimental conditions. Three types of boundary conditions were considered: fully fixed at the cylinder ends (case 1); free axial translations, restrained rotations and radial translations (case 2); only restrained radial translations at the cylinder ends (case 3). A comparison was carried out for the impact conditions of SS-C-1, and the resulting force-displacement curves are displayed in Fig. 3.63.

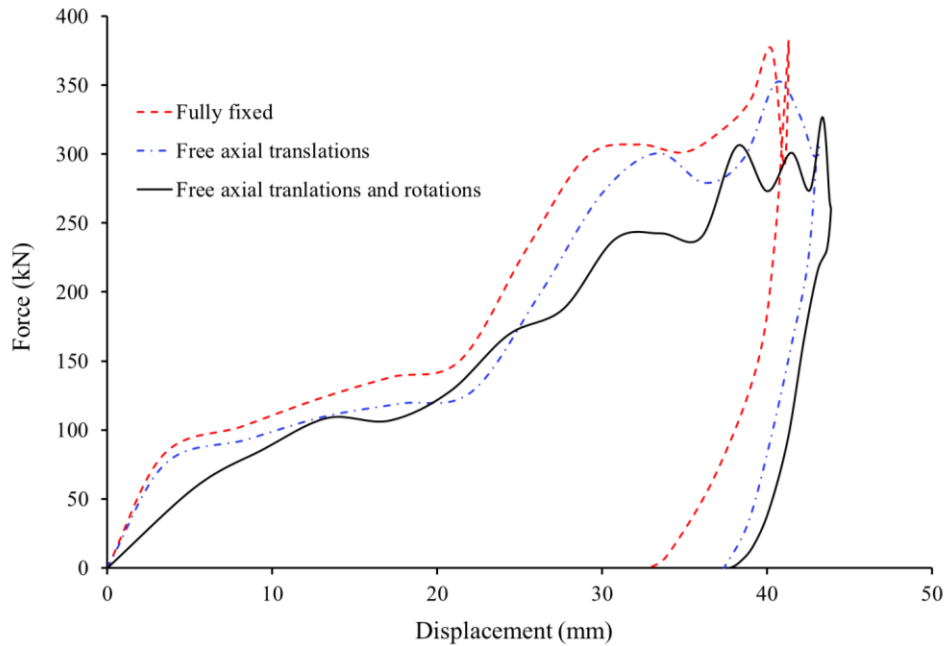


Fig. 3.63 Force-displacement curves for different boundary conditions.

In term of the comparing the maximum permanent deflection prediction for each boundary condition with the experimental result, it is not surprising that the fully fixed condition does not effectively represent the actual case because the upper part of the end plate and ring were not restrained during the tests. Although the energy dissipated by the end plate and the end ring is not significant, their effect on restraining the axial translation of the cylinder ends affects the membrane resistance of the cylinder shell. However, similar results were obtained for case 2 of free axial translations and case 3 of free axial translations and rotations between the test and numerical results. Generally, case 3, which was closely represented the actual case give the best prediction of the maximum permanent deflection. It is concluded that the effect of the boundary conditions for any collision analysis should be considered carefully.

3.4 Parametric study

It is highlighted that the numerical modeling strategy presented to give the reasonably accuracy to compare with experimental results. Therefore, the using nonlinear finite element analysis is capable of predicting the behavior of locally damaged stiffened cylinder with reasonable accuracy. Also, general features of the experimental behavior can be reproduced with the numerical analysis methodology presented satisfactorily. In addition, the problem can be treated in a more detailed manner. Scope exists for parametric studies and more data can be produced via numerical analysis. After validating the numerical strategies by comparing with the experiments from the authors, several parameters are varied to investigate the effects of these changes on the impact response of ring-stiffened cylinders and stringer-stiffened cylinders. Not only the impact conditions such as impact velocity, striking mass but also different impact locations are considered. As basis, the test conditions and the scantlings of RS-C-2 and SS-C-1 are adopted.

3.4.1 Ring-stiffened cylinder

3.4.1.1 Effect of impact location and angle

Details of various impact locations on ring-stiffened cylinder were indicated in Fig. 3.64. The first impact location was set up at the mid-bay of two ring stiffeners. Next, the second and third were also at mid-bay and rotation with 30 degrees and 60 degrees with cross section, respectively. The next impact location was set up on ring stiffener at ring stiffener.

Force-displacement curves with various impact locations can be seen in Fig. 3.65. It is also evident that there are a number of significant differences between force and displacement in the impact locations. The permanent dent depth at mid-bay was larger than that at ring stiffener. As can be seen from the Fig. 3.66, there is a trend that the collision occurred more and more close to the middle of cylinder which have larger of the maximum permanent deflection. It can be explained that the impact response of stiffened cylinder could be improved when loaded at the impact location near by ring members. Moreover, the sharp difference of impact location between 30 degrees and 60 degrees of striker rotation were investigated herein. The permanent deflection of model under impact at striker's 60 degrees location was smaller dramatically than that of striker's 30 degrees at the middle bay of ring stiffened cylinder. By contrast, the different trend was occurred at impact on ring stiffener. The maximum permanent deflection of model under impact at striker with rotation of 60 degrees location was larger dramatically than that of striker's 30 degree at the

middle bay of the ring-stiffened cylinder. Furthermore, the impact locations at each angle is also included for better understanding as shown in Fig. 3.66. As expected, the ratio d/R is larger for impact at mid-ship section at 0° . It is noted that the 0° collision angle is defined the same as direction of mid-ship cross-section which is perpendicular to the longitudinal of the cylinder. Some the samples of deformed shapes are given in Appendix F.1.

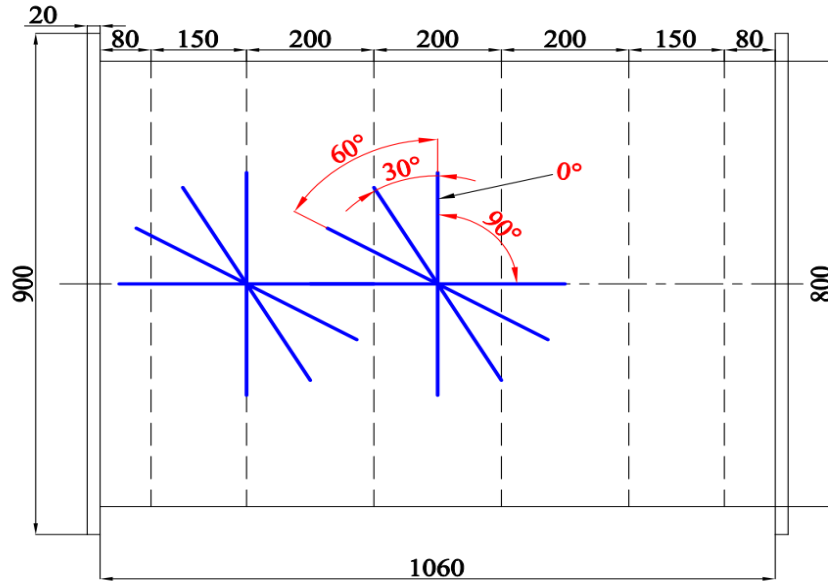


Fig. 3.64 Different impact locations on the ring-stiffened cylinder.

3.4.1.2 Effect of impact velocity

The impact energy is varied by increasing v , the impact velocity. The impact energy is proportional with the square of v , accordingly for larger impact velocities the energy to be dissipated will result larger deformations. The force-displacement curves for various impact velocities, which are shown in Fig. 3.67, remark the strengthening effect of strain rate. For impact velocities higher than 7 m/s, the increase in stiffness due to strain rate effect is clear. It is interesting to note that this difference is not only at the initial stage of loading but also remains throughout the impact until whole impact energy is dissipated. Another important point is that for large deformations the resistance of the ring-stiffened cylinder against denting is decreased. This is due to tripping of all ring-stiffeners.

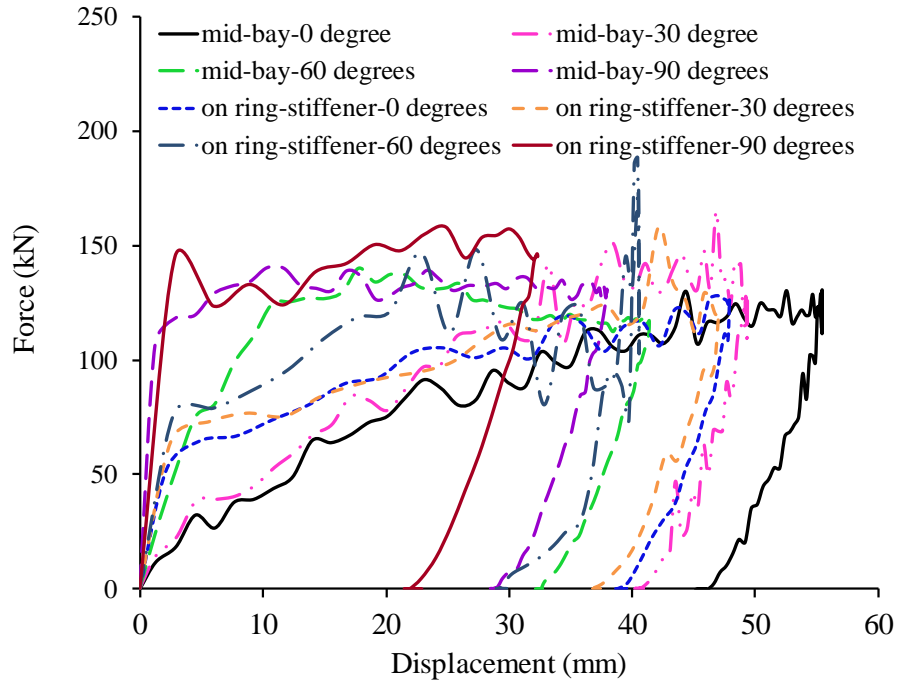


Fig. 3.65 Force-displacement curves with various impact locations on ring-stiffened cylinders.

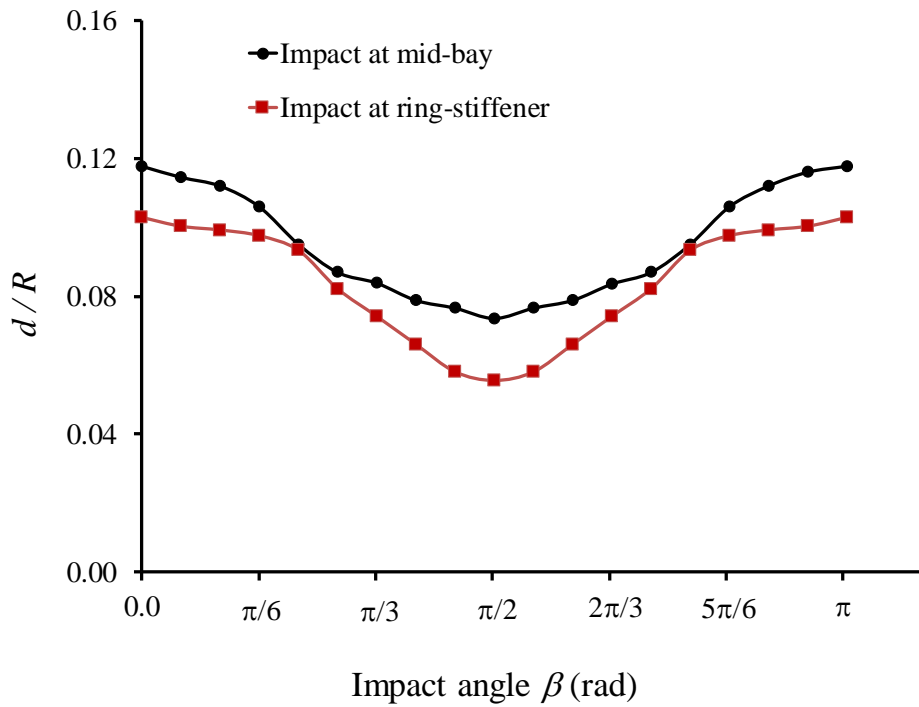


Fig. 3.66 Effect of impact angles.

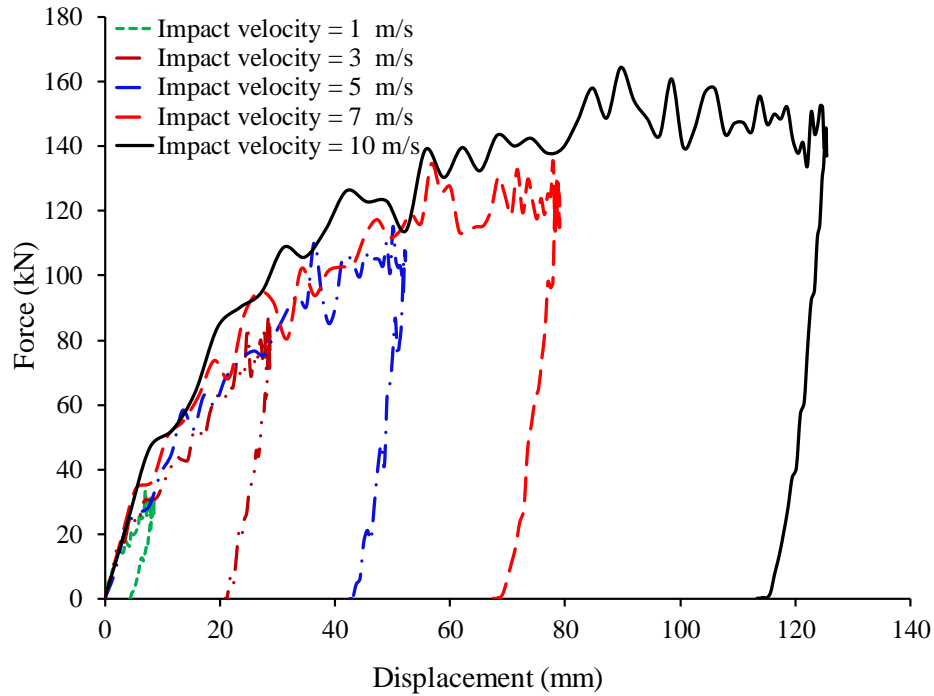


Fig. 3.67 Force-displacement curves with increasing impact velocity on ring-stiffened cylinders.

3.4.1.3 Effect of ring-stiffeners

Firstly, the impact conditions of the RS-C-1 model were used for fully understand the capacity of ring-stiffeners in limiting the damage extents. The number of ring stiffener was varied, with values of 2, 4 and 6. Furthermore, the unstiffened cylinder response is also shown for comparison. It is noted that the overall response tendencies of the force-displacement are quite difference as shown in Fig. 3.68. It is evident that stiffener spacing has a remarkable effect on the resistance of cylinder shell against denting. As the damage zone is bordered with closely spaced stiffeners, the circumferential bending resistance increases even in the initial stage of loading. A significant fraction of the impact energy is dissipated by these stiffeners also as radial deformation, since the contact zone is in the vicinity of the stiffeners.

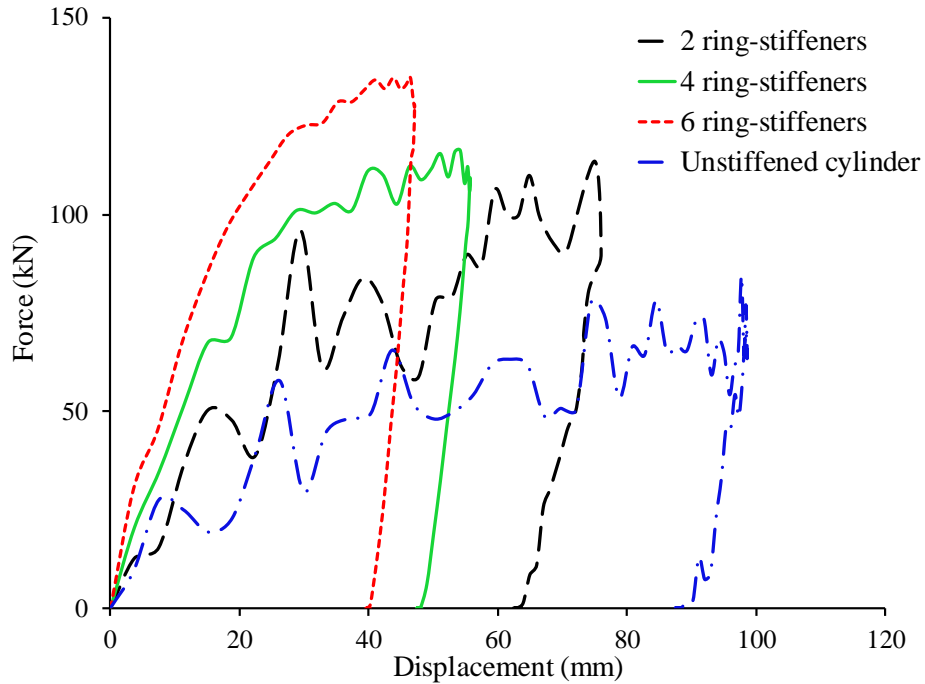
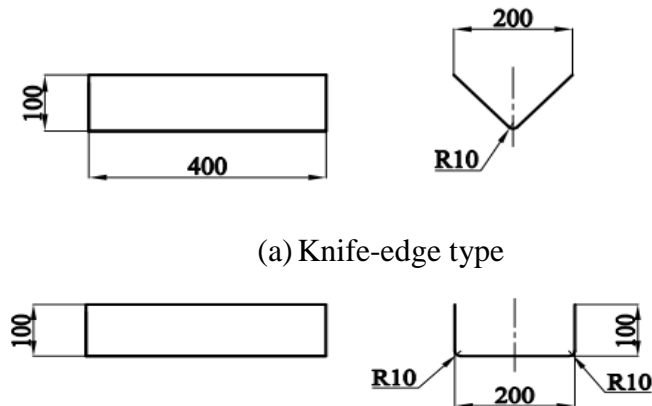


Fig. 3.68 Force-displacement curves with various number of ring-stiffened cylinders.

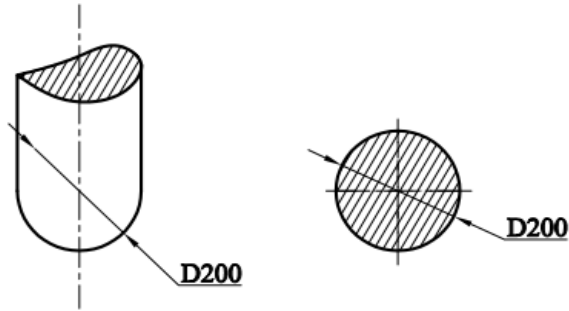
3.4.1.4 Effect of striker header shapes

To assess the effect of various contact areas two additional indenter surfaces were considered, namely, hemispherical and rectangular indenter. Fig. 3.69 shows the three cases considered. The diameter and the contact width of indenting surfaces are same as the ring-stiffener cylinder spacing. The striker mass is 300 kg for all strikers. The corners of the rectangular indenter were filleted. The second case resembles stern or side impact of a berthing vessel and the final case represents bulbous bow impact.



(a) Knife-edge type

(b) Rectangular type



(c) Hemispherical type

Fig. 3.69 Dimensions of striker.

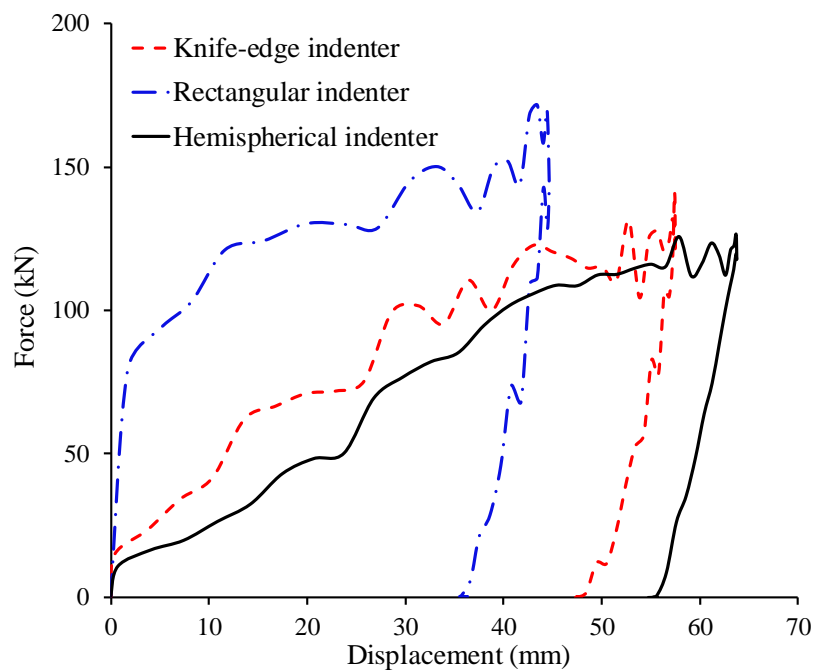


Fig. 3.70 Force-displacement curves for various striker header shapes.

As it is apparent in Fig. 3.70, the most severe case is when the load is applied through a hemispherical indenter which resembles highly localized point loading. The circumferential bending resistance of the cylinder shell cannot be utilized unless the contact area gets large and most of the resistance comes from membrane deformation. Contrary to the hemispherical indenter case, when the load is applied through a rectangular indenter, the resistance is much higher than the knife-edge indenter case. In this case, the load is distributed in a very large area both in circumferential and longitudinal direction at the initiation of the impact. Therefore, especially circumferential resistance is playing a much more important role. The deformed shapes of three type strikers are given in Fig. 3.71.

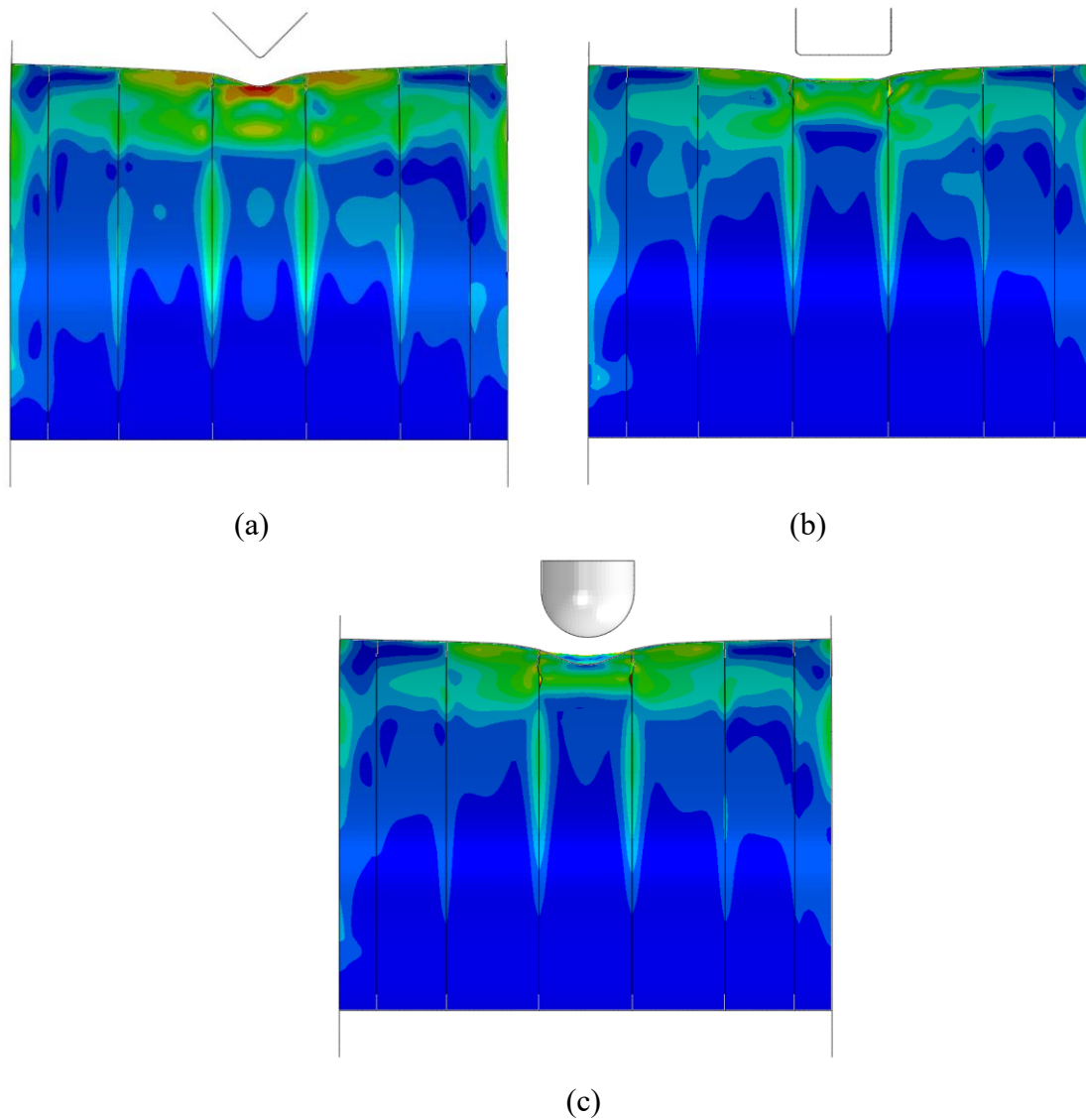


Fig. 3.71 Impact with various indenter surfaces: (a) Knife-edge indenter; (b) rectangular indenter and (c) hemispherical indenter.

3.4.2 Stringer-stiffened cylinder

3.4.2.1 Effect of impact location and angle

In this section, the effects of impact position changes on the responses of stringer-stiffened cylinders under dynamic mass impact were also investigated. The details of the effects of various impact locations on the stringer-stiffened cylinders are illustrated in Fig. 3.72. The relationship between collision force and permanent displacement of denting direction using various impact

locations are illustrated in Fig. 3.73. A number of significant differences are evident between the force and displacement in the impact locations. The permanent dent depths at the mid-bay of the stringer-stiffened cylinders were the largest, while those at the ring stiffeners were the smallest. The reason for this is that when the impact location is close to the ring, the structure cylinder is strengthened, leading to the permanent deflection being reduced sharply. In particular, it can be seen that the deflections decreased significantly, by more than 80% compared to those at mid-bay impact locations. Moreover, the same impact locations with various impact angles also exhibit different permanent displacement values. The permanent dent depth of the stringer-stiffened cylinder exhibits a trend of increasing with a larger impact location angle, created by skewness of the impact striker line and cross-section. Generally, it can be concluded that the impact response of the stiffened cylinder may be improved when loaded at an impact location near ring members.

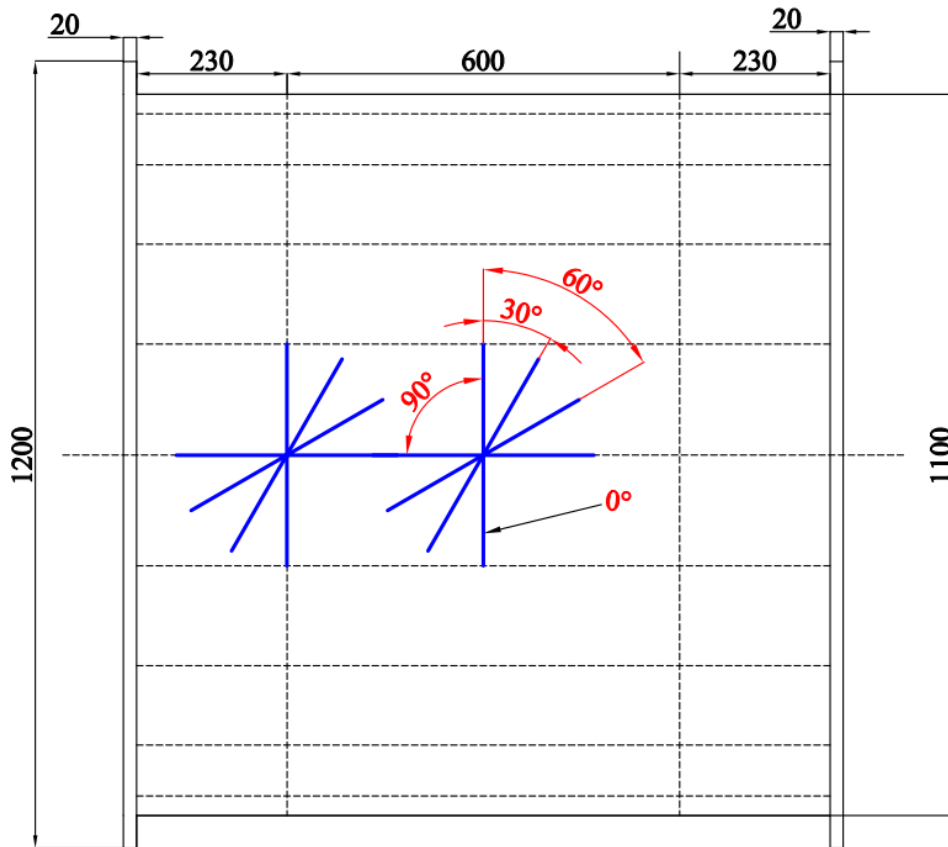


Fig. 3.72 Impact locations on the stringer-stiffened cylinder.

3.4.2.2 Effect of impact velocity

In this part of the study, it is described the response of the stringer-stiffened cylinder when initial velocities are varied. The impact energy is varied by increasing the impact velocity v . The

impact energy is proportional to the square of v ; accordingly, for larger impact velocities, the energy dissipated results in greater deformation. The strain rate is linearly proportional to v . The force-displacement curves for various impact velocities, illustrated in Fig. 3.74, demonstrate the strengthening effect of the strain rate.

For considering the effect of impact velocities, when the impact velocities higher than 8 m/s, an increase in stiffness is evident as a result of the strain rate effect is evident. It is noteworthy that this variation occurs at the initial loading stage and remains throughout the impact duration, until all the impact energy is dissipated. Another critical point is that for large deformations, the resistance of the stringer-stiffened cylinder against denting is decreased, owing to tripping of all the stringer-stiffeners.

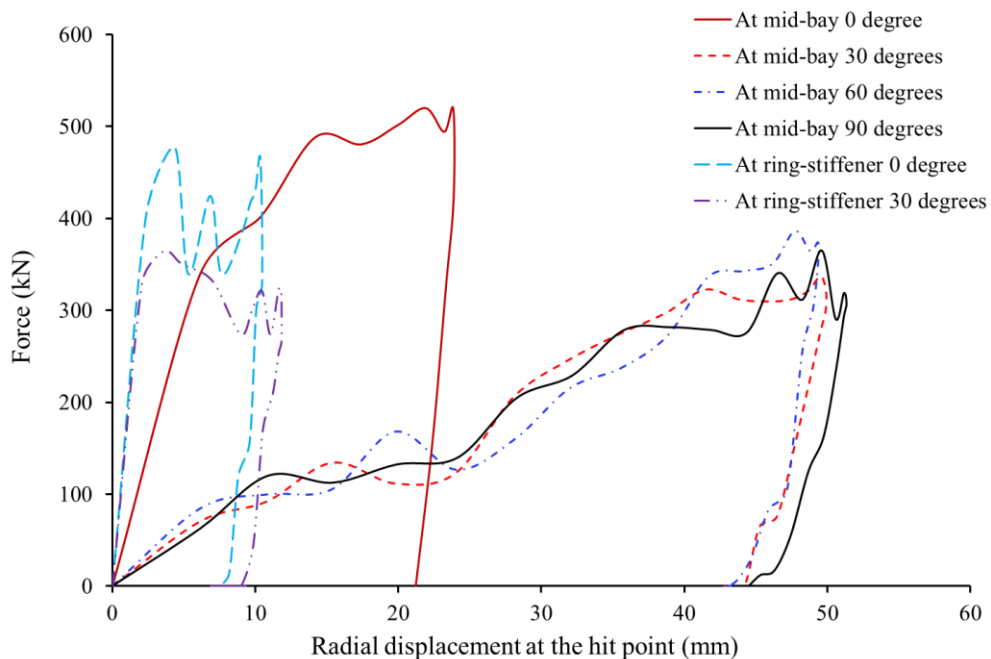


Fig. 3.73 Force-displacement curves with various impact locations on string-stiffened cylinders.

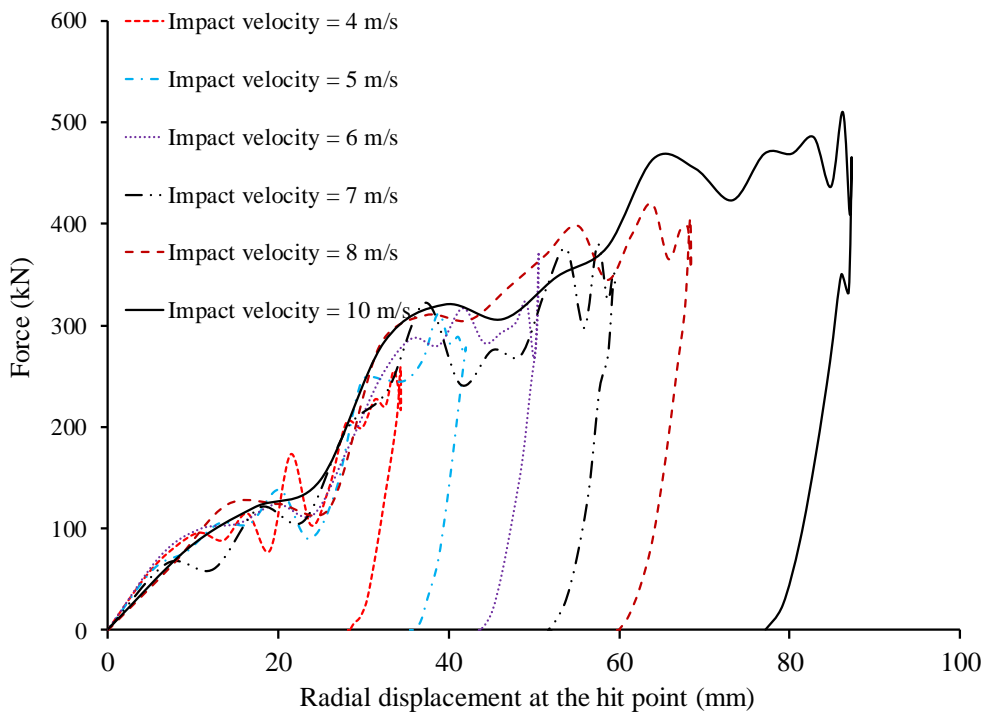


Fig. 3.74 Force-displacement curves with increasing impact velocity of stringer-stiffened cylinder.

3.4.2.3 Effect of stringer-stiffeners

Firstly, the impact conditions of the SS-C-2 model were used for assessing the stringer spacing effect. The number of stringer was varied, with values of 18, 36 and 60. Furthermore, the un-stringer stiffener cylinder response is also shown for comparison. The weight of the stringers in the specimen with 18 stringers was 51.30% of that of the shell plating, while the stringer used in the specimens with 36 and 60 stringers had weights of 108.60 and 180.85% of the shell plating, respectively. It is interesting to note that the overall response tendencies of the force-displacement of these very differently stiffened models are similar, with the exception of the un-stringer stiffener cylinder case, as shown in Fig. 3.75. It is clear that the provision of stringer stiffening did not produce significant beneficial effects in terms of resistance against denting. This should be compared to the increased weight and fabrication complexity when considering their efficiency in containing damage.

Secondly, the effect of the type of stringer-stiffened cylinders and its scantlings are assessed. Instead of flat-bar stiffeners, T-shaped and L-shaped stiffeners are widely used in practice. Therefore, in the first case, the flat-bar stringer stiffeners are replaced with T-shaped stiffeners

having the same weight as the flat-bar stiffeners in the original configuration. In the second case, L-shaped stiffeners are used and its weight also equal to other two types. The scantlings of these three stiffeners are listed in Table 3.18.

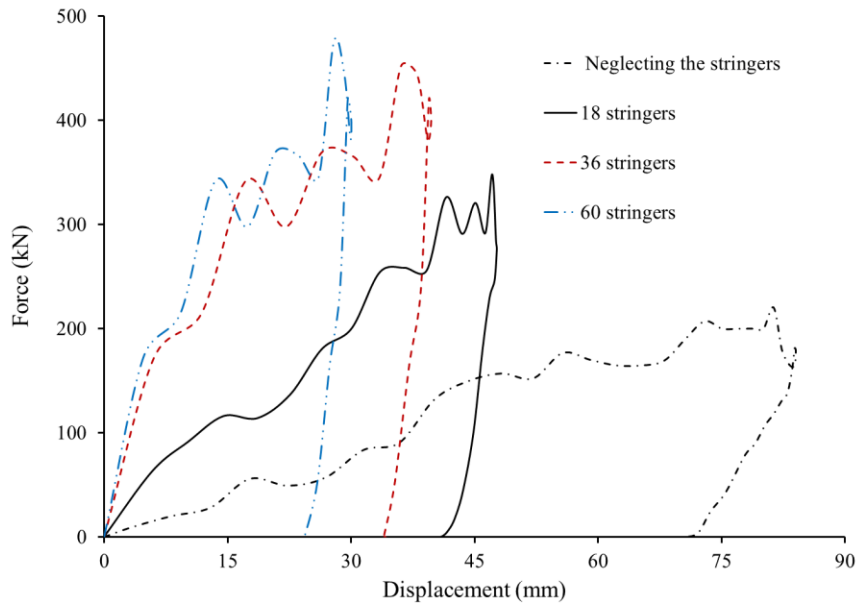


Fig. 3.75 Force-displacement curves for various number of stringer stiffeners.

Table 3.18 Scantlings of stringer-stiffener shapes used in parametric studies.

Scantling	Flat-bar stiffener	T-shaped stiffener	L-shaped stiffener
Web height, h_{sw}	65.0	45.0	50
Web thickness, t_{sw}	5.0	5.0	5.0
Flange width, b_{sf}	-	20	15
Flange thickness, t_{sf}	-	5.0	5.0

The resulting force-displacement curves are shown in Fig. 3.76. There is a slightly decreased of displacement when the stringer-stiffener shape is changed from flat-bar shape to T-stiffener shape and L-stiffener shape. It can be concluded that the scantlings of stringer stiffener shapes are also important for overall the bending resistance of the stringer-stiffener cylinders. Interestingly, the local tripping of stringer-stiffeners has not occurred in the joint of the stringer-stiffeners with ring-stiffeners with the cases of T-stiffener and L-stiffener shape. In general, the resistance of large-diameter cylindrical shells can be increased with adequate scantlings of stiffeners. It is suggested that the design stringer-stiffener dimensions should ensure that the tripping has not occurred. Therefore, a more optimum design would be required to generate the geometry of stringer-stiffeners.

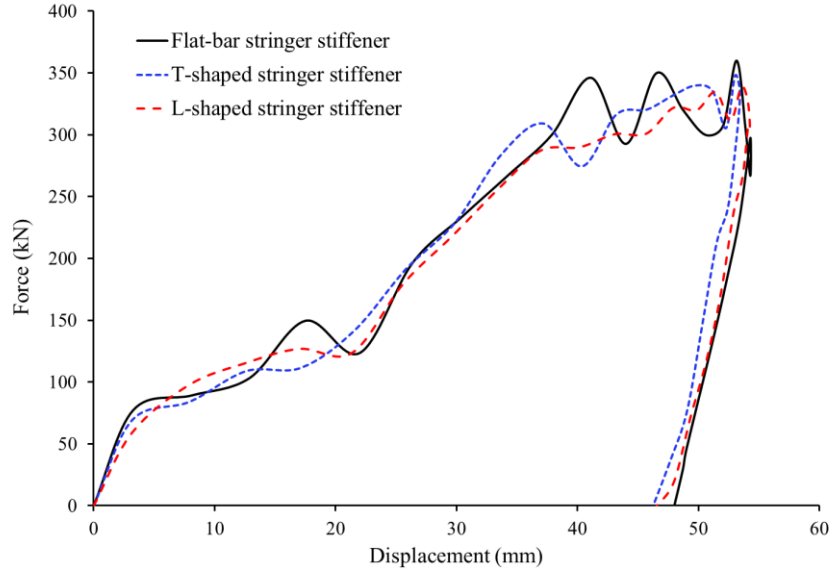


Fig. 3.76 Force-displacement curves for various stringer-stiffener types.

3.4.2.4 Effect of striker header shapes

To investigate the effects of striker header shape on the responses of stringer-stiffened cylinders subjected to dynamic mass impact, three types of striker headers were considered, namely, knife-edge, rectangular and hemispherical indenters. The details of the indenter dimension are given in Fig. 3.69. The striker mass was assumed to be 500 kg and the collision velocities were generated from 4 to 10 m/s. The energy parameter, λ_E , is determined as the ratio between the kinetic energy of striker and the struck structure's energy absorption, like equation (3.15).

$$\lambda_E = \frac{E_k}{E_a} \quad (3.15)$$

where $E_k = \frac{1}{2}mv^2$; Kinetic energy

$$E_a = \frac{\sigma_Y + \sigma_T}{2} \varepsilon_T V_{str}; \text{ Strain energy absorption capacity}$$

The collision analyses were performed with various impact velocities to obtain the damage extents. The results of various striker shape are summarised in Table 3.19 and shown in Fig. 3.76. The most severe case is when the load is applied through a hemispherical indenter which resembles highly localized point loading. The circumferential bending resistance of the cylinder shell cannot be utilized unless the contact area gets large and most of the resistance comes from membrane deformation. Contrary to the hemispherical indenter case, when the load is applied through a rectangular indenter, the resistance is much higher than the knife-edge indenter case. In this case, the load is distributed in a very large area both in circumferential and longitudinal direction at the

initiation of the impact. Furthermore, the results show that when the energy ratio, λ_E , is in the range from 0.5×10^{-3} to 3.1×10^{-3} , the permanent dent depth of the stringer-stiffened cylinder owing to the hemisphere-type indenter was much larger than those of the others. However, interestingly, the permanent dent depths of the three types of striker were approximately the same, when λ_E was almost smaller than 0.12×10^{-3} .

3.5 Derivation of approximate equations to predict the extent damage

In this section, a series of finite element analyses were performed on the design example of a ring/stringer-stiffened cylinder of an actual submarine design concept and on other rings-stiffened cylinders given in the ABS rules [177]. The finite element model was applied with the methods presented in previous section. For each model, a series of finite element analyses were conducted for various dents. To generate damages on the models, a collision analysis was conducted using a rigid knife-edge indenter or hemisphere indenter. In practice, ring/stringer-stiffened cylinder structures are subject to damage in many ways, as a striking ship may collide with these structures by its bow, stern, or side. Therefore, the striking ships could be less or more structurally rigid than the cylinder structures and it leads to less or more absorbed energy from the collision. In this study, a rigid knife-edge striker was applied and it would generate more severe damage than that caused in actual circumstances.

Table 3.19 Summary of collision analysis results with various striker header shapes.

Impact velocity, v (m/s)	Kinetic energy, E_k (J)	$\lambda_E \times 10^3$	Permanent dent depth (mm)		
			Knife-edge	Rectangular	Hemispherical
2.0	1000	0.124	11.6	10.1	10.5
4.0	4000	0.498	26.2	20.8	30.3
6.0	9000	1.120	43.7	33.2	56.4
8.0	16000	1.991	60.1	45.7	74.1
10.0	25000	3.111	77.1	58.7	87.9

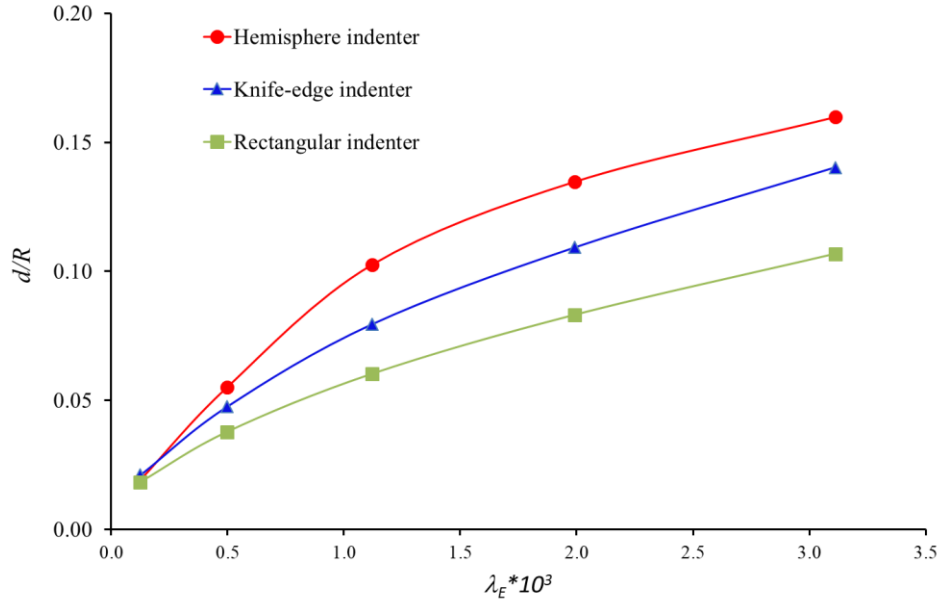


Fig. 3.77 Results from various striker header shapes.

3.5.1 Ring-stiffened cylinder

The dimensions and material properties of the model are listed in Table 3.20. For the collision analysis, the employed velocities were of 1.0 m/s, 2.5 m/s, 5.0 m/s, 7.5 m/s, and 10 m/s. With each velocity, a collision was performed with striker masses of 10 tons, 20 tons, and 50 tons. Therefore, a total of 150 numerical cases were performed. The finite element models were generated with the techniques explained in the previous section. The global mesh size was 80 mm, while the local mesh size was 40 mm. The range of R/t (radius of cylinder/shell thickness) was determined from 97 to 454, and the range of dent depth to radius d/R from 0 to 0.25.

Based on the results calculated for the reference ring-stiffened cylinder models, a simple design formula may be derived by means of a regression analysis in order to predict the maximum permanent dent depth of the ring-stiffened cylinder under dynamic collision. Before performing the regression, the corresponding non-dimensional parameters were assessed to determine the correct dependent parameter that can be used appropriately to derive the non-dimensional dent depth δ_d . The dependence δ_d on the different geometric and material property parameters is presented. The various parameter combinations were also investigated in order to identify the most suitable on which to base δ_d . The trends and degrees of dependence are displayed in detail in Table 3.21 and it can be seen that the variable $\lambda_E = E_k / (\sigma_Y V_{str})$ provides the most suitable basis for δ_d .

Table 3.20 Properties of the reference ring-stiffened cylinders.

Sym.	Unit	RS-1	RS-2	RS-3	RS-4	RS-5	RS-6	RS-7	RS-8	RS-9	RS-10
R	mm	3100	3023	3175	3100	2550	5150	2500	3500	550	3180
t	mm	30	25	20	23	26.2	30	15	12	4.97	7.0
L	mm	12600	15240	10500	10320	14850	16250	11250	7500	1060	6650
L_s	mm	430	3048	840.7	430	450	650	750	400	150	350
σ_Y	MPa	645	754	645	645	827	645	380	276	275	345
E	GPa	206	206	206	206	210	206	205	199	202	199
n_r	[-]	29	5	12	24	33	25	15	19	7	19
h_{rw}	mm	210	214	95.2	180	178	262	190	255	40	120
t_{rw}	mm	19.0	15	11	13	26	16.5	20	11.5	6.0	19
b_{rf}	mm	155	280	76.2	90	102	231	120	76.2	0	90
t_{rf}	mm	19	17	11	23	14	24	20	11.5	0	17
R/t	[-]	103	121	159	135	97	172	167	292	111	454

After the dependent parameters were investigated, the regression analysis was performed with the best-fit evaluation of the numerical results. The best-fit curve from the mean equation numerical data is plotted in Fig. 3.78. In this figure, it is noted that values of permanent dent depth (d) smaller than 0.5% of the cylinder radius (R), which corresponded to the upper limit of tolerable imperfection for ring-stiffened cylinders by PD 5500 [139], were not considered because these values may be assumed as initial imperfections. The accuracy of the best-fit curve was quite good with a mean of the uncertainty modelling factor (X_m) of 0.996 together with a COV of 6.32 %.

Simple formula for predicting the permanent dent depth of ring-stiffened cylinders was derived as equation (3.16). In addition, when considering the safety design, the design equation is provided in Eq. (6.17), which is determined by multiplying mean curve with $(\text{Mean} + 2*\sigma)$. Where σ is standard deviation of mean equation. δ_d is non-dimensional of the permanent dent depth to cylinder radius and the energy parameter λ_E is the ratio of kinetic energy of striker (E_k) to energy absorption capacity of struck structure (E_a) as defined in equation (3.20). Furthermore, Hsu and Jones [144] also provided the energy ratio with different formulations. The static and dynamic energy absorption effectiveness factors ψ and ψ' , respectively, are provided. The static-energy absorption effectiveness factor ψ was defined as the ratio of elastic and plastic strain energy absorption of structural members over the energy absorbed in the same volume of material up to tension fracture. The dynamic energy absorption effectiveness factor ψ' is introduced as the ratio

between total input energy (included kinetic energy) and maximum plastic strain energy absorbed up to failure in the static tension test on material.

Table 3.21 Dependence of δ_d on non-dimensional geometry and material parameters.

Parameter		δ_d	Degree of dependence
L/R			Weak
R/t			Weak
L_s/t			Weak
E/σ_Y			Medium
h_w/t_w			Weak
l_d/R			Weak
$\frac{\sqrt{Lt}}{R} \frac{E}{\sigma_Y}$			Weak
$\frac{E_k}{\sigma_Y \cdot V_{str}}$			Strong

In equation (3.20), the kinetic energy of the striker is proportional to the striker mass (m) and the square of impact velocity (v), and is described in equation (3.21). The static energy absorption capacity E_a was determined by equation (3.22) and here σ_Y is yield strength, σ_T is ultimate strength, and ε_T and V_{str} are the ultimate strain and structure volume, respectively. The structure volume can be rapidly calculated using equation (3.23). Furthermore, the ultimate strength (σ_T) and ultimate strain (ε_T) could be estimated by equations (3.24), (3.25), (3.26), and (3.27). These equations were derived using approximately 7500 tensile test results, including general structural steels and marine structural steels, which were provided by Cho et al. [140].

Generally, the predictions of the extent damage of stiffened cylinder under dynamic mass impact are significant depending on types of indenter shape. Therefore, to consider the effects of striker header shapes such as knife-edge, rectangular and hemispherical indenters, the reduction factor may derive and multiplied together with the proposed formulations. Furthermore, the effects of impact locations and impact angles were also considered as shown in Eqs. (3.18) and (3.19), respectively. The details of these equations are given in Appendix E.

$$\delta_d = \frac{d}{R} = 4.91 C_S C_L C_\beta (\lambda_E)^{0.71} \quad ; \text{ Mean equation} \quad (3.16)$$

$$\delta_d = \frac{d}{R} = 5.16 C_S C_L C_\beta (\lambda_E)^{0.71} \quad ; \text{ Characteristic equation} \quad (3.17)$$

C_S : Indenter shape factor ($C_S = 1$: Hemisphere indenter; $C_S = 0.81$: Knife-edge indenter; $C_S = 0.68$: Rectangular indenter)

C_L : Impact location factor

C_β : Impact angle factor

$$C_L = \text{Exp} \left(-1.55 \left(\frac{x}{L} \right)^{0.57} \right) \quad (3.18)$$

$$C_\beta = 0.139\beta^2 - 0.0437\beta + 1 \quad (3.19)$$

Where

x : distance from collision to mid-span of ring-stiffened cylinder

L : total length of ring-stiffened cylinder

β : impact angle (rad)

$$\lambda_E = \frac{E_k}{E_a} \quad (3.20)$$

$$E_k = \frac{1}{2} m v^2 ; \quad \text{Kinetic energy} \quad (3.21)$$

$$E_a = \frac{\sigma_Y + \sigma_T}{2} \varepsilon_T V_{str}; \quad \text{Strain energy absorption capacity} \quad (3.22)$$

$$V_{str} = V_{shell} + V_{ring-stiffener} = A \cdot L + V_{ring-stiffener} \quad (3.23)$$

- For general structural steel:

$$\frac{\sigma_T}{\sigma_Y} = \left\{ 1 + 0.664 \left(\frac{E}{1000\sigma_Y} \right)^{2.4} \right\} \quad (3.24)$$

$$\frac{\varepsilon_T}{\varepsilon_Y} = 336 \left(\frac{E}{1000\sigma_Y} \right)^{2.52} \quad (3.25)$$

- For marine structural steel:

$$\frac{\sigma_T}{\sigma_Y} = \left\{ 1 + 1.3 \left(\frac{E}{1000\sigma_Y} \right)^{2.5} \right\} \quad (3.26)$$

$$\frac{\varepsilon_T}{\varepsilon_Y} = 320 \left(\frac{E}{1000\sigma_Y} \right)^{1.76} \quad (3.27)$$

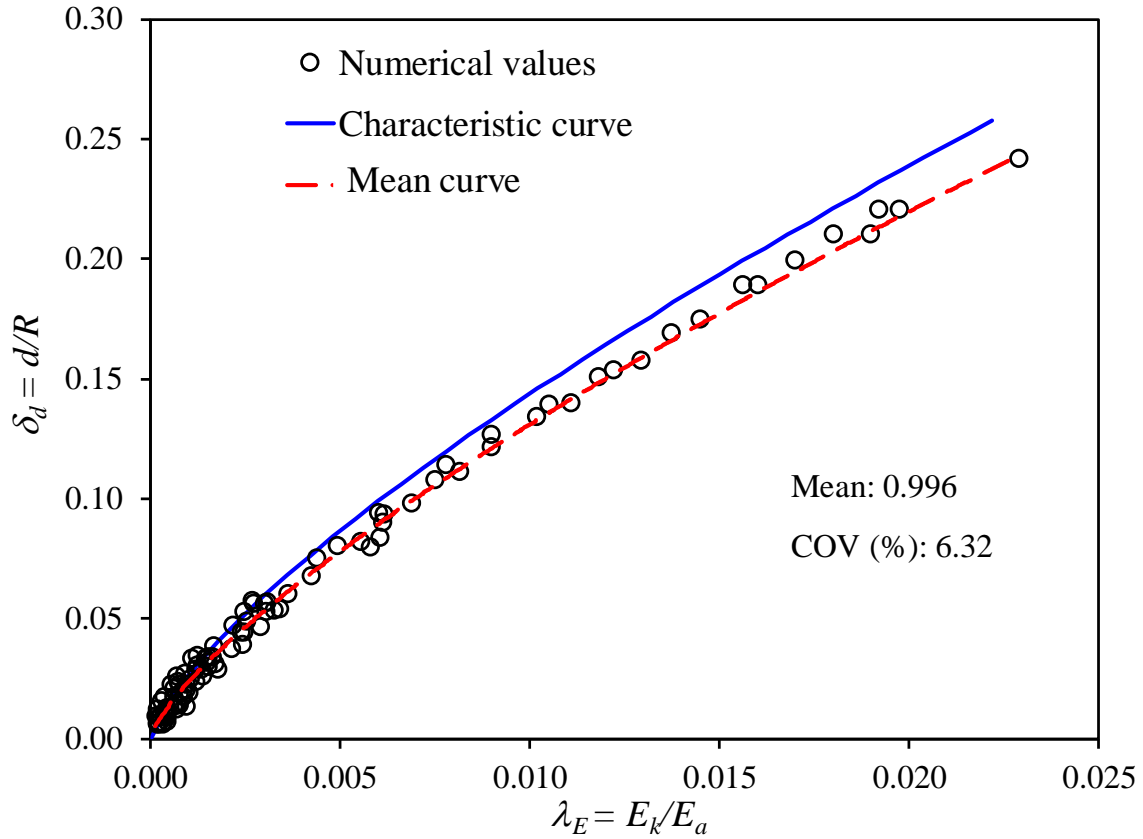


Fig. 3.78 Plotted curve to predict the extent damage for ring-stiffened cylinder.

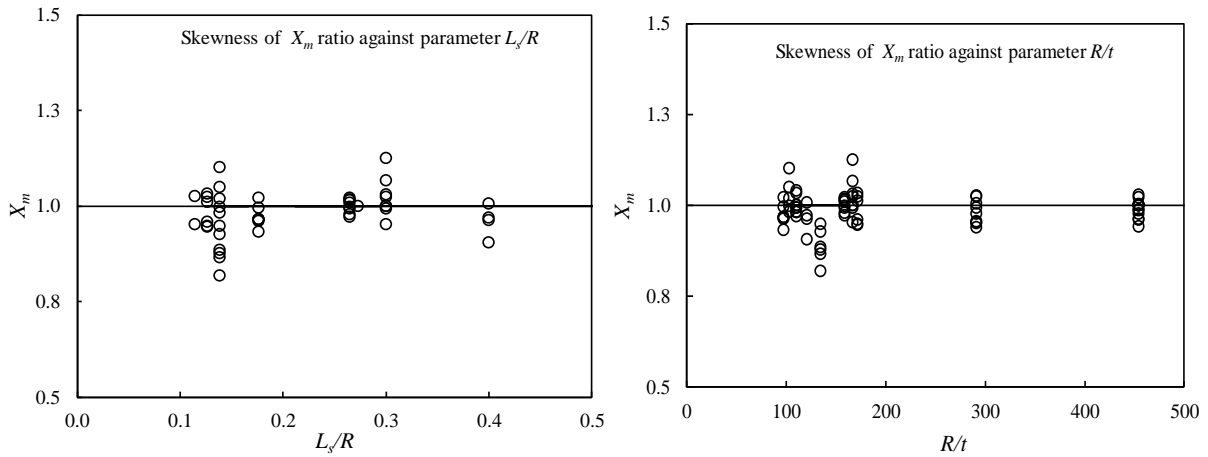


Fig. 3.79 Plotting of the proposed formula against basic parameters L_s/R and R/t for dynamic collision.

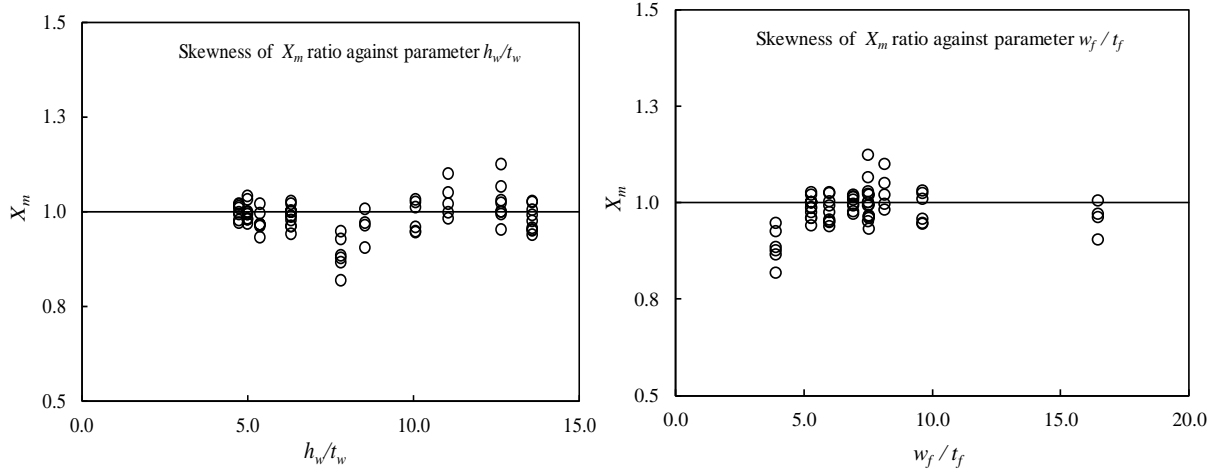


Fig. 3.80 Plotting of the proposed formula against basic parameters h_w/t_w and w_f/t_f for dynamic collision.

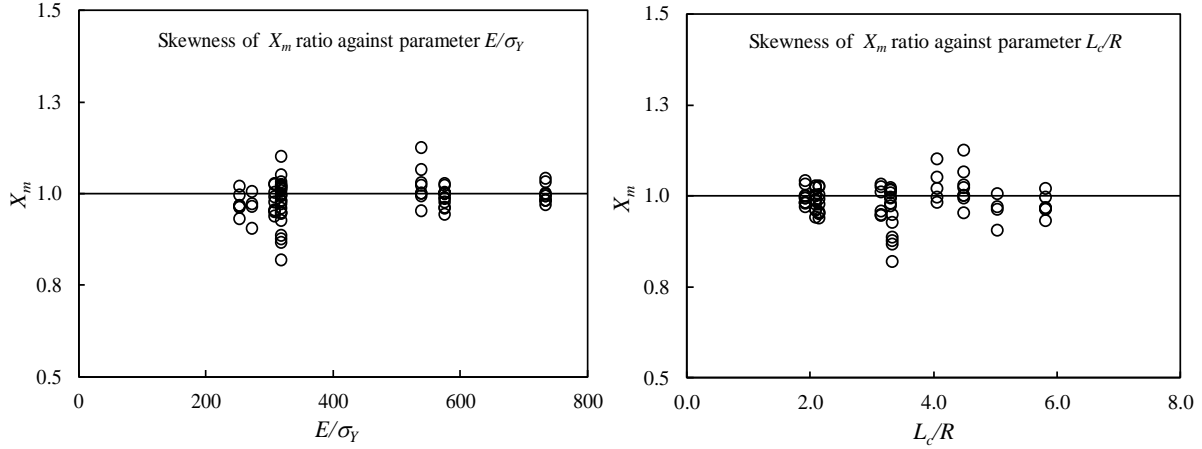


Fig. 3.81 Plotting of the proposed formula against basic parameters E/σ_Y and L_c/R for dynamic collision.

As mentioned in the previous section, Hoo Fatt and Wierzbicki (1991) and Cerik et al. (2015) developed simplified analytical methods to assess collision responses of ring-stiffened cylinders, as indicated in Eqs. (3.28) and (3.29), respectively. In the current study, the force-displacement response of the proposed formulation is expressed in Eqs. (3.30) and (3.31) for mean equation and characteristic equation, respectively. It can be obtained by the derivation of Eqs. (3.16) and (3.17) with respect to d . Where d is the dent depth at the impact point, and m_0 is the fully plastic bending moment of the cylinder wall per unit length ($m_0 = \sigma_0 t^2/4$). The average flow stress σ_0 is calculated by Eq. (3.32). An equivalent thickness t_{eq} is obtained by Eq. (3.33). And m_{eq} is the equivalent bending moment per length. The plastic axial resistance per unit width N_0 is evaluated as $N_0 = \sigma_0 t$.

$$P = 16m_0 \frac{t_{eq}}{t} \sqrt{\frac{\pi D d}{3tR}} \quad (3.28)$$

$$P = 8m_{eq}\sqrt{\frac{\pi d}{8t}} + N_0\sqrt{\frac{\pi td}{2}} \quad (3.29)$$

$$P = 0.15 \frac{E_a}{(C_S C_L C_\beta R)^{1.41}} d^{0.41} \quad ; \text{ Mean equation} \quad (3.30)$$

$$P = 0.14 \frac{E_a}{(C_S C_L C_\beta R)^{1.41}} d^{0.41} \quad ; \text{ Characteristic equation} \quad (3.31)$$

$$\sigma_0 = \frac{\sigma_Y + \sigma_T}{2} \quad (3.32)$$

$$t_{eq} = \sqrt{\frac{4m_{eq}}{\sigma_0}} \quad (3.33)$$

The mean formulation was compared with the existing formulation in the previous studies and the experimental results of two models RS-C-1 and RS-C-2, as shown in Fig. 3.81. It is clear that the force-displacement response of the proposed formulation and Cerik et al. (2015) [115] is a good agreement with the experimental results, while that of Hoo Fatt and Wierzbicki (1991) [129] does not match well with the experimental results. However, the force-displacement response curve of the proposed formulation is small higher than those of experimental results.

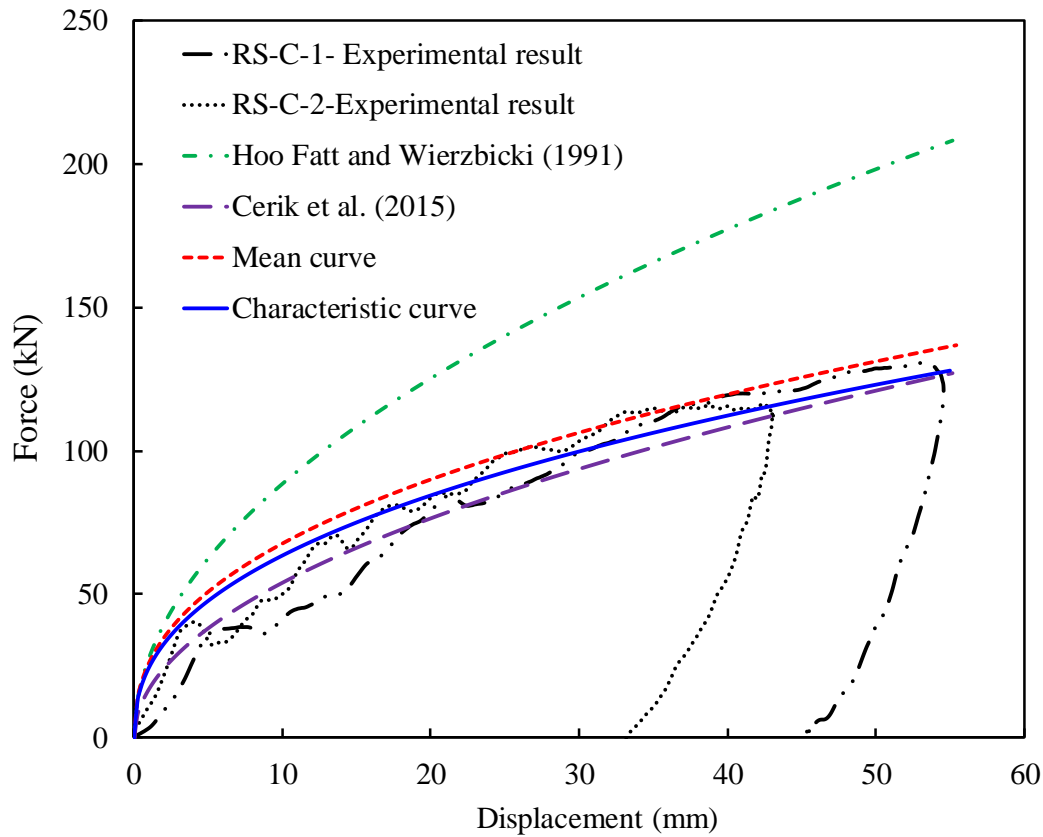


Fig. 3.82 Comparison of proposed formulation and the existing formulations with experimental results.

3.5.2 Stringer-stiffened cylinder

In this section, the simple proposed formulation was derived by a series numerical analysis results of rigorous parametric studies on the actual design of full-scale stringer-stiffened cylinder examples. The dimensions and material properties of the model are listed in Table 3.22. The employed velocities were of 2.5 m/s, 5.0 m/s, 7.5 m/s, and 10 m/s. These selected velocities have represented the collisions of offshore installations with dropped objects from platform decks or floating objects. With each velocity, a collision was performed with striker masses of 10 tons, 20 tons, 50 tons, and 100 tons. Additionally, the collision of offshore installations with supply vessels is also considered. The impact velocities were 1 m/s, 2m/s and 3 m/s. For each velocity, the striker masses were 1000 tons, 3000 tons, 5000 tons, and 7500 tons. It is noted that the added mass was assumed to be 10% to 40% of striker mass. The finite element models were generated with the techniques explained and validated in the previous section. The global mesh size was 100 mm, while the local mesh size was 50 mm. The range of R/t (radius of cylinder/shell thickness) was determined from 159 to 355, and the range of dent depth to radius d/R from 0 to 0.15.

Table 3.22 Properties of the reference stringer-stiffened cylinders.

Sym.	Unit	SS-1	SS-2	SS-3	SS-4	SS-5	SS-6
R	mm	3025	13320	4200	3025	2500	8880
t	mm	19.0	41.5	20.0	12.0	15	25.0
L	mm	10240	17500.0	10500	10240	11250	6600
L_s	mm	2048.0	3500.0	3500	2048	2250	2200
n_r	[-]	4.0	4.0	12.0	4.0	4.0	2.0
h_{rw}	mm	214.0	787.5	700	214.0	190.00	525
t_{rw}	mm	20.0	37.5	12.0	15.0	20	25.0
w_{rf}	mm	200.0	450.0	300	200	150	300
t_{rf}	mm	20.0	45.0	16.0	15.0	20	30.0
n_s	[-]	18.0	36.0	36	18.0	20	60.0
h_{sw}	mm	160.0	450.0	250.0	160.0	150	300
t_{sw}	mm	15.0	37.5	12.0	11.5	20	15.0
w_{sf}	mm	100.0	285.0	90.0	100.0	100	190.0
t_{sf}	mm	15.0	45.0	12.0	11.5	20	19.0
σ_Y	MPa	276.0	345.0	355	276	380	345
E	GPa	205000	206000	206	205000	206000	200000
R/t	[-]	159	321	210	263	167	355

The procedures to derive the formulations for predicting the extent damage of stringer-stiffened cylinder under dynamic mass impact are similar to ring-stiffened cylinders in previous section 3.5.1. After the dependent parameters were investigated, the regression analysis was performed with the best-fit evaluation of the numerical results. The best-fit curve from the proposed equation numerical data is plotted in Fig. 3.83. In this figure, it is noted that values of permanent dent depth (d) smaller than 0.5% of the cylinder radius (R), which corresponded to the upper limit of tolerable imperfection for ring-stiffened cylinders by API [143] were not considered, because these values may be assumed as initial imperfections. The accuracy of the best-fit curve was quite good, with a mean of the uncertainty modelling factor (X_m) of 0.987 together with a COV of 8.60 %.

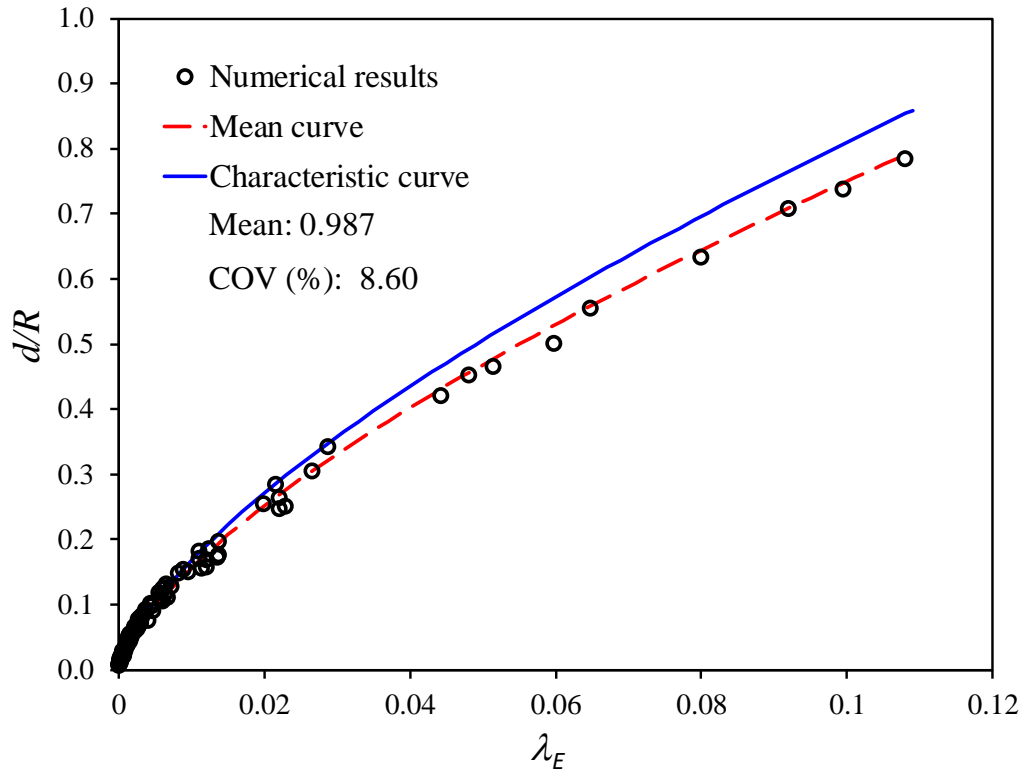


Fig. 3.83 Plotted curve for prediction of extent damage for stringer-stiffened cylinder.

Simple formulations for predicting the permanent dent depth of stringer-stiffened cylinders were derived as Eqs. (3.34) and (3.35). In these equations, the effect of striker header shapes and impact locations as well as impact angles was also considered as the reduction factor C_S , C_L and C_β , respectively. The effects of impact locations and impact angles were considered as Eqs. (3.36) and (3.37), respectively. The results of various striker shape are shown in Fig. 3.84. The most severe case is when the load is applied through a hemispherical indenter which resembles highly

localized point loading. Therefore, the proposed formulation was derived based on the most severe case of a hemispherical indenter.

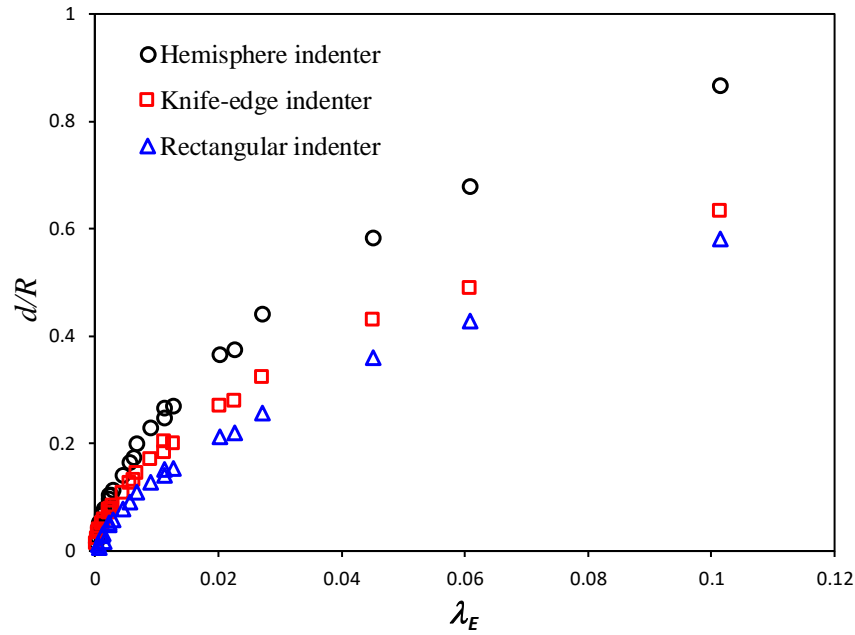


Fig. 3.84 Collision response of stringer-stiffened cylinder with various striker header shapes.

$$\delta_d = \frac{d}{R} = 3.59 C_S C_L C_\beta (\lambda_E)^{0.68} \quad (3.34)$$

$$\delta_d = \frac{d}{R} = 4.16 C_S C_L C_\beta (\lambda_E)^{0.68} \quad (3.35)$$

where

C_S : Indenter shape factor ($C_S = 1$: Hemisphere indenter; $C_S = 0.74$: Knife-edge indenter;

$C_S = 0.63$: Rectangular indenter)

C_L : Impact location factor

C_β : Impact angle factor

$$C_L = \text{Exp} \left(-9.91 \frac{x}{L} \right) \quad (3.36)$$

$$C_\beta = 0.114\beta^2 - 0.346\beta + 1 \quad (3.37)$$

The force-displacement response of the proposed formulation is expressed in Eqs. (3.38) and (3.39) for mean equation and characteristic equation, respectively. It can be obtained by the derivation of Eqs. (3.34) and (3.35) with respect to d .

$$P = 0.224 \frac{E_a}{(C_S C_L C_\beta R)^{1.471}} d^{0.471} \quad ; \text{ Mean equation} \quad (3.38)$$

$$P = 0.18 \frac{E_a}{(C_S C_L C_\beta R)^{1.471}} d^{0.471} \quad ; \text{ Characteristic equation} \quad (3.39)$$

The skewness of the ratios of numerical analysis results to proposed formulation results (X_m) with basic parameters are shown in Figs. 3.85, 3.86, and 3.87. These procedures are important in regression analysis for developing design formulations. It is clear that there is no apparent skewness, which means that there are no significantly affected dependent parameters. Therefore, these basic parameters should be not considered for inclusion in the design of the proposed formulation for predicting the extent of damages under dynamic mass impact.

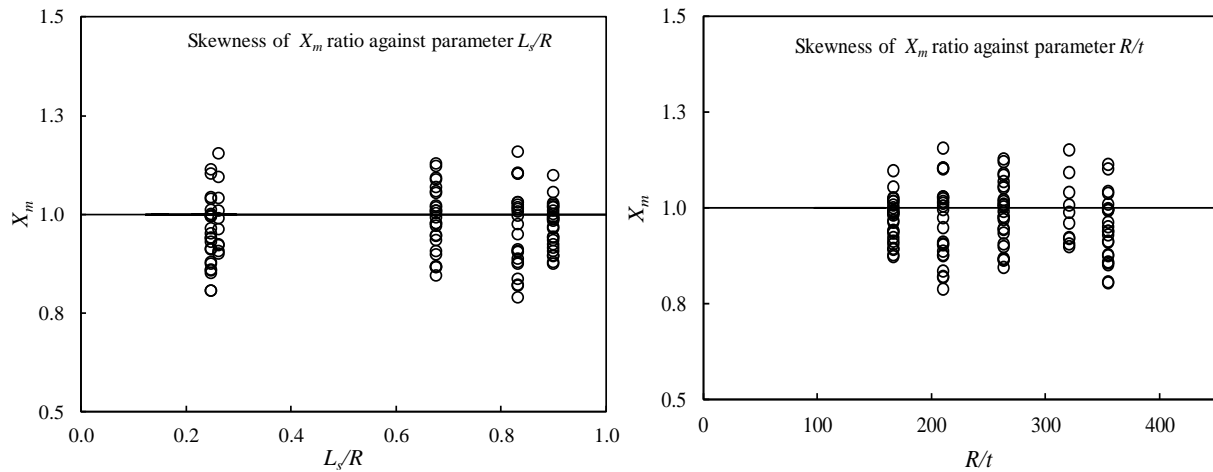


Fig. 3.85 Plotting of the proposed formula against basic parameters L_s/R and R/t .

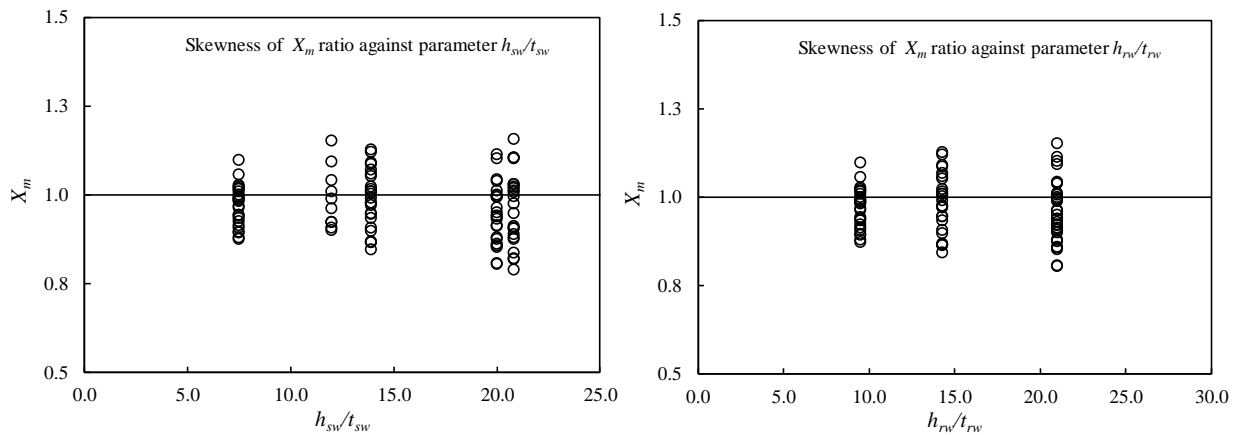


Fig. 3.86 Plotting of the proposed formula against basic parameters h_{sw}/t_{sw} and h_{rw}/t_{rw} .

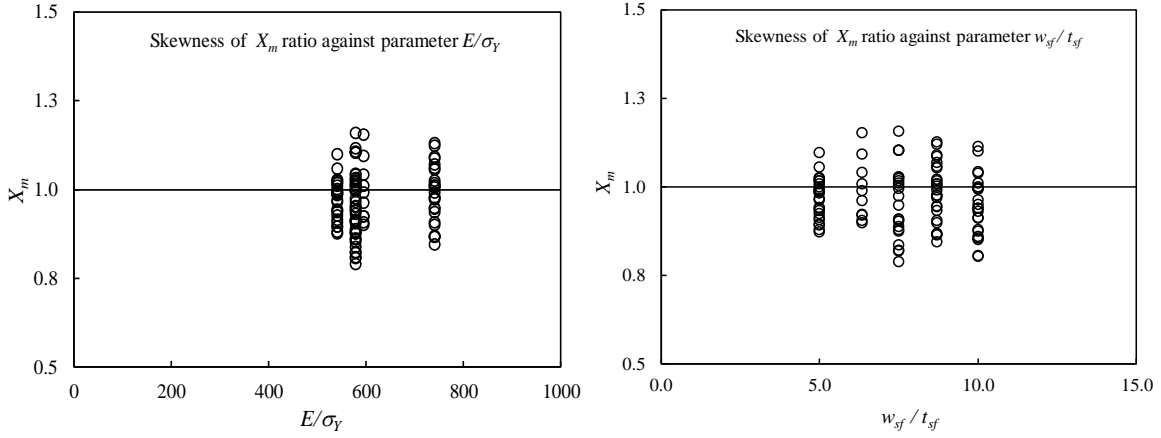


Fig. 3.87 Plotting of the proposed formula against basic parameters E/σ_Y and w_{sf}/t_{sf} .

The proposed formulation was compared with the numerical results of two models SS-C-1 and SS-C-2, as shown in Fig. 3.88. When Eq. 3.34 is equated to the impact energy in the tests, maximum deflection at peak force can be obtained. In comparison with the force-displacement values, the overprediction is observed. However, especially, the maximum resistance is predicted well. It is believed that for a simple tool this inaccuracy is acceptable. This is important when designing the cylinder based on strength design principles.

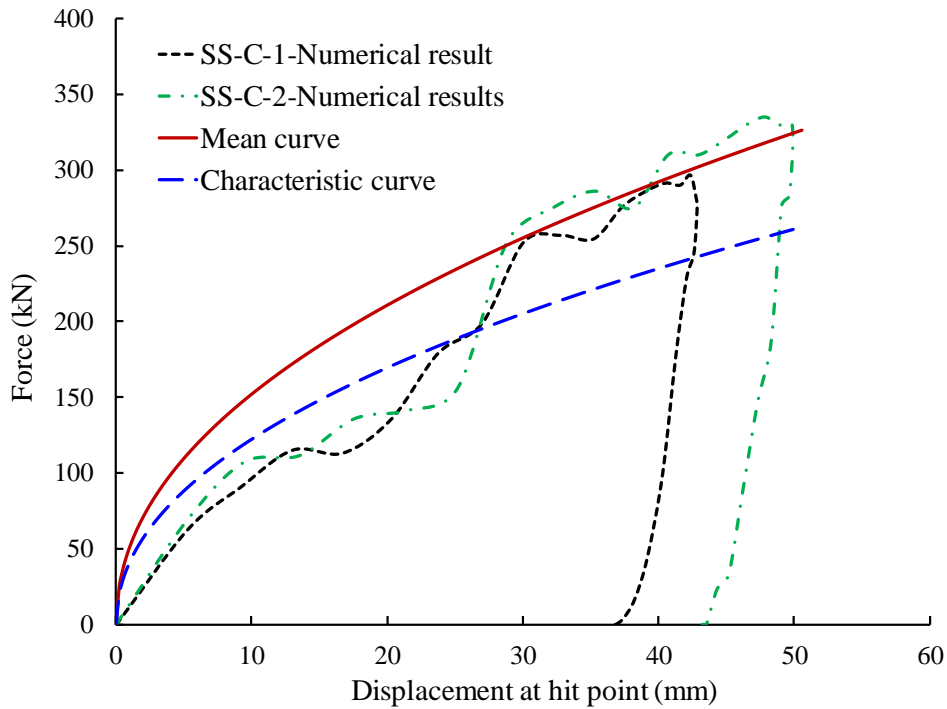


Fig. 3.88 Comparison of proposed model with the numerical results of SS-C-1 and SS-C-2.

3.6 Final remarks

Based on the results of this Chapter, the following conclusions can be drawn:

The dynamic impact tests of ring- and stringer-stiffened cylinder models were successfully conducted in this study. The details of the experimental setups, test procedures and test results are also reported in this Chapter.

For ring-stiffened cylinders, the damage can be described as denting at the impact region. The dent flattens the cross section with a length of the indenter width. At the ends of the flattened dent section, the shell bulges outward. The large dent is limited in the mid-bay. The boundaries of the dent are semi-ellipses. Nonetheless, the damage also spreads by flattening to the adjacent bays in the longitudinal direction. The longitudinal generators deflect inward and cause material stretching in the axial direction because of the end-plate resistance and membrane resistance of the shell. The remainder of the shell is unaffected. This damage shape follows the damage shape of unstiffened cylinders. The end plate and the end ring were sufficiently stiff to maintain circular ends. However, a small degree of rotation was observed on the upper part of these end supports.

For stringer-stiffened cylinders, the damages obtained can be described as a local denting confined at the contact bay. The local dent results in a flattening of the cross-section, with a length equal to that of the indenter and an outward bulging of the zone adjacent to the dent and semi-elliptical-shaped flattened zones in longitudinal direction. The stringer acted as a beam that resisted loading until they formed plastic hinges, while the ring-stiffeners prevented the extent of damage spreading to adjacent bays. Furthermore, it is also noteworthy that local tripping of stringer-stiffeners was apparent near the ring-stiffeners, which was not observed in the previous quasi-static denting tests.

Comparative analysis of denting tests with numerical simulations gave insights on the impact response of ring- and stringer-stiffened cylinder. A good accuracy and reliability of the numerical predictions were achieved for the dynamic mass impact analysis, which can be adopted to perform of further parametric studies for developing design guidelines. The importance of strain rate hardening definition is emphasised. The sensitivity of the numerical simulation accuracy to the strain-rate hardening definition was highlighted. Therefore, it is suggested that the dynamic material properties be used to define plasticity at high strain rates.

The numerical results are very sensitive to the boundary condition definitions. When the boundary conditions are adequately simulated as the test model, good predictions can be expected. Furthermore, the effects of the impact velocities and locations as well as striker header shapes were also investigated in this study in order to clarify the progressive impact responses of ring- and stringer-stiffened cylinders.

A simple formula for predicting the maximum permanent dent depth of ring- and stringer-stiffened cylinders under dynamic mass impact was derived. The accuracy of the proposed formulations has been validated with existing experimental results, and a good agreement was obtained. Thus, in actual cases, when the striking mass, collision velocity, and material parameters, along with the dimension of the ring or stringer-stiffened cylinder structures, were provided, the maximum permanent dent depth was adequately and rapidly predicted with the proposed formulations.

Chapter 4 Fracture response of tubular structures to lateral collision at room and sub-zero temperatures

4.1 Introduction

Tubular member structures are widely used in jackets/legs of fixed offshore platforms and bracings of floating offshore installations, and more recently, as the chord and bracing members for floating offshore wind turbine foundations. The major advantages of tubular structures are good axial compressive loading resistance and low drag resistance force by passing fluid. In addition, these structures are also convenient fabrication and construction. In operational conditions, these structures are not only subjected to dominant compression/tension and hydrostatic pressure but also bending moment owing to ocean waves and winds. Furthermore, during their service lifetime, tubular members may be potentially damaged caused the unexpected forces such as ship collisions, the impact of dropped heavy objects, or slamming. Among these accidents, ship collisions have been highlighted as the most serious ones owing to the damage or even catastrophic loss of the structural integrity [4]. A minor collision will result in only repairable local damage of structure and probably will not call for cease of operation. A major collision, on the other hand will damage tubular structures globally and certainly require a cease of operations. However, it seems extremely uneconomical to design tubular member structures to withstand a major collision and remain operational and it also seems that an attempt to eliminate all collisions can be impractical. Therefore, in order to practice while at the same time economically solve the offshore collision problems, the probability of major collisions should be kept at a low level by defining adequate preventive measures and minor ones should be considered the effects of the damage on the strength and serviceability during the initial design stage for safety concerns [82].

There are many researchers who have studied experiments on the collision of tubular structures. Furnes and Amdahl [180], Søreide et al. [79], Ellinas and Walker [181] provided the experimental investigations on lateral quasi-static impact responses of tubular. Cho [82] reported the dynamic lateral impact tests on small-scale single tubes having simply supported roller conditions. Jones et al. [182] conducted quasi-static and dynamic denting tests on fully fixed boundary conditions for mild steel pipes. Pendersen et al. [183] estimated of collision force between merchant vessels's bow and gravity-supported offshore installations. Amdahl and

Johansen [184] studied the collision of the ship's bow and rigid-jacket tubular, while Amdahl and Eberg [185] considered a rigid ship's bow collision with deformable tubular structures. Recently, Cho et al. [186] provided extensive experimental data of the dynamic impact tests on H-shape tubular members for damage assessment at T-joint of bracing and chord. The impact locations were performed at mid-span and 200 mm away from mid-span.

Theoretical models for the collision of tubular bracings, it is considered the deformation of local denting damage and a global denting damage. The interaction of both local and global damages is the main reason leading to overall bending damage of tubular braces. Therefore, the interaction damage modes are important and should be considered carefully. However, most of the theoretical studies were attracted to solve these modes separately. Furnes and Amdahl [180] and Ellinas and Walker [181] proposed the design curves for assessing local denting damages based on their experimental results. de Oliveira [187], Guedes Soares and Sørense [188], and Sørense and Amdahl [78] developed the theoretical models based on the global beam deformation. The static and dynamic impact responses of metal tubes were investigated by Stronge [189]. Cho [186] proposed the empirical formulations to predict the maximum permanent local deflection and overall bending. These formulations were derived using the results of dynamic impact tests and numerical studies. Paik et al. [190] developed equations for the damaged estimation of tubular members of quasi-static denting.

Recently, Cerik et al. [83] provided the criterion to classify the failure modes of tubular member denting responses based on the extensive numerical results from ABAQUS. The failure modes were separated into three modes: mode 1-dominated by global bending only, mode 2-combination of local denting and beam deformation, mode 3-dominant local shell denting only. It is noted that this research is focused on fully fixed single tubular members under the dynamic impact of knife-edge indenter, and the fracture response is not considered. Furthermore, Cho et al. [186] proposed formulations for predicting the local denting damage and overall bending damage at the impact location of H-shape tubular members. These formulations were derived based on the test data and numerical results. However, it is also not considered the combination of local and global deformation. Until recently, there is no research in the open literature which is accurate and reliable for considering the failure modes of H-shape tubular members under dynamic mass impact. Therefore, in this paper, the interaction between local damage and overall bending damage and joint behavior was taken into account through experimental and numerical results. The failure modes were divided with 2 modes: mode I-plastic damage on bracing only or plastic damage on both bracing & chord, mode II-Plastic damage on bracing and fracture at T-joint.

Nowadays, finite element modeling (FEM) is a powerful tool for predicting ship collisions and groundings. However, one of the main challenges when modeling ship collisions groundings is the satisfactory formulation of the failure criterion to predict the fracture propagation in the ductile material. Thus, these problems are not yet answered accurately and it is still an intensive research topic. Ship and offshore structure collision modellings are very complicated processes. It includes material properties (strain hardening and strain rate effects), geometries, loadings and boundary conditions, others for both striking ships and offshore structures. The numerical analysis of collision needs to input an adequate failure criterion because it is significantly affected by the membrane stretching, crushing and tearing of shells [191]. These progressive failures would be influenced on global structural collapse modes [192].

Recently, many researchers have investigated experiments, theories and developed their FEM for fracture criteria applied in ship collision problems. Generally, there are four main groups of failure criteria applied in FEM of ship collision problems included: equivalent plastic strain criterion [193-206], tri-axial stress state based failure criterion [194, 207-210] and forming limit diagram criterion [211-213] and other types of failure criteria [214-221]. Actually, all fracture criteria also have advantages and drawbacks of each other when applied in ship collision modeling. Interestingly, it is noted that the equivalent plastic strain criterion is the most common criteria used in ship collision modeling. The fracture occurs when the equivalent plastic strain is attained the critical strain (rupture strain). This is the simplest method to solve fracture problems applied in collision simulations of ships. It could be performed easily in an explicit computer code to solve dynamic problems because the stiffness matrix of whole structures is not to assemble and invert [191].

For the equivalent plastic strain criterion, the local crack initiation is assumed to take place when the equivalent plastic strain is obtained the critical strain. This critical strain value can be called fracture strain or maximum plastic strain, which commonly is determined by tensile tests. In ship collision modelling, the range of maximum rupture strain from 10% to 70% [192]. In this study, the simple critical failure strain based on equivalent plastic strain criterion was derived for offshore tubular member and ship collisions. It is a function of the size of fine mesh elements. The reason to choose fine mesh is that the whole ship and offshore structure collisions are very large size, however, fracture occurs only in narrow of the contact areas. In addition, it is very difficult to obtain the fracture phenomena in numerical analysis with the mesh size larger than $5t$ (where t is the thickness of plate) [222]. Therefore, to reduce time of numerical analysis and better to capture the local rupture phenomena, the fine mesh of the impact region and T-joint is selected. Furthermore, the accuracy of the proposed formulation has been established by comparison with the results of tests and finite element analyses.

Nowadays, offshore activities and transportations are increased significantly in arctic regions owing to the expected natural oil and gas resources in the range of 13% of the world's undiscovered oil and gas. Furthermore, the global climate change continues to increase this marine transport in the Arctic Sea as a result of decreasing ice extends. Less ice provides new opportunities for shipping, leading to more intense and rapid development of arctic related technologies. Offshore platform structures may operate at sub-zero temperatures, especially in arctic environments. During service life in the Arctic sea, these structures may potential collision with ships, ice floes or floating objects. Moreover, at sub-zero temperatures, structures may have more brittle behaviour, affecting their performance in service. In the available literature, there are a few studies interested in marine structures at low temperatures [224-225].

Within this context, the aim of this study is three steps. First, the detail results of the dynamic impact tests on bracings joined with two chords of H-shape tubular member at room and sub-zero temperature are provided. The aim of the tests is to provide more realistic information about local denting deformation of tubular wall at the impact location and overall bending deformation of tubular as a beam under lateral impact. The brittleness in tubular members in arctic conditions is also shown by performing impact tests at low temperature. The results of impact tests along with available test results from literature are correlated with numerical analyses performed using commercial finite element analysis package ABAQUS/Explicit. Second, the simple critical failure strain was derived for predicting the fracture response at T-joint of tubular member under low-velocity mass impact. Finally, the proposed formulations for predicting the local denting damage and overall damage are also considered.

4.2 Details of experiments

4.2.1 Test models

4.2.1.1 Dimensions of the test models

The models are H-shape tubulars which consisted one brace and two chords joined to the brace ends by welding. In actual offshore tubular structures, the ranges of D/t ratio are generally used from 20 to 60. In this study, the dimensions of test models were also chosen based on this range of D/t ratio. There were eighteen H-shape tubular models which were fabricated. The dimensions of chords were the same for all models with different dimensions for braces. The experimental models were classified as A, B, C, E, F, G and H series following their brace dimensions. The detail dimensions of each model at room temperature and sub-zero temperature tests are listed in Tables 4.1 and 4.2, respectively. In this table, L is the length, D is the outside

dimeter and t is the thickness of tubular. It is noted that the thicknesses of chord and brace were carefully measured at several points on each chord and brace using ultrasonic measuring instruments and determined by an average value, which is commonly less than nominally value. The dimensions of H-shape tubular member models for H series models were illustrated in Fig. 4.1.

4.2.1.2 Material properties

The material of test models was fabricated from the general-purpose structural steel. The mechanical properties of material were obtained by carry out the uniaxial quasi-static tensile tests. The shape and dimension of tensile test coupons were selected according to the Korean Standard [136], as shown in Fig. 4.2. Six coupons were tested for each series as indicated in Fig. 4.3. The average mechanical properties are given in Table 4.3.

Table 4.1 Measured dimensions of test models for room temperature (unit: mm).

Ref.	Model	Dimension of chord			Dimension of bracing			L_c/D_c	D_c/t_c	L_b/D_b	D_b/t_b
		L_c	D_c	t_c	L_b	D_b	t_b				
Cho et al. [186, 229-231]	A1	1300	114	4.05	1686	76.3	3.11	11.40	28.15	22.10	24.53
	A2	1300	114	4.05	1286	76.3	3.35	11.40	28.15	16.85	22.78
	B2	1300	114	4.04	1268	89.1	3.56	11.40	28.22	14.23	25.03
	C3	1300	114	4.04	886	114.3	4.02	11.40	28.22	7.75	28.43
	E3	1300	114	4.05	886	89.1	2.10	11.40	28.15	9.94	42.43
	F1	1300	114	4.05	1686	114.3	2.00	11.40	28.15	14.75	57.15
	F2	1300	114	4.04	1268	114.3	2.10	11.40	28.22	11.09	54.43
	G1	1300	114	6.02	866	76.0	1.79	11.40	18.94	11.39	42.46
	G2	1300	114	6.02	866	76.0	1.80	11.40	18.94	11.39	42.22
	G3	1300	114	6.00	866	76.0	1.80	11.40	19.00	11.39	42.22
	G4	1300	114	6.05	866	76.0	1.80	11.40	18.84	11.39	42.22
	G5	1300	114	6.05	866	76.0	1.79	11.40	18.84	11.39	42.46
	G6	1300	114	6.05	866	76.0	1.79	11.40	18.84	11.39	42.46
	H1	1300	114	6.07	886	90.0	2.01	11.40	18.78	9.84	44.78
	H2	1300	114	6.00	886	90.0	2.09	11.40	19.00	9.84	43.06
H3	1300	114	6.04	886	90.0	2.08	11.40	18.87	9.84	43.27	
H4	1300	114	6.07	886	90.0	2.08	11.40	18.78	9.84	43.27	
H5	1300	114	6.06	886	90.0	2.03	11.40	18.81	9.84	44.33	

Table 4.2 Measured dimensions of test models for sub-zero temperature (unit: mm).

Ref.	Model	Dimension of chord			Dimension of bracing			L_c/D_c	D_c/t_c	L_b/D_b	D_b/t_b
		L_c	D_c	t_c	L_b	D_b	t_b				
Cho et al.	D2-LT	1300	114	4.08	1268	76.3	1.86	11.40	27.94	16.62	41.02
[229]	D3-LT	1300	114	4.06	886	76.3	1.85	11.40	28.10	11.61	41.24
This study	H6-LT	1300	114	6.04	886	90.0	2.08	11.40	18.87	9.84	43.27

Table 4.3 Material properties of test models.

Model series	A-series	B-series	C-series	E-series	F-series	G-series	H-series
Yield strength, σ_Y (MPa)	401.8	377.4	360.9	360.3	344.7	319.7	317.3
Ultimate tensile strength, σ_T (MPa)	442.9	410.8	419.2	413.5	405.2	418.7	391.1
Young's modulus, E (GPa)	207	207	207	207	207	206	206
Hardening start strain, ε_{HS}	0.0252	0.0327	0.0264	0.0279	0.0268	0.0186	0.0245
Ultimate tensile strain, ε_T	0.1231	0.1349	0.1443	0.1447	0.1548	0.1723	0.1743

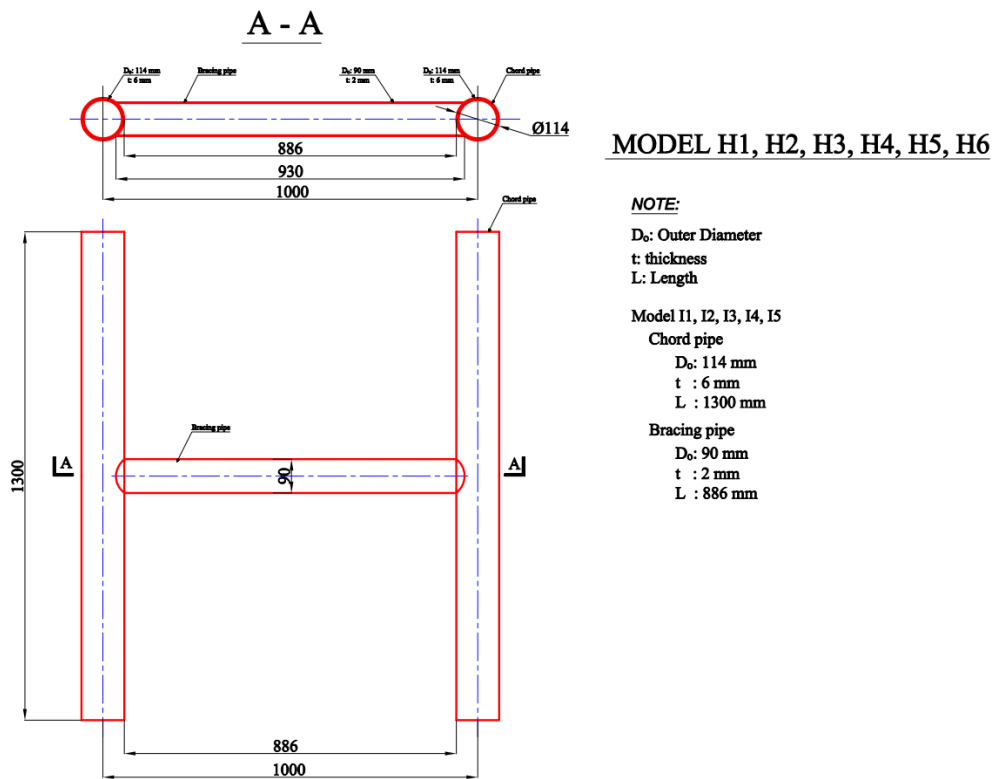


Fig. 4.1 Dimensions of H-shape tubular member models (unit: mm).

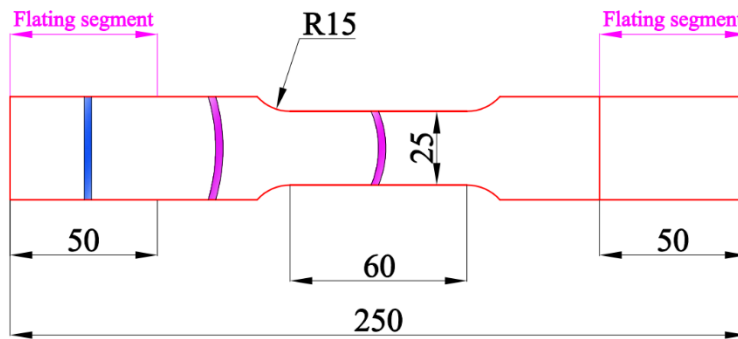


Fig. 4.2 Dimensions of tensile test coupon.



Fig. 4.3 Tensile tests results.

4.2.2 Experimental set-up

4.2.2.1 Experimental set-up at room temperature

The experiments were performed using a drop test machine which was successful in earlier dynamic mass impact tests. The details of the experimental arrangements are indicated in Fig. 4.4. On the top of the testing frame, there is a pulley which guides and holds the striking mass by an electromagnet. The striking mass was attached to a rigid knife-edge indenter. During the drop test, the drop height can be controlled in order to obtain the expected impact energy level. When the electromagnet is disconnected, the striking mass falls freely due to its gravity. The velocity of the striking mass can be simply calculated by equating its potential energy to its kinetic energy prior to impact.

In this study, the different impact energy levels and striking mass types were applied for each model. The shapes and mass arrangement of strikers were designed to minimize the imbalances in free-fall process. Furthermore, to investigate the fracture response at T-joint of tubular, the impact locations were selected around 200 mm, 250 mm, 580 mm, and 590 mm away from the mid-span, respectively. Therefore, the shape of the striker was also required that it cannot touch the chord of tubular during the test. The radius of a knife edge header is 10 mm for the striking mass type I and II. The dimensions of striking mass and its indenter are depicted in Fig. 4.5. The details of impact test conditions for each model are shown in Table 4.4.

For the experimental boundary conditions, the model was firmly clamped and inserted rubber pads grip at both ends of the chord using the support structures, as shown in Fig. 4.4. The support structures of clamps were bolted to a rigid foundation of the loading frames. It is guaranteed that the chords are fully fixed and not allowed any translations and rotations of both ends of chord. In addition, two-direction strain gauges were attached in eight positions at both T-joint regions and impact areas. Among them, four strain gauges were bonded in outer of the shell at the impact region, and the next four strain gauges were placed at both T-joint of the tubular model.

The impact location was moved with various distance values away from the mid-span to investigate the behavior of T-joint. During the impact test, when the striking mass hit the brace of model, the rebounded phenomenon was commonly occurred. Therefore, to protect the model from unexpected damage after the striking mass rebounded, the rubber pads were used for covering all surfaces of model except impact region as indicated in Fig. 4.4.

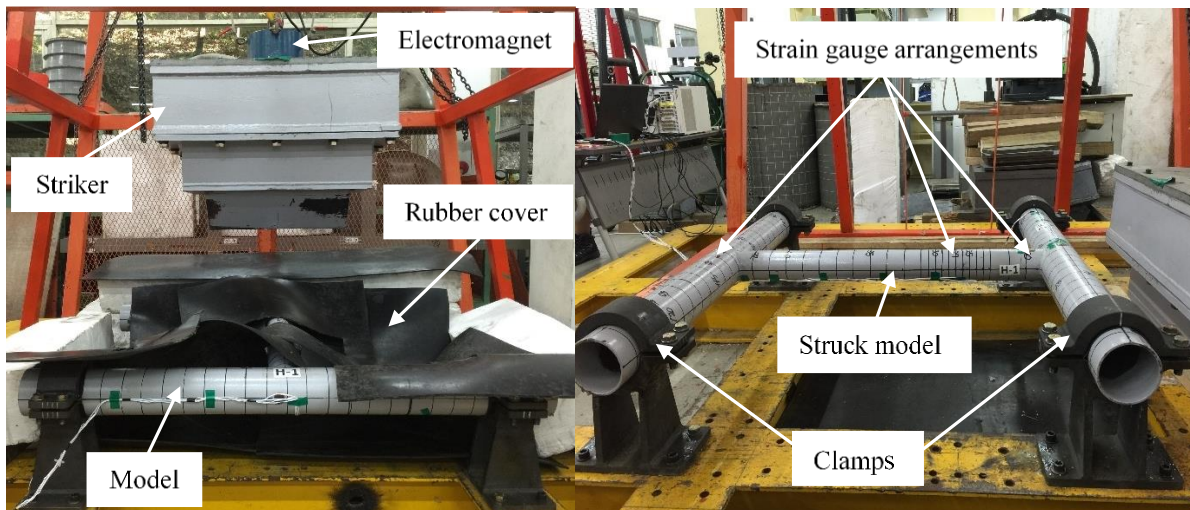


Fig. 4.4 Dynamic mass impact test setup at room temperature.

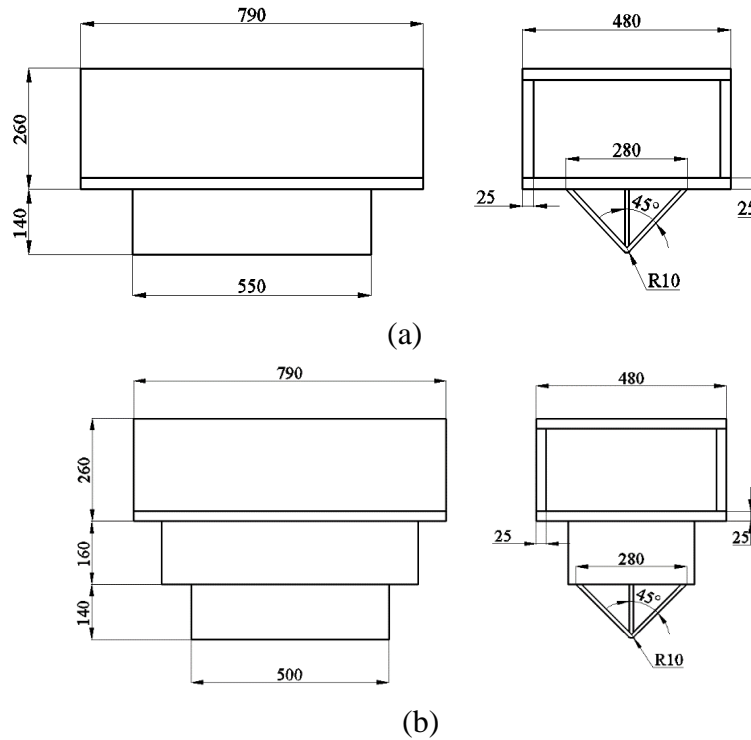


Fig. 4.5 Dimensions of striker mass: (a) Type I; (b) Type II.

Table 4.4 Impact test conditions for tubular members at room temperature.

Model	Velocity (m/s)	Striker mass (Kg)	Kinetic Energy (J)	Striker type	Impact location
A1	5.94	633	11167	II	580 mm away from mid-span
A2	6.57	633	13662	II	250 mm away from mid-span
B2	4.86	460	5433	I	200 mm away from mid-span
C3	5.26	460	6364	I	200 mm away from mid-span
E3	5.25	460	6339	I	200 mm away from mid-span
F1	6.86	633	14894	II	590 mm away from mid-span
F2	5.25	460	6339	I	200 mm away from mid-span
G1	5.13	673	8856	II	200 mm away from mid-span
G2	4.93	673	8179	II	200 mm away from mid-span
G3	4.52	673	6875	II	200 mm away from mid-span
G4	3.81	673	4885	II	200 mm away from mid-span
G5	2.17	673	1585	II	200 mm away from mid-span
G6	2.58	673	2240	II	200 mm away from mid-span
H1	2.58	673	2240	II	200 mm away from mid-span
H2	2.77	673	2582	II	200 mm away from mid-span
H3	2.94	673	2909	II	200 mm away from mid-span
H4	2.39	673	1922	II	200 mm away from mid-span
H5	2.38	673	1906	II	200 mm away from mid-span

4.2.2.2 Experimental set-up at sub-zero temperature

Northern Sweden and Finland are attractive sites for offshore wind turbine installation with good wind conditions. However, for safe operation in arctic conditions, the effects of low temperature should be considered at design stage. Three collision tests at low temperature were performed to study the low temperature brittleness in tubular members. These three models were impacted by striker at 200 mm and 250 mm from the mid-span. The models were kept in cold chambers filled with dry ice and ethanol for a certain time roughly at $-80\text{ }^{\circ}\text{C}$ as shown in Fig. 4.6. The impact conditions for the three models at sub-zero temperature $-50\text{ }^{\circ}\text{C}$ were presented in Table 4.5. The experimental set-up for model D2-LT is described in Fig. 4.7.



Fig. 4.6 Test model OWT-D2-LT in the cold chamber.



Fig. 4.7 Dynamic mass impact test setup at room temperature for model D2-LT.

Table 4.5 Impact test conditions for tubular members at sub-zero temperature.

Model	Velocity (m/s)	Striker mass (kg)	Kinetic Energy (J)	Striker type	Impact location
D2-LT	5.25	460	6339	I	250mm away from mid-span
D3-LT	4.86	460	5433	I	200 mm away from mid-span
H6-LT	2.94	673	2909	II	200 mm away from mid-span

4.2.3 Strain gauge arrangement

For room temperature collision tests, the strain gauge arrangements were placed at five positions to obtain more detail the impact response of the models. At each position two single strain gauges were affixed. First two positions are 80 mm beside the impact point along the generator line. Second strain gauge is 40 mm beside the impact point in circumferential direction. Final two strain gauge positions are located at close to the end of bracing T-joint. Arrangements of strain gauges for room temperature tests are indicated in Fig. 4.8.

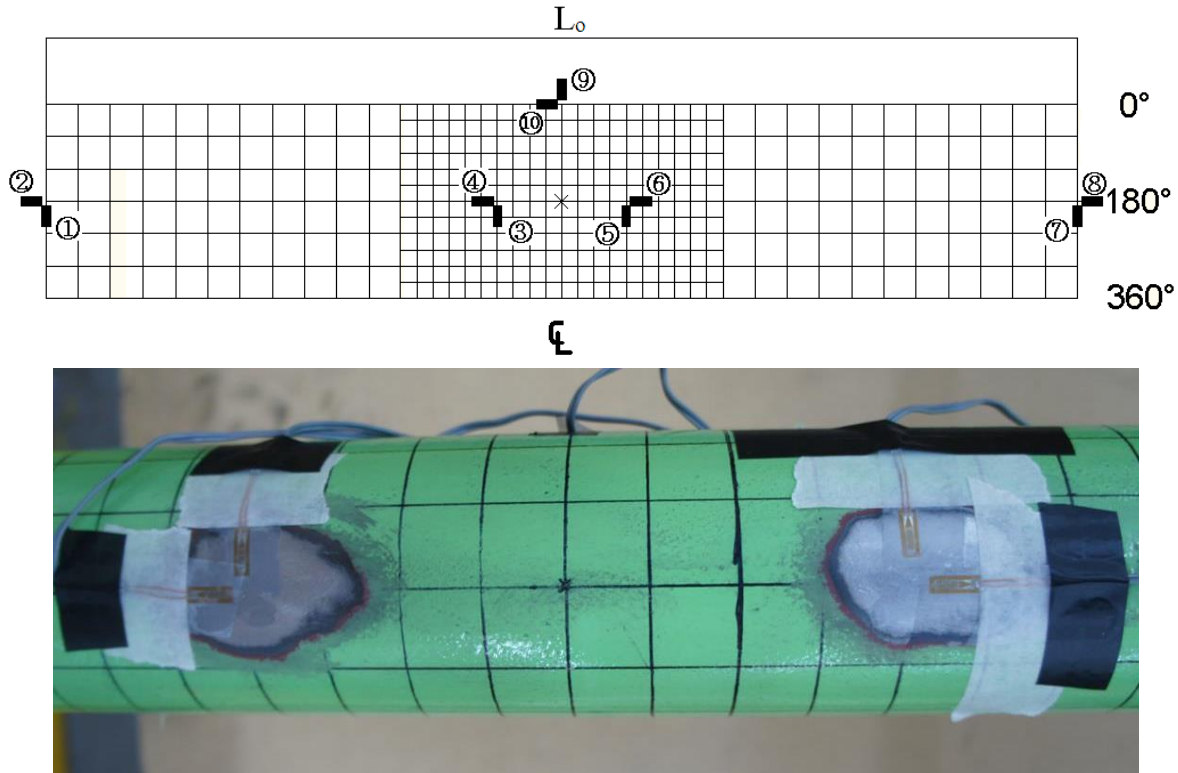


Fig. 4.8 Arrangements of strain gauges for room temperature test.

For sub-zero temperature tests, two-direction strain gauges were bonded in five positions. Among them, four strain gauges were placed on the bracing and another strain gauge was attached on chord member. Furthermore, the temperature histories were measured with five thermocouples attached on the test models. Before the impact test the cold chamber was removed and as soon as the temperature of the model became 50°C the striker was released. The arrangement of thermocouples and strain gauges are given in Fig. 4.9.

4.3 Test results

In this section, the results of the series dynamic mass impact tests were presented. The aim of these series test models was investigated the damages of H-shape tubular member under dynamic mass impact from plastic deformation to complete fracture at T-joint. It means that the impact energies were increased gradually until complete fracture occur by changing the striking masses or drop highs. Therefore, the deformations of the tested models were classified into two groups: plastic damages and fracture damages. First, the plastic damages of the tested models were included local denting, overall bending and overall twisting damages of bracing or both bracing

and chords. Second, the fracture damages were considered according to partial fracture and complete fracture at T-joint.

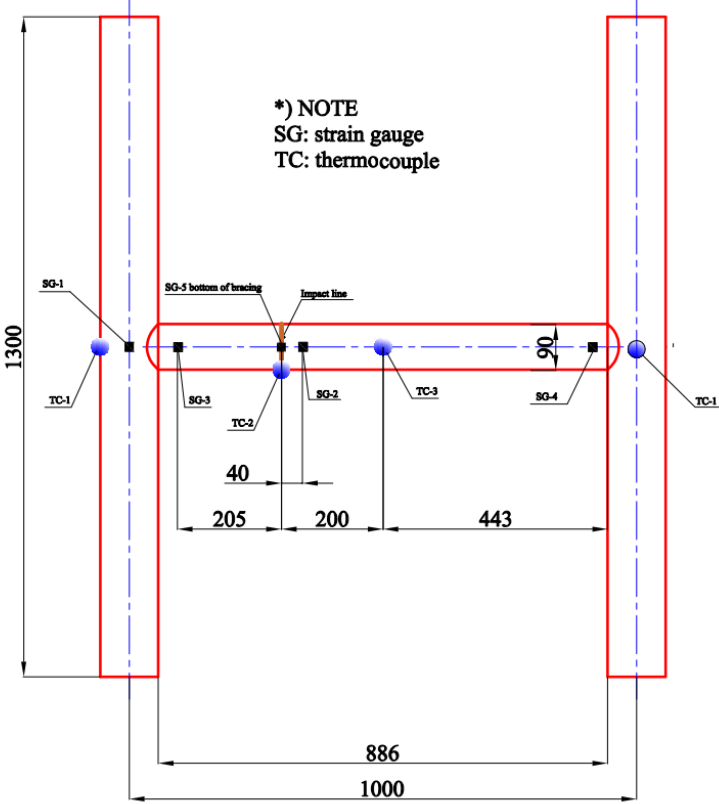


Fig. 4.9 Arrangements of strain gauges and thermocouples for sub-zero temperature test.

4.3.1 Drop test on H-Shape tubular model at room temperature

4.3.1.1 Plastic damage on brace and chord

After experiments, the damage profiles and extents were measured using *CimCore* portable measuring arm device as shown in Fig. 4.10. By doing this, the exact hit location and overall bending damages could be determined. Additionally, the local denting damages can be also measured with a simple way by Vernier calipers as indicated in Fig. 4.11.

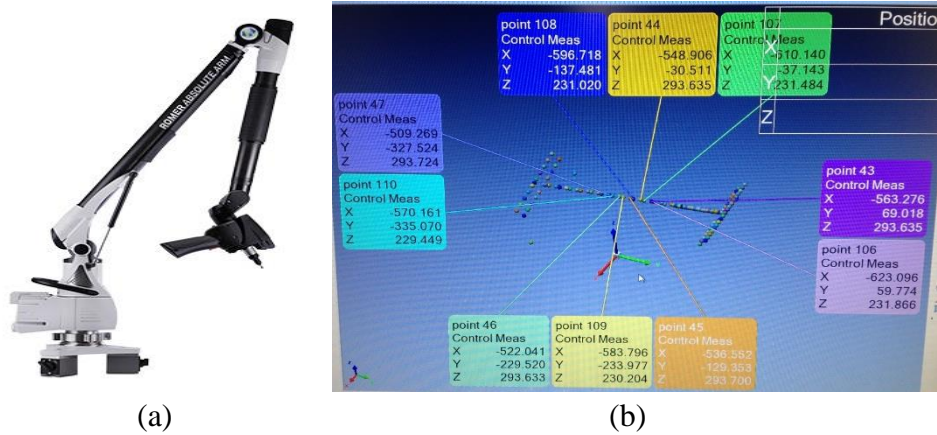


Fig. 4.10 Measurements of deformed shape after collision:
 (a) CimCore device; (b) 3-D coordinates.

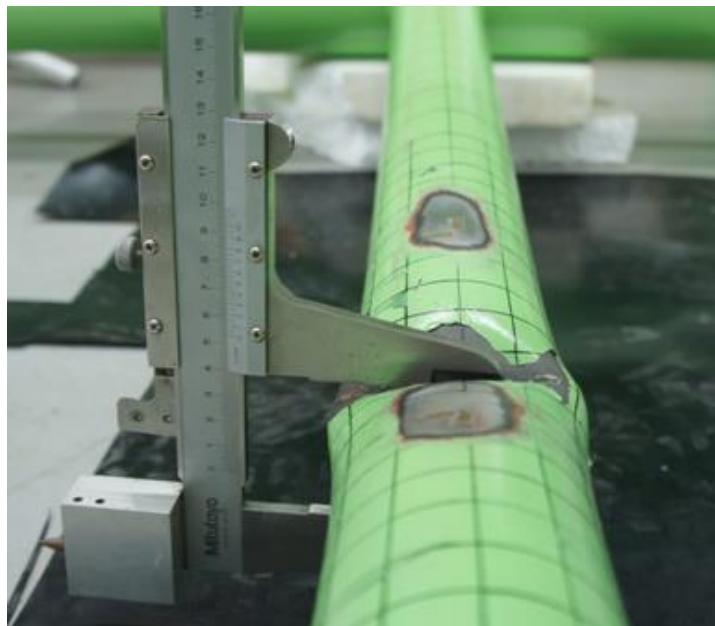


Fig. 4.11 Measuring local denting with Vernier calipers.

The plastic deformations of tubular can be described as two phases. First, local shell denting was occurred only on bracing. Second, the plastic damages were occurred both of the bracing and chord. For the first phase, when the stiffness of chord tubulars much larger than bracing tubulars, the extents of plastic damages occurred only on bracing tubulars including local denting damages (d_a) and overall bending damages (d_o). With the realistic tubular support platforms, the main bearing tubulars are the chords. Thus, when the bracing be damaged, the chord also be affected, but the ability to collapse of the chord structure is small. Therefore, it can be considered as a minor damage.

The deformed shapes of model B2 and C3 are shown in Fig. 4.12. The local denting is occurred mainly on the upper surface of bracing at the impact line as a lateral deflection. It can be

seen that model C3 has a large plastic resistance in bending than that of model B2. The main collision energy is dissipated to local denting deformation.

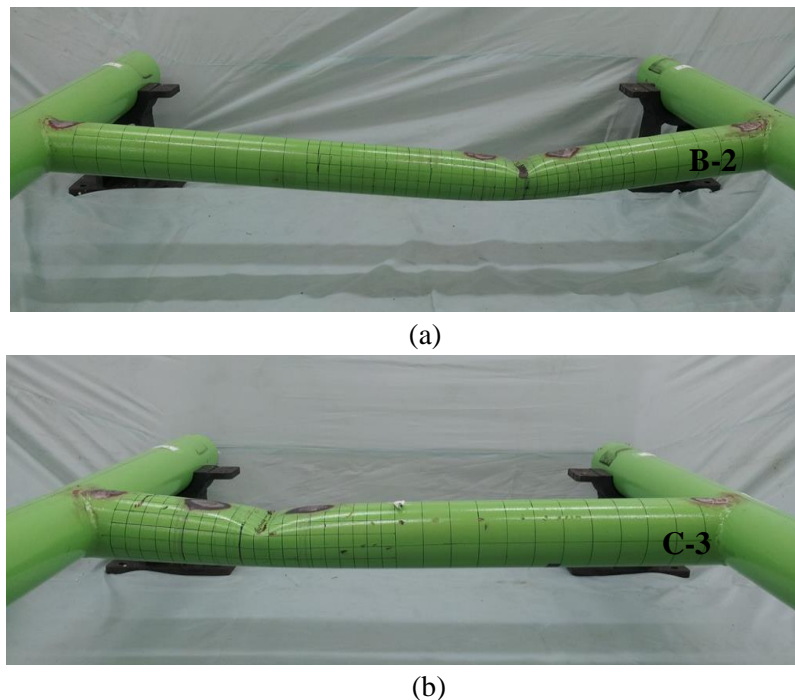
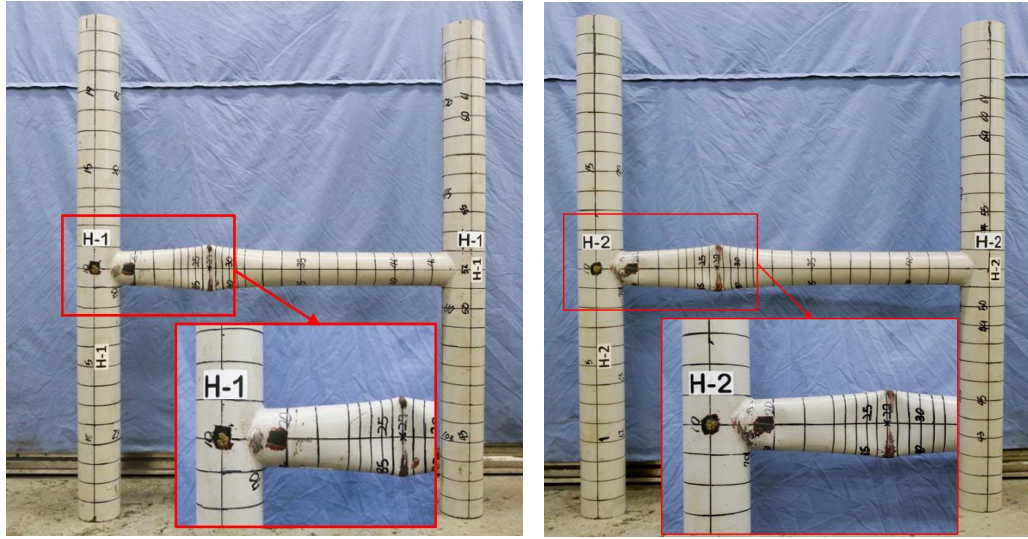
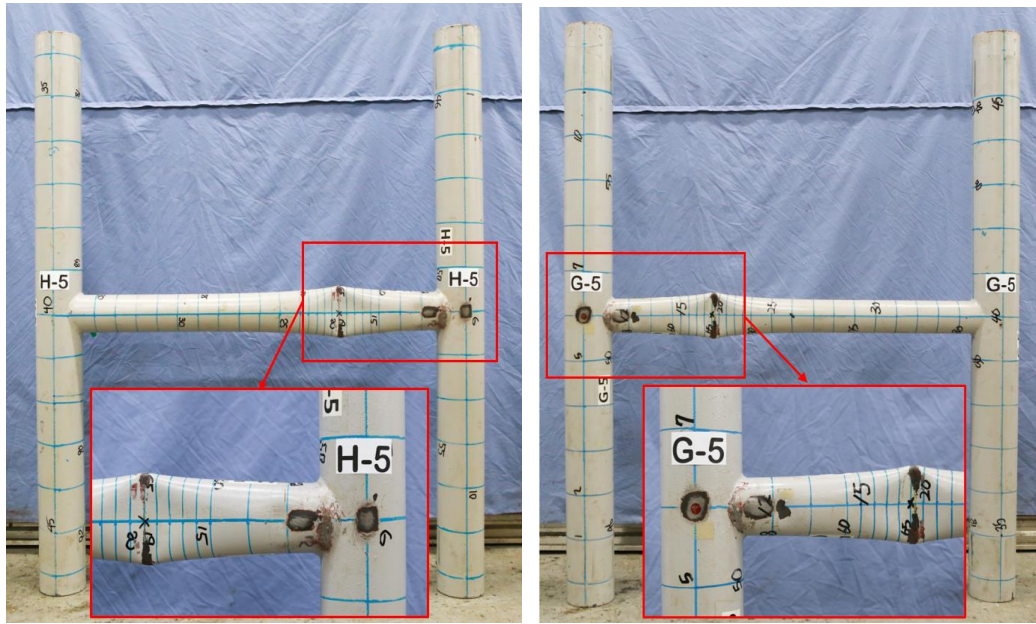


Fig. 4.12 Permanent deformation of models: (a) B2 and (b) C3.

Figs. 4.13 and 4.14 show the damage results of drop tests which the damage occurred on bracing only of model H1, H2, H5 and G5, respectively. It can be seen clearly that there is no damage on the chords. From these figures, the general properties of the extent of damage in tubulars subjected to dynamic impact loading can be described. The local dent damage is confined at the contact line between the tubular and the striker and causes flattening of the tubular cross-section. For moderately large dent depths as observed in these test models, the cross-section is ovalized. Two plastic hinge lines at the boundaries of the flattened zones extending in the longitudinal direction mark the borders of the damage. Due to large deflection, the areas next to the local dent zone are subjected to in-plane deformation as stretching.



(a) (b)
Fig. 4.13 Permanent deformation of models: (a) H1 and (b) H2.



(a) (b)
Fig. 4.14 Permanent deformation of models: (a) H5; (b) G5.

At the end of the tests, the permanent local dent depth d_d and overall bending damage d_o as out-of-straightness of the brace were measured and can be obtained by using Eqs. (1) and (2). In addition, Eqs. (3) and (4) are used to obtain the value of non-dimensional permanent local dent depth δ_d and non-dimensional overall bending damage δ_o , respectively. The quantities for evaluating local denting and overall bending damage extents are shown in Fig. 4.15. In the experiments, there were the deviations of the impact point. The reason may due to the rotations of

the striking mass after it was detached from the electromagnet. It has a large effect on the deformed shape of the tubular at the vicinity of the impact point.

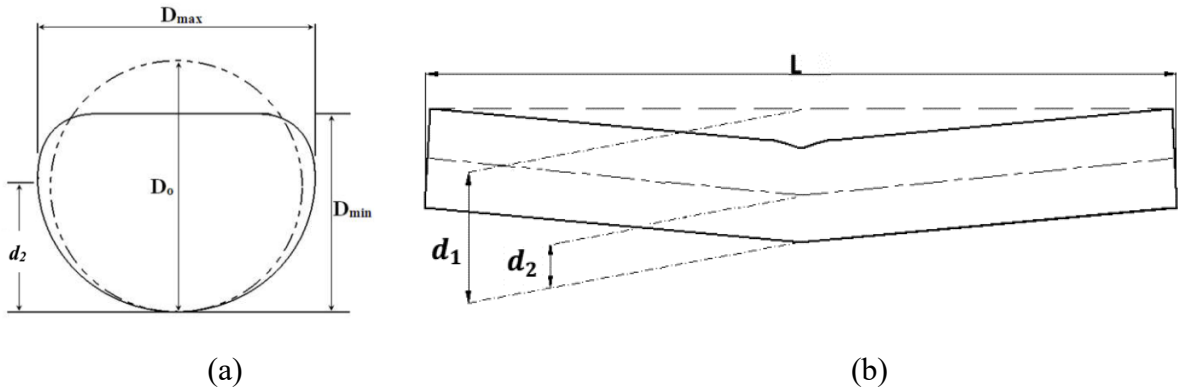


Fig. 4.15 Quantities for evaluating local denting and overall-beam deflection damage extents:
(a) local denting damage and (b) overall bending damage

$$d_d = D_0 - D_{min} \quad (4.1)$$

$$d_o = d_1 - d_2 - \frac{D_0}{2} \quad (4.2)$$

$$\delta_d = \frac{d_d}{D_0} \quad (4.3)$$

$$\delta_o = \frac{d_o}{L} \quad (4.4)$$

For the second phase, the plastic damages were occurred both of the brace and chord. Beside the damages on brace pipes, the damage was also occurred on chord members which near to the impact line in term of local denting, overall bending and overall twisting (d_i) corresponding with three directions X, Y, Z as shown in Fig. 4.16 and Fig. 4.17. In these models, the collision energy effects not only on the bracing but also on the chord. Therefore, with the realistic tubular support platforms, it is a significant damage case because the chords are the main bearing tubulars. Moreover, the residual strength of both chord and bracing can be reduced suddenly due to the imbalance in distribution of total weight from upper blocks. Then, this problem may lead to the collapse of whole structures. In addition, the overall bending damage on bracing members were measured by the calculation approach using equation (4.5). In this equation, the values of parameter a , b , c and d were determined directly from experimental measurement data.

4.3.1.2 Fracture at T-joint

When the stiffness of bracing member is quite smaller compared to that of the chord members, the plastic deformation occurs only on bracing. In these cases, if the collision energy level was increased, the fracture will take account on bracing at T-joint location which near the impact line. Furthermore, if the length of bracing is short, the deformation angle α as in Fig. 4.18

is increased. It means that the overall bending damage on bracing causes to the increase of the rotational deformation angle on bracing member. It is a significant reason leading to the value of shear strain to be increased. When this shear value reached to the shear failure criterion of material properties, fracture damage was taken a place at T-joint location, as shown in Fig. 4.19. When the brace ruptures at the T-joint, it cannot absorb the impact energy anymore. Due to overall bending high tension forces at the welded joints can cause fracture on the bracing. It is noted that the large plastic deformation of bracings which were absorbed the impact energy, leading to decrease the damages on chord. It is improved the safety of entire structures.

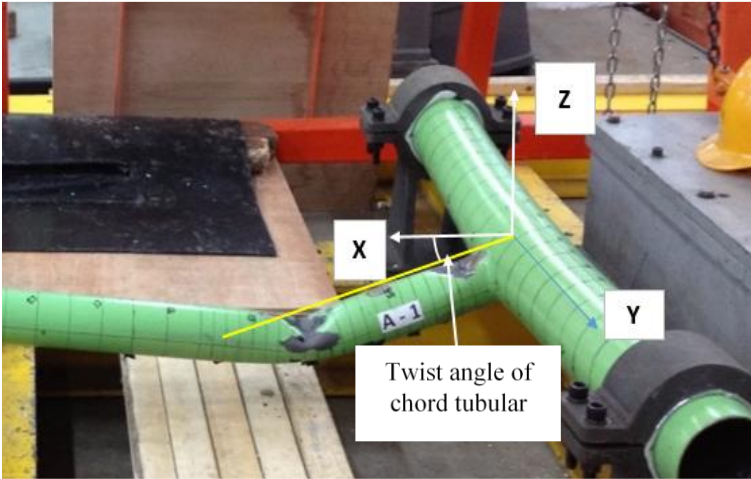
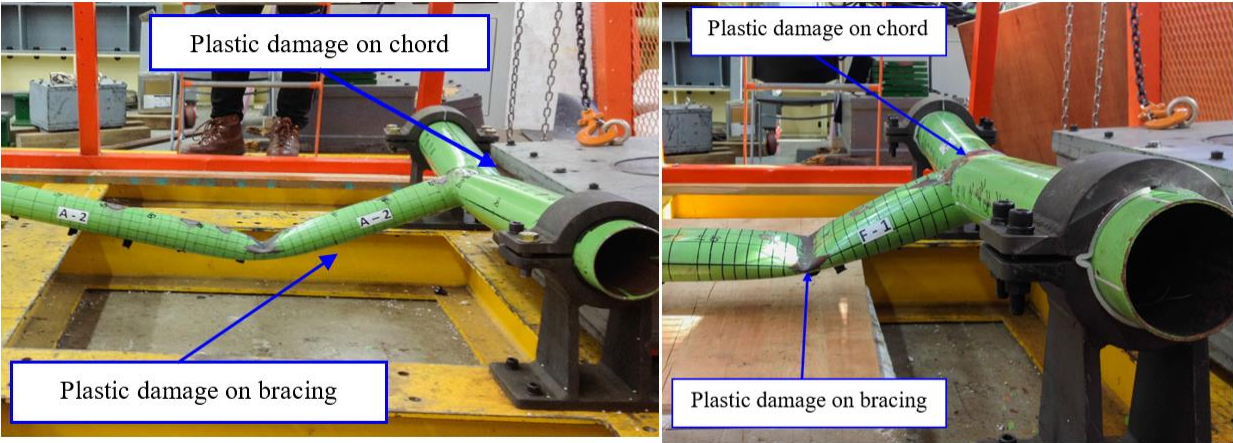


Fig. 4.16 Permanent deformation of model A1.



(a) (b)
Fig. 4.17 Deformed shape of models: (a) A2; (b) F1.

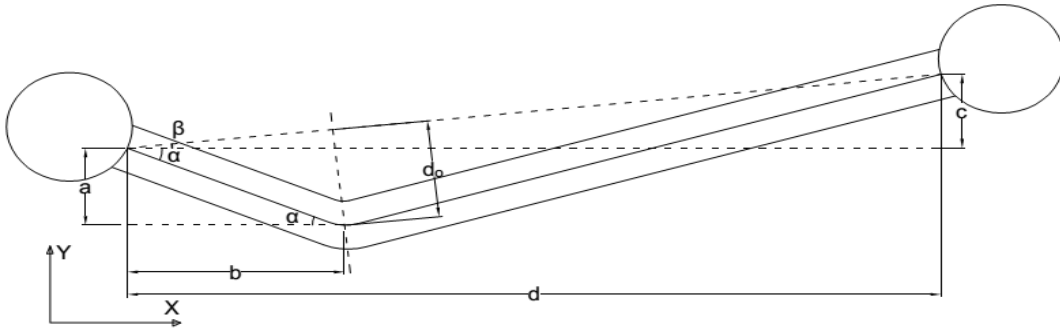


Fig. 4.18 Idealised profiles of a damage on both brace and chord tubular.

$$d_0 = \sin(\alpha + \beta)\sqrt{(a^2 + b^2)} \quad (4.5)$$

$$\tan \alpha = \frac{a}{b} \quad (4.6)$$

$$\tan \beta = \frac{c}{d} \quad (4.7)$$

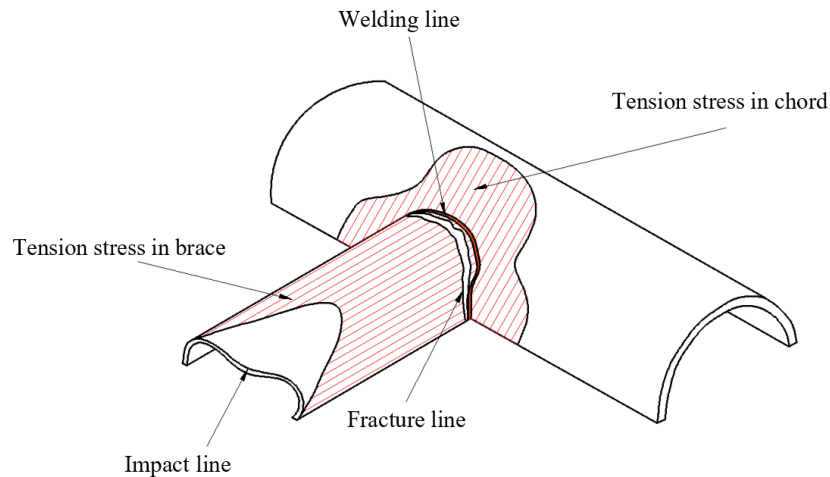


Fig. 4.19 Idealised stress distribution in T-joint of tubular member after denting test.

The partial fracture damages at T-joint locations are depicted in Figs. 4.20 and 4.21 for models E3, G6, H3 and H4, respectively. For all models, the fracture was occurred near the welded joint of bracing and chord. After obtained the partial fracture damages, the collision energies were increased to achieve the complete fracture. The complete fracture damage of model G4 before releasing boundary condition is illustrated in Fig. 4.22. The complete fracture damages and each cross-section of models G1, G2, G3 and G4 are described in Figs. 4.23 and 4.24, respectively. It is noted that cross-section at fracture lines were not smooth and it has some tearing parts. The rotation of the striking mass when it was released from the electromagnet, was one of the most important reason for tearing parts of the cross-section.

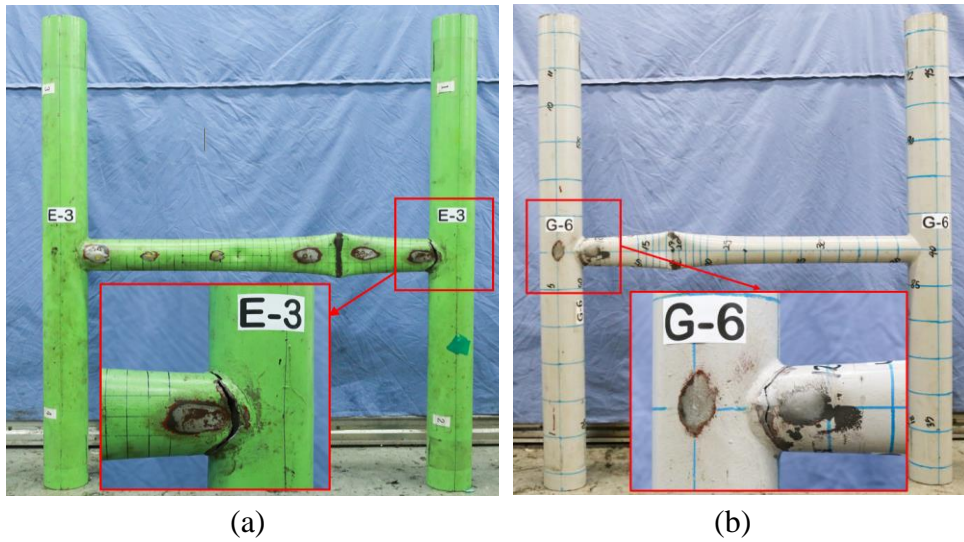


Fig. 4.20 Partial fracture damage of models: (a) E3; (b) G6.

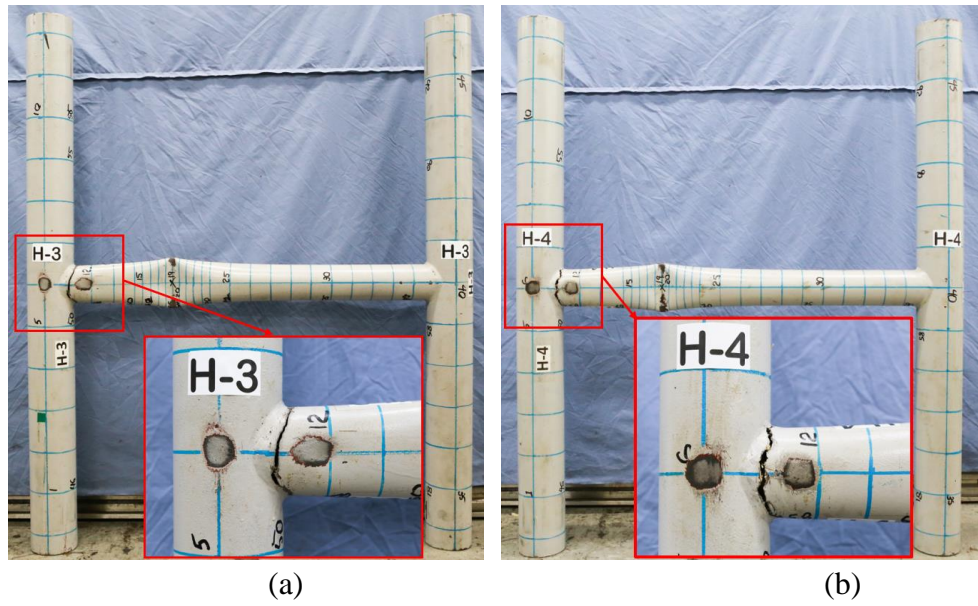
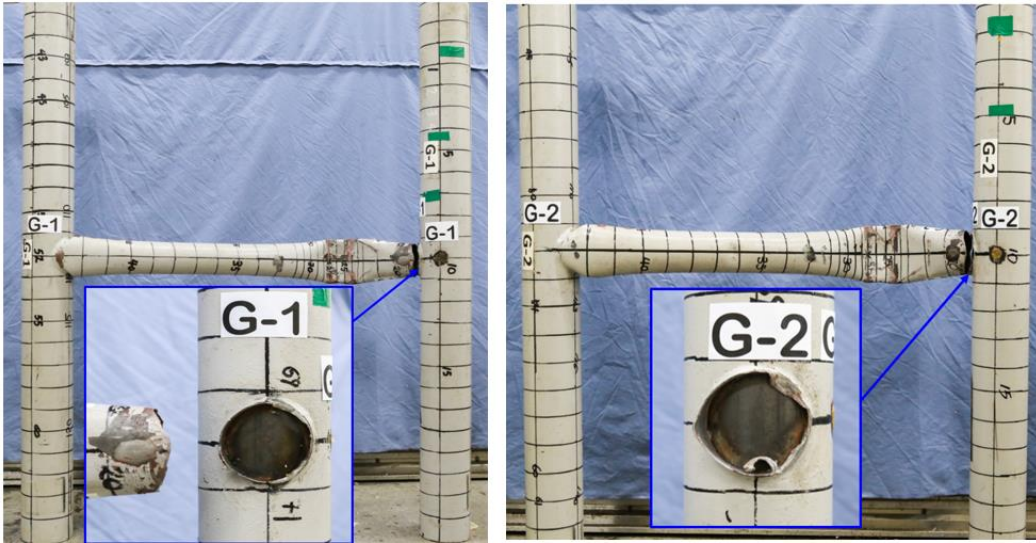


Fig. 4.21 Partial fracture damage of models: (a) H3; (b) H4.



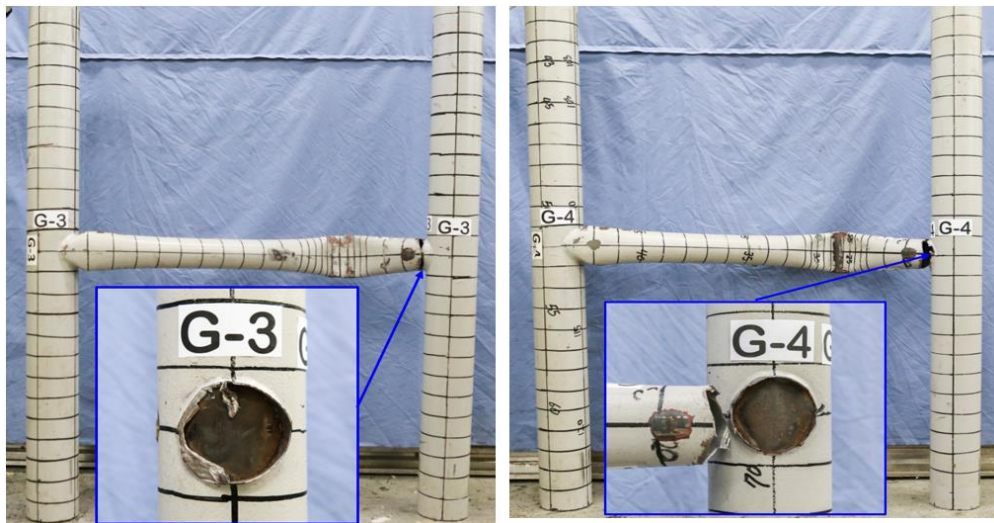
Fig. 4.22 Complete fracture damage of model G4 before releasing boundary condition.



(a)

(b)

Fig. 4.23 Complete fracture damage of models: (a) G1; (b) G2.



(a)

(b)

Fig. 4.24 Complete fracture damage of models: (a) G3; (b) G4.

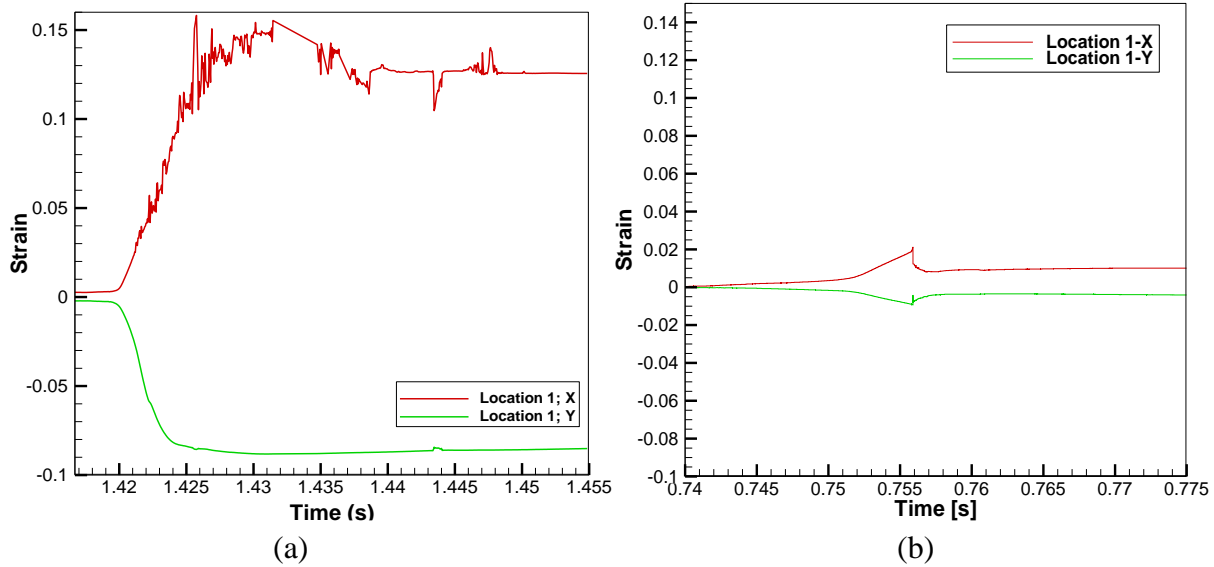


Fig. 4.25 Strain measurement history – Location 1

a) Model F1 – Plastic damage; b) Model G6 – Fracture damage.

The strain measurements provide additional details for understanding the deformation processes. Fig. 4.25 shows the strain gauge values for plastic damage of model F1 compared to the fracture model G6 at location 1. The positive values for tensile strain and negative values for compressive strain. Fig. 4.25 shows that the striker contacted to brace pipe at the impact line around 1.402 (s). It can be seen that the deviation in value of fracture model was smaller than this value of plastic model. Furthermore, Fig. 4.26 shows the strain gauge at location 5 for plastic damage model F1 and fracture model G6 with different scale in value. It can be seen that, for fracture model G6, around 0.755 (s) of drop test period, the values of strain gauge of both of X and Y directions increase to the peak of these values and fracture damage taken a place. After that, these values reduce quickly. This phenomenon is different to the plastic damage cases. It means that the residual stress of fracture damaged model is smaller than this value of plastic damaged model.

The experimental results at room temperature is summarized in Table 4.6. In this table, the measured permanent extents of damages including the dent depth (d_d) and overall damages (d_o) were presented. The failure mode of each model is also provided in this table. It should be noted that the measured values for complete fracture are not included in this table. Because in the actual cases, when the complete fracture occurs, it means that the brace structures are not jointed to chord structures. Therefore, the bracing structures are not contributed to the residual strength of entire structures.

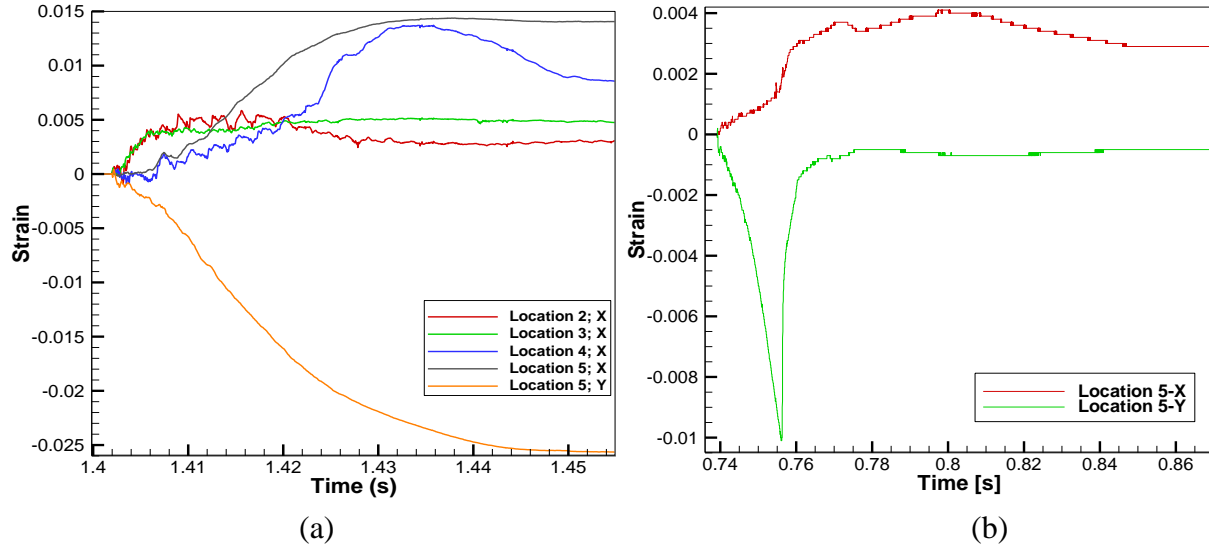


Fig. 4.26 Strain measurement history – location 5:
 (a) model F1 – Plastic damage; (b) G6 – Fracture damage.

Table 4.6 Results of measured damage for each test model at room temperature.

Model	Bracing		Chord		Damage mode
	d_d	d_o	d_d	d_o	
A1	42.60	102.90	19.1	16.8	Plastic
A2	43.40	114.30	37.2	25.6	Plastic
B2	31.55	65.30	-	-	Plastic
C3	34.25	27.75	-	-	Plastic
E3	59.90	64.50	-	-	Partial fracture
F1	93.80	102.60	18.8	13.5	Plastic
F2	59.00	57.75	-	-	Plastic
G1, G2, G3, G4	-	-	-	-	Complete fracture
G5	42.0	28.70	-	-	Plastic
G6	50.0	45.90	-	-	Partial fracture
H1	49.50	23.60	-	-	Plastic
H2	52.0	27.90	-	-	Plastic
H3	56.0	33.20	-	-	Partial fracture
H4	49.50	23.20	-	-	Partial fracture
H5	45.50	14.70	-	-	Plastic

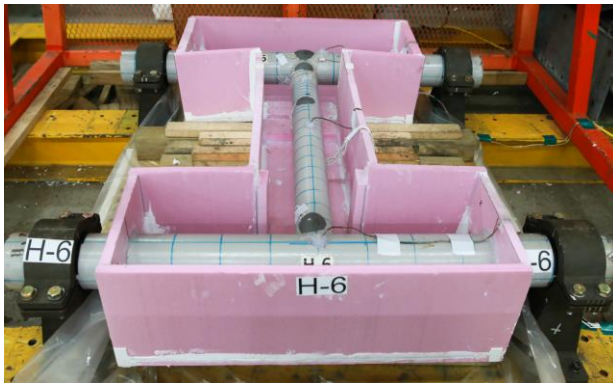
4.3.2 Drop test on H-Shape tubular model at sub-zero temperature

Fig. 4.27 shows the test processes of model H6 including model setting with cold chamber, cooling process, dropt test, and deformed shape after collision test. To represent the Arctic temperatures, cold chambers were fabricated with Styrofoam panels and were glued to the models,

covering the entirety of the model except for the supports, as shown in Fig. 4.27a. The cold chamber was filled with dry ice and ethanol to cool the model. Before filling the cold chamber, four thermocouples were glued onto the model, to measure the temperature during cooling.

The temperature histories were measured with four five thermocouples attached to the test models. Before the impact test the cold chamber was removed and as soon as the temperature of the model became -50°C the striker was released. The temperature measured results using thermocouples is given in Figs. 4.28 and 4.29 for models H6-LT and OWT-D2-LT, respectively. The strain responses during the cooling processes are also measured as shown in Fig. 4.30. It is clear that all strain gauge positions were exhibited a high level of compressive strain. These strains are considered as residual strain due to cooling process.

It is known that at low temperature, although the stiffness and the yield strength of steel increases, little plastic deformation occurs before fracture. Thus brittle type fracture takes place by rapid crack propagation and very small strain energy. This fact obviously results in lower energy absorbing capacity under impact. The deformed shape of model H6-LT is shown in Fig. 4.31. Additionally, the cracks at chords of test models OWT-D2-LT and OWT-D3-LT were given in Figs. 4.32 and 4.33, respectively. It clearly indicates the brittle fracture. This conclusion was confirmed by carefully checking the shell cross-section at crack where no reduction in thickness was observed.



(a)



(b)



Fig. 4.27 Test processes of model H6-LT.

Strain measurement results at room and sub-zero temperature for models H6-LT and H3 were described in Figs. 4.34 and 4.35, respectively. It is noted that the dimensions and impact test conditions of model H6-LT are similar to those of model H3. The main aim of this set model is to investigate the differences in collision behaviors between room temperature and sub-zero temperature. As shown in Figs. 4.34 and 4.35, the strain magnitudes of model H3 is much larger than those of model H6-LT. The comparison of maximum strain measurement at position 2 for each model, which is placed near the impact line, is depicted in Fig. 4.36. It is observed that the strain levels of model H3 are higher than strain levels of model H6-LT with 6.1 times in axial direction and 3.31 times in circumferential direction. Particularly, the fracture of H6-LT occurs earlier than model H3 and the damages generate severer. Finally, the summary of experimental results at sub-zero temperature is shown in Table 4.7.

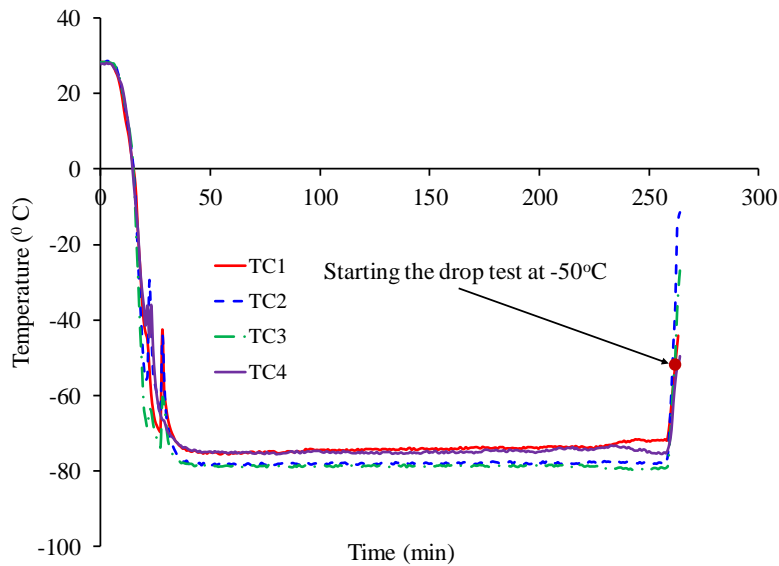


Fig. 4.28 Time history of temperature measured by each thermocouple for model H6-LT.

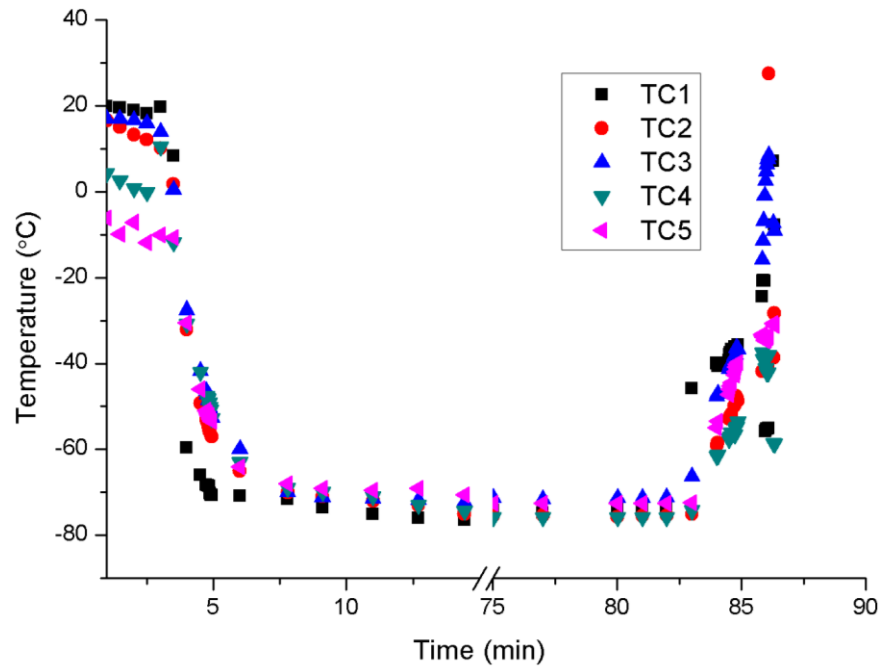


Fig. 4.29 Time history of temperature measured by each thermocouple for model OWT-D2-LT.

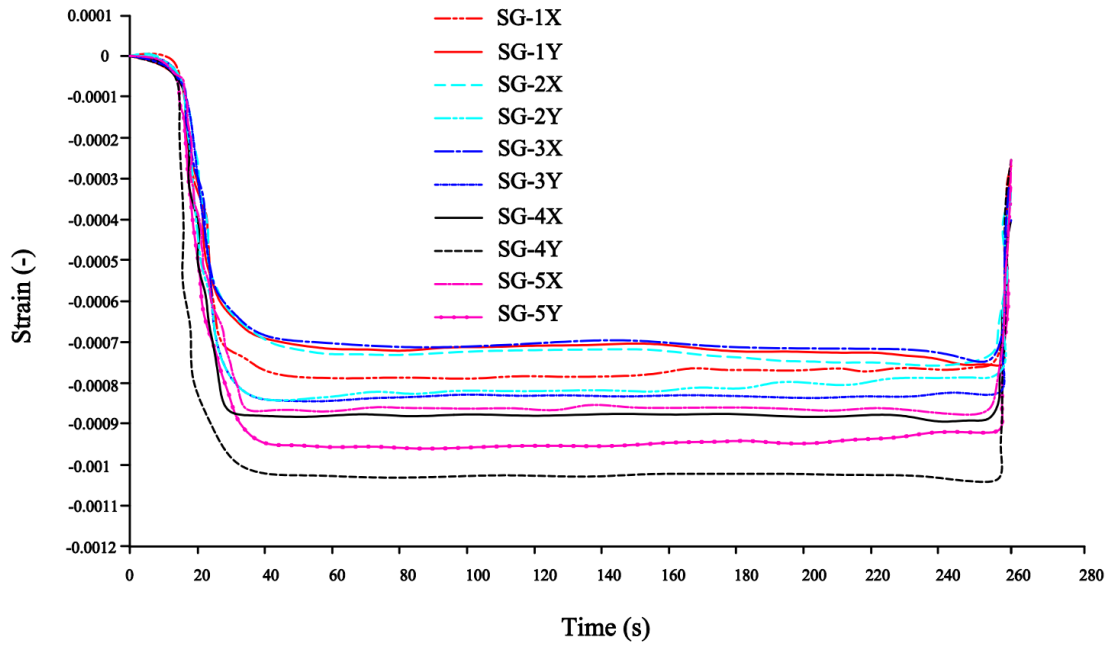


Fig. 4.30 Strain measurement results during cooling time for model H6-LT.

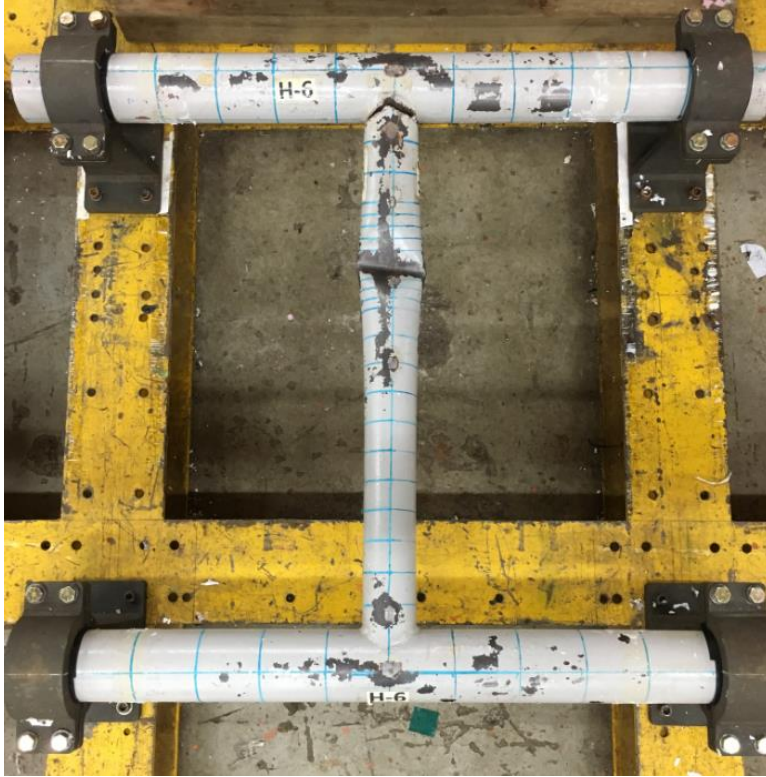


Fig. 4.31 Fracture damage of model H6 with fixed boundary condition.



(a)



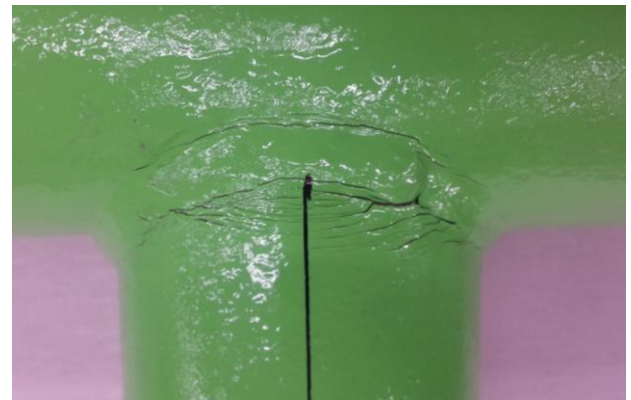
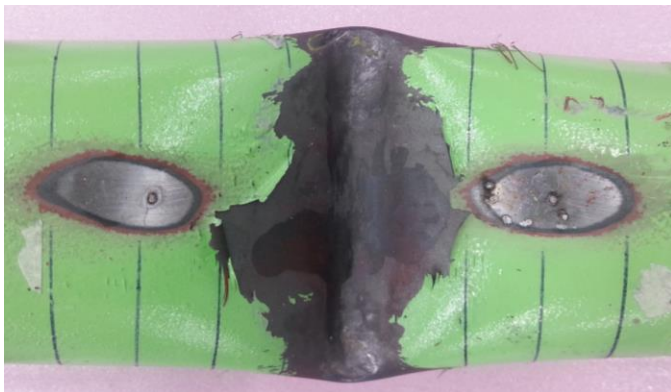
(b)

Fig. 4.32 Deformed shape of model OWT-D2-LT after impact:

(a) At T-joint near the impact point; (b) At impact point and T-joint far from the impact point.



(a)



(b)

Fig. 4.33 Deformed shape of model OWT-D3-LT after impact:

(a) At T-joint near the impact point; (b) At impact point and T-joint far from the impact point.

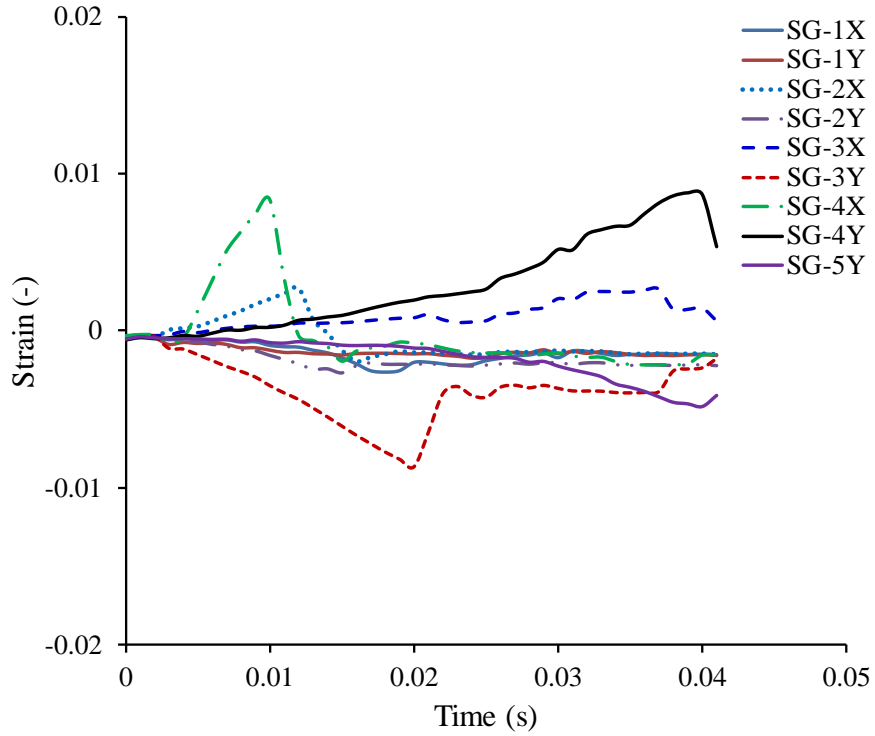


Fig. 4.34 Strain time histories recorded at low-temperature for model H6-LT.

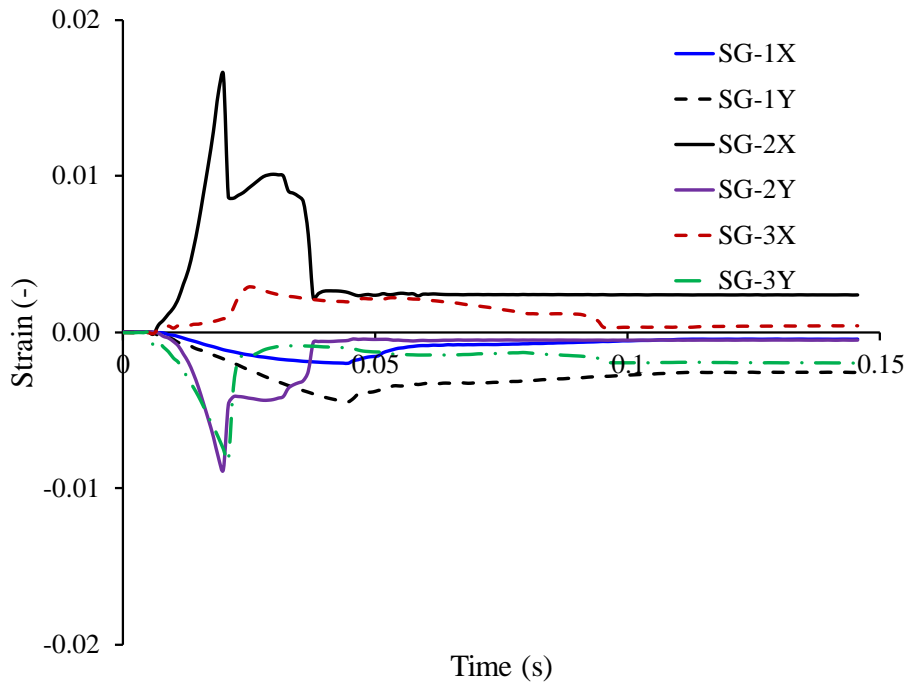


Fig. 4.35 Strain time histories recorded at room temperature for model H3.

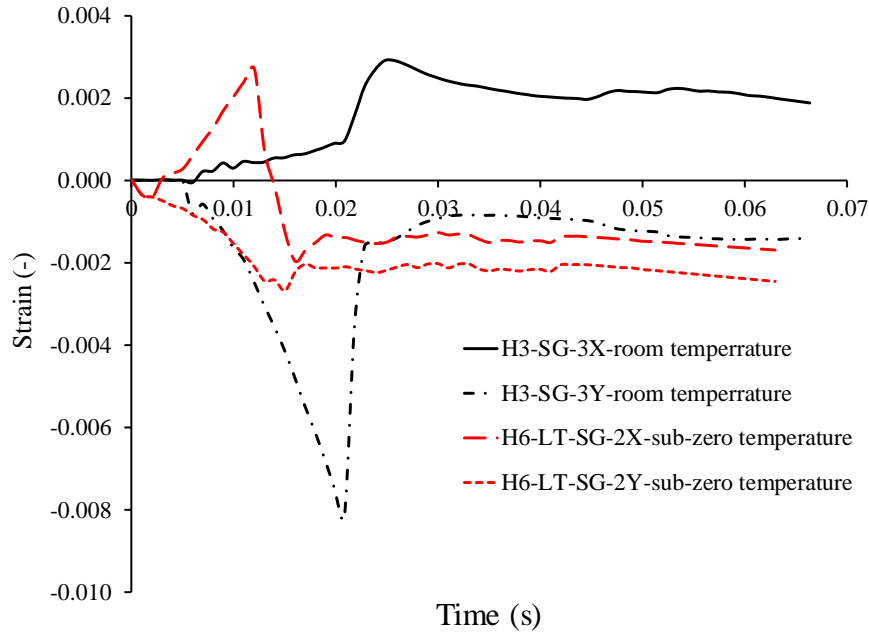


Fig. 4.36 Comparison of strain measurements between room temperature and sub-zero temperature collision.

Table 4.7 Results of measured damage for each test model at sub-zero temperature.

Model	Bracing		Chord		Damage mode
	d_d	d_o	d_d	d_o	
D2-LT	49.25	131.13	19.1	16.8	Fracture
D3-LT	52.0	71.25	37.2	25.6	Fracture
H6-LT	53	89.10	-	-	Fracture

4.4 Numerical simulations of collision test

4.4.1 Finite element modelling

Nonlinear finite element analyses of the test models were performed using the explicit solver of the software package ABAQUS. In the numerical model, both chord and bracing were modelled using four-node doubly curved shell elements S4R, which were accompanied with hourglass control and reduced integration in the ABAQUS library (version 6.14). The residual stress effects of weld joint areas were not considered in the finite element model. The Simpson rule was used with five points throughout the thickness integration. For the knife-edge striker, it was modelled as a rigid body with a 3-D bilinear rigid quadrilateral element (R3D4). A reference node was applied with tie constraint for all the striker elements. The purpose of the reference node was to attach the inertial properties and striking mass velocity during impact. It is noted that the rotations of the striking mass during the impact were also considered in the numerical model.

The optimum mesh size was selected after performing the convergence studies. The mesh size of contact and the T-joint region was two times of the bracing thickness and that for the out region was five times of the bracing thickness. This mesh size is sufficiently fine for capturing the deformed shape and fracture response precisely.

Additionally, during the impact, the model vibrates elastically. Therefore, to reduce these vibrations and rapidly achieve a static equilibrium state, the Rayleigh damping was included in the numerical model. Rayleigh damping can be calculated as following equation (4.8):

$$C = \alpha M_m + \beta K \quad (4.8)$$

where M and K are the mass matrix and stiffness matrix, respectively. The coefficient α is determined as the lowest natural frequency of model, which can be achieved using a modal analysis with a Subspace eigen-solver in ABAQUS library. The coefficient β is the stiffness proportional damping factor. In this study, only mass proportional Rayleigh damping is considered.

4.4.2 Boundary conditions

For the boundary conditions, the ends of both chords of the model were restrained in all degrees of freedom using the thick support structures. The support structures were fully clamped at four bottom bolt holes as the clamped boundary conditions in the experiment. The contact between the indenter and the bracing surface was designed as a general contact algorithm with a penalty method. The coefficient of contact friction is assumed at 0.3 to account for the slipping between the surfaces of indenter and impacted tubular member. The full geometry and boundary conditions of each model is provided in the finite element modelling, as shown in Fig. 4.37.

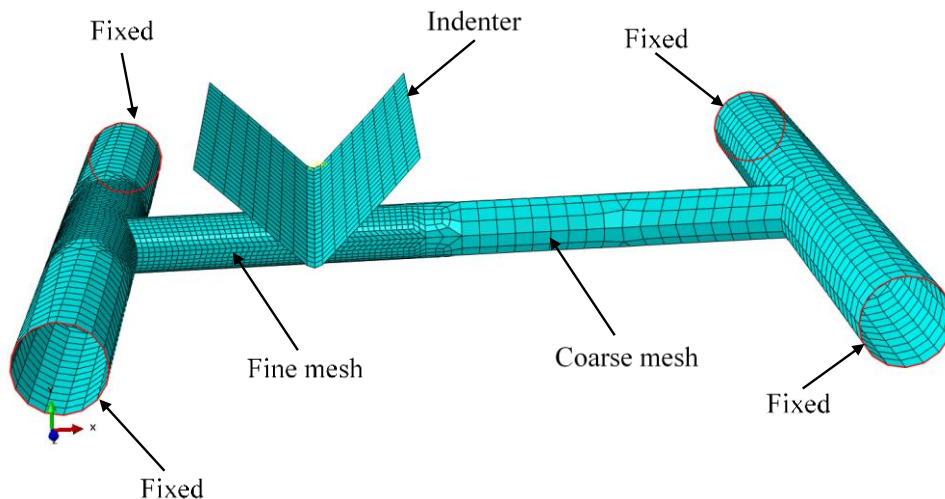


Fig. 4.37 Finite element model for collision analysis.

4.4.3 Material properties definition

To obtain the material definition of collision analysis at room temperature, the formulations provided by Cho et al. [140] were used. The material properties were defined the same procedures as previous section 3.2.2.2 in Chapter 3. In this analysis, the strain rates were generated with various values (10 s⁻¹, 20 s⁻¹, 50 s⁻¹, 70 s⁻¹, 100 s⁻¹ and 150 s⁻¹) for series G model, as shown in Fig. 4.38.

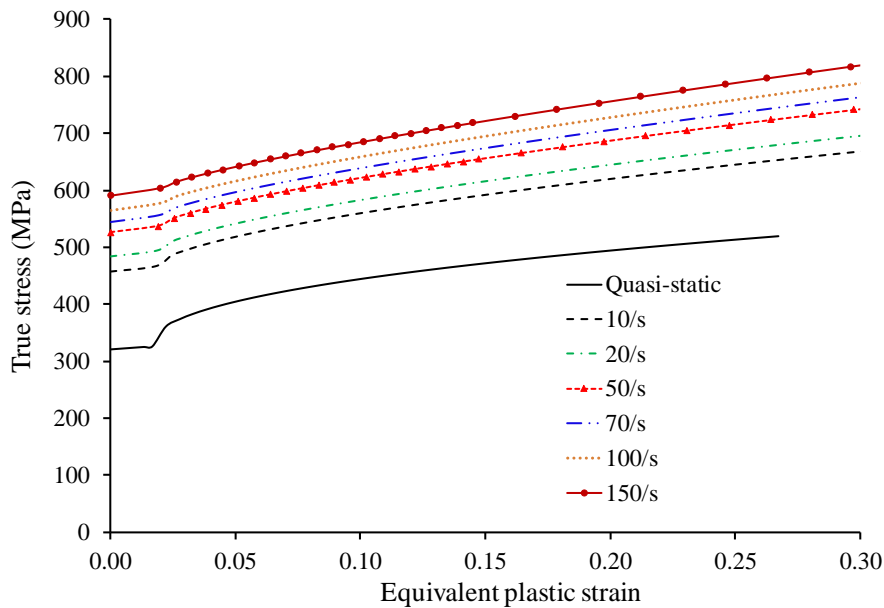


Fig. 4.38 True stress-strain curve at various strain rates for series G model.

For collision analysis at low-temperature, the brittle fracture criterion was applied. Because for mild steel material which behave in a brittle fashion at low temperature may become ductile at high temperature. When the strain rate is increased a ductile material may start to behave in a brittle fashion. Certain materials which are ductile at a given temperature (room temperature), become brittle at sub-zero temperatures. The temperature at which this happens is terms as the ductile brittle transition temperature.

In the other hand, the ductile material which has extensive plastic deformation and energy absorption (“toughness”) before fracture. However, the brittle material which has a little plastic deformation and low energy absorption before fracture. Commonly, the brittle material has comparatively high yield and tensile strength but low toughness due to lack of ductility. The influence of sub-zero temperature on material behavior is shown in Fig. 4.39.

The fracture model used in the present study was the shear fracture criterion. The shear criterion, sometimes referred to as the criterion of equivalent strain, is a phenomenological representation of the initiation of damage due to shear band localization. The criterion presumes that the fracture initiates when the accumulated equivalent plastic strain reaches the material failure strain. This criterion is often used in simulations of ship collision and grounding and has gained popularity due to its simple formulation [223]. In its simplest form, the only input used is the critical fracture strain that is affected by various factors including mesh size, strain rate and low-temperature. It is also affected by material models of the finite element simulation in terms of the stress-strain relationships. In association with this, the DNV [26] and NTSI [29] proposed the values of shear fracture criterion for accidental events: 0.2 for mild steel and 0.15 for high-tensile steel. However, they do not cover the combined effects of low temperature and strain rate.

4.5 Numerical results and discussion

4.5.1 Drop tests at room temperature

Numerical analyses of the test models in current study were performed under similar assumptions as experimental models. First, local denting is evaluated as the vertical distance between deflection of upper surface and bottom surface of the tubular shell at the center of impact line. Overall bending can be obtained from the deflection of cross-section plastic neutral axis.

The comparison between numerical analysis and experimental result for model B2 is described in Fig. 4.40. In this figure, the contours illustrate the equivalent plastic strain distribution. In general, the deformation characteristics of numerical analysis result have a good agreement with the experimental result. The local dent damage is confined at the contact line between the tubular and the striker and causes flattening of the tubular cross-section. It is noted that highly localized plastic strains are indicated at the ends of the impact line. For all of the test models, the cross-section is observed as ovalized shape. The flattened zones are extended in the longitudinal direction with two plastic hinge lines at the borders of the damage. Due to large beam deflection, the areas next to the local dent region are subjected to in-plane deformation as stretching. Consequently, high plastic strains are concentrated at the joints.

The force-displacement response curve is the most important information obtained from finite element analysis for assessing the deformation characteristics. The histories of contact force and striking mass are combined in term of force-displacement relationship. The displacement here corresponds to the overall bending displacement at hit point, which is translated of the neutral axis of bracing. The peak force corresponds to the maximum deformation of tubular members. Then, the displacement is recovered as an elastic springback. The end of the test is determined by zero contact force. The area under the curve corresponds to the plastic deformation energy, which is an

indicator of the crashworthiness of structures subjected to impact. The force-displacement response for model B2 is illustrated in Fig. 4.41. In this figure, the force level is compared with plastic collapse resistance in bending (P_0) for a qualitative understating of the local denting effects. A fixed beam at both ends and subjected to a centrally lateral singular load P was considered. The collapse mechanism consisting of three plastic hinges is depicted in Fig. 4.42.

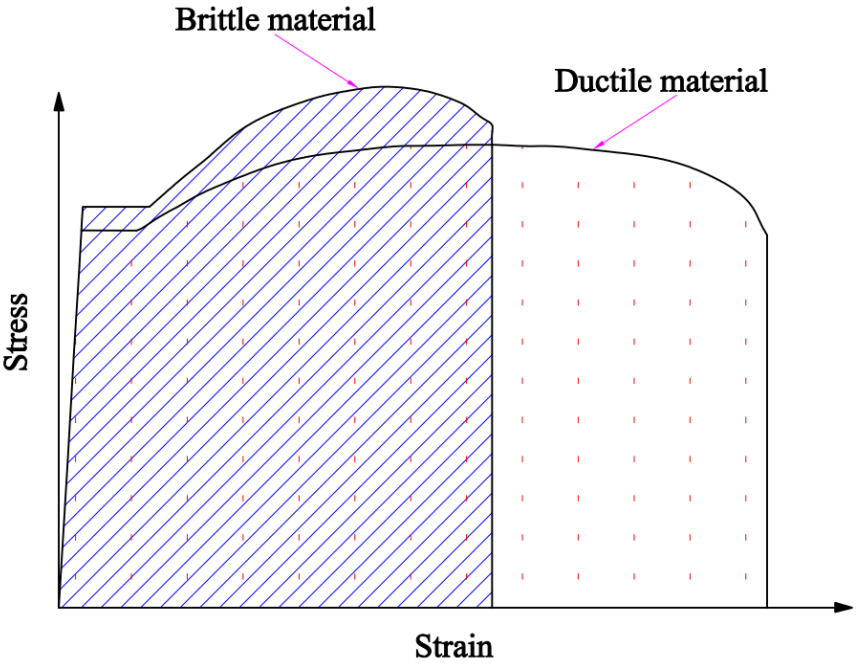
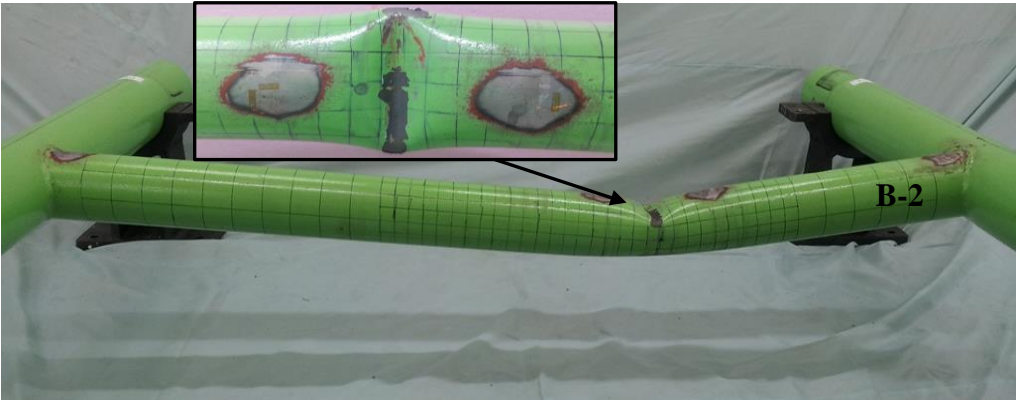


Fig. 4.39 Influence of sub-zero temperature on material behavior [224].



(a)

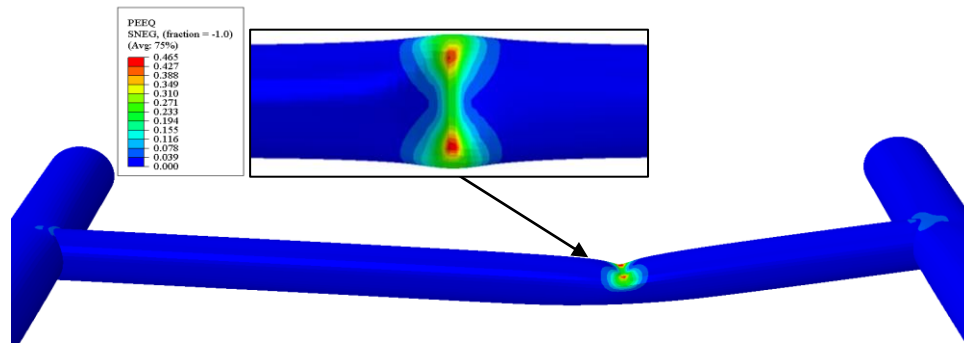


Fig. 4.40 Predicted deformed shape of model compared with test result for model B2:
 (a) test result; (b) numerical result.

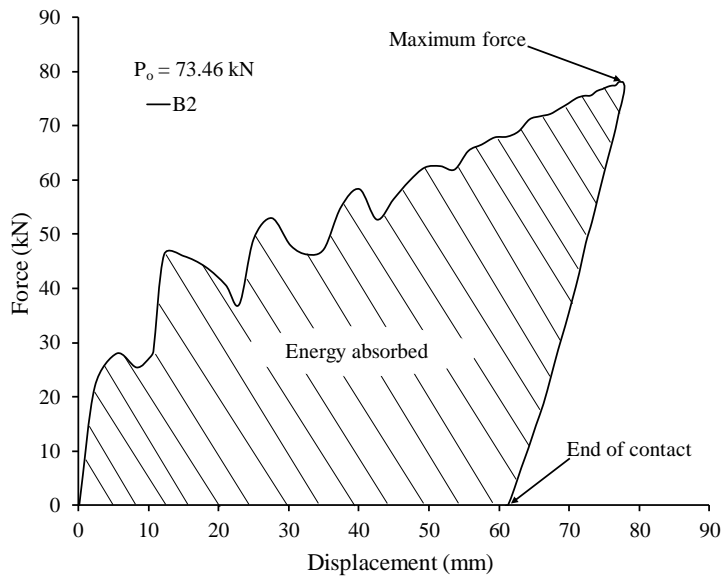


Fig. 4.41 Force-displacement response for model B2.

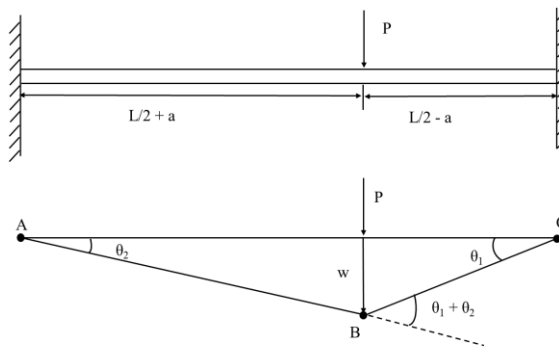


Fig. 4.42 Collapse mechanism of a beam loaded off-center.

The collapse load can be obtained easily by equating the rate of external work done by the lateral force to the rate of internal energy dissipated by the rotation of plastic hinges from equation (4.9) to (4.13). The fully plastic moment capacity M_p of a tubular beam can be calculated by equation (4.14). It is clear that the resistance in bending is proportional with diameter and thickness and inversely proportional with length of the tubular.

$$\dot{E}_{ext} = \dot{E}_{int} \quad (4.9)$$

$$P\dot{w} = M_p\dot{\theta}_1 + M_p(\dot{\theta}_1 + \dot{\theta}_2) + M_p\dot{\theta}_2 \quad (4.10)$$

$$w = \dot{\theta}_1 \left(\frac{L}{2} - a \right) \quad (4.11)$$

$$w = \dot{\theta}_2 \left(\frac{L}{2} + a \right) \quad (4.12)$$

$$P_0 = \frac{M_p \left[2 + \frac{(L-2a)}{\left(\frac{L}{2} + a\right)} \right]}{\frac{L}{2} - a} \quad (4.13)$$

$$M_p = D^2 t \sigma_Y \quad (4.14)$$

The force-displacement curve of model C3 is presented in Fig. 4.43. This model has a large plastic bending collapse resistance. For this model, the local denting deformation is the main energy dissipating mode. In general, the response of force-displacement is almost linear, which was reduced the slope of the curve when the load was increased until reached the maximum impact loading. Then, unloading and elastic spring back occurred.

The force-displacement relationships for model H1, H2, H5 and G5 are shown in Fig. 4.44. The responses of the model are similar to model C3. However, the decreasing slope of the curve is slower than model C3. In general, for the same dimensions, the force-displacement curves follow the similar tendency after reaching the maximum collision force. The behavior of these model can be presented as two stages. The initial impact stage is formed by local shell denting. The second stage occurs when the impact force is increased to exceed the plastic moment capacity, the plastic collapse mechanism is proposed. Thereafter, the resistance of tubular is quickly decreased. Furthermore, based on the deformed shapes of these models in the previous section, the membrane deformation seems to do not occur. Therefore, the membrane effects on these model are not significant powerful.

The predicted deformed shape of models A2 and F1 compared with those of the experimental results are shown in Fig. 4.45. In this figure, the contours of the numerical analysis result are the equivalent plastic strain and von Mises stress for model A2 and F1, respectively. There is a good agreement between numerical analysis results and experimental results. In these model, the plastic damages occurred both of the brace and chord. The kinetic energy is dissipated as local denting damage and overall bending damage for both of the brace and chord. It is clear that the membrane

effects on these model are strongly affected. The force-displacement curves are depicted in Fig. 4.46 for model A1, A2, F1, and F2, respectively. In this figure, the maximum impact forces for all models are much larger than plastic collapse resistance in bending (P_0) of bracing member. It may a reason the damage occurs not only bracing but also chord member.

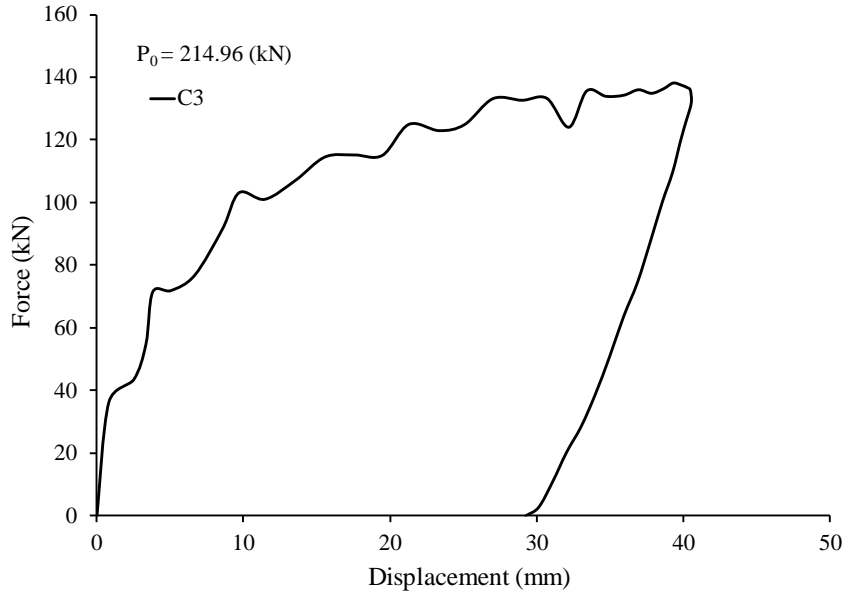


Fig. 4.43 Force-displacement response for model B2.

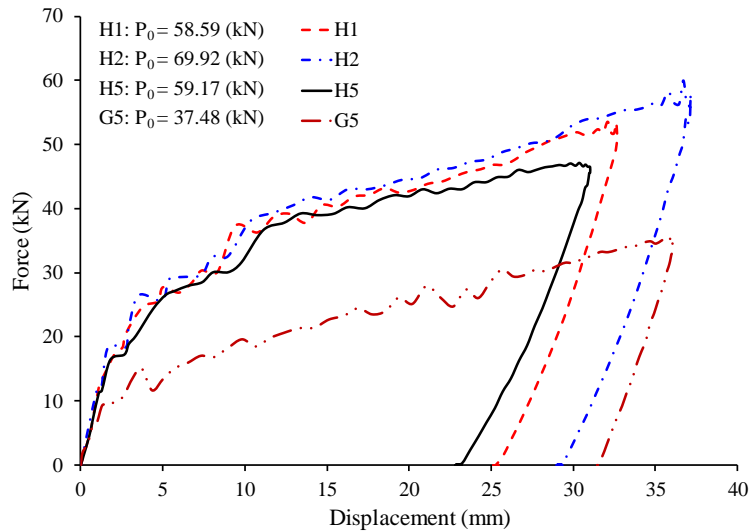
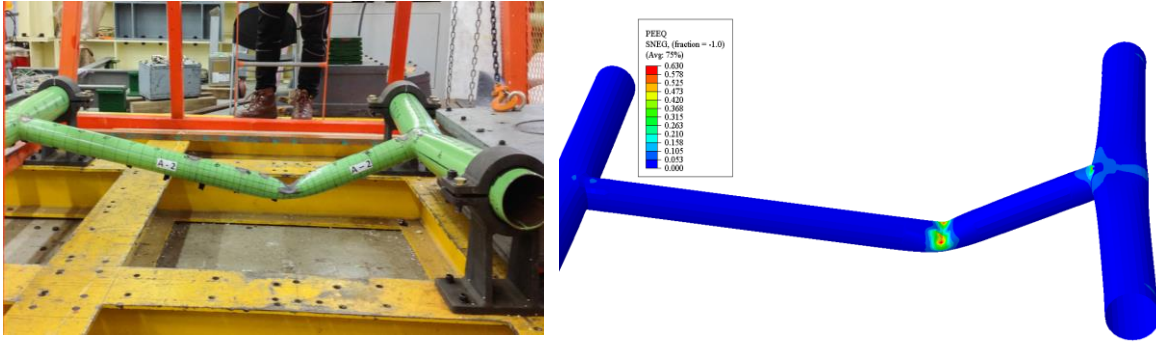
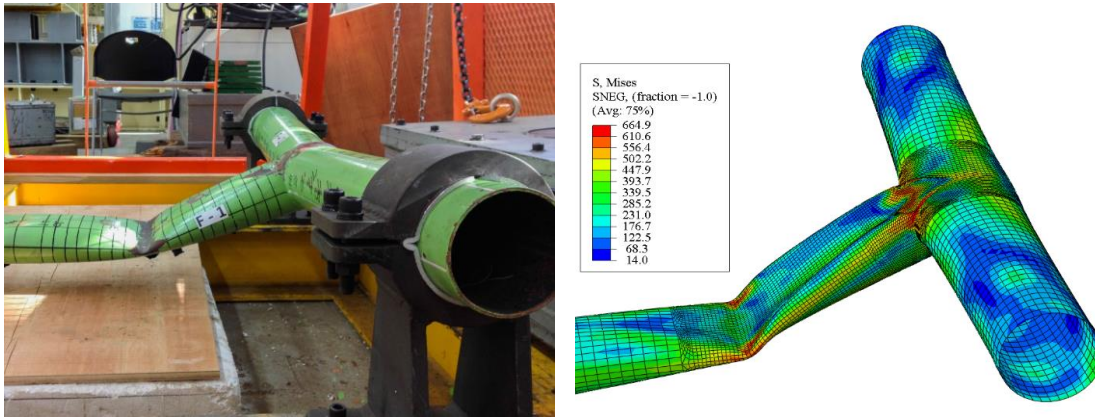


Fig. 4.44 Force-displacement response for different models.



(a)



(b)

Fig. 4.45 Predicted deformed shape of models compared with test results:

(a) model A2; (a) model F1.

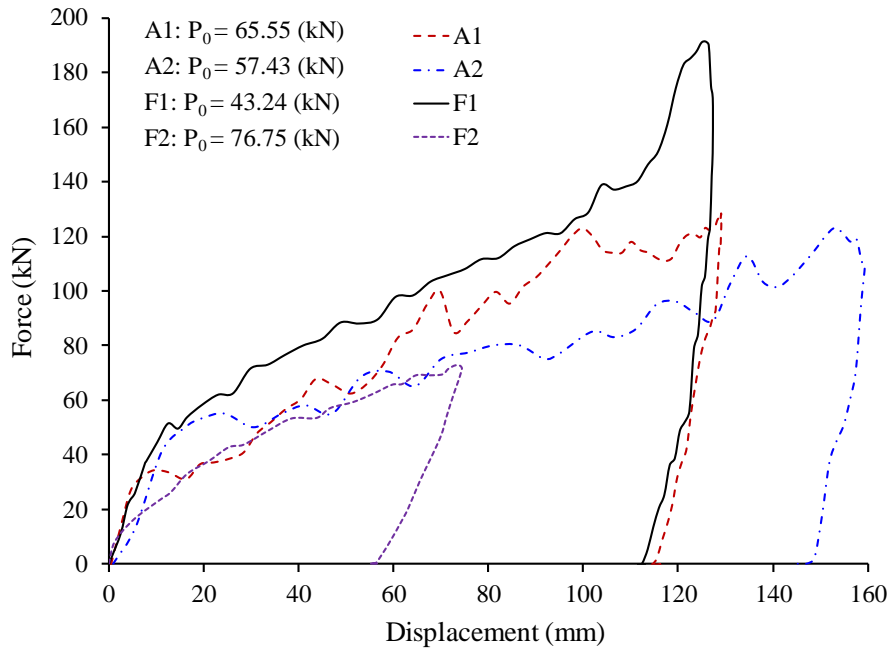


Fig. 4.46 Force-displacement response for different models.

Figs. 4.47 and 4.48 show the comparison of predicted deformed shape of models E3 and G4 with test results. The damage on model E3 is a partial fracture while that of model G4 is a complete fracture, respectively. The deformed shapes observed in tests are captured well by numerical analysis. As mention in the previous section, when the collision energy level was significantly increased, the fracture will take account on bracing at the T-joint location which near the impact line. The energy dissipation of axially restrained tubular is limited by fracture at joints due to excessive membrane straining. It is a typical example of tensile fracture at joint. In the numerical model, the shear fracture criteria were used as fracture criteria. When this shear value reached to the shear failure criterion of material properties, fracture damage occurred at T-joint location.

The force-displacement responses for partial fracture model E3, G6, H3, and H4 are described in Fig. 4.49. There are some differences between fracture damage response and plastic damage response in term of force-displacement curves. First, the slope of impact force curve in fracture damage is decreased slowly. Second, after reached the peak force, where the indenter was completed contact with bracing and move together with striking mass. The reaction force is not decreased rapidly as plastic damage response. In this stage, the damages are still generated continuity before elastic springback occurs.

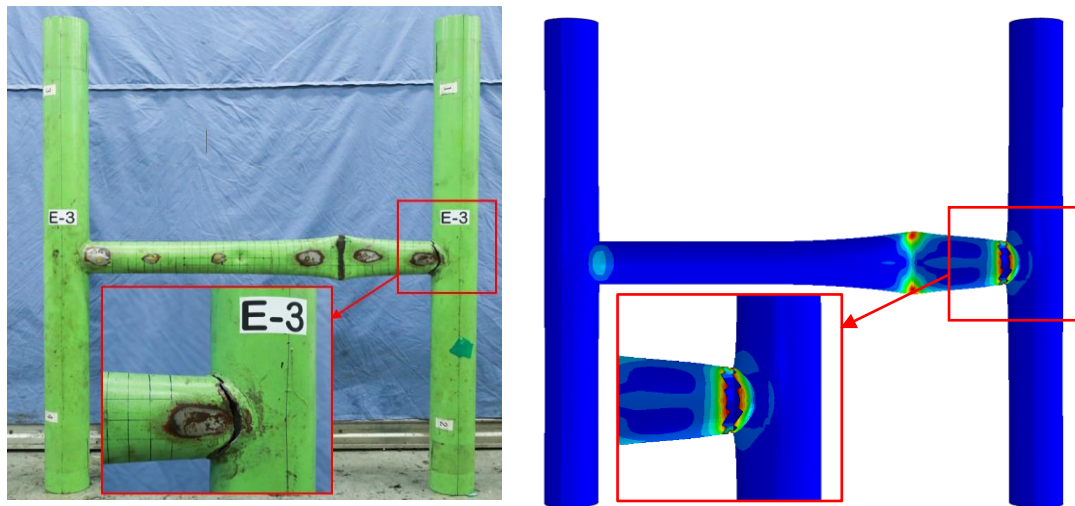


Fig. 4.47 Predicted deformed shape of model compared with test result for model E3.

In order to verify the reasonable accuracy and reliability of the numerical method, the comparison of numerical results with experimental results is summarized in Table 4.8. In this table, the local shell denting and overall bending deformation at the hit point is non-dimensionalised with the diameter of brace tubular member. The uncertainty modelling parameter (X_m), which was defined as the ratio of numerical results to test results, was also included in this table. Additionally, the comparison between numerical results and test results is also displayed in Figs. 4.50 and 4.51. In these figures, the local shell denting and overall bending damage are shown. It can be seen that the mean of modelling uncertainty factor X_m is 1.052 and 1.041 together with quite small COV (coefficient of variation) of 5.12 % and 7.84 % for local shell denting and overall bending damage, respectively. In general, the good accuracy of the numerical method was achieved.

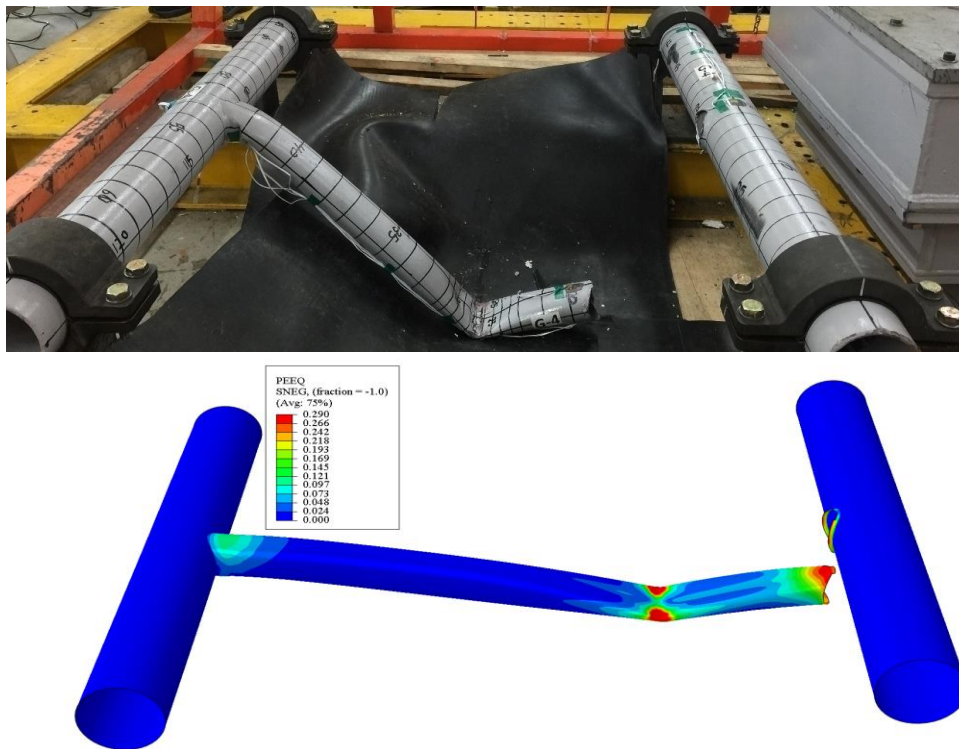


Fig. 4.48 Predicted deformed shape of model compared with test result for model G4.

4.5.2 Drop tests at sub-zero temperature

As in the actual tests, the simulations consisted of two steps: first, inducing the residual stress due to cooling process and second, performing impact analysis. In the first step, the general static Abaqus/Standard was used to induce the residual stress at -50°C . Then, low-temperature

impact test was performed using Abaqus/Explicit. The residual stress during cooling procedure occurred mainly at T-joint of brace and chord, as shown in Fig. 4.52.

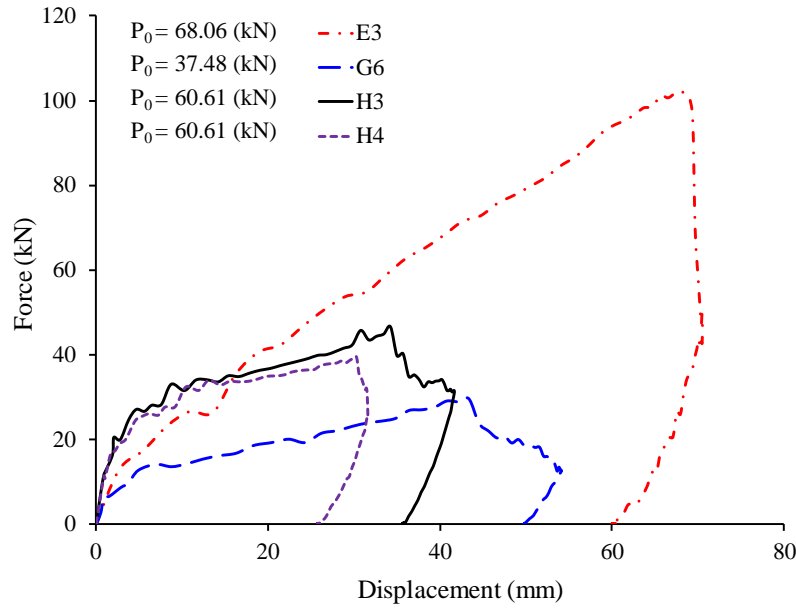


Fig. 4.49 Force-displacement response for different models.

Table 4.8 Comparison of test results and numerical results.

Model	D_b (mm)	Experiment results		Numerical results		Bias (FEA/Test), X_m	
		d_d/D_b (1)	d_o/D_b (2)	d_d/D_b (3)	d_o/D_b (4)	(3)/(1)	(4)/(2)
A1	76	0.56	1.35	0.59	1.41	1.061	1.048
A2	76	0.57	1.85	0.57	1.89	1.001	1.023
B2	89	0.35	0.73	0.38	0.66	1.086	0.907
C3	114	0.30	0.24	0.32	0.25	1.070	1.049
E3	89	0.67	0.72	0.71	0.68	1.052	0.933
F1	114	0.82	0.90	0.88	0.96	1.071	1.065
F2	114	0.52	0.51	0.57	0.49	1.107	0.968
G5	76	0.55	0.38	0.59	0.41	1.071	1.098
G6	76	0.66	0.60	0.71	0.66	1.075	1.085
H1	90	0.55	0.26	0.53	0.28	0.966	1.071
H2	90	0.58	0.31	0.63	0.35	1.093	1.116
H3	90	0.62	0.37	0.57	0.40	0.917	1.077
H4	90	0.55	0.26	0.58	0.31	1.057	1.199
H5	90	0.51	0.27	0.55	0.25	1.097	0.929

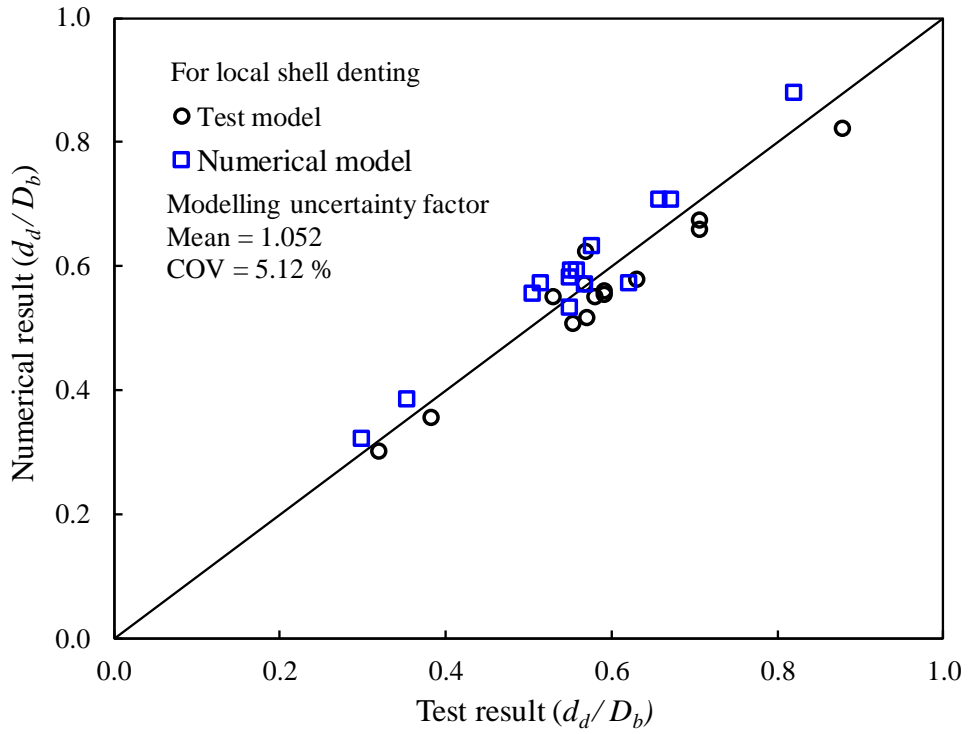


Fig. 4.50 Numerical results compared to test results for predicting local shell denting damage.

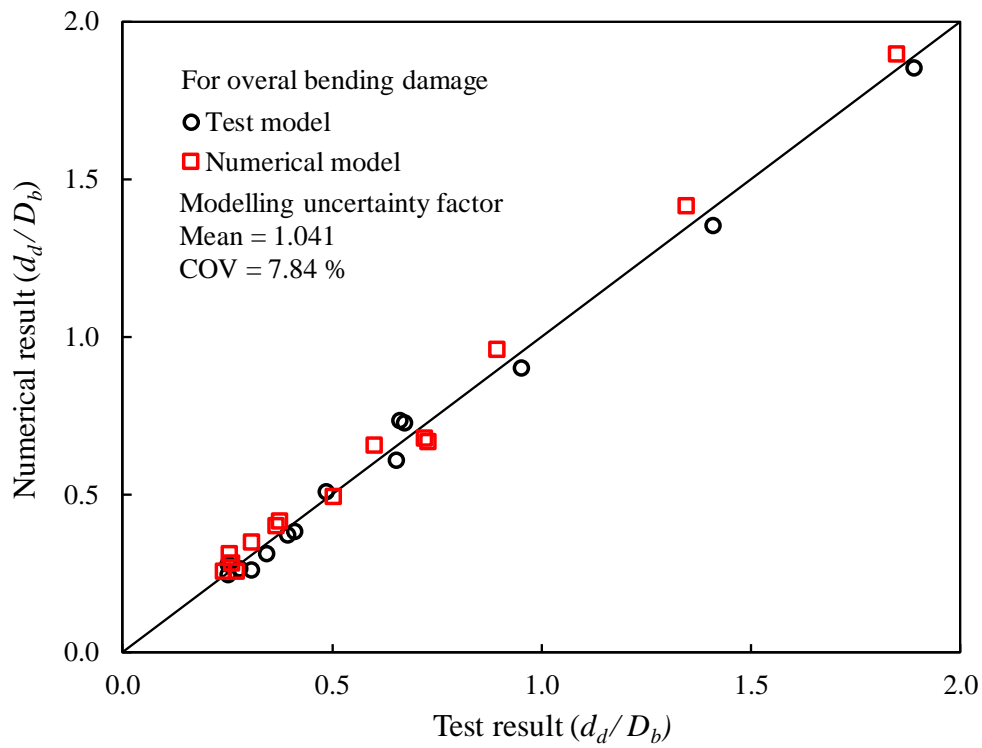


Fig. 4.51 Numerical results compared to test results for predicting overall bending damage.

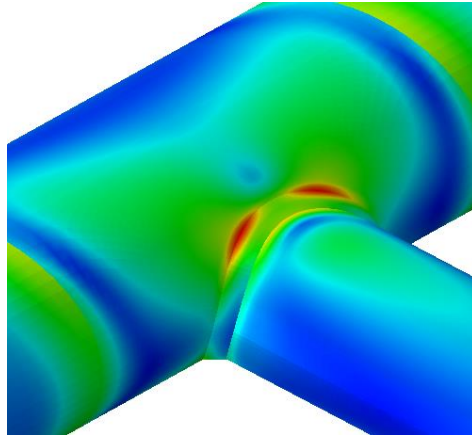


Fig. 4.52 Residual stress distributions at T-joint after cooling process.

Generally, when the material is brittle at low-temperature, the brittle phenomenon is more easily occurred. Therefore, in order to consider the effect on the brittleness of material, numerical was performed using a shear value of 0.2, which is lower three times than the tensile fracture strain of 0.6. The numerical result of model D2-LT was compared with experimental result, as shown in Fig. 4.53.

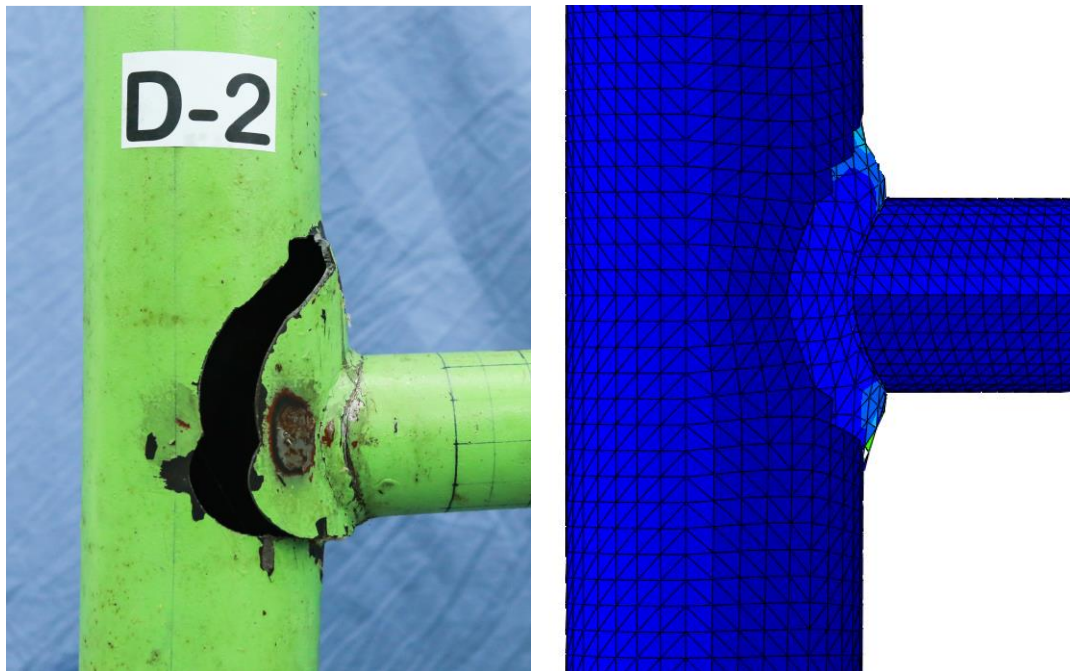


Fig. 4.53 Predicted deformed shape of model compared with test result for model D2-LT.

4.6 Parametric study

4.6.1 Derivation of approximate equation to predict the extent damage

4.6.1.1 Modification factor for maximum deflection

If the horizontal pipe is struck centrally by the striking vessel, the vertical legs will be deformed. In this section, the formulations to predict the maximum deflection and overall bending of ‘standard shape’ protection structures [186]. In the protection structures of caisson tubes, the main horizontal pipes are supported by vertical legs. A main horizontal pipe having two legs is adopted as the standard shape in this study [186].

Regression analysis was also performed for maximum deflection and Eq. (4.15) was obtained. The accuracy of formulation when compared to the numerical results gives a mean of 0.99 together with 6.07 % COV [186].

$$f_{om} = \exp \left\{ 0.03 \left(\frac{D_o}{t} \right)^{-3} + 0.2 \lambda_E^{0.34} - \left(\frac{D_o}{L} \right)^3 \right\} \quad (4.15)$$

Next, the extent of maximum deflection can be obtained by substituting f_{om} to Eq. (4.16).

$$d_{om} = f_{om} \frac{-b + \sqrt{b^2 + 4ac}}{2a} \quad (4.16)$$

where f_{om} : modification factor for maximum deflection

D_o : outside diameter of pipe

λ_E : Energy ratio; it is the ratio of the kinetic energy of the striker to the plastic axial capacity of the main horizontal pipe ($\sigma_Y A L$)

$$\lambda_E = \frac{E_k}{\sigma_Y A L} \quad (4.17)$$

d_{om} : Maximum deflection

L : length of pipe; t : thickness of pipe; A : Cross-sectional area of the horizontal pipe

$$a = \frac{2\sigma_Y}{L_H} \left(A + n A' \frac{l_x^2}{L_V L_H} \right) \quad (4.18)$$

$$b = \frac{4}{L_H} \left(2 M_p + n \frac{l_x}{L_V} M_p' \right) \quad (4.19)$$

$$c = E_k \quad (4.20)$$

A' : Cross-sectional area of the leg pipe

E_k : Kinetic energy of the striking vessel

n : shape factor (see Fig. 4.54)

L_V : Length of leg pipe; L_H : Length of the horizontal pipe.

l_x : Distance between the center of the leg to the fixed end of the main horizontal pipe

M_p : Fully plastic moment of the horizontal pipe; M_p' : Fully plastic moment of the leg

pipe

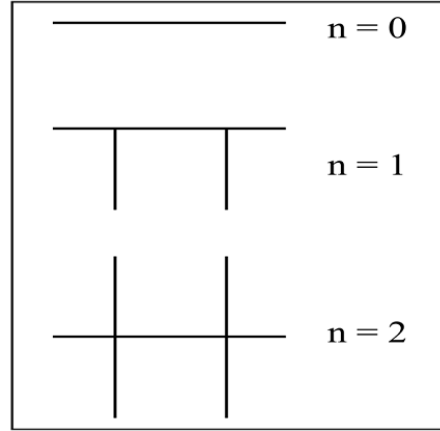


Fig. 4.54 Definition of shape factor.

4.6.1.2 Modification factor for overall bending damage

Based on the regression analysis from numerical results, the modification factor for overall bending damage was proposed in Eq. (4.21). The accuracy of formulation when compared to the numerical results gives a mean of 1.002 together with 6.048 % COV. This modification can be applied to Eq. (4.22) to predict overall bending damage.

$$f_{pp} = \exp \left\{ 0.1 \left(\frac{D_o}{t} \right)^{-3} + 0.17 \lambda_E^{0.1} - \left(\frac{D_o}{L} \right)^2 \right\} \quad (4.21)$$

$$d_{pp} = f_{pp} \frac{-b + \sqrt{b^2 + 4ac}}{2a} \quad (4.22)$$

where f_{pp} : Modification factor for d_{pp} ;

d_{pp} : Permanent deflection of plastic neutral axis point

4.6.1.3 Local denting damage equation

A regression analysis was also performed to investigate the extent of local denting damage at impact point. The proposed equation to predict local denting damage was presented in Eq. (4.23). The accuracy of this equation was verified by comparing to the numerical analysis results was 0.99 of mean and 4.27% of COV.

$$\frac{d_d}{D_o} = 0.92 \left\{ 1 - \exp \left(-1.5 \frac{\lambda_E D_o}{t} \right) \right\} \quad (4.23)$$

4.6.2 Deriving a simple fracture criterion

There are many researchers who derived the formulations using equivalent plastic strain criterion applied in ship collision modeling. Generally, these formulations are used in various mesh-scaling laws depending on the thickness of the shell. Peschmann [205] defined a criterion

for small and large shell thickness. This criterion was derived from experimental and numerical results of ship collision and grounding accidents as follows:

$$\varepsilon_f = \begin{cases} 0.1 + 0.8 \frac{t}{l_e} & \text{if } t \leq 12 \\ 0.08 + 0.65 \frac{t}{l_e} & \text{if } t > 12 \end{cases} \quad (4.24)$$

Hogström et al. [206] provided the failure strain criterion for ship collision and groundings. In this formulation, e_u and c are the uniform strain and Barba constant ($e_u = 0.22$, $c = 0.93$ for shipbuilding steels); w and t are the original width and thickness of the tensile test coupons ($w = 25$ mm; $t = 4$ mm).

$$\varepsilon_f = \ln \left[\exp(e_u) + c \frac{\sqrt{wt}}{l_e} \right] \quad (4.25)$$

Ehlers [208] developed a failure strain equation for hull tanker collision tests as in equation (29). The parameters ε_g and α were measured from the experimental results, with $\varepsilon_g = 0.1466$ and $\alpha = 0.7985$.

$$\varepsilon_f = \varepsilon_g + \alpha \left(\frac{t}{l_e} \right) \quad (4.26)$$

Liu et al. [222] suggested a simple fracture criterion which was derived based on the results of striking bulbous bow collisions with the side shell double-hull ships, according to

$$\varepsilon_f = 0.50 - 0.01 \left(\frac{l_e}{t} \right) \quad (4.27)$$

A simple fracture criterion was proposed by DNV RP-C204 [26] as follows:

$$\varepsilon_f = 0.02 + 0.65 \left(\frac{t}{l_e} \right), \quad \frac{l_e}{t} \geq 5 \quad (4.28)$$

The GL criterion [224] was provided the formulation to predict the rupture strain of the plates from the damaged ship structures. This criterion is defined in equation (32) and (33) for the principal strain (ε_{1f}) and critical through-thickness strain (ε_{3f}) as follows:

$$\varepsilon_1 = \begin{cases} 0.056 + 0.54 \frac{t}{l_e} & \text{if plate structures} \\ 0.079 + 0.76 \frac{t}{l_e} & \text{if beam or trusses} \end{cases}, \quad l_e/t \geq 5 \quad (4.29)$$

$$|\varepsilon_{3f}| = \frac{\varepsilon_{1f}}{1 + \varepsilon_{1f}} \quad (4.30)$$

In this study introduces a new simple critical failure strain for offshore tubular member and ship collisions. It is noted that the formulation was derived when considering the size of fine mesh in the contact area between the offshore tubular member and ship collisions. The results of the numerical analysis are shown in Fig. 4.55. The proposed formulation for predicting the equivalent fracture strain was indicated in equation (4.31). Furthermore, the accuracy of the proposed formulation has been established by comparison with the results of tests and finite element

analyses. The mean of X_m (the ratio between the predicted fracture strain value of proposed formulation and experimental models) was 1.00 together with COV of 6.13 %.

$$\varepsilon_f = 0.471 \left(\frac{l_e}{t} \right)^{-0.524} \quad (4.31)$$

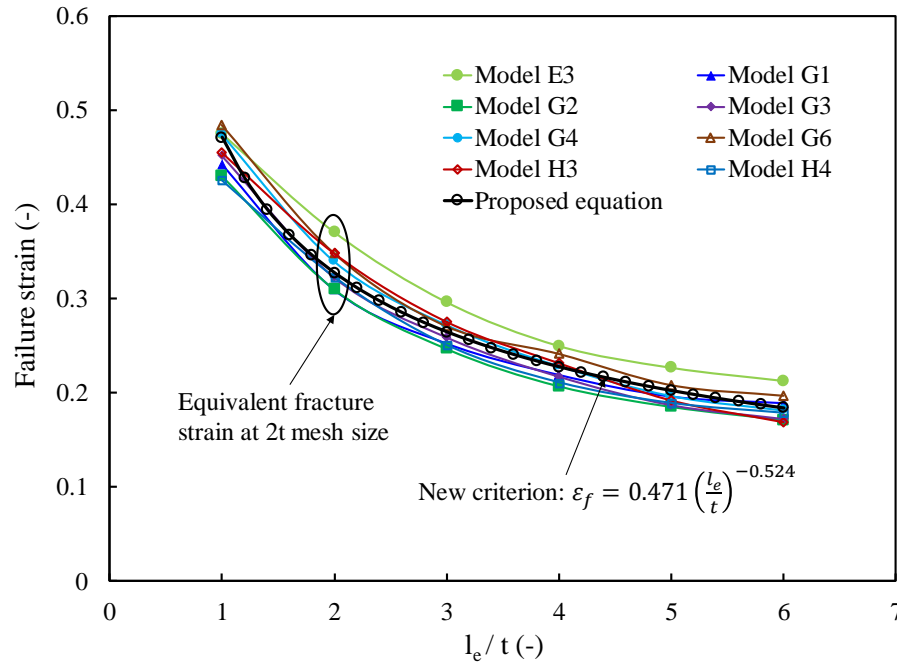


Fig. 4.55 Failure strain of experimental models compared to proposed equation.

Another simple critical failure strain formulation has been derived when considering the size of fine mesh in the contact area between the offshore tubular member and ship collisions. The comparison of the various fracture criteria based on the equivalent fracture strain versus element length curves for ship collision modelling is depicted in Fig. 4.55. Generally, most of the fracture criteria obtained from different researchers have a similar trend. It is described that the length of the element is small following the equivalent rupture strain is large. Failure strain is a function of the size of mesh elements. It is noted that there are small deviations between the proposed equation and DNV (2010) and GL (2014) rules. However, the rupture strain obtained from the proposed equation is much lower than those of other researchers and a slightly higher than DNV (2010) and GL (2014) as shown in Fig. 4.56. The reasons may be because the type of collision scenarios of present test models are different from those of the previous studies. On the other hand, the strain-hardening models included in finite element modelling of the previous studies were different from the current study. It is also one of the main reasons for the deviations between the proposed equation and the previous equation proposed by other researchers.

4.6.3 Failure modes of single and H-shape tubular members

A series of dynamic impact tests included ten plastic damage models, four partial fracture models and four complete fracture models, were successfully conducted in this study. The details of the experimental setup, test procedure and test results are also reported in this paper. The main goal of these tests was to investigate the damage responses at T-joint tubular members.

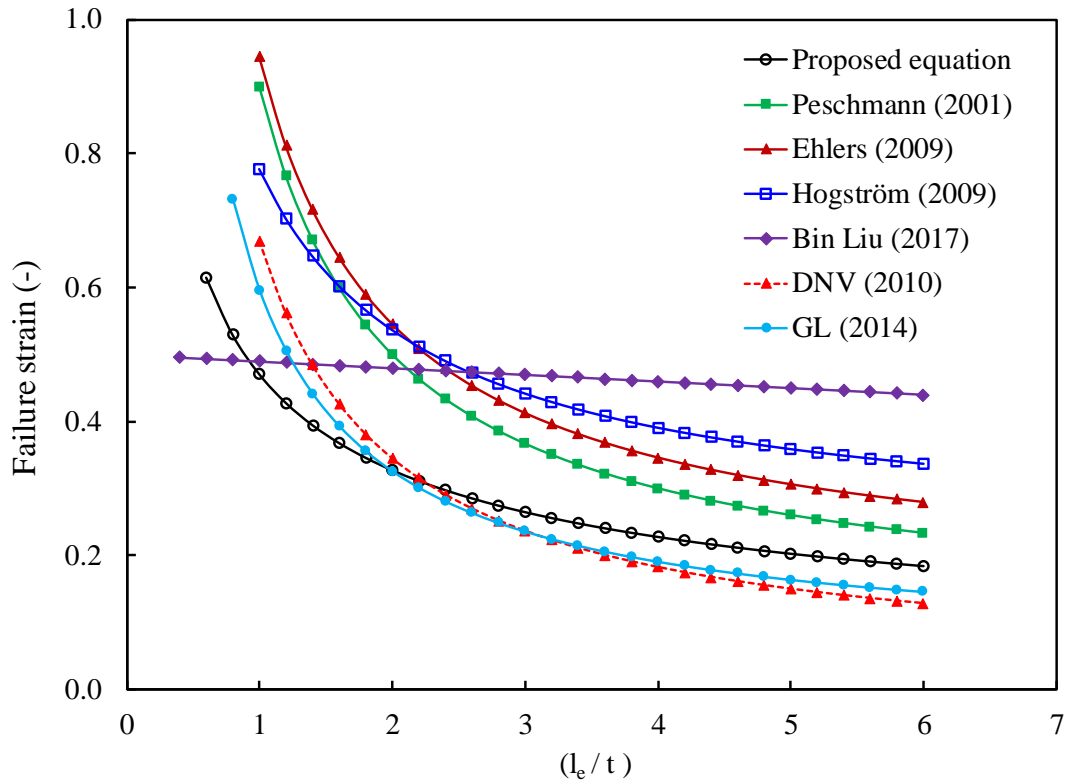


Fig. 4.56 Comparison of the various fracture criteria for ship collision modelling.

In general, the response of tubular members under dynamic mass impact is very complicated because the combination between local shell denting and the overall bending damage. Thus, it is difficult to propose to classify all deformation modes of these structures. The failure modes of experimental results are depicted in Figs. 4.57, 4.58 and 4.59. In these figures, the energy parameter λ_E is defined as the ratio of kinetic energy of striker (E_k) to energy absorption capacity of struck structure (E_a). And P_0 and P_c is plastic collapse load of a fully fixed tubular beam and characteristic force indicating resistance against local denting, respectively.

It can be seen in Figs. 4.57, 4.58 and 4.59 that the failure mode IV (plastic damage on both bracing and chord) is easily classified with energy ratio (λ_E) larger than 0.02. However, failure mode included mode I, mode II and mode III was very complex to classify. It is not straightforward to suggest the simple parameter for classifying all deformation mode and response of tubular members.

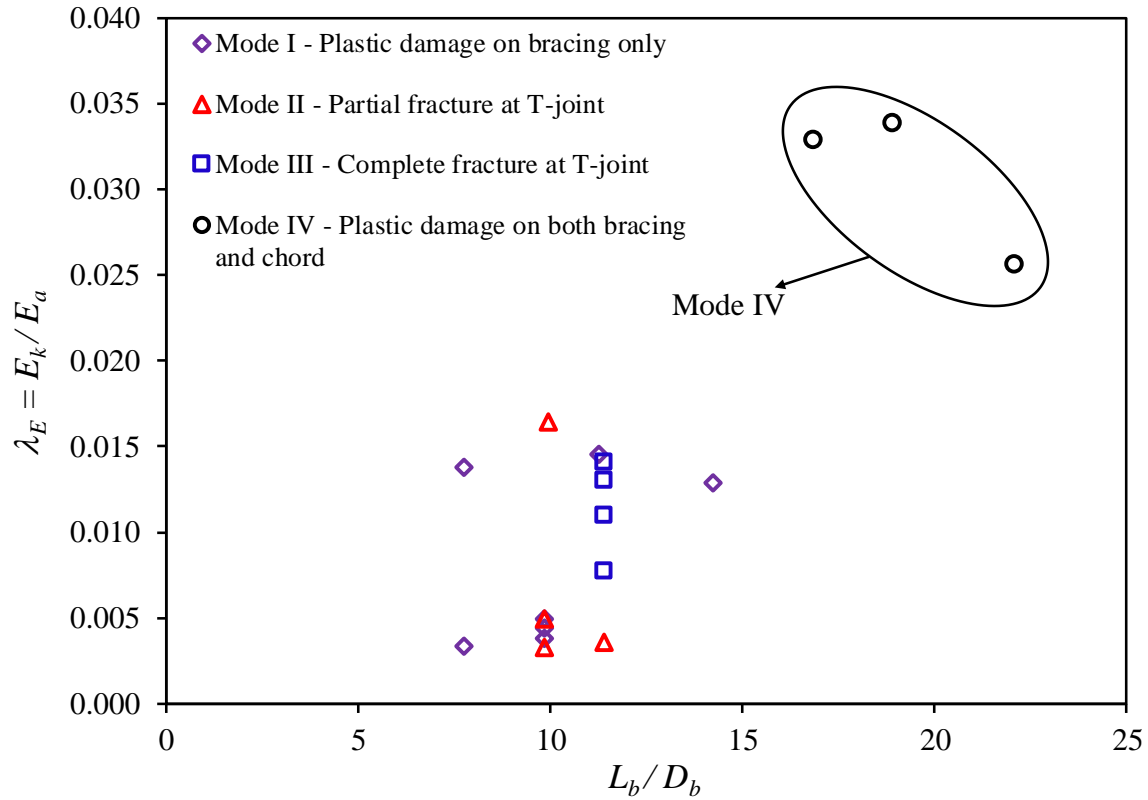


Fig. 4.57 Plotting of failure mode of test models against basic parameters E_k/E_a and L_b/D_b .

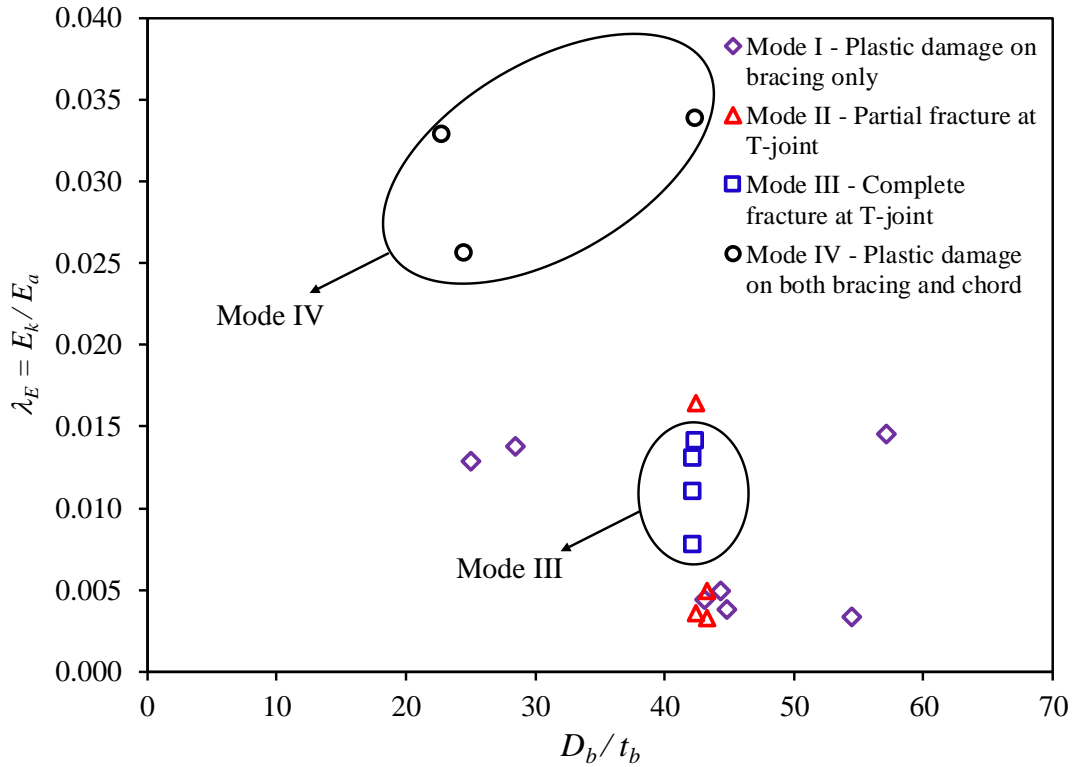


Fig. 4.58 Plotting of failure mode of test models against basic parameters E_k/E_a and D_b/t_b .

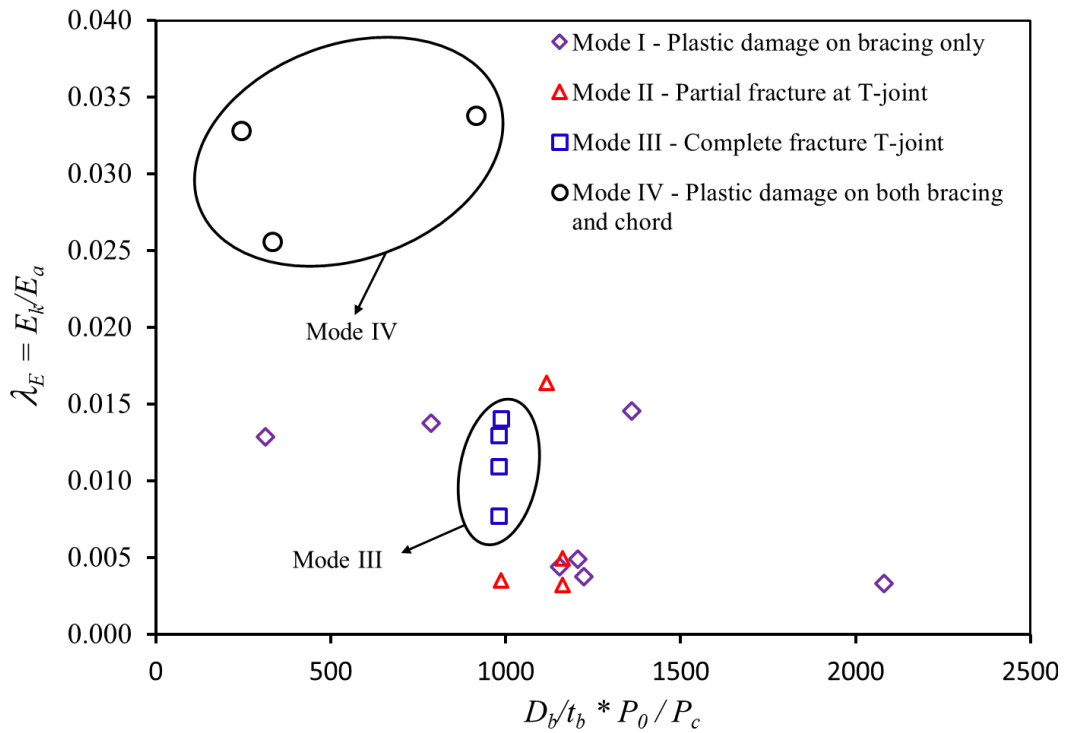


Fig. 4.59 Plotting of failure mode of test models against basic parameters E_k/E_a and $D_b/t_b * P_0/P_c$.

4.7 Final remarks

This Chapter was to provide the series of experimental and numerical results of H-shape tubular members under dynamic mass impact at room and sub-zero temperature. These results were shown insights understanding of the plastic deformation and fracture behavior at T-joint of tubular member during ship collision. The numerical simulations have a good agreement with the experimental results. The predicted local shell denting and overall bending damage are commonly larger than those of test results. The rotation angle of striking mass during free fall and the uncertainty of the dynamic material modelling were the main reason.

The failure modes of tubular member subjected to dynamic mass impact were very complex because the combination between local shell denting and the overall bending damage. It is not straightforward to suggest the simple parameter for classifying all deformation modes and responses of tubular members.

Proposed formulations were provided to predict the maximum deflection, overall bending damage, and local denting damages of FPSO caisson protection structures subjected to attendant vessel collisions. The equations are convenient to use especially in initial design and give the good accuracy and reliability of predictions.

Furthermore, a new simple critical failure strain formulation has been provided when considering the size of fine mesh in the contact area between the offshore tubular member and ship collisions. Commonly, when choosing the failure criterion, it should be considered carefully the type of collision scenarios and definition of the material properties. Even though there are many criterions which have been validated against test results. However, until recently it is still difficult to find a universal failure criterion for all type of various collision scenarios, which has consistently predicted results with the available experimental results. Therefore, most of the fracture criterions have shown drawbacks. These problems are not yet answered accuracy and it is still an intensive research topic. In this study, the good agreement was achieved between numerical simulations and experimental results for eight fracture models. It is shown that the proposed equation (4.31) can be applied to a collision scenario similar to that of the current study.

Chapter 5

Experiments on the residual strength of damaged ring- and stringer-stiffened cylinders subjected to hydrostatic pressure

5.1 Introduction

Ring- and stringer-stiffened cylinder are a well-known structural element as the typical structural component of a tension leg platform, spar, submarines and buoyancy column of a floating offshore wind turbine foundation. During service life, these structural elements are potentially damaged in service, it is necessary to consider the effects of the damage on the strength of the structure and serviceability at the design stage. Thus, it is necessary to understand the form of damage that can potentially occur. The immediate repair of the damage may be difficult and sometimes impossible owing to economic and technical requirements. Therefore, efficient and accurate assessment methods to estimate the damage effects are essential for decision-making through residual strength assessment procedures.

Ultimate strength tests on intact fabricated ring-stiffened cylinders have been reported by many researchers for hydrostatic pressure loading [145-148] and combined axial compression/tension and radial pressure loading [149-155]. As mentioned earlier fabricated ring-stiffened cylinders may contain residual stresses and initial shape imperfections. Many researchers [156-160] have investigated their effects on the ultimate strength of ring-stiffened cylinders subjected to external hydrostatic pressure. Based upon the results of those experimental works together with related theoretical investigations quite accurate and reliable design formulations for predicting the ultimate strength of ring-stiffened cylinders can be found in the BSI [139], GL [161] and ABS [162] Rules. Mackay et al. [163] quantified the accuracy of inter-frame and overall collapse predictions using the submarine design formulae in order to provide a base line for comparison with numerical modelling results.

Regarding the residual strength of a damaged ring-stiffened cylinder, there are only a few studies have been reported in the open literature so far. Harding and Onoufriou [104] reported axial compression tests on damage fabricated ring-stiffened cylinders. The local denting damages were induced by the static application of lateral load. MacKay et al. [54] provided details of experimental and numerical investigations on the strength of damaged pressure hulls which included machined unstiffened and ring-stiffened cylinders with artificial corrosion damage. MacKay et al. [67] conducted numerical analyses of their corroded ring-stiffened models under hydrostatic pressure. Cerik [114] performed numerical predictions of the residual strengths of damaged ring-stiffened cylinders subjected to axial compression.

For stringer-stiffener cylinder structures, several extant studies experimentally described the ultimate strength of intact model for hydrostatic pressure [164-166] and a combination of axial compression/tension and radial pressure [107,109,152, 167-172]. The effects of residual stresses (cold bending and welding) and initial shape imperfections due to the fabrication processes performed on the ultimate strength of stringer-stiffened cylinders subjected to hydrostatic pressure are discussed [156, 173]. Furthermore, the formulations to predict the ultimate strength of stringer-stiffened cylinders were derived by Cho et al. [174], Das et al. [175], DNV [176], API [143], and ABS [177] Rules, which were considerably accurate and reliable. However, there are only a few studies focused on the residual strength of a damaged stringer-stiffened cylinder. Quasi-static denting was conducted to generate the damaged model prior to performing axial compression tests on damaged fabricated stringer-stiffened cylinders [110-112]. Walker et al. [113] also performed quasi-static denting tests on stringer-stiffened cylinders as the first stage and subsequently tested them under a combination of external pressure and axial compression loading. However, until now, there is a lack of the experimental information regarding the dented stringer-stiffened cylinders under pure hydrostatic pressure loadings. Therefore, it is necessary to provide some experimental results of this loading. It may useful to researchers for understanding the responses of the dented stringer-stiffened cylinders under various loadings covering the full ranges of the combinations.

Current design codes do not provide any comprehensive guideline to cover the detrimental effects of damage. Experimental studies have their own difficulties, such that, even series of equivalent intact and damaged models would be tested it would be difficult to correlate two models due to dissimilar imperfections. From this point of view carefully conducted nonlinear finite element analysis may be potentially the effective means of assessment of residual strength, despite the computational costs involved.

In this chapter, the residual strength of the dented ring- and stringer-stiffened cylinders under hydrostatic pressure is investigated through experiments and numerical analysis. After validation the numerical techniques, a rigorous parametric study was performed on both ring- and stringer-stiffened cylinders in order to clarify the residual strength responses.

5.2 Test models

Two series of steel stiffened cylinders were fabricated with different dimensions. The first series for ring-stiffened cylinder included the models, namely, RS-I, RS-II, RS-C-1, RS-C-2, RS-C-3, and RS-C-4. The second series for stringer-stiffened cylinder comprised the models SS-I, SS-C-2, and SS-C-3. Among them, RS-I, RS-II, and SS-I are the intact models, which are used for comparison with the damaged models to determine the ultimate-strength reduction factor.

5.2.1 Material properties

The models were fabricated from a general-purpose structural steel material. The mechanical properties were obtained by performing quasi-static tensile tests and dynamic tensile test results. Detailed explanations of material properties for both ring- and stringer-stiffened cylinder are given in Chapter 3 at Section 3.2.1.2 and 3.3.1.2, respectively.

5.2.2 Damage generation and measurements

To induce damages on the cylinders, a drop test machine was employed. The aim of the collision tests is to obtain the damaged shapes on ring or stringer-stiffened cylinders for the subsequent collapsed tests. The details of damage generation using drop test machine are given in Chapter 3. After the collision tests, hydrostatic pressure tests were performed for assessing the residual strength responses of the ring- and stringer-stiffened cylinders in damaged and intact conditions. The experiments were carried out using a pressure chamber. The maximum pressure of the chamber is tested up to 6.0 MPa, which is equivalent to 600 m of water depth.

5.3 Hydrostatic pressure test on ring-stiffened cylinder

5.3.1 Test procedures

External hydrostatic pressure tests were conducted on two intact and four damaged ring-stiffened cylinder models using a pressure chamber. The inner diameter of the chamber was 1300 mm and the length of the cylinder part was 2800 mm. The maximum testing pressure was 6.0 MPa. One distinctive feature of the chamber was that the deformation of the model could be observed

during testing with the naked eye, and other information, including displacement and strain, could be measured without any difficulties from inside the model. It is noted that a rubber pad was placed to support the free end of the cylinder to reduce the bending moment due to the weight of the test model as shown in Fig. 5.1.

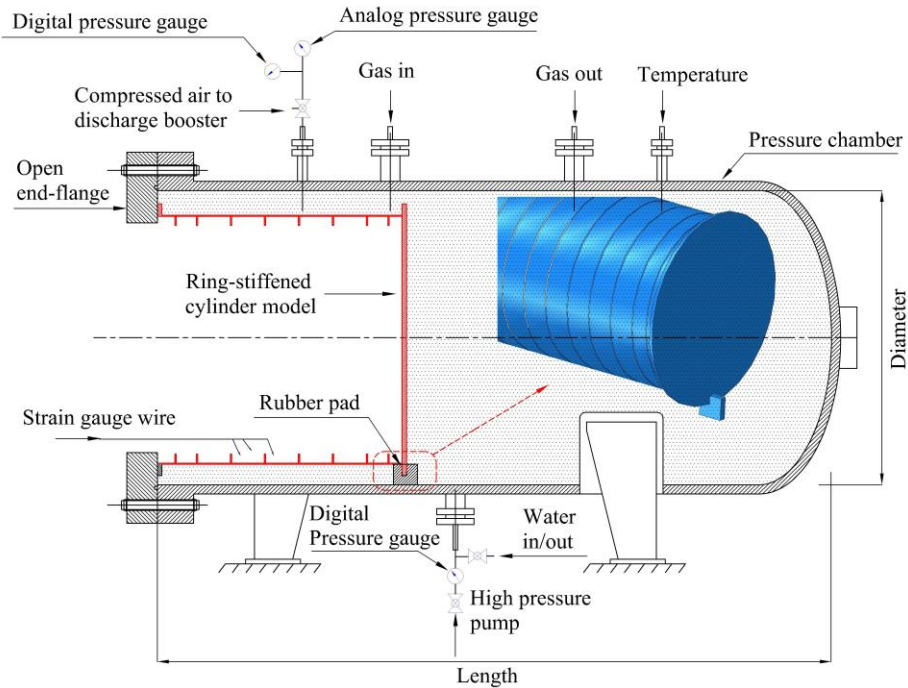


Fig. 5.1 Schematic of the hydrostatic test in pressure chamber.

The model was welded onto the inner surface of the chamber open flange, and then the chamber open flange was fixed with bolts to the main body flange of the chamber. An o-ring was inserted between two flanges to prevent water leakage. The hydrostatic pressure test was conducted using water which supplied to the pressure chamber. The pressure was applied gradually by a *Haskel* air driven high-pressure pump that was operated manually to control the pressure increments. Hydrostatic pressure in the tank was monitored using a pressure gauge. It was calibrated and installed at the top and bottom side. Two types of pressure gauges, analog and digital, were used. Finally, a National Instruments integrated computer was used to record the strain and pressure histories during the experiment.

External pressure was applied to the chamber by closing all the valves, except for the valve connected to the high-pressure pump located at the bottom of the tank. Initially, the pressure loading was increased at approximately 2 bar, and terminated until zero to reckon the stabilization of the pressure chamber at the first stage before hydrostatic pressure test is steadily increased. The increments of the hydrostatic pressure test were divided into three phases: the first 15 % of the

predicted collapse pressure was set by 0.5 bar, from 15–80 % by an additional 1 bar, and from 80% up to the collapse of the model, by the final 0.5 bar increment. Intermittent stops were made to settle the pressure, and check the model until collapse occurred. The collapse of the model was accompanied by a loud bang, followed by a sharp drop in the pressure history.

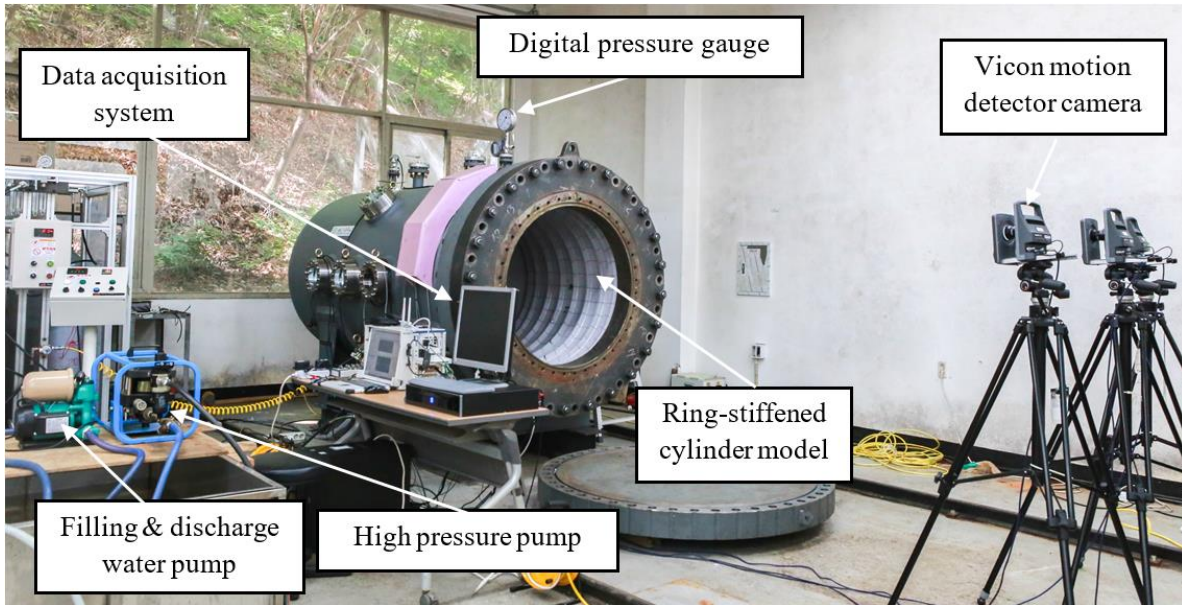
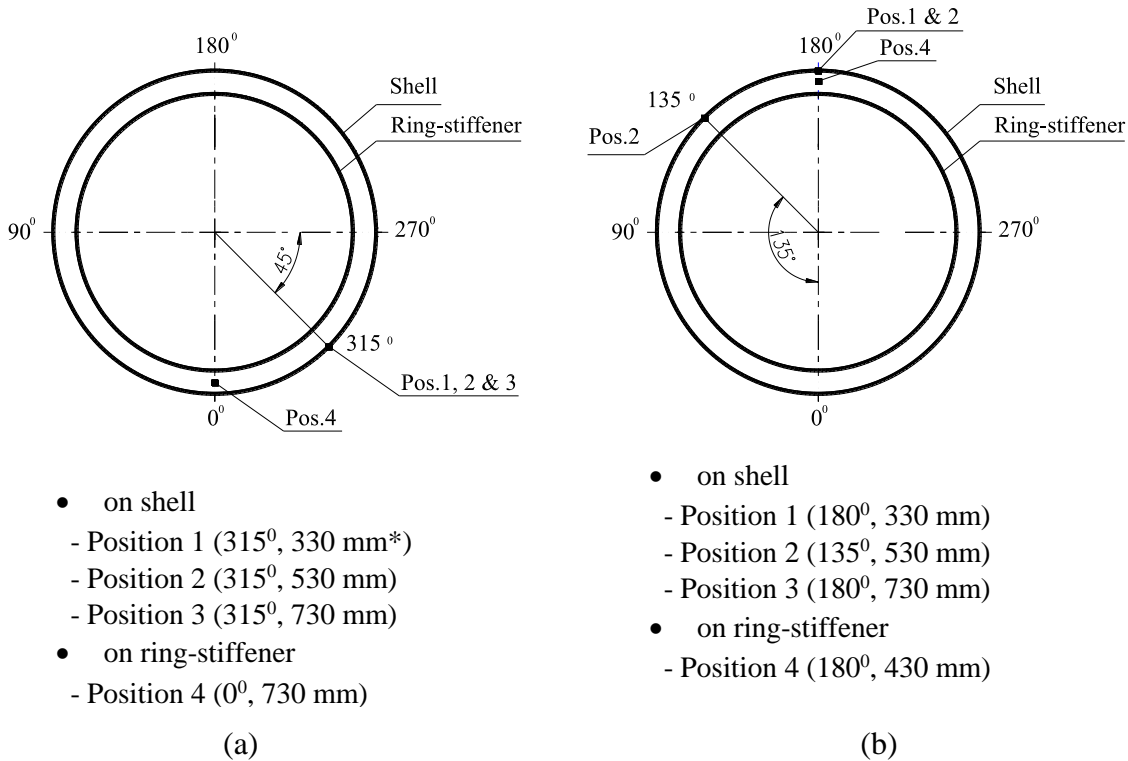


Fig. 5.2 Experimental setup for intact model RS-II under hydrostatic pressure test.

The settings of the hydrostatic pressure experiment are shown in Fig. 5.2. During the test, the pressure was measured by two pressure gauges. One was a digital type, whose signal was continuously recorded by a data logger. The other was an analogue type; its reading was used to confirm the digital signal. The strain data at four positions inside the model were also recorded by a logger signal. The axial shortening at the centre point of the end plate was determined using a Vicon motion detector camera. All the digitally measured data were acquired by the PXI series data acquisition system manufactured by National Instruments, Texas, USA. Additionally, a camera was installed to record the model deformation.

5.3.2 Strain gauge arrangement

To measure the strain response, strain gauges were bonded at four positions. The arrangements of the strain gauges are sketched in Figs. 5.3 & 5.4. Three positions were on the inner surface of the shell and one was at the mid-height of the stiffener. At each position two strain gauges were glued.



note: * indicates the distance from the end-plate

Fig. 5.3 Strain gauge arrangements: (a) model RS-I; (b) models RS-C-1&RS-C-2.

5.3.3 Test results and discussion

5.3.3.1 Intact models: RS-I and RS-II

Fig. 5.5 shows the collapsed shape of the intact model, i.e., model RS-I. When the pressure increased to 1.98 MPa, a local buckling of the shell was visually detected at approximately 10^o-20^o in bay #5. When it reached 2.0 MPa, two more parts of the shell locally buckled at approximately 330^o-350^o in bay #3 and 330^o-340^o in bay #7. Subsequently, when the pressure recorded was 2.16 MPa, a sudden and paramount deformation occurred, showing an overall buckling at 30^o-40^o. Severely tripped stiffeners could be seen, especially in the mid-length of the model. This model showed a typical interactive failure mode between local and overall buckling modes.

For model RS-II, the deformed shape is characterised by a number of shell-buckling lobes, superimposed with overall buckling of the shell and stiffeners, as indicated in Fig. 5.6. Local buckling occurred in bays no.3 and no.6. That local failure was progressed circumferentially for about a quarter of the circular shell, whereas the overall buckling of both models started from the mid-bay of the cylinder towards the end plate.

It is concluded that both models exhibited similar collapsing behaviour. Local collapse occurred on the shell between stiffeners at different bay locations, whereas, in the central bay of the compartments two adjacent stiffeners are tripping, which led to overall buckling. The collapse of models RS-I and RS-II appeared to be the interactive buckling mode.

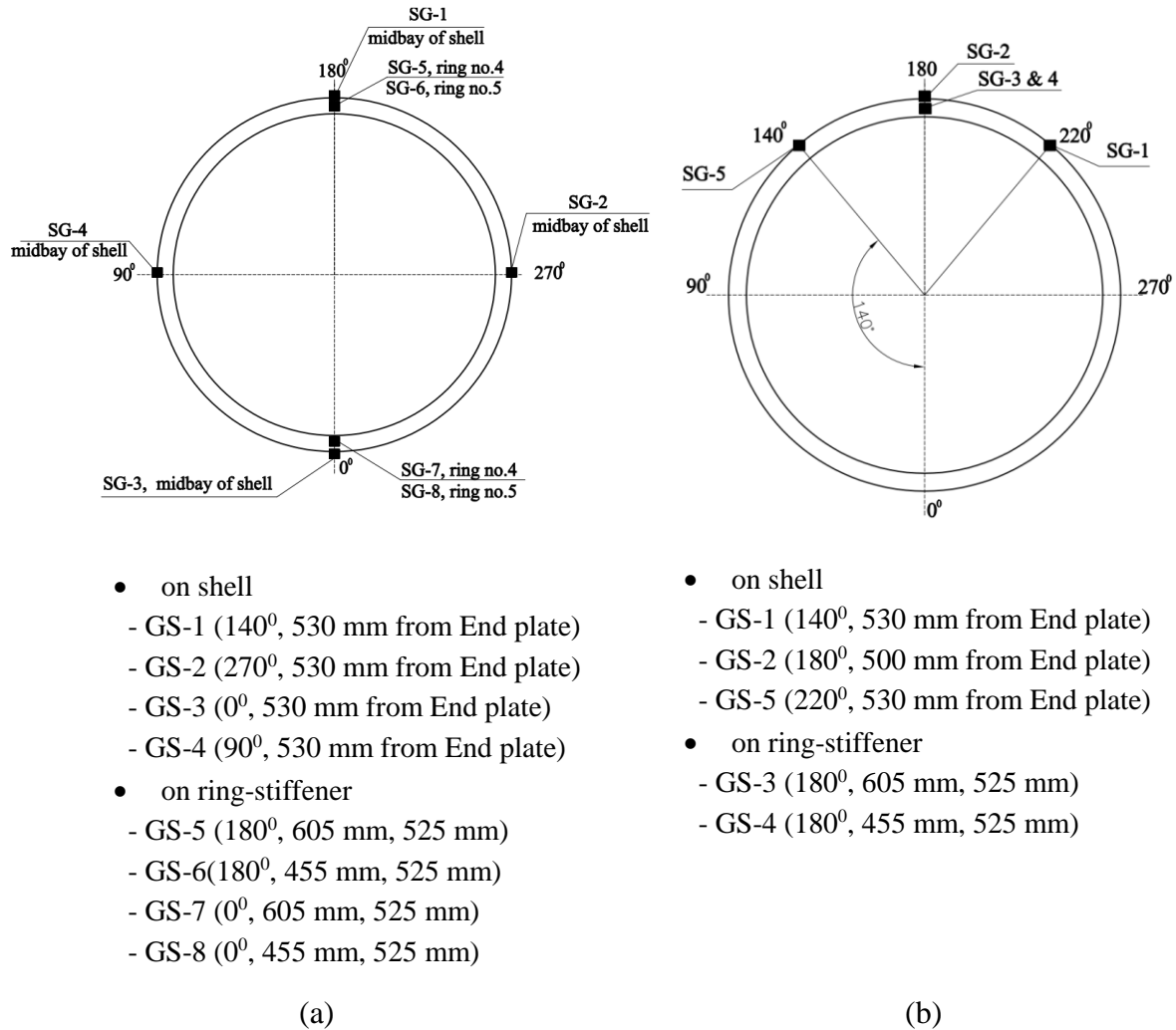


Fig. 5.4 Strain gauge arrangements: (a) model RS-II; (b) models RS-C-3&RS-C-4.

Fig. 5.7 shows the relationship of applied pressure versus axial shortening, where the axial shortening was measured from the displacement of the centre point of the end plate. The small fluctuations shown in the figure was due to time settlements while pressure increases. Instead of controlling the load by the amount of fluid release as typical volume-control, the high pressure pump was handled manually by controlling the valve. Hence, the settlements mean there is a power cut-off of the pump which made intentionally following the load increment procedure. A significant loss of applied pressure occurred immediately after the maximum pressure was reached.

The collapse pressure was found to be approximately 2.16 MPa, for RS-I, and 2.41 MPa for RS-II. This pressure drop resulted from expansion of the fluid volume due to the growth of the model's deformed shape. It indicated the rapid growth in strain with some reduction of the pressure. However, the RS-II model had a higher collapse pressure than R-I. This was related to the thickness of the shell plate and the stiffener geometry.

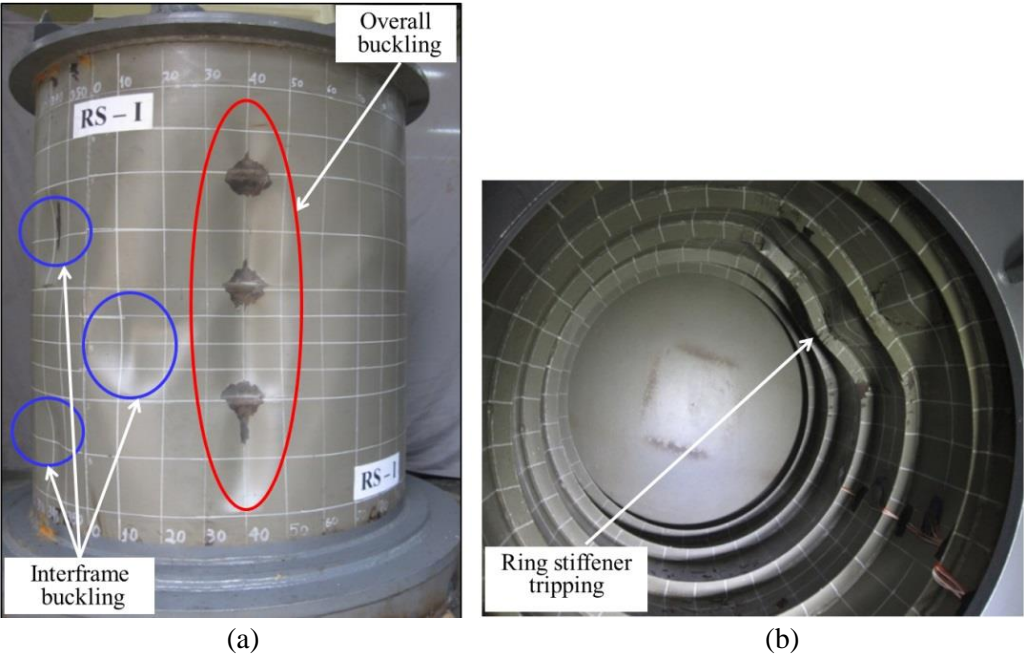


Fig. 5.5 Collapsed shape of the model RS-I: (a) Outside (b) Inside.

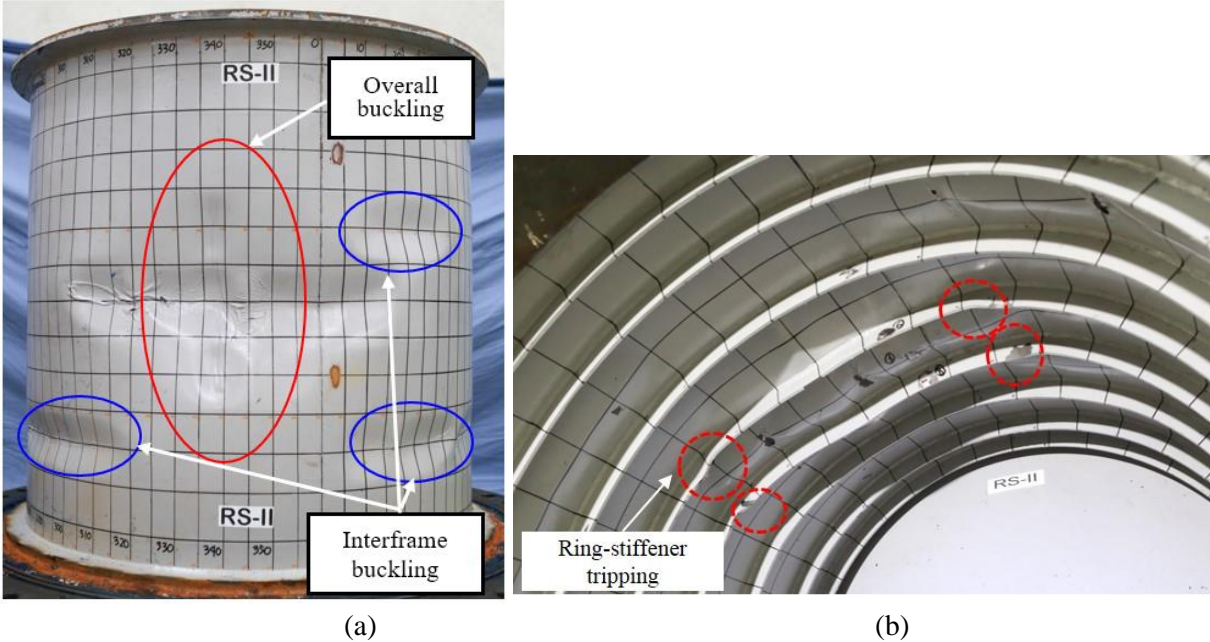


Fig. 5.6 Collapsed shape of the model RS-II: (a) Outside (b) Inside.

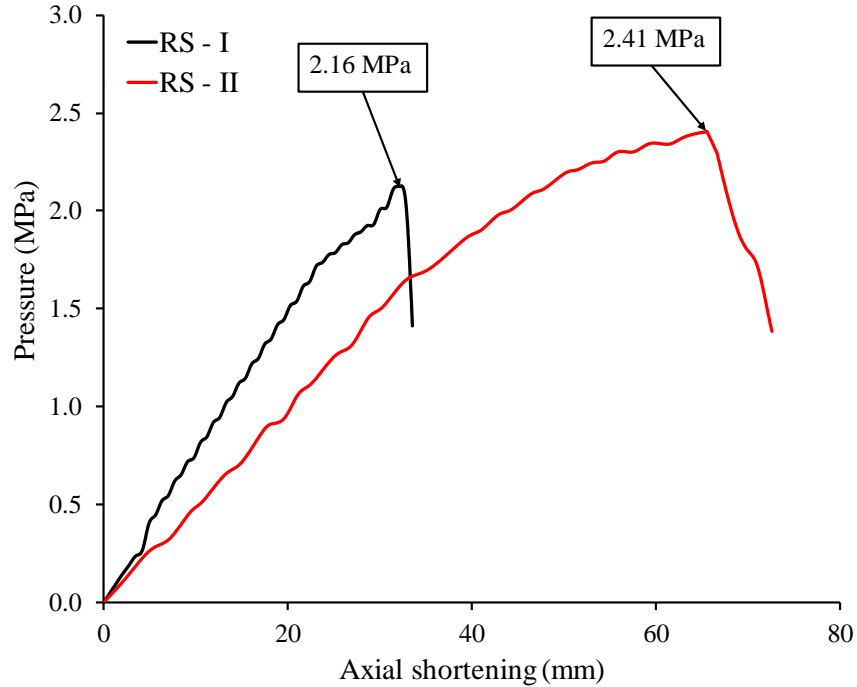


Fig. 5. 7 Axial shortening versus pressure of models RS-I and RS-II.

The strain measurement results for model RS-I are plotted in Fig. 5.8, showing almost linear relationships with pressure up to the collapse pressure. The figure also shows the larger strains at the shell compared with those of the ring-stiffener. For model RS-II, as observed in Fig. 5.9, stiffener tripping was detected by the strain measurement on the stiffener (SG no.5 & 6). The strain was indicated to be tensile on the ring stiffener. The instability on the stiffener led to a general loss of stiffness, followed by buckling of the shell due to high compression, which is shown as negative strain. Overall, the growth of the strain increases significantly in the post-collapse regime, right after the incidence of the limit load. As the applied pressure was decreased, the strain begins to decrease simultaneously with the drop of the pressure, which is the ring-stiffened cylinder model experiencing an unloading of pressure.

5.3.3.2 Damaged models: RS-C-1, RS-C-2, RS-C-3 and RS-C-4

The collapse pressures of the damaged models: RS-C-1, RS-C-2, RS-C-3, and RS-C-4, were 1.40 MPa, 1.65 MPa, 1.90 MPa, and 1.80 MPa, respectively. Compared with the collapse pressure of the intact models, model RS-I, which collapsed at 2.16 MPa, the strength reductions are 35.2 % and 23.6 % for model RS-C-1 and model RS-C-2, respectively. For model RS-C-3 and RS-C-4, the strength reduction when compare with intact model RS-II, which failed at 2.41 MPa, is 21.16% and 25.31%, respectively.

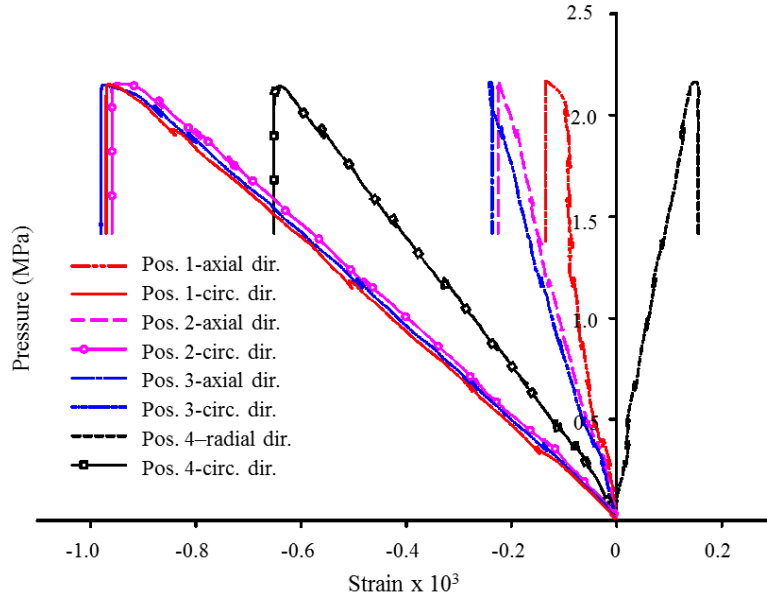


Fig. 5.8 Strain measurement results versus pressure of intact model RS-I.

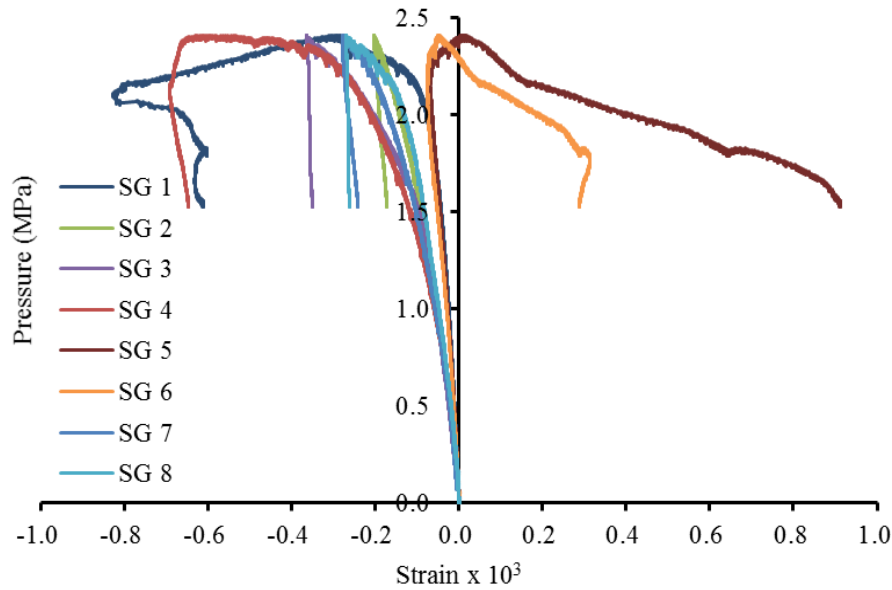


Fig. 5.9 Circumferential strain measurement results versus pressure of intact model RS-II.

The collapsed shape of the damaged models RS-C-1 and RS-C-2 can be seen in Figs. 5.10 and 5.11. Unlike the intact model, model RS-I, which failed according to the interactive failure mode, models RS-C-1 and RS-C-2 were failed by the overall collapse mode. The strain measurement results are depicted against pressure in Fig. 5.12. Probably owing to the existing deformation due to collision damage, some strain gauges bonded on shell (axial direction at

position 1 and circumferential direction at position 4) show high tensile strains. The collapsed shape of model RS-C-3 and RS-C-4 is shown in Fig. 5.13 and Fig. 5.14, respectively. That is quite similar to the collapse shape of models RS-C-1 and RS-C-2 and showing the overall buckling mode. Additionally, the pressure-strain curve for model RS-C-4 were depicted in Fig. 5.15. The strain gauges at positions 2 and 4, which are attached on cylindrical shells and ring-stiffener, respectively, exhibited high tensile strain owing to the sudden collapse of the shell while the strain gauges at positions 1, 3 and 5 exhibited low levels of compressive strain.

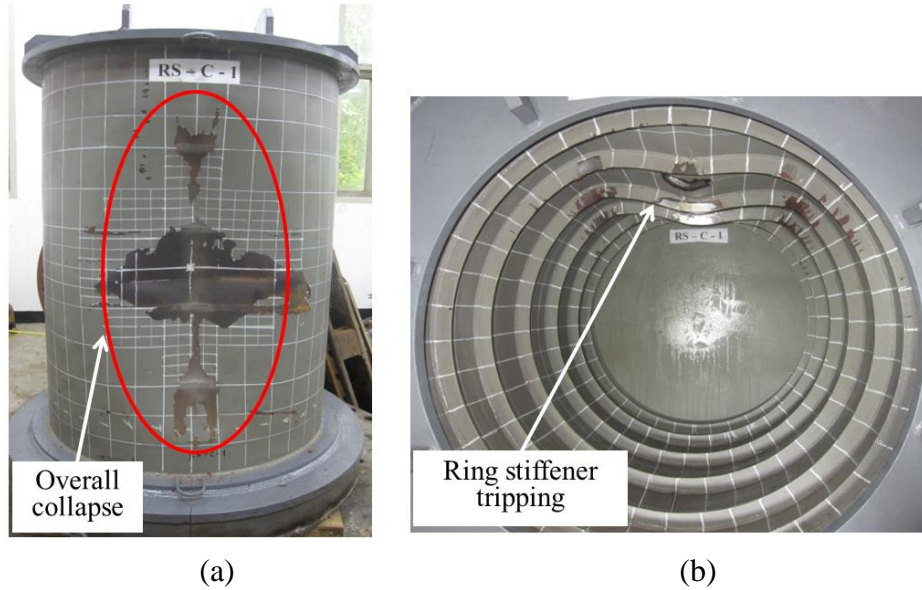


Fig. 5.10 Deformed shape of model RS-C-1: (a) Outside; (b) Inside.

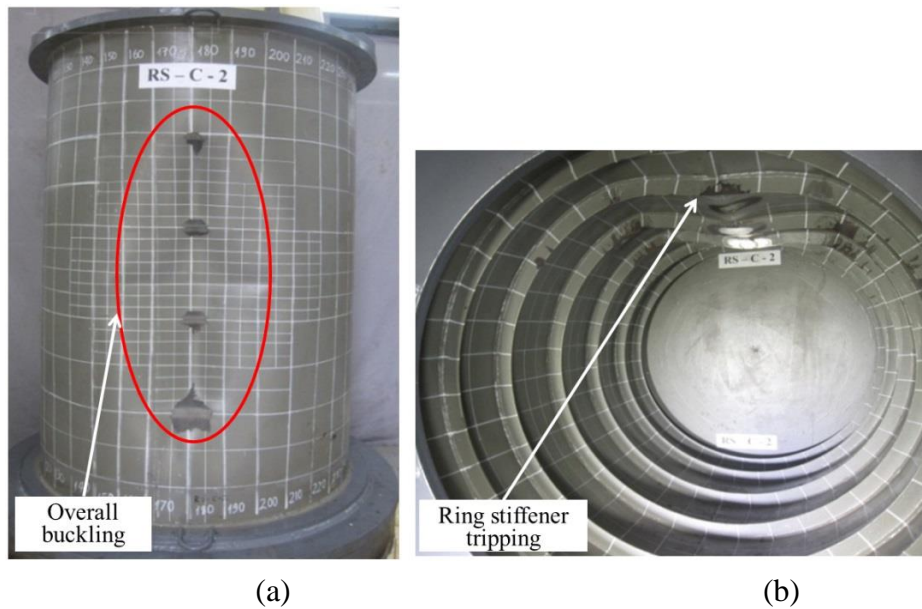


Fig. 5.11 Deformed shape of model RS-C-2: (a) Outside (b) Inside.

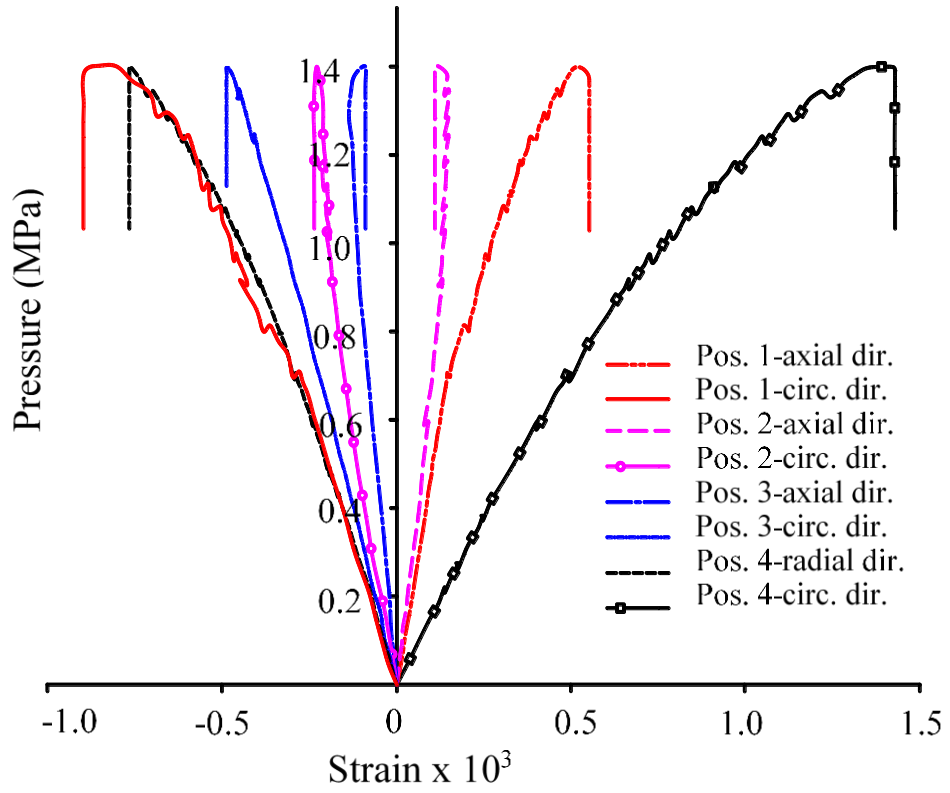


Fig. 5.12 Strain measurement results versus pressure of model RS-C-1.

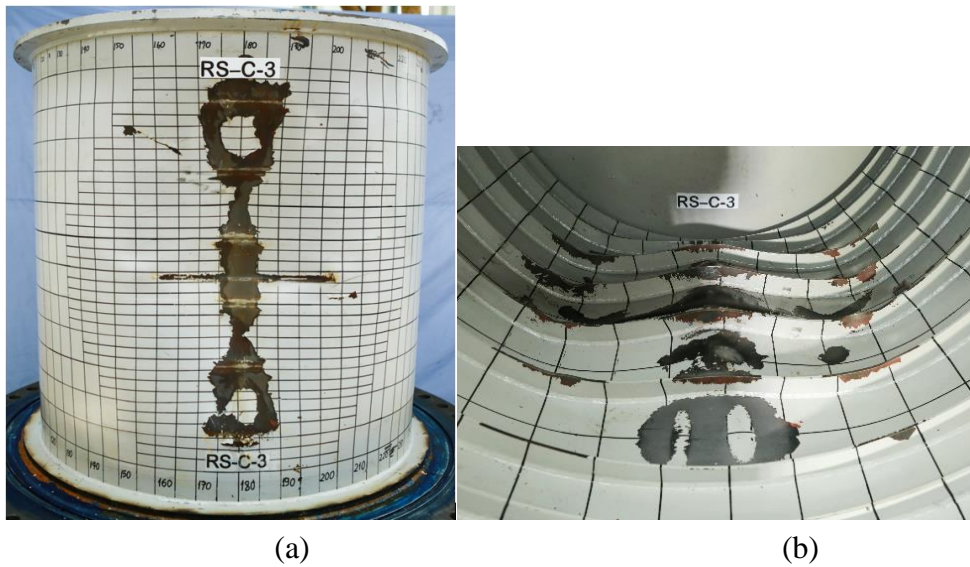


Fig. 5.13 Deformed shape of model RS-C-3: (a) Outside (b) Inside.

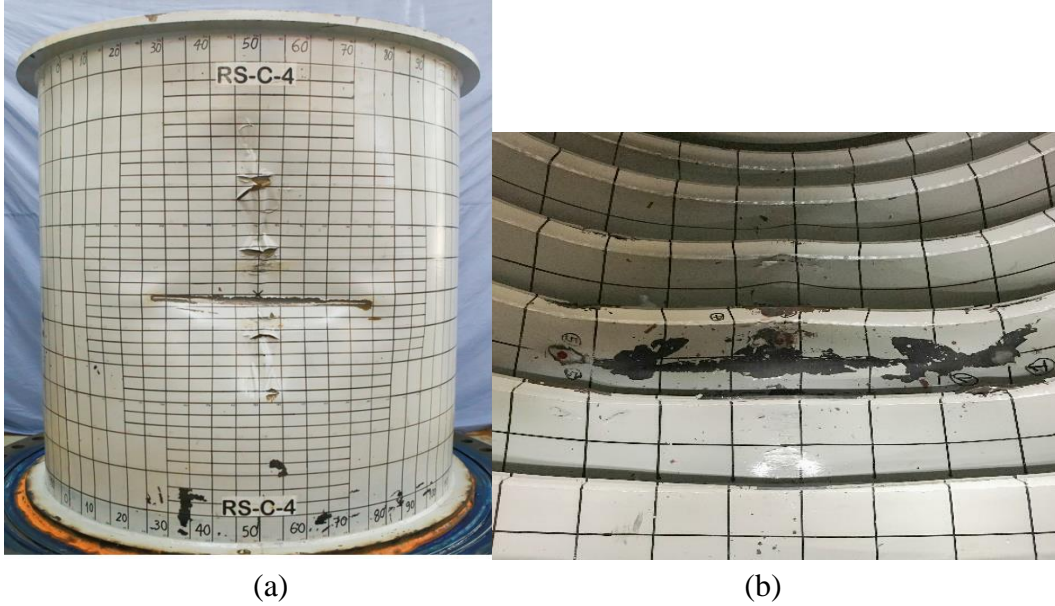


Fig. 5. 14 Deformed shape of model RS-C-4: (a) Outside (b) Inside.

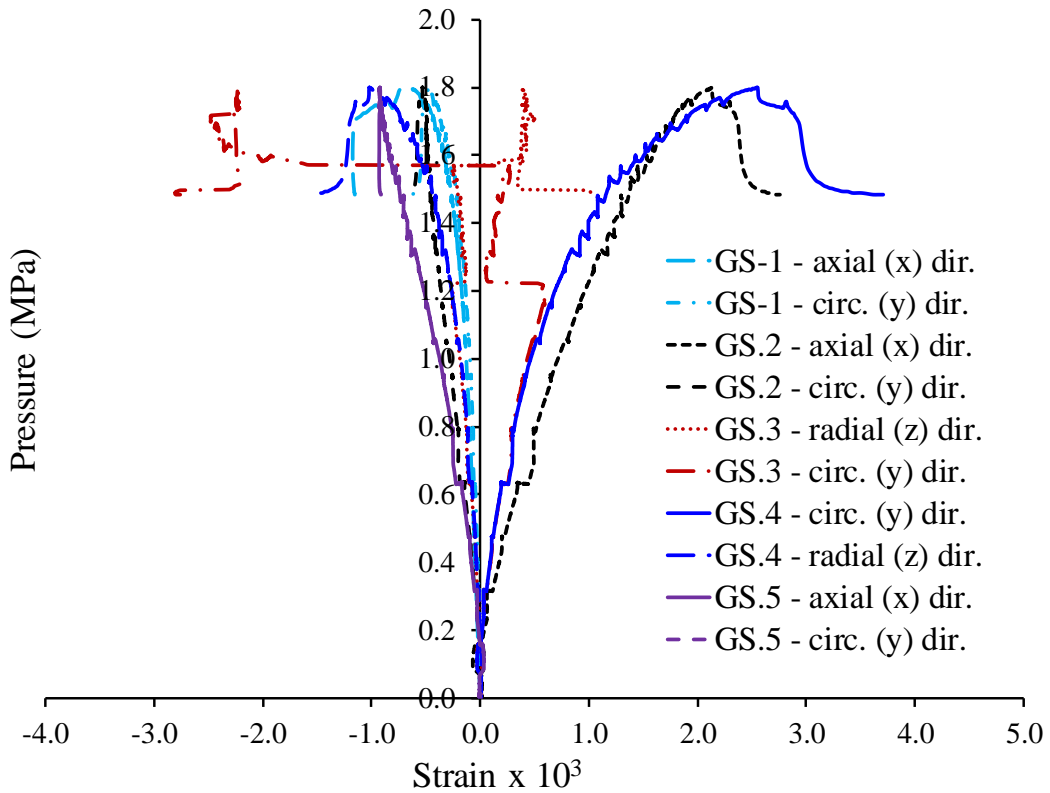


Fig. 5. 15 Strain measurement results versus pressure of model RS-C-4.

5.4 Hydrostatic pressure test on stringer-stiffened cylinder

5.4.1 Test procedures

Hydrostatic pressure testing of three models was performed to assess the residual strength behaviour of the stringer-stiffened cylinders in damaged and intact conditions. The procedures of hydrostatic test on stringer-stiffened cylinders are almost similar to that of ring-stiffened cylinders. The settings of the hydrostatic pressure experiment are shown in Fig. 5.16 and Fig. 5.17. The strain data at 10 positions inside the model were also recorded by a logger signal. The axial shortening at the centre point of the end plate was determined using a Vicon motion detector camera. All the digitally measured data were acquired by the PXI series data acquisition system manufactured by National Instruments, Texas, USA. Additionally, a camera was installed to record the model deformation.

5.4.2 Strain gauge arrangements

Two-direction strain gauges were bonded in eight and ten positions for the intact and two damaged models, respectively. With respect to the intact model SS-I, four strain gauges were attached to the inner cylindrical shell at the mid-bay, and two strain gauges were placed on the mid-height of the stringer stiffener. The next two strain gauges were bonded to the ring-stiffeners. With respect to the damaged models, SS-C-1 and SS-C-2, five strain gauges were on the inner shell surface of the cylinder, and three strain gauges were placed on the mid-height of the stringer-stiffener. The two remaining strain gauges were attached to the ring-stiffener webs. The strain gauge arrangements are shown in Fig.5.18.

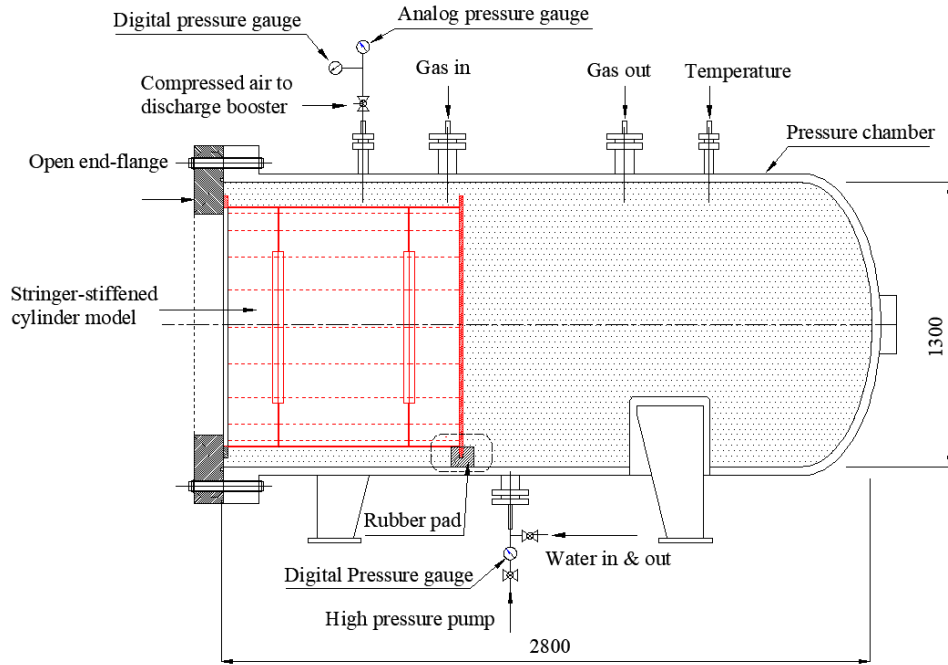


Fig. 5.16 Schematic of hydrostatic pressure test.

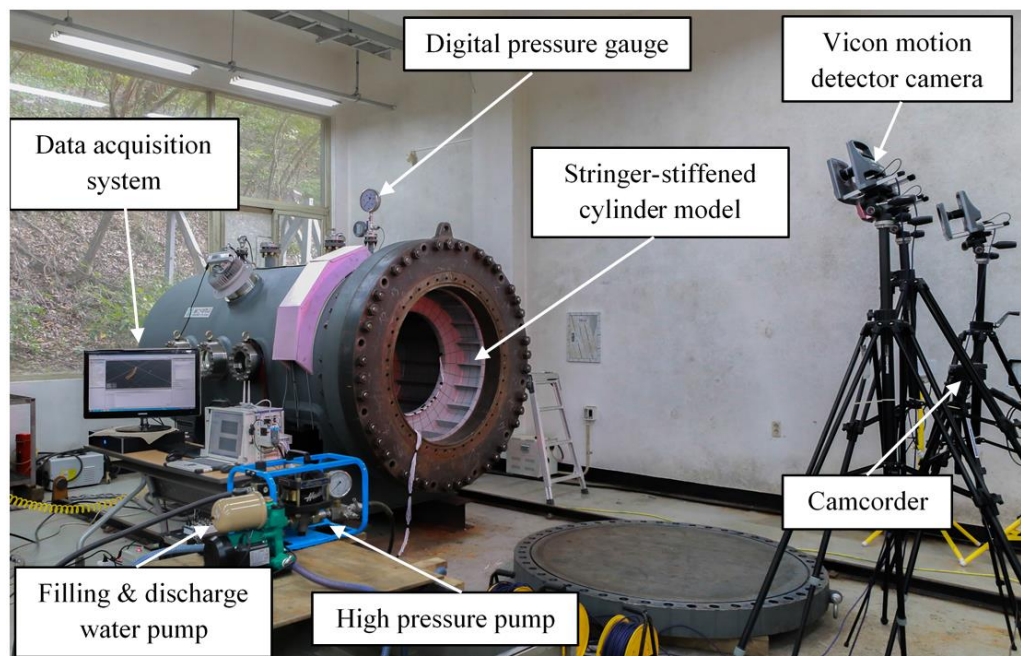
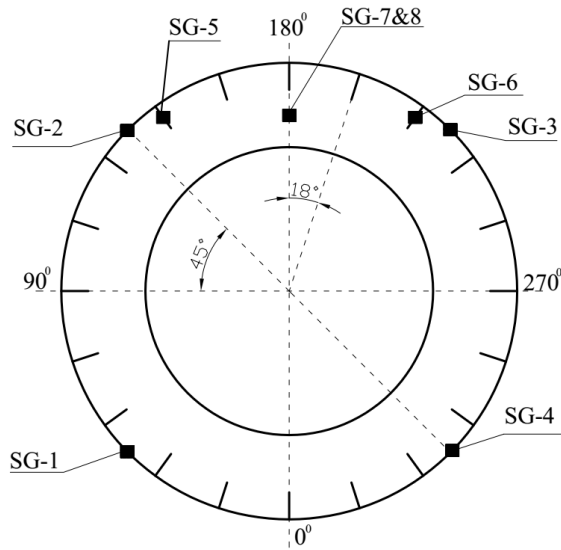
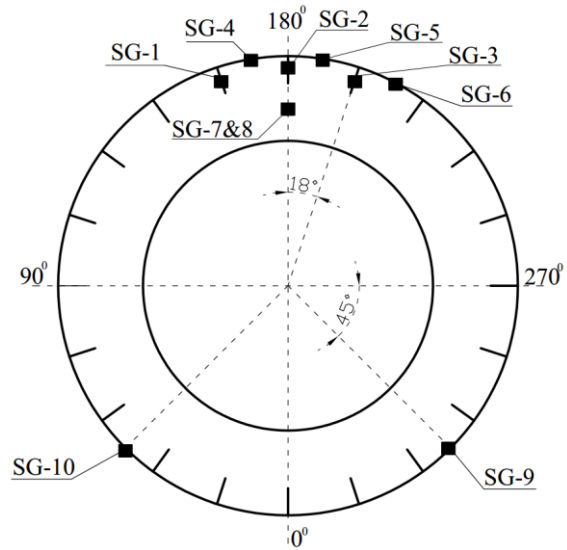


Fig. 5.17 Experimental setup for the hydrostatic pressure test.



- on shell
 - SG-1 (45⁰, 530 mm*)
 - SG-2 (135⁰, 530 mm)
 - SG-3 (225⁰, 530 mm)
 - SG-4 (315⁰, 530 mm)
- on stringer-stiffener
 - SG-5 (144⁰, 530 mm)
 - SG-6 (234⁰, 530 mm)
- on ring-stiffener
 - SG-7 (180⁰, 830 mm, 425 mm)
 - SG-8 (180⁰, 230 mm, 425 mm)

(a)



- on shell
 - SG-4 (170⁰, 500 mm*)
 - SG-5 (190⁰, 500 mm)
 - SG-6 (210⁰, 500 mm)
 - SG-9 (315⁰, 530 mm)
 - SG-10 (45⁰, 530 mm)
- on stringer-stiffener
 - SG-1 (162⁰, 530 mm)
 - SG-2 (180⁰, 530 mm)
 - SG-3 (198⁰, 530 mm)
- on ring-stiffener
 - SG-7 (180⁰, 830 mm, 425 mm)
 - SG-8 (180⁰, 230 mm, 425 mm)

(b)

Note: * indicates the distance from the end plate

Fig. 5.18 Arrangements of the strain gauges: (a) SS-I; (b) SS-C-1 & SS-C-2.

5.4.3 Test results and discussion

5.4.3.1 Intact models: SS-I

The collapse of the structure occurred suddenly and led to the failure of the stringer-stiffened cylinder models. The collapsing phenomenon during the test was demonstrated by a sudden decrease in the applied pressure and was accompanied by a loud noise. A plot of the applied pressure relative to the time history is shown in Fig. 5.19. It is noted that the low fluctuations shown in the figure are due to the time settlements during the pressure increase. When the pressures

increased to 0.62 MPa, a local buckling of the shell between stringer-stiffeners occurred as the first collapse at #1 (210°) by a slight decrease in pressure. The pressure decrease resulted from an expansion of the fluid volume due to the growth of the model's deformed shape. However, the shell could support higher pressures. The pressure slowly increased to 0.66 MPa, and the second collapse occurred at #2 (335°). It was noted that after the event occurred, the system pressure began to increase due to the continuing operation of the pump and regained the previous pressure level due to the recovery of the cylindrical shell. Several instances of local buckling occurred at approximately 0.7 MPa in panel #6 (45°), #7 (100°), #8 (120°), #9 (135°), #10 (155°), and #11(175°), as shown in Fig. 5.19. Subsequently, a significant decrease in pressure was observed at #12 (185°) when the pressure reached 0.72 MPa. Thereafter, the pressure further increased owing to the “hardening up” of the shell, followed by local buckling at panels #13 (30°), #14 (5°), #15 (230°), #16 (245°), #17 (265°), #18 (280°), and #19 (300°). Furthermore, it should be noted that local tripping of the stringer-stiffeners was evident near the ring-stiffeners. Subsequently, the final failure occurred in panel #20 (320°) at a maximum collapse pressure of 0.86 MPa. After the maximum collapse pressure, the pressure was reapplied to generate additional damage until the propagation was complete for all local buckling panels in the longitudinal direction between the ring-stiffeners.

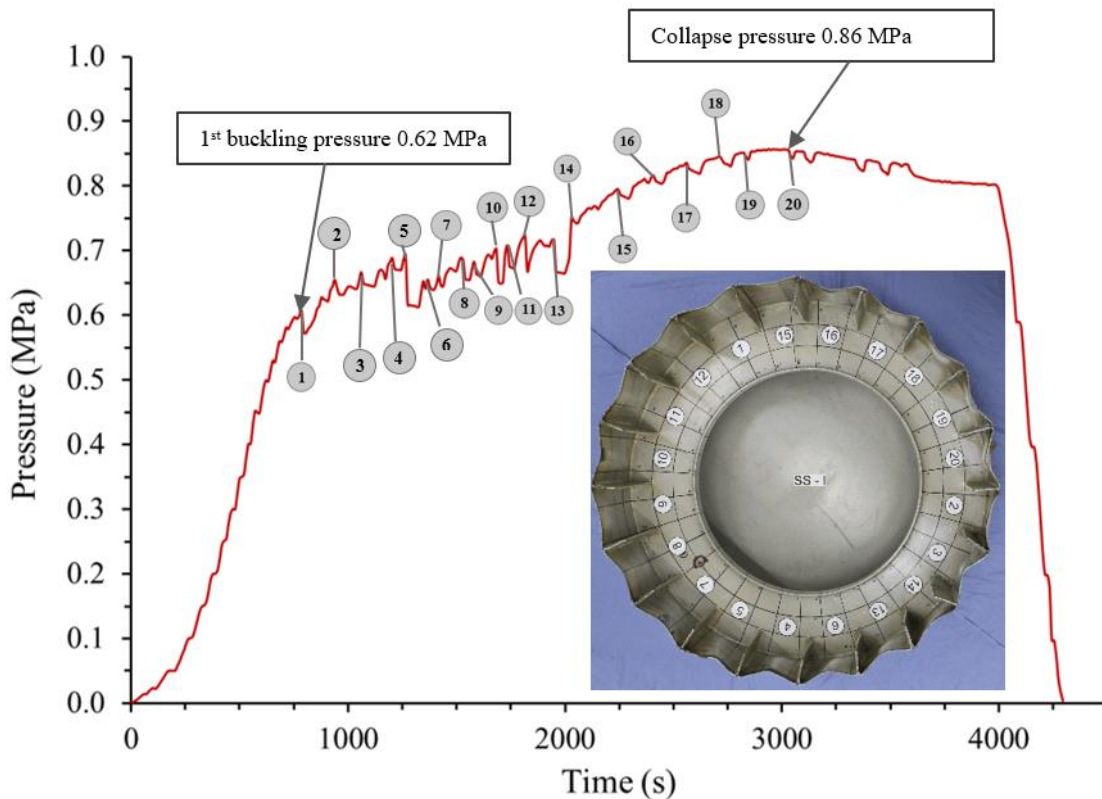


Fig. 5.19 Record of the applied history pressure for model SS-I.

The final collapsed shapes of test models were indicated in Fig. 5.20. Evidently, the local buckling of the cylindrical shell was observed at the stringer-stiffener panels. Furthermore, the extent of local buckling was limited by the stiff and strong ring-stiffeners. It should be noted that local tripping of the stringer-stiffeners occurred near the ring-stiffeners as shown in Fig. 5.21. The stringers acted as beams that resisted the collision loading. Evidently, the ring-stiffeners prevented the damage from spreading to adjacent bays and avoided general buckling of the shell. Additionally, the final collapsed cross-section shape of model SS-I is shown in Fig. 5.22. In the figure, the magnitude of the radial deformed shapes at mid-bay was compared to that of the measured initial deflection and perfect circle. The sequences of collapse are also shown in the figure. The magnitude of initial deflection was exaggerated by 10 times. It is noted that the welding line is located at 0° .

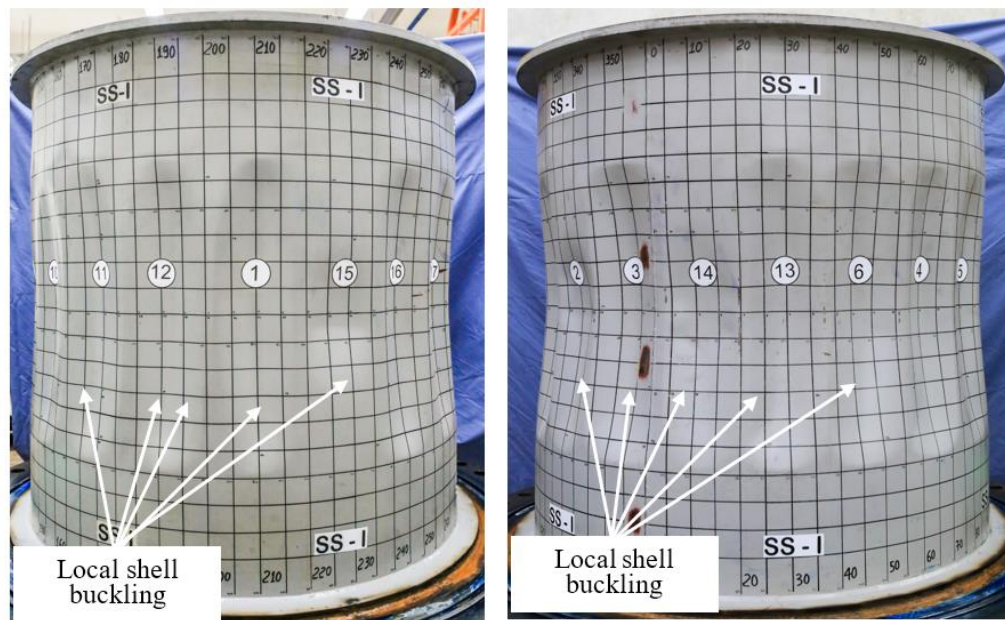


Fig. 5.20 Outside collapse shape of model SS-I.

The axial shortening of the end plate relative to the pressure was recorded by using the Vicon motion detector camera and is shown in Fig. 5.23. When the pressure increased from 0 to approximately 0.62 MPa, the response curve was almost linear. However, after reaching 0.62 MPa, the response curve exhibited some nonlinearity as a certain amount of buckling occurred due to a sudden decrease in pressure. The axial shortening of the end plate was gradually reduced due to structural springback after the releasing pressure as shown in Fig. 5.23. The results of strain measurement are shown in Fig. 5.24. It is noted that the strain of the cylindrical shell exceeds that of the ring-and stringer-stiffener. Specifically, the circumferential strain at positions 1, 2, 3, and 4 (which were bonded at the cylindrical shell) exhibited high tension strain owing to the sudden buckling of the shell.

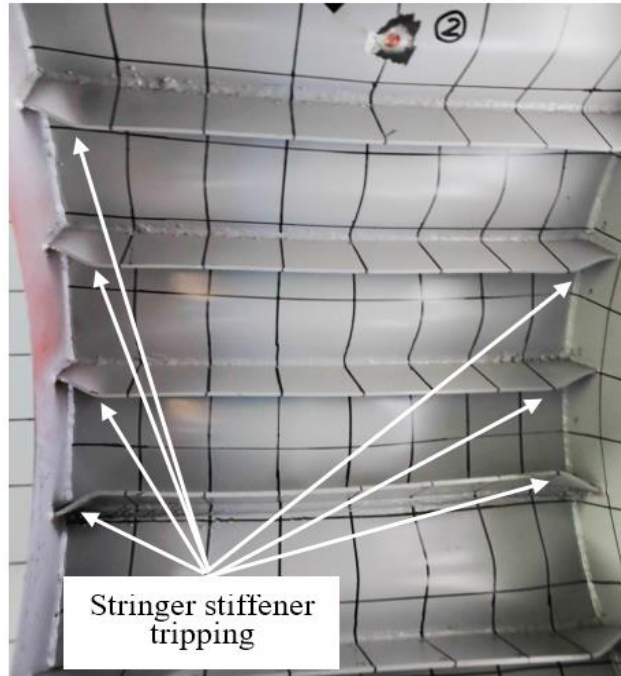


Fig. 5.21 Inside collapse shape of model SS-I.

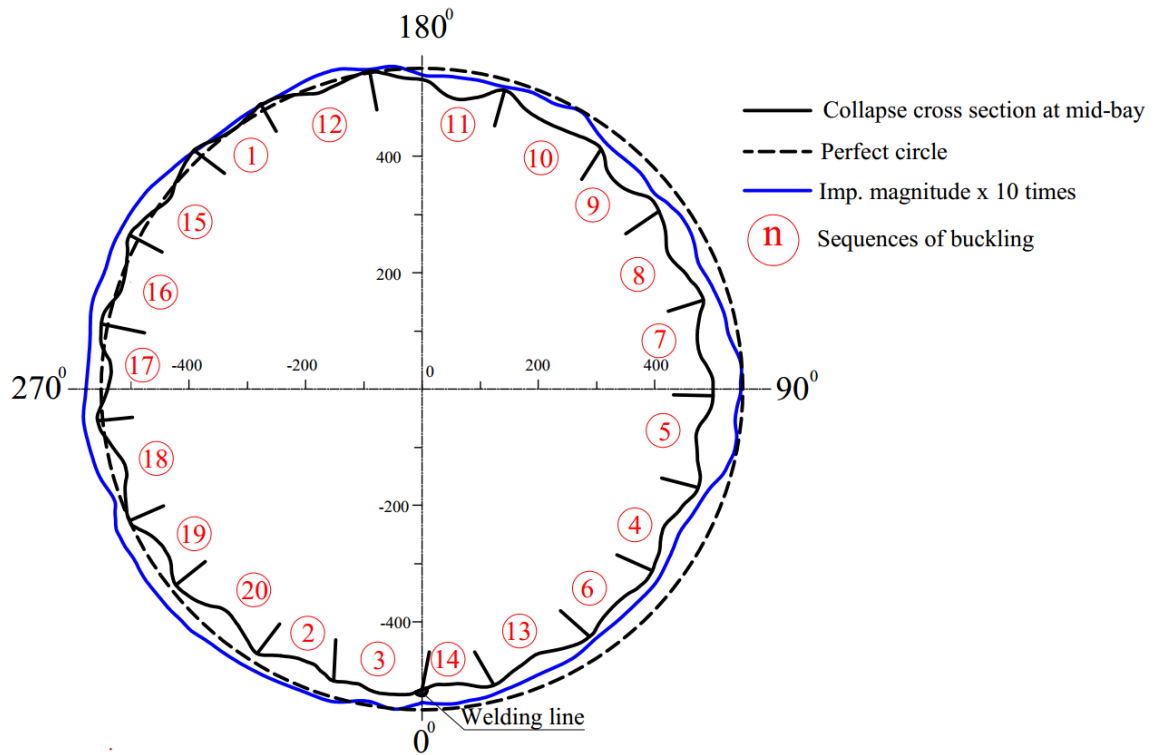


Fig. 5.22 Deformed cross-section shape of model SS-I.

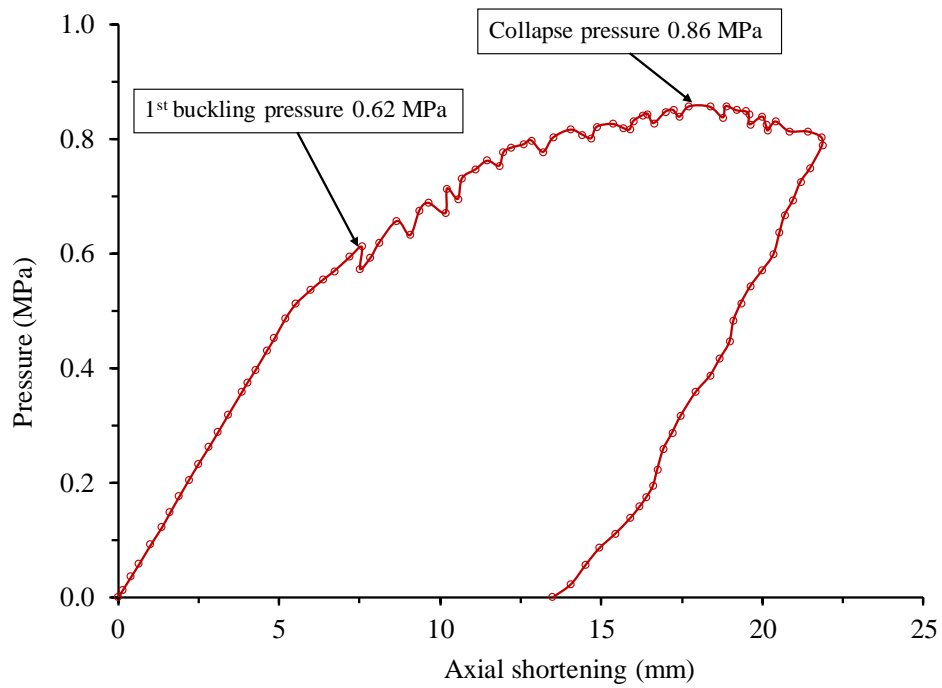


Fig. 5.23 Axial shortening relative to the pressure of intact model SS-I.

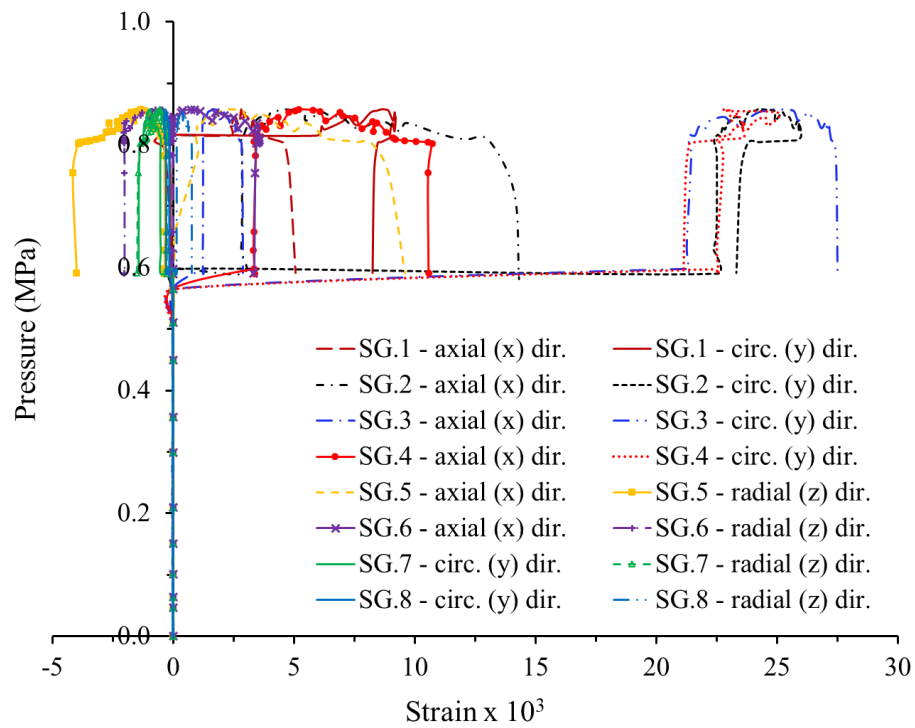


Fig. 5.24 Strain measurement results relative to the pressure of model SS-I.

5.4.3.2 Damaged models: SS-C-1; SS-C-2

After the collision tests, the damaged models were tested under hydrostatic pressure loadings. The relationship between the axial shortening and applied pressure in models SS-C-1 and SS-C-2 is shown in Fig. 5.25. Local buckling was observed when the pressure increased to 0.57 MPa and 0.52 MPa for models SS-C-1 and SS-C-2, respectively. This is denoted as the first collapse pressure of each model. Similar processes occurred for the intact model SS-I in which an initial failure was followed by the recovery of the shell as “hardened-up” to reach a higher pressure level prior to the final collapse of the shell. The maximum collapse pressures of model SS-C-1 and SS-C-2 were 0.83 MPa and 0.85 MPa, respectively. The strength reductions of damaged models when compared to that of the intact model were 3.5% and 1.2% for models SS-C-1 and SS-C-2, respectively. It was concluded that the effects of damages by collisions on the ultimate strength of stringer-stiffened cylinders were extremely low.

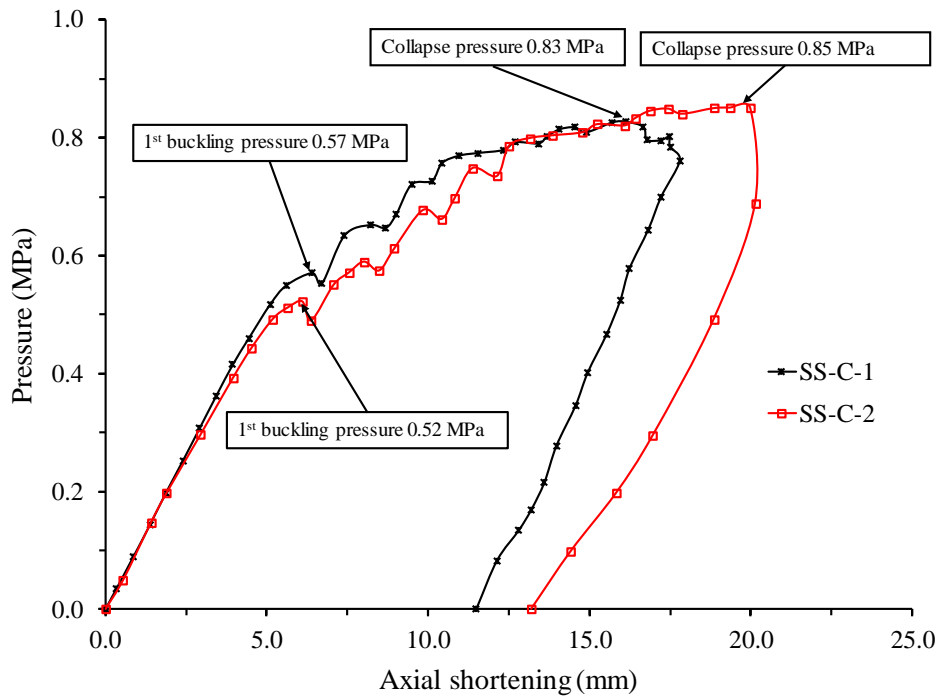


Fig. 5.25 Experimental result of pressure relative to the axial shortening of the models SS-C-1 and SS-C-2.

Figure 5.26 shows the deformed shapes of the damaged model SS-C-1 after the collapse tests. In a manner similar to the intact model SS-I, model SS-C-1 failed owing to the local shell buckling mode. However, the propagation of the deformed shapes of the damaged model started from the initial damaged region and was almost symmetrical to the longitudinal axis. The cylindrical shell collapsed owing to local buckling between the stringer-and ring-stiffener spacing.

Furthermore, the tripping of the stringers also occurred near the ring-stiffeners as shown in Fig. 5.27a. Evidently, the T-ring-stiffeners of the model were sufficiently strong to avoid general buckling of the cylindrical shell. The collapsed cross section at the mid-bay and the denoted sequences of the collapsed shapes are shown in Fig. 5.27b.

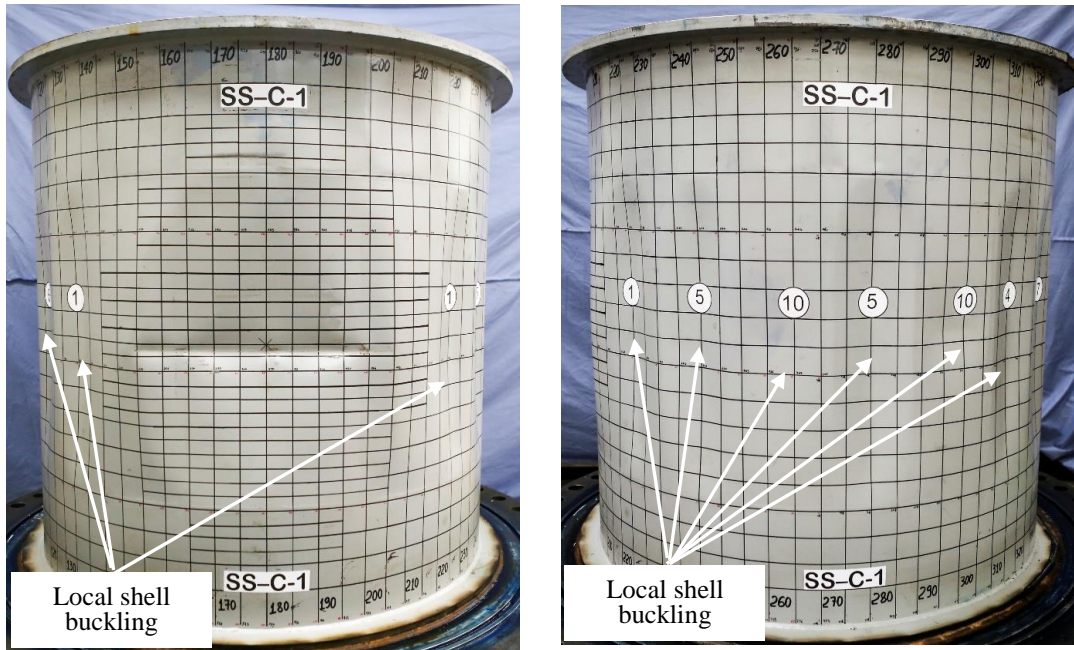
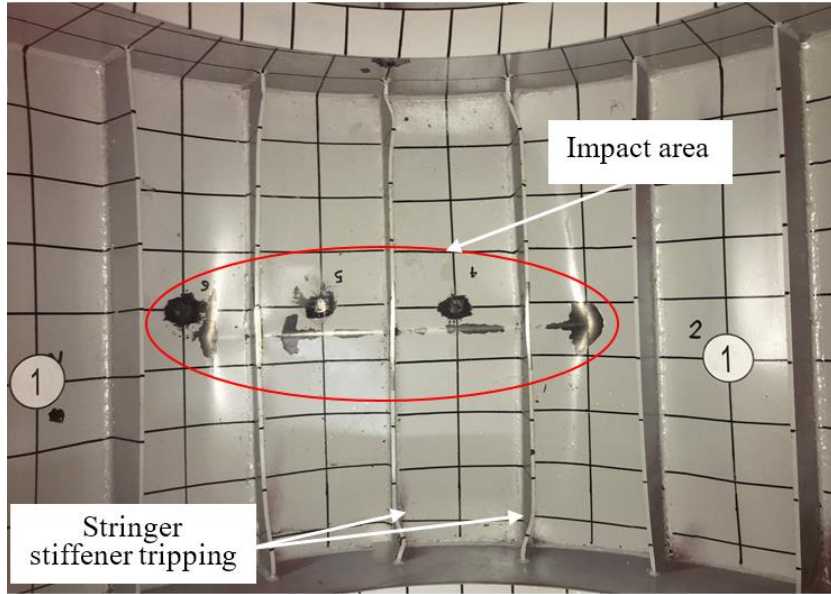
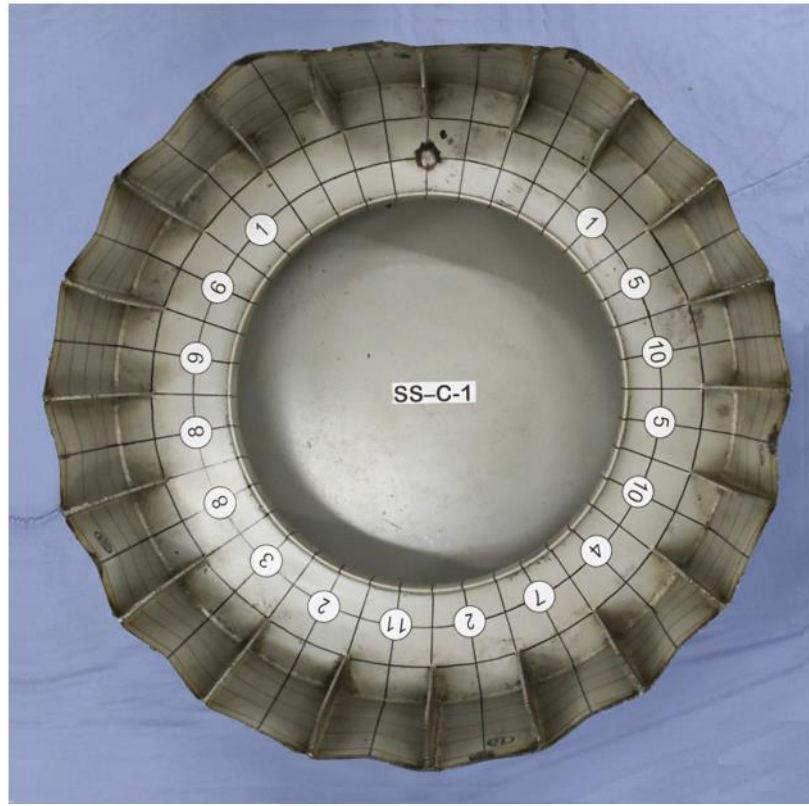


Fig. 5.26 Outside collapse shapes of model SS-C-1.

The results of strain measurement data are shown in Fig. 5.28. The strain gauges at positions 5, 6, 9, and 10, which are attached on cylindrical shells, exhibited high tensile strain owing to the sudden collapse of the shell while the strain gauges at positions 1 to 4 and 7 to 8 exhibited low levels of tensile and compressive strain. The deformation of model SS-C-2 is shown in Fig. 5.29. It is almost identical to the deformed shape of model SS-C-1, and the failure mode also corresponded to local shell buckling. Furthermore, the final collapsed cross-section shape of the model is shown in Fig. 5.30. The magnitude of the radial deformed shapes at mid-bay was compared to that of the measured initial deflection and perfect circle. The sequences of collapse shapes are also shown in the figure. The measured strains are plotted with respect to the pressure of model SS-C-2 in Fig. 5.31. A similar trend is observed with damaged model SS-C-1. However, high levels of the strain values are shown due to the more severe damage generation.



(a)



(b)

Fig. 5.27 Collapse shape of model SS-C-1: (a) inside; (b) cross section.

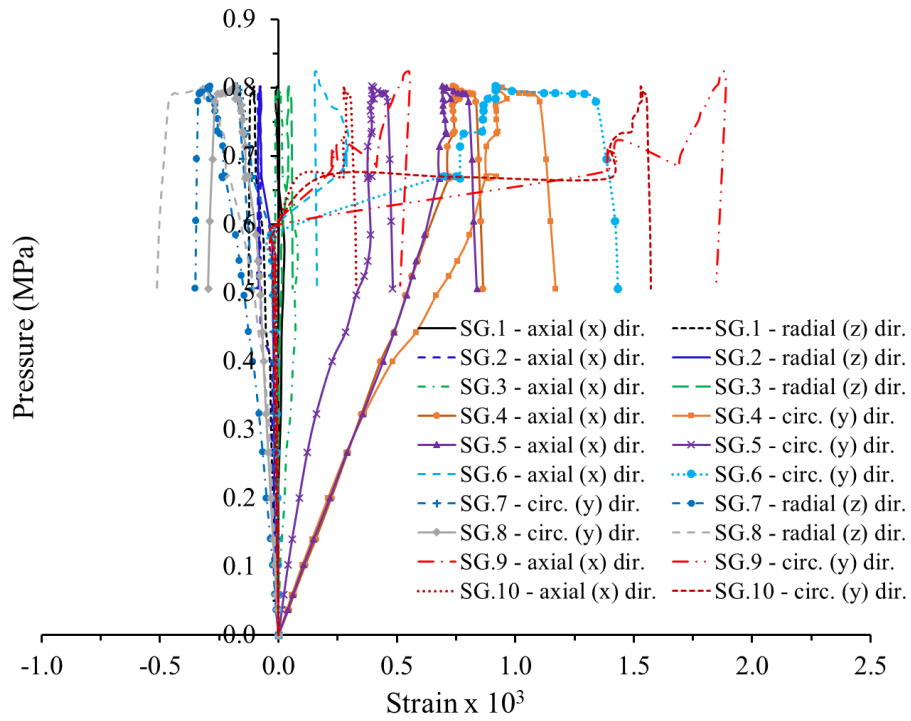


Fig. 5.28 Strain measurement results relative to the pressure of model SS-C-1.

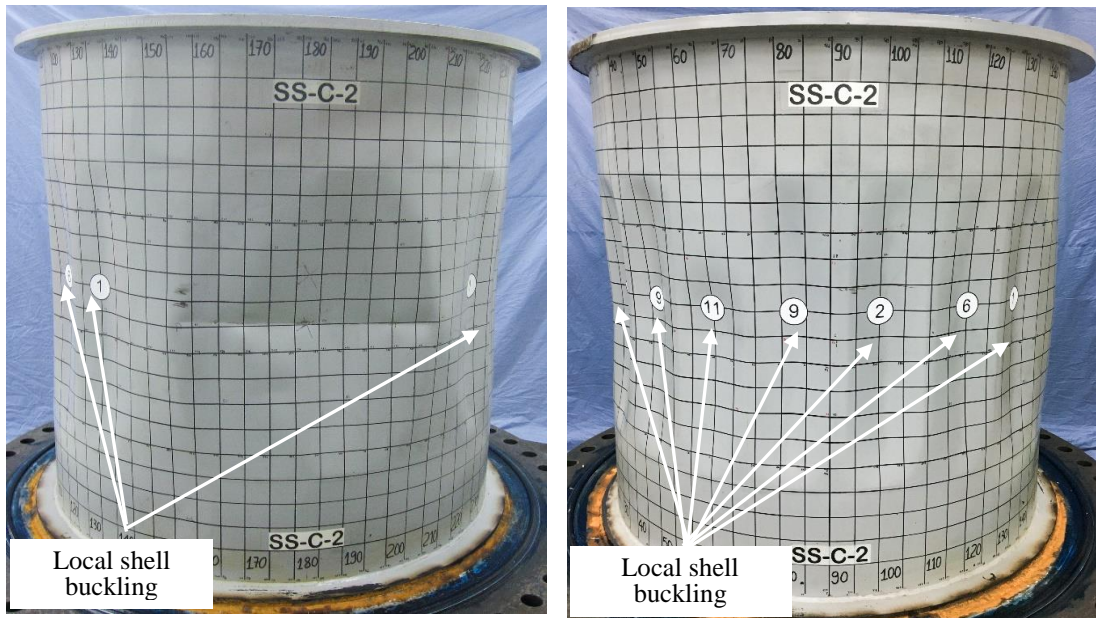


Fig. 5.29 Outside collapse shapes of model SS-C-2.

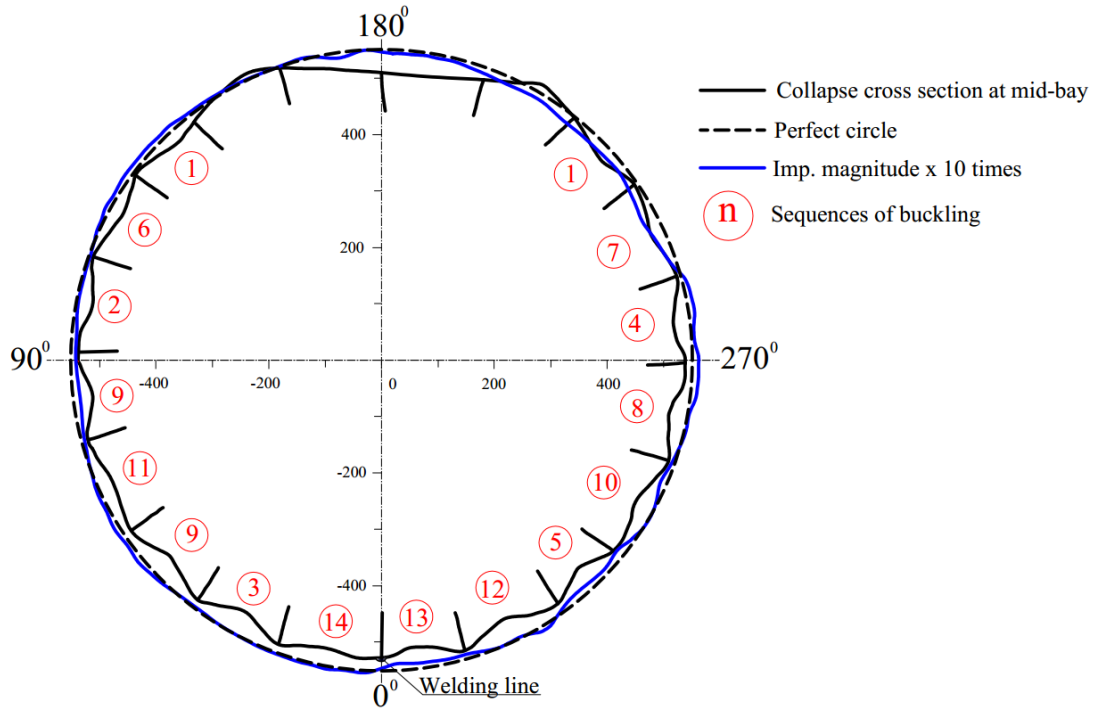


Fig. 5.30 Collapse cross-section shape of model SS-C-2.

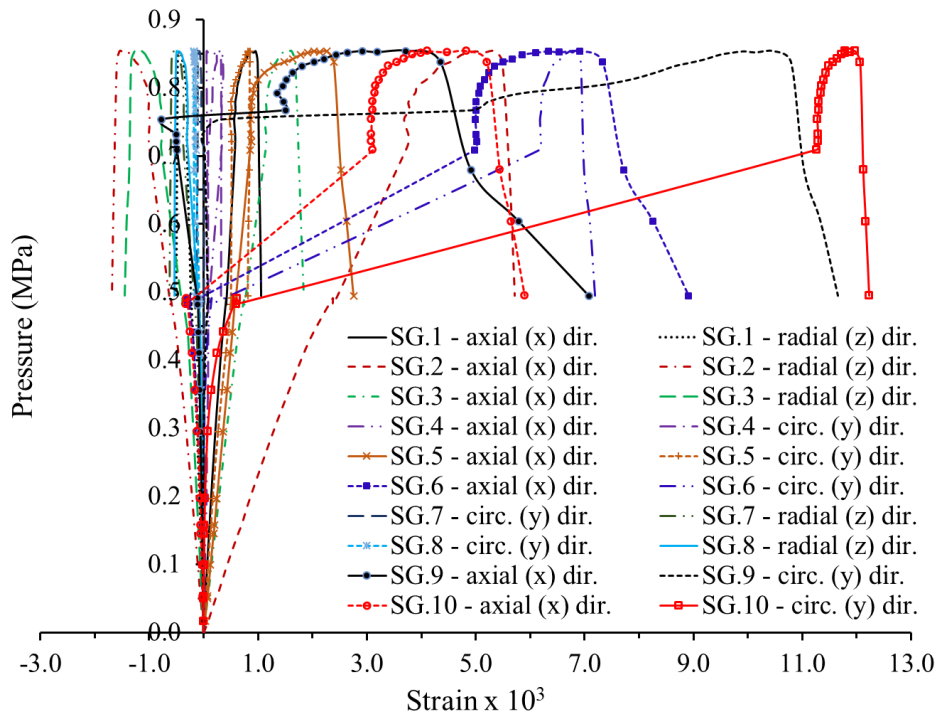


Fig. 5.31 Strain measurement results relative to the pressure of model SS-C-2.

5.5 Numerical analysis

In parallel with the experimental analysis, finite element analysis was utilized to verify the result via the Abaqus FEA software package. The collision process was simulated using a dynamic/explicit method while the collapse under hydrostatic pressure was performed using a modified static Riks method. The same numerical method was applied for both ring- and stringer-stiffened cylinder.

5.5.1 Finite element modelling

Generally, the cylinder wall (shell), stringer-stiffeners, and ring-stiffeners were modelled using four-node curved shell elements (S4R) accompanied with hourglass regulation and reduced integration in Abaqus. The Simpson rule was applied based on five points throughout the thickness integration. Specifically, the knife-edge striker is assumed as a rigid body, and thus the R3D4 element was employed. During the collision simulation, the indenter hit the cylinder surface locally and was defined as the contact constraint by a general contact algorithm involving a penalty method in the software.

The mesh size significantly affects the final result and simulation time. In the study, the optimum mesh size of the whole model is determined by following the visualization of the deformed shape and accurate responsibility of force-displacement. The finer mesh size was observed as 5×5 mm for the contact area and 10×10 mm for other regions. However, the finer mesh size is lower than the thickness of structure, and this can lead to imprecise calculations at the contact area at overlapping structures after rendering thickness. Additionally, a few non-uniform mesh sizes of 10 mm were observed at the ends of the stringer and ring structures. Therefore, to avoid the aforementioned problems, the surfaces of the shell elements were offset outwards and the thickness of the welded joints was maintained.

5.5.2 Residual stresses and initial imperfection

The residual stresses in the fabricated ring-stiffened cylinders may have been caused by cold bending of the shell and welding of the stiffeners to the cylindrical shell. These residual stresses may have affected the strength of the structures. In the cold bending procedures, the steel plates were bent over the desired radius and subsequently the curved structures recovered in the opposite side owing to the elastic springback phenomenon. Thus, permanent deformation was created based

on local plastic behaviour that corresponds to residual stress. The residual stress is distributed in a typical zigzag pattern through the thickness of the shell in both the circumferential and longitudinal directions [178]. When compared with cold bending, the effect of cold rolling on the ultimate strength decreases if the webs of the ring-stiffener are flat bars that are cut from flat plates [69]. Additionally, the cold bending residual stress of the T-ring significantly decreased with respect to the ultimate strength [69, 179].

Numerically, the residual stresses from cold bending were relatively calculated in the cold rolling process as a 2-dimensional stress field. First, the edge of the flat plate was restrained at all degrees of freedom. The other edges of the cylinder were tied to the reference node at the mid-edge, and a rotation was applied to simulate the overbending. Second, the rotations were stopped and subsequently the plate springs back elastically. The process was conducted until the expected shape of the shell was obtained. The procedures were performed in a general quasi-static analysis. In the analysis, the integration points through the shell thickness were increased from 5 to 21. It is noted that the T-ring stiffeners of the model were fabricated in which only the flanges were rolled, and were thus subject to similar residual stress. The flat plate after cold-bending is shown in Fig. 5.32. The cold bending residual stress distribution of model SS-I is given in Fig. 5.33. Here t is the thickness of the cylindrical shell, and z is coordinate with respect to the shell top-plane.

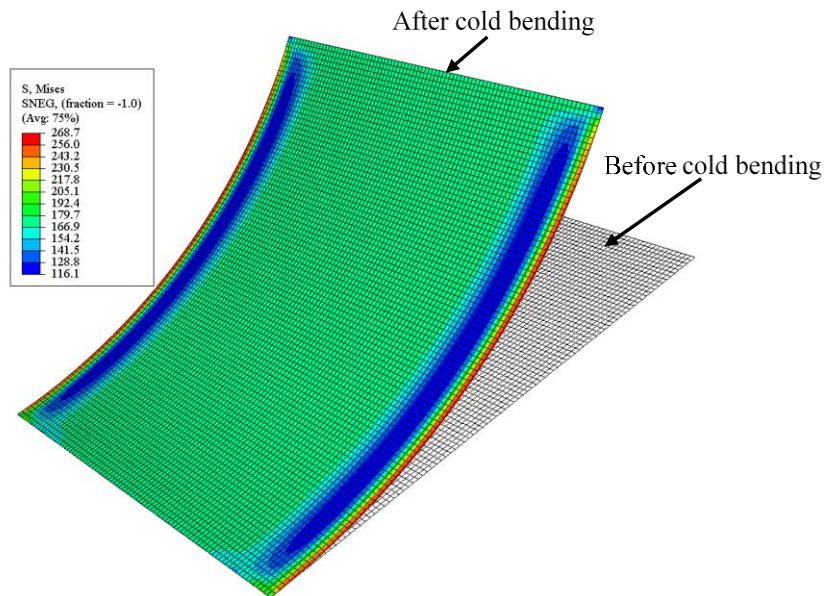


Fig. 5.32 Contour plot of residual stress of typical plate after cold bending.

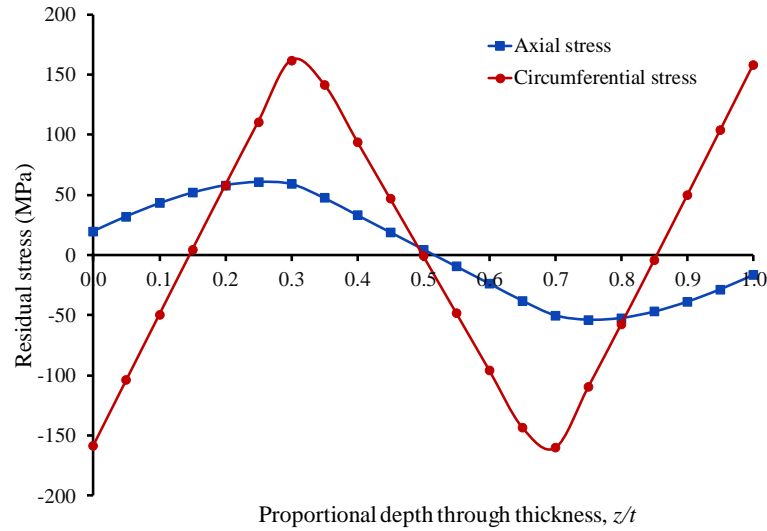


Fig. 5.33 Cold bending residual stress distribution for model SS-I.

Furthermore, during the welding procedures, a high temperature was generated to melt material prior to connecting structures together. The temperature changes also created residual stresses inside structures as well as the surrounding welding area. The volume shrinkage of structures about the welded lines during the cooling procedure after welding led to the distortion of the shell. Specifically, an imbalanced compression distribution between periodic stiffeners appeared. The structures are termed as the "hungry horse". Evidently, the summary of residual stresses from cold bending and welding procedures significantly depended on the strength of final structures [69]. In this study, the residual stresses caused by the welding process were considered, as demonstrated in Fig. 5.34.

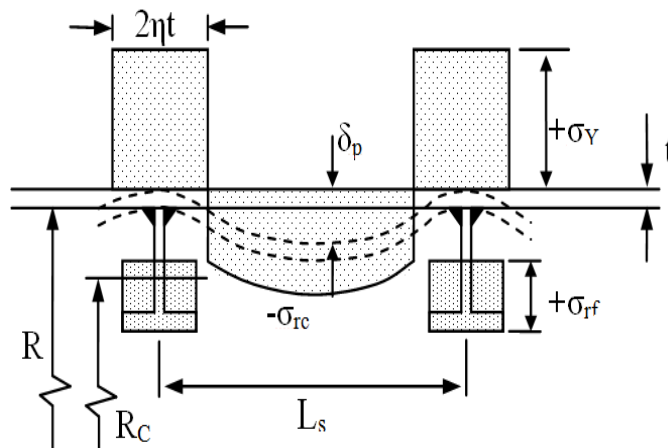


Fig. 5.34 Residual stress distribution caused by stiffener-shell welding [159].

The equations, i.e., eqns (1) ~ (4), for determining the residual stresses due to welding were proposed by Faulkner [159]. The breadth of the tensile stress zone, $2\eta t$, is a characteristic of the

welding procedure and structural configuration, and η ranges from 1.5 to 4.5. Circumferential compressive residual stresses in the shell, σ_{rc} , are the sum of the stresses from the equilibrium balance with tensile circumferential yielding, σ_{rc1} , and stresses associated with the distortion of the shell due to across-the-weld (or transverse) shrinkage weld stresses, σ_{rc2} . The shell distortion is balanced by a tensile stress in the stiffeners, σ_{rf} . In the numerical analyses of this study, η was assumed to be 4 according to Smith and Kirkwood [158] and the inter-frame shell distortion δ_p was assumed to be 10 % of the shell thickness [178]. The welding stresses were derived according to Faulkner's closed-form solutions [159] and those were applied directly to FE models as initial stresses of elements, which were in equilibrium. However, it was not allowed any change in the shape of the model due to the residual stresses due to welding.

$$\sigma_{rc} = \sigma_{rc1} + \sigma_{rc2} \quad (5.1)$$

$$\sigma_{rf} = \frac{(2\delta_p E / \pi R)}{\left[1 + A_f \left(\frac{R}{R_c}\right)^2 / (L_s t)\right]} \quad (5.2)$$

$$\sigma_{rc1} = \frac{2\eta\sigma_Y t}{L_s - 2\eta t} \quad (5.3)$$

$$\sigma_{rc2} = \sigma_{rf} - \frac{\delta_p E}{R} \quad (5.4)$$

where:

σ_{rc} : maximum or mid-region residual compressive stress

σ_{rc1} : residual tensile yield stress due to along-the-weld (or longitudinal) shrinkage

σ_{rc2} : residual compressive stress due to across-the-weld (or transverse) shrinkage

σ_{rf} : residual tension stress in ring-frame

δ_p : inter-frame shell distortion

A_f : cross-sectional area of stiffener

t_s : shell thickness

L_s : stiffener spacing

η : weld tension block width parameter (herein $\eta = 4$)

R_c : radius of frame centre

R : inner radius of cylinder

E : Young's modulus

σ_Y : yield strength

The analysis of the residual stress after welding is shown in Fig. 5.35. Welding residual stresses distribution obtained from analyses for model RS-II are illustrated in Fig.5.36. The welding residual stress distribution of model SS-I is shown in Fig. 5.37. In the study, the geometric imperfections were manually measured as mentioned in the previous section. The geometric imperfections were directly modelled by applying the method of curve and surface fitting in the Abaqus software. Furthermore, the residual stresses from welding and the cold-bending process were precisely induced in the initial stresses of elements in the FE models.

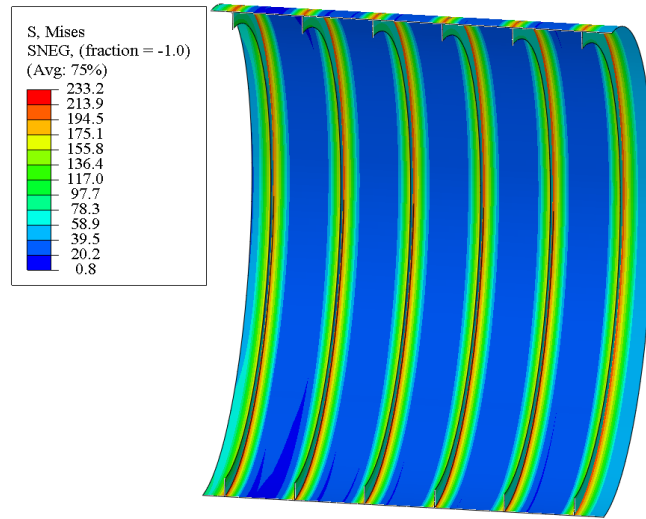


Fig. 5.35 Welding residual stress distribution for model RS-II.

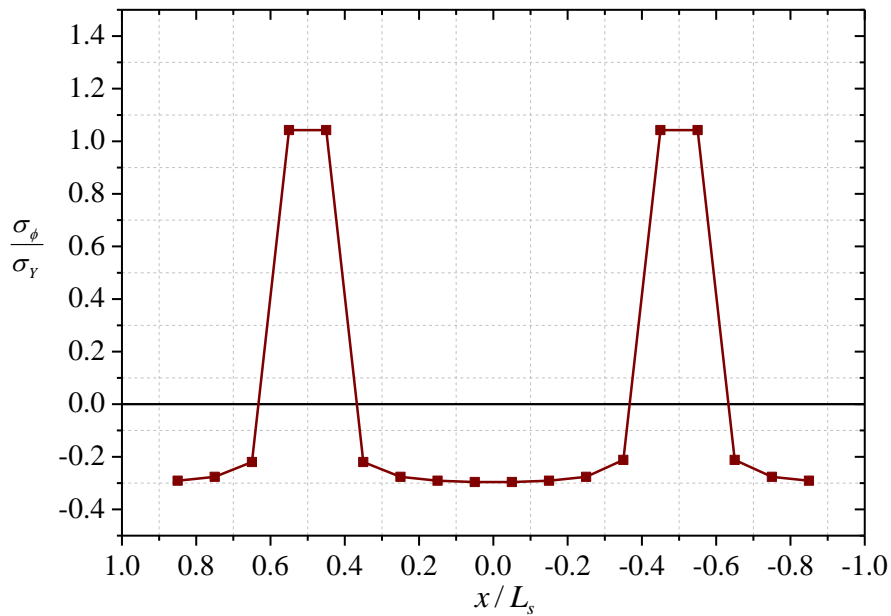


Fig. 5.36 Welding residual stresses distribution obtained from analyses for model RS-II.

5.5.3 Residual strength analysis

As in the experiments, the numerical analysis was performed in two steps: inducing damage and residual strength analysis. When the first step was finished, the damaged model was transferred to residual strength analysis. The first set of step aimed to obtain the updating of the element coordinates in damaged region and the initial stresses distribution of elements. Thus, all residual stresses from collision analysis of models are also included. For the residual strength

analysis, the static Riks solver was applied. It is noted that the material was defined as linear perfectly plastic. The model was fixed at the open end flange, as in the tests indicated in Fig. 5.38. Hydrostatic pressure analysis of three models, including one intact model, were performed to assess the ultimate strength reduction of the stringer-stiffened cylinders in damage and intact conditions.

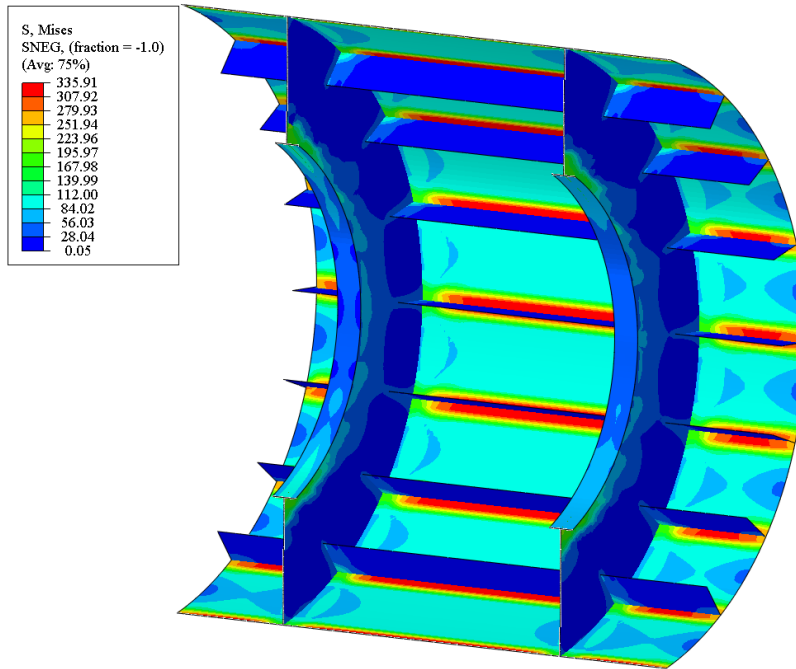


Fig. 5.37 Welding residual stress distribution for model SS-I.

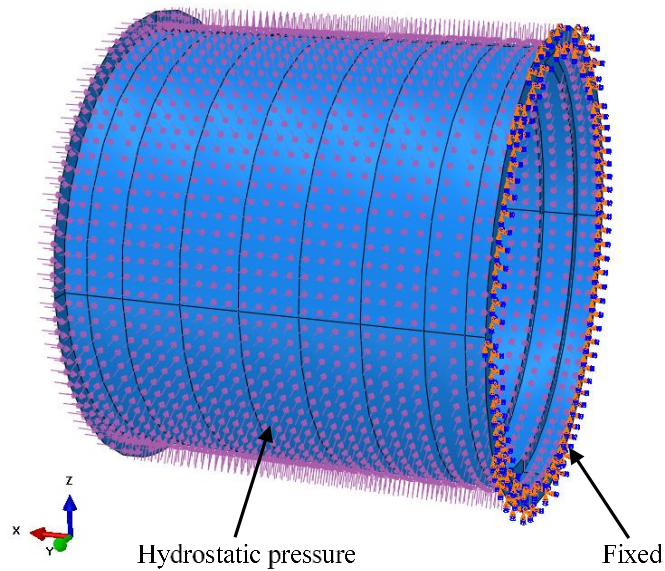


Fig. 5.38 Hydrostatic pressure analysis modelling.

5.5.4 Numerical results and discussions

5.5.4.1 Ring-stiffened cylinder

Fig. 5.39 illustrates the effects of the residual stresses and initial shape imperfections on the ultimate strength of the intact model, model RS-I. When considering the residual stresses only, the collapse pressure was 2.31 MPa; when only the initial shape imperfections were considered, it was 2.19 MPa. However, when considering both, the collapse pressure was reduced to 2.09 MPa. Compared with the experiment result (2.16 MPa), the difference was 3%. Furthermore, the predicted collapse shape of the intact model was compared with the test results, as indicated in Fig. 5.40. The intact model was failed with an interactive buckling mode, which was a combination of inter-frame buckling and overall buckling.

The numerical predictions of the residual strengths of the damaged models, model RS-C-1 and RS-C-2, were 1.36 MPa and 1.59 MPa, respectively. The failure pressure prediction of model RS-C-3 and RS-C-4 was 1.87 MPa and 1.71 MPa. The comparison of strain measurement between test and numerical results are showed in Fig. 5.41. In Figs. 5.42, 5.43, 5.44, and 5.45. the predicted collapse shapes of the two damaged models are compared with those of the experiments. In these figures, the contours indicate the von Mises stress. A good agreement between the predictions and test results can be seen.

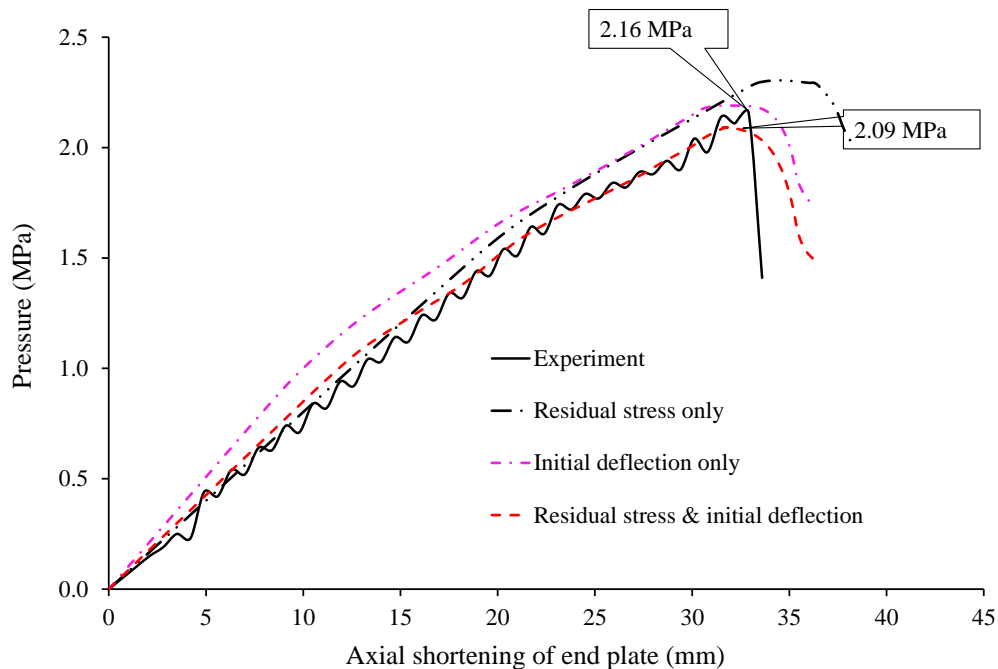


Fig. 5.39 Pressure versus axial shortening curves of model RS-I.

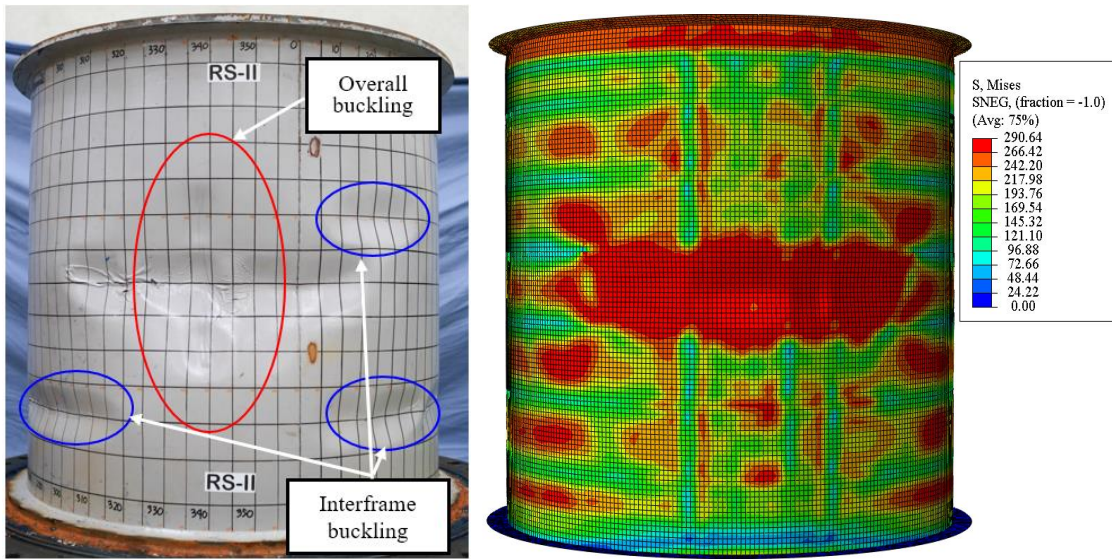


Fig. 5.40 Comparison of numerical predictions with test results for model RS-II.

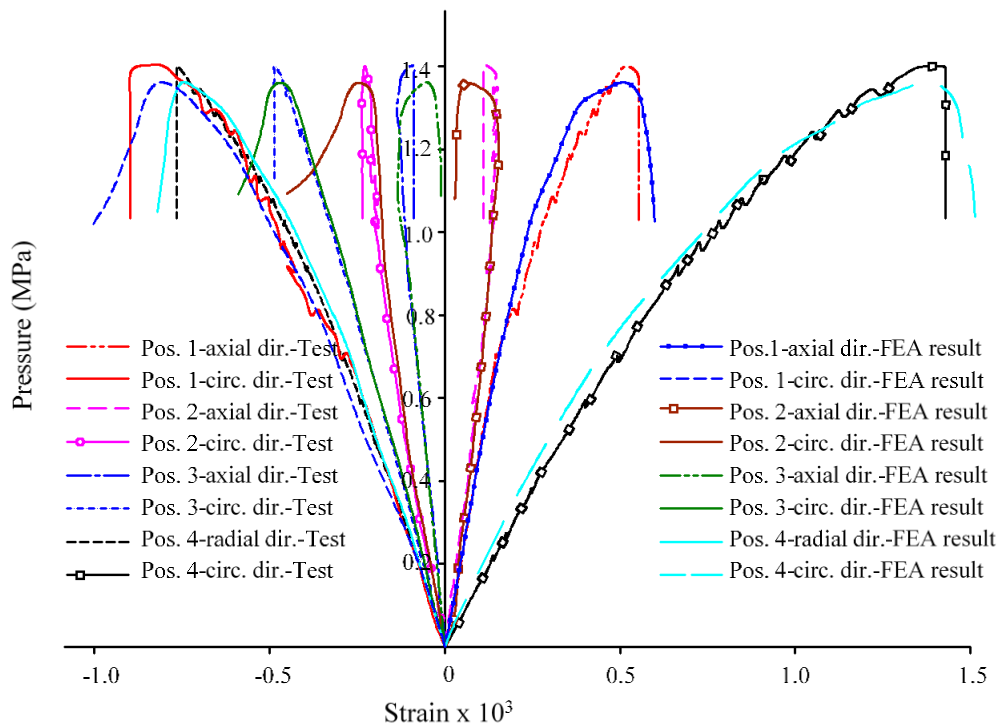


Fig. 5.41 Comparison of strain measurement versus pressure between test and numerical results of model RS-C-1.

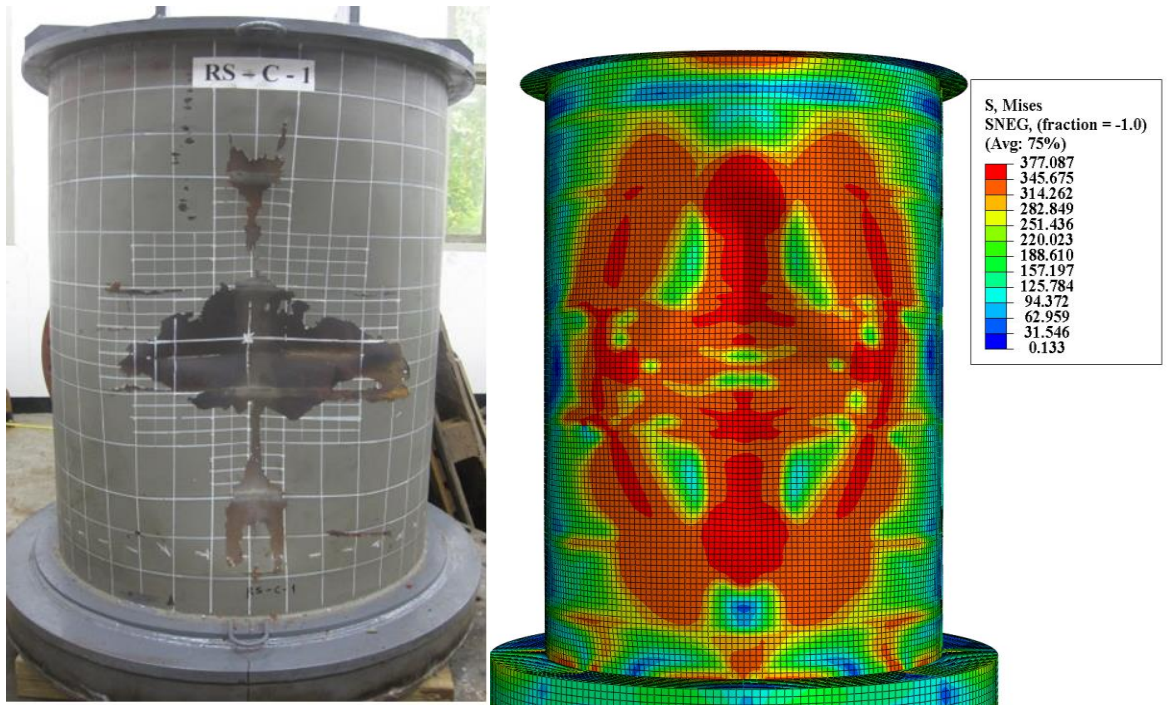


Fig. 5.42 Deformed shape of the test model RS-C-1 compared with numerical results.

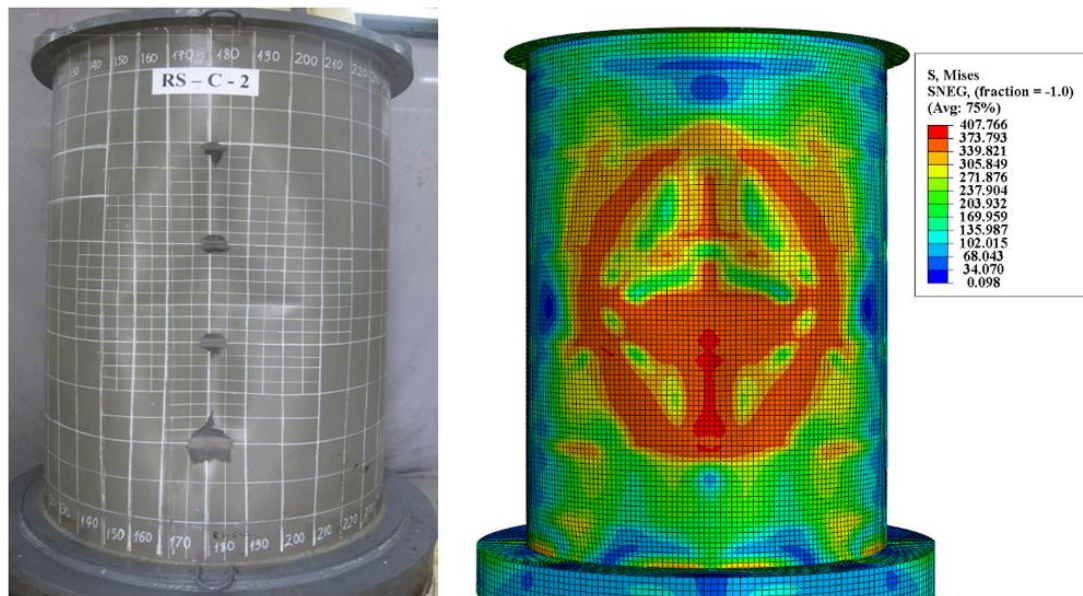
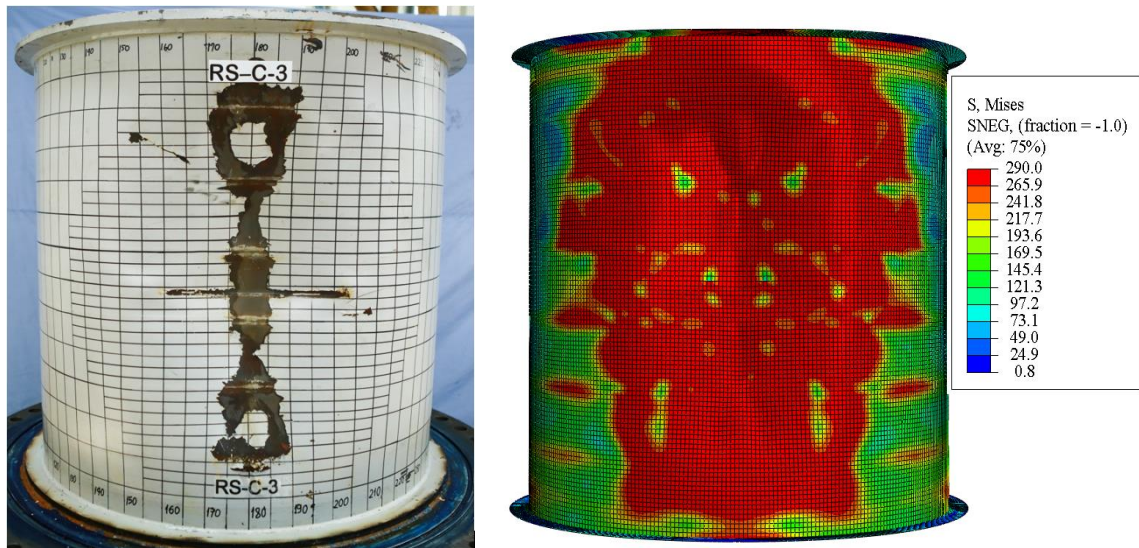
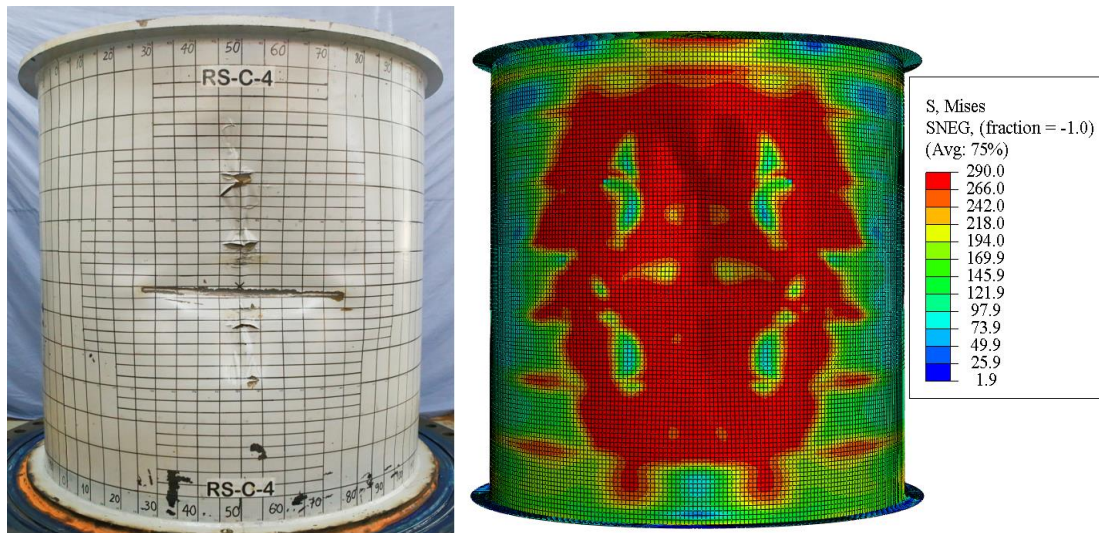


Fig. 5.43 Deformed shape of the test model RS-C-2 compared with numerical results.



(a)



(b)

Fig. 5.44 Predicted collapsed shape of damaged model compared with the test results for models: (a) RS-C-3; (b) RS-C-4.

The comparisons in terms of collapse pressure between the numerical and experimental results are summarised in Table 5.1. The modelling parameter (X_m), which was defined as the ratio of experimental results to nonlinear finite element results, was also included in this table. Furthermore, both numerical and experimental results are compared in Fig. 5.45. The collapse pressure (P_c) values were non-dimensionalised with the yield pressure (P_Y), which was calculated by the proposed equation from PD5500 (BSI, 2009). The mean of the modelling parameter X_m is 1.031. Additionally, the quite small COV is 1.94%, which is non-dimensional of the standard deviation of the uncertainty modelling parameter. Therefore, with the good accuracy of the

numerical analysis methods, it is suggested that the numerical model is able to simulate the progressive collapse behaviour of ring-stiffened cylinder structures and can be used in detailed investigations and parametric studies.

Table 5.1 Comparison of experimental results with numerical results and prediction of some guideline rules.

Model	Collapse pressure (MPa)						
	Test result (1)	Numerical result (2)	PD5500 (3)	GL (4)	Ratio (1)/(2)	Ratio (1)/(3)	Ratio (1)/(4)
RS-I	2.16 (-)	2.09 (-)	2.23	2.36	1.033	0.969	0.915
RS-II	2.41 (-)	2.41	2.77	2.90	1.000	0.870	0.830
RS-C-1	1.40 (-35.2%)	1.36 (-34.9%)	-	-	1.029	-	-
RS-C-2	1.65 (-23.6%)	1.59 (-23.9%)	-	-	1.038	-	-
RS-C-3	1.90 (-21.2%)	1.87 (-22.1%)	-	-	1.029	-	-
RS-C-4	1.80 (-25.3%)	1.71 (-29 %)	-	-	1.038	-	-

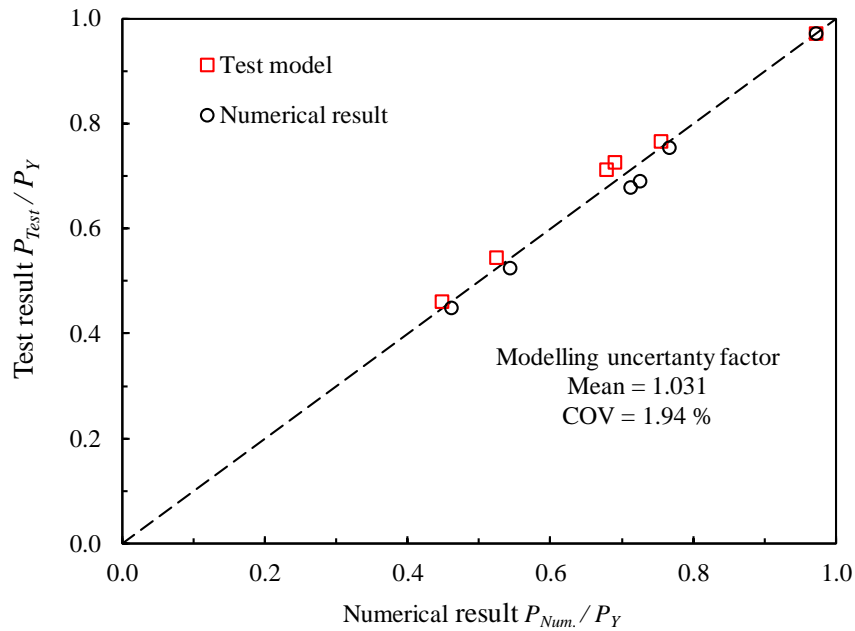


Fig. 5.45 Numerical analysis results compared to test results.

5.5.4.2 Stringer-stiffened cylinder

The effects of residual stresses from cold bending and welding and geometric imperfections on the ultimate strength of model SS-I are shown in Fig. 5.46. The maximum of the collapse

pressure was 0.97 MPa when only the effects of cold bending were considered, and this exceeds the experimental result by 13.1%. When only welding residual stresses were considered, the maximum of the collapse pressure was 0.95 MPa, and this exceeds the experimental result by 10.2%. The collapse pressure was 0.90 MPa when the initial shape imperfections were considered when compared to the test result, which was 4.4% higher. However, in the combined effect of the three types, the collapse pressure was 0.82, and this is 5% lower than the experimental result.

A comparison of the predicted collapsed shape of model SS-I with test results is shown in Figs. 5.47 and 5.48. A reasonable agreement between numerical and experimental results was achieved. Furthermore, the collapse pressure predictions of the damaged SS-C-1 and SS-C-2 models were 0.78 MPa and 0.81 MPa, respectively. The variations in the predicted collapse pressure when compared to those of experimental results were approximately 6% and 4.7 % for models SS-C-1 and SS-C-2, respectively. The reductions in the ultimate strength of damaged models when compared to those of the intact model SS-I were 4.9% and 1.2%, respectively. Additionally, the responses of axial shortening relative to the pressure curves between predictions and test results are plotted in Fig. 5.48. As shown in the figure, the numerical results and test results exhibit reasonable accuracy. The predictions of the collapsed shape of the damaged model were compared to those of the test results as shown in Figs. 5.49 and 5.50. Generally, good agreement was also obtained between the prediction and experimental results. A comparison of the experimental results with the numerical results and predictions of the design rules is summarized in Table 5.2.

Based on the experimental and numerical results, it is clear that the intact and damaged models failed in the local shell buckling mode. This contrasts with previous studies on ring-stiffened cylinders that were presented in section 5.4.4.1 that indicated an interactive mode for the intact model and an overall buckling mode for the damaged model.

Table 5.2 Comparison of the numerical results with the experimental results and prediction of some guideline rules.

Model	Collapse pressure (MPa)						
	Test result (1)	Numerical result (2)	DNV-GL (3)	API (4)	Ratio (1)/(2)	Ratio (1)/(3)	Ratio (1)/(4)
SS-I	0.86 (-)	0.82 (-)	1.04	0.91	1.048	0.827	0.945
SS-C-1	0.83 (-3.5%)	0.78 (-4.9%)	-	-	1.064	-	-
SS-C-2	0.85 (-1.2%)	0.81 (-1.2%)	-	-	1.049	-	-

In contrast to ring-stiffened cylinders, the effects of damages on the ultimate strength of stringer-stiffened cylinders under hydrostatic pressure were extremely low. The strength

reductions were 3.5% and 1.2% when compared to those of the intact model for models SS-C-1 and SS-C-2, respectively. During the collapse tests, after an initial failure occurred with respect to both the intact and damaged models, the shell recovered as “hardened-up” to reach a higher pressure level prior to the final collapse of the shell. However, the propagation of the deformed shapes of the two damaged models started from the initial damaged region and was almost symmetrical to the longitudinal axis.

The test results indicated that the cylindrical shells collapsed owing to local buckling between the ring-and stringer-stiffener spacing. Furthermore, the tripping of the stringers also occurred near the joint between the ring-stiffeners and stringer-stiffeners. It is concluded that the ring-stiffeners were sufficiently strong to guarantee the overall buckling of the cylindrical shell. However, the stringer-stiffeners were not sufficiently strong to resist tripping.

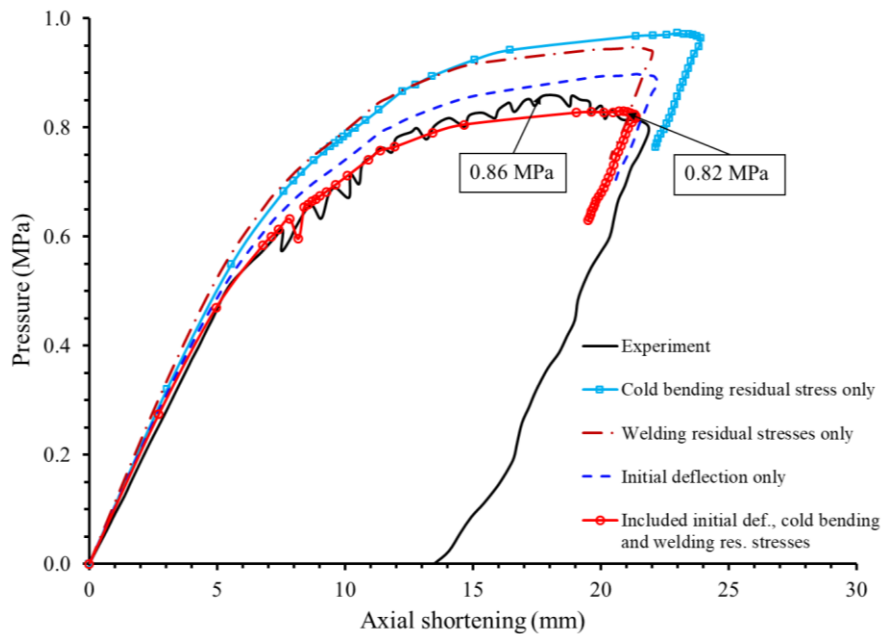


Fig. 5.46 Pressure relative to the axial shortening of intact model SS-I.

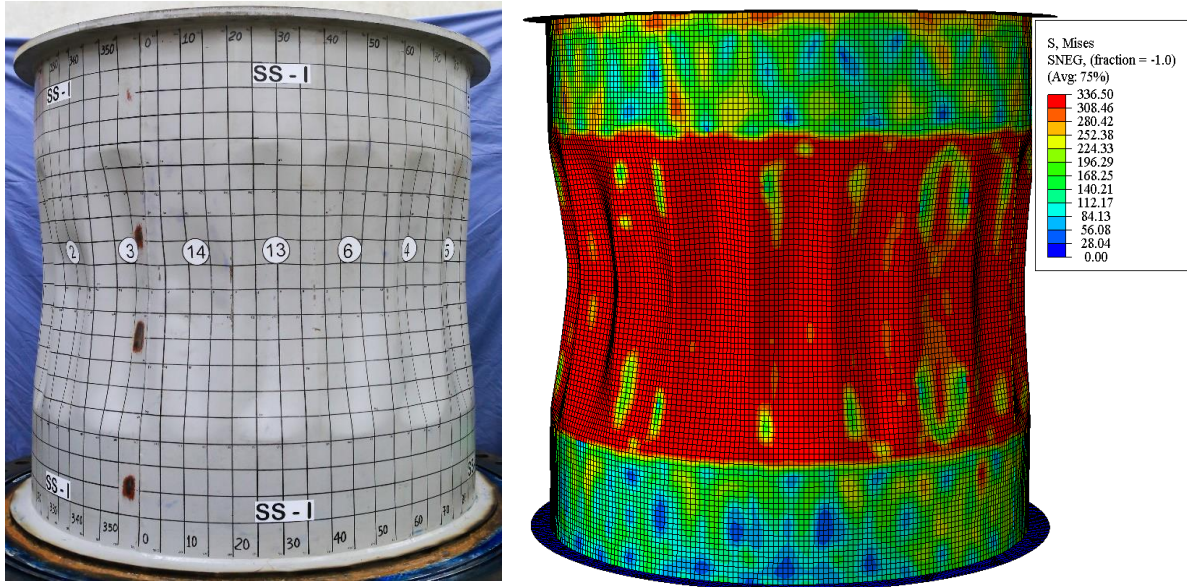


Fig. 5.47 Predicted collapsed shape of model SS-I when compared with the test results.

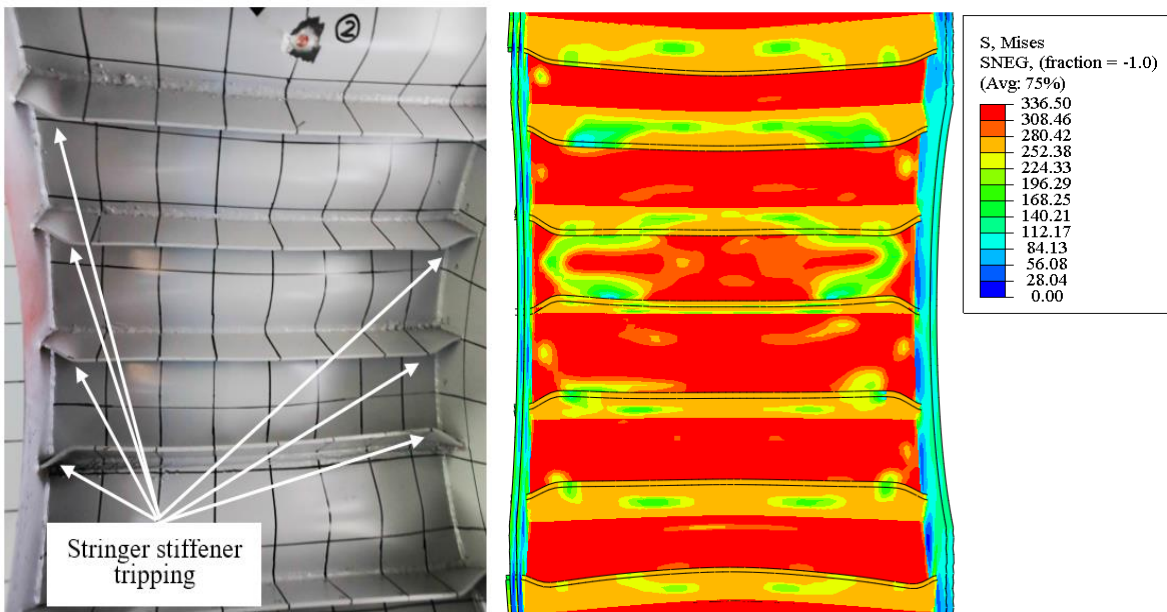


Fig. 5.48 Predicted deformed stringer-stiffener shape when compared with the test results for model SS-I.

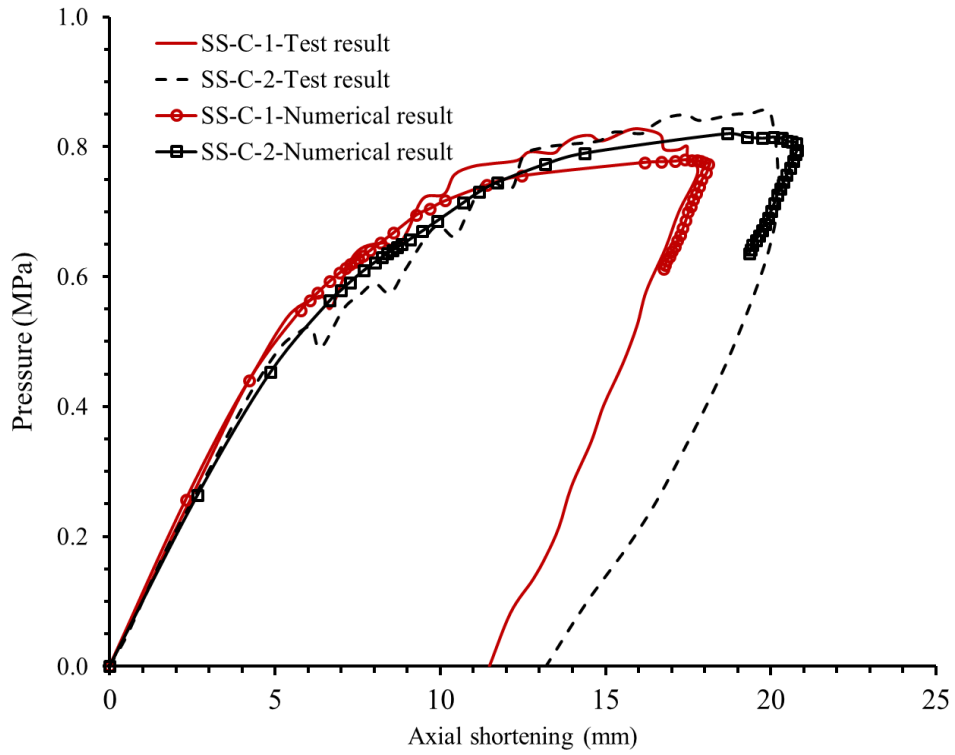


Fig. 5.49 Pressure relative to the axial shortening curves of model SS-C-1 and SS-C-2.

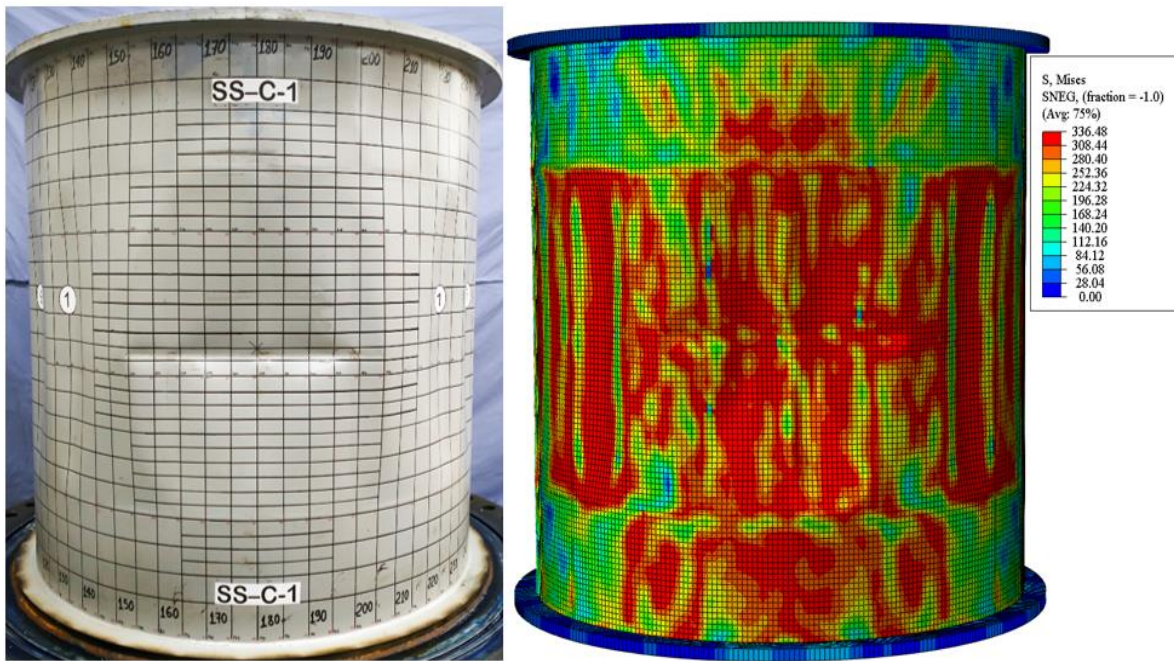


Fig. 5.50 Predicted collapsed shape of test model SS-C-1 when compared with the test results.

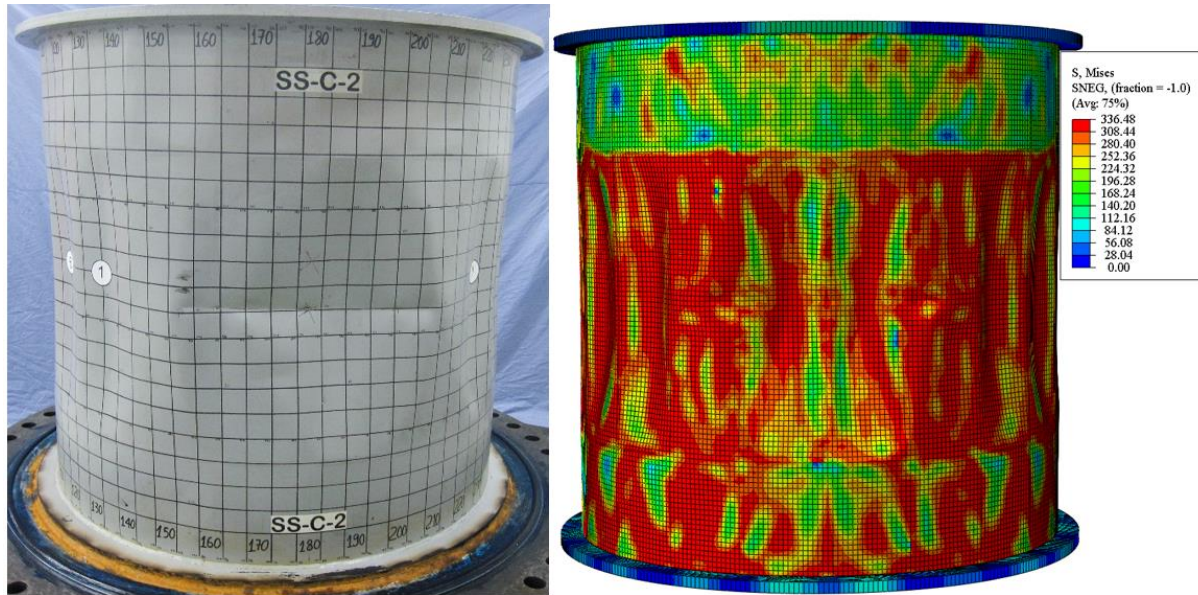


Fig. 5.51 Predicted collapsed shape of test model SS-C-2 when compared with the test results.

5.6 Parametric study

In this section, the parametric study is performed by subsequent the parametric study results from Chapter 3. The aim of the collision tests from the previous Chapter is to obtain the damaged shapes on the ring or stringer-stiffened cylinders for the subsequent collapsed tests.

5.6.1 Ring-stiffened cylinders

5.6.1.1 Effect of impact location

In Fig. 5.52 illustrates the relationship between radial pressure and radial displacement at hit point with various impact locations, which were non-dimensionalized with collapse pressure of intact model (P_{Intact}) and radius of the ring-stiffened cylinder. There are a number of significant different trend in the impact locations. The impact locations close at mid-bay was smaller collapse pressure than impact location at ring stiffener around 10% for each position, which also has the same trend with damaged volume. It can be explained that the resistant response of stiffened cylinder could be improved when loaded at the impact location nearby ring members. Additionally, it can be more understood to see the collapse shape in Fig. 5.53 with damaged impact location in mid-bay and on ring stiffener at 30° skews of striker to cross section

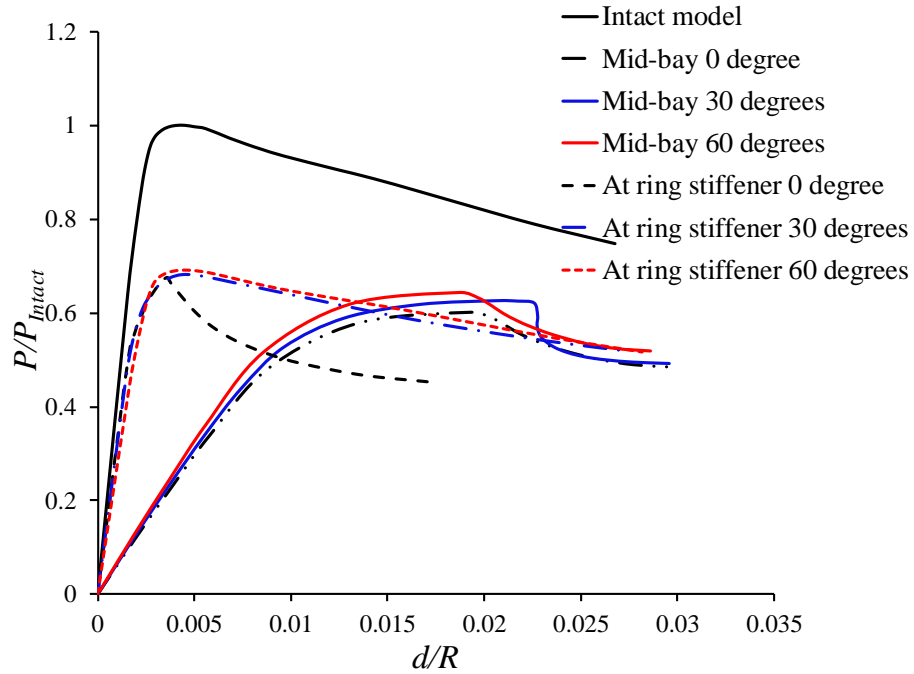


Fig. 5.52 Pressure-radial displacement curves with various impact locations.

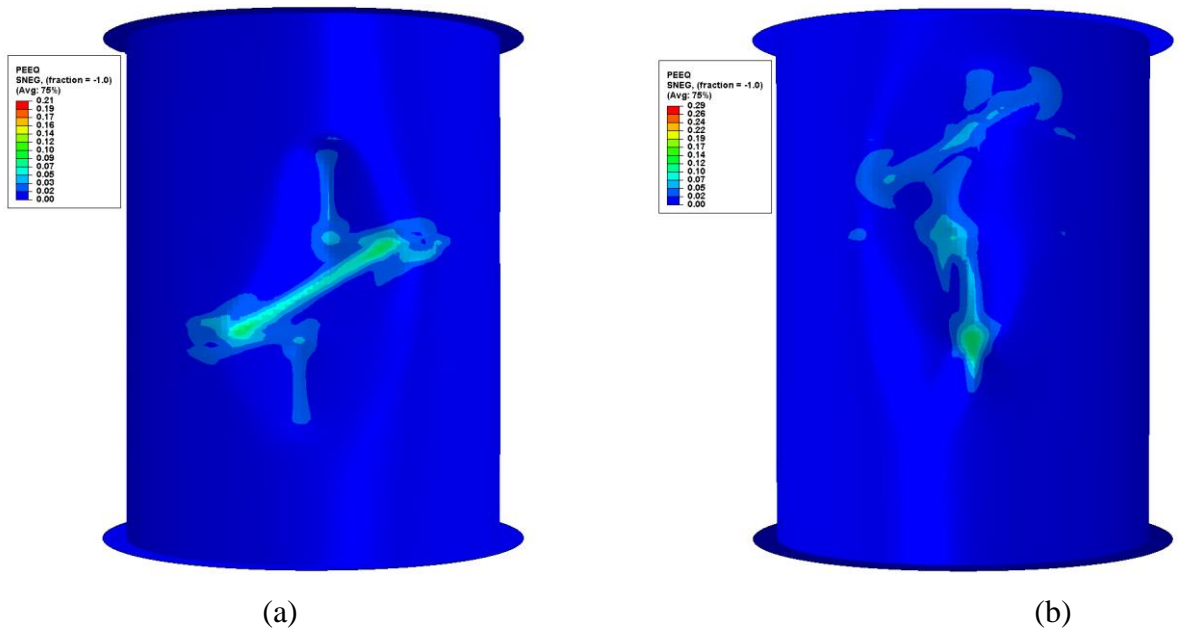


Fig. 5.53 Collapsed shapes: (a) At the mid-bay 30° and (b) At the ring stiffener 30°.

5.6.1.2 Effect of impact velocity

The impact energy is varied by increasing v , the impact velocity. The impact energy is proportional with the square of v , accordingly for larger impact velocities the energy to be

dissipated will result in larger deformations. From Fig. 5.54 it is apparent that the effect of local damage is significant with considerable loss in stiffness and reduction in load carrying capacity. With an increase in dent depth a gradual decrease in ultimate strength is noticeable.

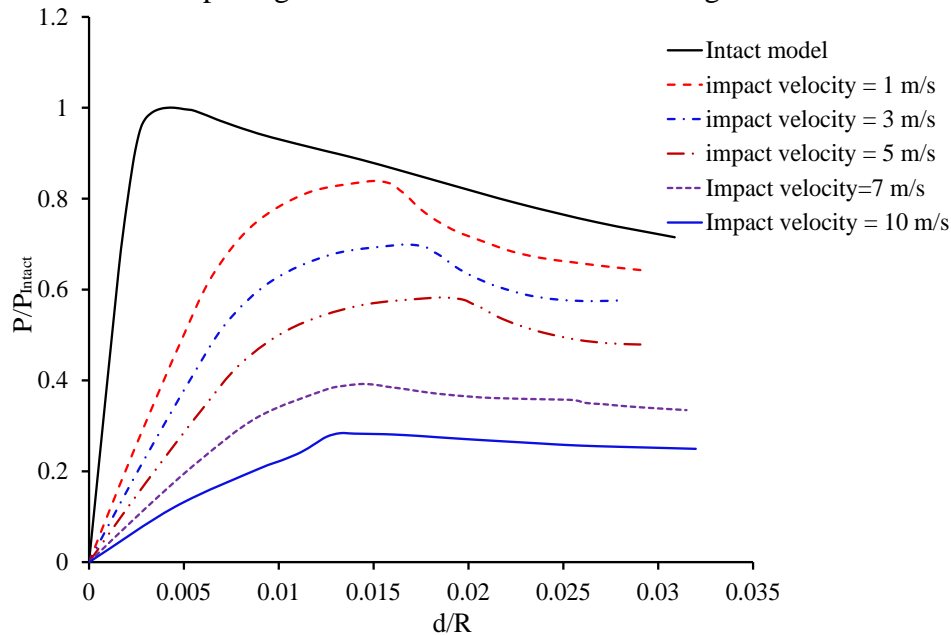


Fig. 5.54 Pressure-radial displacement curves with various impact velocities.

5.6.1.3 Effect of ring-stiffeners

The number of ring stiffener was varied, with values of 2, 4 and 6. The result of pressure-radial displacement curves with various number of ring-stiffened cylinders is shown in Fig. 5.55. It is evident that the number of ring-stiffeners has a remarkable effect on the resistance of cylinder shell against hydrostatic pressure. The residual strength of ring-stiffener cylinder is proportional to the number of ring-stiffeners. Furthermore, the T-shape and flat-bar shaped ring-stiffeners are also considered in Fig. 5.55. Furthermore, the type of ring-stiffener shape is also strongly affected on residual strength of model. The residual strength reduction when changing the T shaped ring-stiffener to flat bar ring-stiffener is 29.2%.

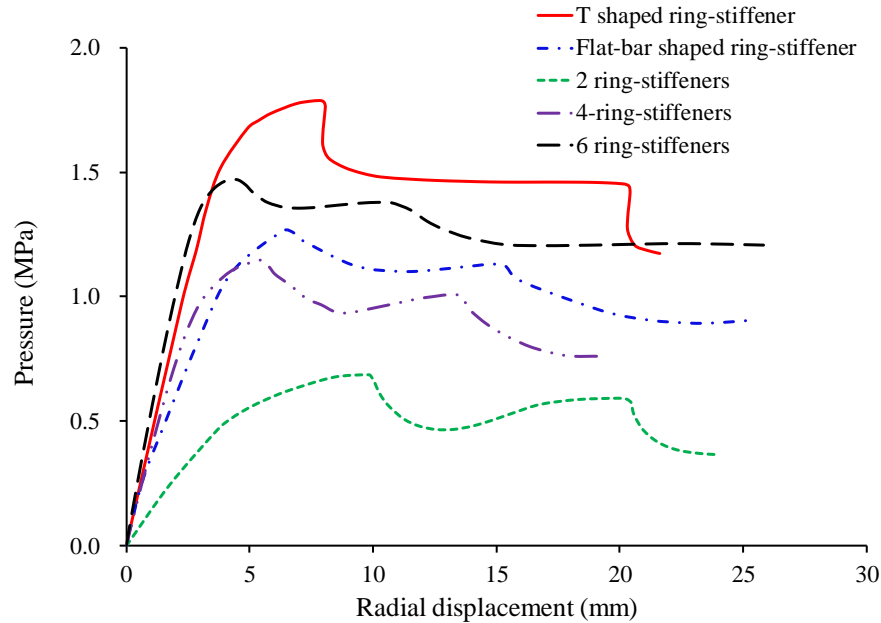


Fig. 5.55 Pressure-radial displacement curves with various number of ring-stiffened cylinders.

5.6.1.4 Effect of striker header shapes

The results of the parametric study are summarized in Table 5.3 and depicted in Fig. 5.56. When the energy ratio, λ_E , was in the range from 0.9×10^{-3} to 1.3×10^{-3} , the residual strength of the damaged ring-stiffened cylinder due to the hemisphere-type indenter was much smaller than those of the other two types. However, quite interestingly, when λ_E was approximately 1.8×10^{-3} , the residual strengths of the three types were nearly the same.

Table 5.3 Summary results of parametric study with various striker shapes.

$\lambda_E \times 10^3$	Collapse pressure (MPa)			Ratio		
	Knife-edge indenter (1)	Rectangular indenter (2)	Hemisphere indenter (3)	(2)/(1)	(3)/(1)	(3)/(2)
Intact model			2.09			
0.88	1.65 (-21%)	1.55 (-26%)	1.48 (-29%)	0.94	0.90	0.95
1.09	1.59 (-24%)	1.48 (-29%)	1.27 (-39%)	0.93	0.80	0.86
1.32	1.39 (-33%)	1.33 (-36%)	1.12 (-46%)	0.96	0.80	0.84
1.57	1.17 (-44%)	1.11 (-47%)	1.07 (-49%)	0.95	0.91	0.96
2.14	1.04 (-50%)	1.02 (-51%)	1.01 (-52%)	0.98	0.97	0.99

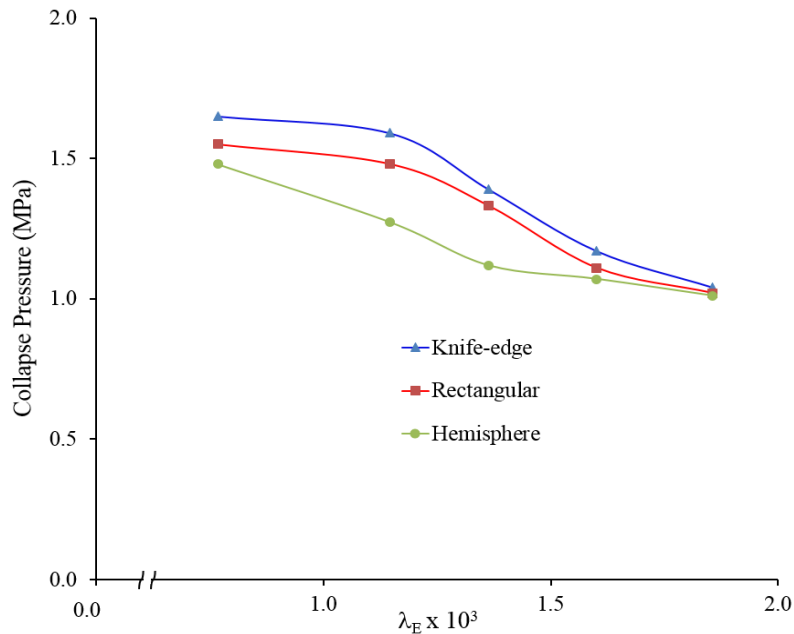


Fig. 5.56 Parametric study results with various striker header shapes.

5.6.2 Stringer-stiffened cylinders

5.6.2.1 Effect of impact location

Fig. 5.57 shows the variation of the ultimate strength of stringer-stiffened cylinder models for various impact locations subjected to hydrostatic pressure. From this figure, it can be inferred that the strength reduction did not vary considerably with impact locations. This might be attributed to the effect of the stringers, as they carry the significant radial load as beam-column elements and are not individually affected by the damage unless positioned closely to the damaged zone.

5.6.2.2 Effect of impact velocity

As in the case of the ring-stiffened cylinder, under radial pressure, the reduction in ultimate strength due to damage is drastic in Fig. 5.58. There are some unstable lines after the collapse pressure. Because of the geometrically nonlinear static problems sometimes involve buckling or collapse behavior, where the load-displacement response shows a negative stiffness and the structure must release strain energy to remain in equilibrium. This is called snap-through. The post-collapse shape for the damaged cylinder as shown in Fig. 5.59 indicates that overall buckling and local shell buckling modes govern the collapse of the cylinder.

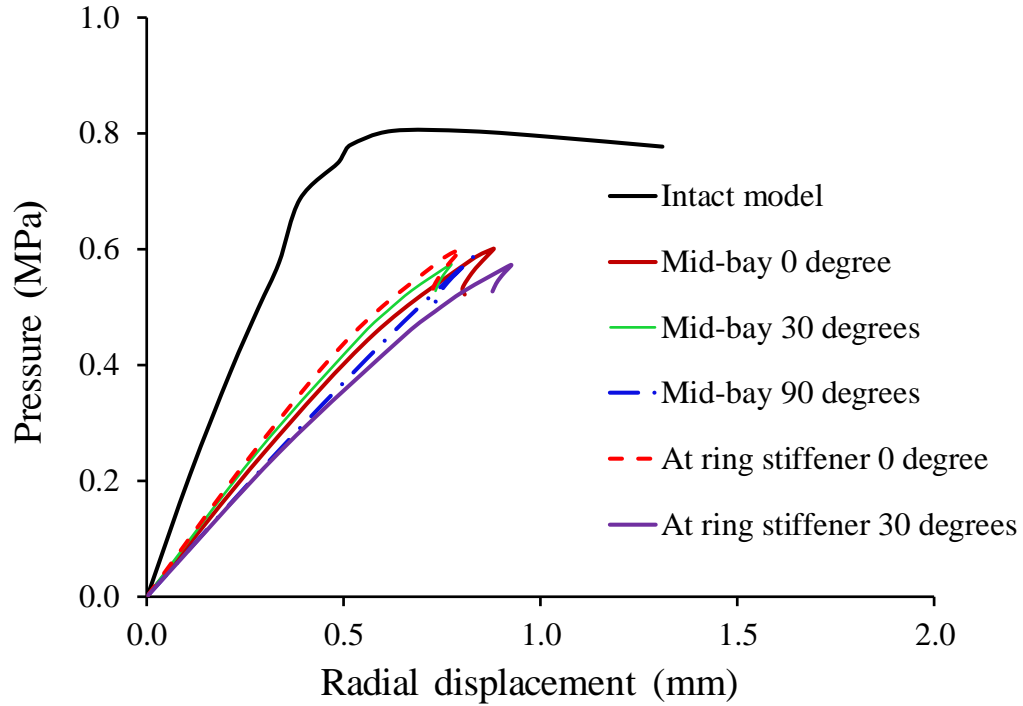


Fig. 5.57 Pressure-radial displacement curves with various impact locations for stringer-stiffened cylinder.

5.6.2.3 Effect of stringer-stiffeners

The effect of the type of stringer-stiffened cylinders and its scantlings are assessed. Instead of flat-bar stiffeners, T-shaped and L-shaped stiffeners are widely used in practice. Therefore, in this section, the flat-bar stringer stiffeners are replaced with T-shaped and L-shaped stiffeners having the same weight as the flat-bar stiffeners in the original configuration. The effect of stringer-stiffened shapes is illustrated in Fig. 5.60. Unlike the case of ring-stiffeners, the stringer-stiffener shapes affect both membrane resistance and circumferential bending resistance. The reduction in the ultimate strength did not increase significantly with increasing the dent depth when changing the shape of stringer-stiffeners. Among three stringer-stiffener shapes, L-shaped stringer-stiffener has a good resistance under hydrostatic pressure.

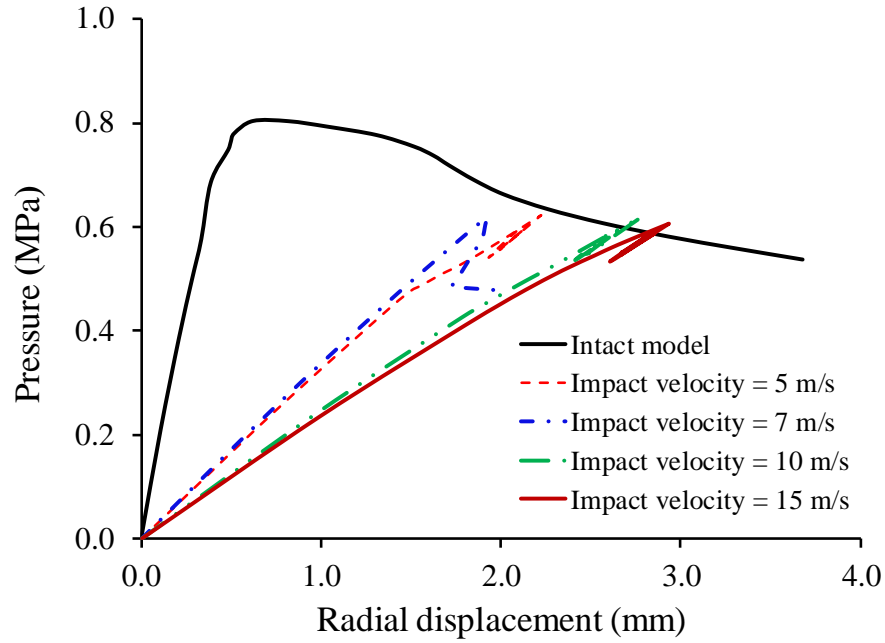


Fig. 5.58 Pressure-radial displacement curves with various impact velocities for stringer-stiffened cylinder.

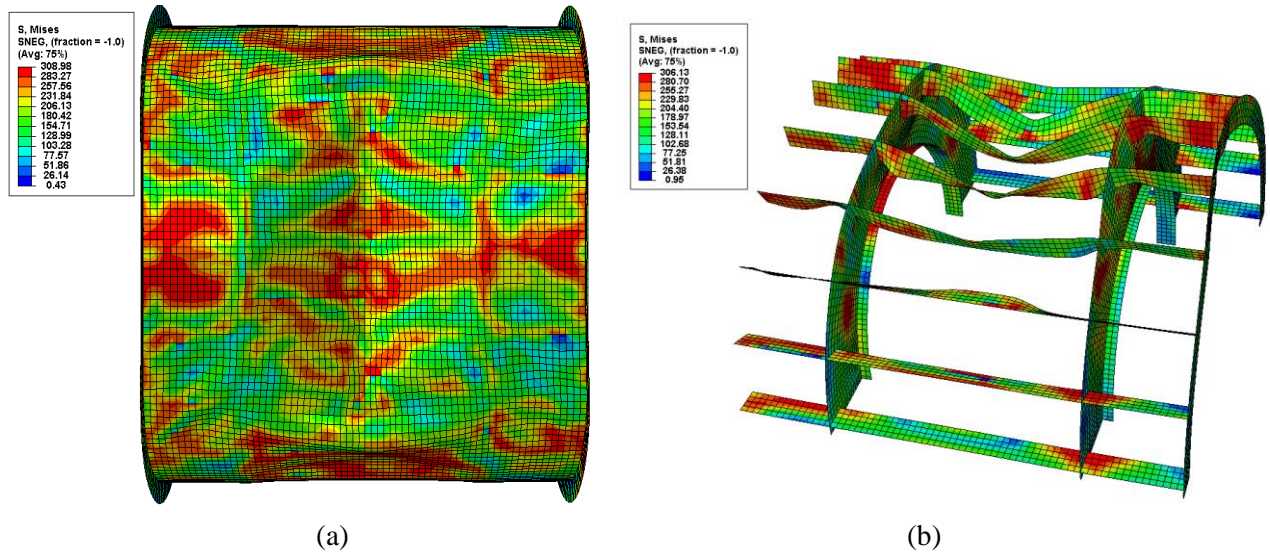


Fig. 5.59 Collapsed shapes: (a) shell, (b) stringer-stiffened cylinder.

5.6.2.4 Effect of striker header shapes

The effect of striker header shapes on stringer-stiffened cylinder was depicted in Fig. 5.61. When the energy ratio, λ_E , was in the range from 1.0×10^{-3} to 1.8×10^{-3} , the residual strength of the damaged stringer-stiffened cylinder due to the hemisphere-type indenter was quite higher than

those of the other two types. However, quite interestingly, when λ_E was approximately 2.0×10^{-3} , the residual strengths of the three types were nearly the same.

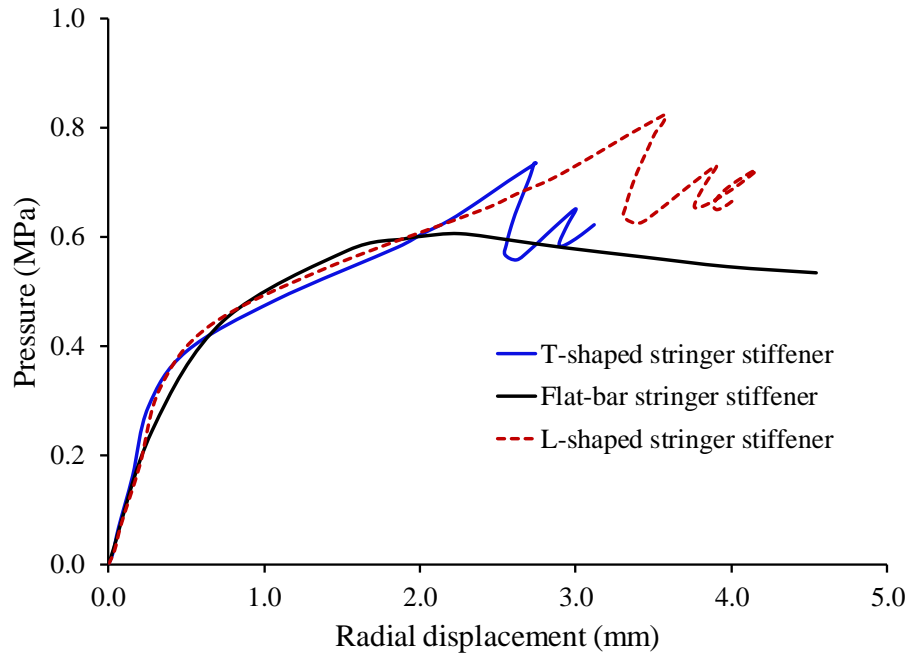


Fig. 5.60 Effect of stringer-stiffener shapes.

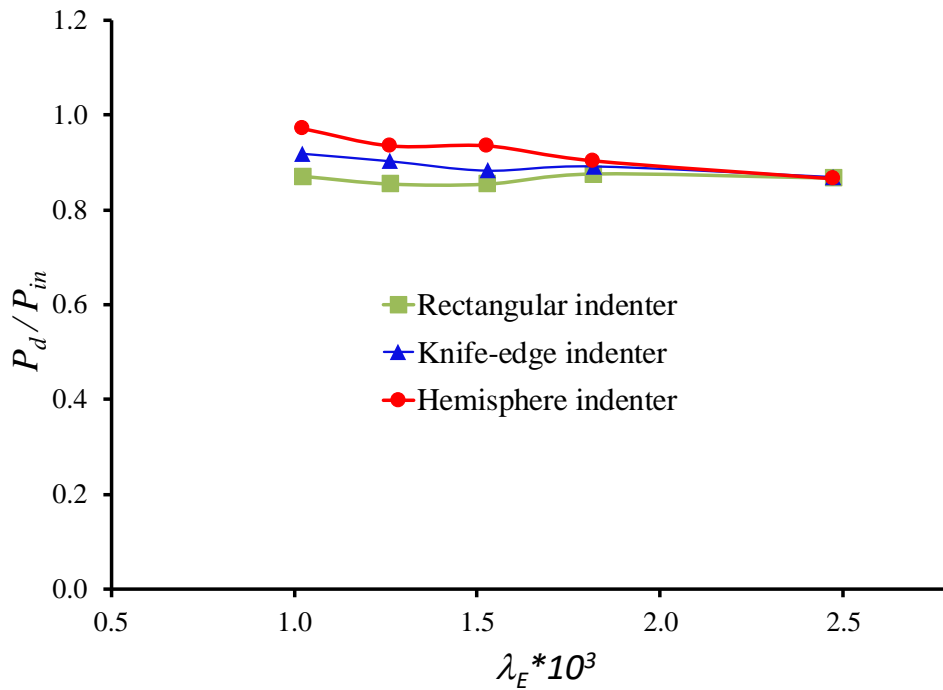


Fig. 5.61 Parametric study results with various striker header shapes for stringer-stiffened cylinder.

5.7 Final remarks

In this chapter the residual strength characteristics of damaged ring- and stringer-stiffened cylinders subjected to hydrostatic pressure were investigated through experimental and numerical prediction results. Based on the results obtained from this chapter following conclusions can be drawn:

To the best of the authors' knowledge, this is the first study that successfully reported on the residual strength tests of damaged ring- and stringer-stiffened cylinders subjected to hydrostatic pressure. In the study, the failure mode of locally damaged ring-stiffened cylinders under hydrostatic pressure was overall buckling even though the corresponding intact model collapsed in an interactive buckling mode. While that of the intact and damaged stringer-stiffened cylinders under hydrostatic pressure failed with respect to the local shell buckling.

The ultimate strength of ring-stiffener cylinder is significant reduced with increasing the dent depth. Contrary to the intact cylinder case, in the post collapse shape of the damaged cylinder the damage spreads to the neighboring bays. The dent causes early tripping of the ring-stiffeners and the inward lobe propagates to the adjacent bays, leading to overall collapse of the cylinder. This is reasonable explanation of the significant reduction in ultimate strength due to damage considering high imperfection sensitivity of overall collapse mode in radial pressure loading case.

For stringer-stiffener cylinders, the cylindrical shell failed several times after an initial failure as evidenced by a sudden decrease in pressure. Subsequently, the shell recovered as "hardened-up" to reach a pressure level higher prior to the final collapse of the shell. The effects of collision damages on the ultimate strength of stringer-stiffened cylinders under hydrostatic pressure were extremely low when compared to those of the intact model, respectively. Due to the large axial bending stiffness of the stringer-stiffened shell wall, the collapse was not sudden and the post-collapse behaviour was unstable. The reduction in the ultimate strength did not increase significantly with increasing the dent depth.

The numerical results indicate that it is necessary to consider residual stresses from cold-bending and welding and the initial shape imperfection in the FEA models. The accuracy and reliability of the numerical prediction were achieved and are adopted to perform further parametric studies to develop design guidelines.

Chapter 6 Predictions on the residual strength of damaged ring- and stringer-stiffened cylinders under hydrostatic pressure

6.1 Introduction

Nowadays, the nonlinear finite element analysis has become an excellent tool for evaluating the collision response and failure of structures in the ocean engineering field [115, 135]. A numerical evaluation of the residual strength of ring- and stringer-stiffened cylinders under hydrostatic pressure was performed by Do et al. [69-70]. It was also applied in some offshore structures, including damaged ring-stiffened cylinders [116-117], pipelines [131], and damaged box girders [132]. Furthermore, a nonlinear finite element analysis was applied to perform ship-collision scenarios and validate the analytical methods [133-134]. Thus, besides its economic efficiency, a carefully performed finite element analysis, validated with reliable test data, could be the most effective way for evaluating the residual strength of damaged ocean engineering structures.

In this chapter, the idea of the current study is to derive the formulations based on the regression analysis of the results of a rigorous parametric study by nonlinear finite element analysis. The residual strength formulations are derived to predict the residual strength of a damaged ring- and stringer-stiffened cylinder under hydrostatic pressure loading. The accuracy and reliability of all the derived formulations are established by comparison with the results of tests and finite element analyses.

6.2. Ring-stiffened cylinder

6.2.1 Description of numerical model

In this section, a series of finite element analyses were performed on the design example of a ring-stiffened cylinder of an actual submarine design concept and on other rings-stiffened cylinders given in the ABS rules [177]. The finite element model was applied with the methods presented in Chapter 5. The dimensions and material properties of the model are listed in Table 6.1. For each model, a series of finite element analyses in which the dent depth varied were

conducted. To generate damages on the models, a collision analysis was conducted using a rigid knife-edge indenter.

The dimensions and material properties of the model are listed in Table 6.1. These design example models are also used for deriving formulations to predict the extent damage of ring-stiffened cylinders under dynamic collision in Chapter 3. A total of 300 numerical cases were performed including 150 collision analyses and 150 residual strength analyses. The finite element models were generated with the techniques explained in the previous section. The global mesh size was 80 mm, while the local mesh size was 40 mm. The range of R/t (radius of cylinder/shell thickness) was determined from 97 to 454, and the range of dent depth to radius d/R from 0 to 0.25.

Table 6.1 Properties of the reference ring-stiffened cylinders.

Sym.	Unit	RS-1	RS-2	RS-3	RS-4	RS-5	RS-6	RS-7	RS-8	RS-9	RS-10
R	mm	3100	3023	3175	3100	2550	5150	2500	3500	550	3180
t	mm	30	25	20	23	26.2	30	15	12	4.97	7.0
L_c	mm	12600	15240	10500	10320	14850	16250	11250	7500	1060	6650
L_s	mm	430	3048	840.7	430	450	650	750	400	150	350
σ_Y	MPa	645	754	645	645	827	645	380	276	275	345
E	GPa	206	206	206	206	210	206	205	199	202	199
n_r	[-]	29	5	12	24	33	25	15	19	7	19
h_w	mm	210	214	95.2	180	178	262	190	255	40	120
t_w	mm	19.0	15	11	13	26	16.5	20	11.5	6.0	19
w_f	mm	155	280	76.2	90	102	231	120	76.2	0	90
t_f	mm	19	17	11	23	14	24	20	11.5	0	17
R/t	[-]	103	121	159	135	97	172	167	292	111	454

6.2.2 Failure mode interaction formula for intact case

For prediction of the failure mode of intact ring-stiffened cylinders, the newest design formulations proposed from Cho et al. [179] were used, which are presented in equations (6.1) to (6.9). These formulations combine all the failure modes of ring-stiffened cylinders under hydrostatic pressure including: shell yielding, local buckling, overall buckling, and ring-stiffened tripping. It is noted that these formulations were also considered the actual initial imperfection shapes and material imperfection as well as the residual stresses from cold bending and welding by using the knockdown factors. The knockdown factors were derived by regression analyses applied to the available test data. The procedures involved in deriving knockdown factor is

described in Fig. 6.1. These formulations have a fair accuracy when compared to the 107 available test models, with X_m (ratios of actual to predicted results) mean of 1.0 together with COV of 7.70%. The accuracy of the provided formulations is better than that of the available recommendation rules by PD 5500, DNV-GL, ABS, and API. Detailed explanations of the design formulation of intact ring-stiffened cylinders are included in Cho et al. [179]. Comparison of the proposed formula and the design code is indicated in Table 6.2.

$$\left(\frac{P_C}{\rho_L P_m} + \frac{P_C}{\rho_{OA} P_n} + \frac{P_C}{\rho_T P_t}\right)^2 + \left(\frac{P_C}{P_Y}\right)^2 = 1 \quad (6.1)$$

where

P_c : collapse pressure

P_m : local buckling pressure

P_n : overall buckling pressure

P_t : tripping pressure

P_Y : yield pressure

ρ_L : local buckling knockdown factor

ρ_{OA} : overall buckling knockdown factor

ρ_T : tripping knockdown factor

$$\rho_T = 2.737 \text{ Exp } \{0.0088 (L_s/R)(\sqrt{(L_s/t)})\}, \text{ for tripping} \quad (6.2)$$

$$\rho_{OA} = 1.055 \text{ Exp } \{0.167 (h_w/t_w)(E/1000\sigma_Y)\}, \text{ for overall buckling} \quad (6.3)$$

$$\rho_L = 0.674 \text{ Exp } \{0.0006 (h_w/t_w)(\sqrt{R L_s/t})(E/1000\sigma_Y)\}, \text{ for local buckling} \quad (6.4)$$

$$P_Y = \frac{\sigma_Y t}{R} \frac{1}{\sqrt{\frac{1}{4} \frac{(1-\nu G)}{2} + (1-\nu G)^2}} \quad (6.5)$$

$$P_m = E \frac{t}{R} \left\{ n^2 - 1 + \frac{1}{2} \left(\frac{\pi R}{L_s} \right)^2 \right\}^{-1} \left[\left\{ n^2 \left(\frac{L_s}{\pi R} \right)^2 + 1 \right\}^{-2} + \frac{t^2}{12R^2(1-\nu^2)} \left\{ n^2 - 1 + \left(\frac{\pi R}{L_s} \right)^2 \right\}^2 \right] \quad (6.6)$$

$$P_n = \frac{(n^2-1)EI_c}{R^3 L_s} + \frac{(Et/R)}{\left[n^2 - 1 + \frac{1}{2} \left(\frac{\pi R}{L_c} \right)^2 \right]} \left\{ \frac{1}{\left[n^2 \left(\frac{L_c}{\pi R} \right)^2 + 1 \right]^2} \right\} \quad (6.7)$$

$$P_t = \frac{\sigma_t P_{yf} R_s}{\sigma_y R_f} \quad (6.8)$$

$$\sigma_t = \frac{G' J + ET_p \left(\frac{n}{R} \right)^2 + k_{0n} \left(\frac{R}{n} \right)^2}{I_o + \frac{k_{0n}}{\xi P_m} \left(\frac{R}{n} \right)^2} \quad (6.9)$$

E is the Young's modulus, ν is defined as the Poisson ratio, n is the wave number, and I_C is the second moment area of the combined cross-section of the ring-frame and the shell that depends on the calculation chosen for the effective breadth of shell plating at the stiffener junction, which contributes to the overall flexural stiffness of the cylinder.

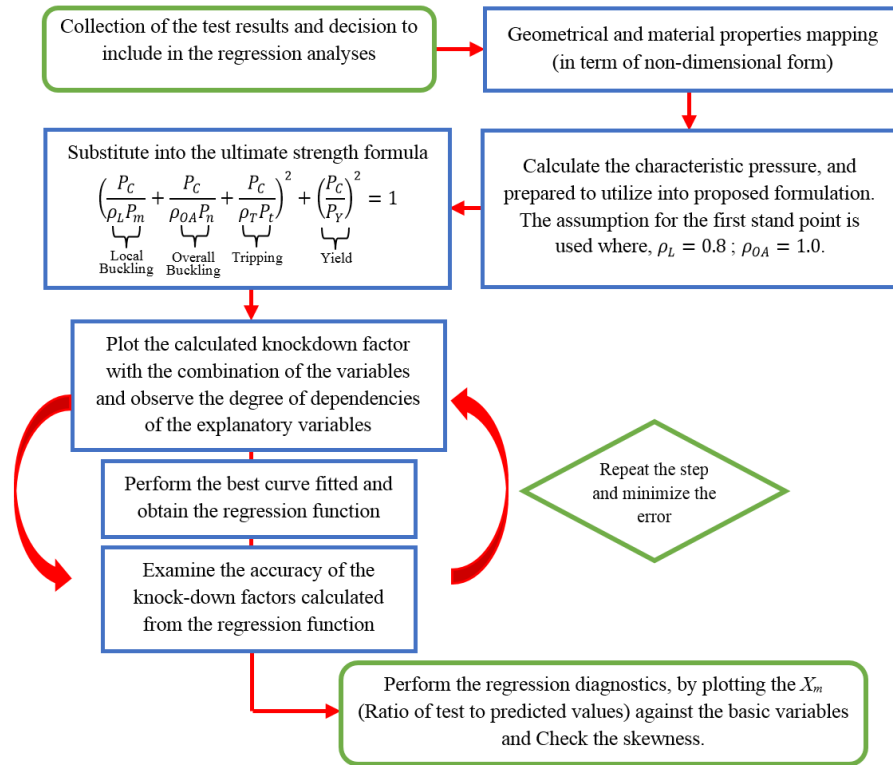


Fig. 6.1 Procedure for the derivation of knockdown factors.

Table 6.2 Comparison of the proposed formula and the design code.

Number of Models	Design Formulations	X_m	
		Mean	COV(%)
107	Proposed Formula	1.00	7.70
	PD 5500	0.96	11.85
	DNV-GL	0.94	13.44
	ABS	1.07	14.18
	API	0.94	14.95

6.2.3 Failure mode formula for damage case

In this section, the formulations to predict the residual strength of damaged ring-stiffened cylinders were derived. A total 150 numerical models, which were generated in the previous

Section, were performed under external hydrostatic pressure. Fig. 6.2 illustrates the collapsed shape of the design example, the submarine model RS-3 ($R/t = 159$; $d/R = 0.016$). This model failed according to the overall buckling mode. The dented area is a main reason of the ring-stiffened tripping, and the damage extended in the longitudinal direction, then leading to overall collapse. In addition, Fig. 6.3 shows the pressure versus radial displacement of the centre point in the dent zone with varying ratio of dent depth to radius (d/R). The effect of local damage is significant, with considerable loss in stiffness and reduction in load carrying capacity. With an increase in dent depth, a gradual decrease in ultimate strength is noticeable.

As in the previous chapter, the same procedure was performed before deriving the formulations in order to find a suitable dependent parameter on which to derive the reduction in ultimate strength, R_u . First, the relations between R_u and various appropriate non-dimensional geometric and material property parameters (L_s/R , R/t , d/R , L_c/R , h_w/t_w , w_f/t_f , and E/σ_Y) were investigated. Combinations of variables such as Z ($Z = \frac{L^2}{Rt} / \sqrt{1-\nu}$: Batdorf slenderness parameter), $\sqrt{Z} \cdot \frac{E}{\sigma_Y}$, and $\frac{\sqrt{Lt}}{R} \frac{E}{\sigma_Y}$ were used. The results show that the d/R ratio (dent depth/radius) had the strongest influence on R_u . After investigating the dependent parameters, the regression analysis was performed with the best-fit evaluation of numerical results. The best-fit curve from numerical data of the approximate formula is plotted in Fig. 6.4. In this figure, the reduction factor R_u was defined as the ratio of collapse pressure of the damaged model to collapse pressure of the intact model. It is noted that the collapse pressure of the intact model was determined using equation (6.1) in Section 6.2.2. Based on the above results, an approximate formula, equation (6.10), was empirically derived using the regression analysis for determining the reduction factor R_u . When considering the safety design, the design equation is given in Eq. (6.11) by multiplying Eq. (6.10) with (Mean + 2* Standard deviation).

$$R_u = \frac{P_{dam.}}{P_{in.}} = Exp(-5.54\delta_d^{1.14}) \quad ; \text{ Mean equation} \quad (6.10)$$

$$R_u = \frac{P_{dam.}}{P_{in.}} = Exp(-0.067 - 5.54\delta_d^{1.14}) \quad ; \text{ Characteristic equation} \quad (6.11)$$

where

$P_{dam.}$: collapse pressure of damaged cylinder

$P_{in.}$: collapse pressure of intact cylinder (Eq. 6.1)

δ_d : non-dimensional dent depth ($\delta_d = d/R$)

The accuracy of the proposed formulation to predict the residual strength of damaged ring-stiffened cylinders was very good, with X_m (ratio of numerical collapse pressure to predicted value) of 0.988 together with COV of 2.68 %. Furthermore, the skewness of the ratios of numerical

analysis results to proposed formulation results (X_m) with basic parameters, including the non-dimensional geometric, material property, and failure mode parameters (L_s/R , R/t , d/R , L_c/R , h_w/t_w , w_f/t_f , E/σ_Y , P_m/P_Y , and P_n/P_Y), are verified, as shown in Figs. 6.5, 6.6, 6.7, and 6.8, where P_Y , P_m , and P_n are the yield pressure, elastic inter-frame buckling pressure, and elastic overall buckling pressure, respectively. P_Y , P_m , P_n and P_t were calculated using equations (6.5), (6.6), (6.7) and (6.8). It is evident that there is no apparent skewness and no sharpness trend line in these figures. It means that the proposed formulation provides acceptable basic parameters.

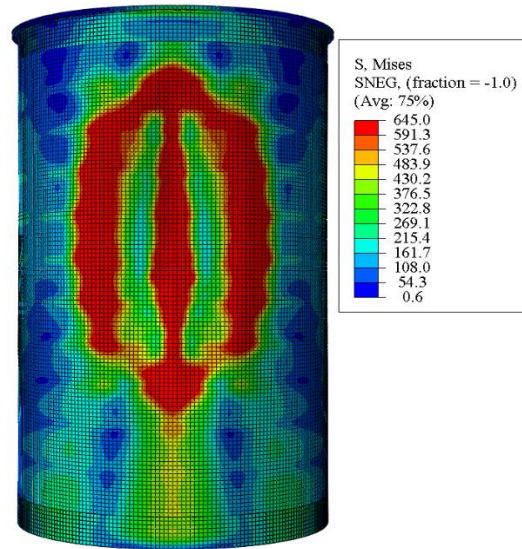


Fig. 6.2 Collapsed shape of damaged model RS-3 ($d/R = 0.016$) under hydrostatic pressure.

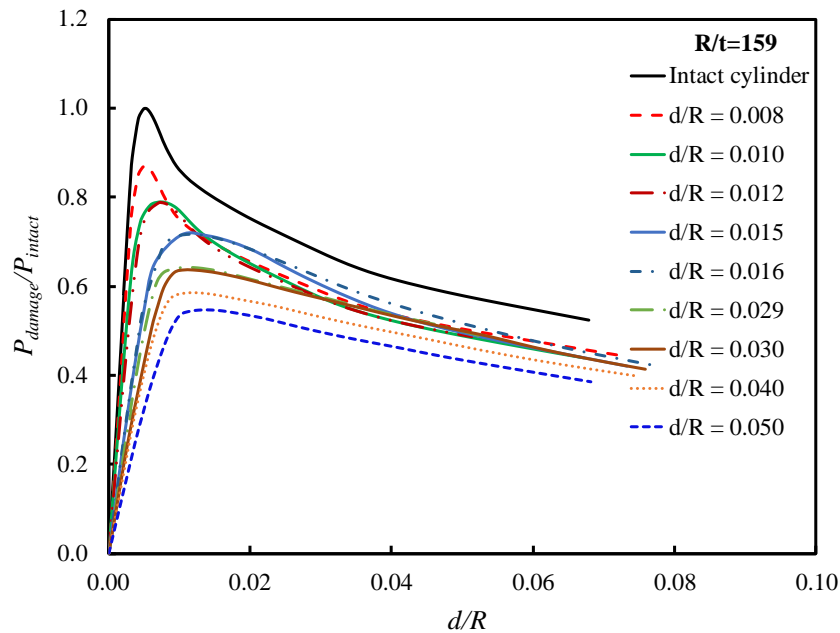


Fig. 6.3 Non-dimensional parameter of pressure versus radial displacement at hit point of model RS-3 ($R/t = 159$).

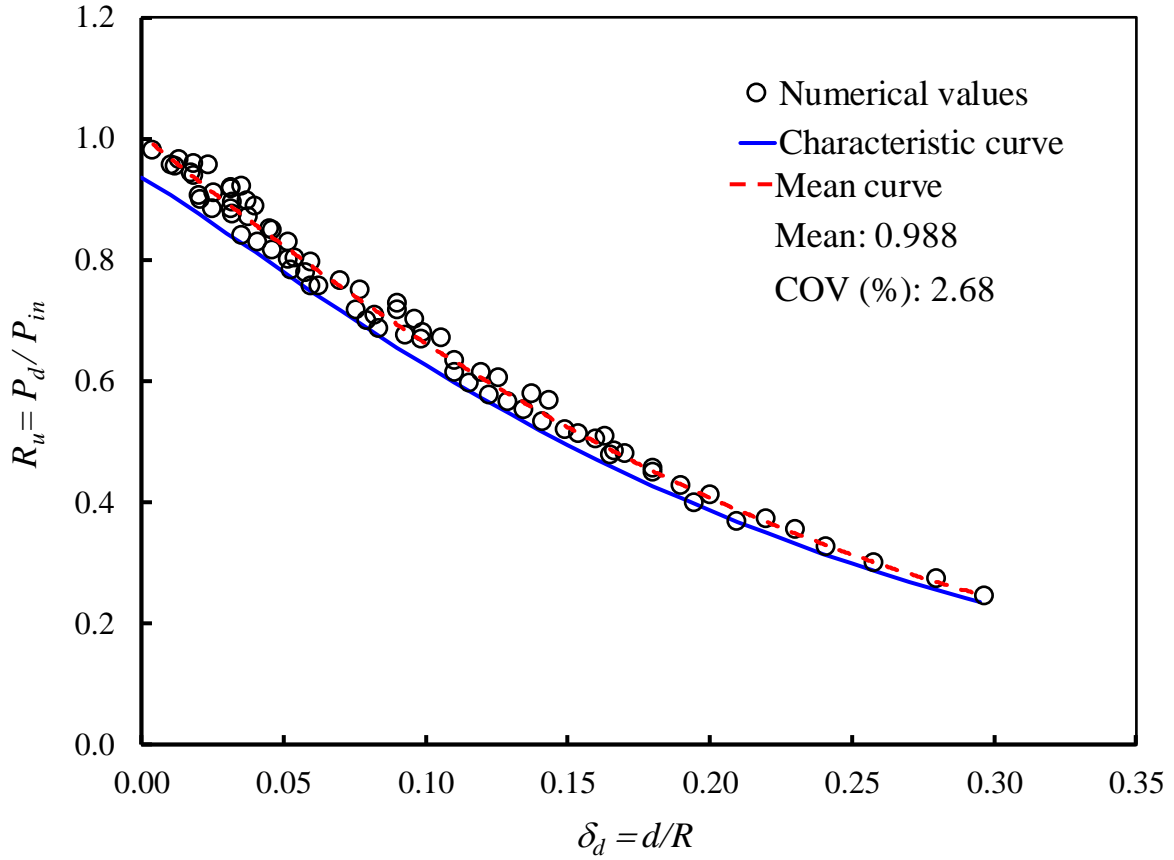


Fig. 6.4 Best-fit curve for prediction of residual strength for ring-stiffener cylinder.

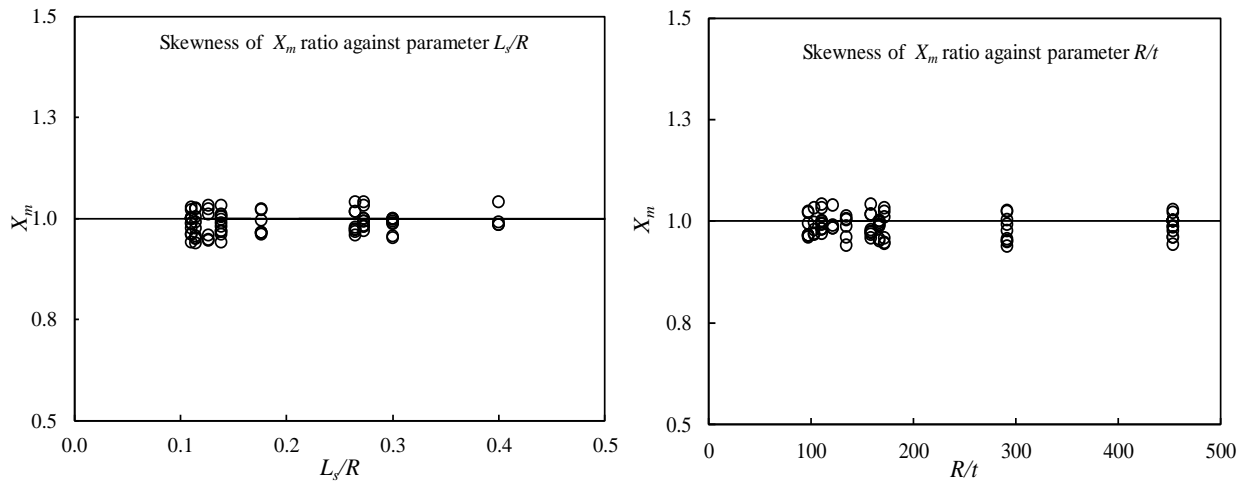


Fig. 6.5 Plotting of X_m against basic parameters L_s/R and R/t for hydrostatic pressure.

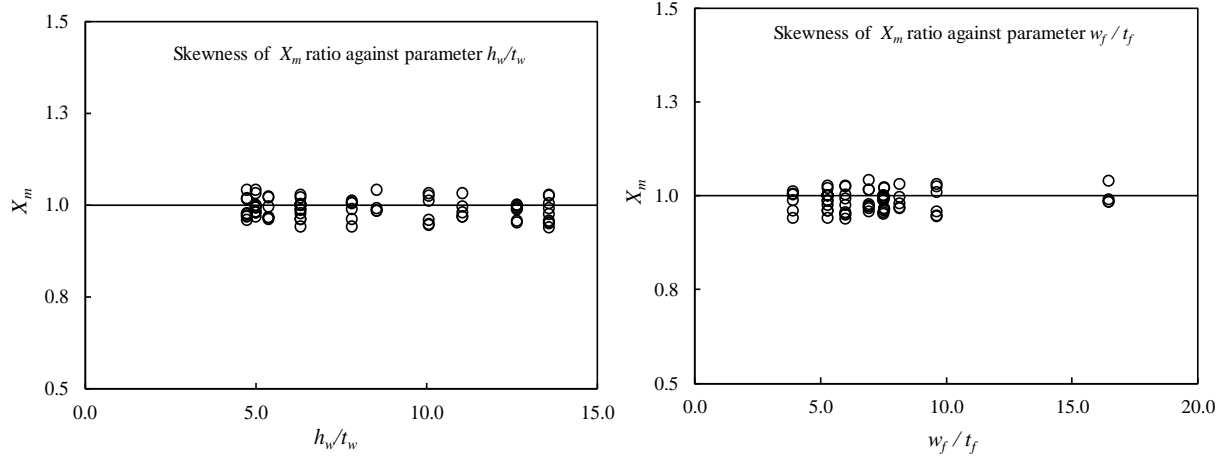


Fig. 6.6 Plotting of X_m against basic parameters h_w/t_w and w_f/t_f for hydrostatic pressure.

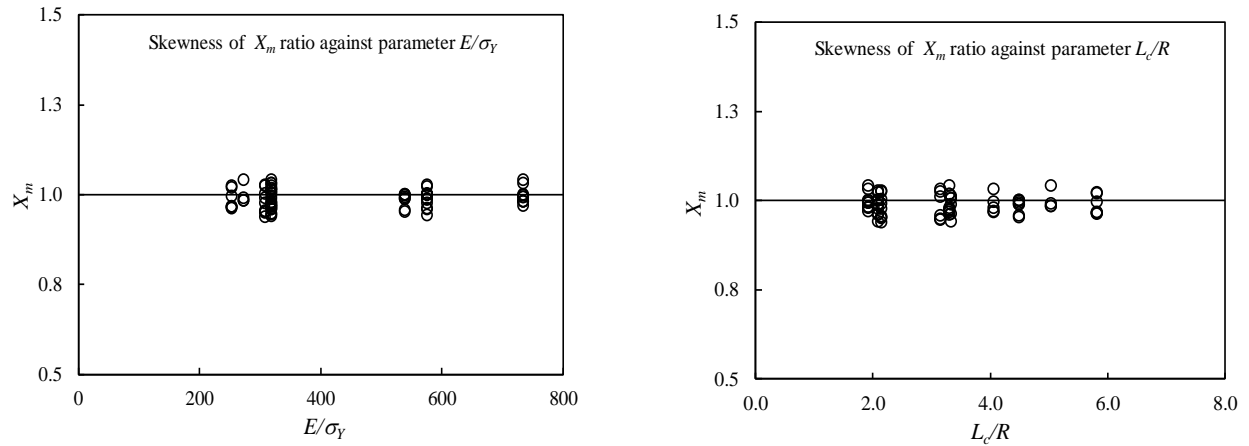


Fig. 6.7 Plotting of X_m against basic parameters E/σ_Y and L_c/R for hydrostatic pressure.

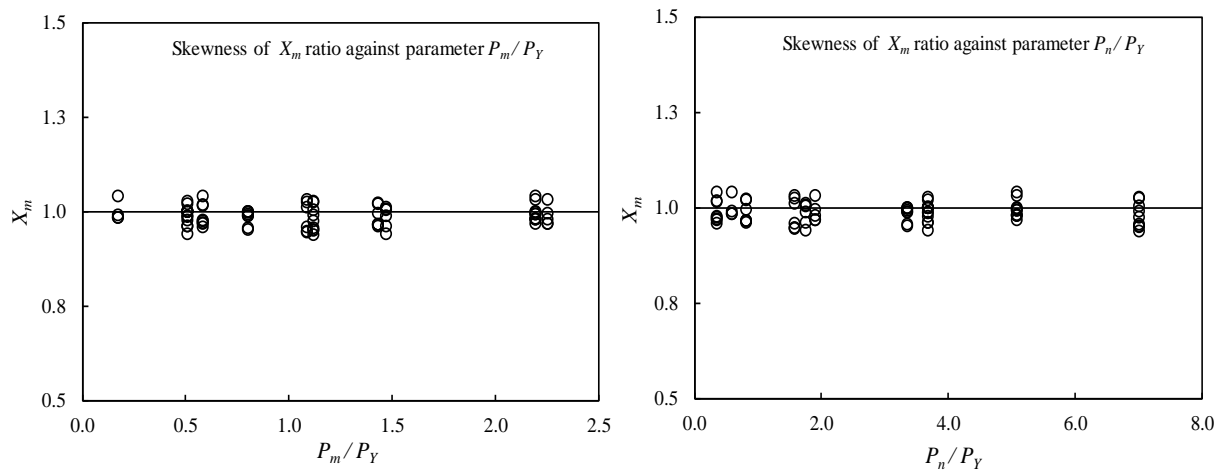


Fig. 6.8 Plotting of X_m against basic parameters P_m/P_Y and P_n/P_Y for hydrostatic pressure.

6.2.4 Accuracy of the proposed formulation

To validate the accuracy of proposed formulation for residual strength prediction, the predicted collapse pressures were compared with those of test results as shown in Table 6.3. The mean of bias between test results over predicted results is 1.026. Furthermore, the comparison of proposed formulation results and the test results is plotted in Fig. 6.9. The collapse pressure was non-dimensionalised with the yield pressure. It is evident that the mean of X_m is 1.026, together with COV of 2.81%. This accuracy is very good for design formulations to predict the residual strength of damaged ring-stiffened cylinders subjected to hydrostatic pressure.

Table 6.3 Comparison of the proposed formulation results with the test results.

	RS-I	RS-C-1	RS-C-2	RS-II	RS-C-3	RS-C-4
Test result, P_c (MPa)	2.16	1.40	1.65	2.41	1.90	1.80
Proposed formulation, P_c (MPa)	2.17	1.35	1.55	2.40	1.89	1.72
Bias (Test/Prop. formulation), X_m	0.995	1.037	1.068	1.004	1.006	1.048

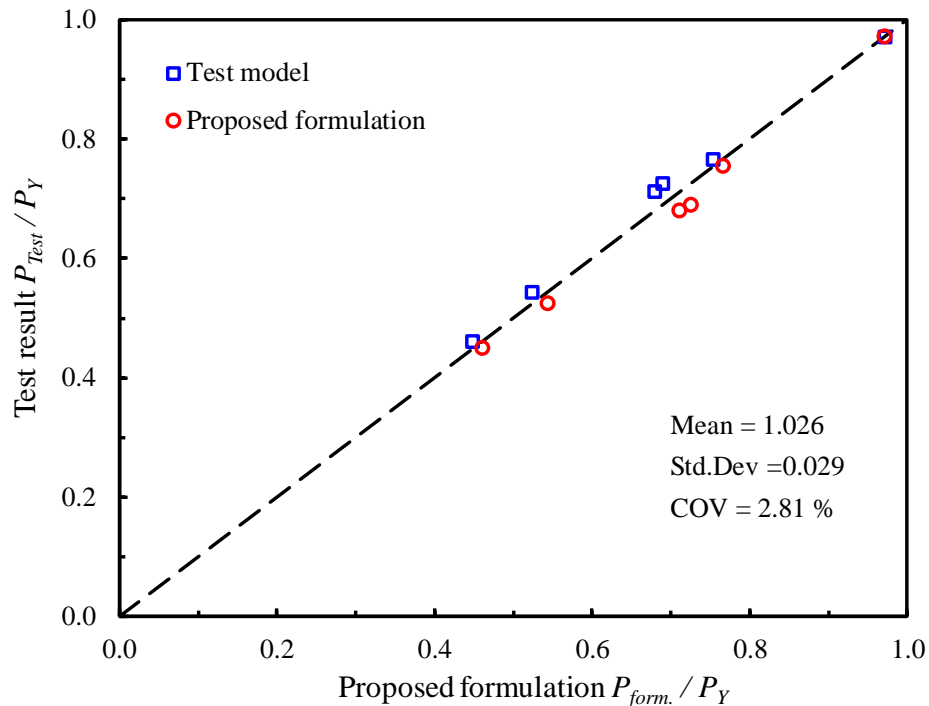


Fig. 6.9 Proposed formulation results compared to test results for predicting residual strength of model under hydrostatic pressure.

6.2.5 Results and discussion

From the numerical results, it is considered that a good accuracy was achieved between the predicted and experimental results for both the collision and residual strength analyses. The mean of the uncertainty modelling factor X_m , of 1.007, tends to unity, together with a COV of 2.84%. It means that the effects of the cold-bending and welding residual stresses and initial shape imperfections, along with the strain-rate hardening, were satisfactorily considered in the finite element modelling. Therefore, the reasonable accuracy and reliability of the proposed nonlinear numerical prediction allow its adoption to perform further parametric studies in order to develop the design formulations.

The formulation to predict the residual strength of damaged ring-stiffened cylinder structures subjected to hydrostatic pressure was also proposed. If the dent depth is known, the reduction factor R_u is quickly predicted by using the proposed equation (6.10). Then, this factor can be multiplied with the collapse pressure of intact cylinders, which is calculated by equation (6.1), to obtain the collapse pressure of the damaged cylinders. Furthermore, the accuracy of the proposed formulation is good when compared to the available test data from the author, with X_m mean of 1.026 and COV of 2.81%. However, the application of the formulas provided by this study is possibly restricted to a range of R/t from 97 to 454 and a range of dent depth to radius d/R from 0 to 0.25. Nevertheless, it is suggested that in future study these proposed formulations may be used for code calibrations, which require simple formulations. Therefore, they can be useful for the purposes of design and serviceability limit state assessment of ring-stiffened cylinders under the risk conditions of marine structures.

6.3. Stringer-stiffened cylinder

6.2.1 Description of test data

In this section, the simple proposed formulation was derived by a series numerical analysis results of rigorous parametric studies on the actual design of full-scale stringer-stiffened cylinder examples as mentioned in section 3.5.2 in Chapter 3. After generating the damages by the dynamic mass impact, these models were subsequent to collapse analysis. The aim of this collision analysis was to obtain an initial geometric deformation, defined with a single parameter, namely the dent depth, for the subsequent collapse analysis. The dimensions and material properties of the model are listed in Table 6.4.

6.2.2 Failure mode equation for intact case

For the formulations to predict the ultimate strength of the intact stringer-stiffened cylinder under hydrostatic pressure, the formulations provided by API were used. The detail of formulations is explained as follows:

$$P_c = \eta P_{eL} \quad (6.12)$$

$$P_{eL} = \frac{Et/R}{n^2+k\lambda^2-1} \left[\frac{(n^2+\lambda^2-1)}{12(1-\nu^2)} \left(\frac{t}{R}\right)^2 + \frac{\lambda^4}{(n^2+\lambda^2)^2} \right] \quad (6.13)$$

$$\lambda = \pi R/L_p \quad (6.14)$$

$$\eta = \begin{cases} 1 & \text{if } \Delta \leq 0.55 \\ \frac{0.45}{\Delta} + 0.18 & \text{if } 0.55 < \Delta \leq 1.6 \\ \frac{1.31}{1+1.15\Delta} & \text{if } 1.6 < \Delta < 6.25 \\ \frac{1}{\Delta} & \text{if } \Delta \geq 6.25 \end{cases} \quad (6.15)$$

$$\Delta = \frac{\sigma_{iej}}{\sigma_Y} \quad (6.16)$$

$$\sigma_{iej} = \alpha_{\theta L} \frac{P_{eL} R_0}{t} K_{\theta L} \quad (6.17)$$

$K_{\theta L} = 1$ if $M_x \geq 3.42$. When $M_x \leq 3.42$ determine $K_{\theta L}$ from Equation (6.15)

$$K_{\theta L} = \begin{cases} 1.0 & \text{for } M_x \geq 3.42 \\ 1 - \varepsilon \Psi & \text{for } M_x \leq 3.42 \end{cases} \quad (6.18)$$

$$\varepsilon = \frac{1-0.3k}{1+L_e t/A} \quad (6.19)$$

$$A = A_r (R/R_r)^2 \quad (6.20)$$

$$M_x = L_r / \sqrt{Rt} \quad (6.21)$$

$$\Psi = \begin{cases} 1.0 & \text{for } M_x \leq 1.26 \\ 1.58 - 0.46M_x & \text{for } 1.26 < M_x \leq 3.42 \\ 0 & \text{for } M_x \geq 3.42 \end{cases} \quad (6.22)$$

$$L_e = 1.56\sqrt{Rt} + t_w \leq L_r \quad (6.23)$$

Where

P_c : collapse pressure;

η : plasticity reduction factor for non-stress relieved shells.

P_{eL} : failure pressure for local buckling mode.

$k = 0.5$ for hydrostatic pressure loading.

n : number of waves into which the shell will buckle in the circumferential direction. It is obtained at the minimum pressure value.

L_p : unsupported length of shell between rings

σ_{iej} : elastic shell buckling stress for fabricated shell

R_r : radius to centroid of stiffening ring

A_r : cross-sectional area of one ring stiffener

t_w : thickness of web of ring stiffener

θ : hoop direction

Ψ : partial safety factor

Table 6.4 Properties of the reference stringer-stiffened cylinders.

Sym.	Unit	SS-1	SS-2	SS-3	SS-4	SS-5	SS-6
R	mm	3025	13320.0	4200	3025	2500	8880
t	mm	19.0	41.5	20.0	12.0	15	25.0
L	mm	10240	17500.0	10500	10240	11250	6600
L_s	mm	2048.0	3500.0	3500	2048	2250	2200
n_r	[-]	4.0	4.0	12.0	4.0	4.0	2.0
h_{rw}	mm	214.0	787.5	700	214.0	190.00	525
t_{rw}	mm	20.0	37.5	12.0	15.0	20	25.0
w_{rf}	mm	200.0	450.0	300	200	150	300
t_{rf}	mm	20.0	45.0	16.0	15.0	20	30.0
n_s	[-]	18.0	36.0	36	18.0	20	60.0
h_{sw}	mm	160.0	450.0	250.0	160.0	150	300
t_{sw}	mm	15.0	37.5	12.0	11.5	20	15.0
w_{sf}	mm	100.0	285.0	90.0	100.0	100	190.0
t_{sf}	mm	15.0	45.0	12.0	11.5	20	19.0
σ_Y	MPa	276.0	345.0	355	276	380	345
E	GPa	205000	206000	206	205000	206000	200000
R/t	[-]	159	321	210	263	167	355

6.2.3 Failure mode formula for damage case

The procedures to derive the formulations for predicting the residual strength of stringer-stiffened cylinder under dynamic mass impact are similar to ring-stiffened cylinders in the previous section. Series of finite element analysis was carried out to evaluate the effect of the dent depth on the reduction in ultimate strength under hydrostatic pressure. The residual strength of stringer-

stiffened cylinders was derived as equation (6.24). After the dependent parameters were investigated, the regression analysis was performed with the best-fit evaluation of the numerical results. The best-fit curve from the proposed equation numerical data is plotted in Fig. 6.10. The accuracy of the best-fit curve was quite good, with a mean of the uncertainty modelling factor (X_m) of 1.01 together with a COV of 3.30 %. The other form of the equation was also derived with a mean of X_m of 1.01 and COV of 3.6%, as illustrated in Eq. (6.25).

$$R_u = \frac{P_{dam}}{P_{in}} = \text{Exp}(-1.796\delta_d) \quad ; \text{Mean equation} \quad (6.24)$$

$$R_u = \frac{P_{dam}}{P_{in}} = 1.246(\delta_d^2) - 1.773(\delta_d) + 1 \quad (6.25)$$

$$R_u = \frac{P_{dam}}{P_{in}} = \text{Exp}(-0.058 - 1.796\delta_d) \quad ; \text{Characteristic equation} \quad (6.26)$$

The skewness of the ratios of numerical analysis results to proposed formulation results (X_m) with basic parameters are shown in Figs. 3.82, 3.83, and 3.84. The skewness of the X_m ratio shows no sharpness trend line. Therefore, the proposed formula provides adequate prediction since it is shown to have less effect on the basic parameters.

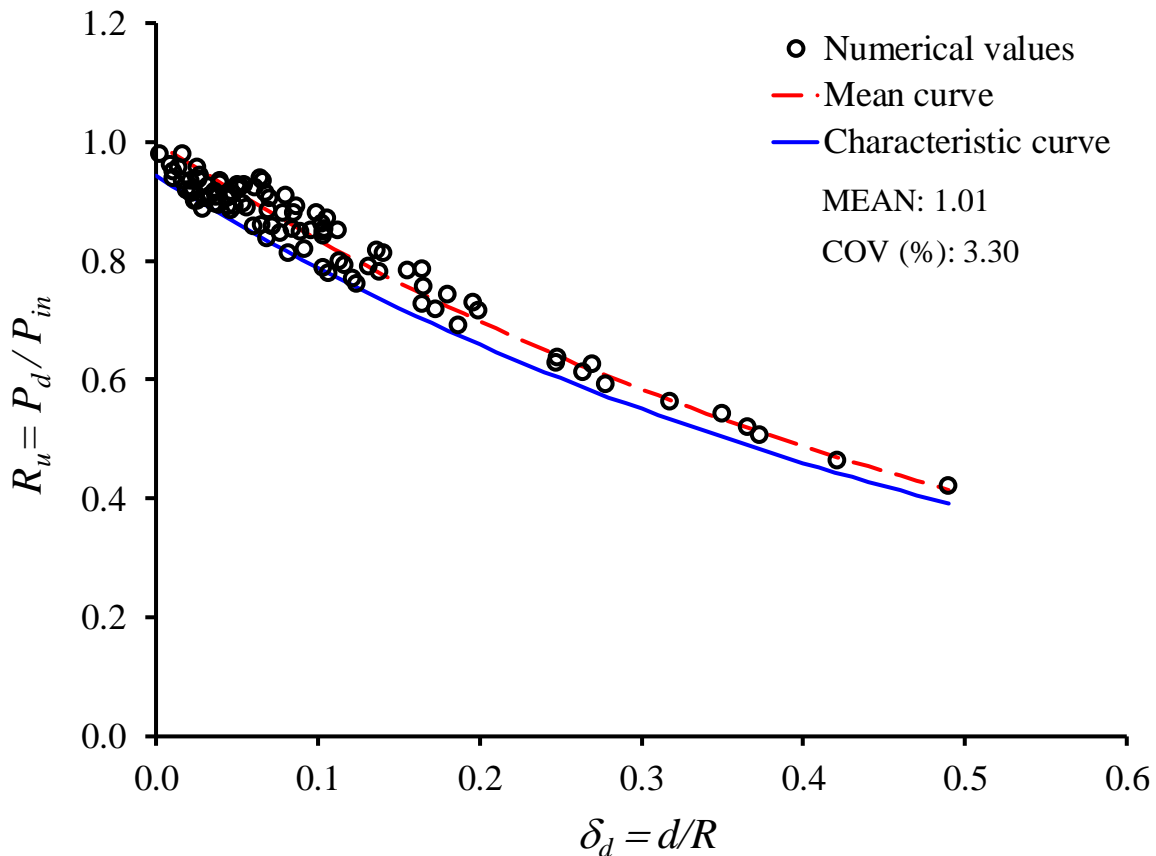


Fig. 6.10 Best-fit curve to predict the residual strength for stringer-stiffened cylinder.

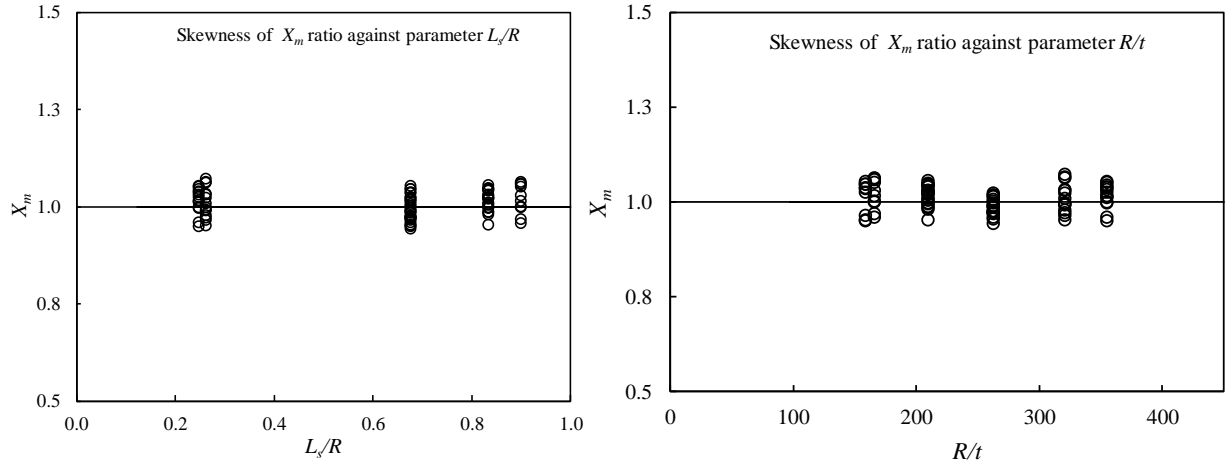


Fig. 6.11 Plotting of the proposed formula against basic parameters L_s/R and R/t .

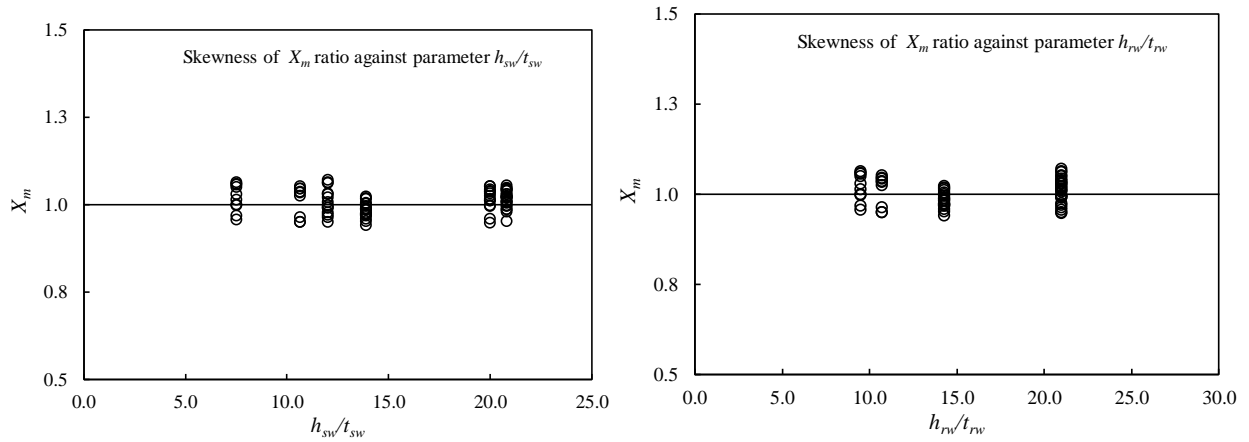


Fig. 6.12 Plotting of the proposed formula against basic parameters h_{sw}/t_{sw} and h_{rw}/t_{rw} .

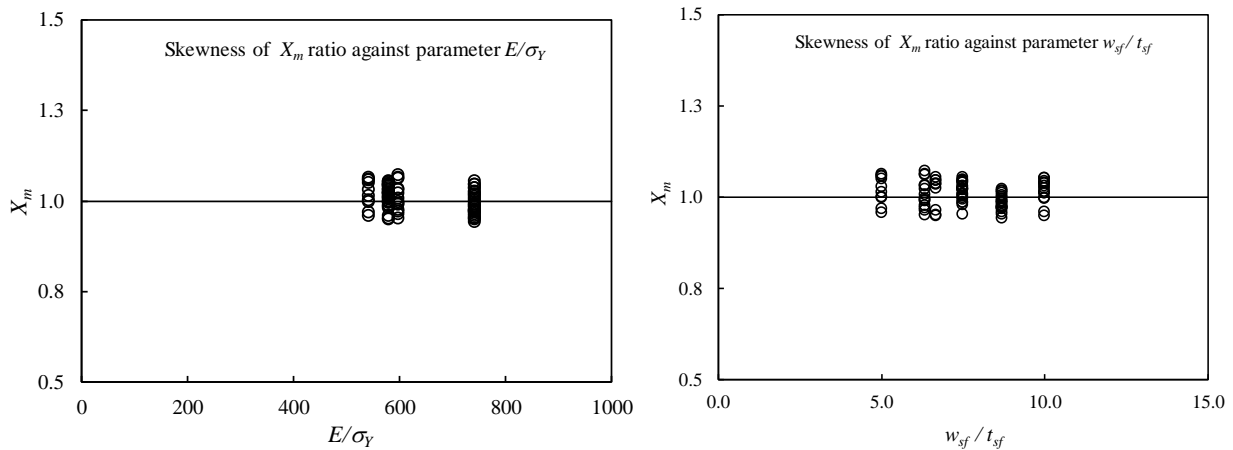


Fig. 6.13 Plotting of the proposed formula against basic parameters E/σ_Y and w_{sf}/t_{sf} .

6.2.4 Accuracy of the proposed formulation

To validate the accuracy of proposed formulation for residual strength prediction, the predicted collapse pressures were compared with those of test results from author as shown in Table 6.5. The mean of bias between test results over predicted results is 1.016. Actually, the number of tests is quite small for validating. Therefore, it needs more experimental work of string-stiffened cylinder under hydrostatic pressure.

Table 6.5 Comparison of the proposed formulation results with the test results.

	SS-I	SS-C-1	SS-C-2
Test result, P_c (MPa)	0.86	0.83	0.85
Proposed formulation, P_c (MPa)	0.91	0.81	0.79
Bias (Test/Prop. formulation), X_m	0.945	1.029	1.076

6.2.5 Results and discussion

The formulation to predict the residual strength of dented stringer-stiffened cylinder structures subjected to hydrostatic pressure was also proposed. If the dent depth is known, the reduction factor R_u is quickly predicted by using the proposed equations (6.23) or (6.24). Then, this factor can be multiplied with the collapse pressure of intact cylinders, which is calculated by equation (6.11), to obtain the collapse pressure of the damaged cylinders. In equation (6.11), the collapse pressure of the intact stringer-stiffened cylinder was calculated according to formulations which provided by API. Furthermore, the accuracy of the proposed formulation is good when compared to the numerical value with X_m mean of 1.01 and COV of 3.30%.

6.4. Final remarks

In this chapter, simple design equations to predict the residual strength of both ring- and stringer-stiffened cylinder under hydrostatic pressure were proposed. These equations have been validated with reliable experimental models provided by the authors. These equations have a very good accuracy, are reliable according to the available test data, and are convenient to use for the purposes of initial design and serviceability limit state assessment of ring- and stringer-stiffened cylinders under the risk conditions of marine structures.

Based on the results of the present study, it is recommended that more advanced and optimal structural designs should be considered in a further parametric study for improving the ultimate strength of stiffened cylinder structures against ship collisions and hydrostatic pressure loadings.

Chapter 7 Residual strength formulations of damaged ring- and stringer-stiffened cylinders under combined axial compression and radial pressure

7.1 Introduction

This Chapter focuses on the load-carrying behavior of damaged ring- and stringer-stiffened cylinders which are typical components of the main legs of tension leg platforms, spars and more recently as buoyancy columns of floating offshore wind turbine foundations subjected to combined axial compression and radial pressure. The case considered in this study corresponds to the residual strength assessment of floating offshore structural columns with damage resulting from collisions with floating subjects or support vessels. A typical damaged column of a platform is shown in Fig. 7.1. Eight small scales ring-stiffened and six stringer-stiffened cylinder models are analysed for validating the numerical techniques. The denting and collapse processes were simulated using Abaqus FEA software package, and a close agreement between the test results and numerical predictions was achieved. Next, based on the regression analysis of the results of a rigorous parametric study on actual design example full-scale stiffened cylinders, the residual strength formulations are derived to predict the residual strength of ring- and stringer-stiffened cylinder under combined loadings.

As mentioned in Chapter 2, there are only a few studies focused on the residual strength of a damaged stiffened cylinder. And there is a limited database of experiments (Ronalds and Dowling [112]; Harding and Onoufriou [104] Walker et al. [49-50]; and research work (Smith and Creswell [36]; Amante et al. [225]; Maddalena et al. [226]). Additionally, recently, there are no rules or design codes which provide any comprehensive guideline to cover the effects of damage on the ultimate strength of stiffened cylinders. Experimental studies may difficulties and costly. Thus, besides its economic efficiency, a carefully performed finite element analysis, validated with reliable test data, could be the most effective way for evaluating the residual strength of damaged ocean engineering structures.



Fig. 7.1 Damaged platform column [225].

7.2 Validation of numerical modeling technique

7.2.1 Description of test data

Fourteen fabricated small scale ring- and stringer-stiffened cylinder models are analysed. Among them eight ring-stiffener cylinder models were reported by Harding and Onoufriou (1995) [104] in the UK. In these experiments the models were artificially dented and subsequently loaded axially in order to determine their residual load carrying capacity. Internal transducers measured the relative displacement of the two end plates in contact with the model, so that the end-shortening can be inferred. The load was applied in small increments and the step size was reduced as the collapse is approached to ensure that nonlinearity in the response and the peak load was accurately measured. The depth of dent in each model is different. Furthermore, Ronalds et al. [112] conducted quasi-static denting tests on four small-scale stringer-stiffened cylinders with lateral loading at mid-span, denoted by 3B1, 3B2, 3B3, and 3B4. Then, these models were subsequently loaded axially until collapsed. All specimens had flat-bar ring-stiffeners dividing the specimens into three bays, which were stiffened in the longitudinal direction by 40 (3B1, 3B2) and 20 (3B3, 3B4) stringer stiffeners, respectively. Other two models R5 and R6 were provided by Walker & McCall (1988) [50] in University of Surrey, UK. This research was to investigate the collapse behavior of the shells subjected to simulated damage and then tested under a combination of external pressure and axial compressive loading. The dimensions and material properties for each model are given in Tables 7.1 and 7.2.

Table 7.1 Properties of the ring-stiffened cylinder models.

		CY-2	CY-3	CY-4	CY-5	CY-6	CY-7	CY-8	CY-9
Radius (mm)	R	160	160	160	160	160	160	160	160
Thickness (mm)	t	0.6	1.2	1.2	0.6	1.2	1.2	0.6	0.6
Total length (mm)	L	200	200	400	400	400	320	96	96
Ring-stiffener spacing (mm)	l	40	40	80	80	80	80	24	24
Yield stress (MPa)	σ_Y	344	342	324	349	324	352	376	376
Elasticity modulus (GPa)	E	201	201	201	201	201	201	201	201
Number of rings	N_r	5	5	5	5	4	4	4	4
Ring-stiffener web height (mm)	h_{rw}	4.8	6.72	4.8	4.8	3	3	3	3
Ring-stiffener web thickness (mm)	t_{rw}	0.6	0.84	0.6	0.6	0.6	0.6	0.6	0.6
Ring-stiffener flange width (mm)	d_f	0	0	0	0	4	4	6	6
Ring-stiffener flange thickness	t_{fj}	0	0	0	0	0.6	0.6	0.84	0.84

Table 7.2 Properties of the orthogonally stiffened cylinder specimens.

Model		3B1	3B2	3B3	3B4	R5	R6
Radius (mm)	R	160	160	160	160	160	160
Thickness (mm)	t	0.6	0.6	0.6	0.6	0.6	0.6
Total length (mm)	L	319	319	319	319	288	288
Inner bay length (mm)	l_{r2}	96	96	96	96	96	96
Outer bay length (mm)	l_{r1}	112	111.5	111.5	111.5	96	96
Yield stress (MPa)	σ_Y	332	332	332	332	387	387
Elasticity modulus (GPa)	E	211	211	211	211	208	208
Number of stringers	N_s	40	40	20	20	40	20
Stringer web height (mm)	h_{sw}	4.8	4.8	4.8	4.8	4.8	4.8

7.2.2 Finite element modeling

The processes of collision damage and collapse under axial compression and radial pressure were numerically simulated using Abaqus FEA software package. The collision was simulated using dynamic/explicit method, while the collapse process was simulated using the modified static Riks method.

In the numerical analysis the shell and ring or stringer stiffeners were modeled with four-node curved shell elements (Abaqus S4R). The elements have hourglass control and reduced integration. Thickness integration was performed using the Simpson rule with five integration points through the thickness. The knife-edge striker was assumed to be rigid and R3D4 element was employed for the striker. The contact between the indenting surface and the struck model was defined using the general contact option in Abaqus, which allows defining the model contact regions with a single interaction. This contact algorithm uses a penalty method as the contact

constraint. The convergence test was performed by changing the mesh sizes of the modeling to select the optimum ones. The global mesh size was determined as 2 mm x 2mm for model all models.

As in the actual tests, the simulations consisted of two steps: first, inducing damage and second, post-damage collapse analysis. The boundary conditions were shown in Fig. 7.2. It is noted that the same numerical techniques are applied for both ring- and stringer-stiffened cylinder. In addition, before performing the first analysis step, initial imperfections were inputted into the models. The best solution is inputted directly measurement imperfection values into modeling models. Because this data not only considering local buckling mode but also including overall buckling mode. Therefore, the collapse shapes were correlated between numerical and experimental results. However, if the measurement imperfection data did not provide, it could be used some formulations and assumptions to determine the imperfection magnitudes. For this goal, it was performed using eigenvalue buckling analyses. In general, the first eigenvalue buckling mode was selected as the initial imperfection shape. In the eigenvalue buckling analysis, fixed boundary conditions at both cylinder ends were assumed. These values were considered when determining the imperfection magnitude associated with the eigenvalue buckling mode.

7.2.3 Validation of numerical method

The test results and the numerical analysis are presented in Table 7.3. The accuracy of the numerical analysis is given as the ratio of The accuracy of the numerical analysis is given as the ratio of the experimental results and numerical results, namely, X_m (modelling uncertainty factor). The mean of modeling uncertainty factor is 0.971, and there is a small COV of 5.99 % by indicating in Table 7.3. In addition, the comparison of force-displacement curves obtained from experimental and numerical results for stringer-stiffener cylinders is indicated in Fig. 7.3. The collapse patterns are also captured well for stringer- and ring-stiffened cylinder as shown in Fig. 7.4 and 7.5, respectively. This further suggests that numerical model is able to progressive collapse behavior of damaged ring- and stringer-stiffened cylinders and can be used to in detailed investigations and parametric studies.

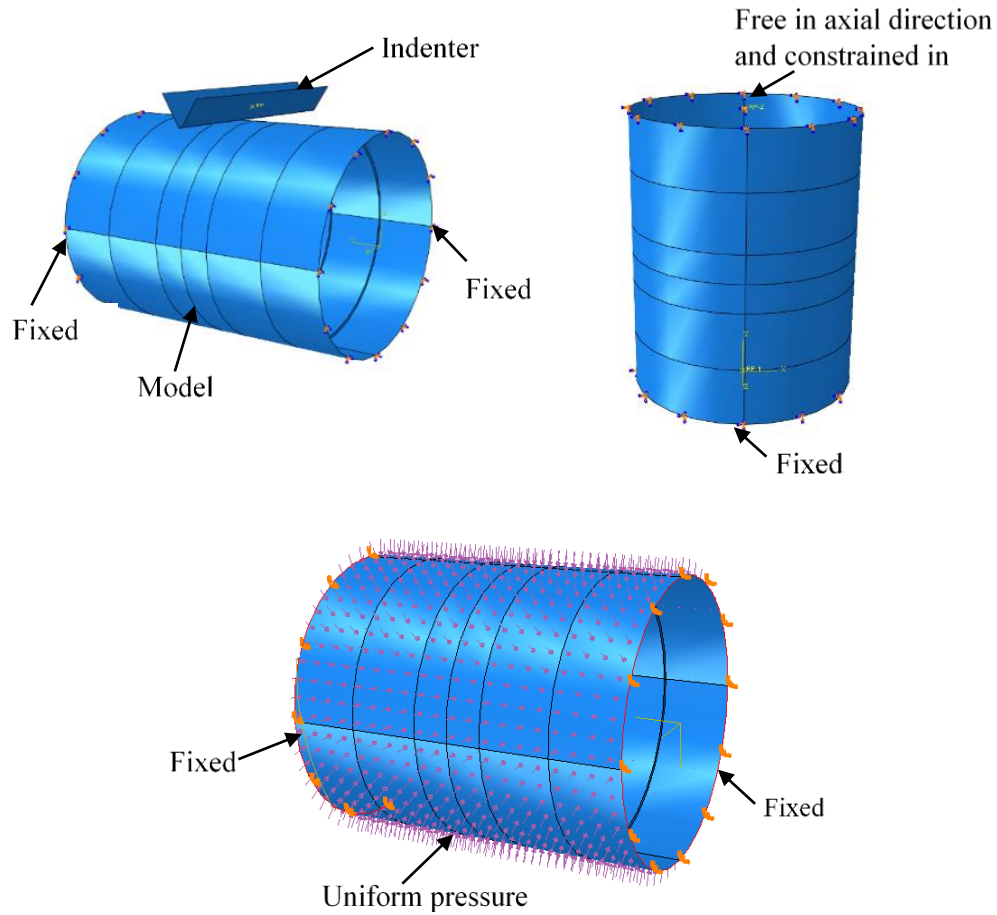


Fig. 7.2 Finite element analysis setup for inducing damage to specimens and post-damage collapse analysis.

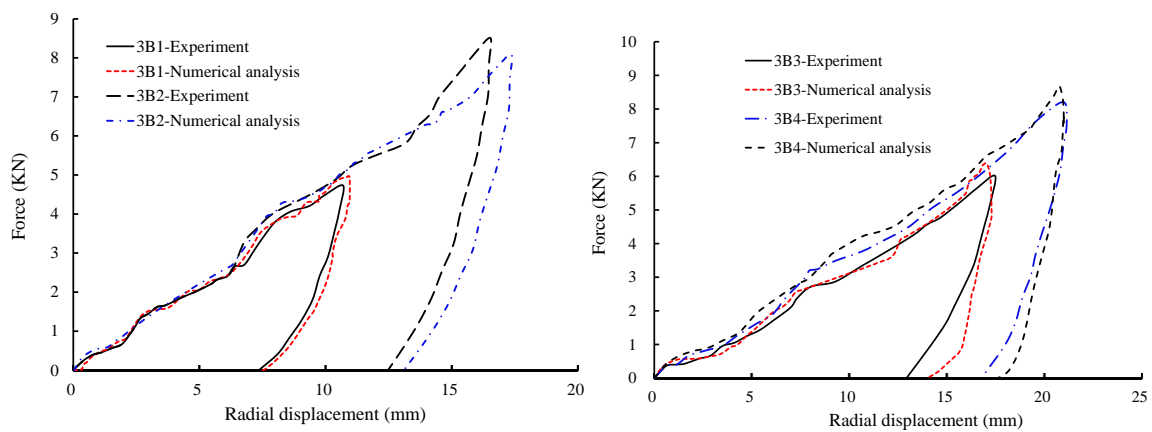


Fig. 7.3 Comparison of force-displacement curves obtained from experimental and numerical results.

Table 7.3 Comparison of experimental results with numerical results.

Model	Experimental result (Mpa)	Numerical result (Mpa)	Ratio X_m (Exp./Num.)
CY-2	271.8	276.9	0.982
CY-3	266.8	289.2	0.922
CY-4	268.9	283.9	0.947
CY-5	212.9	215.7	0.987
CY-6	257.6	281.7	0.915
CY-7	253.4	268.2	0.945
CY-8	225.6	252.8	0.892
CY-9	229.4	251.7	0.911
3B1	318.0	311.5	1.021
3B2	277.0	282	0.982
3B3	202.0	209.5	0.964
3B4	195.0	201.7	0.967
R5	0.36 (P_c)	0.33	1.091
R6	0.30 (P_c)	0.28	1.071
	Mean		0.971
	COV		5.99 %

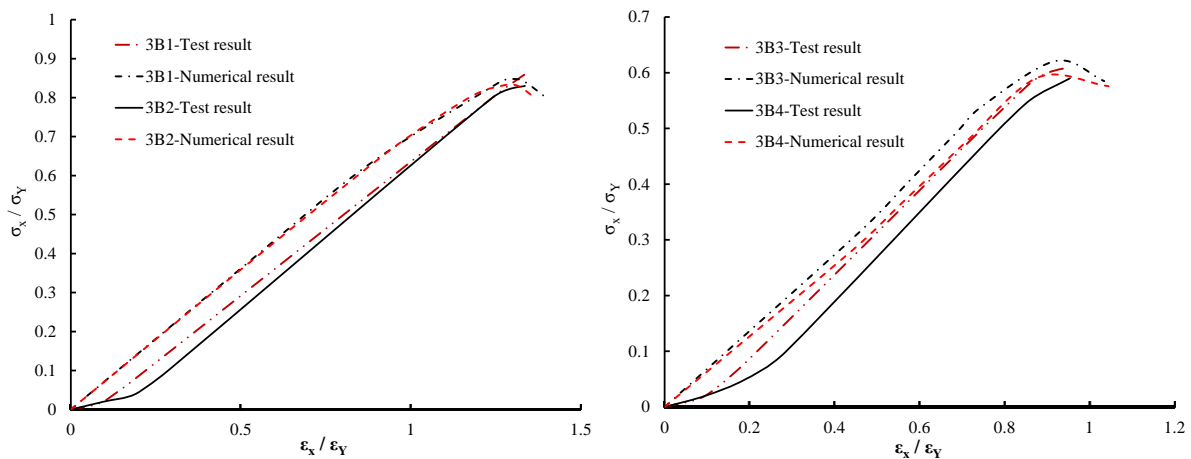
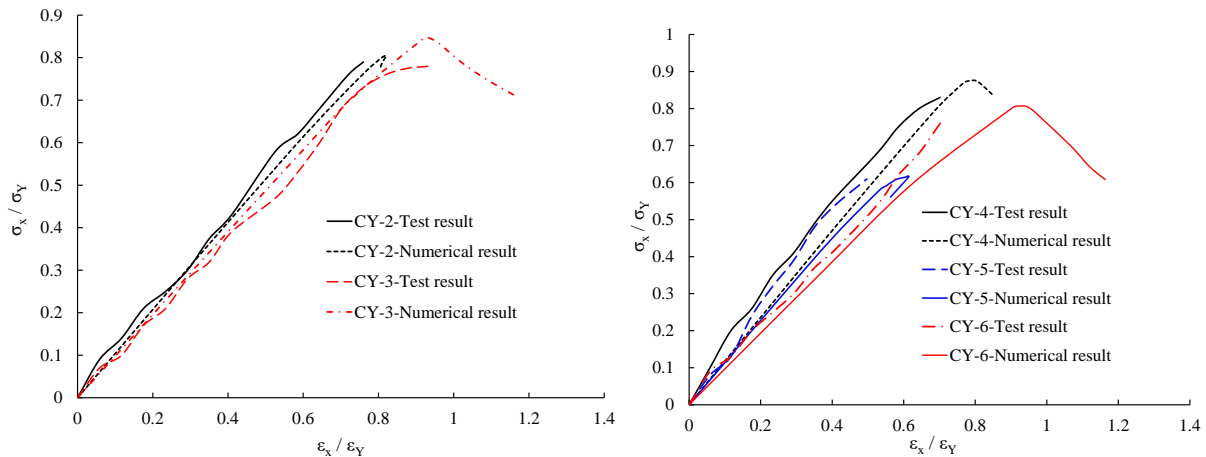


Fig. 7.4 Axial shortening curves for damaged stringer-stiffened cylinder models.



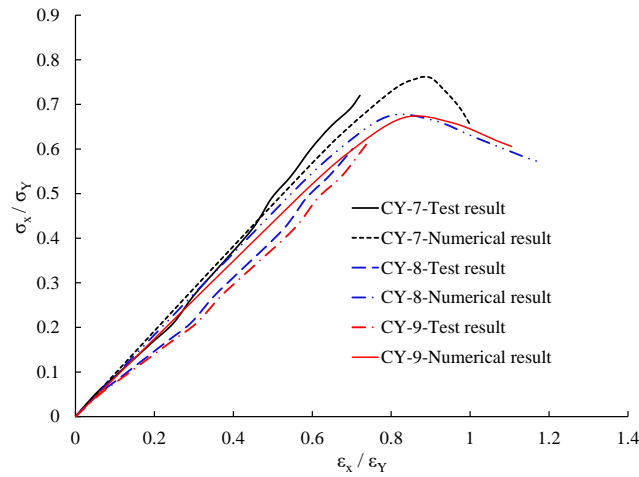


Fig. 7.5 Axial shortening curves for damaged ring-stiffened cylinder models.

7.3. Ring-stiffened cylinder

7.2.1 Description of numerical model

In this section, a series of finite element analyses were performed on the design example of a ring-stiffened cylinder of an actual submarine design concept and on other rings-stiffened cylinders given in the ABS rules [177]. The dimensions and material properties of the model are listed in Table 6.1 in Chapter 6. For each model, a series of finite element analyses in which the dent depth varied were conducted. To generate damages on the models, a collision analysis was conducted using a rigid knife-edge indenter. A total of 600 numerical cases were performed including 150 collision analyses and 450 residual strength analyses. The finite element models were generated with the techniques explained in the previous section. The global mesh size was 80 mm, while the local mesh size was 40 mm. The range of R/t (radius of cylinder/shell thickness) was determined from 97 to 454, and the range of dent depth to radius d/R from 0 to 0.25.

7.2.2 Ultimate strength formulations of intact ring-stiffened cylinder

For prediction of the ultimate strength of intact ring-stiffened cylinders under combined axial compression and radial pressure, the design formulations proposed from Cho et al. [227] were used. This equation has a quite good accuracy when compared to the 30 available test models, with X_m (ratios of actual to predicted results) mean of 1.028 together with COV of 7.9 %. This COV is

acceptable to predict the ultimate strength of ring-stiffened cylinder under combined loadings. The formulations are given in Eq. (7.1).

$$\left(\frac{\sigma_x}{\rho_x \sigma_{xcr}} + \frac{\sigma_\theta}{\rho_\theta \sigma_{\theta cr}}\right)^2 + \left(\frac{\sqrt{\sigma_x^2 - \sigma_x \sigma_\theta + \sigma_\theta^2}}{\sigma_Y}\right)^2 = 1 \quad (7.1)$$

where

$$\rho_x = 0.281 + 19.2X^{-0.518}; \text{ axial compression elasto-plastic knockdown factor} \quad (7.2)$$

$$\rho_\theta = 0.833 + 3510X^{-1.13}; \text{ radial pressure elasto-plastic knockdown factor} \quad (7.3)$$

$$X = \sqrt{Z} \left(\frac{E}{\sigma_Y}\right),$$

$$Z = \frac{\sqrt{1-\nu^2}}{Rt} L^2; \text{ Batdorf slenderness parameter} \quad (7.4)$$

$$\sigma_\theta = \frac{P_r R}{t} (1 - \gamma' G); \text{ average hoop stress at mid-bay} \quad (7.5)$$

$$P_r = \frac{\sigma_\theta t}{R(1-\gamma' G)}; \text{ collapse radial pressure} \quad (7.6)$$

R : shell mean radius

R_s : radius of centroid of ring-frame

$$G = 2\{\sinh(\alpha L/2)\cos(\alpha L/2) + \cosh(\alpha L/2)\sin(\alpha L/2)\} / \{\sinh(\alpha L) + \sin(\alpha L)\} \quad (7.7)$$

$$\gamma' = \frac{A(1-\frac{mv}{2})}{(A+bt)(1+B)}; \quad m = \frac{P_x}{P_r}$$

$A = A_s(R/R_s)^2$; modified ring-frame area; A_s is cross-sectional area of ring-frame.

$$B = 2tN/\alpha(A+bt);$$

$$N = \{\cosh(\alpha L) - \cos(\alpha L)\} / \{\sinh(\alpha L) + \sin(\alpha L)\} \quad (7.8)$$

b : width of ring-frame in contact with shell

$$\alpha L = 1.285 L \sqrt{Rt}$$

σ_Y : static tensile yield stress

σ_x : axial compressive stress

$$\sigma_{xcr} = 0.605Et/R$$

$$\sigma_{\theta cr} = \frac{P_{rm} R}{t} (1 - \gamma'' G); \text{ elastic buckling strength of ideal shell structure under radial pressure} \quad (7.9)$$

$$P_{rm} = \frac{1.4E}{\sqrt{3(1-\nu^2)}} \frac{\left(\frac{t}{R}\right)^2}{\sqrt{Z}}; \text{ von Mises shell buckling pressure under radial pressure alone} \quad (7.10)$$

$$\gamma'' = \frac{A}{(A+bt)(1+B)} \quad (7.11)$$

7.2.3 Deriving residual strength formulations of damaged ring-stiffened cylinder

The Fig. 7.6 illustrates the collapsed shape between an intact case and damaged case with $d/R = 0.03$. It is clear that the collapsed shape of the intact model seems to be symmetry while that of damaged model is asymmetry. Next, Fig. 7.7 shows the pressure versus radial displacement of the center point in dent zone varying the ratio of dent depth over radius d/R . It is observed that the effect of local damage is significant with considerable loss in stiffness and reduction in load carrying capacity. With an increase in dent depth a gradual decrease in ultimate strength is noticeable. The ultimate strength interactive curves for damaged ring-stiffened cylinder under combined loading are shown in Fig. 7.8. For combined loading is performed by keeping the radial pressure constant at several values and applying axial compression until collapsed.

To find a suitable dependent parameter on which to derive reduction ultimate strength R_u , first the relations between R_u and various appropriate non-dimensional geometric and material property parameters (L/R , R/t , d/R and L/t as geometric parameters, E/σ_Y as a material parameter). It was also using combinations of variables as Z ($Z = \left(\frac{L^2}{Rt}\right) / \sqrt{1-\nu}$: Batdorf slenderless parameter), $\sqrt{Z} \cdot \frac{E}{\sigma_Y}$ and $\frac{\sqrt{Lt}}{R} \frac{E}{\sigma_Y}$. The results show that the d/R ratio (dent depth/radius) was the strongest influence on $R_{ux,r}$. The best-fit curve for predicting the residual strength of ring-stiffened cylinder is depicted in Fig. 7.9. Based on the results above a closed-form formula may be derived empirically by regression analysis to predict the reduction factor $R_{ux,r}$ as Eq. (7.12). The accuracy of the proposed formulation to predict the residual strength of damaged ring-stiffened cylinders was quite good, with X_m (ratio of num./prop. values) of 0.986 together with COV of 3.80 %.

$$R_{ux,r} = \frac{\sigma_{xd,r}}{\sigma_{xin,r}} = \text{Exp} \left(-4.95 \frac{d}{R} \right) \quad ; \text{ Mean equation} \quad (7.12)$$

$$R_{ux,r} = \frac{\sigma_{xd,r}}{\sigma_{xin,r}} = \text{Exp} \left(-0.093 - 4.95 \frac{d}{R} \right) \quad ; \text{ Characteristic equation} \quad (7.13)$$

By substituting σ_x of the intact case from Eq. (7.1), the axial compression residual strength of damaged ring-stiffened cylinder can be obtained by Eq. (7.14).

$$\sigma_{xd,r} = \text{Exp} \left(-4.95 \frac{d}{R} \right) \left[\frac{\left(\sqrt{\frac{-3\rho_\theta^2 \rho_x^2 \sigma_\theta^2 \sigma_{\theta cr}^2 \sigma_{xcr}^2 + 4\rho_\theta^2 \rho_x^2 \sigma_\theta^2 \sigma_{\theta cr}^2 \sigma_{xcr}^2 \sigma_Y - 4\rho_\theta^2 \sigma_\theta^2 \sigma_{\theta cr}^2 \sigma_Y + 4\rho_\theta^2 \sigma_\theta^2 \sigma_{\theta cr}^2 \sigma_Y^2 - 2\sigma_\theta \sigma_Y + \rho_\theta \rho_x \sigma_\theta \sigma_{\theta cr} \sigma_{xcr}}{-4\rho_\theta^2 \rho_x^2 \sigma_\theta^2 \sigma_{\theta cr} \sigma_{xcr} \sigma_Y + 4\rho_\theta^2 \sigma_\theta^2 \sigma_{\theta cr}^2 \sigma_Y} \right)}{2\rho_\theta \sigma_{\theta cr} (\rho_x^2 \sigma_{xcr}^2 + \sigma_Y)} \right] \quad (7.14)$$

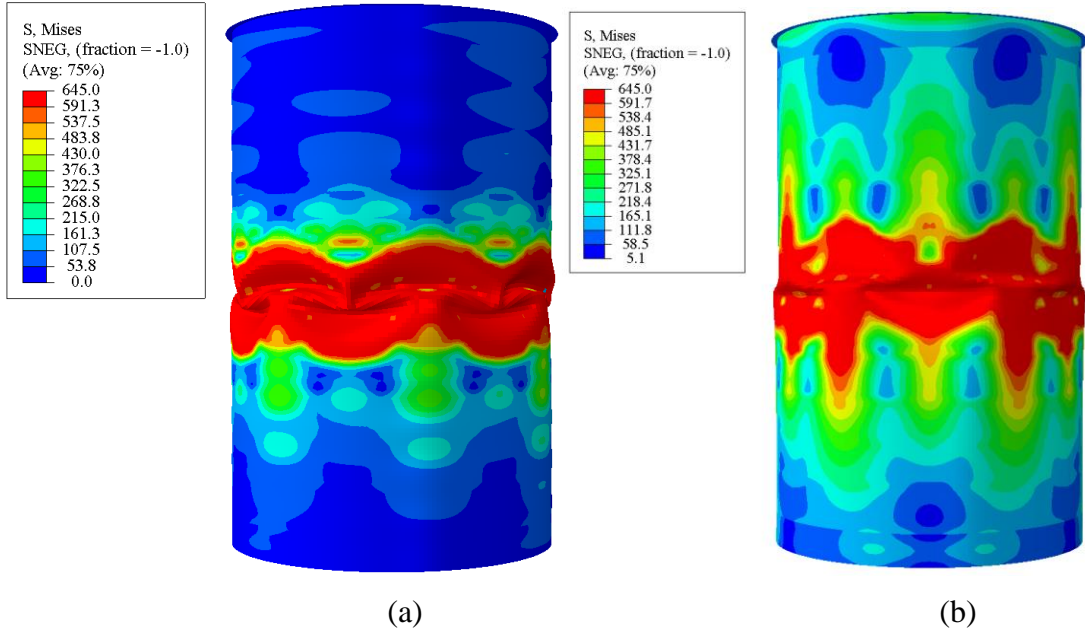


Fig. 7.6 Collapsed shape of ring-stiffened cylinder model ($R/t = 159$) under combined loadings:
(a) intact model; (b) damaged model.

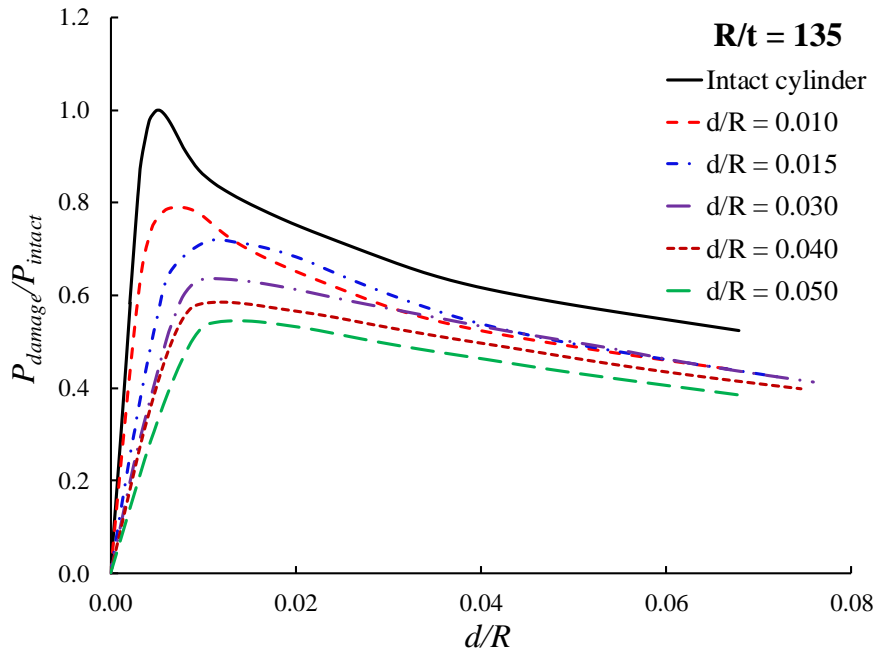


Fig. 7.7 Radial pressure versus displacement curves for the ring-stiffened cylinder model RS-4.

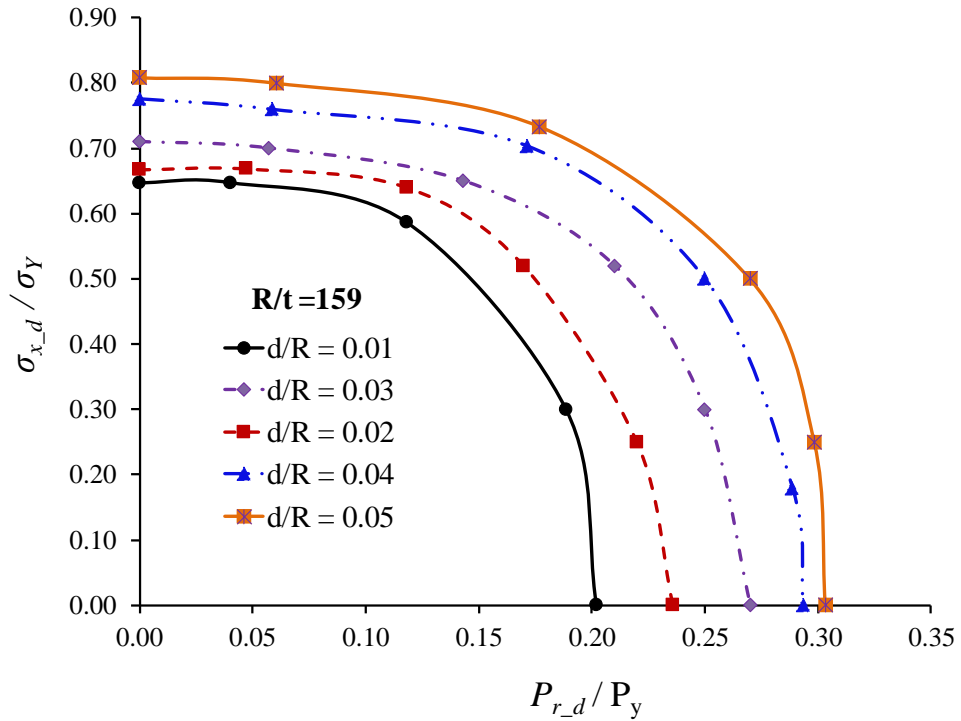


Fig. 7.8 Ultimate strength interaction curves for damaged ring-stiffened cylinders under combined axial compression and radial pressure.

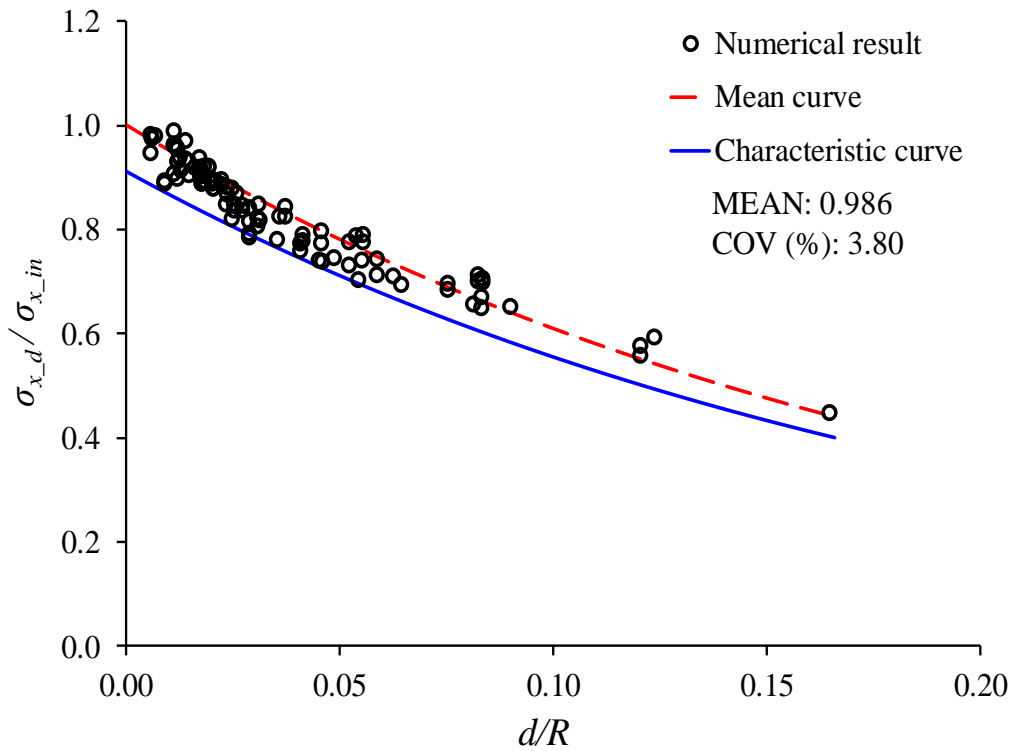


Fig. 7.9 Best-fit curve for prediction of residual strength of ring-stiffened cylinder under combined loading.

7.4. Stringer-stiffened cylinder

7.3.1 Description of numerical model

In this section, the simple proposed formulation was derived by a series numerical analysis results of rigorous parametric studies on the actual design of full-scale stringer-stiffened cylinder examples. The dimensions and material properties of the model are listed in Table 3.20 in Chapter 3. The finite element models were generated with the techniques explained in the previous section. The finite element models were generated with the techniques explained and validated in the previous section. The global mesh size was 100 mm, while the local mesh size was 50 mm. The range of R/t (radius of cylinder/shell thickness) was determined from 159 to 355, and the range of dent depth to radius d/R from 0 to 0.15. Geometry of stringer stiffened cylinder and loadings considered as shown in Fig. 7.10.

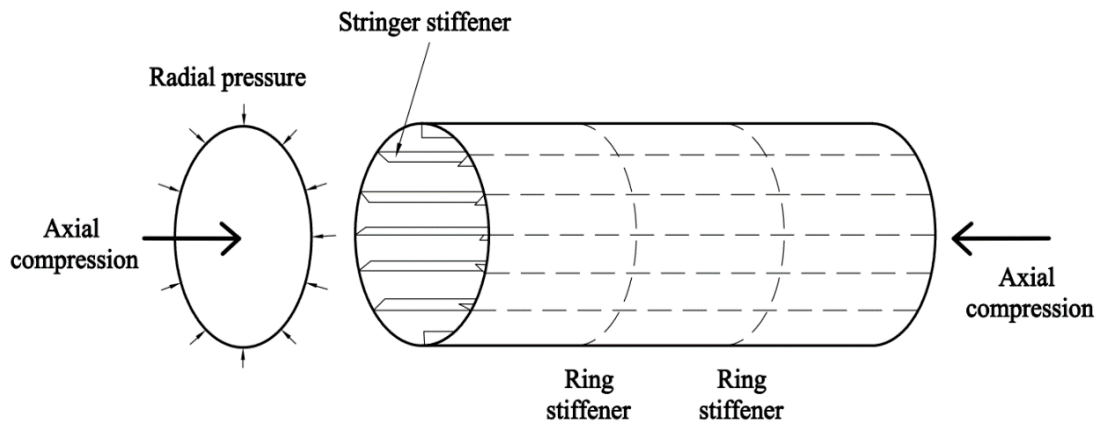


Fig. 7.10 Geometry of stringer stiffened cylinder and loadings considered [227].

7.3.2 Ultimate strength formulations of intact stringer-stiffened cylinder

Most of marine structural members fail in the regime of the interaction between the elastic buckling and yielding. Therefore, any good ultimate strength formulations need to employ inelastic buckling formulae as their basis. Furthermore, for combined loadings more rational treatments are required. For yielding von Mises yield criterion is supported by test results and widely accepted. However, for elastic buckling under combined loads linear interaction of each buckling mode is adopted in some formulations without any verification [228].

In order to accurately predict the ultimate strength of stringer-stiffened cylinders it is necessary to understand its failure mode and then to include all failure modes in the formulation.

The failure modes can be identified as follows: Local shell buckling, stringer/shell collapse between ring frames, stringer tripping, and general instability.

For prediction of the failure mode of intact stringer-stiffened cylinders, the design formulations proposed from Cho et al. [228] were used. These formulations combine all the failure modes of stringer-stiffened cylinders under combined loadings, which are which are presented in equations (7.14). Detailed explanations of the design formulation of intact stringer-stiffened cylinders are included in Cho et al. [228]. These formulations have a fair accuracy when compared to the 90 available test models, with X_m (ratios of actual to predicted results) mean of 1.05 together with COV of 14.3 %. The accuracy of the provided formulations has been compared with those of well-known formulations, such as RCC, API, and DNV formulations. The accuracy of the formula is demonstrated in Table 7.4.

elastic buckling					yielding
$\left(\left\{ \frac{\sigma_x}{\rho_c \sigma_{ec}} + \frac{\sigma_x}{\rho_t \sigma_{et}} + \frac{\sigma_x}{\rho_{oa} \sigma_{oa}} \right\} + \left\{ \frac{\sigma_\theta}{\rho_s C_s (\sigma_{es} + \sigma_{el})} + \frac{\sigma_\theta}{\rho_g (\sigma_{eg} + \sigma_{tr})} \right\} \right)^2 + \left(\frac{\sigma_{eq}}{\sigma_Y} \right)^2 = 1 \quad (7.15)$					
stringer column	stringer tripping	overall column	stringer + shell	general buckling (including ring)	
axial compression			radial pressure		

where

$$\rho_c = 0.2 + 0.4(l/s_e)^{0.3}, \text{ knock-down factor for column buckling of stringer} \quad (7.16)$$

$$\rho_t = 0.122 + 5.9\{A_s/(s_e t)\}^2, \text{ knock-down factor for torsional buckling of stringer} \quad (7.17)$$

$$\rho_{oa} = 0.5, \text{ knock-down factor for overall buckling under axial compression}$$

$$\rho_s = 1.0, \text{ knock-down factor for shell elastic buckling under radial pressure}$$

$$\rho_g = 1.0, \text{ knock-down factor for ring-stiffener buckling under radial pressure}$$

$C_s = 0.5 + 0.03(R/t)^{0.8}$, correction factor for elastic buckling of stringer-stiffened cylinder under radial pressure.

$$\sigma_{eq} = \sqrt{\sigma_x^2 + \sigma_x \sigma_\theta + \sigma_\theta^2}, \text{ von Mises equivalent stress} \quad (7.18)$$

$$\sigma_{ec} = \sigma_e + 0.75\sigma_s, \text{ elastic column buckling stress for stringer and shell} \quad (7.19)$$

$$\sigma_{et} = \sigma_t + 0.75\sigma_s, \text{ elastic tripping stress for stringer and shell} \quad (7.20)$$

$$\sigma_{oa} = \frac{4\pi^2 EI_t}{l_o(A_s + s_e t)n_s}, \text{ elastic overall column buckling stress of stiffened cylinder} \quad (7.21)$$

$$\sigma_{es} = p_{rm} \frac{R}{t}, \text{ elastic buckling stress for unstiffened shell} \quad (7.22)$$

$$\sigma_{el} = \frac{8R}{s_e t l^2} \left\{ \frac{\pi^2 EI_{zs}}{l^2} \left(\frac{4\pi^2}{l^2} EC_w + GJ \right) \right\}^{1/2}, \text{ elastic lateral buckling stress of stringer} \quad (7.23)$$

$$\sigma_{eg} = p_n \frac{R}{t}, \text{ elastic overall buckling stress for shell and ring stiffener} \quad (7.24)$$

$$\sigma_{tr} = \frac{EI_{zr}}{A_r Re_r}, \text{ elastic tripping stress for ring stiffener} \quad (7.25)$$

$$\sigma_e = \frac{4\pi^2 EI}{l^2(A_s + s_e t)}, \text{ elastic buckling stress of the stringer as a column} \quad (7.26)$$

E = Young's modulus

A_s = area of the stringer stiffener

s_e = shell effective width

t = thickness of the shell

l = ring frame spacing

R = radius to center line of shell

I = second moment of the cross-section of the stringer
including the effective shell width

$$\sigma_s = \frac{0.605E(t/R)}{1 + A_s / s_e t}, \text{ elastic buckling stress for unstiffened shell} \quad (7.27)$$

$$\sigma_t = \frac{1}{I_o} \left(GJ + \frac{4\pi^2}{l^2} EC_w \right), \text{ elastic tripping stress of stringer} \quad (7.28)$$

$$J = (b_{sf} t_{sf}^3 + h_{sw} t_{sw}^3) / 3, \text{ St. Venant torsion constant of stringer} \quad (7.29)$$

b_{sf}, t_{sf} = width and thickness of stringer flange respectively

h_{sw}, t_{sw} = height and thickness of stringer web respectively

$$I_o = I_s + A_s e_s^2 + I_{zs}, \text{ moment of inertia of stringer} \quad (7.30)$$

$$I_s = h_{sw}^3 t_{sw} / 12 + b_{sf} t_{sf}^3 / 12 \quad (7.31)$$

$$I_{zs} = h_{sw} t_{sw}^3 / 12 + b_{sf}^3 t_{sf} / 12 \quad (7.32)$$

e_s = distance between stringer centroid (shell excluded) and its toe

$$C_w \approx I_{zs} \left(\frac{h_{sw} + t_{sf}}{2} \right)^2, \text{ torsional warping constant} \quad (7.33)$$

G = shear modulus

I_t = second moment of the whole cross-section of the stringer stiffened cylinder

n_s = number of stringers

$$p_{rm} = \frac{1.4}{\sqrt{3(1-\nu^2)}} \frac{E(t/R)^2}{\sqrt{Z}}, \text{ von Mises bucking pressure under radial pressure alone} \quad (7.34)$$

$$Z = \frac{l^2}{Rt} \sqrt{1-\nu^2}, \text{ Batdorf length parameter}$$

$$p_n = p_{nf} + P_{ns} = \frac{(n^2 - 1)EI_c}{R^3 l} + \frac{Et/R}{(n^2 - 1 + \lambda^2 / 2)(n^2 / \lambda^2 + 1)^2} \quad (n \geq 2), \text{ elastic overall buckling}$$

pressure for shell and ring stiffener (7.35)

$$\lambda = \pi R / l_o$$

I_c = second moment of the cross-section of the ring-stiffener including the effective shell width (width of shell = 0.75L)

e_r = distance between ring centroid (shell excluded) and its toe

I_{zr} = moment of inertia of ring cross-section about its line of symmetry

l_o = overall length of stringer-stiffened cylinder

7.3.3 Deriving residual strength formulations of damaged stringer-stiffened cylinder

For stringer-stiffened cylinders, the effect of radial pressure on the axial load carrying

capacity is not significant unless the radial pressure is close to the collapse pressure. In this study, the radial pressure at $0.2 P_c$ (collapse pressure of damaged model) and $0.5 P_c$ were applied and then performing progressive collapse analysis for axial compressive loading. It is noted that in the combined loading case the collapse patterns observed are similar to the ones in the axial compression case. The comparison of collapsed shape between an intact case and damaged case with $d/R = 0.05$ was described in Fig. 7.11. It is clear that the collapsed shape of the intact model seems to be symmetry while that of damaged model is asymmetry. Because of lack of symmetry in the cross-section of the dented cylinder, the axial stress produced by axial compression applied eccentrically causing an additional moment with respect to the middle surface of the wall. Furthermore, the average axial stress-strain curve of intact model is compared to that of damaged model, as shown in Fig. 7.12. It can be seen in Fig. 7.12 that the reduction in ultimate strength is not to a great extent as the dent depth increases.

Table 7.4 Comparison of the accuracy of existing design formulae and that of the proposed formulation (mean/COV (%)).

Formulation	axial comp. offshore(49)	radial press. Offshore (10)	combined axial comp. and radial press. Offshore (31)	axial comp. aerospace(193)
DNV '82	1.02 (27.1%)	1.45 (40.8%)	1.67 (26.4%)	1.71 (45.7%)
DNV '92	1.10 (30.3%)	2.19 (42.6%)	1.79 (43.3%)	1.83 (34.0%)
API'87	1.07 (19.7%)	1.23 (12.4%)	1.16 (18.4%)	0.90 (67.0%)
ECCS'84	1.20 (28.4%)	-	-	2.23 (33.7%)
ECCS'88	1.02 (32.4%)	-	-	0.68 (71.3%)
RCC'92	1.05 (12.8%)	0.97 (10.4%)	0.97 (17.2%)	1.76 (45.7%)
Proposed	0.99 (12.9%)	0.95 (5.3%)	1.05 (14.3%)	1.16 (32.9%)

The same procedure to derive formulation in the previous section, after investigating the dependent parameter, the regression analysis was performed with the best-fit assessment of numerical results. The best-fit curve for a close form formulation is plotted in Fig. 7.13. In this figure, the reduction factor is defined as the ratio of axial compression strength of damaged model to the axial compression of the intact model. The axial compression strength of intact model under combined loadings was calculated by equation (7.14). The reduction factor $R_{ux,s}$ was empirically derived as Eq. (7.36). Once the ultimate strength of an intact cylinder under combined loadings

$\sigma_{xin,s}$ is calculated, the residual strength can be evaluated by multiplying with the strength reduction factor $R_{ux,s}$ as defined in Eq. (7.38). The accuracy of the proposed formulation to predict the residual strength of damaged stringer-stiffened cylinders was very good, with X_m (ratio of num./prop. values) of 0.998 together with COV of 1.68%.

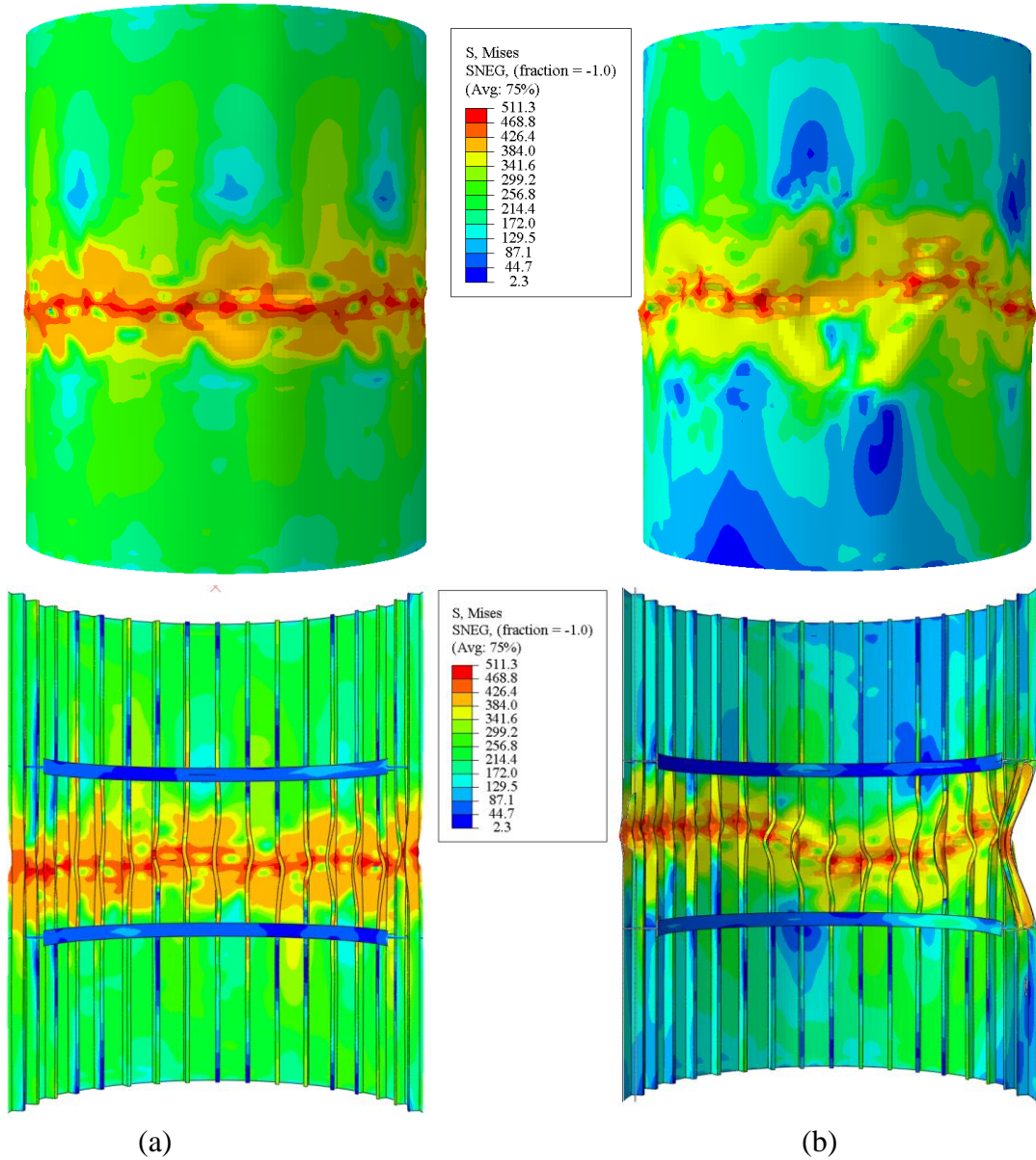


Fig. 7.11 Collapsed shape of stringer-stiffened cylinder model ($R/t = 210$) under combined loadings: (a) intact model; (b) damaged model.

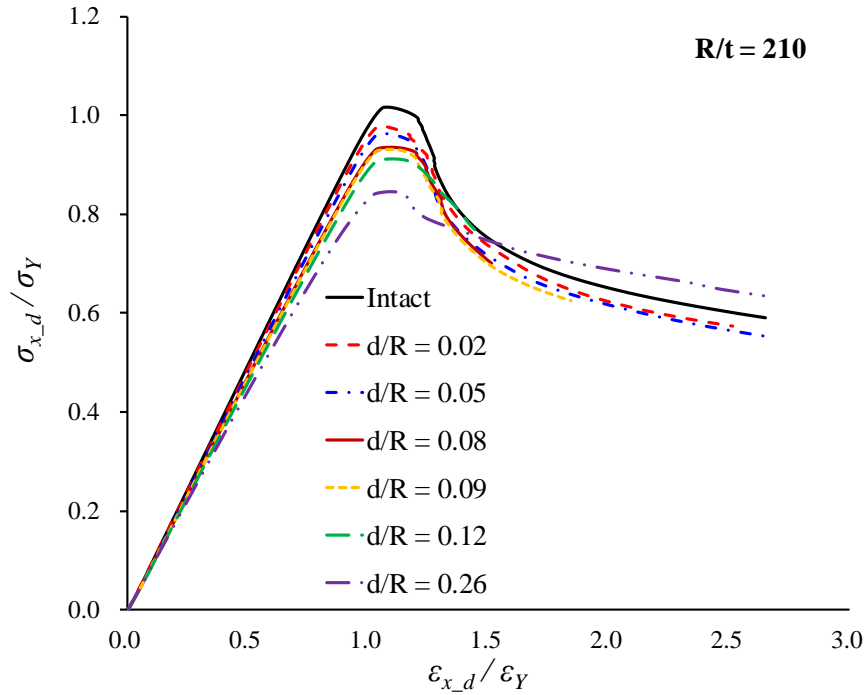


Fig. 7.12 Average axial stress-strain curves for model SS-3 ($R/t = 210$).

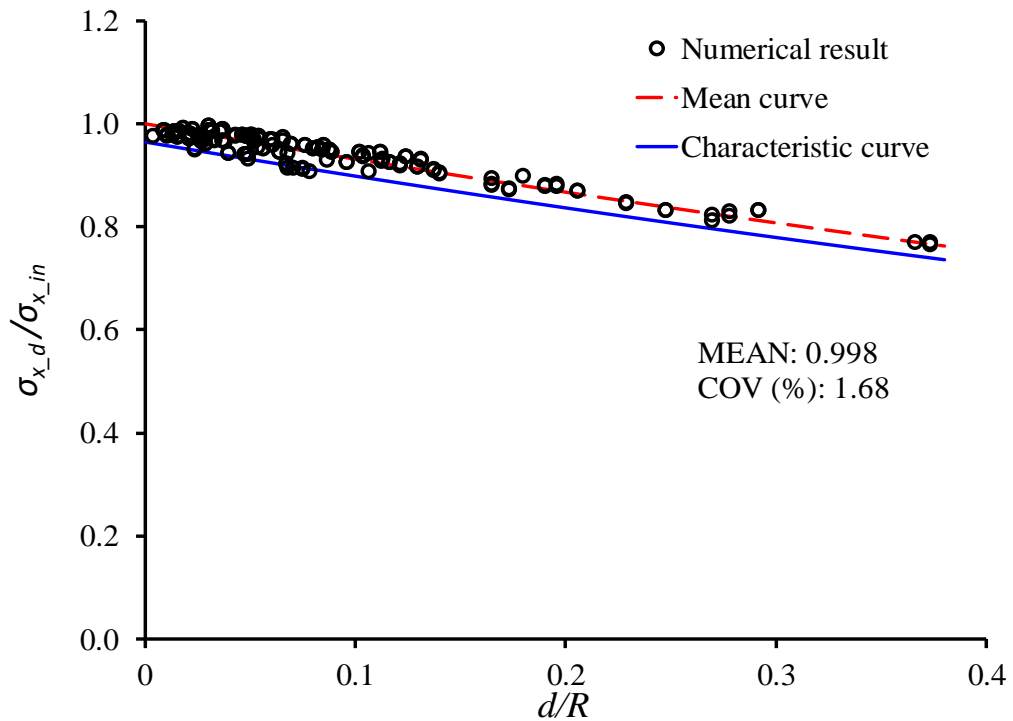


Fig. 7.13 Best-fit curve for prediction of residual strength of stringer-stiffened cylinder under combined loading.

$$R_{ux,s} = \frac{\sigma_{xd,s}}{\sigma_{xin,s}} = Exp\left(-0.711 \frac{d}{R}\right) \quad ; \text{ Mean equation} \quad (7.36)$$

$$R_{ux,s} = \frac{\sigma_{xd,s}}{\sigma_{xin,s}} = Exp\left(-0.036 - 0.711 \frac{d}{R}\right) \quad ; \text{ Characteristic equation} \quad (7.37)$$

By substituting σ_x of the intact case from Eq. (7.15), the axial compression residual strength of damaged stringer-stiffened cylinder can be obtained by Eq. (7.38).

$$\sigma_{xd,s} = Exp\left(-0.711 \frac{d}{R}\right) \left\{ - \left(\frac{\sigma_{\theta} \left[\frac{2}{\rho_s(\sigma_{ec} + \sigma_{es})} + \frac{1}{\rho_g(\sigma_{eg} + \sigma_{tr})} \right] - \frac{\sqrt{(\sigma_{eq} + \sigma_{\gamma})(\sigma_{\gamma} - \sigma_{eq})}}{\sigma_{\gamma}}}{\frac{1}{\rho_c \sigma_{ec}} + \frac{1}{\rho_t \sigma_{et}} + \frac{5}{6 \rho_{oa}}}} \right) \right\} \quad (7.38)$$

7.5 Final remarks

In this chapter the residual strength of both damaged ring- and stringer-stiffened cylinder under combined axial compression and radial pressure were investigated. Based on the numerical results can be shown that the ultimate strength reduction owing to local dented under combined loading does not tend to increase significantly when the dent depth increases. Furthermore, the collapse shape of damaged stiffened cylinder is not symmetry as the intact stiffened cylinder. Because of lack of symmetry in the cross-section of the dented cylinder, the axial stress produced by axial compression applied eccentrically causing an additional moment with respect to the middle surface of the wall.

On the other hand, under combined loading, the axial load carrying capacity of damaged stiffened cylinders is not much affected by radial pressure unless radial pressure is close to its radial collapse pressure. Based on the parametric study results, the approximate formulation for reduction factors were derived for both ring and stringer-stiffened subjected to combined loading. These reduction factors can be multiplied with ultimate strength values obtained for intact cylinders, then the residual strength of damaged cases can be quickly calculated.

Chapter 8 Conclusions and recommendation for future work

8.1 Conclusions

The aim of this thesis is to provide experimental and numerical simulation results for understanding the structural responses of offshore structural components under collision actions. The behavior of thin-walled cylindrical shells with large deflection subjected to localized collision loadings, and their residual strengths has been investigated in this thesis. In addition, some simple formulations for quick checking the extent damage due to collision and residual strength under hydrostatic pressure or combined axial compressive and radial pressure were derived. Both experimental results and nonlinear finite element simulations were extensively used. The focus was given for the rational design and the response of marine structures to against collision loads. Based on the results of the present study, the following conclusions can be drawn:

1. For the first time, the dynamic impact tests of ring- and stringer-stiffened cylinder models have been successfully conducted in this study. The details of the experimental setups, test procedures and test results were also reported in this thesis. Furthermore, the tests were simulated numerically and very good agreements were achieved.
2. For ring-stiffened cylinder, the damage can be described as denting at the impact region. The dent flattens the cross section with a length of the indenter width. At the ends of the flattened dent section, the shell bulges outward. The large dent is limited in the mid-bay. The boundaries of the dent are semi-ellipses. Nonetheless, the damage also spreads by flattening to the adjacent bays in the longitudinal direction. The longitudinal generators deflect inward and cause material stretching in the axial direction because of the end-plate resistance and membrane resistance of the shell. The remainder of the shell is unaffected. This damage shape follows the damage shape of unstiffened cylinders. The end plate and the end ring were sufficiently stiff to maintain circular ends. However, a small degree of rotation was observed on the upper part of these end supports.
3. For stringer-stiffened cylinders, the damages obtained can be described as a local denting confined at the contact bay. The stringer acted as a beam that resisted loading until they formed

plastic hinges, while the ring-stiffeners prevented the extent of damage spreading to adjacent bays. Furthermore, it is also noteworthy that local tripping of stringer-stiffeners was apparent near the ring-stiffeners, which was not observed in the previous quasi-static denting tests.

4. A series of experimental and numerical results of H-shape tubular member under dynamic mass impact at room and sub-zero temperature. These results were shown insights understanding of the plastic deformation and fracture behavior at T-joint of the tubular member during a ship collision. There is a significant difference of fracture response of tubular member at room and sub-zero temperature. The ductile fracture occurs with impact at room temperature while the brittle fracture occurs for the impact at sub-zero temperature. At low temperature, the stiffness and the yield strength of steel increases, little plastic deformation occurs before fracture. Thus brittle type fracture takes place by rapid crack propagation and very small strain energy. Furthermore, the numerical simulations have a good agreement with the experimental results. Finally, a new simple critical failure strain formulation has been provided when considering the size of fine mesh in the contact area between the offshore tubular member and ship collisions.

5. An important feature of the numerical simulations is the dynamic material properties. The sensitivity of the numerical simulation accuracy to the strain-rate hardening definition was presented. The definition of strain rate hardening adopted in the analysis is appropriated for this type of dynamic impact problem. Furthermore, it is suggested that the dynamic material properties be used to define plasticity at high strain rates. When compared to the scaling of quasi-static plasticity with a dynamic hardening factor expressed with Cowper-Symonds equation, the directly inputted the dynamic tensile test results with high levels of strain rate was obtained with a better agreement. Additionally, beside strain rate effects, indenter orientation and hit angle as well as boundary condition definitions should be also considered in numerical simulations.

6. Simple formulations to predict the extent damage of ring- and stringer-stiffened cylinders under dynamic mass impact were provided. The accuracy of the mean formulations has been validated with existing experimental results, and a good agreement was obtained. Thus, in actual cases, when the striking mass, collision velocity, and material parameters, along with the dimension of the ring or stringer-stiffened cylinder structures, were provided, the maximum permanent dent depth was adequately and rapidly predicted with the proposed formulations.

7. To the best of the authors' knowledge, this is the first study that successfully reported on the residual strength tests of damaged ring- or stringer-stiffened cylinders subjected to hydrostatic

pressure. In the study, the failure mode of locally damaged ring-stiffened cylinders under hydrostatic pressure was overall buckling even though the corresponding intact model collapsed in an interactive buckling mode. While that of the intact and damaged stringer-stiffened cylinders under hydrostatic pressure failed with respect to the local shell buckling. The ultimate strength of ring-stiffener cylinder is significant reduced with increasing the dent depth. Contrary to the ring-stiffened cylinder case, the effects of collision damages on the ultimate strength of stringer-stiffened cylinders under hydrostatic pressure were extremely low.

8. The formulations to predict the residual strength of ring- or stringer-stiffened cylinder under hydrostatic pressure or combined axial compression and radial pressure were proposed. These equations have a good accuracy and reliable according to the available test data. It is convenient to use for the purposes of initial design and serviceability limit state assessment of ring- and stringer-stiffened cylinders under the risk conditions of marine structures.

8.2 Recommendations for future work

Because of time constraints as well as deserving to be further investigation, some aspects of importance and interest which were not considered in the thesis. Further research may be recommended as below:

1. Simplified methods for assessing impact response of offshore structural components should be combined with residual strength methods to give quick general view collision consequences. This can further be utilized in reliability or optimization studies for ALS design of offshore structures.
2. The thesis work has mainly focused on cylinder structural type, the other type columns such as square columns with rounded corners, box girder type columns and stiffened panel structures were not considered. Further studies should also cover these components focusing on the conditions of usage in offshore structures.
3. Dynamic tensile test results at sub-zero temperature for the material of tubular member should be provided. This data is valuable to improve the accuracy of brittle fracture analysis at low-temperature. Further investigation on the T-joint tubular members at sub-zero temperatures is also encouraged.

4. Based on the results of the present study, it is recommended that more advanced and optimal structural designs should be considered in a further parametric study for improving the ultimate strength of stiffened cylinder structures against ship collisions and hydrostatic pressure or combined loadings.

5. The proposed formulations for evaluating the residual strength of damaged stiffened cylinders under hydrostatic pressure or combined axial compression and radial pressure are limited to trace the strength of an isolated damaged members. Therefore, the assessment of the residual strength of the whole structures or more complex structures are required. The substructuring method based on finite element modeling can be a solution for this purpose.

6. Fracture modeling is important for the accurate assessment of structural responses in ship collisions. The present simulations used a critical equivalent strain model for simplicity. This can be improved by combining the developed code with advanced fracture models.

References

- [1] HSE. Effective collision risk management for offshore installations. Offshore Technology Report, OTO 1992 052, Health and Safety Executive, UK; 2000.
- [2] IMO 2015. International Maritime Organization, GISIS: Marine Casualties and Incidents, Cited 05. URL <https://gisis.imo.org/Public/MCI/Default.aspx>.
- [3] HSE. Ship/platform collision incident database (2001). Research Report 053. Health and Safety Executive, UK; 2003.
- [4] DNV. Accident statistics for fixed offshore units on the UK continental shelf (1980-2005). HSE Research Report RR566, Sudbury, Suffolk: HSE Books; 2007.
- [5] DNV. Accident statistics for floating offshore units on the UK continental shelf (1980-2005). HSE Research Report RR567, Sudbury, Suffolk: HSE Books; 2007.
- [6] DNV GL. Arctic-the next risk frontier. <https://www.dnvgl.com/technology-innovation/broader-view/arctic/the-arctic-riskpicture.html>.
- [7] Hill BT. Ship Iceberg collision database. National Research Council Canada, 2009. IceData.com.

- [8] Kvitrud A. Collision between platforms and ships in Norway in the period 2001-2010. In: 30th International Conference on Ocean, Offshore and Arctic engineering. Rotterdam, Netherlands: ASME; 2011. p. 637-41.
- [9] Fire & Blast Information Group (2005). Mumbai High North Platform. Retrieved from <http://www.fabig.com/Accidents/Mumbai+High+North.htm>.
- [10] IOPCF. Annual report 2005, International Oil Pollution Compensation Funds.
- [11] Harding JE, Onoufriou A, Tsang SK. Collisions—What is the danger to offshore rigs?. *Journal of Constructional Steel Research* 1983; 3(2):31–38.
- [12] HSE. Buckling of offshore structural components – Report of the UK Cohesive Buckling Research Programme 1983-1985. Offshore Technology Report, OTH/90/329, Health and Safety Executive, UK; 1992.
- [13] HSE. Protection of offshore installations against impact - background report. Offshore Technology Report, OTI 88/535, Health and Safety Executive, UK; 1988.
- [14] Amdahl J. Energy absorption in ship-platform impacts. Dr. Ing. Thesis. Division of Marine Structures, Report UR-83-34, The Norwegian Institute of Technology, Trondheim, Norway; 1983.
- [15] Ellinas CP, Valsgård S. Collisions and damage of offshore structures: a state-of-the-art. *Journal of Energy Resources Technology* 1985; 107(3):297-314.
- [16] Fumes O, and Amdahl J. Computer simulation ship-platform Impacts of offshore collisions. *Applied Ocean Research* 1980; 2(3):119-127.
- [17] Minorsky V. An analysis of ship collisions with reference to protection of nuclear power plants. Sharp (George G.) Inc., New York; 1958.
- [18] Pedersen PT, Zhang S. On impact mechanics in ship collisions. *Marine Structures* 1998; 11(10): 295–329.
- [19] Stronge WJ. Impact mechanics. Cambridge University Press; 2004.
- [20] Brown, A. J. 2002. Collision scenarios and probabilistic collision damage. *Marine Structures* 2002; 15:335-364.
- [21] Tabri, K. 2012. Influence of coupling in the prediction of ship collision damage. *Ships and Offshore Structures* 2012; 7:47-54.
- [22] Wang G, Spencer J, Chen Y. Assessment of a ship’s performance in accidents. *Marine Structures* 2002; 14(4-5):313-333.
- [23] Det norske Veritas. Design against accidental loads. Technical Note for Fixed Offshore Installations. TNA 101,1981.
- [24] Det norske Veritas Impact Loads from Boats. Technical Note for Fixed Offshore Installations. TNA 202,1981.
- [25] Paik JK, Thayamballi AK. Ship-shaped offshore installations: design building, and operation. Cambridge UK: Cambridge University Press; 2007.
- [26] DNV. Design against accidental loads. Recommended Practice. DNV-RP–C204; Det Norske Veritas; 2010.

- [27] API. API Recommended practice 2A-WSD: Recommended practice for planning, designing and constructing fixed offshore platforms – working stress design. American Petroleum Institute; 2000.
- [28] BSH. Standard – Design of Offshore Wind Turbines. Bundesamt für Seeschifffahrt und Hydrographie (Federal Maritime and Hydrographic Agency), Hamburg and Rostock, Germany; 2007.
- [29] NORSOK Standard N-004. Design of steel structures, Appendix A, design against accidental actions; 2004.
- [30] Amdahl J. Energy absorption in ship-platform impacts. Dr. Ing. Thesis. Division of Marine Structures, Report UR-83-34, The Norwegian Institute of Technology, Trondheim, Norway; 1983.
- [31] American Petroleum Institute. Recommended Practice for Planning, Designing, and Constructing Fixed Offshore Platforms. API RP 2A, Washington DC; 1984.
- [32] Det norske Veritas Rules for the Design, Construction and inspection of Offshore Structures Appendix C: Steel Structures. Hovik, Norway; 1982.
- [33] Pippard A. M. and Chitty L. Experiment on the Plastic failure of cylindrical shells. The Institution of Civil Engineering Problems; 1948. p. 2-29.
- [34] Zayas V. A. and Dao B. V. Experimental and Analytical Comparisons Of Semisubmersible Offshore Rig Damage Resulting from a Ship Collision. Proceedings 17th OTC, Houston, OTC Paper 4888;1985. p. 413-422.
- [35] Smith CS, Dow RS. Residual Strength of Damaged Steel Ships and Offshore Structures. J. of Constructional Steel Research 1981;1(4):2-15.
- [36] Smith CS, Creswell DT. Effects of damage on the strength of ring-stiffened cylinders under External Pressure. Proceedings of the Third International Symposium on Practical Design of Ship and Mobile Units, Trondheim, Norway;1977. p. 1004-1015.
- [37] Frieze PA, Sachinis A. Compressive strength of stress-relieved ring-stiffened cylinders Including local damage. Proceedings of Conference, Marine and Offshore Safety, University of Glasgow, ed. Frieze P. A. et al., Elsevier Science Publishers, Amsterdam;1984. p. 341-362.
- [38] Onoufriou A, Harding JE. Residual Strength of Damaged Ring-Stiffened Cylinders. Proceedings of Conf., OMAE, Dallas, Texas.;1985. p. 537-545.
- [39] Onoufriou A, Harding JE. Effect of Imperfect Damage on the Residual Strength of Ring Stiffened Cylinders. Proceedings of Conf., OMAE, Tokyo, Japan;1986. p. 315-322.
- [40] Onoufriou A, Elnashai AS, Harding JE, Dowling PJ. Numerical Modelling of damage to Ring Stiffened Cylinders. Proceedings of OMAE Conf., Dallas, Texas.;1987. p. 281-289.
- [41] Onoufriou A. Collapse of damaged ring stiffened cylinders. Ph. D Thesis, Imperial College, University of London; 1987.
- [42] Ronalds B. F. and Dowling, P. J. Damage of orthogonally stiffened BOSS '85, Delft;1985. p.419-428.

- [43] Ronalds BF, Dowling PJ. Buckling of intact and damaged offshore shell structures. Proceedings of Conf. Advances in Marine Structures Smith C. S. and Clarke J. D. cds., Elsevier Applied Science 1986;201-218.
- [44] Ronalds BF, Dowling PJ. Finite deformations of stringer stiffened plates and shells under knife-edge Loading. Proceedings of Conf., OMAE, Tokyo, Japan;1986. p. 323-331.
- [45] Ronalds BF. Mechanics of dented orthogonally stiffened cylinders. Ph. D Thesis, Imperial College, University of London;1985.
- [46] Ronalds BF, Dowling PJ. Local damage effects in cylinders stiffened by rings and stringers. Proceedings of Conf. Steel Construction Offshore/Onshore, imperial College, London; 1987.
- [47] Kwok MK, McCall S, Walker AC. The behaviour of damaged cylindrical shells subjected to static and dynamic loading. Applied Solid Mechanics 2, Tooth A. S. and Spence J. eds., Elsevier Applied Science 1987;2:155-178.
- [48] Walker AC, McCall S, Kwok R. Strength of damaged shells under pressure and axial loading. Proceedings of Conf. Steel Construction Offshore/Onshore, Imperial London; 1987.
- [49] Walker AC, McCall S, Thorpe TW. Strength of damaged ring and orthogonally stiffened shells Part I: Plain ring stiffened shells. Thin-Walled Structures 1987;5:425-453.
- [50] Walker AC, McCall S, Thorpe TW. Strength of Damaged Ring and Orthogonally Stiffened Shells Part II: T-Ring and Orthogonally Stiffened Shells. Thin-Walled Structures, 1987;6:19-50.
- [51] Tsang SK., Harding JE, Walker AC, Andronicou A. Buckling of Ring Stiffened Cylinders Subjected to Combined Pressure and Axial Compressive Loading. Proceedings ASME Conf. on Pressure Vessels and Piping Technology, Oregon;1983. p. 2-8.
- [52] Tsang SK, Harding JE. Buckling behaviour under pressure of cylindrical shells reinforced by light ring stiffeners. Proceedings Instn Civ. Engrs, Part 2, Vol. 79, p. 365-381,1985.
- [53] Tsang S. K. and Harding J. E. A plastic mechanism formulation for the general instability of ring-stiffened cylinders under pressure-dominated loadings. Int. J. Mech. Sci., Vol. 27, No. 6, p. 409-422,1985.
- [54] Tsang S. K. Collapse of Ring Stiffened Cylindrical Pressure Shells under Combined External and Axial Compression. Ph. D Thesis, Imperial College, University of London, 1985.
- [55] Galletly G. D. Buckling of Fabricated Cylinders Subjected to Compressive Axial Loads and/or External Pressure—A Comparison of Several Codes. PVP-57 Pressure Vessel Design (G. E. O. Widera ed.), Book No. H00214, ASME, New York, p. 29-47,1982.
- [56] Galletly GD, Pemsing K. On design procedures for the buckling of cylinders under axial compression and external Pressure. Trans. ASME, J. Press. Vess. Tech.;1984. p.134-142.
- [57] Galletly GD, Pemsing K. Buckling of cylinders under Combined External Pressure and Axial Compression. Collapse: The Buckling of structures in theory and practice,

- Proceedings IUTAM Symp., Thompson T. and Hunt G. W. eds., Cambridge University Press.; 1983. p. 502-527.
- [58] Frieze PA, Cho SR, Faulkner D. Strength of ring-stiffened cylinders under combined loads. Proceedings 16th OTC, Houston, OTC Paper 4714;1984. p. 39-48.
- [59] Miller CD. Buckling of axially compressed cylinders. Proceedings ASCE Struct. Div., vol. 103, no. ST3;1977. p. 695-721.
- [60] Miller CD. Summary of Buckling tests on fabricated steel cylindrical shells in USA. Buckling of shells in offshore structures, Harding J. E., Dowling P. J. and Agelidis N., Granada, London; 1982. p. 429-472.
- [61] Ellinas CP, Croll JGA. Overall Buckling of ring-stiffened cylinders. Proceedings Insm. Civ. Engrs, Part 2;1981. p.637-661.
- [62] Croll JGA, Ellinas CPA. Design formulation for axisymmetric collapse of stiffened and unstiffened cylinders. Trans. ASME, J. of Energy Resources Technology, vol. 107;1985. p.350-355.
- [63] Croll JGA. Axisymmetric elastic-plastic buckling of axial and pressure loaded cylinders. Proceedings Instn. Mech. Engrs, vol. 198C, No. 16;1982. p.243-259.
- [64] Croll JGA. Lower bound methods in shell buckling. Developments in Thin-Walled Structures - 3, Rhodes J. and Walker A. C. eds., Elsevier Applied Science, London;1985. p.117-163.
- [65] Raymond MKK. Mechanics of damaged thin-walled cylindrical shells. Ph. D Thesis, University of Surrey;1991.
- [66] McCall S. Experimental study of repair methods for damaged cylindrical shells subjected to axial and hydrostatic compression. Ph. D Thesis, University of Surrey, March 1996.
- [67] MacKay JA, Smith MJ, van Keulen F, Bosman TN, Pegg NG. Experimental investigation of the strength and stability of submarine pressure hulls with and without artificial corrosion damage. Mar Structs 2010; 23:339-59.
- [68] MacKay JR, Jiang L, Glas AH. Accuracy of nonlinear finite element collapse predictions for submarine pressure hulls with and without artificial corrosion damage. Mar Struct 2011; 24:292-317.
- [69] Cho S-R, Do QT, Shin HK. Residual strength of damaged ring-stiffened cylinders subjected to external hydrostatic pressure. Mar Structs 2017;56:186–205.
- [70] Do QT, Muttaqie T, Shin HK, Cho S-R. Dynamic lateral mass impact on steel stringer-stiffened cylinders. Int J Impact Eng 2018;116:105–26.
- [71] Do QT, Muttaqie T, Park S, Shin HK, Cho S-R. Ultimate strength of intact and dented steel stringer-stiffened cylinders under hydrostatic pressure. Thin-Walled Struct 2018;132:442–460.
- [72] Do QT, Muttaqie T, Park S, Shin HK, Cho S-R. Predicting the collision damage of steel ring-stiffened cylinders and their residual strength under hydrostatic pressure. Ocean Eng 2018;169:326–43.

- [73] Thomas SG. Large Deformation of thin-walled circular tube under transverse loading- Part 1,11 and 111. *Int. J. Mech, Sci.* 1976;3:501-509.
- [74] Amdahl J. Impact capacity of steel platforms and tests on large deformations of tubes under transverse loading. Veritas Report No. 80-0036;1980.
- [75] Fumes O, and Amdahl J. Ship collisions with offshore platforms. *Intermaritec 80, Hamburg*;1980. p. 310-328.
- [76] Pettersen E, Johnsen KR. New non-linear methods for estimation of collision resistance of mobil offshore units. *Proceedings 13th OTC, Houston, OTC Paper 4135*;1981. p.173-186.
- [77] Pettersen E. Assessment of impact damage by means of a simplified approach. *Non-Linear Faulkner D. et al eds., Integrity of Offshore Structures, Applied Science Publishers*;1981. p. 317-338.
- [78] Soreide TH, Amdahl J. Deformation characteristics of tubular members with reference to impact loads from collision and dropped objects. *Norwegian Maritime Research, No. 2*;1982. p. 3-12.
- [79] Søreide TH, Moan T, Amdahl J. Analysis of ship/platform impacts. *BOSS '82*;1982. p.257-278.
- [80] Storheim M, Amdahl J. Design of offshore structures against accidental ship collisions. *Mar Struct 2014*;37:135–72.
- [81] Yu Z, Amdahl J. Full six degrees of freedom coupled dynamic simulation of ship collision and grounding accidents. *Mar Struct 2016*;47:1–22.
- [82] Cho SR. Design approximations for offshore tubulars against collisions. PhD thesis. Faculty of Engineering, University of Glasgow, Glasgow, UK; 1987.
- [83] Cerik BC, Shin HK, Cho SR. A comparative study on damage assessment of tubular members subjected to mass impact. *Mar Struct 2016*;46:1–29.
- [84] Liu K, Liu B, Wang Z, Wang G (George), Guedes Soares C. An experimental and numerical study on the behaviour of tubular components and T-joints subjected to transverse impact loading. *Int J Impact Eng 2018*;120:16–30.
- [85] Smith CS, Kirkwood W, Swan JW. Buckling strength and post-collapse behavior of tubular bracing members including damage effects. *BOSS '79*;1979. p. 303-326.
- [86] Smith CS, Somerville WL, Swan JW. Residual strength and stiffness of damaged Steel bracing members. *Proceedings 13th OTC, Houston, OTC Paper 3981*;1981. p.273-282.
- [87] Smith CS. Strength and stiffness of damaged tubular beam columns. *Buckling of shells in offshore structures, Granada, London*;1982. p. 1-24.
- [88] Smith CS. Assessment of damage in offshore steel platforms. *Proceedings of Conf., Marine and offshore safety, Glasgow, eds., Frieze et al.,1984.* p. 279-307.
- [89] Taby J, Moan T, Rashed SMH. Theoretical and experimental study of the behaviour of damaged tubular members in offshore structures. *Norwegian Maritime Research, No. 2*;1981. p. 26-33.
- [90] Taby J, Moan T. Collapse and residual strength of damaged tubular members. *BOSS '85, Delft*;1985.

- [91] Ellinas CP. Ultimate strength of damaged tubular bracing Members. Proceedings of ASCE, J. of Structural Division, Vol. 109, No. 2;1983. p.245-259.
- [92] Ueda Y, Rashed SMH. Behaviour of damaged tubular structural members. Trans ASME J. Energy Resources Technology, Vol. 107;1985. p.343-349.
- [93] Griffiths DR, Wickens HG. The effects of damage on circular tubular compression members. Proceedings of the 3 rd. International Conference on Space Structures, University of Surrey, U. K.;1984. p. 381-387.
- [94] NORSOK-N003. Action and action effects;2007.
- [95] NORSOK-N004. Design of steel structures;2004.
- [96] DNV-RP-C204, Recommended practice DNV-RP-C204. DET NORSKE VERITAS; 2010.
- [97] DNV-RP-C208. Determination of Structural Capacity by Non-linear FE analysis Methods. Det Norske Veritas;2013.
- [98] DNV. Impact loads from boats. Technical Note for Fixed Offshore Installations TN A, 202;1981.
- [99] DNV. Safety principles and arrangements. Offshore Standard. DNV-OS–A101, Det Norske Veritas; 2011.
- [100] DNV. Design of offshore steel structures, general (LRFD method). Offshore Standard. DNVOS–C101, Det Norske Veritas; 2011.
- [101] Moan T, Amdahl J, Gerhard E. Assessment of ship impact risk to offshore structures-new NORSOK N-003 guidelines. Proceedings of the 3rd Offshore Structural Reliability Conference (OSRC 2016);2016.
- [102] ABS. Guidance notes on accidental load analysis and design for offshore structures. American Bureau of Shipping; 2013.
- [103] Walker AC, Kwok M. Process of damage in thin-walled cylindrical shells. In: Smith, Clarke, editors. Advances in Marine Structures. London, UK: Elsevier Applied Science Publishers; 1986. p. 111-136.
- [104] Harding JE, Onoufriou A. Behaviour of ring-stiffened cylindrical members damaged by local denting. J Constr Steel Res 1995;33(3):237-257.
- [105] Karroum CG, Reid SR, Li S. Indentation of ring-stiffened cylinders by wedge- shaped indenters e Part 1: An experimental and finite element investiga- tion. Int J Mech Sci 2007;49(1):13-38.
- [106] Ellinas CP, Supple WJ, Walker AC. Buckling of offshore structures: a state-of-the art-review of the buckling of offshore structures. Houston, USA: Gulf Publishing Company;1984.
- [107] Harding JE, Dowling PJ, Valsgard S, Walker AC. The buckling design of stringer-stiffened shells subject to combined pressure and axial compression. Offshore Technol Conf 1983.
- [108] Das PK, Subin KK, Pretheesh PC. A re-visit on design and analysis of stiffened shell structures for offshore applications Advances in Marine Structures. Guedes Soares & Fricke (eds.). Taylor & Francis Group : London, UK; 2011. p. 119-131.

- [109] Das PK, Faulkner D, Zimmer RA. Selection of robust strength models for efficient design of ring and stringer stiffened cylinders under combined loads. Proc 11th Int Conf Ocean Offshore Arct Eng -OMAE 1992 1992:417–26.
- [110] Ronalds BF, Dowling PJ. A denting mechanism for orthogonally cylinders. Int. J. Mech 1987; 29(10):743-59.
- [111] Ronalds B, Dowling PJ. Stiffening of steel cylindrical shells for accidental lateral impact. In: Proceedings of Institution of Civil Engineers 1987;83(4):799-814.
- [112] Ronalds BF, Dowling PJ. Collision resistance of orthogonally stiffened shell structures. J Constr Steel Res 1988;9:179–94.
- [113] Walker AC, McCall S. Experimental investigation of damaged stiffened cylindrical shells. Thin-Walled Struct 1998;30:79–94.
- [114] Cerik BC. Ultimate strength of locally damaged steel stiffened cylinders under axial compression. Thin-Walled Struct 2015; 95:138–151.
- [115] Cerik BC, Shin HK, Cho SR. On the resistance of steel ring-stiffened cylinders subjected to low-velocity mass impact. Int J Impact Eng 2015; 84:108-23.
- [116] Prabu B, Raviprakash A V, Venkatraman A. Parametric study on buckling behaviour of dented short carbon steel cylindrical shell subjected to uniform axial compression. Thin-Walled Struct 2010;48:639–49.
- [117] Rathinam N, Prabu B. Numerical study on influence of dent parameters on critical buckling pressure of thin cylindrical shell subjected to uniform lateral pressure. Thin-Walled Struct 2015;88:1–15.
- [118] Karroum CG, Reid SR, Li S. Indentation of ring-stiffened cylinders by wedge-shaped indenters-Part 2: Scale model tests. Int J Mech Sci 2007;49:39–53.
- [119] Villavicencio R, Guedes Soares C. Numerical modelling of the boundary conditions on beams struck transversely by a mass. Int J Impact Eng 2011; 38:384–96.
- [120] Villavicencio R, Guedes Soares C. Numerical modelling of laterally impacted plates reinforced by free and end connected stiffeners. Eng Struct 2012; 44:46–62.
- [121] Villavicencio R, Guedes Soares C. Impact response of rectangular and square stiffened plates supported on two opposite edges. Thin-Walled Struct 2013; 68:164–82.
- [122] Villavicencio R, Kim YH, Cho SR, Guedes Soares C. Deformation process of web girders in small-scale tanker double hull structures subjected to lateral impact. Mar Struct 2013; 32:84-112.
- [123] Jones N. The credibility of predictions for structural designs subjected to large dynamic loadings causing inelastic behaviour. Int J Impact Eng 2013; 53:106–14.
- [124] Hoo Fatt MS, Wierzbicki T. Damage of plastic cylinders under localized pressure loading. Int J Mech Sci 1991;33(12):999-1016.
- [125] Hoo Fatt MS, Wierzbicki T. Impact damage on long plastic cylinders. Int J Offshore Polar Eng 1992;2(2):147-156.
- [126] Wierzbicki T, Hoo Fatt MS. Impact response of a string-on-plastic foundation. Int J Impact Eng 1992;21(36):21-36.

- [127] Wierzbicki T, Hoo Fatt MS. Damage assessment of cylinders due to impact and explosive loading. *Int J Impact Eng* 1993;13(2):215-41.
- [128] Moussouros M, Hoo Fatt MS. Effect of shear on plastic denting of cylinders. *Int J Mech Sci* 1995;37(4):355-371.
- [129] Hoo Fatt MS, Wierzbicki T. Denting analysis of ring stiffened cylindrical shells. *Int J Offshore Polar Eng* 1991;1(2):137-145.
- [130] Wierzbicki T, Suh MS. Indentation of tubes under combined loading. *Int J Mech Sci* 1988;30(3-4):229-48.
- [131] Ramasamy R, Tuan Ya TMYS. Nonlinear finite element analysis of collapse and post-collapse behaviour in dented submarine pipelines. *Applied Ocean Research* 2014;46:116–123.
- [132] Benson S, AbuBakar A, Dow RS. A comparison of computational methods to predict the progressive collapse behaviour of a damaged box girder. *Engineering Structures* 2013;48: 266-280.
- [133] Hong L, Amdahl J. Crushing resistance of web girders in ship collision and grounding. *Marine Structures* 2008;21:374–401.
- [134] Hong L, Amdahl J. Rapid assessment of ship grounding over large contact surfaces. *Ships and Offshore Structures* 2012;7:5–19.
- [135] Liu B. Analytical method to assess double-hull ship structures subjected to bulbous bow collision. *Ocean Engineering* 2017;142:27–38.
- [136] Korean Standard. Method of tensile test for metallic materials. KS B 0802; 2008.
- [137] ISO, ISO 26203-2:2011 Metallic materials-Tensile testing at high strain rates - Part 2: Servo-hydraulic and other test systems; 2011.
- [138] Kendrick SB. Shape imperfection in cylinders and spheres: Their importance in design and methods of measurement. *Journal of Strain Analysis for Engineering Design* 1977; 12(2): 117–122.
- [139] PD 5500. Specification for unfired fusion welded pressure vessels. British Standard Institution, London, UK; 2009.
- [140] Cho SR, Choi SI, Son SK. Dynamic material properties of marine steels under impact loadings. In: *Proceedings of the 2015 World Congress on Advances in Structural Engineering and Mechanics, ASEM15*, Incheon, Korea; 2015.
- [141] Cowper GR, Symonds PS. Strain-hardening and strain-rate effects in the impact loading of cantilever beams. In: *Technical Report, No. 28*. Division of Applied Mathematics, Brown University; 1957.
- [142] Lee HJ, Kim SB. A study on application of material properties in ship collision analysis. In: *Proceedings of the Annual Autumn Conference of the Social of Naval Architecture of Korea*, Jeju, Korea; 2007.
- [143] API, *Bulletin on Stability Design of Cylindrical Shells*, API Bulletin 2U, 3rd ed., Washington; 2004.

- [144] Hsu SS, Jones N. Quasi-static and dynamic axial crushing of thin-walled circular stainless steel, mild steel and aluminium alloy tubes. *International Journal of Crashworthiness* 2004;9:195–217.
- [145] Kendrick SB. Analysis of results of static pressure tests of Chatham submarine models. Naval Construction Research Establishment, Dunfermline, report no. R218; 1955.
- [146] Kendrick SB. Structure design of submarine pressure vessels. Naval Construction Research Establishment, Dunfermline, report no. R483; 1964.
- [147] Miller CD, Kinra RK. External pressure tests of ring-stiffened fabricated cylinders. In: *Offshore Tech Conference, OTC 4107*; 1981.
- [148] Cho SR, So HY. Ultimate strength tests on ring-stiffened cylinders and conical shells subjected to hydrostatic pressure. In: *Proceedings of the 17th Asian-Pacific Technical Exchange and Advisory Meeting on Marine Structures, Taiwan*; 2003. p. 579-588.
- [149] Dowling PJ, Harding JE. Experimental behavior of ring and stringer stiffened shells. In: *Buckling of Shells in Offshore Structures*, ed. by Harding JE, London, Granada; 1982. p. 73-107.
- [150] Sridharan P, Walker AC. Experimental investigation of the buckling behaviour of stiffened cylindrical shells. In: *UK Department of energy report OT-R7835*; 1980.
- [151] Odland J. An experimental investigation of the buckling strength of the ring-stiffened cylinder shells under axial compression. In: *Norwegian Maritime Research* 1981; 4:22-39.
- [152] Miller CD. Summary of buckling tests on fabricated steel cylindrical shells in USA. In: *Buckling of Shells in Offshore Structures*, ed. by Harding JE, London, Granada; 1982. p. 429-471.
- [153] Buckling of test of 8 fabricated ring-stiffened cylinders under axial compression. In: *Mitsubishi Heavy Industries Ltd*; 1982.
- [154] Miller CD. Buckling of axial compressed cylinders. *J Struct Div Trans, ASCE* 1977; 103:695-721.
- [155] Miller CD, Kinra RK. Tension and collapse tests of fabricated steel cylinders. In: *Offshore Tech Conference, OTC 4218*; 1982.
- [156] Krenzke MA. Effects of initial deflections and residual welding stresses on elastic behavior and collapse of stiffened cylinders subjected to external hydrostatic pressure. Report 1327, Washington DC; 1960.
- [157] Bushnell D. Effect of cold bending and welding on buckling of ring-stiffened cylinders. *Comput Struct* 1970;12:291-307.
- [158] Smith CS, Kirkwood W. Influence of initial deformations and residual stresses on inelastic flexural buckling of stiffened plates and shells. In: *Steel Plated Structures*. London: Granada Publishing Limited; 1977. p.838-864.
- [159] Faulkner D. Effects of residual stresses on the ductile strength of plane welded grillages and of ring stiffened cylinders. *Strain Analysis* 1977;12:130-139.

- [160] Kendrick S. The influence of shape imperfections and residual stress on the collapse of stiffened cylinders. In: Conference on Significance of Deviations from Design Shape, Institute of Mechanical Engineers; 1979. p.25–35.
- [161] GL. Rules for the classification and construction of ship technology. Part 5 underwater technology. Annex A - Calculation of the pressure hull, Germanischer Lloyd, Hamburg, Germany; 2009.
- [162] ABS. Rules for building and classing underwater vehicles, systems and hyperbaric facilities. American Bureau of Shipping, Houston, USA; 2002.
- [163] MacKay JR, van Keulen F, Smith MJ. Quantifying the accuracy of numerical collapse predictions for the design of submarine pressure hulls. *Thin Wall Struct* 2011; 49:145-156.
- [164] Agelidis N, Dowling PJ. The strength of stringer stiffened cylinders. Proceedings of the 3rd international colloquium on stability of metal structures, Paris; 1984. p.169-178.
- [165] Dowling PJ, Harding JE, Agelidis N, Fahy W. Buckling of orthogonally stiffened cylindrical shells used in offshore engineering, in: Imperial college report; 1986.
- [166] Krasovsky VL, Kostyrko VV. Experimental studying of buckling of stringer cylindrical shells under axial compression, *Thin-Walled Struct* 2007;45:877-882.
- [167] Kinra RK. Hydrostatic and axial collapse tests of stiffened cylinders, in: Proceedings of Offshore technology conference, OTC 2685; 1976. p.765-788.
- [168] Dowling PJ. The collapse of stiffened cylinders, in: Proceedings of International conference on steel plated structure, Ed. PJ Dowling, et al., Crosby Lockwood Staples, London; 1977. p.791-808.
- [169] Green DR, Nelson HM. Compression tests on large-scale stringer stiffened tubes, in: Proceedings of Buckling of shells in offshore structures, Ed. Harding, Dowling and Agelidis, Granada, London; 1982. p.25-43.
- [170] Dowling PJ, Harrding JE. Experimental behaviour of ring and stringer stiffened shells, in: Proceedings of Buckling of shells in offshore structures, Ed. Harding, Dowling and Agelidis. Granada, London; 1982. p.73-107.
- [171] McCall S, Walker AC. Buckling tests on stringer-stiffened cylinder models subject to load combinations, Det Norske Veritas, in: Report 80-0299; 1982.
- [172] Weller T, Singer J, Nachmani S. Recent experimental studies on the buckling of stringer-stiffened cylindrical shells, in: TAE report 100, Technion-1970, Israel institute of technology, Department of Aeronautical Engineering, Haifa, Israel;1970.
- [173] Lennon RF. The Effects of cold forming and welding residual stress states on the buckling resistance of orthogonally stiffened cylinders, *Appl. Mech. Mater* 2006; 6:509–518.
- [174] Cho S-R, Lee SB. Ultimate strength formulation for stringer-stiffened cylinders subjected to combined axial compression and radial pressure, *Journal of Ocean Engineering and Technology* 1998;1:41-55.
- [175] Das PK, Subin KK, Pretheesh PC. A revisit on design and analysis of stiffened shell structures for offshore applications, in: Guedes Soares C, Fricke W (Eds.), *Advances in Marine Structures*, CRC Press, London; 2011. p.119-131.

- [176] Det Norske Veritas, DNV RP-C202: Buckling Strength of Shells, Det Nor Verit AS 27;2013.
- [177] ABS, Guide for Buckling and Ultimate Strength Assessment for Offshore Structures;2014.
- [178] Cerik BC, Cho S-R. Numerical investigation on the ultimate strength of stiffened cylindrical shells considering residual stresses and shakedown, *J. Mar. Sci. Technol.* 2013; 18:524–534.
- [179] Cho S-R, Muttaqie T, Do QT, Kim S, Kim SM, Han DH. Experimental investigations on the failure modes of ring-stiffened cylinders under external hydrostatic pressure, *Int. J. Nav. Archit. Ocean Eng* 2018;10:711-729.
- [180] Furnes O, Amdahl J. Ship collisions with offshore platforms. Intermaritec, Hamburg, Germany;1980. p. 310-318.
- [181] Ellinas CP, Walker AC. Damage on tubular bracing members. Proceedings of IABSE Colloquium on Ship Collision with Bridges and Offshore Structures, Copenhagen, Denmark; 1983. p.253-261.
- [182] Jones N, Birch SE, Birch RS, Zhu L, Brown M. An experimental study on the lateral impact of fully clamped mild steel pipes. *Proc Inst Mech Eng Part E J Process Mech Eng* 1992; 206:111-27.
- [183] Pedersen PT, Valsgard S, Olsen D. Ship impact: bow collisions. *Int. J. Impact Eng* 1993;13:163-187.
- [184] Amdahl J, Johansen A. High-energy ship collision with jacket legs. Proceedings of the International Offshore and Polar Engineering Conference (ISOPE 2001), ISBN 1-880653-55-9 (Vol. IV);2001.
- [185] Amdahl J, Eberg E. Ship collision with offshore structure. Moan (Ed.), *Structural Dynamics – EURO DYN’93*. Balkema, Rotterdam, (ISBN 90 5410 336 1). 1993.
- [186] Cho S-R, Le DNC, Jeong JH, Frieze PA, Shin HK. Development of simple design-oriented procedure for predicting the collision damage of FPSO caisson protection structures. *Ocean Engineering* 2017;142:458-69.
- [187] de Oliveira JG. The behaviour of steel offshore structures under accidental collisions. Proceedings of the offshore technology conference, Houston, USA; 1982. p. 187-98.
- [188] Soares CG, Søreide TH. Plastic analysis of laterally loaded circular tubes. *Journal of Structural Engineering (United States)* 1983;109:451-67.
- [189] Stronge WJ. Impact on metal tubes: indentation and perforation. Jones N, Wierzbicki T, editors. *Structural crashworthiness and failure*. London: Elsevier Applied Science; 1993. p. 165-88.
- [190] Paik JK, Shin BC, Chang YK. Damage estimation for offshore tubular members under quasi static loading. *Journal of the Society of Naval Architects of Korea* 1989; 26(4): 81–93.
- [191] Moan T. Development of accidental collapse limit state criteria for offshore structures. *Structural Safety* 2009; 31:124-35.

- [192] Calle MAG, Alves M. A review-analysis on material failure modeling in ship collision. *Ocean Engineering* 2015;106:20-38.
- [193] Zhang L, Egge ED, Bruhns H. Approval procedure concept for alternative arrangements. *Proceedings of the International Conference on Collision and Grounding of Ships and Offshore Structures, ICCGS 2004, Tokyo, Japan;2004.*
- [194] Lehmann E, Yu X. On ductile rupture criteria for structural tear in the case of ship collision and grounding. *Practical design of ships and mobile units, Elsevier Science, B.V;1998.*
- [195] Lehmann E, Egge ED, Scharrer M, Zhang L. Calculation of collision with the aid of linear FE models. *Proceedings of the 8th International Symposium on Practical design of ships and other floating structures, PRADS; 2001; 2:1293-1300.*
- [196] Servis DP, Samuelides M. Ship collision analysis using finite elements. *National Technical University of Athens, Internal Report;1999.*
- [197] Kitamura O. FEM approach to the simulation of collision and grounding damage. *Mar Struct* 2002;15:403–28.
- [198] Wang G, Arita K, Liu D. Behavior of a double hull in a variety of stranding or collision scenarios. *Mar Struct* 2000;13:147-87.
- [199] Yamada Y, Endo H, Pedersen PT. Numerical study on the effect on buffer bow structure in ship-ship collision. *Proceedings of the 15th International Offshore and Polar Engineering Conference, Seoul, Korea; 2005. p.604-11.*
- [200] Yagi S, Kumamoto H, Muragishi O, Takaoka Y, Shimoda T. A study on collision buffer characteristic of sharp entrance angle bow structure. *Mar Struct* 2009;22:12-23.
- [201] Wiśniewski K, Kołakowski P. The effect of selected parameters on ship collision results by dynamic FE simulations. *Finite Elem Anal Des* 2003;39:985-1006.
- [202] Yamada Y. Bulbous buffer bows: a measure to reduce oil spill in tanker collisions. *Department of Mechanical Engineering, Technical University of Denmark, DTU, Ph.D. Thesis;2006.*
- [203] Hogström P. RoPax ship collision - a methodology for survivability analysis. *Department of shipping and marine technology, Chalmers University of Technology , Ph.D. Thesis;2012.*
- [204] Ehlers S. The influence of the material relation on the accuracy of collision simulations. *Mar Struct* 2010;23:462–74.
- [205] Peschmann J. Energy absorption computations of ship steel structures under collision and grounding. *Technical University of Hamburg, Ph.D. Thesis;2001.*
- [206] Hogström P, Ringsberg JW, Johnson E. An experimental and numerical study of the effects of length scale and strain state on the necking and fracture behaviours in sheet metals. *Int J Impact Eng* 2009;36:1194–203.
- [207] Törnqvist R. Design of crashworthy ship structures. *Technical University of Denmark, Ph.D. Thesis;2003.*

- [208] Ehlers S, Broekhuijsen J, Alsos HS, Biehl F, Tabri K. Simulating collision response of ship side structures: a failure criteria benchmark study. *Int. Shipbuild. Prog.* 55; 2008. p. 128-144.
- [209] Kõrgesaar M, Romanoff J. Influence of softening on fracture propagation in large-scale shell structures. *Int J Solids Struct* 2013;50:3911–21.
- [210] Alsos HS, Amdahl J. On the resistance to penetration of stiffened plates, Part I - Experiments. *Int J Impact Eng* 2009;36:799–807.
- [211] Alsos HS, Hopperstad OS, Törnqvist R, Amdahl J. Analytical and numerical analysis of sheet metal instability using a stress based criterion. *Int J Solids Struct* 2008;45:2042–55.
- [212] Abubakar A, Dow RS. Simulation of ship grounding damage using the finite element method. *Int J Solids Struct* 2013;50:623–36.
- [213] Jie M, Cheng CH, Chan LC, Chow CL. Forming limit diagrams of strain-rate-dependent sheet metals. *Int J Mech Sci* 2009;51:269–75.
- [214] Bai Y, Bendiksen E, Pedersen PT. Collapse analysis of ship hulls. *Mar Struct* 1993; 6:485–507.
- [215] Glykas A, Das PK, Barltrop N. Application of failure and fracture criteria during a tanker head-on collision. *Ocean Eng* 2001;28:375–95.
- [216] Servis D, Samuelides M. Implementation of the T-failure criterion in finite element methodologies. *Comput Struct* 2006;84:196–214.
- [217] Jones N. On the dynamic inelastic failure of beams *Structural Failure*, Ed.. Wiley, New York, USA; 1989. p.133-159.
- [218] Paik JK. Practical techniques for finite element modeling to simulate structural crashworthiness in ship collisions and grounding (Part I: Theory). *Ships Offshore Struct* 2007;2:69-80.
- [219] Paik JK. Practical techniques for finite element modelling to simulate structural crashworthiness in ship collisions and grounding (Part II: Verification). *Ships Offshore Struct* 2007; 2: 81-85.
- [220] Gagnon RE, Wang J. Numerical simulations of a tanker collision with a bergy bit incorporating hydrodynamics, a validated ice model and damage to the vessel. *Cold Reg Sci Technol* 2012; 81: 26-35.
- [221] Woelke PB, Shields MD, Abboud NN, Hutchinson JW. Simulations of ductile fracture in an idealized ship grounding scenario using phenomenological damage and cohesive zone models. *Comput Mater Sci* 2013;80:79-95.
- [222] Liu B, Villavicencio R, Zhang S, Guedes Soares C. A simple criterion to evaluate the rupture of materials in ship collision simulations. *Mar Struct* 2017; 54:92-111.
- [223] Kim KJ, Lee JH, Park DK, Jung BG, Han X, Paik JK. An experimental and numerical study on nonlinear impact responses of steel-plated structures in an Arctic environment. *Int J Impact Eng* 2016; 93:99-115.
- [224] Sören Ehlers, Erling Østby. Increased crashworthiness due to arctic conditions-The influence of sub-zero temperature. *Mar Struct* 2012; 28:86-100.

- [225] Amante DA, Trovado L, Estefen SF. Residual strength assessment of semi-submersible platform column due to supply vessel collision, in: Proceedings of OMAE 2008, Estoril, Portugal; 2008. p.15-20.
- [226] Maddalena M, Netto TA, Cyrino JCR. On the structural integrity of damaged columns of semisubmersible platforms. *International Journal of Computer Applications in Technology* 2012; 43(3): 190–198.
- [227] Cho S-R, Frieze PA. Strength formulation for ring-stiffened cylinder under combined axial loading and radial pressure. *J. Construct. Steel Research* 1988; 9:3-34.
- [228] Cho S-R, Lee S-B. Ultimate strength formulation for stringer-stiffened cylinders subjected to combined axial compression and radial pressure. *International journal of Ocean Engineering and Technology* 1998; 1(1): 41-55.
- [229] Cho S-R, Seo BS, Cerik BC, Shin HK. Experimental and numerical investigations on the collision between offshore wind turbine support structures and service vessels. ICCGS; 2012.
- [230] Cho S-R, Seo BS, Cerik BC, Shin HK. Experimental and numerical investigations on the collision between offshore wind turbine support structures and service vessels. In: Amdahl J, Ehlers S, Leira BJ, editors. *Collision and grounding of ships and offshore structures*. London: CRC Press; 2013. p. 281-287.
- [231] Cho S-R, Le DNC, Shin HK. Plastic and fracture damages at T-joint of offshore tubular structures under collisions, TEAM 2016, Mokpo, Rep. of Korea; 2016.

List of publications

International Journal

- [1] Sang-Rai Cho, **Quang Thang Do**, Hyun Kyoung Shin. Residual strength of damaged ring-stiffened cylinders subjected to external hydrostatic pressure. *Marine Structures* 2017; 56:186–205.
- [2] **Quang Thang Do**, Teguh Muttaqie, Hyun Kyoung Shin, Sang-Rai Cho. Dynamic lateral mass impact on steel stringer-stiffened cylinders. *International Journal of Impact Engineering* 2018; 116:105–26.
- [3] **Quang Thang Do**, Teguh Muttaqie, Sang-Hyun Park, Hyun Kyoung Shin, Sang-Rai Cho. Ultimate strength of intact and dented steel stringer-stiffened cylinders under hydrostatic pressure. *Thin-Walled Structures* 2018; 132:442–60.
- [4] **Quang Thang Do**, Teguh Muttaqie, Sang-Hyun Park, Hyun Kyoung Shin, Sang-Rai Cho. Predicting the collision damage of steel ring-stiffened cylinders and their residual strength under hydrostatic pressure. *Ocean Engineering* 2018; 169:326–43.
- [5] **Quang Thang Do**, Teguh Muttaqie, Dinh Ngoc Can Le, Byeong-Soo Seo, Sang-Hyun Park, Hyun Kyoung Shin, Sang-Rai Cho. Fracture response and failure mode of H-shape tubular structures under dynamic mass impact. *International Journal of Impact Engineering*. (under preparation).
- [6] Sang-Rai Cho, Teguh Muttaqie, **Quang Thang Do**, Ha Young So, Jung-Min Sohn. Ultimate strength formulation considering failure mode interactions of ring-stiffened cylinders subjected to hydrostatic pressure. *Ocean Engineering* 2018; 161: 242–256.
- [7] Sang-Rai Cho, Teguh Muttaqie, **Quang Thang Do**, Kim S, Kim SM, Han D-H. Experimental investigations on the failure modes of ring-stiffened cylinders under external hydrostatic pressure. *International Journal of Naval Architecture and Ocean Engineering* 2018; 10:711-729.

International Conference

- [1] Quang Thang Do, Hyun Kyoung Shin, Cho Sang-Rai. Numerical investigations on the collapse behavior of damaged stringer-stiffened cylinders subjected to hydrostatic pressure In: Proceeding of Annual Spring Meeting of the Society of Naval Architects of Korea (SNAK), Busan, South Korea, 2016.
- [2] Quang Thang Do, Hyun Kyoung Shin, Cho Sang-Rai. Residual strength formulation for damaged ring-stiffened cylinders subjected to combined axial compression and radial pressure. In: Proceeding of Annual Autumn Meeting of the Society of Naval Architects of Korea (SNAK), Changwon, South Korea, 2016.
- [3] Quang Thang Do, Hyun Kyoung Shin, Hyun Heong Ahn, Jung Tae Kim, Cho Sang-Rai. Residual strength of damaged ring-stiffened cylinders subjected to hydrostatic pressure. In: Proceeding of the 7th International Conference on Collision and Grounding of Ships and Offshore Structures (ICCGS), Ulsan, South Korea, 2016.
- [4] Quang Thang Do, Hyun Kyoung Shin, Cho Sang-Rai. Numerical investigations on the buckling collapse behavior of dented ring-stiffened cylinders under combined axial compression and radial pressure. In: Proceeding of the 30th Asian-Pacific Technical Exchange and Advisory Meeting on Marine Structures (TEAM), Mokpo, South Korea, 2016.
- [5] Cho Sang-Rai, Teguh Muttaqie, Quang Thang Do. Derivation of strength formulation considering frame tripping for ring-stiffened cylindrical shell subjected to hydrostatic pressure. In: Proceeding of Annual Spring Meeting of the Society of Naval Architects of Korea (SNAK), Busan, South Korea, 2016.
- [6] Quang Thang Do, Hyun Kyoung Shin, Cho Sang-Rai. Residual strength of damaged stringer-stiffened cylinders subjected to hydrostatic pressure. In: Proceeding of Annual Spring Meeting of the Society of Naval Architects of Korea (SNAK), Busan, South Korea, 2017.
- [7] Quang Thang Do, Teguh Muttaqie, Hyun Kyoung Shin, Cho Sang-Rai. Numerical investigation on the responses of steel stringer-stiffened cylinders subjected to dynamic lateral mass impact. In: Proceeding of Annual Autumn Meeting of the Society of Naval Architects of Korea (SNAK), Yeosu, South Korea, 2017.
- [8] Quang Thang Do, Teguh Muttaqie, Hyun Kyoung Shin, Cho Sang-Rai. On the resistance of stringer-stiffened cylinders subjected to dynamic lateral mass impact. In: Proceeding of the

- 31th Asian-Pacific Technical Exchange and Advisory Meeting on Marine Structures (TEAM), Osaka, Japan, 2017.
- [9] Quang Thang Do, Teguh Muttaqie, Sang-Hyun Park, Hyun Kyoung Shin, Cho Sang-Rai. Residual strength of stringer-stiffened cylinder subjected to external hydrostatic pressure. In: Proceeding of the 3rd International Conference on Safety And Reliability of Ships, Offshore & Subsea Structures, Wuhan University of Technology, China, 2018.
- [10] Quang Thang Do, Sang-Hyun Park, Hyun Kyoung Shin, Kyu Nam Cho, Cho Sang-Rai. Ultimate strength formulations of intact and dented ring-stiffened cylinders under external hydrostatic pressure. In: Proceeding of the 32th Asian-Pacific Technical Exchange and Advisory Meeting on Marine Structures (TEAM), Wuhan University of Technology, China, 2018.
- [11] Quang Thang Do, Teguh Muttaqie, Sang-Hyun Park, Hyun Kyoung Shin, Cho Sang-Rai. Predicting the ultimate residual strength of dented steel stiffened cylinder subjected to combined axial compression and radial pressure. In: Proceeding of Progress in the Analysis and Design of Marine Structure, Dubrovnik, Croatia, 2019 (Submitted).

Appendix A: Imperfection measurement results for stiffened cylinder

RS-I	1st stiffener	2nd bay	2nd stiffener	3rd bay	3rd stiffener	4th bay	4th stiffener	5th bay	5th stiffener	6th bay	6th stiffener
Degree	p (mm)	p (mm)	p (mm)								
0	1.11	1.17	1.07	1.75	2.25	2.13	2.33	2.06	1.92	2.70	1.45
10	0.60	0.39	-1.14	-1.31	-1.54	-1.59	-1.64	-1.31	-1.16	-1.35	-0.92
20	0.04	0.20	0.01	-0.22	-0.33	-0.12	0.01	-0.38	-0.30	-0.48	-0.22
30	0.27	0.20	0.10	0.24	0.14	0.33	0.25	0.32	0.21	0.38	0.07
40	-0.85	-1.17	0.71	0.58	0.42	0.60	0.53	0.70	0.39	0.59	0.22
50	0.23	0.66	0.74	0.65	0.45	0.70	0.48	0.78	0.40	0.55	0.19
60	0.06	-0.38	-0.33	-0.16	-0.02	-0.20	-0.26	-0.32	-0.27	-0.55	-0.45
70	-0.40	-0.38	-0.20	0.20	-0.01	-0.25	-0.23	-0.02	0.01	-0.36	0.34
80	-0.17	0.01	0.04	0.06	0.16	-0.13	-0.23	-0.02	-0.01	0.05	-0.04
90	-0.20	-0.19	-0.13	-0.28	-0.12	-0.29	-0.21	-0.40	-0.07	-0.43	-0.30
100	-0.11	-0.08	-0.07	-0.02	-0.16	-0.15	-0.15	-0.42	-0.25	-0.25	-0.03
110	-0.18	-0.32	-0.01	-0.23	-0.07	-0.23	-0.15	-0.17	-0.12	-0.38	-0.26
120	-0.26	-0.10	-0.01	-0.15	0.03	-0.14	-0.15	-0.16	-0.16	-0.23	-0.10
130	-0.20	-0.16	-0.06	-0.15	-0.16	-0.12	-0.24	-0.26	-0.14	-0.16	0.03
140	-0.22	-0.08	-0.09	-0.11	0.12	-0.16	-0.33	-0.25	-0.11	-0.18	0.01
150	-0.15	-0.13	-0.12	-0.13	-0.03	-0.18	-0.10	-0.25	-0.10	-0.25	-0.02
160	-0.12	-0.11	-0.03	-0.08	-0.10	-0.14	-0.18	-0.19	-0.32	-0.39	-0.08
170	-0.17	-0.11	0.01	-0.12	-0.17	-0.19	-0.20	-0.21	-0.04	-0.17	-0.06
180	-0.31	-0.17	0.07	-0.16	0.03	-0.24	-0.10	-0.18	-0.07	-0.11	-0.07
190	-0.10	-0.11	0.01	-0.03	0.04	-0.05	-0.16	-0.20	-0.18	-0.30	-0.15
200	-0.22	-0.19	-0.12	-0.12	0.00	-0.14	-0.22	-0.32	-0.21	-0.28	-0.07
210	-0.09	-0.12	0.00	-0.05	-0.11	-0.16	-0.14	-0.17	-0.04	-0.12	-0.05
220	-0.18	-0.10	0.07	-0.14	-0.03	-0.31	-0.25	-0.30	-0.19	-0.23	0.00
230	-0.23	-0.07	-0.12	-0.03	-0.05	-0.14	-0.21	-0.16	-0.23	-0.36	-0.19

240	0.60	-0.37	-0.05	-0.29	0.06	-0.18	-0.05	-0.34	-0.15	-0.33	-0.11
250	-0.11	-0.15	0.04	-0.04	-0.08	-0.15	-0.29	-0.16	-0.01	-0.19	-0.07
260	-0.15	0.10	0.21	0.17	0.12	-0.01	-0.01	0.01	0.02	0.05	0.04
270	-0.09	-0.09	-0.19	-0.27	-0.24	-0.40	-0.37	-0.43	-0.18	-0.39	-0.08
280	-0.21	-0.30	-0.07	-0.39	-0.32	-0.30	-0.19	-0.31	-0.13	-0.27	-0.03
290	-0.47	-0.33	-0.20	-0.12	0.04	-0.18	-0.33	-0.32	-0.28	-0.23	-0.12
300	0.34	0.27	0.19	0.37	0.21	0.27	0.04	0.12	-0.14	-0.03	0.08
310	-0.51	-0.42	-0.13	-0.49	-0.28	-0.56	-0.28	-0.63	-0.20	-0.71	-0.30
320	-0.36	-0.24	-0.15	-0.27	-0.19	-0.30	-0.43	-0.25	-0.15	-0.15	-0.17
330	0.00	0.33	0.18	0.25	0.24	0.30	0.38	0.36	0.19	0.48	-0.02
340	-0.66	-1.05	-0.37	-0.88	-0.82	-1.09	-1.03	-1.41	-0.61	-1.26	-0.33
350	0.03	0.28	-0.38	-0.19	-0.16	0.08	0.09	0.35	-0.25	0.00	0.11

RS-C-1	1st stiffener	2nd bay	2nd stiffener	3rd bay	3rd stiffener	4th bay	4th stiffener	5th bay	5th stiffener	6th bay	6th stiffener
Degree	p (mm)	p (mm)	p (mm)								
0	0.66	1.15	0.82	1.43	0.54	1.02	0.63	0.71	0.56	0.86	0.66
10	0.18	-0.03	-1.21	0.17	0.00	-0.11	0.10	0.18	0.14	0.03	-0.04
20	-0.29	-0.48	-0.19	-0.63	-0.63	-0.53	-0.41	-0.61	-0.59	-0.56	-0.35
30	-0.19	-0.21	-0.06	-0.45	-0.51	-0.30	-0.35	-0.09	-0.39	-0.26	-0.22
40	0.31	0.43	0.33	0.48	0.57	0.55	0.44	0.47	0.66	0.42	0.17
50	-0.09	-0.31	-0.11	-0.14	-0.23	0.08	0.09	0.01	-0.23	-0.04	0.26
60	0.03	-0.18	-0.47	-0.18	0.33	-0.11	-0.17	-0.12	-0.20	-0.09	-0.20
70	0.21	0.24	0.44	0.30	0.00	0.25	0.35	0.36	0.38	0.36	0.58
80	-0.26	-0.37	-0.14	-0.32	-0.41	-0.45	-0.37	-0.21	-0.34	-0.14	-0.15
90	0.07	-0.08	0.01	-0.19	0.18	0.01	0.04	0.04	0.11	0.00	-0.02
100	0.10	-0.17	-0.17	-0.07	-0.21	0.12	0.21	0.17	0.18	0.23	0.28
110	0.12	-0.02	-0.03	-0.05	0.26	0.08	0.01	0.17	-0.05	0.08	0.13
120	0.14	0.01	0.08	-0.24	-0.25	0.02	-0.04	-0.06	-0.04	-0.02	-0.01
130	0.14	-0.09	0.13	-0.15	-0.13	-0.07	0.01	0.01	-0.02	-0.03	0.03
140	-0.06	-0.18	-0.23	-0.10	0.06	0.04	-0.06	0.12	-0.06	-0.04	0.11
150	0.07	-0.05	0.11	-0.11	-0.10	-0.03	-0.07	0.01	-0.16	-0.19	-0.04
160	0.02	-0.12	0.01	-0.24	-0.06	-0.23	-0.14	-0.17	-0.27	-0.07	0.01
170	-0.02	-0.21	-0.18	-0.28	-0.05	-0.05	-0.04	-0.08	0.00	0.02	-0.05
180	-0.07	-0.29	-0.07	-0.24	-0.04	-0.03	-0.02	0.11	0.05	0.01	-0.02
190	0.00	-0.14	-0.17	-0.19	-0.13	-0.10	-0.01	0.03	-0.04	0.01	0.03
200	-0.05	-0.06	0.11	-0.21	-0.20	0.00	-0.04	-0.05	-0.21	-0.13	-0.05
210	0.00	-0.06	-0.09	-0.12	0.03	-0.15	-0.18	-0.09	-0.04	0.02	0.02
220	0.10	-0.12	0.16	-0.13	0.00	-0.17	-0.22	-0.08	-0.04	-0.06	0.01
230	0.05	-0.08	-0.03	-0.09	-0.05	-0.07	0.13	0.02	-0.05	-0.13	0.07
240	0.18	-0.13	-0.07	-0.05	-0.05	-0.02	-0.16	-0.13	-0.25	-0.07	-0.08
250	0.05	-0.24	-0.09	-0.09	-0.19	-0.18	-0.17	0.00	0.00	-0.02	-0.07

260	-0.10	-0.07	-0.01	-0.27	0.03	-0.11	-0.05	0.08	0.15	-0.02	-0.03
270	-0.10	-0.30	-0.29	-0.21	0.23	-0.06	-0.04	-0.08	-0.20	-0.08	0.03
280	-0.01	0.14	0.39	0.10	0.27	0.06	0.01	0.11	0.14	0.10	0.09
290	0.39	0.22	0.24	0.03	0.20	-0.05	-0.03	0.03	0.00	0.12	0.23
300	0.39	0.09	0.29	-0.06	-0.35	-0.05	0.04	0.16	0.03	0.11	0.11
310	-0.16	-0.21	-0.34	-0.20	-0.08	-0.05	-0.06	-0.01	-0.03	-0.01	0.00
320	-0.28	-0.50	-0.21	-0.43	0.14	-0.29	-0.09	-0.27	0.19	-0.37	0.03
330	-0.06	0.12	0.04	0.27	0.28	0.36	0.03	0.34	0.01	0.25	-0.01
340	-0.32	-0.71	-0.29	-0.73	-0.23	-0.63	-0.23	-0.64	-0.42	-0.66	-0.35
350	-0.37	0.52	0.27	0.61	0.21	0.64	0.38	0.46	0.81	0.64	-0.28

RS-C-2	1st stiffener	2nd bay	2nd stiffener	3rd bay	3rd stiffener	4th bay	4th stiffener	5th bay	5th stiffener	6th bay	6th stiffener
Degree	p (mm)	p (mm)	p (mm)								
0	1.61	1.95	1.29	1.19	1.25	0.49	0.50	0.57	0.16	0.75	1.46
10	-0.39	-0.66	-0.37	-0.60	-0.27	-0.50	-0.52	-0.25	0.17	-0.03	-0.13
20	-0.19	-0.02	-0.05	0.37	0.40	0.49	0.44	0.28	0.02	0.00	-0.23
30	-0.03	0.00	0.04	-0.25	-0.69	-0.19	-0.06	-0.16	0.23	0.12	0.08
40	-0.01	-0.22	-0.08	-0.21	-0.03	-0.29	-0.33	-0.26	-0.29	-0.27	-0.24
50	-0.08	0.08	0.08	0.14	0.11	0.24	0.33	0.38	0.16	0.18	0.02
60	0.12	0.10	0.07	0.08	-0.27	0.15	0.12	0.08	0.11	-0.01	-0.11
70	-0.04	-0.03	-0.17	-0.09	-0.10	-0.07	-0.14	-0.11	-0.40	-0.24	-0.14
80	-0.01	-0.07	-0.04	0.03	0.05	-0.04	-0.08	-0.08	-0.03	-0.08	-0.18
90	-0.14	-0.07	-0.06	-0.10	0.01	0.01	0.16	-0.08	-0.13	-0.05	-0.14
100	0.07	0.04	0.13	0.20	0.03	0.14	0.03	0.06	0.15	0.08	-0.09
110	0.01	-0.03	-0.25	-0.01	0.14	-0.06	-0.24	0.15	0.05	0.01	-0.22
120	-0.06	-0.09	0.06	-0.08	-0.03	-0.08	-0.09	-0.06	-0.06	-0.05	-0.01
130	-0.05	-0.01	-0.12	-0.04	-0.08	-0.12	-0.12	-0.04	-0.20	-0.13	-0.08

140	-0.09	-0.12	-0.14	-0.16	-0.01	-0.13	-0.05	-0.11	-0.03	-0.10	-0.29
150	0.09	-0.13	-0.19	-0.06	0.03	0.02	0.10	-0.14	-0.15	-0.07	-0.06
160	-0.04	-0.06	-0.08	0.08	0.13	0.14	0.11	-0.07	0.14	0.09	-0.07
170	-0.02	0.13	0.11	0.09	0.17	0.13	-0.01	0.08	0.02	0.03	-0.08
180	0.02	0.01	-0.04	0.06	0.15	-0.04	0.05	0.11	0.26	0.15	0.01
190	-0.14	-0.11	-0.20	-0.02	0.00	0.05	0.08	0.06	0.08	-0.02	-0.06
200	-0.02	-0.04	-0.04	0.01	0.11	0.11	0.03	-0.14	-0.41	-0.25	-0.27
210	-0.04	-0.02	0.06	0.01	0.11	-0.04	-0.10	-0.07	-0.04	-0.12	-0.22
220	-0.03	-0.06	-0.10	-0.12	-0.22	-0.12	-0.08	-0.07	0.09	-0.03	-0.21
230	-0.05	-0.06	-0.09	0.03	0.03	-0.03	0.03	-0.01	-0.15	0.03	-0.12
240	-0.08	-0.05	-0.07	-0.02	0.12	0.17	-0.05	-0.12	-0.03	-0.19	-0.21
250	0.24	0.00	-0.07	0.04	0.05	-0.07	0.08	-0.11	-0.12	-0.06	-0.05
260	-0.35	0.03	-0.05	-0.08	-0.09	-0.11	-0.15	-0.12	-0.04	0.10	-0.12
270	0.41	-0.10	-0.09	-0.23	-0.14	-0.22	-0.25	-0.04	0.16	0.06	-0.10
280	-0.37	-0.23	-0.19	-0.15	0.01	-0.08	0.01	-0.15	-0.26	-0.40	-0.23
290	0.24	0.28	0.09	0.42	0.27	0.45	0.17	0.20	-0.14	0.18	-0.03
300	-0.58	-0.48	-0.40	-0.35	0.00	-0.25	0.00	-0.27	-0.13	-0.18	-0.20
310	-0.03	-0.04	-0.05	0.10	-0.20	0.08	-0.04	0.09	0.08	0.02	-0.04
320	-0.16	-0.18	-0.11	-0.19	0.08	-0.11	-0.20	-0.14	-0.28	-0.13	-0.18
330	0.04	-0.07	0.01	-0.19	-0.26	-0.27	-0.26	-0.46	-0.05	-0.33	-0.56
340	-0.15	-0.05	-0.11	-0.04	0.48	0.05	0.32	0.08	0.08	0.33	0.33
350	-0.39	-0.59	-0.30	-0.21	-0.67	0.05	-0.16	0.12	0.19	-0.37	-0.19

Imperfection amplitude measurement for SS-1-Axial direction																					
Deg.	0	70	120	170	220	270	320	370	420	470	520	570	620	670	720	770	820	870	920	970	1045
0	0.21	0.26	0.30	0.47	0.38	0.32	0.24	0.61	0.51	0.61	0.59	0.51	0.80	0.92	1.18	1.18	0.80	0.51	0.59	0.61	0.51
10	-0.19	0.25	0.45	0.27	0.19	0.55	0.42	0.31	0.43	0.31	0.21	0.41	0.21	0.41	0.39	0.39	0.21	0.41	0.21	0.31	0.43
20	-0.31	1.15	0.30	-0.05	-0.44	0.96	0.07	-0.25	-0.32	-0.25	-0.51	-0.24	-0.46	-0.15	-0.38	-0.38	-0.46	-0.24	-0.51	-0.25	-0.32
30	-0.69	-0.09	0.11	-0.62	-0.82	-0.57	-0.35	-0.52	0.17	-0.52	-0.69	-0.98	-1.25	-0.80	-0.87	-0.87	-1.25	-0.98	-0.69	-0.52	0.17
40	-0.68	-0.43	-0.32	-1.05	-0.97	-0.80	-0.29	-0.88	-1.23	-0.88	-1.33	-1.55	-1.85	-1.49	-1.61	-1.61	-1.85	-1.55	-1.33	-0.88	-1.23
50	-0.86	-0.76	0.03	-0.85	-0.96	-0.94	-0.77	-1.17	-1.54	-1.17	-1.77	-2.03	-2.48	-2.10	-2.22	-2.22	-2.48	-2.03	-1.77	-1.17	-1.54
60	-1.14	-1.07	-0.87	-2.00	-1.81	-2.21	-1.72	-2.41	-3.05	-2.41	-2.61	-3.03	-2.88	-3.15	-3.19	-3.19	-2.88	-3.03	-2.61	-2.41	-3.05
70	-1.32	-1.06	-1.03	-2.01	-2.04	-2.41	-2.07	-2.94	-3.70	-2.94	-3.28	-3.83	-4.00	-3.85	-3.91	-3.91	-4.00	-3.83	-3.28	-2.94	-3.70
80	-1.07	-0.83	-1.37	-2.77	-2.78	-3.22	-2.77	-3.32	-3.82	-3.32	-3.88	-4.55	-4.25	-4.20	-4.15	-4.15	-4.25	-4.55	-3.88	-3.32	-3.82
90	-1.24	-1.44	-2.47	-4.23	-3.41	-4.45	-3.40	-4.76	-5.27	-4.76	-5.13	-5.35	-5.35	-5.52	-4.08	-4.08	-5.35	-5.35	-5.13	-4.76	-5.27
100	-0.55	-0.74	-1.46	-2.94	-2.61	-3.49	-3.18	-4.22	-4.72	-4.22	-4.90	-5.18	-5.25	-4.95	-4.30	-4.30	-5.25	-5.18	-4.90	-4.22	-4.72
110	-0.25	-0.08	-0.79	-2.18	-2.50	-3.04	-2.94	-3.98	-4.63	-3.98	-4.64	-5.21	-5.47	-5.19	-5.25	-5.25	-5.47	-5.21	-4.64	-3.98	-4.63
120	-0.36	0.18	-0.31	-1.58	-1.81	-2.58	-2.37	-3.54	-4.15	-3.54	-4.05	-4.37	-4.47	-4.73	-3.87	-3.87	-4.47	-4.37	-4.05	-3.54	-4.15
130	0.21	0.98	0.51	-0.27	-0.48	-0.83	-0.70	-1.96	-2.17	-1.96	-2.77	-3.18	-3.11	-3.52	-3.39	-3.39	-3.11	-3.18	-2.77	-1.96	-2.17
140	0.28	0.64	0.50	-0.36	-0.61	-0.82	-0.11	-1.46	-1.77	-1.46	-2.10	-2.42	-2.82	-2.73	-2.75	-2.75	-2.82	-2.42	-2.10	-1.46	-1.77
150	0.31	0.84	0.49	-0.26	-0.06	-0.44	-0.23	-0.34	-0.52	-0.34	-0.78	-1.54	-1.65	-1.27	-1.40	-1.40	-1.65	-1.54	-0.78	-0.34	-0.52
160	0.37	0.64	0.27	-0.17	-0.07	-0.37	-0.16	-0.14	-0.22	-0.14	-0.47	-0.82	-0.68	-0.53	-0.50	-0.50	-0.68	-0.82	-0.47	-0.14	-0.22
170	0.25	0.43	0.29	0.14	0.09	-0.06	0.05	0.35	0.29	0.35	0.18	-0.11	0.18	0.50	0.71	0.71	0.18	-0.11	0.18	0.35	0.29
180	0.21	0.26	0.30	0.47	0.39	0.32	0.25	0.61	0.51	0.61	0.62	0.58	0.86	0.99	1.30	1.30	0.86	0.58	0.62	0.61	0.51
190	0.13	0.12	0.08	0.41	0.54	0.53	0.50	0.82	0.83	0.82	1.00	1.02	1.30	0.89	0.81	0.81	1.30	1.02	1.00	0.82	0.83
200	-0.08	-0.04	0.05	0.57	0.68	0.74	0.62	1.06	1.16	1.06	1.13	1.43	1.95	1.68	1.37	1.37	1.95	1.43	1.13	1.06	1.16
210	-0.14	-0.24	-0.01	0.66	0.76	0.77	0.64	1.43	1.48	1.43	1.63	1.99	1.91	2.33	2.06	2.06	1.91	1.99	1.63	1.43	1.48
220	-0.28	-0.30	-0.17	0.62	0.73	0.72	0.64	1.58	1.77	1.58	2.13	2.59	2.48	2.88	3.06	3.06	2.48	2.59	2.13	1.58	1.77
230	0.07	-0.49	-0.15	0.98	1.08	1.12	1.07	2.10	2.30	2.10	2.62	3.33	3.23	3.43	3.04	3.04	3.23	3.33	2.62	2.10	2.30
240	0.35	-0.44	0.08	1.28	1.38	1.84	1.47	2.47	2.72	2.47	3.09	3.76	3.82	3.85	3.21	3.21	3.82	3.76	3.09	2.47	2.72
250	0.40	-0.16	0.22	1.45	1.50	1.94	1.64	2.61	3.02	2.61	3.43	4.08	4.11	4.00	3.34	3.34	4.11	4.08	3.43	2.61	3.02

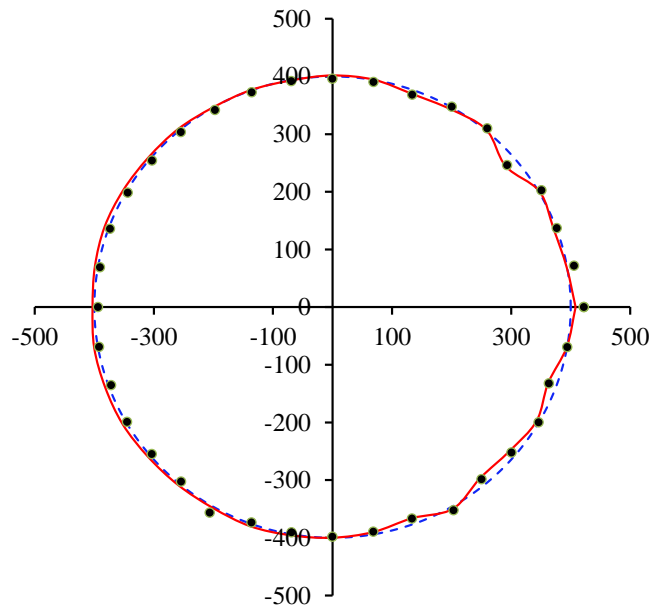
Imperfection amplitude measurement for SS-1-Axial direction																					
Deg.	0	70	120	170	220	270	320	370	420	470	520	570	620	670	720	770	820	870	920	970	1045
260	0.47	0.03	0.41	1.75	1.55	2.18	1.65	2.80	3.33	2.80	3.50	4.06	4.06	4.09	3.92	3.92	4.06	4.06	3.50	2.80	3.33
270	0.55	0.28	0.46	2.20	2.21	2.56	2.00	3.09	3.59	3.09	3.71	4.12	3.82	3.77	3.41	3.41	3.82	4.12	3.71	3.09	3.59
280	0.82	0.28	0.69	1.93	1.86	2.30	2.18	2.49	3.11	2.49	2.86	3.52	3.26	3.21	3.03	3.03	3.26	3.52	2.86	2.49	3.11
290	1.01	0.37	0.69	1.62	1.55	1.86	1.46	2.03	2.51	2.03	2.51	3.02	2.53	2.70	2.77	2.77	2.53	3.02	2.51	2.03	2.51
300	0.65	0.37	0.52	1.28	1.12	1.42	1.09	1.66	2.10	1.66	2.17	2.52	2.58	2.26	2.41	2.41	2.58	2.52	2.17	1.66	2.10
310	1.13	0.33	0.48	0.85	1.17	1.60	1.19	1.34	1.86	1.34	1.90	2.04	2.30	1.69	1.69	1.69	2.30	2.04	1.90	1.34	1.86
320	0.54	0.15	0.56	1.31	1.23	1.45	1.21	1.08	1.61	1.08	1.65	1.62	1.96	1.27	0.90	0.90	1.96	1.62	1.65	1.08	1.61
330	0.22	0.06	0.47	1.20	1.07	1.20	1.04	0.87	1.25	0.87	1.30	1.26	1.49	0.97	0.90	0.90	1.49	1.26	1.30	0.87	1.25
340	0.30	0.14	0.28	0.86	0.96	1.02	0.90	1.03	1.18	1.03	1.10	1.07	1.29	0.87	0.74	0.74	1.29	1.07	1.10	1.03	1.18
350	0.46	0.10	0.13	0.55	0.55	0.52	0.50	0.95	0.88	0.95	0.98	0.92	1.04	0.53	0.42	0.42	1.04	0.92	0.98	0.95	0.88
360	0.21	0.26	0.30	0.47	0.38	0.32	0.24	0.61	0.51	0.61	0.59	0.51	0.80	0.92	1.18	1.18	0.80	0.51	0.59	0.61	0.51



Fig. A. 1 Measurements of initial shape imperfections.

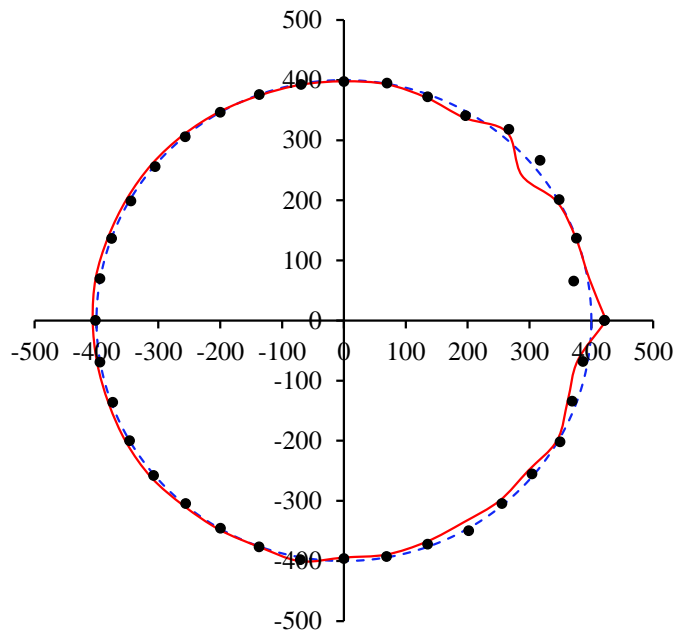
Appendix B: Typical circumferential shape imperfection pattern observed in test models

Imp. magnitude x 20 exaggerated at 1st ring-stiffener
RS-I -model



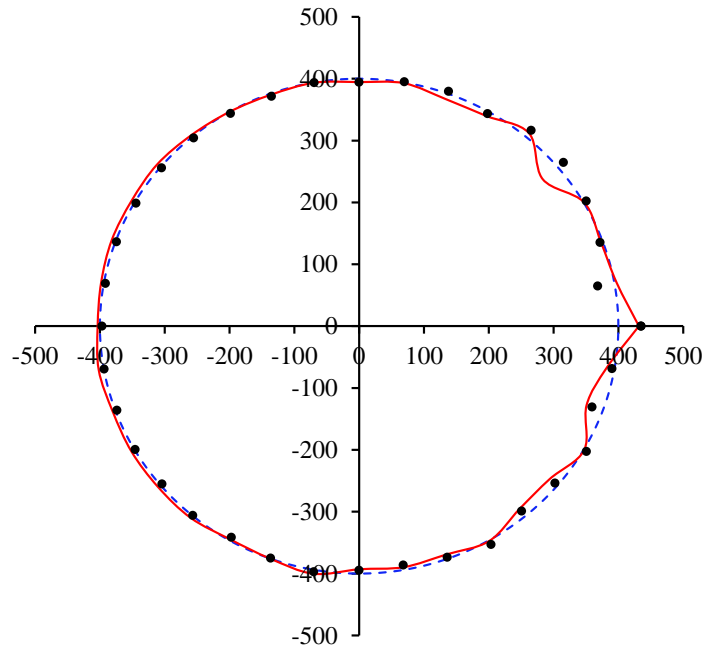
-- Real Circle • Measured point — Fourier Functional

Imp. magnitude x 20 exaggerated at 2nd ring-stiffener
RS-I -model



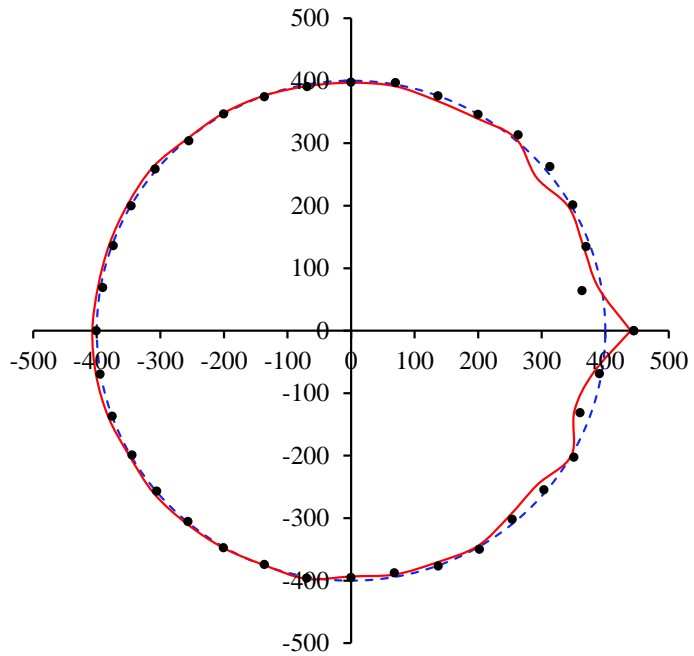
-- Real Circle • Measured Point — Fourier Functional

Imp. magitude x 20 exaggerated at 3rd bay
RS-I -model

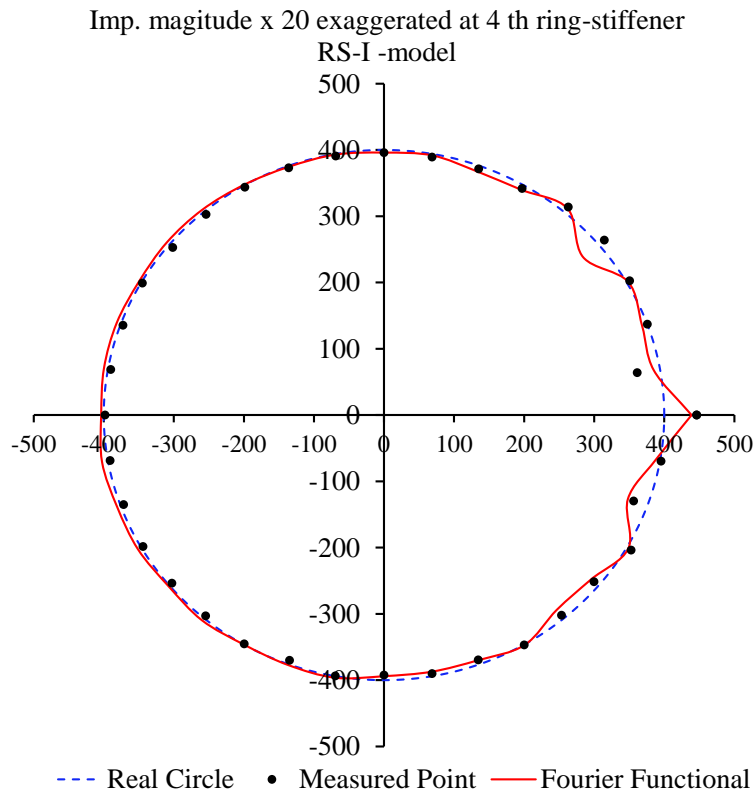
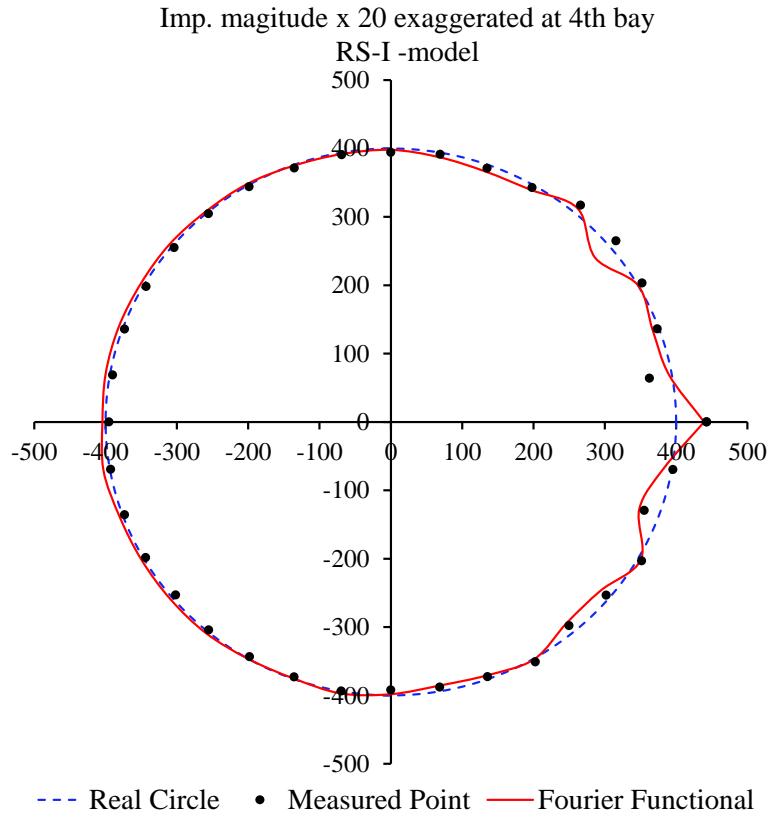


-- Real Circle • Measured Point — Fourier Functional

Imp. magitude x 20 exaggerated at 3rd ring-stiffener
RS-I -model



-- Real Circle • Measured Point — Fourier Functional



Appendix C: Properties of tensile test coupons and details of test results for stiffened cylinder models

Detail of tensile test result on each coupon for models: RS-I, RS-C-1, and RS-C-2

RS-I Cylinder shell	Thickness (mm)			Average thickness (mm)	Width (mm)			Average width (mm)	Average cross-sectional area (mm ²)
	Coupon ID #	t ₁	t ₂		t ₃	t _{ave}	w ₁		
1	3.84	3.82	3.81	3.82	24.77	24.79	24.81	24.79	94.78
2	3.83	3.82	3.82	3.82	24.80	24.84	24.8	24.81	94.87
3	3.82	3.83	3.82	3.82	24.83	24.83	24.81	24.82	94.91
4	3.82	3.82	3.85	3.83	24.81	24.78	24.8	24.80	94.97
5	3.83	3.83	3.82	3.83	24.78	24.78	24.78	24.78	94.82
6	3.82	3.82	3.85	3.83	24.85	24.78	24.79	24.81	95.01

RS-I Ring-stiffeners	Thickness (mm)			Average thickness (mm)	Width (mm)			Average width (mm)	Average cross-sectional area (mm ²)
	Coupon ID #	t ₁	t ₂		t ₃	t _{ave}	w ₁		
1	3.80	3.78	3.82	3.80	24.81	24.79	24.77	24.79	94.20
2	3.80	3.80	3.81	3.80	24.81	24.87	24.81	24.83	94.44
3	3.78	3.77	3.76	3.77	24.83	24.81	24.77	24.80	93.51
4	3.80	3.80	3.81	3.80	24.83	24.83	24.84	24.83	94.45
5	3.80	3.79	3.80	3.80	24.93	24.86	24.86	24.88	94.47
6	3.80	3.79	3.80	3.80	24.93	24.86	24.91	24.90	94.54

RS-C-1 Cylinder shell	Thickness (mm)			Average thickness (mm)	Width (mm)			Average width (mm)	Average cross-sectional area (mm ²)
	Coupon ID #	t ₁	t ₂		t ₃	t _{ave}	w ₁		
1	3.80	3.82	3.81	3.81	24.85	24.83	24.83	24.84	94.63
2	3.81	3.82	3.81	3.81	24.81	24.79	24.81	24.80	94.58
3	3.82	3.81	3.82	3.82	24.79	24.83	24.80	24.81	94.68
4	3.82	3.83	3.82	3.82	24.81	24.78	24.81	24.80	94.82
5	3.82	3.82	3.83	3.82	24.79	24.80	24.80	24.80	94.81
6	3.82	3.82	3.82	3.82	24.82	24.87	24.82	24.84	94.88

RS-C-1 Ring-stiffeners	Thickness (mm)			Average thickness (mm)	Width (mm)			Average width (mm)	Average cross-sectional area (mm ²)
	Coupon ID #	t ₁	t ₂		t ₃	t _{ave}	w ₁		
1	3.81	3.83	3.83	3.82	24.77	24.84	24.80	24.80	94.83
2	3.82	3.83	3.83	3.83	24.83	24.82	24.80	24.82	94.97
3	3.81	3.82	3.82	3.82	24.79	24.81	24.82	24.81	94.68
4	3.82	3.81	3.82	3.82	24.77	24.77	24.81	24.78	94.59
5	3.83	3.83	3.83	3.83	24.78	24.79	24.77	24.78	94.91
6	3.82	3.82	3.83	3.82	24.83	24.84	24.88	24.85	95.01

RS-C-2 Cylinder shell	Thickness (mm)			Average thickness (mm)	Width (mm)			Average width (mm)	Average cross-sectional area (mm ²)
Coupon ID #	t ₁	t ₂	t ₃	t _{ave}	w ₁	w ₂	w ₃	w _{ave}	A _{ave}
1	3.77	3.75	3.76	3.76	24.84	24.90	24.87	24.87	93.51
2	3.80	3.80	3.81	3.80	24.82	24.83	24.88	24.84	94.49
3	3.79	3.79	3.81	3.80	24.95	24.93	24.96	24.95	94.71
4	3.78	3.78	3.79	3.78	24.78	24.79	24.80	24.79	93.79
5	3.79	3.78	3.78	3.78	24.88	24.87	24.83	24.86	94.05
6	3.80	3.76	3.75	3.77	24.89	24.81	24.79	24.83	93.61

RS-C-2 Ring-stiffeners	Thickness (mm)			Average thickness (mm)	Width (mm)			Average width (mm)	Average cross-sectional area (mm ²)
Coupon ID #	t ₁	t ₂	t ₃	t _{ave}	w ₁	w ₂	w ₃	w _{ave}	A _{ave}
1	3.76	3.76	3.76	3.76	24.79	24.75	24.82	24.79	93.20
2	3.79	3.79	3.79	3.79	24.89	24.84	24.84	24.86	94.21
3	3.79	3.79	3.80	3.79	24.85	24.89	24.86	24.87	94.33
4	3.80	3.80	3.80	3.80	24.82	24.72	24.76	24.77	94.11
5	3.76	3.76	3.76	3.76	24.77	24.84	24.78	24.80	93.24
6	3.80	3.79	3.80	3.80	24.81	24.87	24.87	24.85	94.35

Dynamic tensile test coupon for ring-stiffened cylinder models: RS-I, RS-C-1 and RS-C-2

Coupon ID #	Thickness (mm)			Average thickness (mm)	Width (mm)			Average width (mm)	Average cross-sectional area (mm ²)
	t ₁	t ₂	t ₃	t _{ave}	w ₁	w ₂	w ₃	w _{ave}	A _{ave}
DT-1	2.29	2.14	2.28	2.24	10.02	10.00	9.96	9.99	22.35
DT-2	1.92	1.93	1.92	1.92	9.98	10.01	10.01	10.00	19.23
DT-3	2.07	2.07	2.06	2.07	10.03	10.06	9.96	10.02	20.70
DT-4	2.14	2.13	2.12	2.13	10.13	10.06	10.12	10.10	21.52
DT-5	2.08	2.10	2.11	2.10	10.01	10.00	10.01	10.01	20.98
DT-6	2.09	2.12	2.11	2.11	10.03	10.04	9.98	10.02	21.10
DT-7	2.13	2.14	2.14	2.14	10.09	10.00	10.03	10.04	21.45
DT-8	2.10	2.11	2.11	2.11	10.06	10.03	10.04	10.04	21.16
DT-9	2.12	2.12	2.12	2.12	9.99	10.01	10.01	10.00	21.21
DT-10	2.10	2.11	2.11	2.11	10.01	9.96	10.02	10.00	21.06
DT-11	2.13	2.11	2.13	2.12	9.39	9.28	9.99	9.55	20.28
DT-12	2.03	2.05	2.09	2.06	10.04	9.98	10.03	10.02	20.60
DT-13	2.00	2.01	2.01	2.01	9.97	10.00	10.00	9.99	20.05
DT-14	2.16	2.16	2.23	2.18	9.99	10.01	9.96	9.99	21.80
DT-15	1.94	1.94	1.96	1.95	10.01	9.99	10.00	10.00	19.47
DT-16	1.93	1.93	1.93	1.93	10.01	10.03	10.03	10.02	19.35
DT-17	1.95	1.96	1.96	1.96	9.97	9.98	9.97	9.97	19.51
DT-18	2.05	2.05	2.06	2.05	9.98	10.00	10.01	10.00	20.53
DT-19	2.06	2.05	2.06	2.06	9.99	10.00	9.97	9.99	20.54
DT-20	2.03	2.05	2.06	2.05	9.98	10.02	10.00	10.00	20.47
DT-21	2.06	2.07	2.07	2.07	10.00	10.03	9.99	10.01	20.68
DT-22	2.18	2.17	2.19	2.18	9.96	9.95	9.93	9.95	21.68
			Mean	2.07			Mean	9.99	20.71
			Std. dev.	0.08			Std. dev.	0.10	0.83
			COV %	4.0%			COV %	1.0%	4.0%

Dimensions of the dynamic tensile coupons for S1-Ring & stringer stiffener - 5mm

Specimen	Measured thickness (mm)				Measured width (mm)				A (mm ²)	
	1	2	3	Mean	1	2	3	Mean		
S1-1	1.97	1.98	1.97	1.97	5.97	5.97	5.98	5.97	11.79	
S1-2	1.98	1.98	1.98	1.98	5.99	6.00	5.98	5.99	11.86	
S1-3	1.97	1.98	1.98	1.98	5.99	6.00	5.99	5.99	11.85	
S1-4	2.00	1.99	1.98	1.99	6.01	5.99	6.00	6.00	11.94	
S1-5	1.97	1.98	1.98	1.98	6.01	6.00	5.99	6.00	11.86	
S1-6	1.98	1.97	1.98	1.98	6.01	6.00	6.00	6.00	11.87	
S1-7	1.99	1.98	1.99	1.99	5.97	5.97	5.98	5.97	11.87	
S1-8	1.98	1.98	1.97	1.98	6.00	5.99	5.99	5.99	11.85	
S1-9	1.97	1.98	1.99	1.98	5.97	5.98	5.99	5.98	11.84	
MEAN				1.98	MEAN				5.99	11.86
Std. dev.				0.01	Std. dev.				0.01	0.04
COV%				0.27	COV%				0.19	0.33

Dimensions of the dynamic tensile coupons for S2-Cylinder shell- mmm

Specimen	Measured thickness (mm)				Measured width (mm)				A (mm ²)	
	1	2	3	Mean	1	2	3	Mean		
S2-1	1.96	1.96	1.98	1.97	5.95	5.97	6.02	5.98	11.76	
S2-2	1.98	1.98	2.00	1.99	5.98	5.98	5.97	5.98	11.87	
S2-3	1.97	1.97	1.98	1.97	6.00	6.00	5.97	5.99	11.82	
S2-4	1.97	1.97	1.98	1.97	5.96	5.97	5.97	5.97	11.77	
S2-5	1.97	1.97	1.97	1.97	5.96	5.97	5.98	5.97	11.76	
S2-6	1.97	1.98	1.97	1.97	5.96	5.96	5.97	5.96	11.77	
S2-7	1.97	1.96	1.97	1.97	5.96	5.97	5.97	5.97	11.73	
S2-8	1.97	1.98	1.97	1.97	5.96	5.98	5.98	5.97	11.79	
S2-9	1.97	1.97	1.98	1.97	5.97	5.96	5.96	5.96	11.77	
S2-10	1.97	1.98	1.98	1.98	5.96	5.96	5.97	5.96	11.79	
MEAN				1.97	MEAN				5.97	11.78
Std. dev.				0.01	Std. dev.				0.01	0.04
COV%				0.29	COV%				0.15	0.33

Parent plate	Coupon ID	E (MPa)	σ_Y (MPa)	σ_T (MPa)	ϵ_Y	ϵ_{yp}	ϵ_T	ϵ_f
RS-I-1	#1	177000	298.3	394.9	0.00168	0.01950	0.20000	0.38000
RS-I-1	#2	205000	301.8	392.4	0.00147	0.02460	0.19600	0.36700
RS-I-1	#3	247000	306.8	399.3	0.00124	0.01710	0.19400	0.36800
RS-I-1	#4	198000	307.7	400.9	0.00155	0.02380	0.19600	0.37900
RS-I-1	#5	193000	317.9	403.8	0.00164	0.02840	0.19600	0.37200
	Mean	205000	306.5	398.3	0.00152	0.02268	0.19640	0.37320
	Std. dev.	26403.0	7.40	4.60	0.00018	0.00444	0.00219	0.00606
	COV %	12.91	2.42	1.16	11.66	19.58	1.12	1.62
RS-I-2	#1	204000	304.3	392.6	0.00149	0.01890	0.19400	0.36700
RS-I-2	#2	174000	310.8	398.3	0.00179	0.02380	0.19700	0.36500
RS-I-2	#3	216000	305.2	393.8	0.00141	0.02180	0.19100	0.35700
RS-I-2	#4	232000	309.0	396.9	0.00133	0.02330	0.19700	0.37800
RS-I-2	#5	201000	306.0	400.6	0.00152	0.02050	0.19200	0.37000
	Mean	206000	307.1	396.4	0.00151	0.02166	0.19420	0.36740
	Std. dev.	21360.6	2.70	3.30	0.00017	0.00202	0.00277	0.00764
	COV %	10.39	0.90	0.83	11.37	9.31	1.43	2.08

Parent plate	Coupon ID	E (Mpa)	σ_Y (Mpa)	σ_T (Mpa)	ϵ_Y	ϵ_{yp}	ϵ_T	ϵ_f
RS-C-1-1	#1	208000	296.2	393.6	0.00142	0.02180	0.19600	0.37700
RS-C-1-1	#2	160000	295.7	392.8	0.00184	0.02040	0.19900	0.37800
RS-C-1-1	#3	198000	293.1	389.4	0.00147	0.02210	0.20100	0.38300
RS-C-1-1	#4	193000	317.4	403.6	0.00165	0.02660	0.19400	0.36900
RS-C-1-1	#5	197000	308.5	401.6	0.00157	0.02260	0.19000	0.37300
	Mean	191000	302.2	396.2	0.00159	0.02270	0.19600	0.37600
	Std. dev.	18182.3	10.4	6.1	0.00016	0.00233	0.00430	0.00529
	COV %	9.50	3.44	1.54	10.36	10.26	2.19	1.41
RS-C-1-2	#1	178000	312.5	403.9	0.00176	0.02230	0.19200	0.36400
RS-C-1-2	#2	196000	313.6	402.6	0.00160	0.02200	0.19500	0.37100
RS-C-1-2	#3	226000	296.3	390.0	0.00131	0.01960	0.20400	0.37400
RS-C-1-2	#4	197000	291.1	391.5	0.00148	0.01950	0.19600	0.37500
RS-C-1-2	#5	205000	319.7	404.7	0.00156	0.02500	0.19700	0.36700
	Mean	200000	306.6	398.6	0.00154	0.02168	0.19680	0.37020
	Std. dev.	17392.1	12.30	7.20	0.00016	0.00227	0.00444	0.00466
	COV %	8.69	4.00	1.80	10.62	10.46	2.26	1.26

Parent plate	Coupon ID	E (Mpa)	σ_Y (Mpa)	σ_T (Mpa)	ϵ_Y	ϵ_{yp}	ϵ_T	ϵ_f
RS-C-2-1	#1	197000	299.6	388.6	0.00152	0.02080	0.19500	0.36800
RS-C-2-1	#2	196000	310.3	398.1	0.00158	0.02160	0.19700	0.36900
RS-C-2-1	#3	178000	311.0	399.7	0.00175	0.02330	0.19800	0.37400
RS-C-2-1	#4	208000	312.9	400.0	0.00150	0.02360	0.19000	0.36900
RS-C-2-1	#5	209000	311.2	400.3	0.00149	0.02280	0.18900	0.36200
	Mean	198000	309.0	397.3	0.00157	0.02242	0.19380	0.36840
	Std. dev.	12496.1	5.4	4.9	0.00011	0.00118	0.00409	0.00428
	COV %	6.32	1.73	1.24	6.72	5.28	2.11	1.16
RS-C-2-2	#1	242000	299.9	394.8	0.00124	0.02230	0.19400	0.36700
RS-C-2-2	#2	206000	315.0	401.3	0.00153	0.02270	0.19300	0.36700
RS-C-2-2	#3	230000	302.6	395.5	0.00131	0.02040	0.18900	0.36200
RS-C-2-2	#4	209000	309.1	396	0.00147	0.02120	0.19500	0.36700
RS-C-2-2	#5	170000	304.2	394.2	0.00178	0.02040	0.19300	0.36800
	Mean	212000	306.1	396.4	0.00147	0.02140	0.19280	0.36620
	Std. dev.	27478.7	6.00	2.80	0.00021	0.00107	0.00228	0.00239
	COV %	12.98	1.95	0.72	14.48	4.98	1.18	0.65

For all coupons

	E (Mpa)	σ_u (Mpa)	σ_Y (Mpa)	σ_T (Mpa)	ϵ_Y	ϵ_{yp}	ϵ_T	ϵ_f
Mean	202000	316.3	306.2	397.2	0.001532	0.0221	0.195	0.370
Std. dev.	20360.6	10.1	7.6	4.7	0.00016	0.0023	0.0035	0.0059
COV %	10.1	3.2	2.5	1.2	10.4	10.5	1.8	1.6

Detail of tensile test result on each coupon for models: RS-II, RS-C-3, and RS-C-4

Coupon test	E (MPa)	Yield Stress (MPa)	Yield Strain	Ultimate tensile Stress (MPa)	Ultimate Tensile Strain	Hardening start strain	Fracture strain
TS-1	206000	275.1	0.0033	374.8	0.2333	0.0140	0.4687
TS-2	202000	269.0	0.0033	367.3	0.2359	0.0146	0.4699
TS-3	200000	279.2	0.0034	370.1	0.2379	0.0146	0.4711
TS-4	200000	265.7	0.0034	364.9	0.2335	0.0148	0.4614
TS-5	206000	272.7	0.0033	368.3	0.2347	0.0142	0.4810
TS-6	202000	277.7	0.0033	368.0	0.2378	0.0143	0.4712
TS-7	204000	278.3	0.0034	372.5	0.2318	0.0154	0.4799
TS-8	201000	275.3	0.0034	375.6	0.2333	0.0141	0.4687
TS-9	201000	281.2	0.0034	373.4	0.2334	0.0146	0.4758
Mean	202000	274.9	0.0034	370.5	0.23	0.01	0.47
Std. dev.	$\frac{2304.5}{2}$	5.01	0.00006	3.68	0.0021	0.0004	0.01
COV %	1.14	1.82	1.72	0.99	0.91	2.92	1.29

Coupon test	E (MPa)	Yield Stress (MPa)	Yield Strain	Ultimate tensile Stress (MPa)	Ultimate Tensile Strain	Hardening start strain	Fracture strain
TR-1	196000	294.4	0.0035	447.0	0.2152	0.0119	0.4234
TR-3	192000	290.7	0.0035	444.9	0.2167	0.0118	0.4191
TR-4	198000	286.7	0.0035	444.2	0.2174	0.0120	0.4240
TR-5	198000	288.4	0.0035	445.0	0.2182	0.0120	0.4205
TR-6	199000	289.2	0.0035	446.1	0.2145	0.0121	0.4204
TR-7	198000	294.0	0.0035	444.4	0.2241	0.0120	0.4200
TR-8	198000	292.0	0.0035	445.6	0.2251	0.0122	0.4258
TR-9	198000	289.9	0.0035	445.0	0.2171	0.0126	0.4258
Mean	197000	290.6	0.0035	445.5	0.2185	0.0121	0.4224
Std. dev.	2159.30	2.69	0.00003	1.23	0.0039	0.0002	0.0027
COV %	1.09	0.93	0.71	0.28	1.80	2.07	0.64

Detail of tensile test result on each coupon for models: SS-I, SS-C-1, and SS-C-2

Cylinder shell							
Coupon ID	E (Mpa)	σ_Y (Mpa)	ϵ_Y	σ_T (Mpa)	ϵ_T	ϵ_{HS}	ϵ_f
T-S-1	208000	331.8	0.00360	413.0	0.17410	0.02184	0.38612
T-S-2	209000	331.8	0.00363	414.4	0.17204	0.02147	0.37694
T-S-3	210000	341.2	0.00318	421.8	0.17410	0.02551	0.39877
T-S-4	211000	340.2	0.00316	417.4	0.17443	0.02175	0.38847
T-S-5	205000	339.5	0.00345	421.5	0.17044	0.02173	0.36336
T-S-6	219000	331.2	0.00335	413.9	0.17125	0.02134	0.37230
Mean	210000	335.9	0.00339	417.0	0.17273	0.02227	0.38099
Std. dev.	4719.4	4.83	0.00	3.90	0.00	0.00	0.01
COV %	2.25	1.44	5.95	0.93	0.99	7.16	3.32
Ring-stiffener flange							
Coupon ID	E (Mpa)	σ_Y (Mpa)	ϵ_Y	σ_T (Mpa)	ϵ_T	ϵ_{HS}	ϵ_f
T-EF-1	199000	275.4	0.00338	395.5	0.21935	-	0.44394
T-EF-2	202000	264.7	0.00338	397.2	0.22829	-	0.44073
T-EF-3	206000	274.3	0.00332	395.1	0.22939	-	0.46687
T-EF-4	197000	260.0	0.00335	394.8	0.23459	-	0.46566
T-EF-5	206000	253.7	0.00333	389.7	0.23355	-	0.47343
T-EF-6	209000	263.3	0.00325	394.9	0.23022	-	0.47279
Mean	203000	265.2	0.00333	394.5	0.22923	-	0.46057
Std. dev.	4498.9	8.38	0.00	2.53	0.01	-	0.01
COV %	2.22	3.16	1.46	0.64	2.37	-	3.15

Stringer stiffener							
Coupon ID	E (Mpa)	σ_Y (Mpa)	ϵ_Y	σ_T (Mpa)	ϵ_T	ϵ_{HS}	ϵ_f
T-SG-1	211000	266.7	0.00332	393.5	0.22737	-	0.46863
T-SG-2	213000	275.1	0.00329	394.5	0.23044	-	0.45565
T-SG-3	202000	255.7	0.00325	386.4	0.23045	-	0.47431
T-SG-4	217000	254.4	0.00318	387.2	0.22369	-	0.45575
T-SG-5	190000	288.1	0.00353	389.8	0.22710	-	0.45091
T-SG-6	205000	248.8	0.00330	385.8	0.23364	-	0.46787
Mean	206000	264.8	0.00331	389.5	0.22878	-	0.46219
Std. dev.	9741.28	14.82	0.00	3.72	0.00	-	0.01
COV %	4.72	5.60	3.52	0.96	1.51	-	2.01

Ring-stiffener web							
Coupon ID	E (Mpa)	σ_Y (Mpa)	ϵ_Y	σ_T (Mpa)	ϵ_T	ϵ_{HS}	ϵ_f
T-R-1	201000	264.5	0.00331	387.5	0.23346	-	0.45746
T-R-2	201000	255.1	0.00335	391.6	0.23355	-	0.47343
T-R-3	206000	253.7	0.00333	389.7	0.23355	-	0.47343
T-R-4	199000	252.9	0.00326	389.7	0.23355	-	0.47343
T-R-5	211000	275.9	0.00334	397.3	0.22939	-	0.46687
T-R-6	201000	251.3	0.00326	387.3	0.23355	-	0.47343
Mean	203000	258.9	0.00331	390.5	0.23284	-	0.46967
Std. dev.	4564.82	9.57	0.00	3.67	0.00	-	0.01
COV %	2.25	3.70	1.20	0.94	0.73	-	1.39



Fig. C.1 Shell coupon tensile test results for ring-stiffened cylinder model.



Fig. C.2 Ring-stiffener coupon tensile test results for ring-stiffened cylinder model.

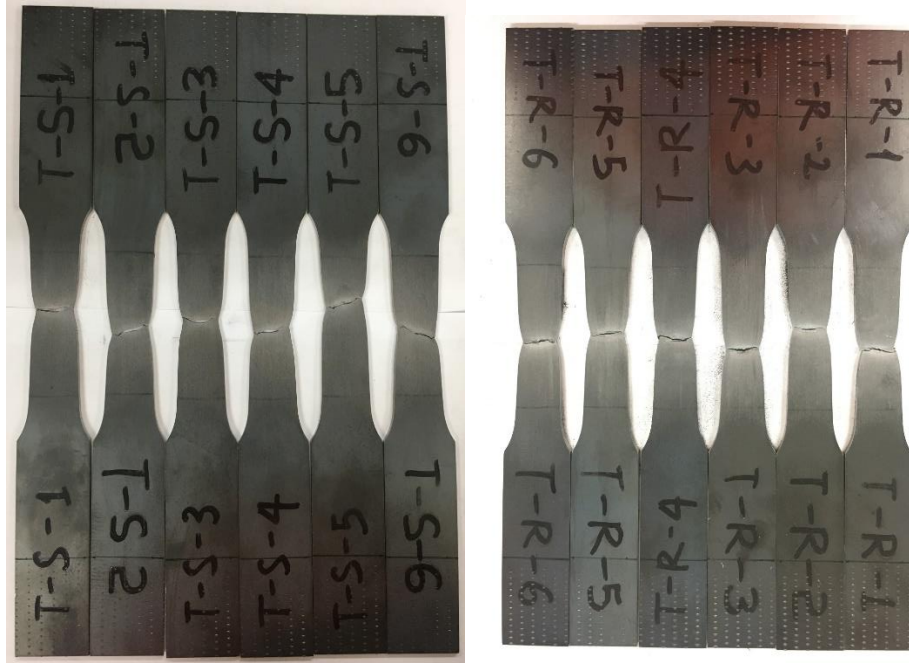


Fig. C.3 Coupon tensile test results for stringer-stiffener cylinder model.

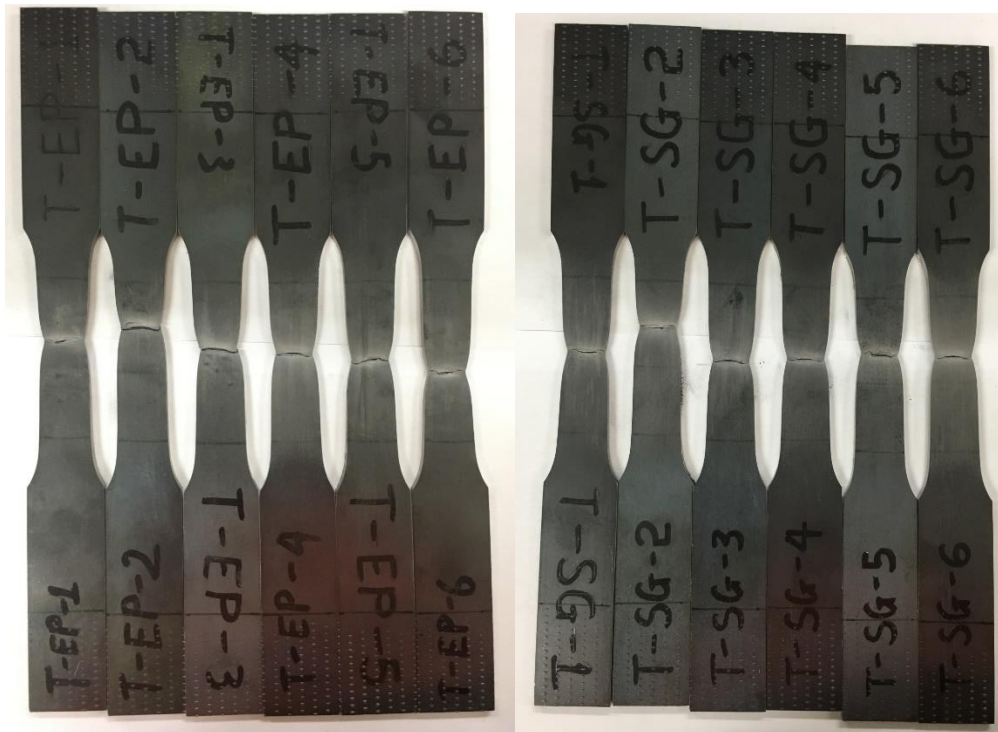


Fig. C.4 Coupon tensile test results for stringer-stiffener cylinder.

Dynamic tensile test set-up

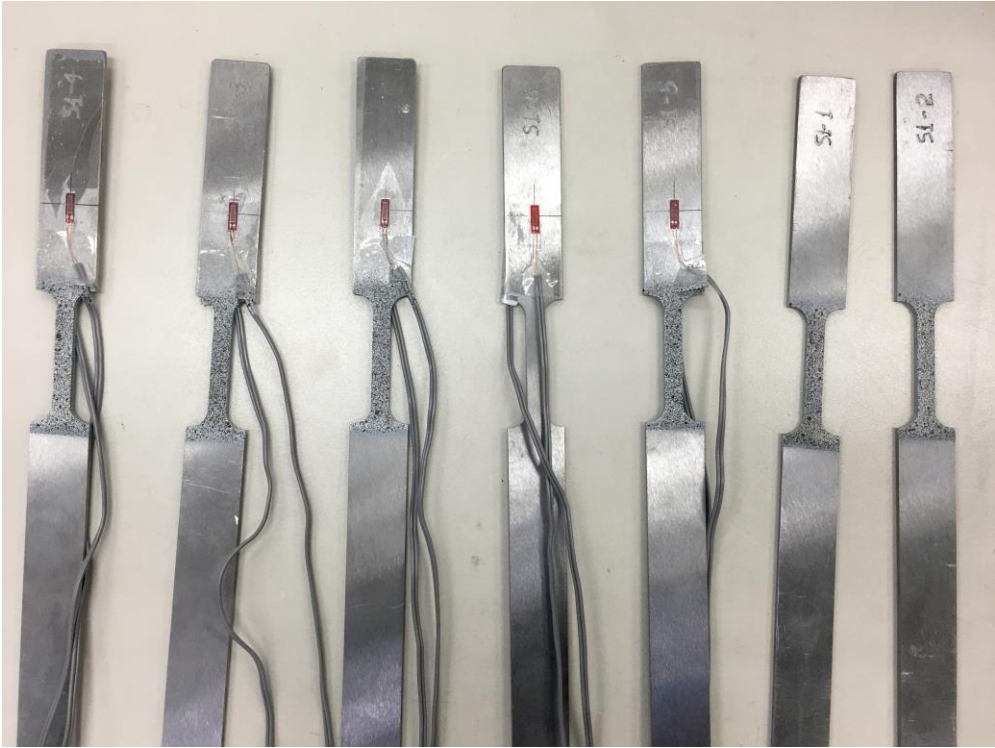
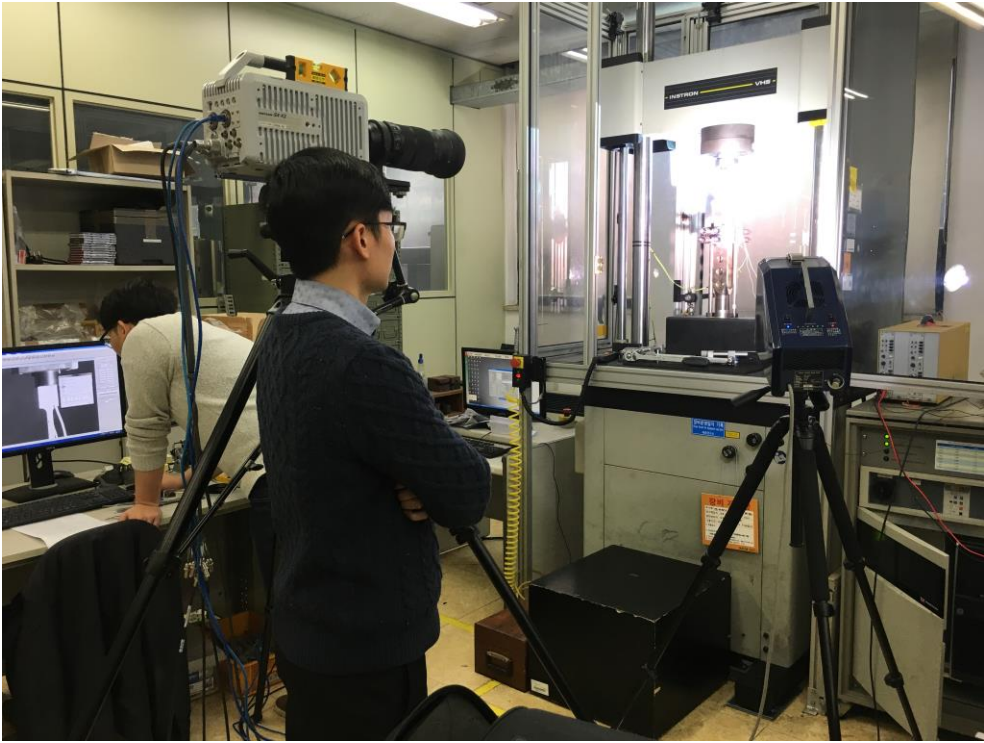


Fig. C.5 Dynamic tensile test set-up.

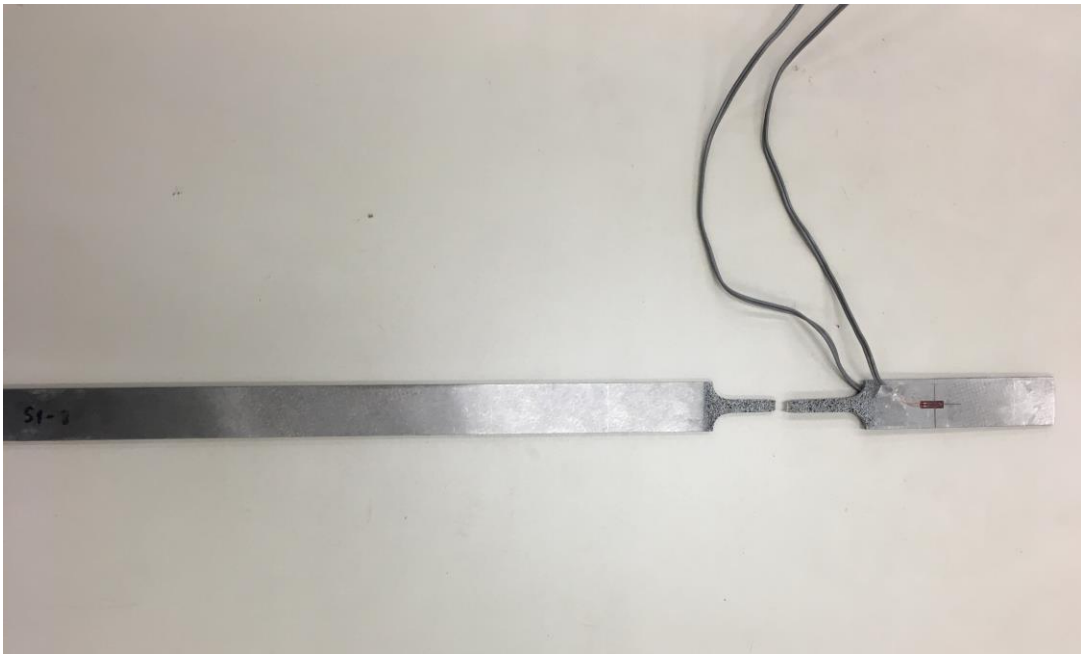
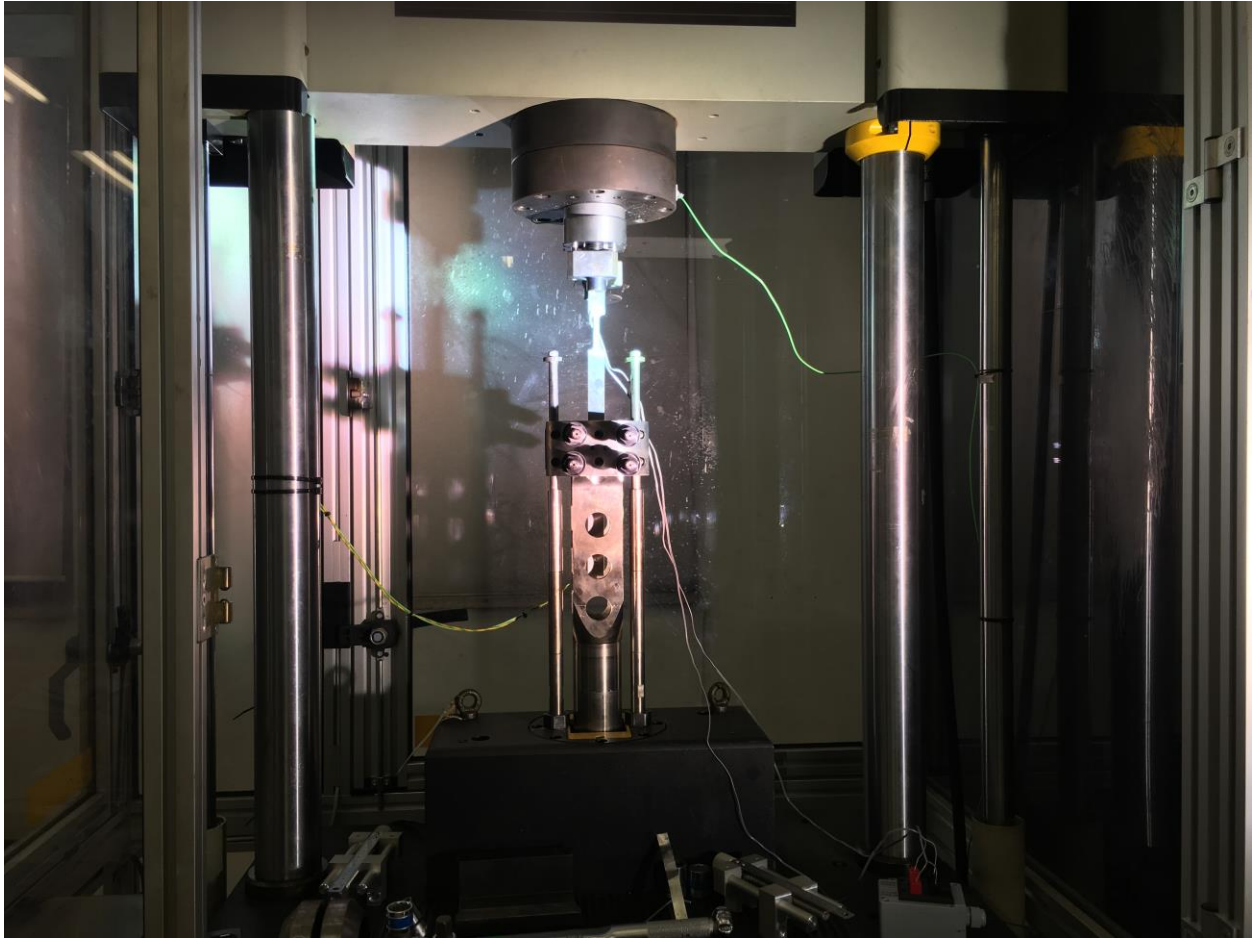
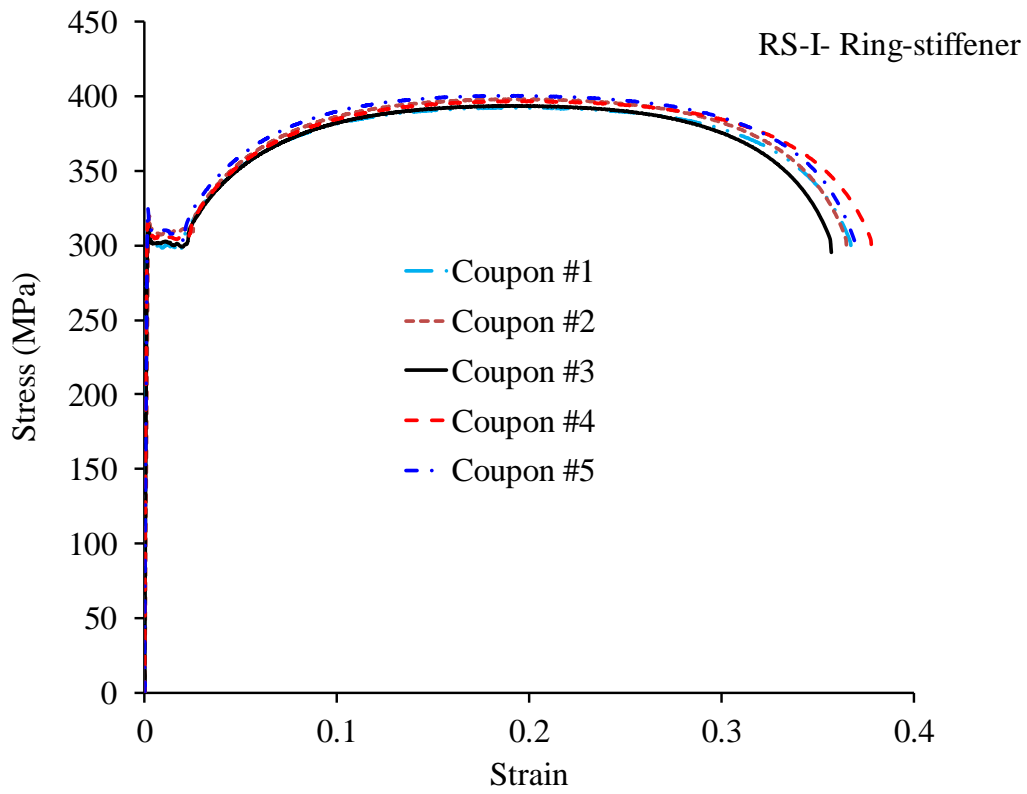
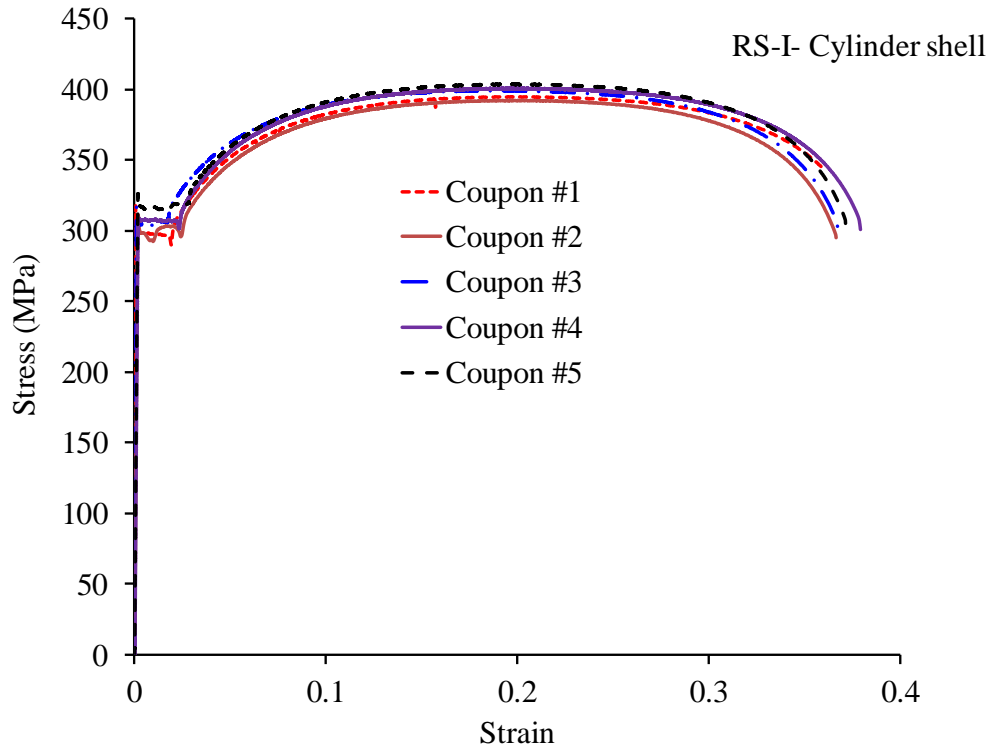
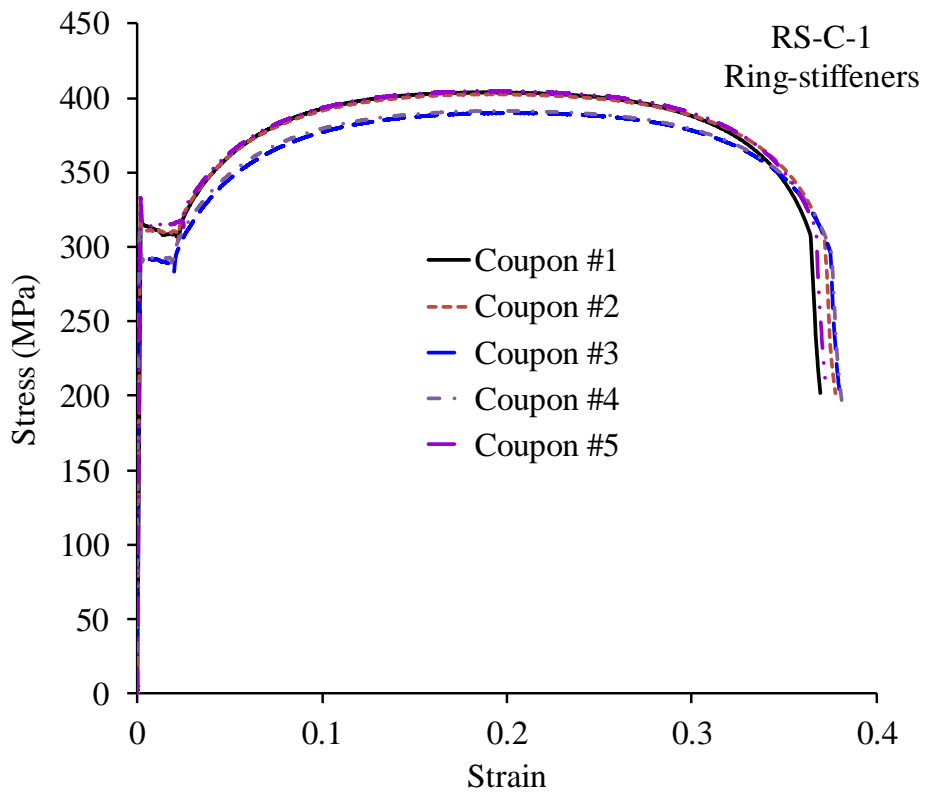
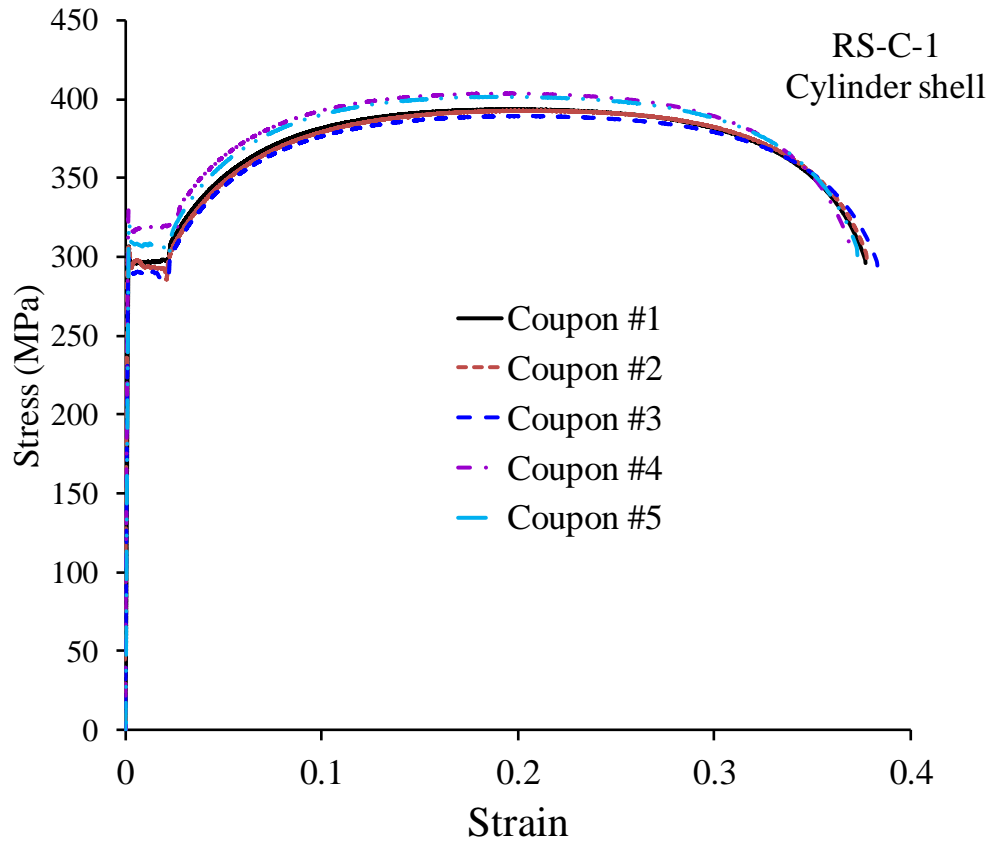
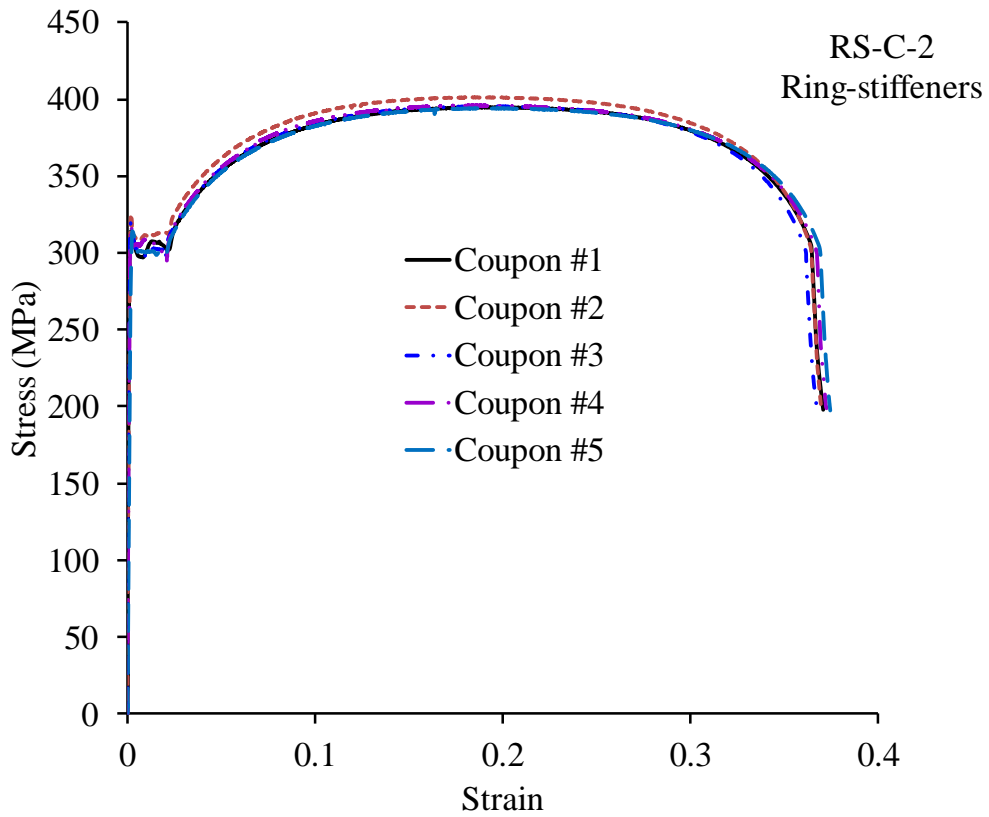
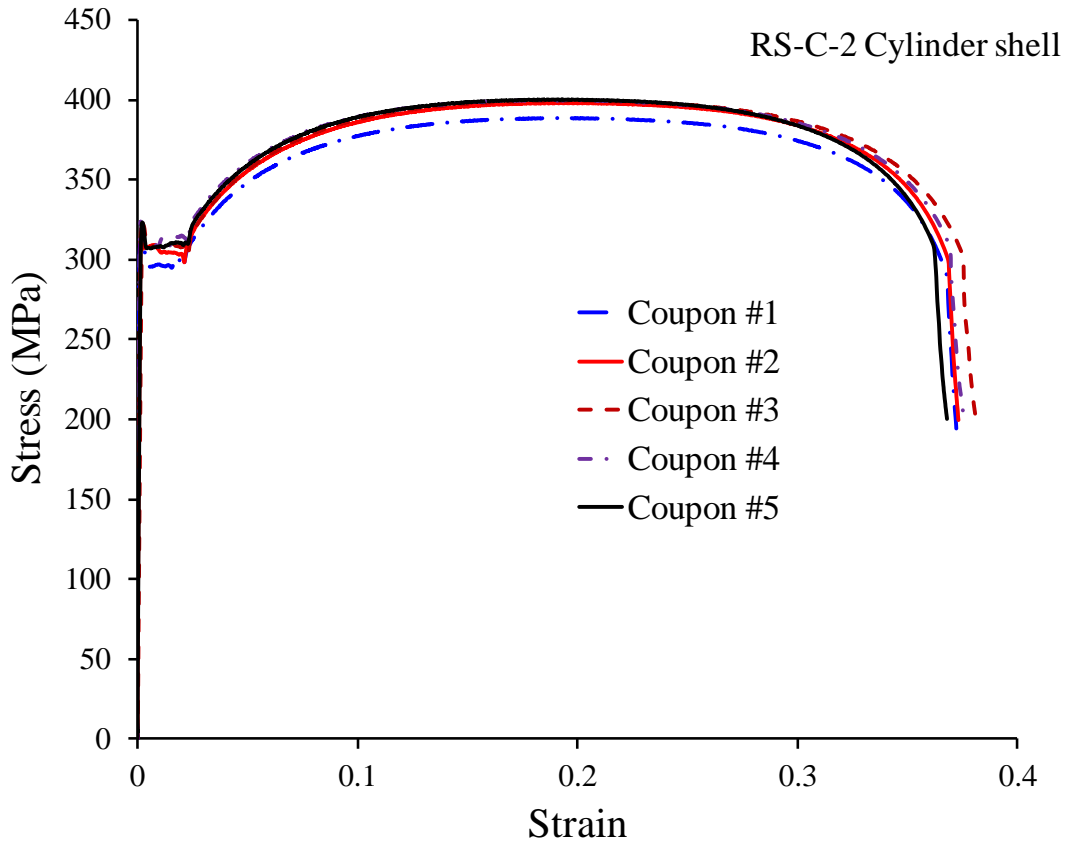


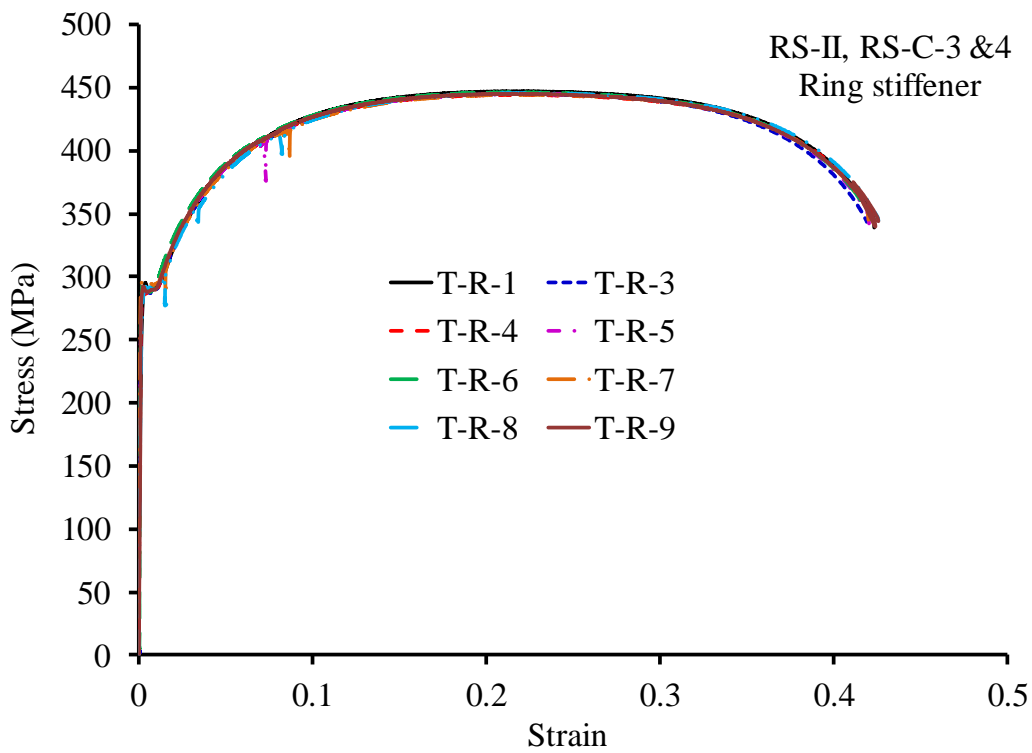
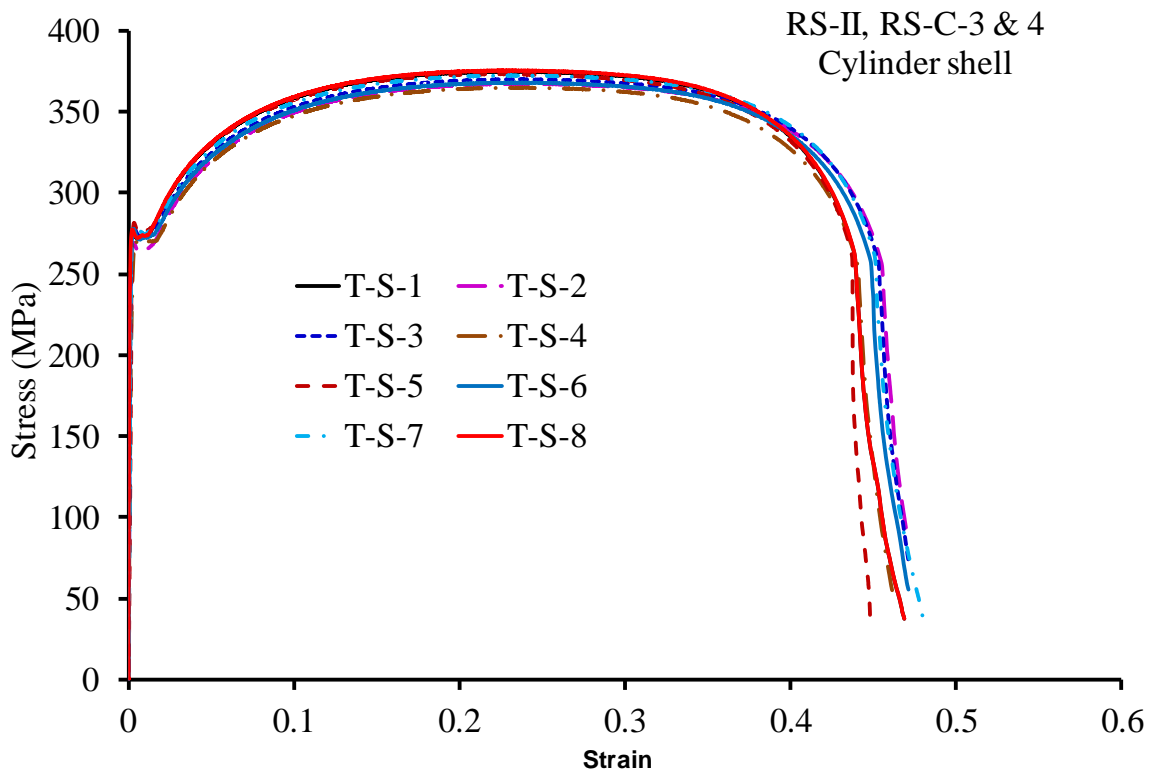
Fig. C.6 Coupon for dynamic tensile test after testing.

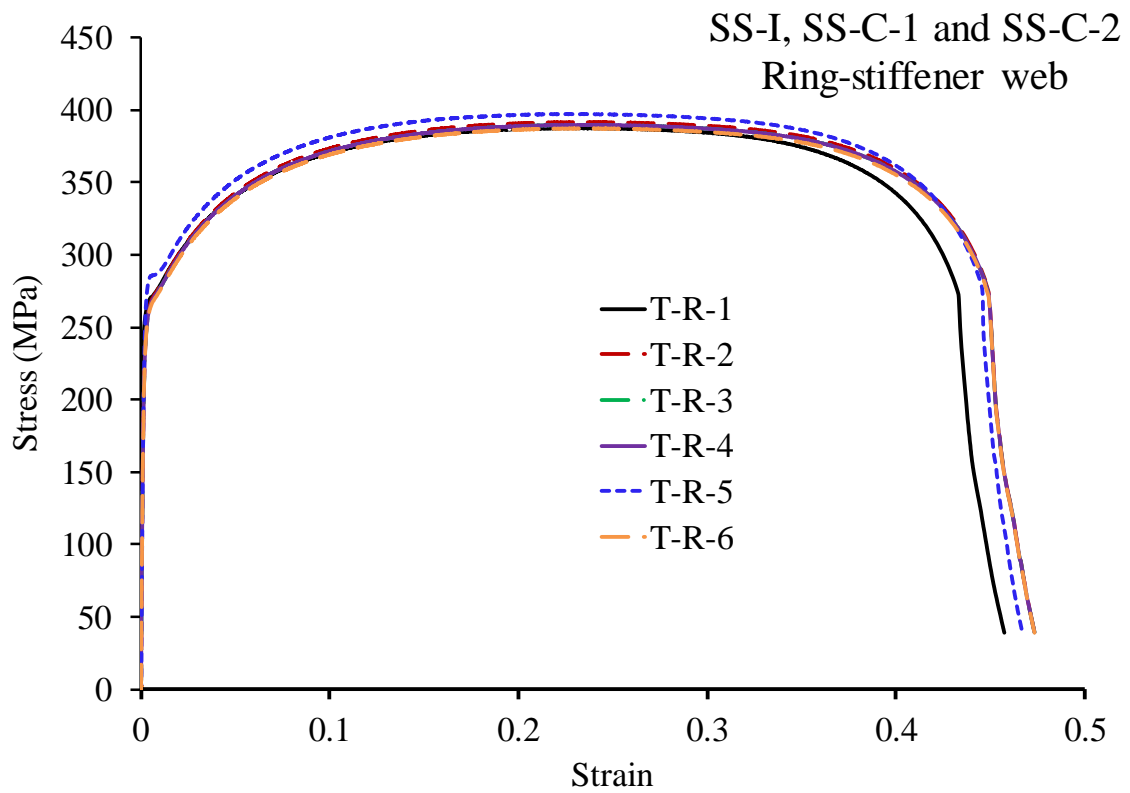
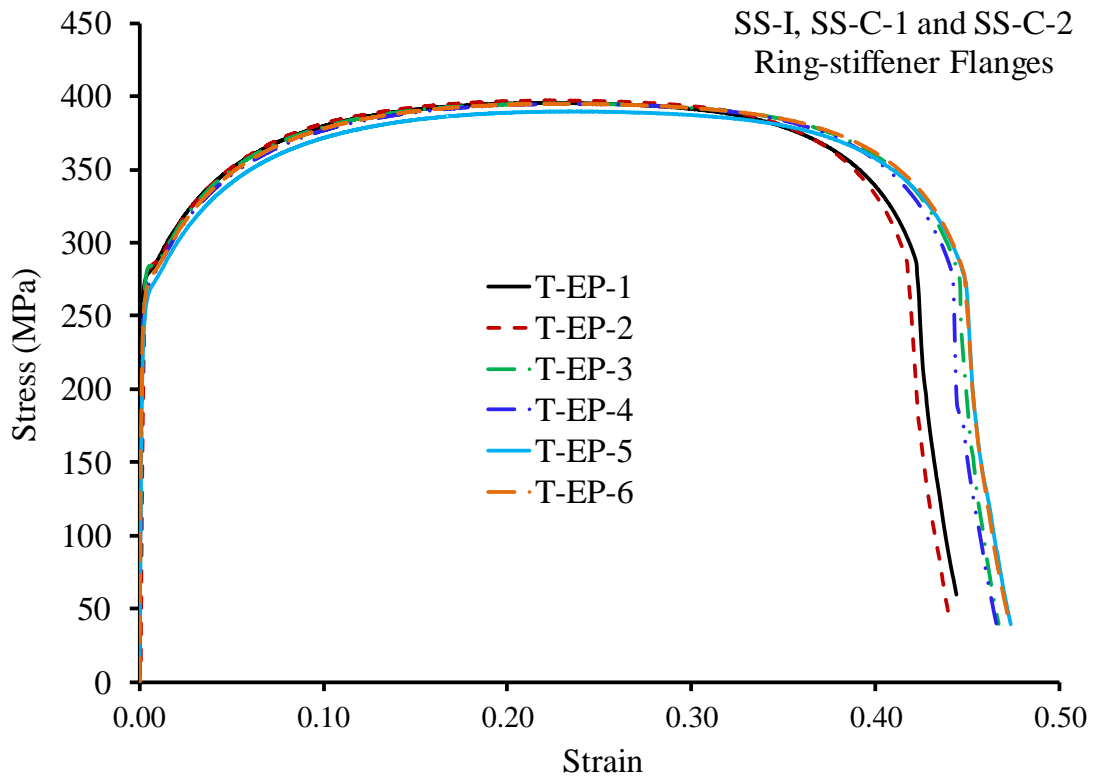
Tensile test curves

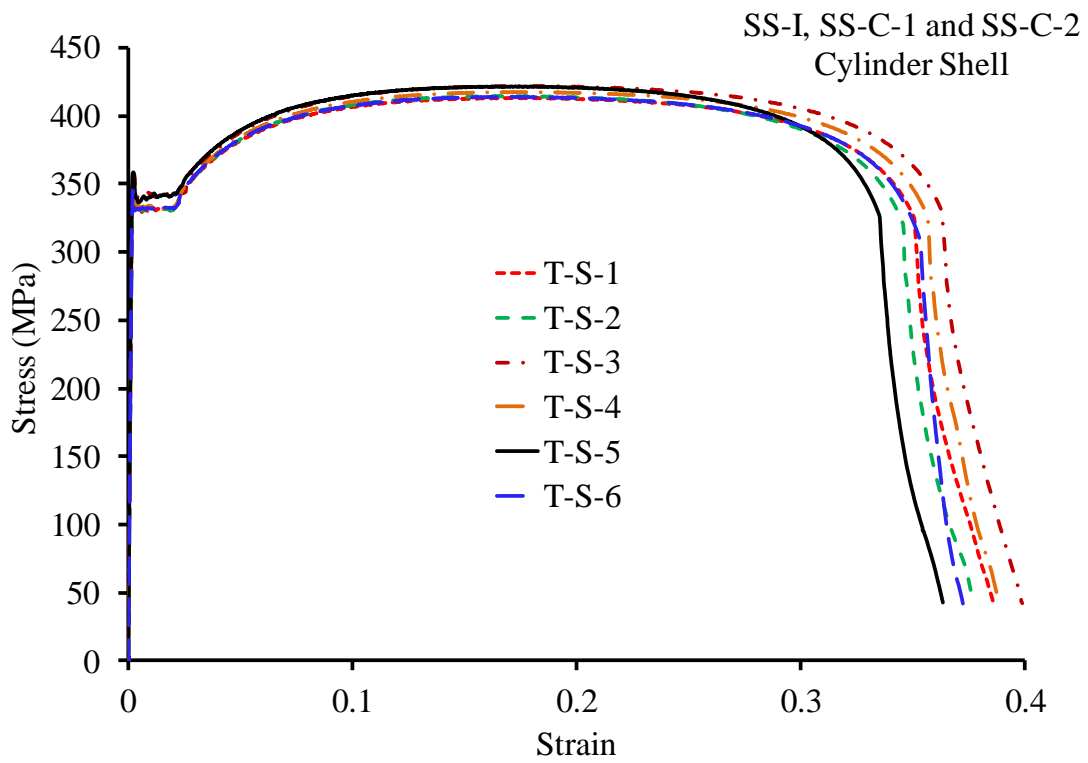
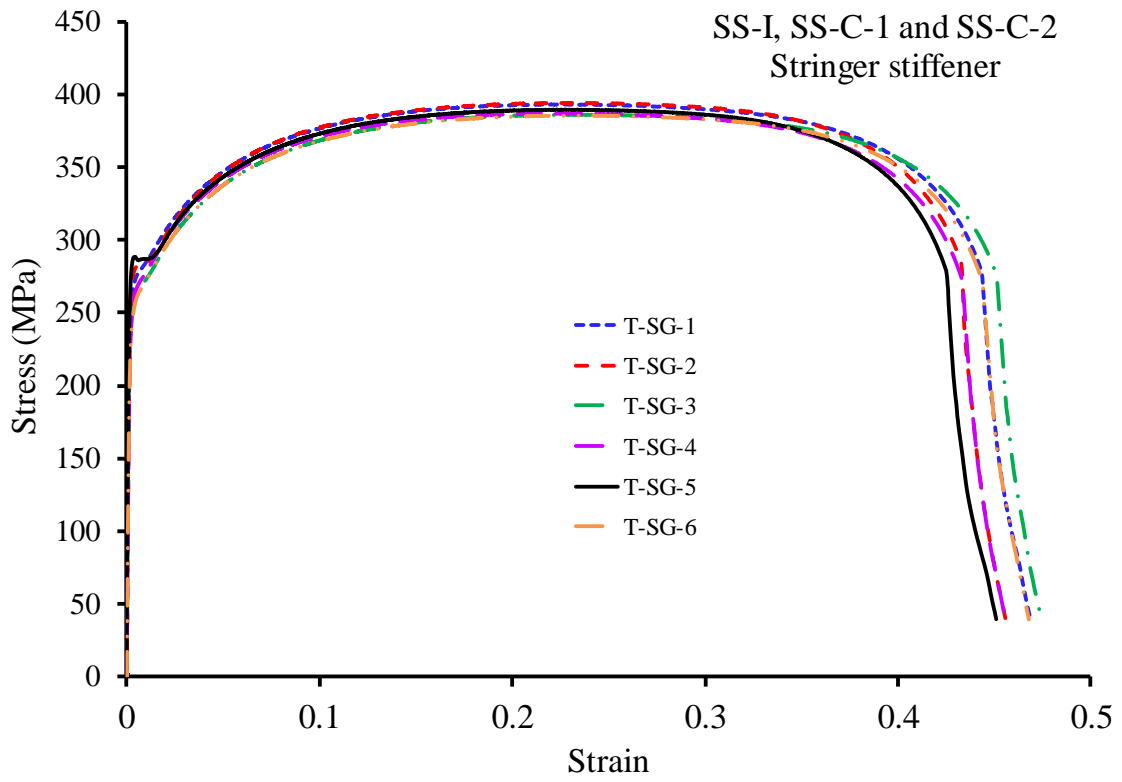




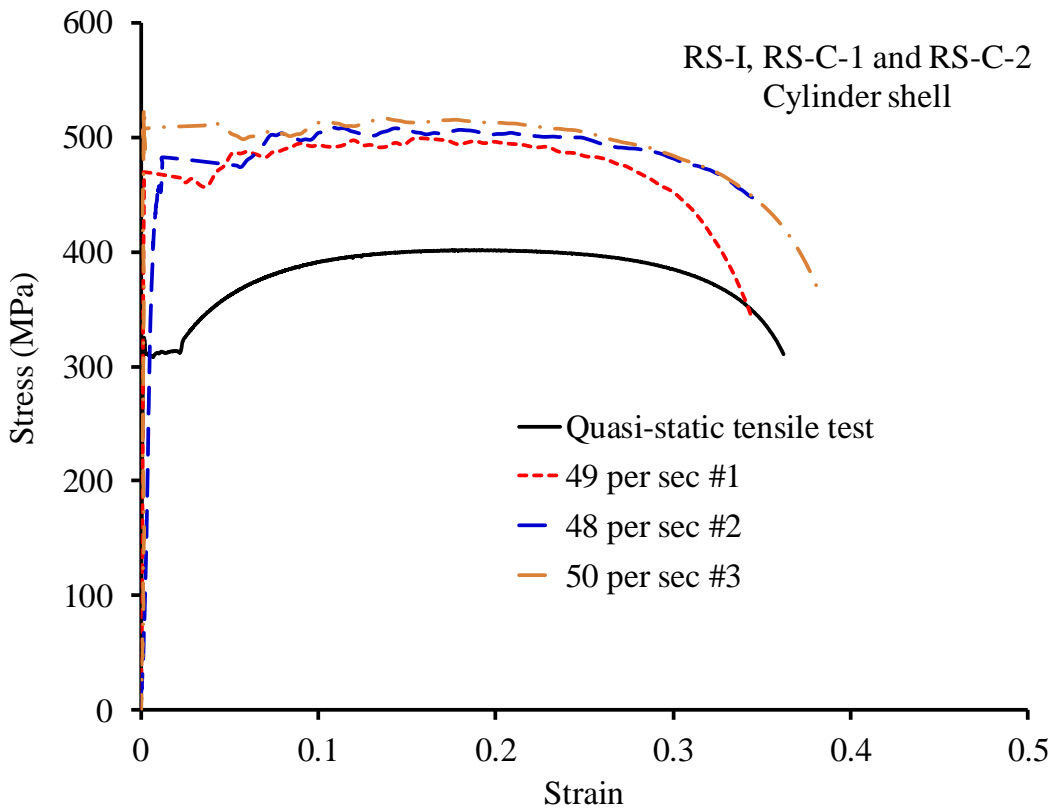
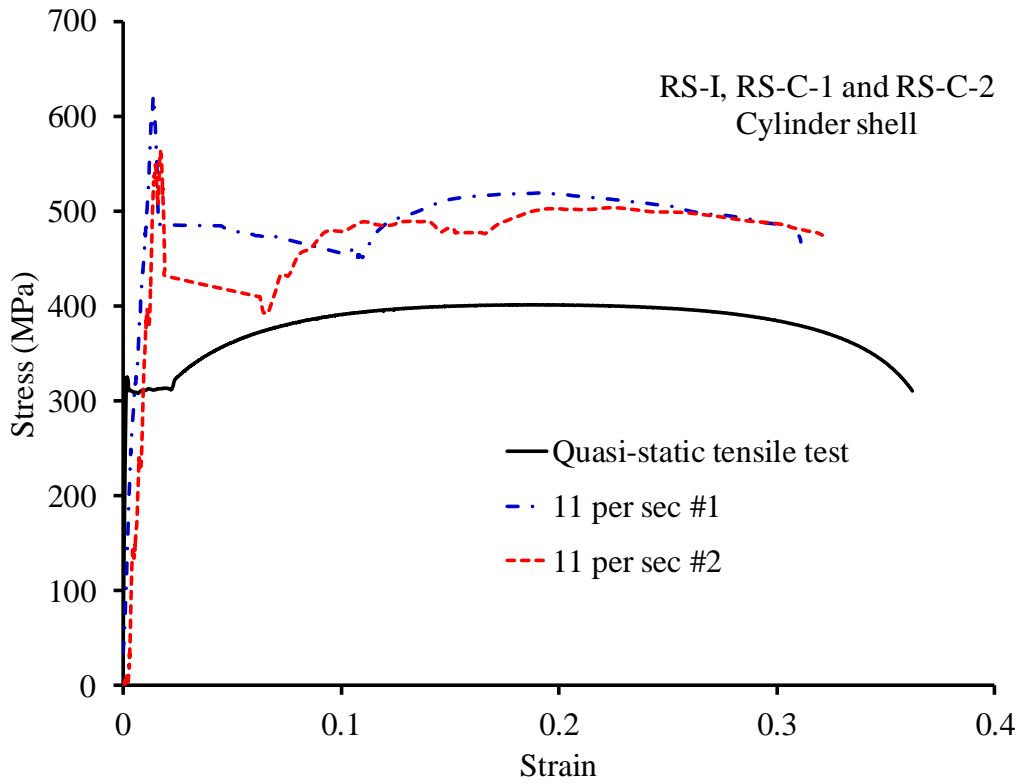


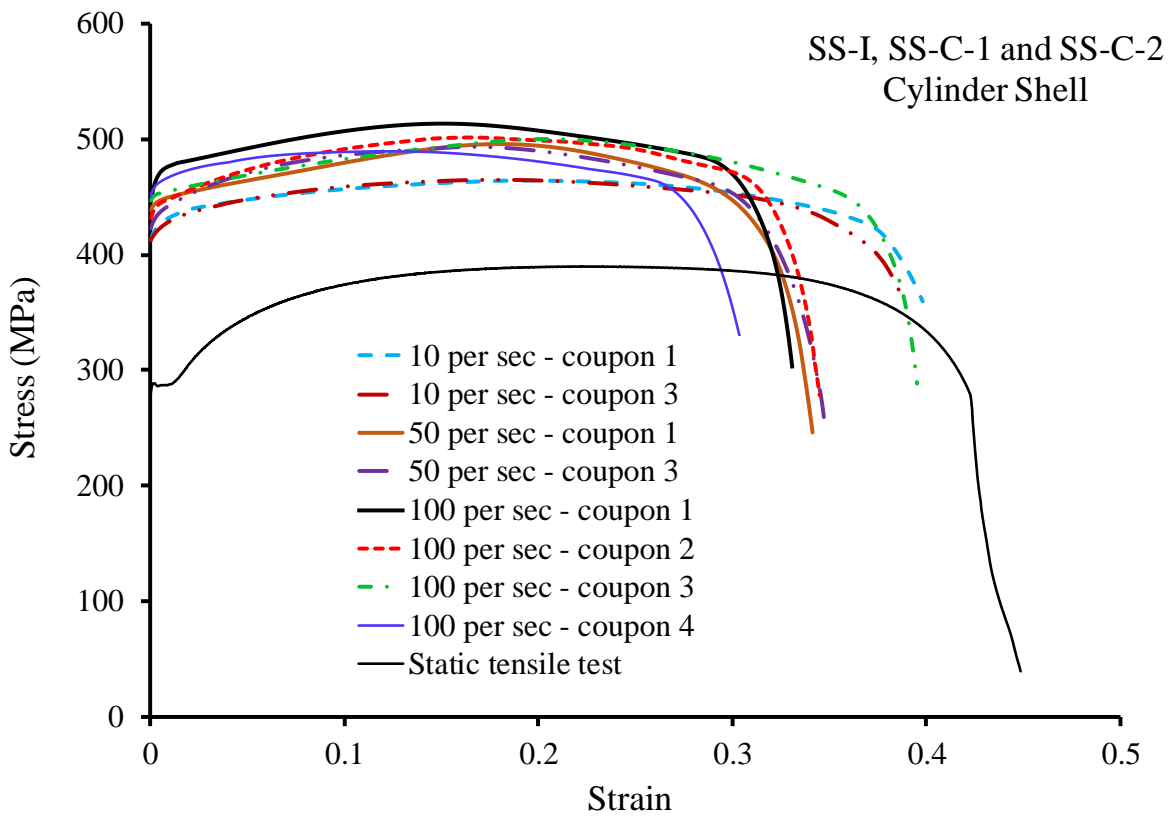
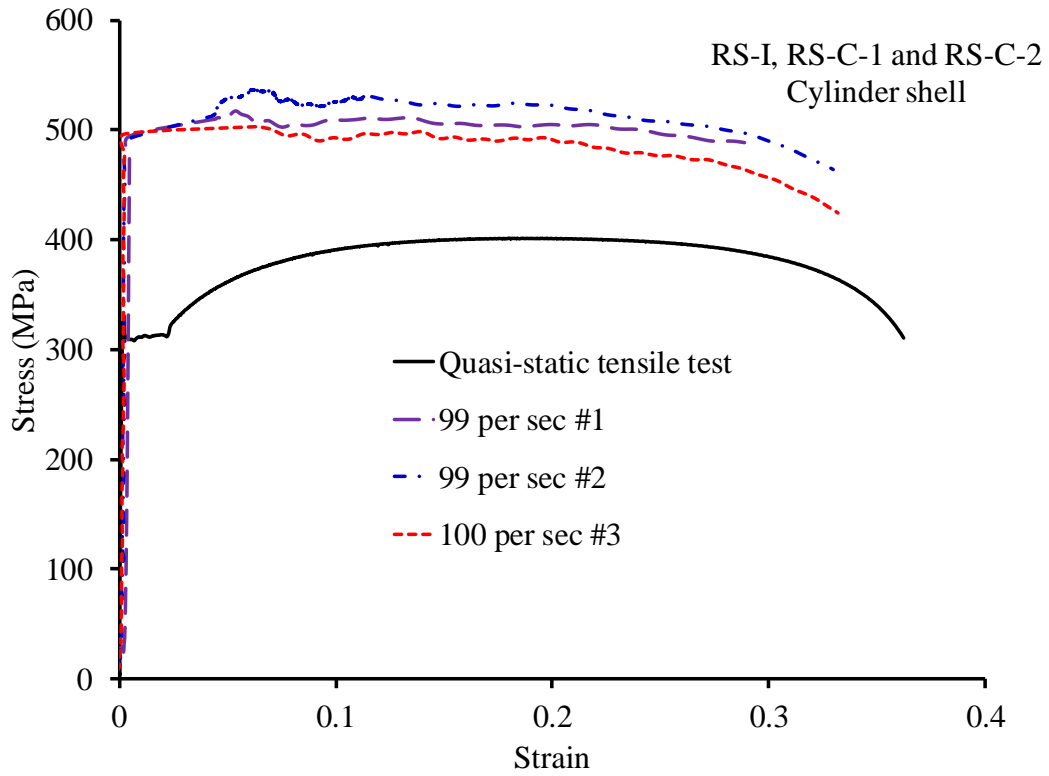






Dynamic tensile test curves





Appendix D: Experiments

D.1 Measured damage extents for ring-and stringer-stiffened models Longitudinal damage profiles

RS-C-1									
Center		10 degrees		20 degrees		-10 degrees		-20 degrees	
x	z	x	z	x	z	x	z	x	z
1041.3	401.0	1041.4	394.8	1043.0	378.0	1043.4	396.4	1044.5	380.9
1013.0	399.8	1006.6	393.6	1025.6	377.7	1022.0	395.6	1011.2	379.8
981.8	398.7	981.0	393.1	999.3	377.0	987.4	394.2	977.6	379.1
945.8	398.0	949.4	392.2	977.0	376.7	954.4	393.9	947.1	379.3
911.4	397.2	907.6	391.4	950.8	376.4	913.5	393.5	915.3	378.9
870.2	395.5	875.7	390.5	927.9	376.6	872.9	392.4	890.5	378.8
828.3	393.5	845.8	389.2	903.5	376.0	826.8	391.0	848.4	377.6
791.1	392.4	810.7	388.1	865.0	374.9	775.2	389.7	848.4	377.6
790.6	392.4	810.7	388.1	828.6	374.4	751.7	388.9	817.1	377.5
744.2	390.7	786.5	387.5	800.1	373.6	724.0	387.9	778.5	377.2
707.0	388.9	756.5	386.4	757.1	372.8	697.6	386.7	737.1	376.9
667.4	386.1	727.1	385.2	728.0	372.1	670.5	385.3	699.1	375.9
634.0	382.0	699.1	383.8	699.6	371.5	637.4	382.6	661.5	374.8
615.1	378.3	674.2	382.3	677.4	370.6	608.8	378.7	635.0	373.5
580.9	367.9	647.7	379.8	651.0	369.3	585.6	372.5	615.4	372.9
558.9	361.8	624.8	377.4	622.9	367.7	562.7	364.7	596.4	372.4
527.1	367.5	607.8	373.8	597.9	365.3	557.6	364.3	576.0	369.6
527.0	367.5	592.8	369.2	567.6	357.5	546.4	367.1	564.0	366.7
497.9	374.9	572.2	361.9	556.2	354.4	531.3	371.8	545.4	370.1
490.1	376.7	559.1	358.0	543.3	357.5	513.1	376.6	525.9	373.2
483.5	378.2	543.1	360.2	530.9	361.3	492.9	380.2	494.4	374.6
468.2	381.3	527.4	364.4	513.9	365.3	469.5	382.9	472.8	374.6
450.1	384.2	509.4	369.1	504.4	366.9	469.5	382.9	440.5	373.6
418.7	387.3	489.7	373.8	494.2	367.9	449.2	384.4	415.3	374.3
382.2	389.6	481.6	375.5	469.3	369.6	425.3	385.9	392.7	374.7
351.4	390.8	471.6	377.4	446.8	369.6	396.0	387.0	408.7	374.6
322.8	391.4	452.4	380.5	423.4	370.4	362.2	387.8	371.7	375.3
286.2	392.1	428.7	383.0	399.0	371.1	332.0	388.4	328.7	375.6
267.1	392.7	404.4	384.1	368.7	371.6	302.8	388.8	291.2	375.9
229.1	393.6	381.6	385.2	341.7	371.6	265.8	389.2	250.9	375.6
186.0	394.9	354.3	386.2	319.6	372.5	233.2	389.9	218.4	375.7
179.8	395.1	332.6	386.7	287.4	372.9	184.8	390.8	172.6	377.1
158.6	395.6	306.0	387.4	252.7	372.7	161.7	391.5	133.5	377.0

RS-C-1									
Center		10 degrees		20 degrees		-10 degrees		-20 degrees	
x	z	x	z	x	z	x	z	x	z
151.5	395.8	279.8	387.9	228.6	372.7	136.0	391.7	86.7	377.0
127.6	396.0	252.9	388.4	196.6	373.2	99.9	391.7	51.9	377.1
94.5	396.3	231.7	388.8	163.8	373.7	62.5	392.2	10.7	378.6
81.5	396.5	197.3	389.2	131.7	373.6	32.4	393.0		
43.9	397.6	161.4	390.1	95.7	373.4	11.5	394.0		
40.3	397.7	126.2	390.1	67.0	373.4				
23.8	398.5	85.7	390.8	12.2	373.5				
		53.3	391.5						
		13.5	393.2						

RS-C-2									
Center		10 degrees		20 degrees		-10 degrees		-20 degrees	
x	z	x	z	x	z	x	z	x	z
1045.7	401.9	1046.5	395.6	1048.0	377.2	1046.8	392.4	1046.5	374.4
1009.2	400.9	1015.2	394.8	1009.9	377.1	1018.9	391.6	1013.6	373.7
973.1	400.4	975.1	394.3	975.7	376.1	975.7	390.6	975.8	372.7
915.0	399.7	937.8	393.9	939.9	376.4	944.0	390.4	933.2	373.2
897.3	399.2	897.9	393.5	897.0	376.2	900.3	390.1	899.7	372.9
862.1	398.0	862.4	392.4	863.6	375.5	862.9	389.4	860.2	371.8
823.8	396.8	826.3	391.8	824.2	375.2	825.6	388.1	828.2	371.7
800.3	396.2	799.4	391.3	800.0	374.9	801.7	387.4	800.1	371.3
773.9	395.7	774.8	391.2	772.1	374.7	776.5	387.2	779.9	371.3
750.5	395.1	747.4	390.3	751.0	374.5	750.7	386.9	752.2	371.5
724.9	394.3	725.2	389.7	726.9	374.8	723.0	386.4	725.0	370.6
702.4	393.4	701.8	389.1	702.0	374.7	701.9	385.8	699.0	370.7
673.2	391.8	673.0	388.0	672.6	373.7	673.6	385.0	677.9	370.3
651.1	390.1	649.8	386.7	674.0	373.6	651.9	384.2	650.5	369.9
625.4	387.7	626.3	385.4	652.4	373.1	626.3	382.7	628.4	368.7
600.2	382.8	598.0	381.8	652.6	373.2	600.2	380.4	604.1	369.0
587.4	379.5	573.1	375.9	628.7	372.4	573.9	375.5	576.3	369.5
575.8	376.3	549.4	368.8	603.1	372.5	551.5	368.9	553.0	367.3
565.2	373.4	545.8	368.2	574.8	372.2	541.2	370.3	529.5	369.8
553.4	370.5	529.3	371.5	549.0	367.4	527.9	373.9	503.6	370.2
550.0	369.8	503.7	378.0	543.7	366.6	516.6	376.7	480.0	369.5
543.9	369.5	478.5	382.6	529.3	369.8	503.4	379.1	452.4	368.2
537.4	370.5	453.9	385.4	502.7	373.1	490.4	380.8	428.1	368.1
532.3	371.5	429.1	387.0	478.6	373.6	481.5	381.6	402.8	368.0

RS-C-2									
Center		10 degrees		20 degrees		-10 degrees		-20 degrees	
x	z	x	z	x	z	x	z	x	z
524.1	373.3	405.5	387.7	452.0	372.8	466.9	382.4	377.2	368.4
510.8	376.4	381.4	388.6	430.2	372.6	452.2	382.9	352.4	367.7
496.8	379.6	355.6	389.1	404.3	373.2	436.6	383.2	330.6	368.4
482.2	382.7	330.8	389.6	382.2	373.6	428.9	383.4	276.6	367.5
466.4	385.5	306.4	390.0	356.4	374.0	415.1	383.7	226.2	366.6
452.6	387.5	280.7	390.3	331.5	374.4	404.3	384.0	191.3	367.7
439.6	388.9	256.2	390.3	303.5	374.4	391.7	384.2	158.4	367.7
429.3	389.8	228.6	390.6	282.2	374.3	378.4	384.7	119.6	367.3
415.7	390.2	195.5	391.2	253.7	373.8	366.6	384.8	83.5	367.4
405.8	390.5	160.4	392.0	229.6	373.6	354.3	385.0	10.6	369.6
390.9	391.4	127.7	392.1	197.2	374.4	342.4	385.3		
379.6	392.1	81.9	391.7	161.1	374.8	330.2	385.4		
365.5	392.8	46.3	392.3	128.2	374.6	311.7	385.7		
343.4	393.7	9.7	393.7	84.0	374.1	290.3	385.9		
318.3	394.3			46.7	374.2	259.4	385.9		
291.6	394.8			9.3	374.7	230.5	385.9		
265.2	395.0					198.3	386.4		
243.0	395.2					173.3	387.0		
210.9	395.7					151.1	387.2		
185.6	396.4					119.2	386.6		
160.7	396.9					90.3	386.6		
129.9	397.0					80.2	386.6		
94.3	396.9					52.8	387.0		
70.2	396.9					10.2	388.4		

* Center is the top generator. x is the longitudinal coordinate where x = 1060 corresponds to the end ring. z is the vertical coordinate.

RS-C-3									
170 degrees		175 degrees		180 degrees-center		185 degrees		190 degrees	
x	z	x	z	x	z	x	z	x	z
3.5	553.6	0.3	553.4	2.4	553.2	4.2	553.4	4.0	553.2
70.7	552.1	68.1	551.7	43.0	552.4	70.9	551.3	69.9	551.5
96.6	551.5	94.5	551.1	119.3	550.2	120.8	550.5	94.1	551.0
119.0	551.2	120.6	550.7	148.9	550.9	146.3	550.9	121.7	550.7
146.6	551.5	147.5	551.0	174.7	550.6	172.9	550.6	145.9	551.1
172.1	551.3	172.2	550.8	200.8	550.3	197.8	550.4	195.4	550.7
196.4	551.2	196.0	550.7	225.3	549.9	223.6	550.1	221.3	550.5
221.7	551.0	220.6	550.4	247.6	549.3	248.3	549.5	247.3	550.0
247.2	550.6	248.0	549.8	271.5	548.5	272.2	548.8	271.7	549.6
270.4	549.9	271.4	549.1	297.1	547.7	299.5	548.3	299.3	549.3
297.5	549.5	296.9	548.2	323.1	546.2	320.7	547.5	322.0	548.7
322.0	548.8	321.0	546.7	345.3	546.4	348.9	547.3	347.0	548.5
345.8	548.8	346.5	547.1	370.8	546.4	371.4	547.0	370.9	548.3
371.2	548.7	370.9	547.2	397.7	545.7	396.9	546.2	397.2	547.6
397.9	548.1	396.5	546.6	420.9	544.3	422.4	544.8	422.0	546.5
422.4	547.1	422.6	545.2	448.2	542.0	450.0	542.6	449.2	544.9
445.7	545.8	447.5	543.3	473.8	537.9	472.9	539.0	476.3	541.4
474.0	542.5	474.4	539.2	496.5	532.0	489.5	535.1	490.0	538.8
496.9	538.4	499.1	533.0	520.9	524.7	503.0	531.1	509.1	534.1
510.7	535.2	522.1	526.5	535.2	521.3	518.5	526.6	521.1	530.6
523.6	532.0	533.8	523.7	544.3	522.6	532.9	522.8	535.7	527.2
534.1	529.9	546.2	525.8	555.4	526.3	540.1	522.9	548.1	530.0
540.2	530.5	559.0	529.9	568.4	530.9	557.4	528.3	564.1	534.7
546.1	531.8	568.1	532.9	585.5	535.9	570.5	532.7	574.9	537.6
555.5	534.4	585.0	537.5	598.1	538.3	594.6	538.8	596.6	542.0
569.5	537.9	596.2	539.5	619.9	541.1	619.0	541.8	610.8	543.5
595.0	542.6	619.4	542.4	644.8	543.3	642.2	543.9	629.4	545.2
621.4	545.1	645.0	544.5	670.9	544.8	670.6	545.4	644.6	546.0
644.4	546.5	669.6	545.6	698.2	545.7	696.0	546.1	673.3	547.2
669.8	547.4	695.9	546.5	720.6	546.3	723.3	546.8	696.9	547.7
694.8	548.0	721.0	547.0	745.6	547.2	745.7	547.7	720.0	548.1
720.8	548.4	744.1	547.8	769.6	547.4	768.7	547.9	743.4	548.8
745.8	549.1	770.0	547.9	792.4	547.9	792.7	548.4	769.0	549.0
768.1	549.1	794.1	548.3	814.5	548.3	814.1	548.7	791.2	549.2
791.9	549.3	813.5	548.5	835.7	548.6	836.3	549.0	810.2	549.5
815.2	549.5	838.8	548.8	861.3	548.8	862.2	549.2	835.7	549.7
838.4	549.6	863.0	548.9	896.5	549.4	896.6	549.7	866.1	549.8
863.8	549.6	892.4	549.4	920.4	549.1	922.8	549.3	897.9	550.2

RS-C-3									
170 degrees		175 degrees		180 degrees-center		185 degrees		190 degrees	
x	z	x	z	x	z	x	z	x	z
892.6	549.9	918.6	549.1	972.5	549.8	948.7	549.6	919.4	549.7
919.5	549.6	946.2	549.4	1038.6	551.6	972.2	550.0	950.2	549.7
944.0	549.7	973.4	549.8			1035.0	551.3	974.5	550.2
974.2	550.1	1038.0	551.4					1038.3	551.2
1038.3	551.6								

RS-C-4									
40 degrees		45 degrees		50 degrees-center		55 degrees		60 degrees	
x	z	x	z	x	z	x	z	x	z
5.3	554.5	4.2	554.7	4.3	555.0	4.5	555.4	3.4	555.7
57.2	553.2	55.2	553.2	54.1	553.5	53.8	553.7	53.2	553.9
89.8	552.0	88.0	552.0	105.4	551.5	90.4	552.2	87.2	552.6
119.5	551.3	119.1	551.0	117.4	551.0	122.5	551.2	118.2	551.8
147.9	550.9	147.3	550.5	148.0	550.4	146.6	550.8	146.6	551.5
175.8	549.5	173.9	549.0	173.2	549.1	172.1	549.8	172.3	550.6
200.8	548.2	199.4	546.8	200.3	547.1	197.6	549.0	200.1	550.1
225.1	547.0	224.2	544.7	223.3	545.5	222.5	548.0	221.4	549.6
250.4	546.7	247.9	544.4	248.9	544.9	248.7	547.1	249.6	548.8
276.2	547.3	275.6	546.0	275.5	545.7	274.2	546.5	272.4	548.2
300.1	547.5	297.8	546.5	299.0	545.9	297.8	546.4	299.6	547.8
326.0	546.7	327.1	545.6	326.6	545.1	324.3	545.6	324.7	547.0
347.1	546.2	350.7	544.8	349.3	544.4	349.3	544.9	349.4	546.3
375.4	545.3	376.5	543.7	374.0	543.4	375.2	543.9	374.1	545.6
401.5	544.0	402.0	542.3	399.5	541.8	398.1	542.6	399.8	544.4
425.1	542.5	425.1	540.4	425.2	539.4	425.6	540.3	425.1	542.8
450.2	540.4	450.8	537.4	450.5	536.2	449.9	537.4	446.9	540.9
473.4	536.6	473.7	532.8	474.3	531.1	473.9	532.6	474.8	536.3
499.1	530.2	498.6	525.1	497.9	523.6	498.2	525.2	496.9	530.6
532.5	520.5	522.0	517.2	524.3	514.7	522.8	516.9	523.3	522.7
547.4	523.8	536.3	514.1	537.8	511.9	537.7	513.2	536.9	518.9
571.9	530.8	552.5	518.9	559.0	518.5	555.9	518.8	555.8	523.9
596.0	535.4	595.9	531.3	593.7	529.1	578.1	526.5	582.0	532.0
620.6	538.2	623.5	535.4	621.9	533.7	619.1	534.5	611.9	537.0
647.3	540.2	645.5	537.4	646.7	536.5	644.4	537.2	644.7	540.2
669.9	541.1	668.0	538.9	670.1	538.3	669.6	539.2	670.9	541.7
696.4	541.9	695.8	540.1	694.8	539.5	694.8	540.3	693.9	542.5

RS-C-4									
40 degrees		45 degrees		50 degrees-center		55 degrees		60 degrees	
x	z	x	z	x	z	x	z	x	z
723.4	542.5	720.7	540.9	722.6	540.4	720.2	541.1	720.7	543.1
747.5	542.9	745.5	541.7	746.9	541.2	744.6	541.8	746.7	543.6
771.7	543.0	771.8	541.9	769.6	541.5	769.6	542.0	770.6	543.8
797.7	543.4	793.7	542.3	795.7	542.1	793.5	542.4	794.2	544.0
821.6	543.7	819.2	542.8	820.7	542.6	819.8	542.9	822.9	544.3
847.0	543.7	845.6	543.1	844.4	542.9	845.0	543.1	844.7	544.4
872.3	543.7	868.7	543.1	868.7	543.0	870.7	543.3	871.0	544.5
896.6	543.7	895.6	543.3	894.5	543.2	894.8	543.4	895.5	544.5
926.4	543.3	924.5	543.0	894.5	543.2	926.5	543.4	929.0	544.3
956.5	543.4	965.5	543.7	935.1	543.1	964.5	544.2	955.7	544.6
983.3	544.0	983.9	544.2	989.1	544.3	984.9	544.8	984.7	545.2
1037.3	544.4	1037.0	544.6	1034.8	544.9	1036.3	545.1	1038.1	545.3

Transverse damage profiles

RS-C-1									
Dent line		730 mm		630 mm		430 mm		330 mm	
y	z	y	z	y	z	y	z	y	z
306.1	271.9	252.5	316.4	255.0	317.0	252.9	314.1	303.9	270.3
292.2	287.2	236.6	327.2	236.1	328.8	228.5	330.5	280.4	293.5
282.0	297.3	218.4	338.0	213.9	340.0	197.3	347.8	253.0	315.1
267.0	311.0	195.4	349.8	195.1	348.3	181.5	355.3	225.7	332.2
248.5	325.9	167.4	361.4	161.6	360.3	164.5	362.3	209.8	340.9
224.5	341.5	147.5	368.2	135.3	367.7	150.0	367.6	194.7	348.2
200.4	349.2	117.3	376.5	120.0	371.2	136.6	372.0	181.3	354.1
178.9	350.2	80.3	383.5	102.4	374.0	120.6	376.6	163.1	361.2
155.2	352.9	60.6	386.2	86.6	376.0	103.0	380.9	148.1	366.3
135.7	354.0	24.4	389.0	70.7	377.6	87.0	384.1	135.4	370.0
114.7	355.5	-9.0	390.0	49.6	379.4	71.2	386.6	120.1	374.1
98.3	356.1	-41.8	389.4	27.5	380.4	55.7	388.5	101.7	378.1
70.5	357.6	-72.4	386.9	15.7	380.6	38.1	390.0	86.4	380.6
57.1	358.3	-96.9	383.4	-1.0	381.8	22.5	390.8	69.2	382.7
32.3	359.7	-125.3	377.4	-17.3	382.1	4.6	391.2	54.7	384.0
17.2	360.7	-146.7	371.3	-30.9	382.2	-6.7	391.3	38.6	384.9
2.0	361.8	-169.5	363.3	-42.9	382.4	-62.0	388.4	22.9	385.6
-8.7	362.3	-186.6	356.1	-58.4	381.9	-93.6	383.6	4.9	386.6
-28.1	363.0	-209.0	344.9	-67.0	381.3	-109.2	380.2	-8.2	387.1
-44.6	363.6	-235.8	328.7	-77.1	380.7	-126.4	375.8	-24.7	387.4
-62.4	364.3	-245.3	322.0	-93.7	379.2	-141.0	371.3	-42.2	387.0
-78.6	365.0			-108.2	377.2	-154.9	366.4	-61.5	385.6
-93.5	365.5			-128.1	373.4	-170.5	360.3	-76.2	384.0
-111.9	366.0			-145.0	369.3	-188.3	352.3	-92.6	381.5
-129.8	366.5			-165.3	363.4	-200.3	346.3	-107.7	378.7
-157.0	366.2			-178.9	358.8	-217.3	336.9	-125.4	374.4
-172.5	365.1			-190.4	354.4	-231.0	328.4	-142.5	369.4
-191.7	359.7			-207.0	347.1	-243.6	319.8	-156.7	364.6
-216.9	346.2			-221.3	339.7	-256.9	309.8	-171.2	359.4
-236.2	333.2			-248.0	322.2	-268.5	300.3	-187.8	352.6
-248.5	323.9					-280.7	289.4	-202.4	345.8
						-294.3	276.0	-216.4	338.6
								-246.1	320.2
								-271.4	300.2
								-295.3	277.0

RS-C-2									
Dent line		730 mm		630 mm		430 mm		330 mm	
y	z	y	z	y	z	y	z	y	z
223.8	339.5	238.7	324.9	264.2	306.9	262.7	304.4	262.8	306.4
207.7	349.7	205.0	345.8	249.2	318.9	242.7	320.0	249.3	317.0
188.7	359.1	173.1	361.4	236.3	328.0	227.2	330.7	233.5	327.9
170.2	363.9	155.7	368.4	222.7	336.6	203.1	345.2	220.1	336.2
135.2	366.7	136.4	375.0	204.9	346.3	188.1	353.0	203.1	345.6
115.8	367.3	118.1	380.2	188.6	353.9	169.1	361.8	187.8	353.1
101.2	367.7	100.7	384.4	172.1	360.8	153.0	368.2	169.9	361.0
85.6	368.0	85.3	387.3	156.1	366.5	136.1	374.0	156.1	366.3
68.7	368.3	69.4	389.8	137.6	372.3	120.4	378.7	137.1	372.5
44.1	368.8	49.7	392.0	120.1	376.9	102.7	383.2	119.9	377.4
28.3	369.1	28.5	393.6	101.9	380.7	85.4	386.8	101.9	381.6
10.4	369.4	11.3	394.2	86.6	383.3	66.7	389.7	84.1	384.8
-8.0	369.4	-5.7	394.3	68.4	385.4	46.5	392.1	67.8	386.9
-26.8	368.9	-24.3	393.9	49.8	386.8	27.0	393.5	49.1	388.7
-42.4	369.0	-41.1	392.8	28.2	387.6	9.2	394.1	27.6	389.5
-63.5	368.9	-64.9	390.5	10.1	387.7	-13.6	394.0	9.5	389.7
-88.2	368.7	-91.9	386.3	-7.1	387.9	-30.2	393.4	-8.9	389.8
-104.5	368.6	-105.8	383.3	-23.2	387.6	-47.1	392.1	-25.5	389.8
-104.5	368.6	-116.2	380.9	-42.3	387.4	-65.1	390.0	-43.5	389.2
-119.5	368.6	-133.6	376.1	-66.3	385.7	-91.0	385.5	-67.0	387.2
-135.7	368.1	-150.0	370.8	-88.8	383.0	-105.4	382.3	-92.5	383.3
-149.6	367.1	-165.5	365.0	-104.2	380.4	-121.8	378.0	-106.4	380.5
-168.3	365.2	-177.2	360.1	-116.9	377.7	-136.2	373.6	-118.0	377.9
-181.6	362.1	-194.9	351.8	-132.4	373.9	-151.4	368.4	-135.6	373.0
-196.6	355.9	-207.7	344.9	-148.3	369.4	-168.7	361.6	-151.5	367.8
-210.6	348.0			-148.3	369.4	-180.1	356.5	-166.0	362.4
				-164.2	364.1	-194.5	349.5	-179.9	356.7
				-180.3	357.9	-205.4	343.7	-191.3	351.5
				-192.9	352.5	-231.7	327.8	-207.4	343.3
				-209.4	344.4	-260.4	306.6		

* y is the transverse coordinate where $y = 0$ corresponds to the center line. z is the vertical coordinate. Coordinates are given for certain longitudinal position, for example $x = 630$ mm corresponds to the position of one of the ring-stiffener bordering the mid-bay.

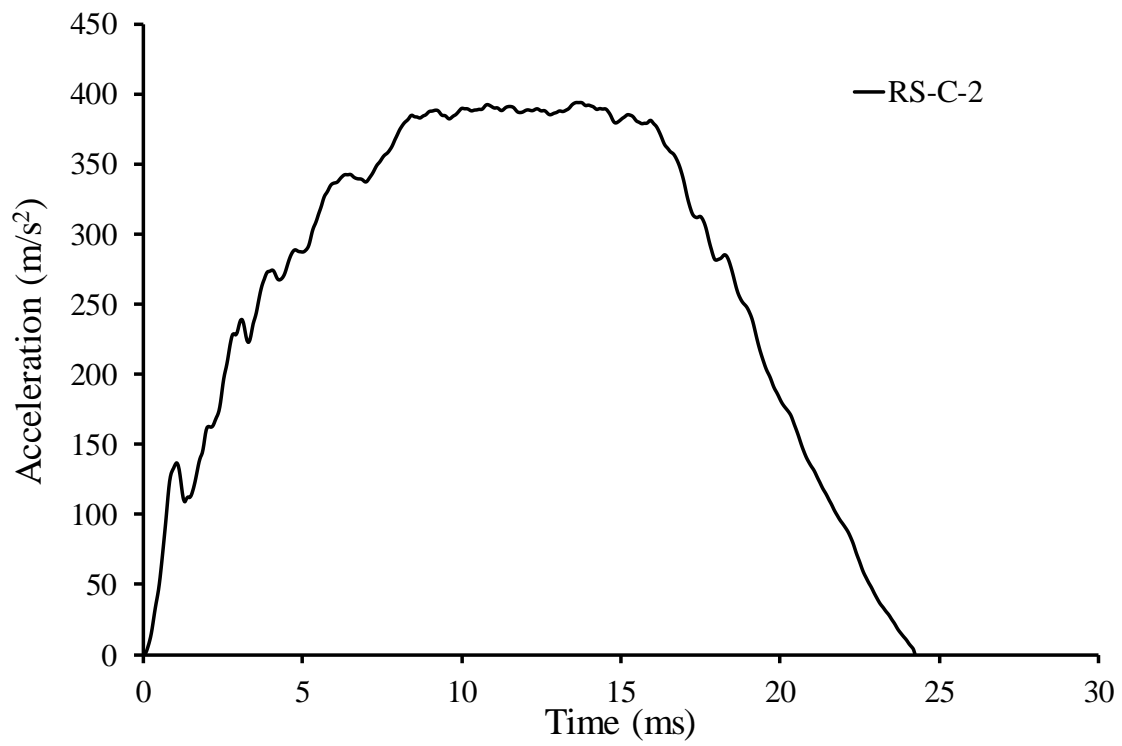
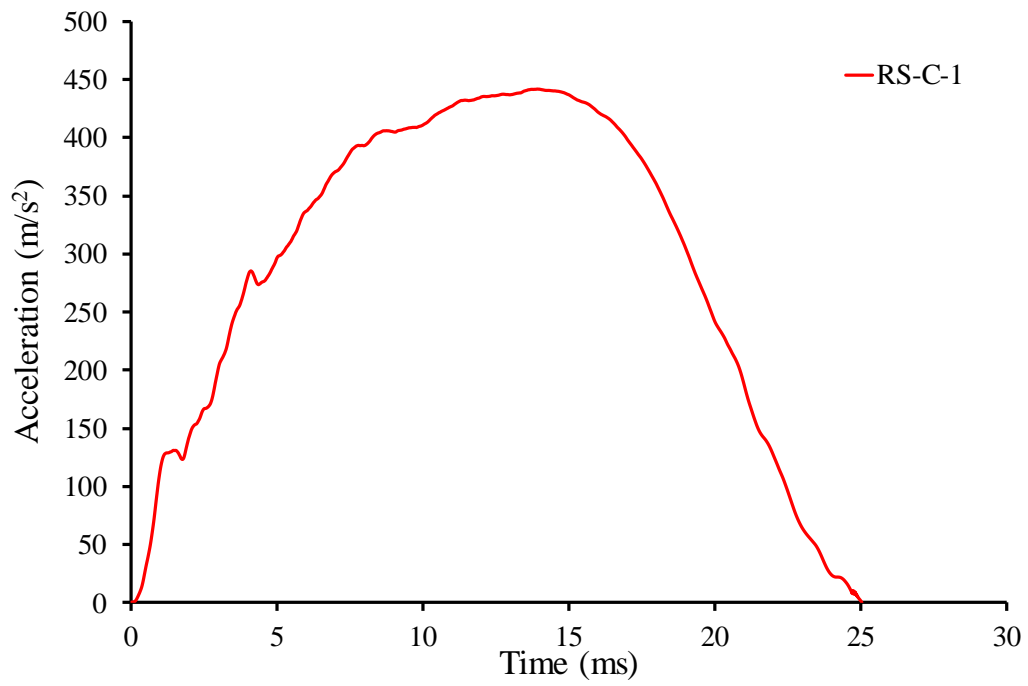
RS-C-3					
Dent line		555 mm		605mm	
y	z	y	z	y	z
0.1	0.3	1109.7	2.8	7.7	95.7
1.6	47.6	1107.7	50.4	17.9	143.1
7.3	94.7	1102.1	96.3	32.4	190.1
17.3	142.2	1091.9	144.6	48.8	232.0
31.5	189.0	1077.4	190.0	71.2	276.1
49.1	233.5	1058.9	235.2	97.5	317.9
70.9	276.7	1037.2	277.6	126.7	357.0
96.9	318.0	1011.0	318.8	156.8	390.4
125.8	356.4	981.7	357.4	193.0	425.0
157.1	391.6	950.4	392.0	230.1	453.5
192.7	425.2	910.0	429.1	272.3	479.9
231.2	455.0	872.9	456.7	316.8	500.5
272.1	481.1	830.7	481.9	361.0	515.1
287.8	489.8	787.0	501.9	409.0	526.4
300.8	496.3	739.9	518.2	455.0	533.3
314.4	502.5	692.6	530.0	504.2	536.6
326.7	507.4	646.4	537.4	533.2	537.1
339.9	511.9	596.1	541.1	549.9	537.5
350.7	514.7	549.2	542.0	584.7	536.9
361.3	516.6	503.5	540.8	598.6	536.8
379.5	518.2	455.9	536.6	647.0	533.7
398.5	519.3	408.9	528.5	692.3	527.7
409.7	519.8	363.3	516.7	740.0	517.1
426.5	520.3	315.8	499.7	787.5	502.1
442.7	520.7	272.5	479.0	830.6	483.1
455.7	520.9	232.7	454.6	871.8	458.6
468.7	521.0	193.2	425.0	910.7	429.2
482.3	521.1	159.4	393.0	951.0	391.8
501.0	521.2	126.3	356.4	981.6	357.7
510.2	521.1	98.1	319.2	1010.4	319.7
525.8	521.2	70.7	276.4	1035.9	279.2
537.1	521.3	49.7	234.3	1058.5	235.5
548.4	521.2	32.3	191.0	1077.4	190.0
563.7	521.0	17.0	142.4	1091.1	145.5
579.8	520.9	7.6	95.4	1101.7	96.7
596.07	520.80	1.76	46.76	1107.98	49.77
604.68	520.51			1109.56	1.44
617.62	520.25			1110.02	1.25

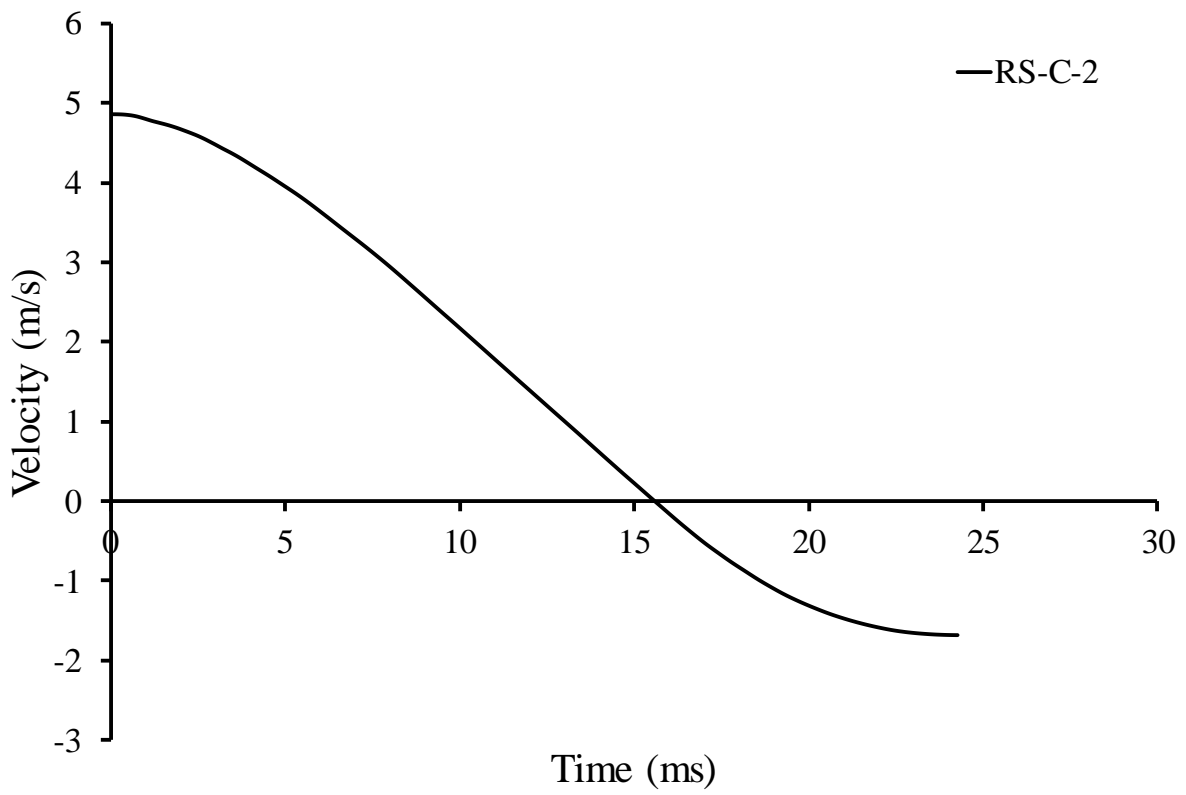
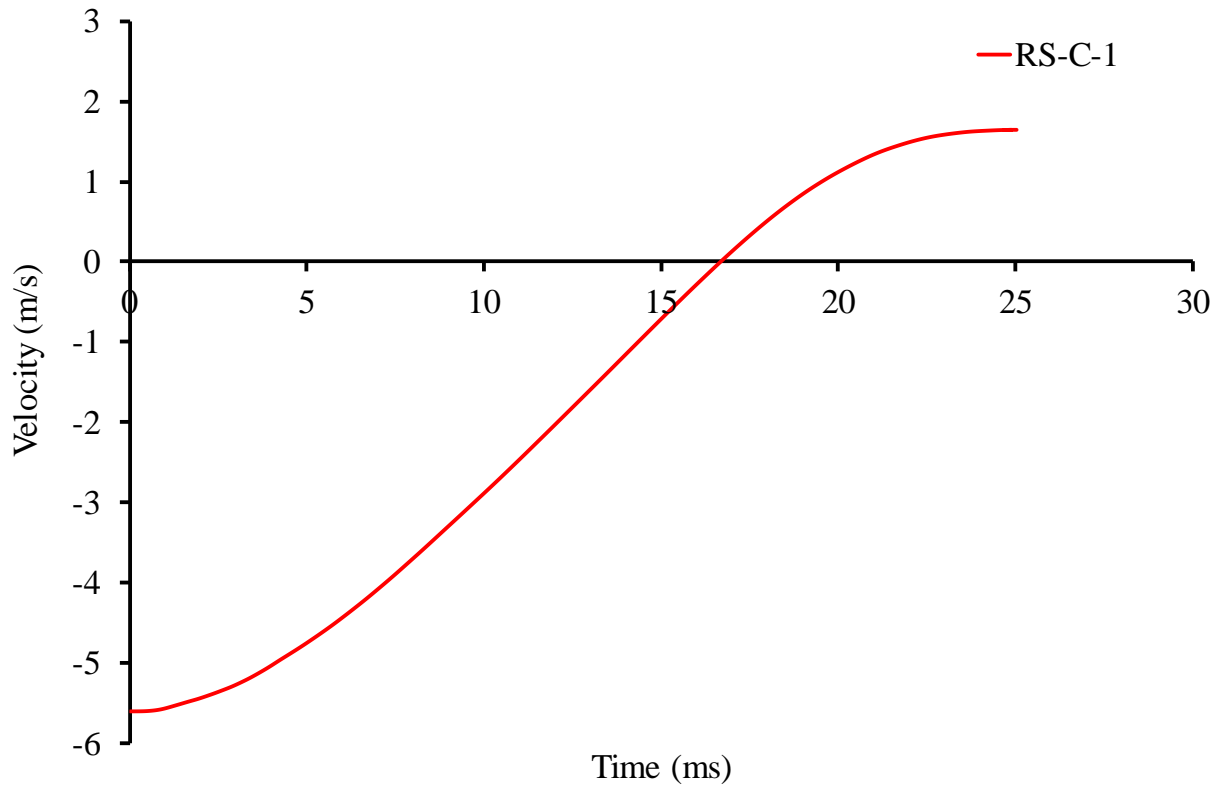
629.84	519.95				
642.50	519.73				
655.60	519.39				
671.63	518.93				
685.405	518.553				
698.955	518.047				
713.97	517.337				
728.444	516.428				
742.338	515.323				
757.474	513.645				
770.795	510.682				
781.403	507.515				

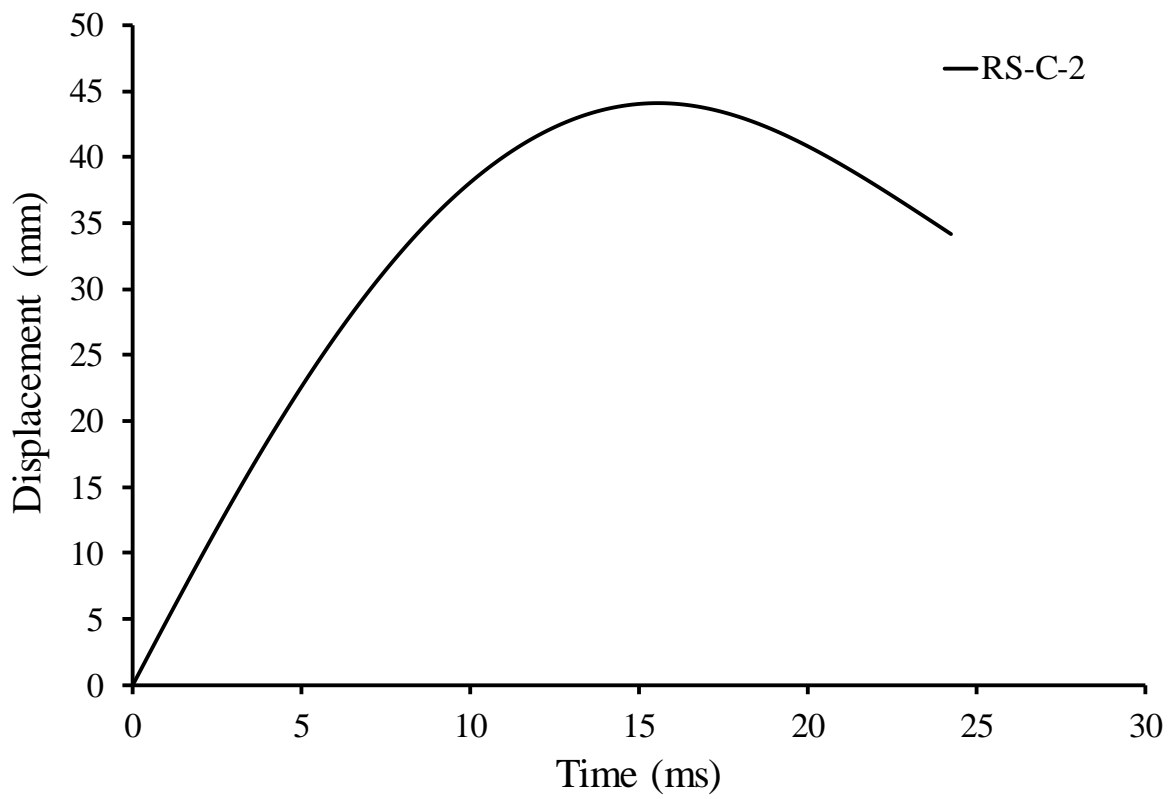
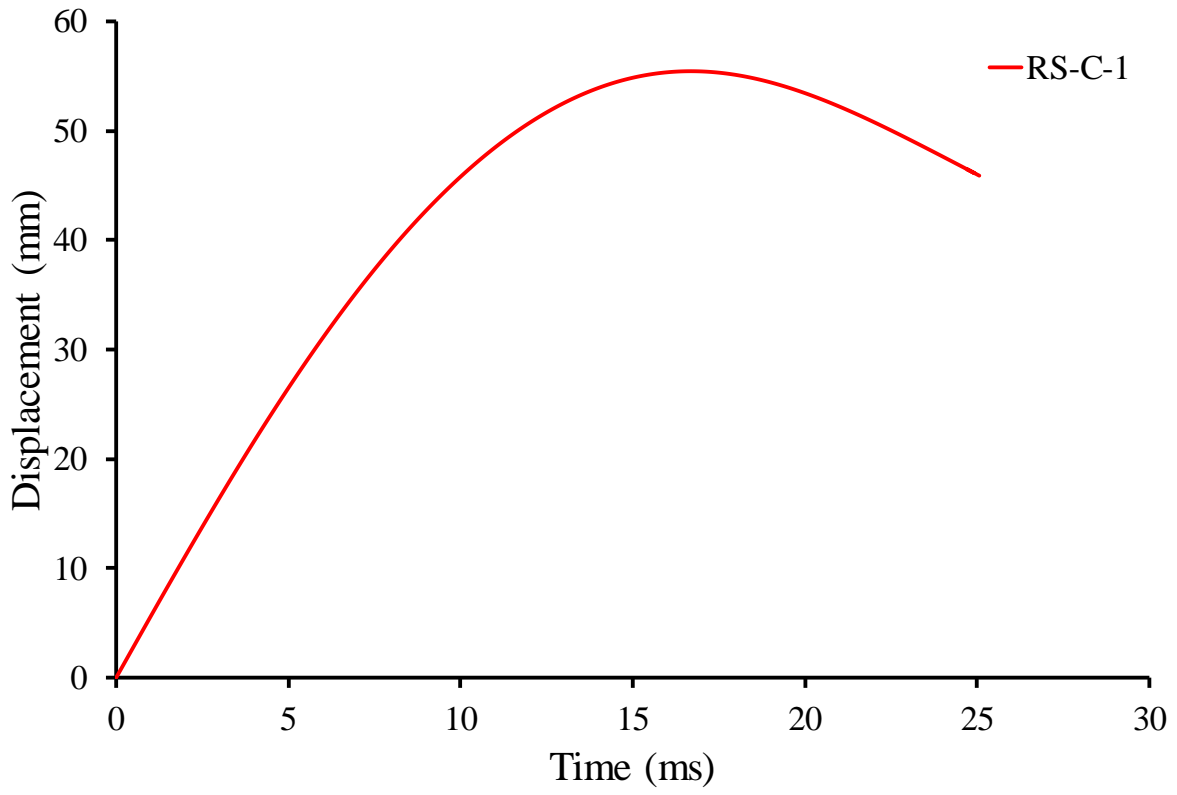
RS-C-4					
Dent line		555 mm		605 mm	
y	z	y	z	y	z
-0.7	0.6	1106.7	45.4	1.7	48.0
1.6	49.0	1100.6	93.3	8.8	97.6
8.4	96.5	1090.9	140.1	19.4	144.3
19.4	145.3	1077.8	184.9	33.1	189.2
33.0	189.4	1060.2	229.8	51.1	232.9
50.7	232.8	1038.8	272.7	74.4	276.1
74.0	276.0	1014.3	312.6	100.6	317.1
100.7	317.2	984.4	353.3	124.5	350.4
125.9	351.9	951.8	390.0	162.3	392.3
161.9	392.3	917.9	421.8	198.3	425.6
198.0	426.3	879.5	451.2	199.2	426.5
234.4	455.9	838.8	475.7	236.0	455.5
277.6	483.2	792.2	497.1	279.1	480.4
320.6	503.9	746.8	512.4	324.3	499.9
345.8	509.7	701.7	523.6	368.7	513.6
370.6	511.1	655.3	530.7	416.0	523.1
396.8	512.0	605.2	534.9	415.9	523.1
417.3	512.3	557.7	536.0	463.5	527.6
462.7	512.7	509.4	535.4	510.9	529.8
486.1	512.5	462.7	532.8	557.9	529.6
510.6	512.3	414.9	526.3	605.0	527.9
533.5	512.2	322.4	499.2	654.0	525.2
557.7	511.9	279.8	480.1	701.3	519.3
570.5	511.5	237.7	456.0	748.1	509.3
586.7	511.1	199.9	427.4	794.4	495.1

RS-C-4					
Dent line		555 mm		605 mm	
601.8	510.8	163.1	393.6	838.1	476.7
620.9	510.3	134.8	363.2	879.1	452.2
639.9	509.6	100.8	318.7	880.8	451.0
651.6	509.2	73.1	275.0	918.0	422.0
676.8	508.3	50.6	233.0	953.1	388.6
698.07	507.48	32.87	189.07	985.75	352.06
726.80	506.11	19.23	143.81	1014.88	311.49
746.21	504.95	8.50	96.22	1038.53	272.65
765.45	503.46			1060.69	229.23
781.46	501.73			1038.45	272.79
792.11	499.55			1060.83	228.82
815.48	491.00				
831.19	483.51				
855.57	469.50				
879.97	452.94				
902.83	435.46				
918.07	422.65				
938.718	403.639				
952.772	389.499				
984.779	353.224				
1014.227	313.143				
1038.405	273.597				
1059.975	230.768				
1060.183	230.5				

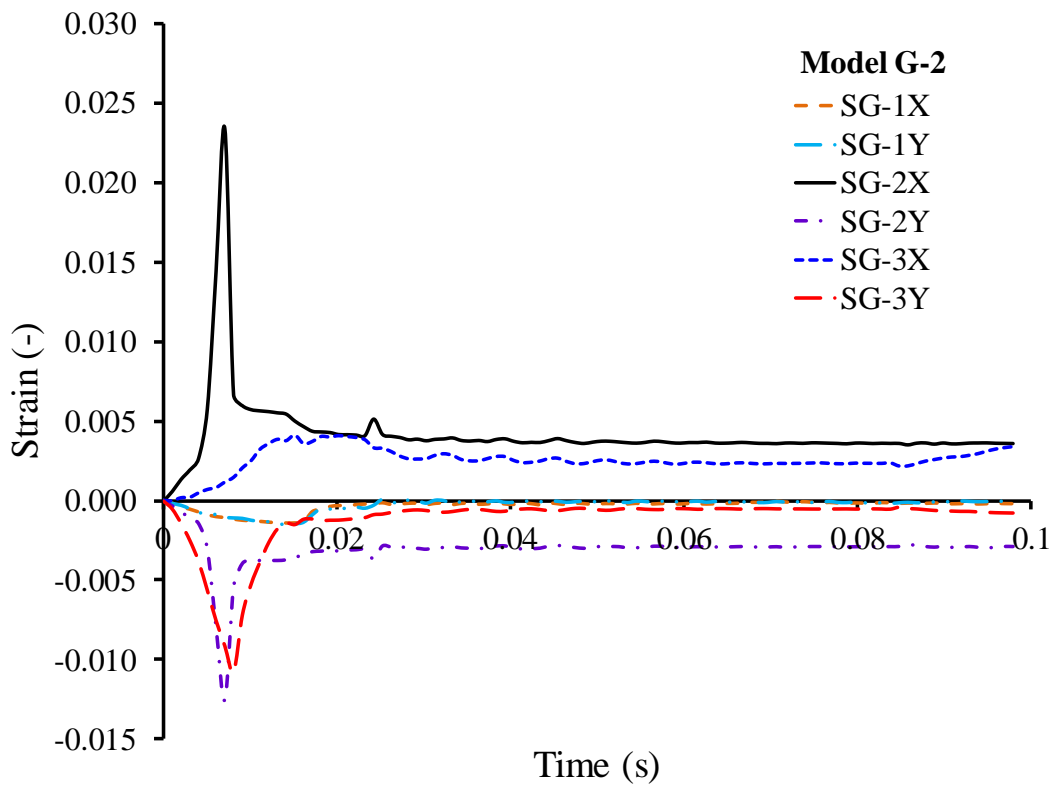
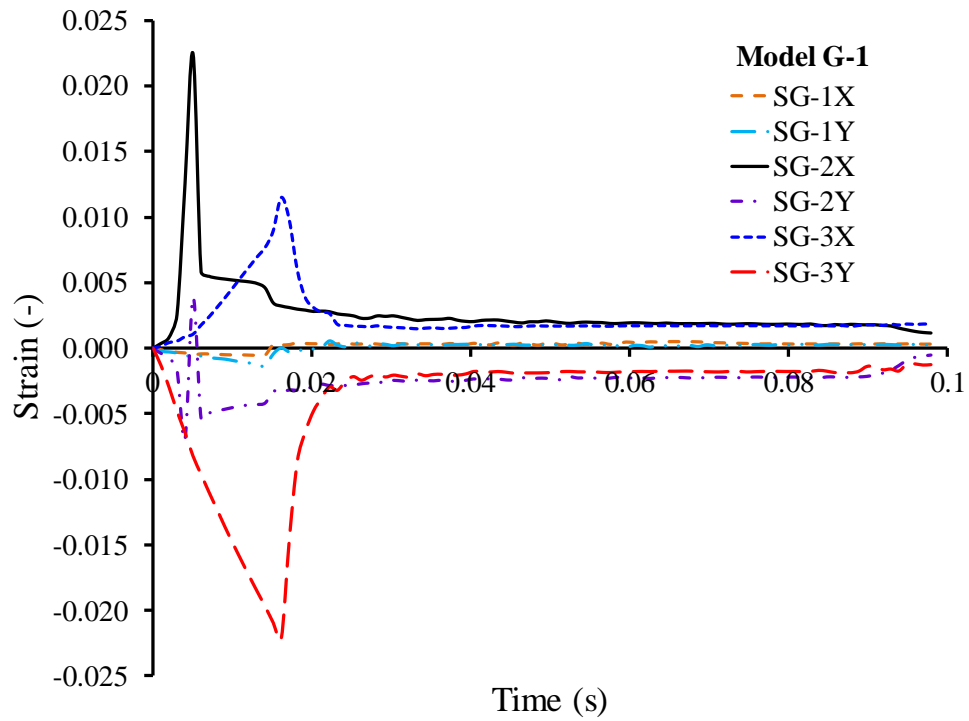
D.2 Accelerometer measurements

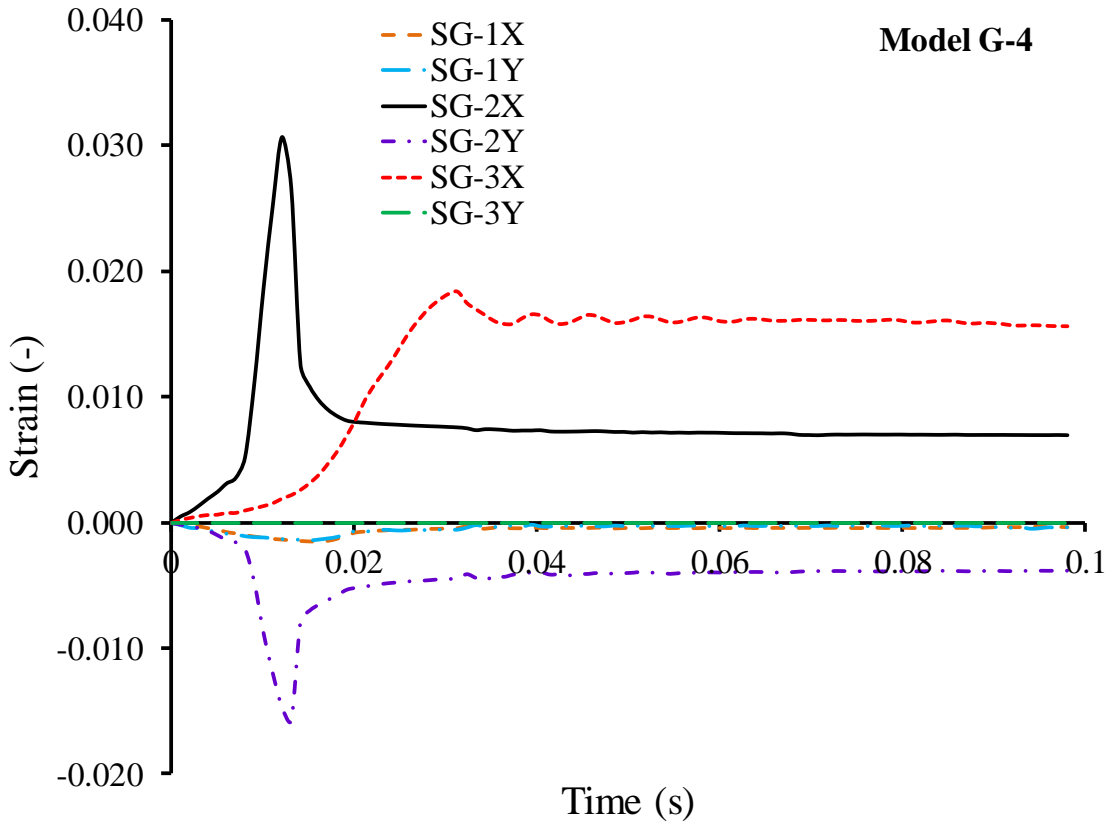
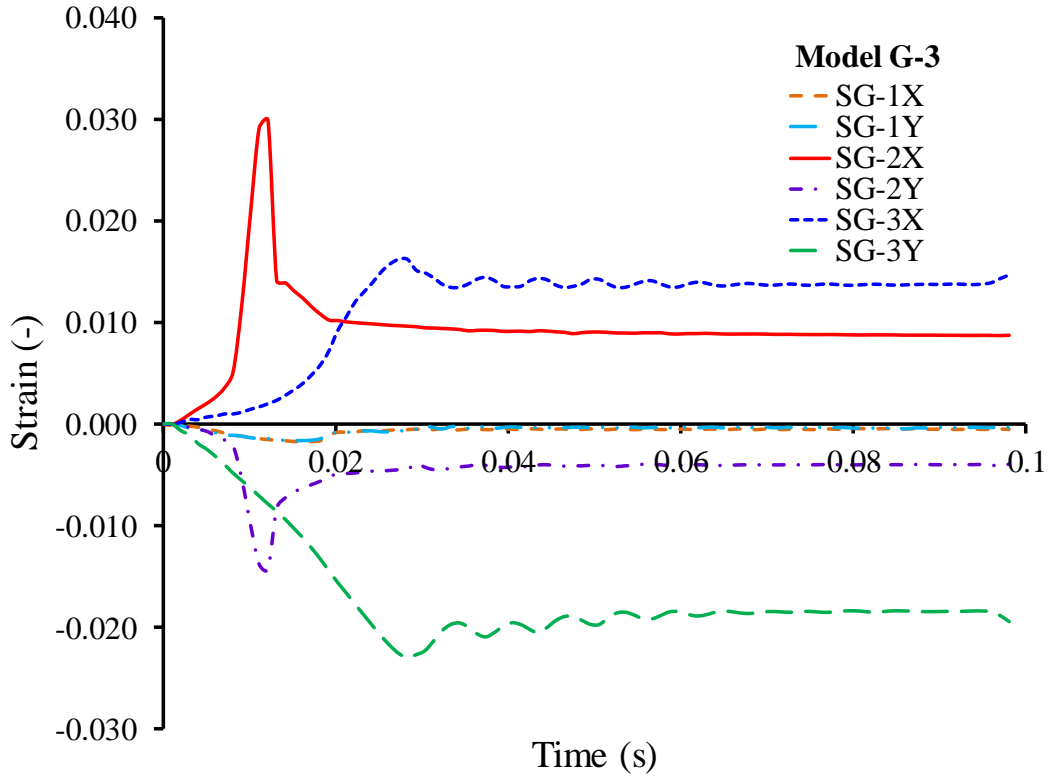


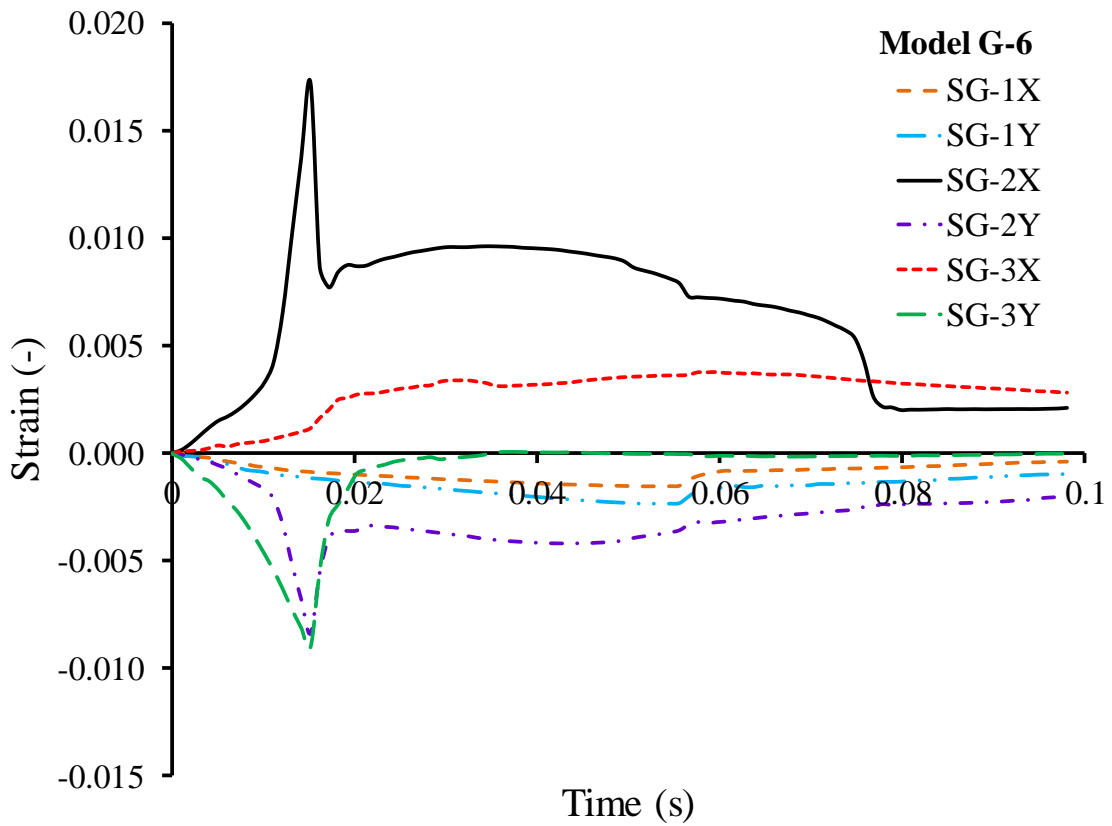
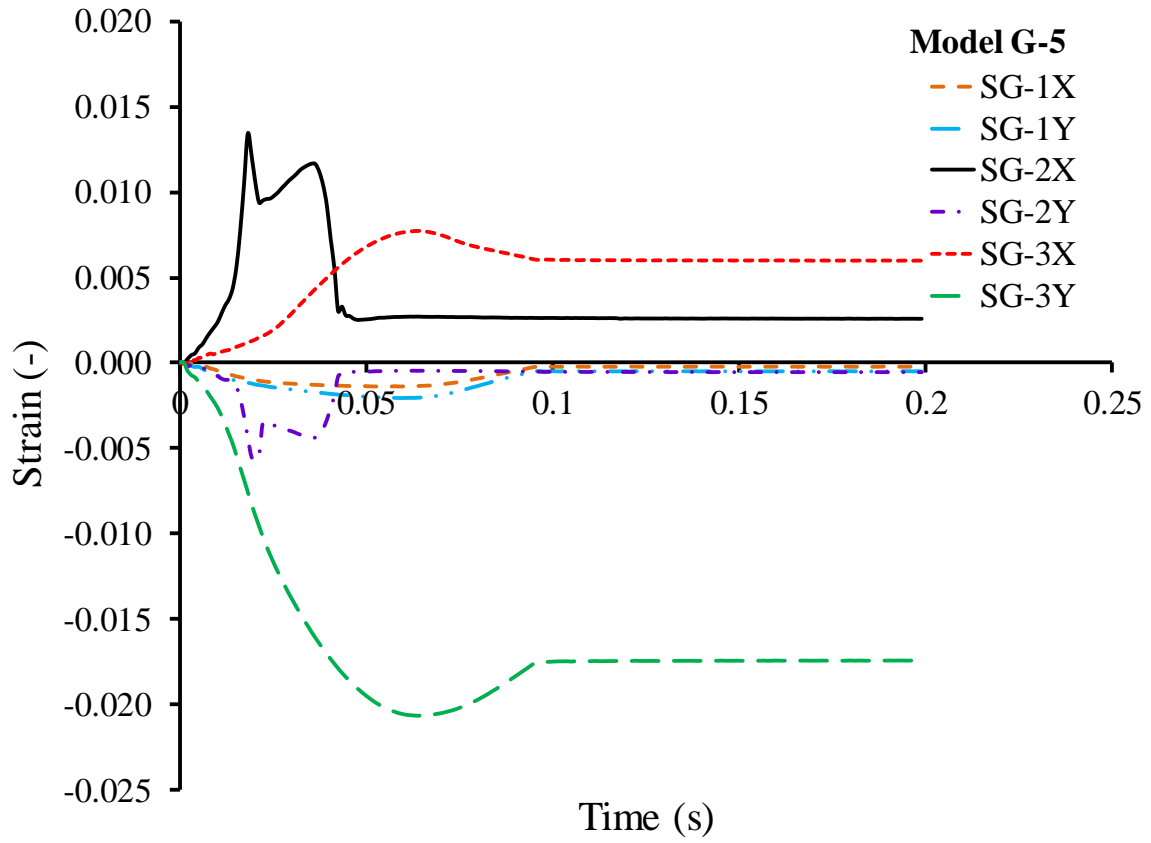


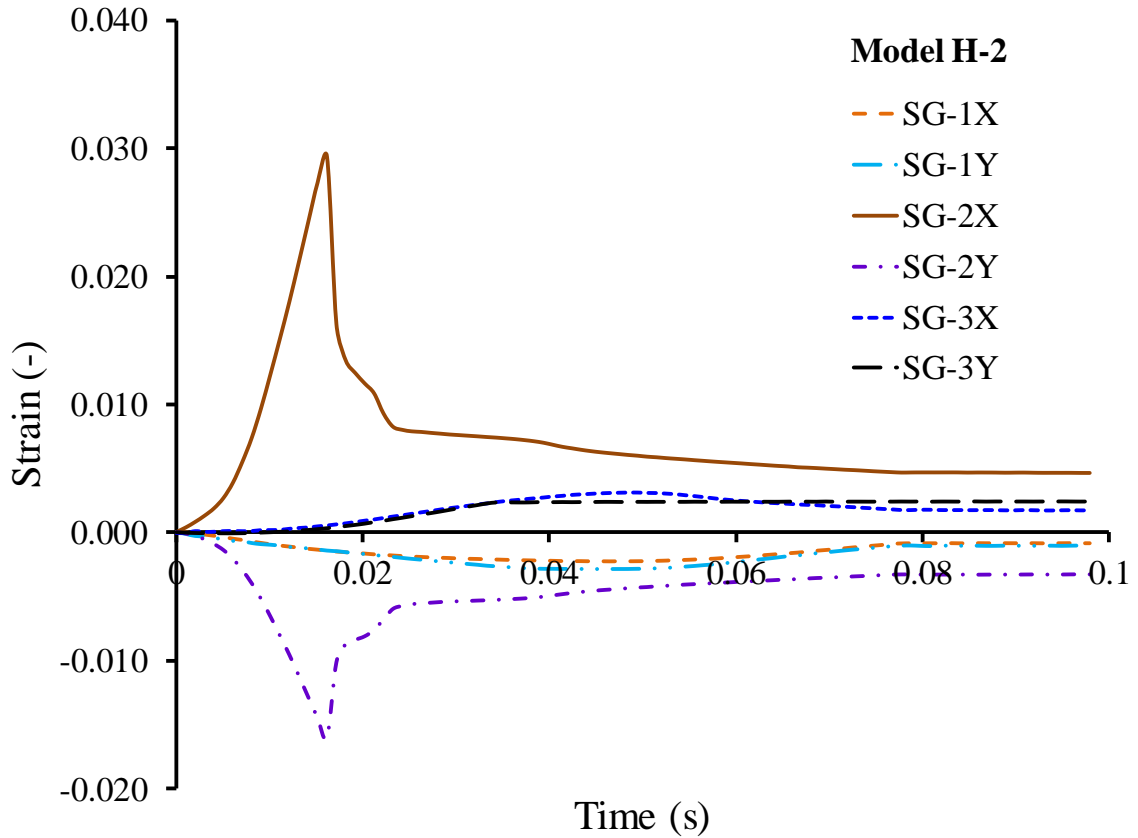
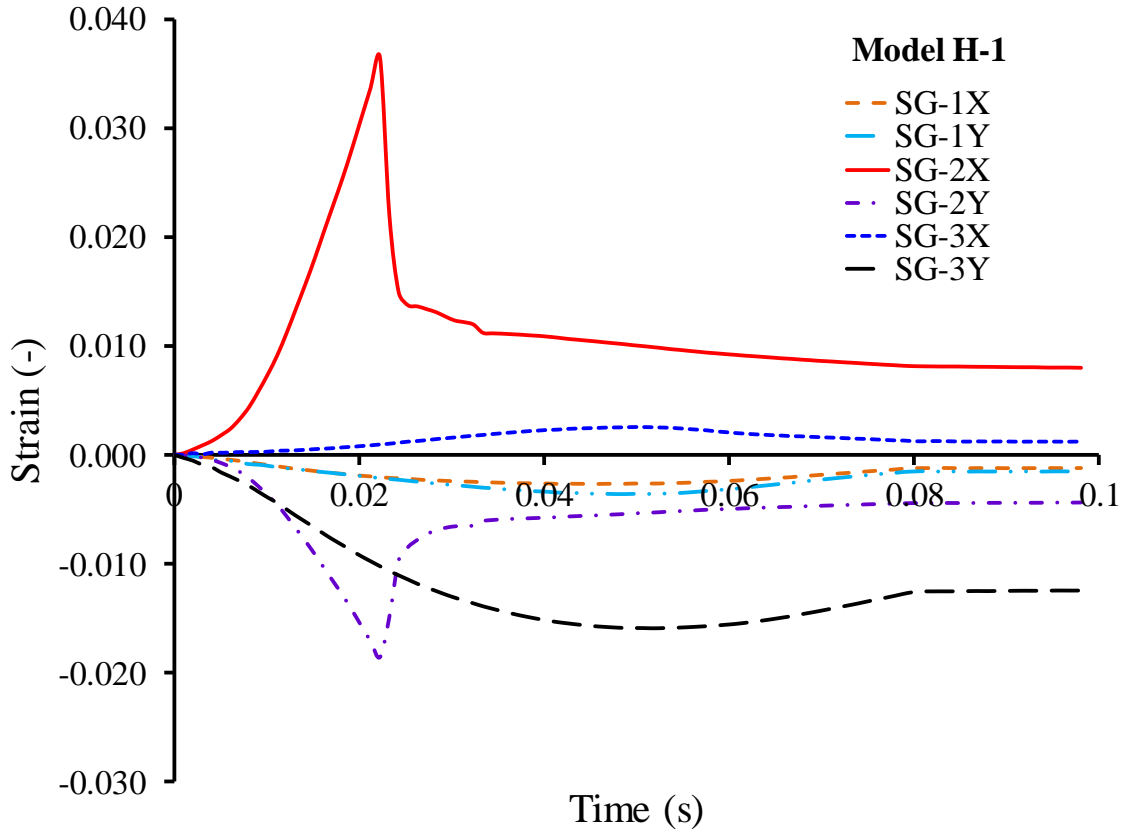


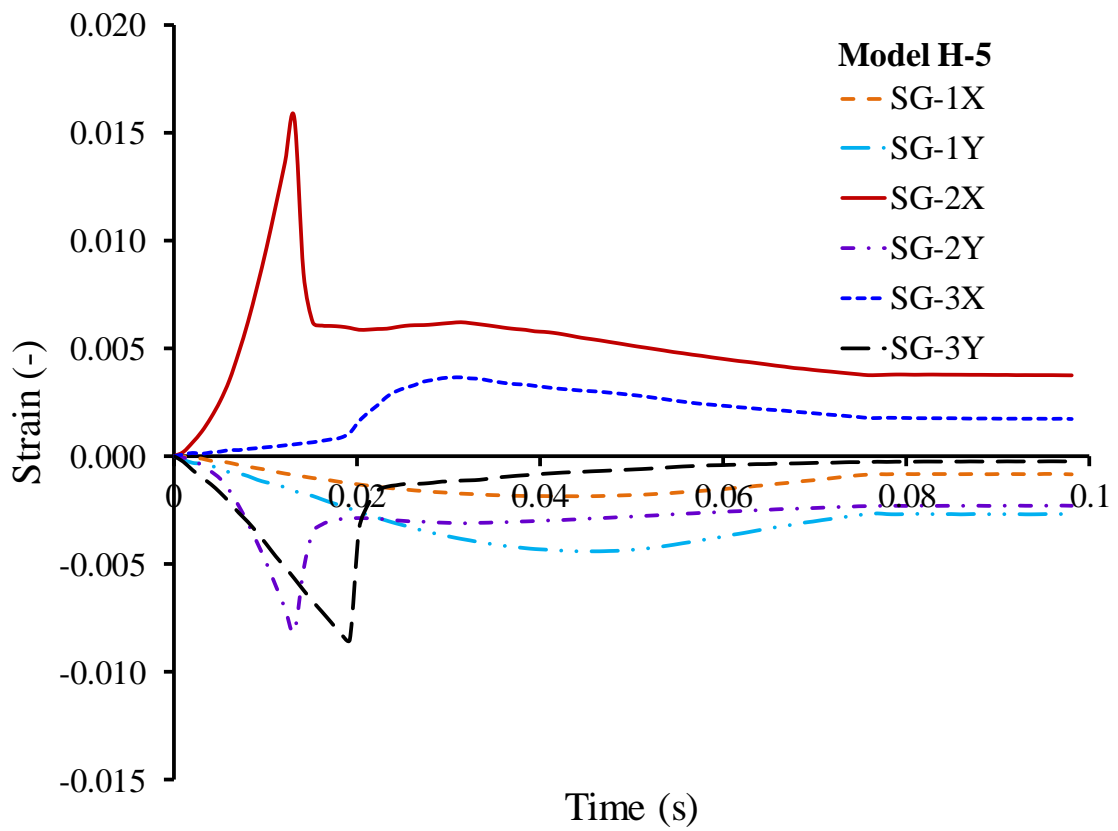
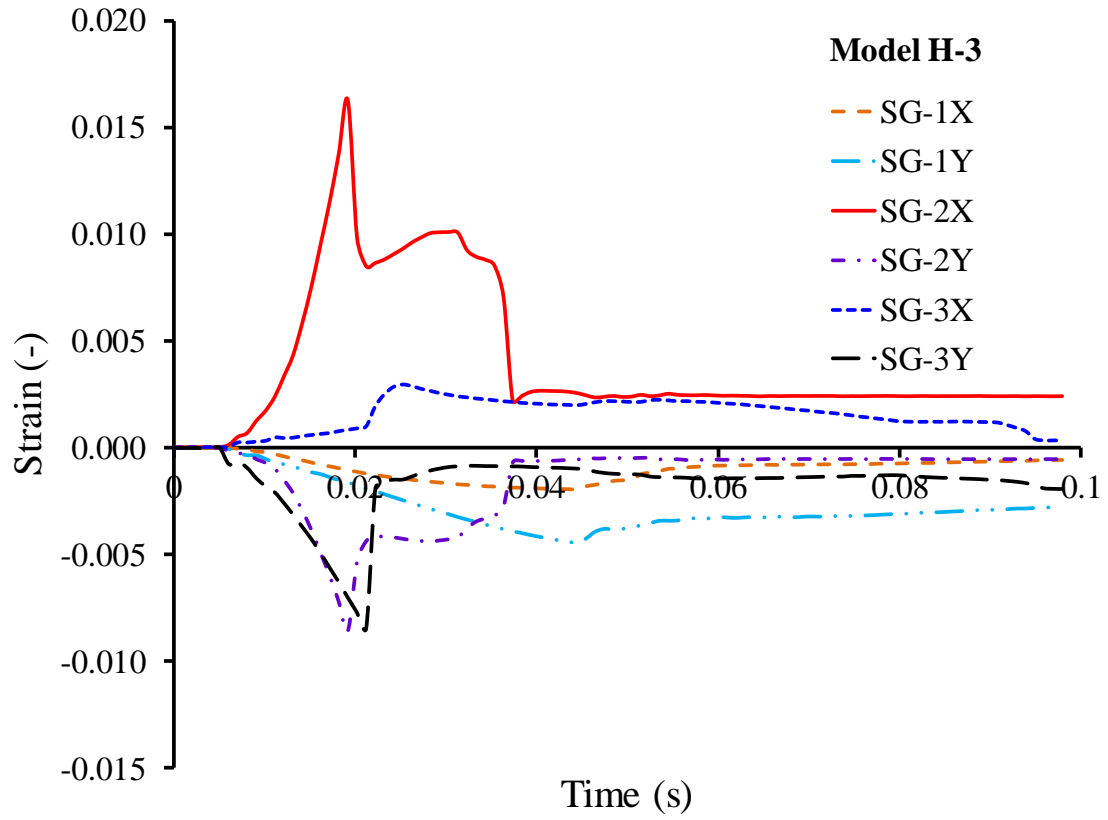
D.3 Strain measurement for tubular test models











D.4 Deformed shape of the experimental models



Fig. D4.1 Deformed shape of model A1.



Fig. D4.2 Deformed shape of model A2.



Fig. D4.3 Deformed shape of model F1.



Fig. D4.4 Deformed shape of model D2.

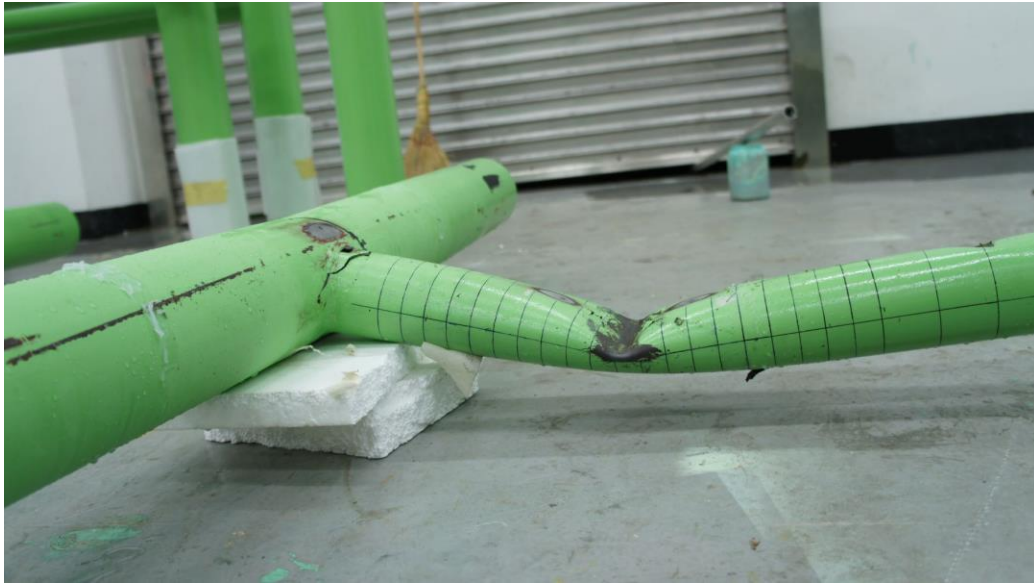


Fig. D4.5 Deformed shape of model D3.

Appendix E: Effects of impact location and angles on the extent damage of ring- and stringer-stiffened cylinder

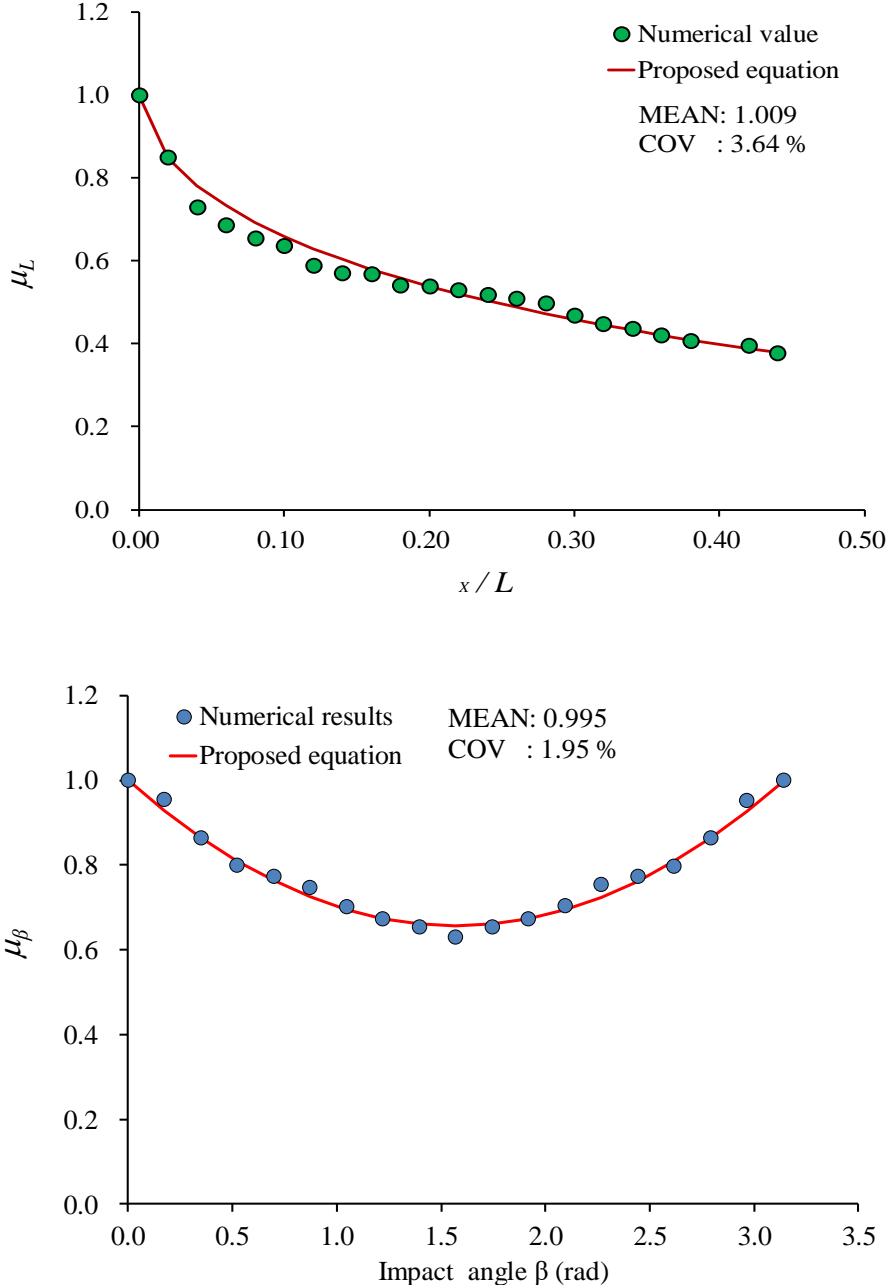


Fig. E.1 Effects of impact location and angles on the extent damage of ring-stiffened cylinder.

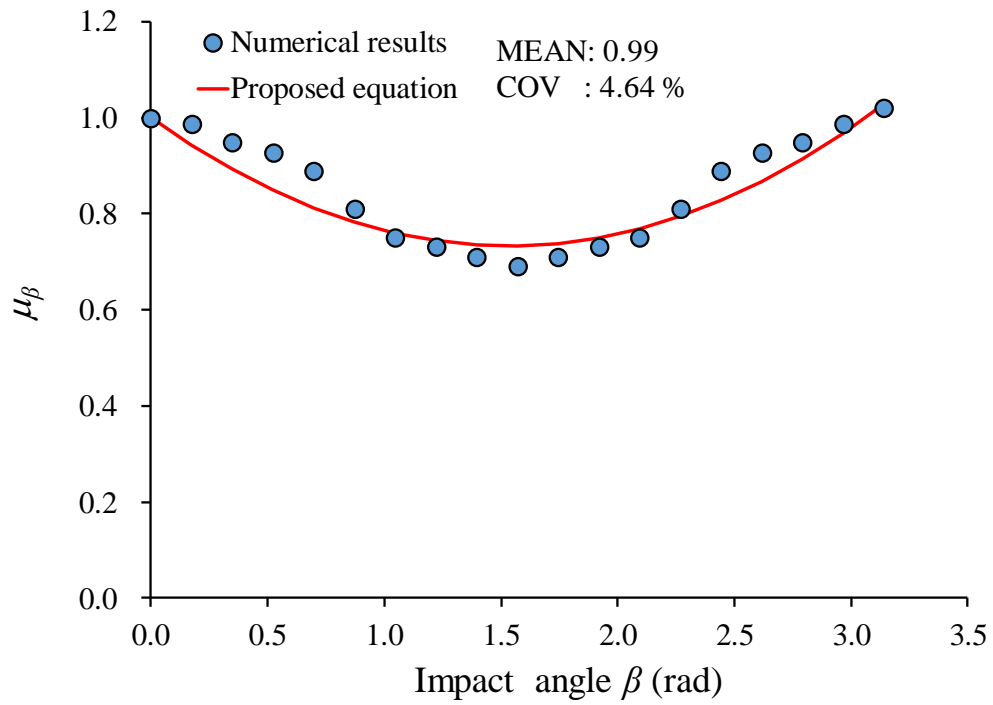
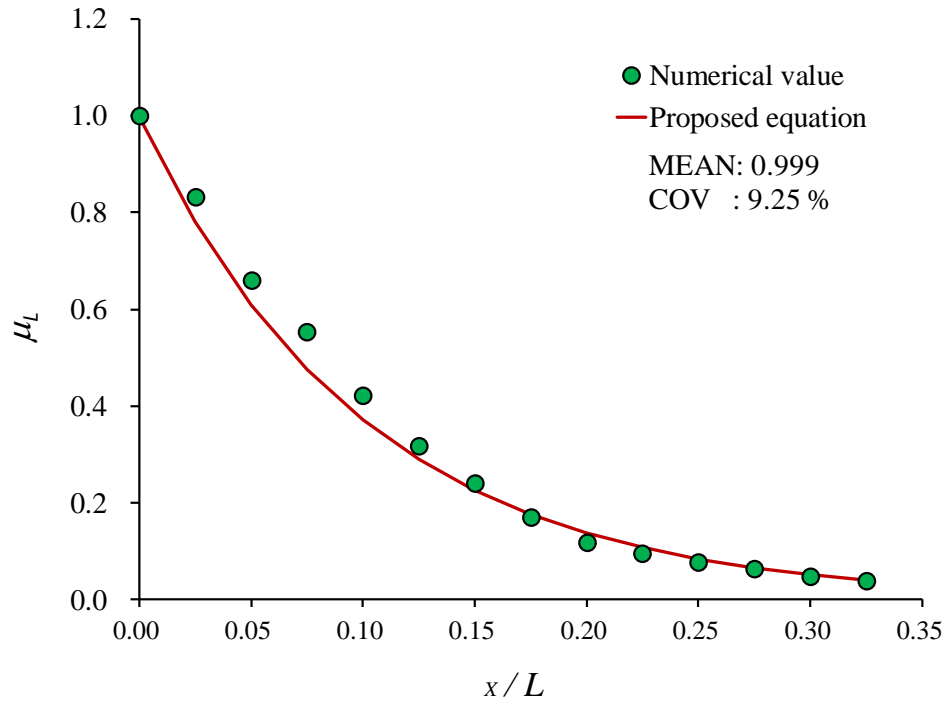


Fig. E.2 Effects of impact location and angles on the extent damage of stringer-stiffened cylinder.

Appendix F: Numerical analysis results

F.1 Deformed shape of the numerical models

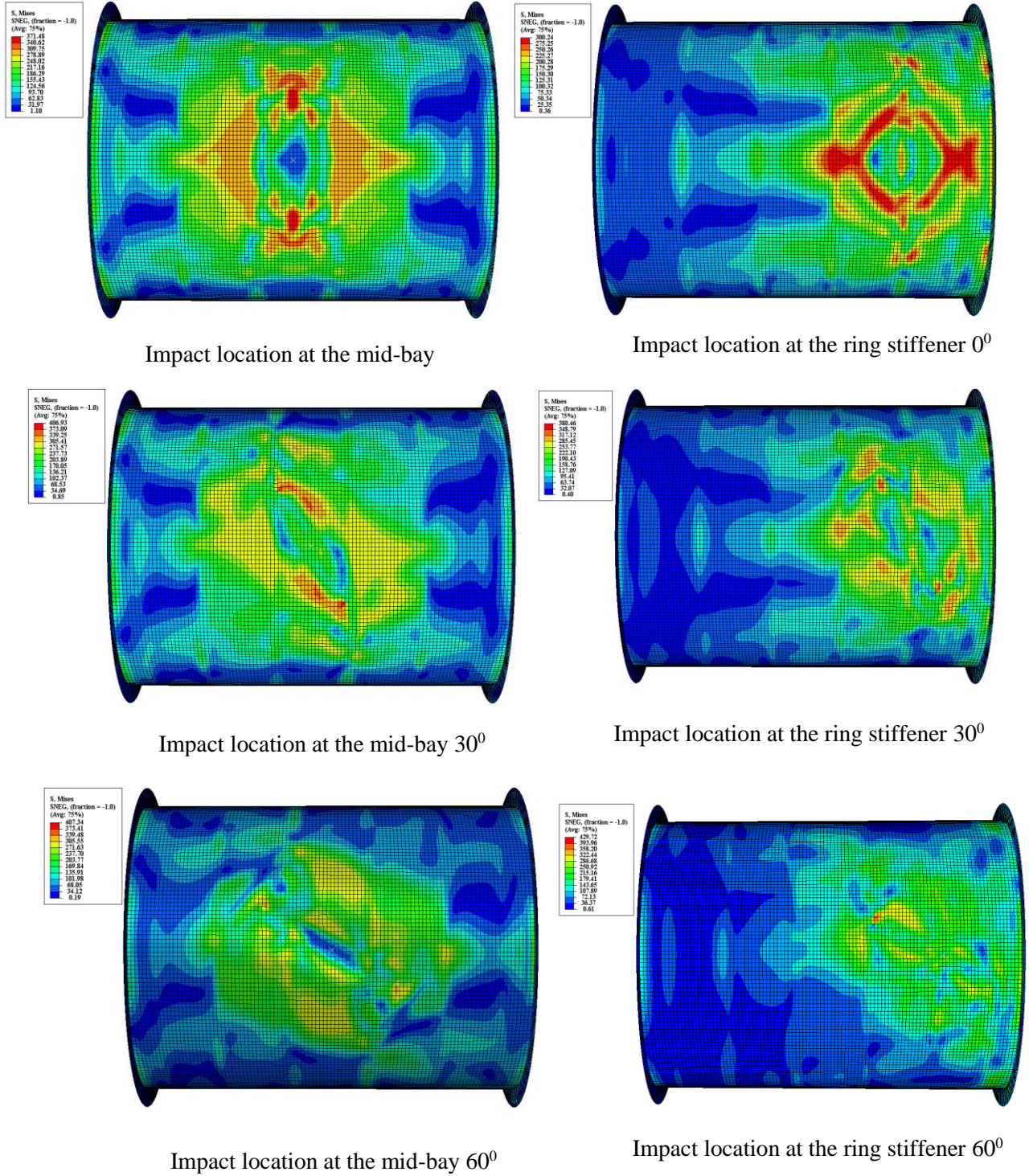
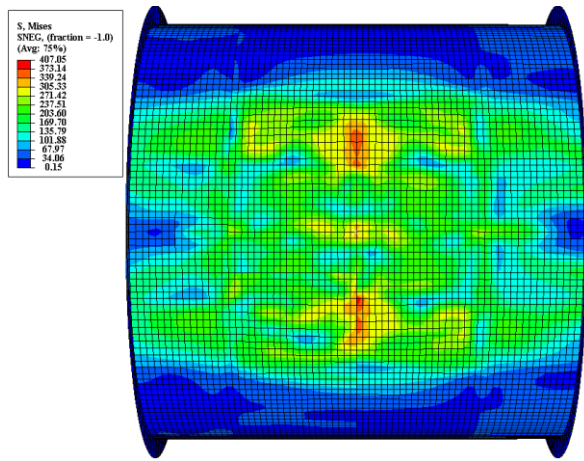
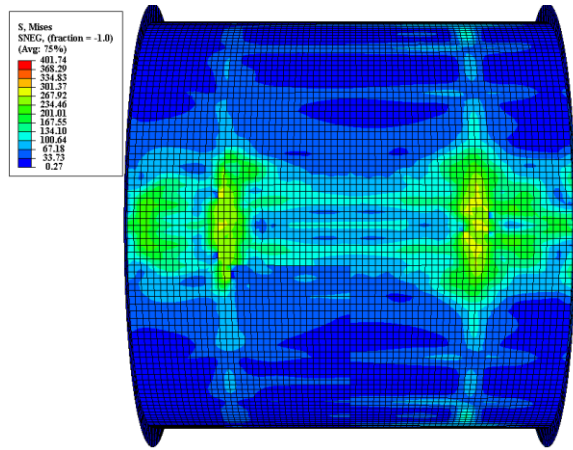


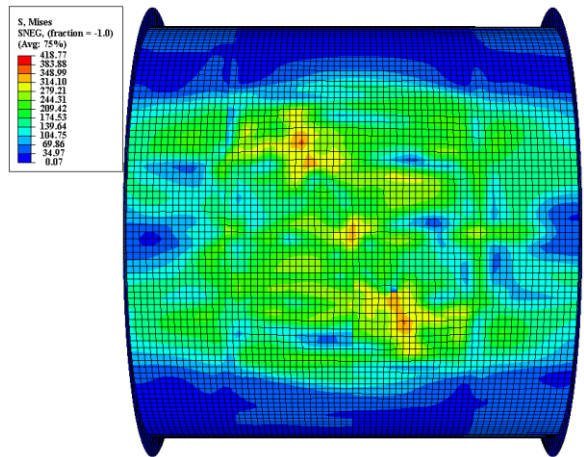
Fig. F.1 Deformed shape of the various impact locations on ring-stiffened cylinders.



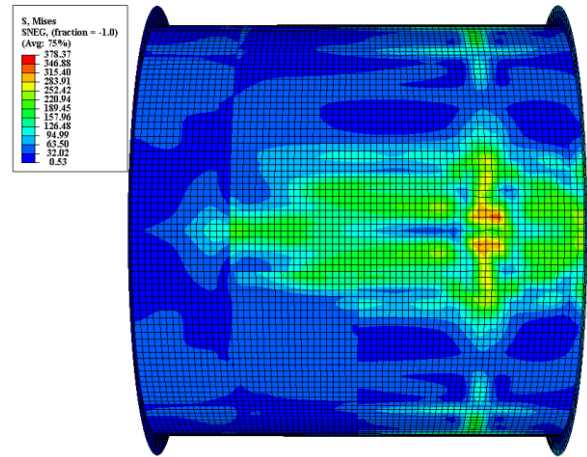
Impact location at the mid-bay 0°



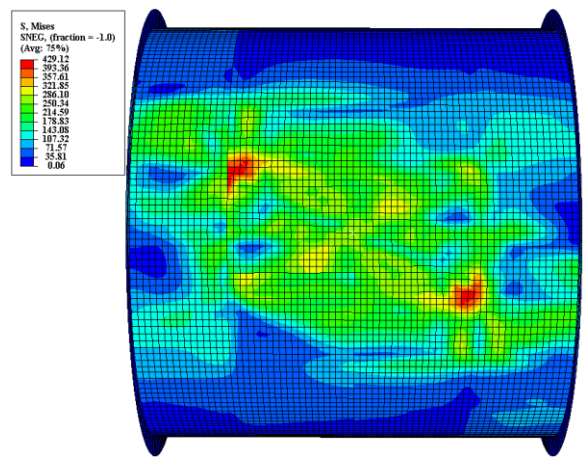
Impact location at the mid-bay 90°



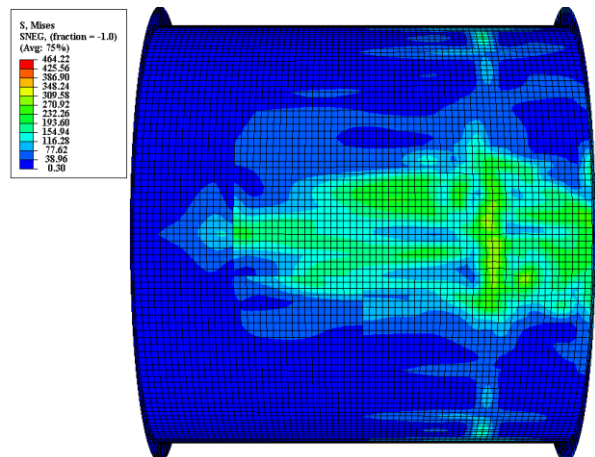
Impact location at the mid-bay 30°



Impact location at the stringer stiffener 0°



Impact location at the mid-bay 60°



Impact location at the stringer stiffener 30°

Fig. F.2 Deformed shape of the various impact locations on stringer-stiffened cylinders.

F.2 Results of permanent deflection for ring- or stringer-stiffened cylinder under mass impact

Table F.2.1 Comparison of prediction and parametric study result for permanent deflection of the ring-stiffened cylinder under mass impact.

Model	Collision cases	Velocity, v (mm/s)	Striker mass, m (ton)	Structural volume, V_{str} (mm ³)	Kinetic energy, E_k (mJ)	Energy absorption, E_a (mJ)	$\lambda_E = E_k/E_a$	Dent depth, d (mm)		X_m (Num./Eq. (3.16))
								Num.	Eq. (3.16)	
RS-1	Case 1	2500	10	11050688248	31250000	993912642885	0.000031	8.25	7.84	1.053
			20		62500000		0.000063	14.21	12.82	1.108
			50		156250000		0.000157	27.29	24.57	1.111
	Case 2	5000	10		125000000		0.000126	20.61	20.97	0.983
			20		250000000		0.000252	37.01	34.30	1.079
			50		625000000		0.000629	69.68	65.75	1.060
	Case 3	7500	10		281250000		0.000283	39.24	37.30	1.052
			20		562500000		0.000566	62.69	61.01	1.028
			50		1406250000		0.001415	116.01	116.93	0.992
	Case 4	10000	10		500000000		0.000503	56.98	56.12	1.015
			20		1000000000		0.001006	95.26	91.79	1.038
			50		2500000000		0.002515	192.35	175.93	1.093

Model	Collision cases	Velocity, v (mm/s)	Striker mass, m (ton)	Structural volume, V_{str} (mm ³)	Kinetic energy, E_k (mJ)	Energy absorption, E_a (mJ)	$\lambda_E = E_k/E_a$	Dent depth, d (mm)		X_m (Num./Eq. (3.16))
								Num.	Eq. (3.16)	
RS-2	Case 1	2500	10	7772089487	31250000	717253120408	0.000044	-	-	-
			20		62500000		0.000087	-	-	-
			50		156250000		0.000218	-	-	-
	Case 2	5000	10		125000000		0.000174	-	-	-
			20		250000000		0.000349	-	-	-
			50		625000000		0.000871	78.44	80.83	0.970
	Case 3	7500	10		281250000		0.000392	45.31	45.85	0.988
			20		562500000		0.000784	75.64	75.00	1.009
			50		1406250000		0.001961	156.23	143.75	1.087
	Case 4	10000	10		500000000		0.000697	68.57	68.98	0.994
			20		1000000000		0.001394	115.29	112.84	1.022
			50		2500000000		0.003486	235.69	216.28	1.090

Model	Collision cases	Velocity, v (mm/s)	Striker mass, m (ton)	Structural volume, V_{str} (mm ³)	Kinetic energy, E_k (mJ)	Energy absorption, E_a (mJ)	$\square_E = E_k/E_a$	Dent depth, d (mm)		X_m (Num./Eq. (3.16))
								Num.	Eq. (3.16)	
RS-3	Case 1	2500	10	4632383801	31250000	416642359575	0.000075	-	-	-
			20		62500000		0.000150	-	-	-
			50		156250000		0.000375	49.04	46.65	1.051
	Case 2	5000	10		125000000		0.000300	34.60	39.82	0.869
			20		250000000		0.000600	67.12	65.14	1.030
			50		625000000		0.001500	135.68	124.84	1.087
	Case 3	7500	10		281250000		0.000675	78.02	70.82	1.102
			20		562500000		0.001350	135.64	115.84	1.171
			50		1406250000		0.003375	230.45	222.03	1.038
	Case 4	10000	10		500000000		0.001200	125.80	106.55	1.181
			20		1000000000		0.002400	189.35	174.29	1.086
			50		2500000000		0.006000	350.40	334.05	1.049

Model	Collision cases	Velocity, v (mm/s)	Striker mass, m (ton)	Structural volume, V_{str} (mm ³)	Kinetic energy, E_k (mJ)	Energy absorption, E_a (mJ)	$\square_E = E_k/E_a$	Dent depth, d (mm)		X_m (Num./Eq. (3.16))
								Num.	Eq. (3.16)	
RS-4	Case 1	2500	10	6479379999	31250000	582763494384	0.000054	10.69	11.45	0.933
			20		62500000		0.000107	17.75	18.73	0.947
			50		156250000		0.000268	34.39	35.90	0.958
	Case 2	5000	10		125000000		0.000214	21.81	30.64	0.712
			20		250000000		0.000429	48.03	50.11	0.958
			50		625000000		0.001072	109.84	96.05	1.144
	Case 3	7500	10		281250000		0.000483	52.15	54.49	0.957
			20		562500000		0.000965	94.75	89.13	1.063
			50		1406250000		0.002413	196.77	170.83	1.152
	Case 4	10000	10		500000000		0.000858	85.89	81.98	1.048
			20		1000000000		0.001716	142.56	134.10	1.063
			50		2500000000		0.004290	304.20	257.02	1.184

Model	Collision cases	Velocity, v (mm/s)	Striker mass, m (ton)	Structural volume, V_{str} (mm ³)	Kinetic energy, E_k (mJ)	Energy absorption, E_a (mJ)	$\lambda_E = E_k/E_a$	Dent depth, d (mm)		X_m (Num./Eq. (3.16))
								Num.	Eq. (3.16)	
RS-5	Case 1	2500	10	9218814098	31250000	879082094343	0.000036	8.05	7.03	1.145
			20		62500000		0.000071	11.21	11.51	0.974
			50		156250000		0.000178	24.34	22.05	1.104
	Case 2	5000	10		125000000		0.000142	15.53	18.82	0.825
			20		250000000		0.000284	28.81	30.79	0.936
			50		625000000		0.000711	63.48	59.01	1.076
	Case 3	7500	10		281250000		0.000320	29.58	33.47	0.884
			20		562500000		0.000640	52.34	54.76	0.956
			50		1406250000		0.001600	112.80	104.95	1.075
	Case 4	10000	10		500000000		0.000569	44.74	50.36	0.888
			20		1000000000		0.001138	80.03	82.38	0.971
			50		2500000000		0.002844	172.52	157.90	1.093

Model	Collision cases	Velocity, v (mm/s)	Striker mass, m (ton)	Structural volume, V_{str} (mm ³)	Kinetic energy, E_k (mJ)	Energy absorption, E_a (mJ)	$\lambda_E = E_k/E_a$	Dent depth, d (mm)		X_m (Num./Eq. (3.16))
								Num.	Eq. (3.16)	
RS-6	Case 1	2500	10	23641037299	31250000	2126304292952	0.000015	-	-	-
			20		62500000		0.000029	-	-	-
			50		156250000		0.000073	-	-	-
	Case 2	5000	10		125000000		0.000059	-	-	-
			20		250000000		0.000118	33.19	33.21	0.999
			50		625000000		0.000294	63.79	63.66	1.002
	Case 3	7500	10		281250000		0.000132	38.20	36.11	1.058
			20		562500000		0.000265	58.75	59.07	0.995
			50		1406250000		0.000661	109.09	113.21	0.964
	Case 4	10000	10		500000000		0.000235	56.67	54.33	1.043
			20		1000000000		0.000470	84.34	88.87	0.949
			50		2500000000		0.001176	163.53	170.33	0.960

Model	Collision cases	Velocity, v (mm/s)	Striker mass, m (ton)	Structural volume, V_{str} (mm ³)	Kinetic energy, E_k (mJ)	Energy absorption, E_a (mJ)	$\lambda_E = E_k/E_a$	Dent depth, d (mm)		X_m (Num./Eq. (3.16))
								Num.	Eq. (3.16)	
RS-7	Case 1	2500	10	2642766645	31250000	228977109478	0.000136	22.34	17.92	1.246
			20		62500000		0.000273	31.25	29.32	1.066
			50		156250000		0.000682	72.76	56.19	1.295
	Case 2	5000	10		125000000		0.000546	54.26	47.96	1.131
			20		250000000		0.001092	92.56	78.45	1.180
			50		625000000		0.002730	156.47	150.36	1.041
	Case 3	7500	10		281250000		0.001228	95.63	85.29	1.121
			20		562500000		0.002457	147.06	139.52	1.054
			50		1406250000		0.006141	260.61	267.41	0.975
	Case 4	10000	10		500000000		0.002184	131.35	128.33	1.024
			20		1000000000		0.004367	209.09	209.92	0.996
			50		2500000000		0.010918	384.36	402.34	0.955

Model	Collision cases	Velocity, v (mm/s)	Striker mass, m (ton)	Structural volume, V_{str} (mm ³)	Kinetic energy, E_k (mJ)	Energy absorption, E_a (mJ)	$\lambda_E = E_k/E_a$	Dent depth, d (mm)		X_m (Num./Eq. (3.16))
								Num.	Eq. (3.16)	
RS-8	Case 1	2500	10	4906180087	31250000	428539600675	0.000073	21.09	16.08	1.311
			20		62500000		0.000146	31.63	26.30	1.202
			50		156250000		0.000365	58.28	50.41	1.156
	Case 2	5000	10		125000000		0.000292	50.53	43.03	1.175
			20		250000000		0.000583	72.46	70.38	1.030
			50		625000000		0.001458	129.24	134.89	0.958
	Case 3	7500	10		281250000		0.000656	73.48	76.52	0.960
			20		562500000		0.001313	114.75	125.17	0.917
			50		1406250000		0.003281	228.42	239.91	0.952
	Case 4	10000	10		500000000		0.001167	99.86	115.13	0.867
			20		1000000000		0.002334	171.15	188.33	0.909
			50		2500000000		0.005834	349.49	360.96	0.968

Model	Collision cases	Velocity, v (mm/s)	Striker mass, m (ton)	Structural volume, V_{str} (mm ³)	Kinetic energy, E_k (mJ)	Energy absorption, E_a (mJ)	$\lambda_E = E_k/E_a$	Dent depth, d (mm)		X_m (Num./Eq. (3.16))
								Num.	Eq. (3.16)	
RS-9	Case 1	2500	0.30	18123336	937500	1208653177	0.000776	13.35	13.54	0.986
			0.6		1875000		0.001551	20.46	22.15	0.924
			1.0		3125000		0.002586	29.05	31.83	0.913
	Case 2	5000	0.30		3750000		0.003103	31.50	36.23	0.870
			0.6		7500000		0.006205	53.61	59.26	0.905
			1.0		12500000		0.010342	80.12	85.17	0.941
	Case 3	7500	0.30		8437500		0.006981	57.32	64.43	0.890
			0.6		16875000		0.013962	99.09	105.40	0.940
			1.0		28125000		0.023270	147.66	151.48	0.975
	Case 4	10000	0.30		15000000		0.012411	88.72	96.94	0.915
			0.6		30000000		0.024821	152.84	158.58	0.964
			1.0		50000000		0.041368	228.01	227.91	1.000

Model	Collision cases	Velocity, v (mm/s)	Striker mass, m (ton)	Structural volume, V_{str} (mm ³)	Kinetic energy, E_k (mJ)	Energy absorption, E_a (mJ)	$\square_E = E_k/E_a$	Dent depth, d (mm)		X_m (Num./Eq. (3.16))
								Num.	Eq. (3.16)	
RS-10	Case 1	2500	10	2332474523	31250000	127222524424	0.000246	36.93	33.73	1.095
			20		62500000		0.000491	54.45	55.18	0.987
			50		156250000		0.001228	101.94	105.75	0.964
	Case 2	5000	10		125000000		0.000983	79.15	90.26	0.877
			20		250000000		0.001965	143.42	147.65	0.971
			50		625000000		0.004913	286.11	282.98	1.011
	Case 3	7500	10		281250000		0.002211	146.35	160.53	0.912
			20		562500000		0.004421	258.88	262.59	0.986
			50		1406250000		0.011053	523.90	503.28	1.041
	Case 4	10000	10		500000000		0.003930	470.53	241.52	1.948
			20		1000000000		0.007860	393.68	395.08	0.996
			50		2500000000		0.019651	792.52	757.23	1.047

Table F.2.2 Comparison of prediction and parametric study result for permanent deflection of the stringer-stiffened cylinder under mass impact.

Model	Collision cases	Velocity, v (mm/s)	Striker mass, m (ton)	Structural volume, V_{str} (mm ³)	Kinetic energy, E_k (mJ)	Energy absorption, E_a (mJ)	$\lambda_E = E_k/E_a$	Dent depth, d (mm)		X_m (Num./Eq. (3.34))
								Num.	Eq.(3.34)	
SS-2	Case 1	2500	10	95306421226	31250000	5531023413830	0.000006	-	-	-
			20		62500000		0.000011	-	-	-
			50		156250000		0.000028	-	-	-
			100		312500000		0.000056	-	-	-
	Case 2	5000	10		125000000		0.000023	-	-	-
			20		250000000		0.000045	-	-	-
			50		625000000		0.000113	-	-	-
			100		1250000000		0.000226	112.60	117.39	0.96
	Case 3	7500	10		281250000		0.000051	44.15	42.57	1.04
			20		562500000		0.000102	65.89	68.20	0.97
			50		1406250000		0.000254	125.14	127.18	0.98
			100		2812500000		0.000508	213.19	203.75	1.05
	Case 4	10000	10		500000000		0.000090	65.23	62.95	1.04
			20		1000000000		0.000181	108.62	100.86	1.08
			50		2500000000		0.000452	198.45	188.07	1.06
			100		5000000000		0.000904	320.78	301.32	1.06
	Case 5	1000	1000		500000000		0.000090	61.23	62.95	0.97
			3000		1500000000		0.000271	143.17	132.88	1.08
			5000		2500000000		0.000452	203.12	188.07	1.08
	Case 6	2000	1000		2000000000		0.000362	176.05	161.59	1.09
			3000		6000000000		0.001085	379.93	341.09	1.11
			5000		10000000000		0.001808	525.20	482.75	1.09
	Case 7	3000	1000		4500000000		0.000814	301.25	280.48	1.07
			3000		13500000000		0.002441	558.98	592.04	0.94
			5000		22500000000		0.004068	866.69	837.93	1.03

Model	Collision cases	Velocity, v (mm/s)	Striker mass, m (ton)	Structural volume, V_{str} (mm ³)	Kinetic energy, E_k (mJ)	Energy absorption, E_a (mJ)	$\lambda_E = E_k/E_a$	Dent depth, d (mm)		X_m (Num./Eq. (3.34))
								Num.	Eq.(3.34)	
SS-3	Case 1	2500	10	7684526133	31250000	436829204444	0.00007	15.33	16.93	0.91
			20		62500000		0.00014	25.67	27.12	0.95
			50		156250000		0.00036	56.96	50.58	1.13
			100		312500000		0.00072	90.05	81.03	1.11
	Case 2	5000	10		125000000		0.00029	46.32	43.46	1.07
			20		250000000		0.00057	76.34	69.62	1.10
			50		625000000		0.00143	136.18	129.83	1.05
			100		1250000000		0.00286	201.19	208.00	0.97
	Case 3	7500	10		281250000		0.00064	81.16	75.43	1.08
			20		562500000		0.00129	126.53	120.85	1.05
			50		1406250000		0.00322	212.44	225.34	0.94
			100		2812500000		0.00644	356.23	361.03	0.99
	Case 4	10000	10		500000000		0.00114	116.65	111.55	1.05
			20		1000000000		0.00229	175.37	178.72	0.98
			50		2500000000		0.00572	284.47	333.24	0.85
			100		5000000000		0.01145	495.33	533.90	0.93
	Case 5	1000	1000		500000000		0.00114	121.35	111.55	1.09
			3000		1500000000		0.00343	223.72	235.45	0.95
			5000		2500000000		0.00572	293.67	333.24	0.88
	Case 6	2000	1000		2000000000		0.00458	259.07	286.33	0.90
			3000		6000000000		0.01374	569.91	604.37	0.94
			5000		10000000000		0.02289	865.64	855.39	1.01
	Case 7	3000	1000		4500000000		0.01030	487.73	496.99	0.98
			3000		13500000000		0.03090	999.68	1049.04	0.95
			5000		22500000000		0.05151	1362.0	1484.73	0.92

Model	Collision cases	Velocity, v (mm/s)	Striker mass, m (ton)	Structural volume, V_{str} (mm ³)	Kinetic energy, E_k (mJ)	Energy absorption, E_a (mJ)	$\lambda_E = E_k/E_a$	Dent depth, d (mm)		X_m (Num./Eq. (3.34))
								Num.	Eq.(3.34)	
SS-4	Case 1	2500	10	3230080656	31250000	221606454067	0.00014	22.69	19.34	1.17
			20		62500000		0.00028	36.63	30.99	1.18
			50		156250000		0.00071	58.85	57.79	1.02
			100		312500000		0.00141	108.87	92.59	1.18
	Case 2	5000	10		125000000		0.00056	55.30	49.65	1.11
			20		250000000		0.00113	82.00	79.55	1.03
			50		625000000		0.00282	169.65	148.34	1.14
			100		1250000000		0.00564	249.32	237.66	1.05
	Case 3	7500	10		281250000		0.00127	96.54	86.19	1.12
			20		562500000		0.00254	157.07	138.08	1.14
			50		1406250000		0.00635	261.93	257.48	1.02
			100		2812500000		0.01269	408.42	412.51	0.99
	Case 4	10000	10		500000000		0.00226	144.96	127.45	1.14
			20		1000000000		0.00451	212.05	204.20	1.04
			50		2500000000		0.01128	374.81	380.76	0.98
			100		5000000000		0.02256	565.05	610.04	0.93
	Case 5	1000	1000		500000000		0.00226	126.18	127.45	0.99
			3000		1500000000		0.00677	301.49	269.03	1.12
			5000		2500000000		0.01128	401.42	380.76	1.05
	Case 6	2000	1000		2000000000		0.00903	346.73	327.16	1.06
			3000		6000000000		0.02708	665.44	690.56	0.96
			5000		10000000000		0.04513	881.49	977.36	0.90
	Case 7	3000	1000		4500000000		0.02031	553.79	567.86	0.98
			3000		13500000000		0.06092	1126.68	1198.62	0.94
			5000		22500000000		0.10153	1510.21	1696.44	0.89

Model	Collision cases	Velocity, v (mm/s)	Striker mass, m (ton)	Structural volume, V_{str} (mm ³)	Kinetic energy, E_k (mJ)	Energy absorption, E_a (mJ)	$\lambda_E = E_k/E_a$	Dent depth, d (mm)		X_m (Num./Eq. (3.34))
								Num.	Eq.(3.34)	
SS-5	Case 1	2500	10	4168307142	31250000	225866807805	0.00014	16.98	15.78	1.08
			20		62500000		0.00028	29.02	25.28	1.15
			50		156250000		0.00069	47.83	47.15	1.01
			100		312500000		0.00138	76.05	75.53	1.01
	Case 2	5000	10		125000000		0.00055	36.94	40.51	0.91
			20		250000000		0.00111	69.59	64.90	1.07
			50		625000000		0.00277	132.70	121.02	1.10
			100		1250000000		0.00553	217.01	193.89	1.12
	Case 3	7500	10		281250000		0.00125	74.69	70.31	1.06
			20		562500000		0.00249	131.13	112.65	1.16
			50		1406250000		0.00623	230.12	210.05	1.10
			100		2812500000		0.01245	342.95	336.53	1.02
	Case 4	10000	10		500000000		0.00221	119.16	103.98	1.15
			20		1000000000		0.00443	186.89	166.59	1.12
			50		2500000000		0.01107	315.13	310.63	1.01
			100		5000000000		0.02214	486.90	497.68	0.98
	Case 5	1000	1000		500000000		0.00221	115.62	103.98	1.11
			3000		1500000000		0.00664	242.45	219.48	1.10
			5000		2500000000		0.01107	336.68	310.63	1.08
	Case 6	2000	1000		2000000000		0.00885	284.36	266.90	1.07
			3000		6000000000		0.02656	564.23	563.36	1.00
			5000		10000000000		0.04427	777.71	797.35	0.98
	Case 7	3000	1000		4500000000		0.01992	468.34	463.27	1.01
			3000		13500000000		0.05977	909.72	977.85	0.93
			5000		22500000000		0.09962	1239.6	1383.98	0.90

Model	Collision cases	Velocity, v (mm/s)	Striker mass, m (ton)	Structural volume, V_{str} (mm ³)	Kinetic energy, E_k (mJ)	Energy absorption, E_a (mJ)	$\lambda_E = E_k/E_a$	Dent depth, d (mm)		X_m (Num./Eq. (3.34))
								Num.	Eq.(3.34)	
SS-6	Case 1	2500	10	14762320468	31250000	814150671913	0.00004	-	-	-
			20		62500000		0.00008	-	-	-
			50		156250000		0.00019	72.41	70.03	1.03
			100		312500000		0.00038	124.02	112.19	1.11
	Case 2	5000	10		125000000		0.00015	57.71	60.17	0.96
			20		250000000		0.00031	102.98	96.40	1.07
			50		625000000		0.00077	191.11	179.75	1.06
			100		1250000000		0.00154	291.42	287.98	1.01
	Case 3	7500	10		281250000		0.00035	109.14	104.43	1.05
			20		562500000		0.00069	177.84	167.32	1.06
			50		1406250000		0.00173	308.49	311.99	0.99
			100		2812500000		0.00345	465.76	499.85	0.93
	Case 4	10000	10		500000000		0.00061	162.30	154.44	1.05
			20		1000000000		0.00123	250.64	247.43	1.01
			50		2500000000		0.00307	430.02	461.38	0.93
			100		5000000000		0.00614	690.62	739.20	0.93
	Case 5	1000	1000		500000000		0.00061	174.60	154.44	1.13
			3000		1500000000		0.00184	330.34	325.99	1.01
			5000		2500000000		0.00307	443.55	461.38	0.96
	Case 6	2000	1000		2000000000		0.00246	385.62	396.42	0.97
			3000		6000000000		0.00737	840.15	836.76	1.00
			5000		10000000000		0.01228	1104.0	1184.29	0.93
	Case 7	3000	1000		4500000000		0.00553	621.58	688.09	0.90
			3000		13500000000		0.01658	1495.7	1452.40	1.03
			5000		22500000000		0.02764	1991.71	2055.63	0.97

Model	Collision cases	Velocity, v (mm/s)	Striker mass, m (ton)	Structural volume, V_{str} (mm ³)	Kinetic energy, E_k (mJ)	Energy absorption, E_a (mJ)	$\lambda_E = E_k/E_a$	Dent depth, d (mm)		X_m (Num./Eq. (3.34))
								Num.	Eq.(3.34)	
SS-6	Case 1	2500	10	14762320468	31250000	814150671913	0.00004	-	-	-
			20		62500000		0.00008	-	-	-
			50		156250000		0.00019	72.41	70.03	1.03
			100		312500000		0.00038	124.02	112.19	1.11
	Case 2	5000	10		125000000		0.00015	57.71	60.17	0.96
			20		250000000		0.00031	102.98	96.40	1.07
			50		625000000		0.00077	191.11	179.75	1.06
			100		1250000000		0.00154	291.42	287.98	1.01
	Case 3	7500	10		281250000		0.00035	109.14	104.43	1.05
			20		562500000		0.00069	177.84	167.32	1.06
			50		1406250000		0.00173	308.49	311.99	0.99
			100		2812500000		0.00345	465.76	499.85	0.93
	Case 4	10000	10		500000000		0.00061	162.30	154.44	1.05
			20		1000000000		0.00123	250.64	247.43	1.01
			50		2500000000		0.00307	430.02	461.38	0.93
			100		5000000000		0.00614	690.62	739.20	0.93
	Case 5	1000	1000		500000000		0.00061	174.60	154.44	1.13
			3000		1500000000		0.00184	330.34	325.99	1.01
			5000		2500000000		0.00307	443.55	461.38	0.96
	Case 6	2000	1000		2000000000		0.00246	385.62	396.42	0.97
			3000		6000000000		0.00737	840.15	836.76	1.00
			5000		10000000000		0.01228	1104.00	1184.29	0.93
	Case 7	3000	1000		4500000000		0.00553	621.58	688.09	0.90
			3000		13500000000		0.01658	1495.79	1452.40	1.03
			5000		22500000000		0.02764	1991.71	2055.63	0.97

F.3 Residual strength of damaged ring- or stringer-stiffened cylinder under hydrostatic pressure

Table F3. 1 Comparison of the proposed formulation results with numerical results for residual strength of damaged ring-stiffened cylinder under external hydrostatic pressure.

Model	Collision cases	Velocity, v (mm/s)	Striker mass, m (ton)	$\delta_d = d/R$	P_{intact} (Mpa)	P_{damage} (Mpa)	$R_u = P_{dam}/P_{in.}$		X_m (Num./Eq. (6.10))	
							Num. result	Eq.(6.10)		
RS-1	Case 1	2500	10	-	6.591	-	-	-	-	
			20	-		-	-	-	-	
			50	-		-	-	-	-	
	Case 2	5000	10	-		-	-	-	-	-
			20	0.01194		7.20	1.092	0.965	1.132	
			50	0.02248		6.65	1.009	0.929	1.086	
	Case 3	7500	10	0.01266		7.15	1.085	0.963	1.127	
			20	0.02022		5.98	0.907	0.937	0.967	
			50	0.03742		4.82	0.731	0.877	0.833	
	Case 4	10000	10	0.01838		6.19	0.940	0.943	0.996	
			20	0.03073		5.29	0.803	0.901	0.891	
			50	0.06205		4.93	0.749	0.792	0.945	

Model	Collision cases	Velocity, v (mm/s)	Striker mass, m (ton)	$\delta_d = d/R$	P_{intact} (Mpa)	P_{damage} (Mpa)	$R_u = P_{dam}/P_{in.}$		X_m (Num./Eq. (6.10))	
							Num. result	Eq.(6.10)		
RS-2	Case 1	2500	10	-	2.190	-	-	-	-	
			20	-		-	-	-	-	
			50	-		-	-	-	-	
	Case 2	5000	10	-		-	-	-	-	-
			20	-		-	-	-	-	-
			50	0.02595		1.86	0.850	0.917	0.926	
	Case 3	7500	10	0.01499		1.93	0.880	0.955	0.921	
			20	0.02502		2.00	0.912	0.921	0.991	
			50	0.05168		2.02	0.922	0.828	1.114	
	Case 4	10000	10	0.02268		1.88	0.858	0.929	0.924	
			20	0.03814		1.83	0.834	0.875	0.953	
			50	0.07797		1.61	0.735	0.739	0.995	

Model	Collision cases	Velocity, v (mm/s)	Striker mass, m (ton)	$\delta_d = d/R$	P_{intact} (Mpa)	P_{damage} (Mpa)	$R_u = P_{dam}/P_{in.}$		X_m (Num./Eq. (6.10))
							Num. result	Eq.(6.10)	
RS-3	Case 1	2500	10	-	1.503	-	-	-	-
			20	-		-	-	-	-
			50	0.01545		1.44	0.960	0.953	1.007
	Case 2	5000	10	0.01090		1.57	1.047	0.968	1.081
			20	0.02114		1.28	0.851	0.934	0.911
			50	0.04273		1.19	0.790	0.859	0.920
	Case 3	7500	10	0.02457		1.17	0.777	0.922	0.843
			20	0.04272		1.13	0.752	0.859	0.876
			50	0.07258		1.17	0.777	0.757	1.026
	Case 4	10000	10	0.03962		1.23	0.818	0.870	0.941
			20	0.05964		1.22	0.813	0.800	1.016
			50	0.11036		0.92	0.610	0.638	0.956

Model	Collision cases	Velocity, v (mm/s)	Striker mass, m (ton)	$\delta_d = d/R$	P_{intact} (Mpa)	P_{damage} (Mpa)	$R_u = P_{dam}/P_{in.}$		X_m (Num./Eq. (6.10))
							Num. result	Eq.(6.10)	
RS-4	Case 1	2500	10	0.00345	4.331	-	-	-	-
			20	0.00572		-	-	-	-
			50	0.01109		-	-	-	-
	Case 2	5000	10	0.00703		4.12	0.951	0.981	0.970
			20	0.01549		4.26	0.983	0.953	1.032
			50	0.03543		3.82	0.882	0.884	0.997
	Case 3	7500	10	0.01682		4.18	0.966	0.949	1.018
			20	0.03057		3.77	0.871	0.901	0.966
			50	0.06347		3.14	0.725	0.787	0.920
	Case 4	10000	10	0.02771		3.81	0.880	0.911	0.965
			20	0.04599		3.11	0.718	0.847	0.848
			50	0.09813		2.66	0.615	0.675	0.911

Model	Collision cases	Velocity, v (mm/s)	Striker mass, m (ton)	$\delta_d = d/R$	P_{intact} (Mpa)	P_{damage} (Mpa)	$R_u = P_{dam}/P_{in.}$		X_m (Num./Eq. (6.10))
							Num. result	Eq.(6.10)	
RS-5	Case 1	2500	10	0.00316	5.894	5.56	0.943	0.992	0.950
			20	0.00440		5.97	1.012	0.989	1.024
			50	0.00954		5.76	0.977	0.973	1.004
	Case 2	5000	10	0.00609		5.30	0.899	0.984	0.914
			20	0.01130		5.95	1.009	0.967	1.043
			50	0.02490		5.63	0.956	0.921	1.037
	Case 3	7500	10	0.01160		5.16	0.876	0.966	0.907
			20	0.02053		5.83	0.989	0.936	1.057
			50	0.04423		5.30	0.900	0.854	1.054
	Case 4	10000	10	0.01755		5.05	0.857	0.946	0.906
			20	0.03138		5.19	0.880	0.898	0.980
			50	0.06766		4.63	0.786	0.773	1.016

Model	Collision cases	Velocity, v (mm/s)	Striker mass, m (ton)	$\delta_d = d/R$	P_{intact} (Mpa)	P_{damage} (Mpa)	$R_u = P_{dam}/P_{in.}$		X_m (Num./Eq. (6.10))	
							Num. result	Eq.(6.10)		
RS-6	Case 1	2500	10	-	2.888	-	-	-	-	
			20	-		-	-	-	-	
			50	-		-	-	-	-	
	Case 2	5000	10	-		-	-	-	-	-
			20	0.00645		3.25	1.126	0.983	1.146	
			50	0.01239		2.44	0.845	0.964	0.877	
	Case 3	7500	10	0.00742		2.86	0.989	0.980	1.010	
			20	0.01141		2.63	0.909	0.967	0.940	
			50	0.02118		2.28	0.790	0.934	0.845	
	Case 4	10000	10	0.01100		2.30	0.795	0.968	0.821	
			20	0.01638		2.57	0.891	0.950	0.937	
			50	0.03175		2.23	0.773	0.897	0.861	

Model	Collision cases	Velocity, v (mm/s)	Striker mass, m (ton)	$\delta_d = d/R$	P_{intact} (Mpa)	P_{damage} (Mpa)	$R_u = P_{dam}/P_{in.}$		X_m (Num./Eq. (6.10))
							Num. result	Eq.(6.10)	
RS-7	Case 1	2500	10	0.00894	1.702	-	-	-	-
			20	0.01250		-	-	-	-
			50	0.02910		-	-	-	-
	Case 2	5000	10	0.02170		1.55	0.910	0.932	0.976
			20	0.03702		1.43	0.840	0.879	0.956
			50	0.06259		1.29	0.756	0.790	0.956
	Case 3	7500	10	0.03825		1.45	0.852	0.874	0.974
			20	0.05882		1.28	0.752	0.803	0.936
			50	0.10424		1.11	0.652	0.657	0.993
	Case 4	10000	10	0.05254		1.25	0.734	0.825	0.891
			20	0.08363		1.17	0.686	0.721	0.951
			50	0.15374		0.81	0.477	0.519	0.919

Model	Collision cases	Velocity, v (mm/s)	Striker mass, m (ton)	$\delta_d = d/R$	P_{intact} (Mpa)	P_{damage} (Mpa)	$R_u = P_{dam}/P_{in.}$		X_m (Num./Eq. (6.10))
							Num. result	Eq.(6.10)	
RS-8	Case 1	2500	10	0.00602	1.910	2.07	1.082	0.984	1.100
			20	0.00904		1.92	1.005	0.974	1.032
			50	0.01665		1.76	0.919	0.949	0.968
	Case 2	5000	10	0.01444		1.82	0.953	0.957	0.996
			20	0.02070		1.64	0.860	0.936	0.920
			50	0.03693		1.58	0.826	0.879	0.940
	Case 3	7500	10	0.02099		1.50	0.783	0.935	0.838
			20	0.03279		1.45	0.761	0.894	0.852
			50	0.06526		1.27	0.666	0.781	0.852
	Case 4	10000	10	0.02853		1.43	0.751	0.908	0.827
			20	0.04890		1.33	0.696	0.837	0.832
			50	0.09986		1.19	0.624	0.670	0.931

Model	Collision cases	Velocity, v (mm/s)	Striker mass, m (ton)	$\delta_d = d/R$	P_{intact} (Mpa)	P_{damage} (Mpa)	$R_u = P_{dam}/P_{in.}$		X_m (Num./Eq. (6.10))
							Num. result	Eq.(6.10)	
RS-9	Case 1	2500	0.3	0.02427	2.430	2.20	0.905	0.923	0.981
			0.6	0.03721		2.04	0.838	0.878	0.954
			1.0	0.05282		1.81	0.746	0.824	0.905
	Case 2	5000	0.3	0.05728		1.75	0.719	0.808	0.889
			0.6	0.09747		1.68	0.689	0.677	1.018
			1.0	0.14568		1.37	0.562	0.540	1.041
	Case 3	7500	0.3	0.10422		1.33	0.547	0.657	0.833
			0.6	0.18017		0.95	0.390	0.456	0.855
			1.0	0.26847		0.70	0.289	0.290	0.995
	Case 4	10000	0.3	0.16131		1.11	0.457	0.500	0.914
			0.6	0.27788		0.69	0.284	0.276	1.027
			1.0	0.41456		0.35	0.144	0.131	1.095

Model	Collision cases	Velocity, v (mm/s)	Striker mass, m (ton)	$\delta_d = d/R$	P_{intact} (Mpa)	P_{damage} (Mpa)	$R_u = P_{dam}/P_{in.}$		X_m (Num./Eq. (6.10))
							Num. result	Eq.(6.10)	
RS-10	Case 1	2500	0.3	0.01191	1.451	1.28	0.884	0.965	0.916
			0.6	0.01756		1.30	0.897	0.946	0.948
			1.0	0.03288		1.27	0.874	0.893	0.979
	Case 2	5000	0.3	0.02553		1.28	0.884	0.919	0.963
			0.6	0.04627		1.23	0.851	0.846	1.005
			1.0	0.09229		0.89	0.614	0.693	0.886
	Case 3	7500	0.3	0.04721		1.23	0.848	0.843	1.006
			0.6	0.08351		0.97	0.671	0.721	0.930
			1.0	0.16900		0.76	0.523	0.482	1.086
	Case 4	10000	0.3	0.15178		0.82	0.566	0.524	1.080
			0.6	0.12699		0.78	0.541	0.590	0.916
			1.0	0.25565		0.44	0.306	0.310	0.987

Table F3. 2 Comparison of the proposed formulation results with numerical results for residual strength of damaged stringer-stiffened cylinder under external hydrostatic pressure.

Model	Collision cases	Velocity, v (mm/s)	Striker mass, m (ton)	$\delta_d = d/R$	P_{intact} (Mpa)	P_{damage} (Mpa)	$R_u = P_{dam.}/ P_{in.}$		X_m (Num./Eq. (6.24))
							Num. result	Eq.(6.24)	
SS-1	Case 1	2500	10	-	1.188	-	-	-	-
			20	0.01752		1.01	0.852	0.969	0.879
			50	0.03712		1.03	0.870	0.936	0.930
			100	0.05949		1.04	0.877	0.899	0.976
	Case 2	5000	10	0.03040		1.00	0.843	0.947	0.891
			20	0.05046		1.06	0.888	0.913	0.973
			50	0.08799		1.10	0.922	0.854	1.080
			100	0.12947		0.98	0.829	0.793	1.046
	Case 3	7500	10	0.05399		1.08	0.911	0.908	1.004
			20	0.08233		1.11	0.932	0.863	1.081
			50	0.13757		0.95	0.801	0.781	1.025
			100	0.20580		0.66	0.559	0.691	0.809
	Case 4	10000	10	0.07630		1.12	0.942	0.872	1.080
			20	0.11331		1.05	0.887	0.816	1.087
			50	0.19030		0.79	0.665	0.711	0.936
			100	0.291912		0.64	0.535	0.592	0.904

Model	Collision cases	Velocity, v (mm/s)	Striker mass, m (ton)	$\delta_d = d/R$	P_{intact} (Mpa)	P_{damage} (Mpa)	$R_u = P_{dam.} / P_{in.}$		X_m (Num./Eq. (6.24))	
							Num. result	Eq.(6.24)		
SS-2	Case 1	2500	10	-	0.729	-	-	-	-	
			20	-		-	-	-	-	
			50	-		-	-	-	-	
			100	-		-	-	-	-	
	Case 2	5000	10	-		-	-	-	-	-
			20	-		-	-	-	-	
			50	-		-	-	-	-	
			100	0.00845		0.70	0.954	0.985	0.968	
	Case 3	7500	10	0.00331		0.69	0.943	0.994	0.948	
			20	0.00495		0.66	0.904	0.991	0.912	
			50	0.00940		0.63	0.861	0.983	0.875	
			100	0.01601		0.69	0.949	0.972	0.977	
	Case 4	10000	10	0.00490		0.68	0.932	0.991	0.940	
			20	0.00815		0.66	0.905	0.985	0.918	
			50	0.01490		0.65	0.891	0.974	0.915	
			100	0.024083		0.63	0.868	0.958	0.907	
	Case 5	1000	1000	0.004597		0.62	0.847	0.992	0.855	
			3000	0.010749		0.60	0.827	0.981	0.843	
			5000	0.015249		0.59	0.806	0.973	0.829	
	Case 6	2000	1000	0.013217		0.67	0.923	0.977	0.945	
			3000	0.028523		0.66	0.902	0.950	0.950	
			5000	0.039429		0.58	0.799	0.932	0.858	
	Case 7	3000	1000	0.022616		0.60	0.820	0.960	0.854	
			3000	0.041965		0.58	0.799	0.927	0.862	
			5000	0.065067		0.60	0.820	0.890	0.921	

Model	Collision cases	Velocity, v (mm/s)	Striker mass, m (ton)	$\delta_d = d/R$	P_{intact} (Mpa)	P_{damage} (Mpa)	$R_u = P_{dam}/P_{in.}$		X_m (Num./Eq. (6.24))
							Num. result	Eq.(6.24)	
SS-3	Case 1	2500	10	0.00365	0.845	-	-	-	-
			20	0.00611		0.78	0.927	0.989	0.937
			50	0.01356		0.78	0.928	0.976	0.951
			100	0.02144		0.81	0.955	0.962	0.993
	Case 2	5000	10	0.01103		0.77	0.915	0.980	0.934
			20	0.01818		0.79	0.933	0.968	0.964
			50	0.03242		0.81	0.956	0.943	1.014
			100	0.04790		0.79	0.938	0.918	1.023
	Case 3	7500	10	0.01932		0.81	0.954	0.966	0.987
			20	0.03013		0.81	0.956	0.947	1.010
			50	0.05058		0.78	0.929	0.913	1.017
			100	0.08482		0.71	0.838	0.859	0.976
	Case 4	10000	10	0.02777		0.81	0.963	0.951	1.012
			20	0.04176		0.81	0.962	0.928	1.037
			50	0.06773		0.74	0.870	0.885	0.983
			100	0.117935		0.55	0.648	0.809	0.801
	Case 5	1000	1000	0.028893		0.82	0.969	0.949	1.021
			3000	0.053267		0.78	0.924	0.909	1.016
			5000	0.069922		0.73	0.862	0.882	0.977
	Case 6	2000	1000	0.061684		0.77	0.916	0.895	1.023
			3000	0.135694		0.56	0.665	0.784	0.849
			5000	0.206106		0.54	0.633	0.691	0.917
	Case 7	3000	1000	0.116126		0.61	0.725	0.812	0.894
			3000	0.238019		0.57	0.671	0.652	1.029
			5000	0.324286		0.52	0.613	0.559	1.097

Model	Collision cases	Velocity, v (mm/s)	Striker mass, m (ton)	$\delta_d = d/R$	P_{intact} (Mpa)	P_{damage} (Mpa)	$R_u = P_{dam}/P_{in.}$		X_m (Num./Eq. (6.24))
							Num. result	Eq.(6.24)	
SS-4	Case 1	2500	10	0.00750	0.425	-	-	-	-
			20	0.01211		0.41	0.958	0.978	0.979
			50	0.01945		0.39	0.926	0.966	0.959
			100	0.03599		0.39	0.907	0.937	0.968
	Case 2	5000	10	0.01828		0.38	0.905	0.968	0.936
			20	0.02711		0.41	0.965	0.952	1.013
			50	0.05608		0.39	0.911	0.904	1.008
			100	0.08242		0.36	0.846	0.862	0.981
	Case 3	7500	10	0.03191		0.38	0.904	0.944	0.958
			20	0.05192		0.36	0.853	0.911	0.937
			50	0.08659		0.29	0.688	0.856	0.803
			100	0.13501		0.27	0.644	0.785	0.821
	Case 4	10000	10	0.04792		0.38	0.904	0.918	0.986
			20	0.07010		0.36	0.853	0.882	0.968
			50	0.12391		0.29	0.688	0.800	0.859
			100	0.186792		0.22	0.527	0.715	0.736
	Case 5	1000	1000	0.041711		0.38	0.900	0.928	0.971
			3000	0.099667		0.35	0.816	0.836	0.977
			5000	0.132702		0.34	0.800	0.788	1.015
	Case 6	2000	1000	0.114623		0.36	0.852	0.814	1.047
			3000	0.219979		0.30	0.715	0.674	1.061
			5000	0.291403		0.27	0.635	0.593	1.072
	Case 7	3000	1000	0.183072		0.25	0.593	0.720	0.824
			3000	0.372455		0.24	0.555	0.512	1.084
			5000	0.499244		0.20	0.471	0.408	1.154

Model	Collision cases	Velocity, v (mm/s)	Striker mass, m (ton)	$\delta_d = d/R$	P_{intact} (Mpa)	P_{damage} (Mpa)	$R_u = P_{dam}/P_{in.}$		X_m (Num./Eq. (6.24))
							Num. result	Eq.(6.24)	
SS-5	Case 1	2500	10	0.00679	1.142	-	-	-	-
			20	0.01161		-	-	-	-
			50	0.01913		1.05	0.923	0.966	0.955
			100	0.03042		1.13	0.989	0.947	1.045
	Case 2	5000	10	0.01478		1.06	0.931	0.974	0.956
			20	0.02783		0.97	0.849	0.951	0.893
			50	0.05308		0.96	0.839	0.909	0.923
			100	0.08680		0.87	0.762	0.856	0.890
	Case 3	7500	10	0.02988		0.94	0.823	0.948	0.868
			20	0.05245		0.92	0.807	0.910	0.886
			50	0.09205		0.88	0.774	0.848	0.913
			100	0.13718		0.87	0.758	0.782	0.970
	Case 4	10000	10	0.04766		0.87	0.758	0.918	0.826
			20	0.07475		0.87	0.761	0.874	0.871
			50	0.12605		0.85	0.743	0.797	0.932
			100	0.194759		0.82	0.721	0.705	1.023
	Case 5	1000	1000	0.04625		0.97	0.848	0.920	0.921
			3000	0.096979		0.95	0.832	0.840	0.990
			5000	0.134671		0.86	0.753	0.785	0.959
	Case 6	2000	1000	0.113745		0.93	0.814	0.815	0.999
			3000	0.225694		0.85	0.744	0.667	1.116
			5000	0.311084		0.71	0.623	0.572	1.090
	Case 7	3000	1000	0.187335		0.75	0.657	0.714	0.919
			3000	0.363888		0.65	0.569	0.520	1.094
			5000	0.495842		0.49	0.429	0.410	1.045

Model	Collision cases	Velocity, v (mm/s)	Striker mass, m (ton)	$\delta_d = d/R$	P_{intact} (Mpa)	P_{damage} (Mpa)	$R_u = P_{dam.}/P_{in.}$		X_m (Num./Eq. (6.24))
							Num. result	Eq.(6.24)	
SS-6	Case 1	2500	10	-	0.902	-	-	-	-
			20	-		-	-	-	-
			50	0.00815		-	-	-	-
			100	0.01397		-	-	-	-
	Case 2	5000	10	0.00650		-	-	-	-
			20	0.01160		0.95	1.054	0.979	1.076
			50	0.02152		0.83	0.918	0.962	0.954
			100	0.03282		0.82	0.911	0.943	0.967
	Case 3	7500	10	0.01229		0.86	0.956	0.978	0.977
			20	0.02003		0.83	0.920	0.965	0.954
			50	0.03474		0.83	0.916	0.940	0.975
			100	0.05245		0.79	0.876	0.910	0.962
	Case 4	10000	10	0.01828		0.81	0.898	0.968	0.928
			20	0.02823		0.75	0.831	0.951	0.875
			50	0.04843		0.74	0.820	0.917	0.895
			100	0.077773		0.69	0.765	0.870	0.880
	Case 5	1000	1000	0.019662		0.88	0.976	0.965	1.011
			3000	0.0372		0.84	0.931	0.935	0.996
			5000	0.049949		0.75	0.831	0.914	0.910
	Case 6	2000	1000	0.043426		0.82	0.909	0.925	0.983
			3000	0.094612		0.76	0.843	0.844	0.999
			5000	0.124324		0.69	0.765	0.800	0.956
	Case 7	3000	1000	0.069998		0.65	0.721	0.882	0.817
			3000	0.168444		0.61	0.676	0.739	0.915
			5000	0.224292		0.52	0.576	0.668	0.862

F.4 Residual strength of damaged ring- or stringer-stiffened cylinder under combined axial compression and radial pressure

Table F4.1 Comparison of the proposed formulation results with numerical results for residual strength of damaged ring-stiffened cylinder under combined axial compression and radial pressure.

Model	Collision cases	Velocity, v (mm/s)	Striker mass, m (ton)	$\delta_d = d/R$	$0.2P_{c_damage}$ (Mpa)	$\sigma_{xin,r}$ (Mpa)	$\sigma_{xd,r}$ (Mpa)	$R_{ux,r} = \sigma_{xd,r} / \sigma_{xin,r}$		X_m (Num./Eq. (7.12))	
								Num. result	Eq.(7.12)		
RS-1	Case 1	2500	10	-	-	651.2	-	-	-	-	
			20	-	-		-	-	-	-	
			50	-	-		-	-	-	-	
	Case 2	5000	10	-	-		-	-	-	-	-
			20	0.01194	1.44		604.80	0.929	0.943	0.985	
			50	0.02248	1.33		560.50	0.861	0.895	0.962	
	Case 3	7500	10	0.01266	1.25		592.50	0.910	0.939	0.969	
			20	0.02022	1.20		561.20	0.862	0.905	0.952	
			50	0.03742	0.76		558.60	0.858	0.831	1.032	
	Case 4	10000	10	0.01838	1.24		554.20	0.851	0.913	0.932	
			20	0.03073	1.06		541.30	0.831	0.859	0.968	
			50	0.06205	0.75		500.50	0.769	0.736	1.045	

Model	Collision cases	Velocity, v (mm/s)	Striker mass, m (ton)	$\delta_d = d/R$	$0.5P_{c_damage}$ (Mpa)	$\sigma_{xin,r}$ (Mpa)	$\sigma_{xd,r}$ (Mpa)	$R_{ux,r} = \sigma_{xd,r} / \sigma_{xin,r}$		X_m (Num./Eq. (7.12))	
								Num. result	Eq.(7.12)		
RS-1	Case 1	2500	10	-	-	651.2	-	-	-	-	
			20	-	-		-	-	-	-	
			50	-	-		-	-	-	-	
	Case 2	5000	10	-	-		-	-	-	-	-
			20	0.01194	3.60		603.30	0.926	0.943	0.983	
			50	0.02248	3.33		566.00	0.869	0.895	0.971	
	Case 3	7500	10	0.01266	3.13		593.40	0.911	0.939	0.970	
			20	0.02022	2.99		565.70	0.869	0.905	0.960	
			50	0.03742	1.91		547.30	0.840	0.831	1.011	
	Case 4	10000	10	0.01838	3.10		564.30	0.867	0.913	0.949	
			20	0.03073	2.65		520.35	0.799	0.859	0.930	
			50	0.06205	1.87		495.80	0.761	0.736	1.035	

Model	Collision cases	Velocity, v (mm/s)	Striker mass, m (ton)	$\delta_d = d/R$	$0.2P_{c_damage}$ (Mpa)	$\sigma_{xin,r}$ (Mpa)	$\sigma_{xd,r}$ (Mpa)	$R_{ux,r} = \sigma_{xd,r} / \sigma_{xin,r}$		X_m (Num./Eq. (7.12))
								Num. result	Eq.(7.12)	
RS-2	Case 1	2500	10	-		633.0	-	-	-	-
			20	-			-	-	-	-
			50	-			-	-	-	-
	Case 2	5000	10	-			-	-	-	-
			20	-			-	-	-	-
			50	0.02595	0.22		597.26	0.944	0.879	1.073
	Case 3	7500	10	0.01499	0.24		608.92	0.962	0.928	1.036
			20	0.02502	0.23		585.45	0.925	0.884	1.047
			50	0.05168	0.22		535.48	0.846	0.774	1.093
	Case 4	10000	10	0.02268	0.21		599.33	0.947	0.894	1.059
			20	0.03814	0.21		537.71	0.849	0.828	1.026
			50	0.07797	0.25		472.13	0.746	0.680	1.097

Model	Collision cases	Velocity, v (mm/s)	Striker mass, m (ton)	$\delta_d = d/R$	$0.5P_{c_damage}$ (Mpa)	$\sigma_{xin,r}$ (Mpa)	$\sigma_{xd,r}$ (Mpa)	$R_{ux,r} = \sigma_{xd,r} / \sigma_{xin,r}$		X_m (Num./Eq. (7.12))
								Num. result	Eq.(7.12)	
RS-2	Case 1	2500	10	-		633.0	-	-	-	-
			20	-			-	-	-	-
			50	-			-	-	-	-
	Case 2	5000	10	-			-	-	-	-
			20	-			-	-	-	-
			50	0.02595	0.55		602.31	0.952	0.879	1.082
	Case 3	7500	10	0.01499	0.61		608.17	0.961	0.928	1.035
			20	0.02502	0.58		593.75	0.938	0.884	1.062
			50	0.05168	0.56		588.67	0.930	0.774	1.201
	Case 4	10000	10	0.02268	0.52		596.91	0.943	0.894	1.055
			20	0.03814	0.52		533.38	0.843	0.828	1.018
			50	0.07797	0.62		459.36	0.726	0.680	1.067

Model	Collision cases	Velocity, v (mm/s)	Striker mass, m (ton)	$\delta_d = d/R$	$0.2P_{c,damage}$ (Mpa)	$\sigma_{xin,r}$ (Mpa)	$\sigma_{xd,r}$ (Mpa)	$R_{ux,r} = \sigma_{xd,r} / \sigma_{xin,r}$		X_m (Num./Eq. (7.12))
								Num. result	Eq.(7.12)	
RS-3	Case 1	2500	10	-		520.2	-	-	-	-
			20	-			-	-	-	-
			50	-			-	-	-	-
	Case 2	5000	10	0.01090	0.26		468.94	0.901	0.947	0.951
			20	0.02114	0.21		466.14	0.896	0.901	0.995
			50	0.04273	0.11		460.22	0.885	0.809	1.093
	Case 3	7500	10	0.02457	0.18		473.72	0.911	0.885	1.028
			20	0.04272	0.14		473.77	0.911	0.809	1.125
			50	0.07258	0.07		399.05	0.767	0.698	1.099
	Case 4	10000	10	0.03962	0.14		469.56	0.903	0.822	1.098
			20	0.05964	0.10		443.10	0.852	0.744	1.144
			50	0.11036	0.11		335.65	0.645	0.579	1.114

Model	Collision cases	Velocity, v (mm/s)	Striker mass, m (ton)	$\delta_d = d/R$	$0.5P_{c,damage}$ (Mpa)	$\sigma_{xin,r}$ (Mpa)	$\sigma_{xd,r}$ (Mpa)	$R_{ux,r} = \sigma_{xd,r} / \sigma_{xin,r}$		X_m (Num./Eq. (7.12))
								Num. result	Eq.(7.12)	
RS-3	Case 1	2500	10	-		520.2	-	-	-	-
			20	-			-	-	-	-
			50	-			-	-	-	-
	Case 2	5000	10	0.01090	0.66		466.14	0.896	0.947	0.946
			20	0.02114	0.53		466.93	0.898	0.901	0.997
			50	0.04273	0.29		468.45	0.901	0.809	1.113
	Case 3	7500	10	0.02457	0.44		468.79	0.901	0.885	1.018
			20	0.04272	0.35		459.05	0.882	0.809	1.090
			50	0.07258	0.19		422.84	0.813	0.698	1.164
	Case 4	10000	10	0.03962	0.34		461.92	0.888	0.822	1.080
			20	0.05964	0.26		428.10	0.823	0.744	1.106
			50	0.11036	0.26		321.56	0.618	0.579	1.067

Model	Collision cases	Velocity, v (mm/s)	Striker mass, m (ton)	$\delta_d = d/R$	$0.2P_{c_damage}$ (Mpa)	$\sigma_{xin,r}$ (Mpa)	$\sigma_{xd,r}$ (Mpa)	$R_{ux,r} = \sigma_{xd,r} / \sigma_{xin,r}$		X_m (Num./Eq. (7.12))
								Num. result	Eq.(7.12)	
RS-4	Case 1	2500	10	0.00345	-	611.0	-	-	-	-
			20	0.00572	-		-	-	-	-
			50	0.01109	-		-	-	-	-
	Case 2	5000	10	0.00703	0.89		589.36	0.965	0.966	0.999
			20	0.01549	0.85		551.10	0.902	0.926	0.974
			50	0.03543	0.78		492.21	0.806	0.839	0.960
	Case 3	7500	10	0.01682	0.84		541.50	0.886	0.920	0.963
			20	0.03057	0.75		479.00	0.784	0.860	0.912
			50	0.06347	0.63		435.86	0.713	0.730	0.977
	Case 4	10000	10	0.02771	0.76		478.23	0.783	0.872	0.898
			20	0.04599	0.62		511.10	0.836	0.796	1.050
			50	0.09813	0.53		405.20	0.663	0.615	1.078

Model	Collision cases	Velocity, v (mm/s)	Striker mass, m (ton)	$\delta_d = d/R$	$0.5P_{c_damage}$ (Mpa)	$\sigma_{xin,r}$ (Mpa)	$\sigma_{xd,r}$ (Mpa)	$R_{ux,r} = \sigma_{xd,r} / \sigma_{xin,r}$		X_m (Num./Eq. (7.12))
								Num. result	Eq.(7.12)	
RS-4	Case 1	2500	10	0.00345	-	611.0	-	-	-	-
			20	0.00572	-		-	-	-	-
			50	0.01109	-		-	-	-	-
	Case 2	5000	10	0.00703	2.23		572.35	0.937	0.966	0.970
			20	0.01549	2.13		501.30	0.820	0.926	0.886
			50	0.03543	1.95		485.13	0.794	0.839	0.946
	Case 3	7500	10	0.01682	2.09		511.26	0.837	0.920	0.909
			20	0.03057	1.89		471.15	0.771	0.860	0.897
			50	0.06347	1.57		441.30	0.722	0.730	0.989
	Case 4	10000	10	0.02771	1.90		446.82	0.731	0.872	0.839
			20	0.04599	1.56		421.19	0.689	0.796	0.866
			50	0.09813	1.33		412.20	0.675	0.615	1.097

Model	Collision cases	Velocity, v (mm/s)	Striker mass, m (ton)	$\delta_d = d/R$	$0.2P_{c_damage}$ (Mpa)	$\sigma_{xin,r}$ (Mpa)	$\sigma_{xd,r}$ (Mpa)	$R_{ux,r} = \sigma_{xd,r} / \sigma_{xin,r}$		X_m (Num./Eq. (7.12))
								Num. result	Eq.(7.12)	
RS-5	Case 1	2500	10	0.00316	-	806.97	-	-	-	-
			20	0.00440	-		-	-	-	-
			50	0.00954	-		-	-	-	-
	Case 2	5000	10	0.00609	1.21		795.64	0.986	0.970	1.016
			20	0.01130	1.08		710.90	0.881	0.946	0.932
			50	0.02490	1.05		675.49	0.837	0.884	0.947
	Case 3	7500	10	0.01160	0.94		711.12	0.881	0.944	0.933
			20	0.02053	1.06		648.80	0.804	0.903	0.890
			50	0.04423	0.95		613.21	0.760	0.803	0.946
	Case 4	10000	10	0.01755	0.92		669.70	0.830	0.917	0.905
			20	0.03138	0.94		603.80	0.748	0.856	0.874
			50	0.06766	0.89		565.87	0.701	0.715	0.980

Model	Collision cases	Velocity, v (mm/s)	Striker mass, m (ton)	$\delta_d = d/R$	$0.2P_{c_damage}$ (Mpa)	$\sigma_{xin,r}$ (Mpa)	$\sigma_{xd,r}$ (Mpa)	$R_{ux,r} = \sigma_{xd,r} / \sigma_{xin,r}$		X_m (Num./Eq. (7.12))
								Num. result	Eq.(7.12)	
RS-5	Case 1	2500	10	0.00316	-	806.97	-	-	-	-
			20	0.00440	-		-	-	-	-
			50	0.00954	-		-	-	-	-
	Case 2	5000	10	0.00609	3.03		744.13	0.922	0.970	0.950
			20	0.01130	2.70		709.60	0.879	0.946	0.930
			50	0.02490	2.63		659.31	0.817	0.884	0.924
	Case 3	7500	10	0.01160	2.35		709.00	0.879	0.944	0.931
			20	0.02053	2.65		648.60	0.804	0.903	0.890
			50	0.04423	2.38		622.15	0.771	0.803	0.960
	Case 4	10000	10	0.01755	2.30		665.30	0.824	0.917	0.899
			20	0.03138	2.36		618.56	0.767	0.856	0.895
			50	0.06766	2.23		558.73	0.692	0.715	0.968

Model	Collision cases	Velocity, v (mm/s)	Striker mass, m (ton)	$\delta_d = d/R$	$0.2P_{c_damage}$ (Mpa)	$\sigma_{xin,r}$ (Mpa)	$\sigma_{xd,r}$ (Mpa)	$R_{ux,r} = \sigma_{xd,r} / \sigma_{xin,r}$		X_m (Num./Eq. (7.12))
								Num. result	Eq.(7.12)	
RS-6	Case 1	2500	10	-		550.0	-	-	-	-
			20	-			-	-	-	-
			50	-			-	-	-	-
	Case 2	5000	10	-			-	-	-	-
			20	0.00645	0.93		512.80	0.932	0.969	0.963
			50	0.01239	0.70		512.80	0.932	0.941	0.991
	Case 3	7500	10	0.00742	0.82		527.10	0.958	0.964	0.994
			20	0.01141	0.79		479.86	0.872	0.945	0.923
			50	0.02118	0.65		422.20	0.768	0.900	0.852
	Case 4	10000	10	0.01100	0.81		468.65	0.852	0.947	0.900
			20	0.01638	0.74		443.20	0.806	0.922	0.874
			50	0.03175	0.58		422.20	0.768	0.855	0.898

Model	Collision cases	Velocity, v (mm/s)	Striker mass, m (ton)	$\delta_d = d/R$	$0.5P_{c_damage}$ (Mpa)	$\sigma_{xin,r}$ (Mpa)	$\sigma_{xd,r}$ (Mpa)	$R_{ux,r} = \sigma_{xd,r} / \sigma_{xin,r}$		X_m (Num./Eq. (7.12))
								Num. result	Eq.(7.12)	
RS-6	Case 1	2500	10	-		550.0	-	-	-	-
			20	-			-	-	-	-
			50	-			-	-	-	-
	Case 2	5000	10	-			-	-	-	-
			20	0.00645	2.32		509.00	0.925	0.969	0.955
			50	0.01239	1.74		453.20	0.824	0.941	0.876
	Case 3	7500	10	0.00742	2.04		507.60	0.923	0.964	0.957
			20	0.01141	1.98		489.13	0.889	0.945	0.941
			50	0.02118	1.63		421.00	0.765	0.900	0.850
	Case 4	10000	10	0.01100	2.03		479.54	0.872	0.947	0.921
			20	0.01638	1.84		441.60	0.803	0.922	0.871
			50	0.03175	1.45		419.60	0.763	0.855	0.893

Model	Collision cases	Velocity, v (mm/s)	Striker mass, m (ton)	$\delta_d = d/R$	$0.2P_{c_damage}$ (Mpa)	$\sigma_{xin,r}$ (Mpa)	$\sigma_{xd,r}$ (Mpa)	$R_{ux,r} = \sigma_{xd,r} / \sigma_{xin,r}$		X_m (Num./Eq. (7.12))
								Num. result	Eq.(7.12)	
RS-7	Case 1	2500	10	0.00894	-	330.0	-	-	-	-
			20	0.01250	-		-	-	-	-
			50	0.02910	-		-	-	-	-
	Case 2	5000	10	0.02170	0.31		301.62	0.914	0.898	1.018
			20	0.03702	0.29		289.39	0.877	0.833	1.053
			50	0.06259	0.26		261.08	0.791	0.734	1.078
	Case 3	7500	10	0.03825	0.28		278.25	0.843	0.828	1.019
			20	0.05882	0.22		289.89	0.878	0.747	1.175
			50	0.10424	0.21		214.22	0.649	0.597	1.088
	Case 4	10000	10	0.05254	0.25		235.38	0.713	0.771	0.925
			20	0.08363	0.23		217.62	0.659	0.661	0.998
			50	0.15374	0.19		175.79	0.533	0.467	1.140

Model	Collision cases	Velocity, v (mm/s)	Striker mass, m (ton)	$\delta_d = d/R$	$0.5P_{c_damage}$ (Mpa)	$\sigma_{xin,r}$ (Mpa)	$\sigma_{xd,r}$ (Mpa)	$R_{ux,r} = \sigma_{xd,r} / \sigma_{xin,r}$		X_m (Num./Eq. (7.12))
								Num. result	Eq.(7.12)	
RS-7	Case 1	2500	10	0.00894	-	330.0	-	-	-	-
			20	0.01250	-		-	-	-	-
			50	0.02910	-		-	-	-	-
	Case 2	5000	10	0.02170	0.77		297.95	0.903	0.898	1.005
			20	0.03702	0.73		281.26	0.852	0.833	1.024
			50	0.06259	0.64		267.26	0.810	0.734	1.104
	Case 3	7500	10	0.03825	0.70		272.39	0.825	0.828	0.997
			20	0.05882	0.54		286.13	0.867	0.747	1.160
			50	0.10424	0.53		214.26	0.649	0.597	1.088
	Case 4	10000	10	0.05254	0.63		219.98	0.667	0.771	0.865
			20	0.08363	0.58		215.82	0.654	0.661	0.989
			50	0.15374	0.48		135.29	0.410	0.467	0.878

Model	Collision cases	Velocity, v (mm/s)	Striker mass, m (ton)	$\delta_d = d/R$	$0.2P_{c_damage}$ (Mpa)	$\sigma_{xin,r}$ (Mpa)	$\sigma_{xd,r}$ (Mpa)	$R_{ux,r} = \sigma_{xd,r} / \sigma_{xin,r}$		X_m (Num./Eq. (7.12))
								Num. result	Eq.(7.12)	
RS-8	Case 1	2500	10	0.00602	-	412.0	-	-	-	-
			20	0.00904	-		-	-	-	
			50	0.01665	0.35		363.50	0.882	0.921	0.958
	Case 2	5000	10	0.01444	0.34		389.87	0.946	0.931	1.016
			20	0.02070	0.33		357.20	0.867	0.903	0.961
			50	0.03693	0.26		319.20	0.775	0.833	0.930
	Case 3	7500	10	0.02099	0.30		350.20	0.850	0.901	0.943
			20	0.03279	0.27		325.40	0.790	0.850	0.929
			50	0.06526	0.19		276.90	0.672	0.724	0.928
	Case 4	10000	10	0.02853	0.27		337.10	0.818	0.868	0.942
			20	0.04890	0.22		294.60	0.715	0.785	0.911
			50	0.09986	0.16		243.00	0.590	0.610	0.967

Model	Collision cases	Velocity, v (mm/s)	Striker mass, m (ton)	$\delta_d = d/R$	$0.5P_{c_damage}$ (Mpa)	$\sigma_{xin,r}$ (Mpa)	$\sigma_{xd,r}$ (Mpa)	$R_{ux,r} = \sigma_{xd,r} / \sigma_{xin,r}$		X_m (Num./Eq. (7.12))
								Num. result	Eq.(7.12)	
RS-8	Case 1	2500	10	0.00602	-	412.0	-	-	-	-
			20	0.00904	-		-	-	-	
			50	0.01665	0.88		376.70	0.914	0.921	0.993
	Case 2	5000	10	0.01444	0.85		382.56	0.929	0.931	0.997
			20	0.02070	0.82		364.00	0.883	0.903	0.979
			50	0.03693	0.64		313.60	0.761	0.833	0.914
	Case 3	7500	10	0.02099	0.75		356.70	0.866	0.901	0.961
			20	0.03279	0.68		329.20	0.799	0.850	0.940
			50	0.06526	0.49		272.80	0.662	0.724	0.915
	Case 4	10000	10	0.02853	0.67		342.30	0.831	0.868	0.957
			20	0.04890	0.55		300.60	0.730	0.785	0.929
			50	0.09986	0.40		247.40	0.600	0.610	0.984

Model	Collision cases	Velocity, v (mm/s)	Striker mass, m (ton)	$\delta_d = d/R$	$0.2P_{c_damage}$ (Mpa)	$\sigma_{xin,r}$ (Mpa)	$\sigma_{xd,r}$ (Mpa)	$R_{ux,r} = \sigma_{xd,r} / \sigma_{xin,r}$		X_m (Num./Eq. (7.12))
								Num. result	Eq.(7.12)	
RS-10	Case 1	2500	0.3	0.01191	-	215.0	-	-	-	-
			0.6	0.01756	-		-	-	-	-
			1.0	0.03288	-		-	-	-	-
	Case 2	5000	0.3	0.02553	0.26		172.69	0.803	0.881	0.911
			0.6	0.04627	0.25		164.70	0.766	0.795	0.963
			1.0	0.09229	0.18		151.28	0.704	0.633	1.111
	Case 3	7500	0.3	0.04721	0.25		171.04	0.796	0.792	1.005
			0.6	0.08351	0.19		152.30	0.708	0.661	1.071
			1.0	0.16900	0.12		103.16	0.480	0.433	1.108
	Case 4	10000	0.3	0.15178	0.08		117.41	0.546	0.472	1.158
			0.6	0.12699	0.15		115.97	0.539	0.533	1.011
			1.0	0.25565	0.41		71.23	0.331	0.282	1.174

Model	Collision cases	Velocity, v (mm/s)	Striker mass, m (ton)	$\delta_d = d/R$	$0.5P_{c_damage}$ (Mpa)	$\sigma_{xin,r}$ (Mpa)	$\sigma_{xd,r}$ (Mpa)	$R_{ux,r} = \sigma_{xd,r} / \sigma_{xin,r}$		X_m (Num./Eq. (7.12))
								Num. result	Eq.(7.12)	
RS-10	Case 1	2500	0.3	0.01191	-	215.0	-	-	-	-
			0.6	0.01756	-		-	-	-	-
			1.0	0.03288	-		-	-	-	-
	Case 2	5000	0.3	0.02553	0.64		189.90	0.883	0.881	1.002
			0.6	0.04627	0.62		165.29	0.769	0.795	0.967
			1.0	0.09229	0.45		151.28	0.704	0.633	1.111
	Case 3	7500	0.3	0.04721	0.62		177.89	0.827	0.792	1.045
			0.6	0.08351	0.49		156.32	0.727	0.661	1.099
			1.0	0.16900	0.29		95.89	0.446	0.433	1.030
	Case 4	10000	0.3	0.15178	0.21		113.27	0.527	0.472	1.117
			0.6	0.12699	0.37		92.36	0.430	0.533	0.805
			1.0	0.25565	1.03		63.19	0.294	0.282	1.042

Table F4.2 Comparison of the proposed formulation results with numerical results for residual strength of damaged stringer-stiffened cylinder under combined axial compression and radial pressure.

Model	Collision cases	Velocity, v (mm/s)	Striker mass, m (ton)	$\delta_d = d/R$	$0.2P_{c,damage}$ (Mpa)	$\sigma_{xin,r}$ (Mpa)	$\sigma_{xd,r}$ (Mpa)	$R_{ux,r} = \sigma_{xd,r} / \sigma_{xin,r}$		X_m (Num./Eq. (7.36))
								Num. result	Eq.(7.36)	
SS-1	Case 1	2500	10	-	-	270.0	-	-	-	-
			20	0.0175	0.202		271.98	1.007	0.988	1.020
			50	0.0371	0.207		266.91	0.989	0.974	1.015
			100	0.0595	0.208		261.95	0.970	0.959	1.012
	Case 2	5000	10	0.0304	0.200		268.61	0.995	0.979	1.017
			20	0.0505	0.211		263.91	0.977	0.965	1.013
			50	0.0880	0.219		256.39	0.950	0.939	1.011
			100	0.1295	0.197		247.48	0.917	0.912	1.005
	Case 3	7500	10	0.0540	0.217		263.24	0.975	0.962	1.013
			20	0.0823	0.221		257.56	0.954	0.943	1.011
			50	0.1376	0.190		246.25	0.912	0.907	1.006
			100	0.2058	0.133		234.89	0.870	0.864	1.007
	Case 4	10000	10	0.0763	0.224		258.81	0.959	0.947	1.012
			20	0.1133	0.211		251.74	0.932	0.923	1.011
			50	0.1903	0.176		237.22	0.879	0.873	1.006
			100	0.2919	0.121		224.58	0.832	0.813	1.024

Model	Collision cases	Velocity, v (mm/s)	Striker mass, m (ton)	$\delta_d = d/R$	$0.5P_{c,damage}$ (Mpa)	$\sigma_{xin,r}$ (Mpa)	$\sigma_{xd,r}$ (Mpa)	$R_{ux,r} = \sigma_{xd,r} / \sigma_{xin,r}$		X_m (Num./Eq. (7.36))
								Num. result	Eq.(7.36)	
SS-1	Case 1	2500	10	-	-	270.0	-	-	-	-
			20	0.0175	0.506		272.13	1.008	0.988	1.021
			50	0.0371	0.517		266.98	0.989	0.974	1.015
			100	0.0595	0.521		261.98	0.970	0.959	1.012
	Case 2	5000	10	0.0304	0.501		268.63	0.995	0.979	1.017
			20	0.0505	0.528		261.59	0.969	0.965	1.004
			50	0.0880	0.548		256.48	0.950	0.939	1.011
			100	0.1295	0.492		247.33	0.916	0.912	1.004
	Case 3	7500	10	0.0540	0.541		263.21	0.975	0.962	1.013
			20	0.0823	0.554		257.62	0.954	0.943	1.012
			50	0.1376	0.476		245.75	0.910	0.907	1.004
			100	0.2058	0.332		234.84	0.870	0.864	1.007
	Case 4	10000	10	0.0763	0.559		258.98	0.959	0.947	1.013
			20	0.1133	0.527		242.28	0.897	0.923	0.973
			50	0.1903	0.440		237.79	0.881	0.873	1.008
			100	0.2919	0.303		224.75	0.832	0.813	1.024

Model	Collision cases	Velocity, v (mm/s)	Striker mass, m (ton)	$\delta_d = d/R$	$0.2P_{c_damage}$ (Mpa)	$\sigma_{xin,r}$ (Mpa)	$\sigma_{xd,r}$ (Mpa)	$R_{ux,r} = \sigma_{xd,r} / \sigma_{xin,r}$		X_m (Num./Eq. (7.36))	
								Num. result	Eq.(7.36)		
SS-2	Case 1	2500	10	-	-	350.2	-	-	-	-	
			20	-	-		-	-	-	-	
			50	-	-		-	-	-	-	
			100	-	-		-	-	-	-	
	Case 2	5000	10	-	-		-	-	-	-	-
			20	-	-		-	-	-	-	
			50	-	-		-	-	-	-	
			100	0.00845	0.122		338.36	0.966	0.994	0.972	
	Case 3	7500	10	0.00331	0.122		342.42	0.978	0.998	0.980	
			20	0.00495	0.122		335.34	0.958	0.996	0.961	
			50	0.00940	0.123		333.37	0.952	0.993	0.958	
			100	0.01601	0.121		329.13	0.940	0.989	0.951	
	Case 4	10000	10	0.00490	0.125		340.64	0.973	0.997	0.976	
			20	0.00815	0.119		335.47	0.958	0.994	0.964	
			50	0.01490	0.115		330.99	0.945	0.989	0.955	
			100	0.02408	0.122		312.35	0.892	0.983	0.907	

Model	Collision cases	Velocity, v (mm/s)	Striker mass, m (ton)	$\delta_d = d/R$	$0.5P_{c, damage}$ (Mpa)	$\sigma_{xin,r}$ (Mpa)	$\sigma_{xd,r}$ (Mpa)	$R_{ux,r} = \sigma_{xd,r} / \sigma_{xin,r}$		X_m (Num./Eq. (7.36))	
								Num. result	Eq.(7.36)		
SS-2	Case 1	2500	10	-	-	350.2	-	-	-	-	
			20	-	-		-	-	-	-	
			50	-	-		-	-	-	-	
			100	-	-		-	-	-	-	
	Case 2	5000	10	-	-		-	-	-	-	-
			20	-	-		-	-	-	-	
			50	-	-		-	-	-	-	
			100	0.00845	0.305		318.98	0.911	0.994	0.916	
	Case 3	7500	10	0.00331	0.305		342.49	0.978	0.998	0.980	
			20	0.00495	0.305		339.75	0.970	0.996	0.974	
			50	0.00940	0.308		332.43	0.949	0.993	0.956	
			100	0.01601	0.303		329.46	0.941	0.989	0.952	
	Case 4	10000	10	0.00490	0.312		338.65	0.967	0.997	0.970	
			20	0.00815	0.298		335.39	0.958	0.994	0.963	
			50	0.01490	0.287		331.17	0.946	0.989	0.956	
			100	0.02408	0.305		330.85	0.945	0.983	0.961	

Model	Collision cases	Velocity, v (mm/s)	Striker mass, m (ton)	$\delta_d = d/R$	$0.2P_{c_damage}$ (Mpa)	$\sigma_{xin,r}$ (Mpa)	$\sigma_{xd,r}$ (Mpa)	$R_{ux,r} = \sigma_{xd,r} / \sigma_{xin,r}$		X_m (Num./Eq. (7.36))
								Num. result	Eq.(7.36)	
SS-3	Case 1	2500	10	-	-	350.0	-	-	-	-
			20	0.00611	0.157		354.21	1.012	0.996	1.016
			50	0.01356	0.157		346.31	0.989	0.990	0.999
			100	0.02144	0.161		344.32	0.984	0.985	0.999
	Case 2	5000	10	0.01103	0.155		346.93	0.991	0.992	0.999
			20	0.01818	0.158		345.23	0.986	0.987	0.999
			50	0.03242	0.162		339.78	0.971	0.977	0.993
			100	0.04790	0.159		332.99	0.951	0.967	0.984
	Case 3	7500	10	0.01932	0.161		345.07	0.986	0.986	1.000
			20	0.03013	0.162		340.94	0.974	0.979	0.995
			50	0.05058	0.157		331.87	0.948	0.965	0.983
			100	0.08482	0.142		321.37	0.918	0.941	0.975
	Case 4	10000	10	0.02777	0.163		341.95	0.977	0.980	0.996
			20	0.04176	0.163		336.03	0.960	0.971	0.989
			50	0.06773	0.147		324.84	0.928	0.953	0.974
			100	0.11794	0.110		312.74	0.894	0.920	0.972
	Case 5	1000	1000	0.02889	0.164		341.31	0.975	0.980	0.995
			3000	0.05327	0.156		330.37	0.944	0.963	0.980
			5000	0.06992	0.146		323.62	0.925	0.952	0.972

Model	Collision cases	Velocity, v (mm/s)	Striker mass, m (ton)	$\delta_d = d/R$	$0.5P_{c, damage}$ (Mpa)	$\sigma_{xin,r}$ (Mpa)	$\sigma_{xd,r}$ (Mpa)	$R_{ux,r} = \sigma_{xd,r} / \sigma_{xin,r}$		X_m (Num./Eq. (7.36))
								Num. result	Eq.(7.36)	
SS-3	Case 1	2500	10	-	-	350.0	-	-	-	-
			20	0.00611	0.392		347.17	0.992	0.996	0.996
			50	0.01356	0.392		342.32	0.978	0.990	0.988
			100	0.02144	0.404		344.32	0.984	0.985	0.999
	Case 2	5000	10	0.01103	0.387		339.92	0.971	0.992	0.979
			20	0.01818	0.394		335.17	0.958	0.987	0.970
			50	0.03242	0.404		339.06	0.969	0.977	0.991
			100	0.04790	0.396		333.05	0.952	0.967	0.985
	Case 3	7500	10	0.01932	0.403		345.03	0.986	0.986	0.999
			20	0.03013	0.404		340.95	0.974	0.979	0.995
			50	0.05058	0.392		331.99	0.949	0.965	0.983
			100	0.08482	0.354		322.62	0.922	0.941	0.979
	Case 4	10000	10	0.02777	0.407		341.98	0.977	0.980	0.997
			20	0.04176	0.407		336.00	0.960	0.971	0.989
			50	0.06773	0.368		324.89	0.928	0.953	0.974
			100	0.11794	0.274		311.91	0.891	0.920	0.969
	Case 5	1000	1000	0.02889	0.409		341.30	0.975	0.980	0.995
			3000	0.05327	0.390		330.49	0.944	0.963	0.981
			5000	0.06992	0.364		323.69	0.925	0.952	0.972

Model	Collision cases	Velocity, v (mm/s)	Striker mass, m (ton)	$\delta_d = d/R$	$0.2P_{c, damage}$ (Mpa)	$\sigma_{xin,r}$ (Mpa)	$\sigma_{xd,r}$ (Mpa)	$R_{ux,r} = \sigma_{xd,r} / \sigma_{xin,r}$		X_m (Num./Eq. (7.36))
								Num. result	Eq.(7.36)	
SS-4	Case 1	2500	10	-	-	268.9	-	-	-	-
			20	0.0121	0.075		246.18	0.915	0.991	0.923
			50	0.0195	0.079		245.92	0.914	0.986	0.927
			100	0.0360	0.077		229.98	0.855	0.975	0.877
	Case 2	5000	10	0.0183	0.077		247.82	0.922	0.987	0.934
			20	0.0271	0.082		233.43	0.868	0.981	0.885
			50	0.0561	0.077		239.98	0.892	0.961	0.929
			100	0.0824	0.072		223.60	0.831	0.943	0.882
	Case 3	7500	10	0.0319	0.077		232.06	0.863	0.978	0.883
			20	0.0519	0.073		237.37	0.883	0.964	0.916
			50	0.0866	0.058		220.93	0.821	0.940	0.874
			100	0.1350	0.045		208.68	0.776	0.908	0.854
	Case 4	10000	10	0.0479	0.077		234.74	0.873	0.967	0.903
			20	0.0701	0.073		229.51	0.853	0.951	0.897
			50	0.1239	0.058		211.25	0.786	0.916	0.858
			100	0.1868	0.045		192.69	0.717	0.876	0.818
	Case 5	1000	1000	0.0417	0.077		231.29	0.860	0.971	0.886
			3000	0.0997	0.069		228.56	0.850	0.932	0.912
			5000	0.1327	0.028		219.68	0.817	0.910	0.898
	Case 6	2000	1000	0.1146	0.084		224.60	0.835	0.922	0.906
			3000	0.2200	0.061		215.37	0.801	0.855	0.936
			5000	0.2914	0.051		210.09	0.781	0.813	0.961
	Case 7	3000	1000	0.1831	0.048		214.60	0.798	0.878	0.909
			3000	0.3725	0.047		189.36	0.704	0.767	0.918
			5000	0.4992	0.040		167.23	0.622	0.701	0.887

Model	Collision cases	Velocity, v (mm/s)	Striker mass, m (ton)	$\delta_d = d/R$	$0.5P_{c,damage}$ (Mpa)	$\sigma_{xin,r}$ (Mpa)	$\sigma_{xd,r}$ (Mpa)	$R_{ux,r} = \sigma_{xd,r} / \sigma_{xin,r}$		X_m (Num./Eq. (7.36))
								Num. result	Eq.(7.36)	
SS-4	Case 1	2500	10	-	-	268.9	-	-	-	-
			20	0.0121	0.189		245.77	0.914	0.991	0.922
			50	0.0195	0.197		244.83	0.910	0.986	0.923
			100	0.0360	0.193		229.42	0.853	0.975	0.875
	Case 2	5000	10	0.0183	0.192		248.10	0.923	0.987	0.935
			20	0.0271	0.205		233.81	0.869	0.981	0.886
			50	0.0561	0.194		239.55	0.891	0.961	0.927
			100	0.0824	0.180		223.89	0.833	0.943	0.883
	Case 3	7500	10	0.0319	0.192		232.06	0.863	0.978	0.883
			20	0.0519	0.181		237.99	0.885	0.964	0.918
			50	0.0866	0.146		221.46	0.823	0.940	0.876
			100	0.1350	0.112		206.10	0.766	0.908	0.844
	Case 4	10000	10	0.0479	0.192		234.82	0.873	0.967	0.903
			20	0.0701	0.181		229.26	0.852	0.951	0.896
			50	0.1239	0.146		211.20	0.785	0.916	0.858
			100	0.1868	0.112		191.54	0.712	0.876	0.813
	Case 5	1000	1000	0.0417	0.191		219.73	0.817	0.971	0.842
			3000	0.0997	0.173		217.13	0.807	0.932	0.867
			5000	0.1327	0.070		208.70	0.776	0.910	0.853
	Case 6	2000	1000	0.1146	0.211		213.37	0.793	0.922	0.861
			3000	0.2200	0.152		204.60	0.761	0.855	0.890
			5000	0.2914	0.128		199.59	0.742	0.813	0.913
	Case 7	3000	1000	0.1831	0.121		203.87	0.758	0.878	0.863
			3000	0.3725	0.118		179.89	0.669	0.767	0.872
			5000	0.4992	0.100		158.87	0.591	0.701	0.842

Model	Collision cases	Velocity, v (mm/s)	Striker mass, m (ton)	$\delta_d = d/R$	$0.2P_{c_damage}$ (Mpa)	$\sigma_{xin,r}$ (Mpa)	$\sigma_{xd,r}$ (Mpa)	$R_{ux,r} = \sigma_{xd,r} / \sigma_{xin,r}$		X_m (Num./Eq. (7.36))
								Num. result	Eq.(7.36)	
SS-5	Case 1	2500	10	-	-	495.0	-	-	-	-
			20	-	-		-	-	-	-
			50	0.0191	0.246		462.31	0.934	0.986	0.947
			100	0.0304	0.251		438.86	0.887	0.979	0.906
	Case 2	5000	10	0.0148	0.246		458.37	0.926	0.990	0.936
			20	0.0278	0.213		444.74	0.898	0.980	0.916
			50	0.0531	0.174		420.82	0.850	0.963	0.883
			100	0.0868	0.174		441.35	0.892	0.940	0.948
	Case 3	7500	10	0.0299	0.214		438.72	0.886	0.979	0.905
			20	0.0525	0.180		418.18	0.845	0.963	0.877
			50	0.0920	0.180		439.54	0.888	0.937	0.948
			100	0.1372	0.167		413.63	0.836	0.907	0.921
	Case 4	10000	10	0.0477	0.175		444.66	0.898	0.967	0.929
			20	0.0748	0.173		420.02	0.848	0.948	0.895
			50	0.1261	0.170		409.61	0.827	0.914	0.905
			100	0.1948	0.158		395.35	0.799	0.871	0.917

Model	Collision cases	Velocity, v (mm/s)	Striker mass, m (ton)	$\delta_d = d/R$	$0.5P_{c_damage}$ (Mpa)	$\sigma_{xin,r}$ (Mpa)	$\sigma_{xd,r}$ (Mpa)	$R_{ux,r} = \sigma_{xd,r} / \sigma_{xin,r}$		X_m (Num./Eq. (7.36))
								Num. result	Eq.(7.36)	
SS-5	Case 1	2500	10	-	-	495.0	-	-	-	-
			20	-	-		-	-	-	-
			50	0.0191	0.615		455.30	0.920	0.986	0.932
			100	0.0304	0.627		435.56	0.880	0.979	0.899
	Case 2	5000	10	0.0148	0.615		458.24	0.926	0.990	0.935
			20	0.0278	0.532		444.13	0.897	0.980	0.915
			50	0.0531	0.435		420.47	0.849	0.963	0.882
			100	0.0868	0.434		441.06	0.891	0.940	0.948
	Case 3	7500	10	0.0299	0.535		442.65	0.894	0.979	0.913
			20	0.0525	0.449		430.92	0.870	0.963	0.904
			50	0.0920	0.451		438.59	0.886	0.937	0.946
			100	0.1372	0.417		416.47	0.841	0.907	0.927
	Case 4	10000	10	0.0477	0.438		418.40	0.845	0.967	0.874
			20	0.0748	0.433		444.25	0.897	0.948	0.946
			50	0.1261	0.425		423.04	0.855	0.914	0.935
			100	0.1948	0.395		389.33	0.786	0.871	0.903

Model	Collision cases	Velocity, v (mm/s)	Striker mass, m (ton)	$\delta_d = d/R$	$0.2P_{c_damage}$ (Mpa)	$\sigma_{xin,r}$ (Mpa)	$\sigma_{xd,r}$ (Mpa)	$R_{ux,r} = \sigma_{xd,r} / \sigma_{xin,r}$		X_m (Num./Eq. (7.36))	
								Num. result	Eq.(7.36)		
SS-6	Case 1	2500	10	-	-	352.4	-	-	-	-	
			20	-	-		-	-	-	-	
			50	-	-		-	-	-	-	
			100	-	-		-	-	-	-	
	Case 2	5000	10	-	-		-	-	-	-	-
			20	0.0116	0.204		348.01	0.988	0.992	0.996	
			50	0.0215	0.166		346.68	0.984	0.985	0.999	
			100	0.0328	0.164		343.83	0.976	0.977	0.999	
	Case 3	7500	10	0.0123	0.207		347.18	0.985	0.991	0.994	
			20	0.0200	0.200		346.98	0.985	0.986	0.999	
			50	0.0347	0.165		342.23	0.971	0.976	0.995	
			100	0.0525	1.612		338.19	0.960	0.963	0.996	
	Case 4	10000	10	0.0183	0.205		347.17	0.985	0.987	0.998	
			20	0.0282	0.166		345.18	0.980	0.980	0.999	
			50	0.0484	0.168		340.79	0.967	0.966	1.001	
			100	0.0778	0.165		335.25	0.951	0.946	1.005	
	Case 5	1000	1000	0.0197	1.674		345.87	0.981	0.986	0.995	
			3000	0.0372	0.199		342.59	0.972	0.974	0.998	
			5000	0.0499	0.166		340.27	0.966	0.965	1.000	
	Case 6	2000	1000	0.0434	0.168		341.39	0.969	0.970	0.999	
			3000	0.0946	0.174		333.28	0.946	0.935	1.012	
			5000	0.1243	0.165		327.58	0.930	0.915	1.015	
	Case 7	3000	1000	0.0700	0.166		336.01	0.953	0.951	1.002	
			3000	0.1684	0.146		333.21	0.946	0.887	1.066	
			5000	0.2243	0.145		315.29	0.895	0.853	1.049	

Model	Collision cases	Velocity, v (mm/s)	Striker mass, m (ton)	$\delta_d = d/R$	$0.5P_{c, damage}$ (Mpa)	$\sigma_{xin,r}$ (Mpa)	$\sigma_{xd,r}$ (Mpa)	$R_{ux,r} = \sigma_{xd,r} / \sigma_{xin,r}$		X_m (Num./Eq. (7.36))	
								Num. result	Eq.(7.36)		
SS-6	Case 1	2500	10	-	-	352.4	-	-	-	-	
			20	-	-		-	-	-	-	
			50	-	-		-	-	-	-	
			100	-	-		-	-	-	-	
	Case 2	5000	10	-	-		-	-	-	-	-
			20	0.0116	0.510		348.00	0.988	0.992	0.996	
			50	0.0215	0.414		327.15	0.928	0.985	0.943	
			100	0.0328	0.411		314.97	0.894	0.977	0.915	
	Case 3	7500	10	0.0123	0.519		347.86	0.987	0.991	0.996	
			20	0.0200	0.499		343.46	0.975	0.986	0.989	
			50	0.0347	0.413		343.46	0.975	0.976	0.999	
			100	0.0525	4.030		336.25	0.954	0.963	0.990	
	Case 4	10000	10	0.0183	0.513		347.16	0.985	0.987	0.998	
			20	0.0282	0.414		345.23	0.980	0.980	1.000	
			50	0.0484	0.420		340.83	0.967	0.966	1.001	
			100	0.0778	0.412		335.34	0.952	0.946	1.006	
	Case 5	1000	1000	0.0197	4.185		328.69	0.933	0.986	0.946	
			3000	0.0372	0.498		342.43	0.972	0.974	0.998	
			5000	0.0499	0.414		319.72	0.907	0.965	0.940	
	Case 6	2000	1000	0.0434	0.421		341.02	0.968	0.970	0.998	
			3000	0.0946	0.435		333.30	0.946	0.935	1.012	
			5000	0.1243	0.413		272.94	0.775	0.915	0.846	
	Case 7	3000	1000	0.0700	0.415		279.14	0.792	0.951	0.833	
			3000	0.1684	0.365		268.59	0.762	0.887	0.859	
			5000	0.2243	0.362		259.78	0.737	0.853	0.865	